

**A general approach to search for supersymmetry
at the LHC by combining signal enhanced
kinematic regions using the ATLAS detector**

Inauguraldissertation

der Philosophisch-naturwissenschaftlichen Fakultät
der Universität Bern

vorgelegt von

Basil Schneider
von Obersiggenthal



Leiter der Arbeit:

Prof. Dr. Antonio Ereditato

Albert Einstein Center for Fundamental Physics
Laboratorium für Hochenergiephysik
Physikalisches Institut

**A general approach to search for supersymmetry
at the LHC by combining signal enhanced
kinematic regions using the ATLAS detector**

Inauguraldissertation
der Philosophisch-naturwissenschaftlichen Fakultät
der Universität Bern

vorgelegt von

Basil Schneider

von Obersiggenthal

Leiter der Arbeit:

Prof. Dr. Antonio Ereditato

Albert Einstein Center for Fundamental Physics
Laboratorium für Hochenergiephysik
Physikalisches Institut

Von der Philosophisch-naturwissenschaftlichen Fakultät angenommen.

Bern, 17. Juni 2014

Der Dekan
Prof. Dr. Silvio Decurtins

*To my mother.
To Jasna.*

Publications

I am co-author of 156 papers published by the ATLAS collaboration. For a complete list, see <http://inspirehep.net/author/profile/B.Schneider.1>. I provided substantial contributions for the following publications:

- ATLAS Collaboration, *Search for supersymmetry in events with four or more leptons in $\sqrt{s} = 8$ TeV pp collisions with the ATLAS detector*, arXiv:1405.5086 [hep-ex].
- ATLAS Collaboration, *Search for direct production of charginos and neutralinos in events with three leptons and missing transverse momentum in $\sqrt{s} = 8$ TeV pp collisions with the ATLAS detector*, JHEP **1404** (2014) 169, 10.1007/JHEP04(2014)169, arXiv:1402.7029 [hep-ex].
- B. Schneider on behalf of the ATLAS collaboration, *Search for direct production of charginos and neutralinos in events with three leptons and missing transverse momentum in 21 fb^{-1} of pp collisions at $\sqrt{s} = 8$ TeV with the ATLAS detector*, ATL-PHYS-PROC-2013-145, (Poster: ATL-PHYS-SLIDE-2013-350).
- ATLAS Collaboration, *Search for supersymmetry in events with four or more leptons in 21 fb^{-1} of pp collisions at $\sqrt{s} = 8$ TeV with the ATLAS detector*, ATLAS-CONF-2013-036.
- ATLAS Collaboration, *Search for direct production of charginos and neutralinos in events with three leptons and missing transverse momentum in 21 fb^{-1} of pp collisions at $\sqrt{s} = 8$ TeV with the ATLAS detector*, ATLAS-CONF-2013-035.
- ATLAS Collaboration, *Search for direct production of charginos and neutralinos in events with three leptons and missing transverse momentum in 13.0 fb^{-1} of pp collisions at $\sqrt{s} = 8$ TeV with the ATLAS detector*, ATLAS-CONF-2012-154.
- ATLAS Collaboration, *Search for Supersymmetry in events with four or more leptons in 13 fb^{-1} pp collisions at $\sqrt{s} = 8$ TeV with the ATLAS detector*, ATLAS-CONF-2012-153.
- ATLAS Collaboration, *Search for direct production of charginos and neutralinos in events with three leptons and missing transverse momentum in $\sqrt{s} = 7$ TeV pp collisions with the ATLAS detector*, Phys.Lett. **B718** (2013) 841-859, arXiv:1208.3144 [hep-ex].
- L. Ancu, B. Schneider et al. (15 authors), *The ATLAS IBL BOC Demonstrator*, ATL-INDET-PROC-2011-038.
- B. Schneider on behalf of the ATLAS collaboration, *SUSY Searches at ATLAS in Multilepton Final States with Jets and Missing Transverse Energy*, ATL-PHYS-PROC-2011-201, (Poster: ATL-PHYS-SLIDE-2011-423).

For the following internal notes I provided substantial contributions and am listed as author:

- *Search for supersymmetry in events with four or more leptons in $\sqrt{s} = 8$ TeV pp collisions with the ATLAS detector,*
ATL-COM-PHYS-2013-1621.
- *Search for supersymmetry in events with three leptons and missing transverse momentum in 21 fb^{-1} pp collisions at $\sqrt{s} = 8$ TeV with the ATLAS detector,*
ATL-PHYS-INT-2013-021.
- *Search for supersymmetry in events with three leptons and missing transverse momentum in 20.3 fb^{-1} pp collisions at $\sqrt{s} = 8$ TeV with the ATLAS detector,*
ATL-COM-PHYS-2013-888.
- *Search for Supersymmetry in events with four or more leptons in 20.7 fb^{-1} pp collisions at $\sqrt{s} = 8$ TeV with the ATLAS detector,*
ATL-COM-PHYS-2012-1819.
- *Search for Supersymmetry in events with four or more leptons in 13 fb^{-1} pp collisions at $\sqrt{s} = 8$ TeV with the ATLAS detector,*
ATL-PHYS-INT-2012-096.
- *Search for supersymmetry in events with three leptons and missing transverse momentum in 13 fb^{-1} pp collisions at $\sqrt{s} = 8$ TeV with the ATLAS detector,*
ATL-PHYS-INT-2012-095.
- *SUSY Searches in the Final States with Three Leptons and Missing Transverse Momentum at ATLAS,*
ATL-PHYS-INT-2012-059.

Personal contributions

The ATLAS experiment is a large international collaboration. Publications are always the work of a large number of people. Here I summarize the relevant contributions that I made in the framework of the collaboration. Most of these items are further explained in this thesis. The thesis is the result of my own work. When the work made by others is used, this is explicitly referenced.

Hardware

- I tested optical receivers to be used for the readout of the insertable b -layer for reliability, frequency and input sensitivity. I defined the tests and performed them. The experiments and its results are described in Chapter 3.
- To document the tests of the optical receivers, I set up a Twiki site [1] and presented the results on different insertable b -layer general meetings.
- I built up the hardware activities at the University of Bern. With my efforts, the lab became known throughout the insertable b -layer community. The University of Bern is still active in this field and considered as expert in terms of optical receivers, thanks to my contributions.

Analysis

- The binned signal region used in a supersymmetry search published in JHEP [2] is completely my idea and my work. It is the main topic of this thesis and explained in detail in Chapter 5. It has also been combined with another search for SUSY in a final state with two leptons [3] and was presented in the CERN courier journal [4].
- I used my expertise and gave guidance for the optimization of the signal regions with at least one tau in [2].
- I carried out the statistical interpretation for various publications, all searching for supersymmetry in either three lepton or four lepton final states [2, 5, 6, 7, 8, 9, 10]. The statistical interpretation is subject of the Chapters 8 and 9.
- For the statistical interpretation, I provided p -values, visible cross-sections, exclusion limit contours and upper limits on model cross-sections. The results are in the corresponding publications, in Chapter 9 I discuss the results from [2].
- I was responsible for the calculations to derive limits with asymptotic formulae or with Monte Carlo pseudo-experiments. I was also comparing results of these two methods to make a decision if the asymptotic formulae are good enough for our purpose. For the case of the latest paper [2], the situation and findings are outlined in Section 9.5.
- For the latest paper [2] alone, I generated more than $2.5 \cdot 10^8$ Monte Carlo pseudo-experiments. This was done on a batch-system at the University of Bern with about 1500 cores. I was solely responsible for this undertaking using scripts that I partially developed.
- To speed up the process of determining the upper limits on the model cross-sections with Monte Carlo pseudo-experiments, I implemented a faster and more precise

method than the one currently used as standard. This is explained in more detail in Section 9.3.

- To validate the results from the statistical machinery I set up and conducted many tests, e.g. how to compare the results from a multi-region fit with different single-region fits, the method is outlined in Section 5.5.
- For the statistical interpretation I created a RootCore package [11] for analyzers to store their relevant events and to have a standardized framework to carry out the statistical interpretation. This package is used in the electroweak supersymmetry search groups with final states of two light leptons, two taus, three and four leptons.
- I collected a package of scripts [12] of which I have written most of them myself, to carry out the statistical interpretation with the aforementioned RootCore package. These scripts rely on HistFitter [13]. They are used in the electroweak supersymmetry search groups with final states of two light leptons, three leptons and four leptons.
- I made the final exclusion limit contour plots for the supersymmetry searches with a final state of three leptons [2, 6, 8].
- I was part of a small team setting up a RootCore package called “Common Code”, a central framework to do the cutflow in different electroweak supersymmetry analyses.
- I set up a framework for a simultaneous fit method to determine the most important background, WZ , in a supersymmetry search with three leptons in the final state. This method was applied in [5, 6].
- In [2], I provided most of the figures.
- I presented two analyses with three leptons in the final state [2, 8] on a SUSY-approval.
- I was selected to present posters on the supersymmetry searches in a final state with three leptons at the PLHC conference 2011 in Perugia [14] and at the 1st LHC Physics conference 2013 in Barcelona [15].

Abstract

The Standard Model of particle physics is a very successful theory, but it cannot describe e.g. gravity or explain the hierarchy problem. Supersymmetry is a proposed extension to the Standard Model that would solve some of its shortcomings by introducing a relation between fermions and bosons through the existence of a supersymmetric partner to every particle in the Standard Model. Since it is a broken symmetry, supersymmetric particles are heavier than their Standard Model counterparts. No supersymmetric particle has been observed to date.

The ATLAS experiment at the Large Hadron Collider is a multi-purpose detector to measure parameters in the Standard Model and conduct searches for new particles. Searching for supersymmetric particles is one of the main goals of the experiment. In 2012, 20.3 fb^{-1} of data at a centre-of-mass energy of $\sqrt{s} = 8 \text{ TeV}$ was collected by ATLAS.

In this thesis, I analyzed the ATLAS data and developed a novel statistical approach that bins a signal enhanced region in phase space into many sub-regions. In a later step, these regions are statistically combined to enhance the sensitivity to a supersymmetric signal. The use of modern likelihood techniques allows to apply my method in a consistent and general way to supersymmetry searches. It can also be applied to other searches. Since no excess in data is observed, I set limits on masses of the supersymmetric particles. The results are compared with another search, which interpreted its results in the same models. My method led to an observed improvement of the limit on the supersymmetric particle masses at the 95 % confidence level of up to 100 GeV, only by only improving the search method, without the need of additional data.

I also tested optical receiver components which are built into the readout chain of a new detector subsystem. The tests carried out are also explained in this thesis.

Contents

Introduction	1
1 Theory	5
1.1 The Standard Model	5
1.2 Supersymmetry	6
2 The ATLAS experiment at the Large Hadron Collider	9
2.1 The Large Hadron Collider	9
2.2 The ATLAS detector	12
2.3 Reconstruction	17
2.4 Trigger and data acquisition	19
3 IBL	21
3.1 Rx requirements	22
3.2 Experimental setup	24
3.3 Low Frequency tests	25
3.4 Input sensitivity	25
4 Search for electroweakly produced supersymmetry	31
4.1 Motivation	31
4.2 SUSY models	31
4.3 Irreducible background	36
4.4 Reducible Background	41
4.5 Preselection	45
4.6 Object definition	46
4.7 Matrix Method	49
5 Binning the signal region	53
5.1 Signal grid optimization	53
5.2 Basic selection	56
5.3 Discriminating variables	56
5.4 Binning approach	57
5.5 Signal region optimization	59
5.6 The $3\ell Z$ veto	64
5.7 Signal region breakdown	72
5.8 Other signal regions	76
5.9 Systematic uncertainties	76
5.10 Acceptance & Efficiency	80
6 Validation of background modeling	89
6.1 Validation regions	89
6.2 Signal contamination	102
7 Events in the signal region	103

8 Statistical Test	107
8.1 p -values	107
8.2 The likelihood function	109
8.3 Test statistic	110
8.4 CL_s	111
8.5 Sampling distributions	113
8.6 Expected values and the Asimov dataset	115
9 Statistical Interpretation	119
9.1 Discovery p -value	119
9.2 Exclusion limits	119
9.3 Upper limits on the model cross-sections	142
9.4 Fit results	150
9.5 Asymptotic limits vs. pseudo-experiments	153
Conclusions	157
Acknowledgements	163
Appendix A Signal region event yields and sensitivities	165
Appendix B Systematic uncertainties	177
Appendix C Distributions in VR0τb-binned	189
Appendix D Distributions in binned signal region	209
Appendix E CL_s per bin	229
Appendix F Upper limit on model cross-section scans in μ	243
List of Tables	260
List of Figures	263
References	273

Introduction

The studies presented in this thesis were performed at the ATLAS experiment at the Large Hadron Collider (LHC) at CERN in Geneva. The LHC reaches the highest energy collisions ever achieved with a particle accelerator, allowing to extend human knowledge in fundamental particle physics. ATLAS is a multi-purpose detector recording LHC collisions. In 2012, the LHC delivered a dataset to the ATLAS experiment corresponding to 20.3 fb^{-1} of proton-proton collision events at a centre-of-mass energy of 8 TeV. Together with the 5 fb^{-1} at 7 TeV, this concludes run 1. During 2013 and 2014, the LHC is being upgraded to achieve centre-of-mass collisions up to 14 TeV. In 2015 the LHC will resume the physics program at a planned centre-of-mass energy of 13 TeV.

The discovery of the Higgs boson is the highlight of the searches conducted with the data in run 1. All searches for a supersymmetric signal are in good agreement with the Standard Model and stringent limits on the masses of different supersymmetric particles are set. Although the parameter space of supersymmetry has been narrowed, there is still plenty of room for a supersymmetric signal that could solve e.g. the hierarchy problem and provide an excellent dark matter candidate.

Discovering supersymmetry is one of the main goals of the LHC. Searches are conducted in various kinematic signal enhanced regions in phase space by looking for an excess of events in data. The main topic of my thesis is to generalize this approach by not just using one such signal region, but by splitting it into many orthogonal regions and combining them statistically. By splitting the signal region into many subregions, more information about data events in the phase space can be obtained, leading to sensitivity in many diverse supersymmetric scenarios and more stringent limits, compared to the standard approach.

I will give here a short overview of the Standard Model and illustrate the most important motivations for supersymmetric searches and an improved statistical method to optimize searches for it. The Standard Model is the theory describing elementary particles and their interactions. Particles that make up the known matter around us are called fermions, which are further divided into leptons and quarks, both are arranged in three different generations. In the language of the Standard Model - Quantum Field Theory - the interaction of these matter particles happens via an exchange of other particles, these force carrying particles are called bosons. All particles of the Standard Model have been observed, the latest being the Higgs boson, which was discovered in 2012 simultaneously by the ATLAS experiment and CMS, the other multi-purpose detector situated at the LHC. I am co-author of the ATLAS publication [16] in which the discovery of the Higgs boson was announced.

The Standard Model has proven to be very successful, withstanding countless tests and being confirmed at ever higher accuracies. Nonetheless, we know that the Standard Model is not complete, since many open questions remain that cannot be answered within the framework of the Standard Model itself. The most obvious of these open issues is gravity, which is not part of the Standard Model. A widely accepted quantized theory of gravity does not even exist.

Another unresolved issue is the hierarchy problem of the Higgs mass. Since the Higgs couples to the mass of every particle, it receives itself radiative corrections to its mass. These corrections add up to a very high Higgs mass, much larger than the one observed at roughly 125 GeV. The small Higgs mass can be addressed by cancellations of quantum corrections, but it is not clear how they occur. Either there is a delicate fine-tuning of these very large quantum corrections of the order of the Planck mass of 10^{19} GeV, that lead to a cancellation of these large terms and to a Higgs mass of about 10^2 GeV or there

is a framework in which these cancellations happen naturally. One such framework is supersymmetry (SUSY). SUSY protects the small Higgs mass from quantum corrections by proposing a bosonic superpartner to every fermion in the Standard Model and a fermionic superpartner to every boson in the Standard Model. All quantum numbers of these superpartners should be equal to the ones of their Standard Model partners, except for the spin, which differs by $1/2 \hbar$. For the rest of the thesis I work in natural units and set $\hbar = c = 1$.

The question remains, why we have observed all Standard Model particles, but none of the SUSY partners yet. The explanation is that they do not have the same mass, i.e. SUSY is a broken symmetry. A SUSY symmetry breaking mechanism results in higher masses for the SUSY particles than for their Standard Model equivalents. Different breaking mechanisms are proposed.

SUSY can also explain other shortcomings of the Standard Model. Careful observation of the dynamics in our Universe led to the conclusion that ordinary matter can only make up around 4 % of the energy matter content of the Universe. The predominant matter in our Universe is believed to be made out of particles we don't know, called dark matter. If the lightest SUSY particle is stable, it provides an excellent dark matter candidate.

Finding SUSY is thus one of the major goals of the physics program at the LHC, but so far no SUSY has been observed. Instead, the Standard Model was confirmed at ever higher accuracies, including the discovery of the Higgs boson. Since SUSY predicts a large amount of so far undetected particles and has many parameters with unpredicted values related to the symmetry breaking mechanism, the parameter space is huge and a SUSY search compulsorily has to make many assumptions. Negative search results can only exclude a small part of the parameter space.

A rather clean signature to look for SUSY is a final state with exactly three leptons, since in this final state there is hardly any background coming from strong interactions, a predominant background present at a hadron collider. I worked on finding SUSY in this final state, where I carried out the statistical interpretation of many searches and personally developed a general approach to search for a SUSY signal by combining many signal enhanced kinematic regions and optimizing them for maximum sensitivity. Optimizing this region means finding a portion of the parameter space, where a SUSY signal can stand out from the otherwise overwhelming Standard Model background, given a SUSY signal of the hypothesized form exists. By subdividing the signal enhanced region into many subregions, more information about the observations in the parameter space is gathered and the sensitivity to different SUSY models is substantially enhanced and broadened. This process is subsequently called *binning* the signal region. With my method I also introduce more robust statistical methods. My results will show a strong improvement over previous results, by only applying a more subtle search technique, without any additional data. This is published in a paper on arXiv and JHEP.

The data I analyzed in this thesis was collected by the ATLAS experiment. The ATLAS detector is the largest detector at the LHC, a multi-purpose detector to measure and search for many physics objects. In 2013 and 2014, the LHC is not delivering collisions, giving the accelerator but also the detectors the chance to upgrade their instruments. During this shutdown, ATLAS plans to upgrade the inner detector with an additional fourth layer, the insertable *b*-layer (IBL), to act as replacement for failing detector parts and allow for greater vertexing precision in the physics run to come. The IBL also introduces a new readout technology. In particular, new optical readout components will be used. Commercial products of these readout components exist, but they needed to be tested for reliability, low frequency and input sensitivity behaviour. I will describe these tests that I carried out, proving that two of the three suppliers tested meet our requirements and are

matching our needs. These components are built into the readout chain of the detector during the writing of this thesis.

My thesis is structured as follows: Chapter 1 gives a very brief introduction into the Standard Model and SUSY, only the key points important to my work are introduced with no claim to be complete. The ATLAS detector is discussed in Chapter 2. It is a vast subject, but only a brief overview is given here. In Chapter 3 I discuss the IBL in more detail, introducing the readout chain and explain the experiments carried out to test the optical receivers. The following chapters address my work in analyzing the LHC data to search for a SUSY signal. Chapter 4 gives an overview of the analysis. My aforementioned contribution, the binned region to search for a SUSY signal, is presented in great detail in Chapter 5. Before looking at LHC data in my binned signal enhanced region, the background modeling was tested in dedicated validation regions. This is subject of Chapter 6. Chapter 7 then compares the results of the background expectation in my region with the observations made in the LHC data. A general overview of the statistical interpretation of results in high energy physics is given in Chapter 8 and the usage of these methods to extract results on ATLAS data is shown in Chapter 9. A concluding statement is given at the end to wrap up the thesis.

1 Theory

The theory of the Standard Model is a vast subject. I will only introduce the particles and interactions on a sketchy level. For more details, see the many textbooks that have been written about this subject. I describe some of the shortcomings of the Standard Model and explain why Supersymmetry would solve these issues. For the part about Supersymmetry, I mainly follow [17, 18].

1.1 The Standard Model

The Standard Model of particle physics is one of the best experimentally tested theories of mankind. It describes the known elementary particles and its interactions with the exception of gravity. For our purpose this is not an issue, since gravitational interactions of particles are so weak. Omitting this force does not alter the predictions of the Standard Model. But it's already clear at this stage that the Standard Model cannot be the final theory of particle interactions since it is not complete.

The particles of the Standard Model are divided into fermions and bosons. Fermions are particles that make up all matter we know. Their intrinsic angular momentum, i.e. spin is $1/2$ and they are divided into quarks and leptons. The quarks are called up, down, strange, charm, bottom and top quark. The up, charm and top quark carry an electric charge of $2/3 e$, where e is the elementary charge and the down, strange and bottom quark carry $-1/3 e$. Due to these symmetries, the quarks are classified into three different families, each with an up-type quark and a down-type quark,

$$\begin{pmatrix} u \\ d \end{pmatrix}, \begin{pmatrix} c \\ s \end{pmatrix}, \begin{pmatrix} t \\ b \end{pmatrix}. \quad (1)$$

In nature we do not observe free quarks but only compound objects like protons, neutrons or pions. These compound objects are called hadrons. Quark-antiquark pairs make up mesons, while three quarks make up baryons. The fact that there are no free quarks observed in nature is called confinement. The strong charge is called color charge, it can take on the values red, green or blue or one of its anticolor. Due to confinement, only colorless singlet states can freely propagate. Thus, every quark can pair up with another quark carrying its anti color charge to become a colorless singlet state, a meson. Another possibility is three quarks with three different (anti) colors that combine to become a colorless singlet state called baryon.

The leptons have a similar structure: electrons, muons and taus are the charged leptons with an electric charge of $-1 e$. The electrically neutral leptons are called neutrinos, since they only interact weakly. They are called electron neutrino, muon neutrino and tau neutrino. Also the leptons can be classified into three families, each with a charged lepton and a neutrino,

$$\begin{pmatrix} e \\ \nu_e \end{pmatrix}, \begin{pmatrix} \mu \\ \nu_\mu \end{pmatrix}, \begin{pmatrix} \tau \\ \nu_\tau \end{pmatrix}. \quad (2)$$

None of the leptons carry color charge.

When fermions interact with each other, e.g. in a scattering experiment, they do so by exchanging other particles, that are called bosons. Depending which boson is exchanged, a different type of interaction occurs. The exchange of gluons is characteristic for the strong interaction. Gluons carry no electric charge, but always a color and an anticolor. They couple to the color charges, that's why leptons do not feel the strong interaction. Since only colorless singlet state particles can freely propagate, the force can not be carried over long distances and therefore is only very short-ranged.

Photons are exchanged in electromagnetic interactions, they couple to the electric charge. They don't carry color charge nor electric charge. Since the photon mass is zero and they do not couple to each other, the interaction is long-ranged.

Finally, in a weak interaction process either a W^+ , a W^- or a Z boson is exchanged. The sign of the W indicate their electric charge, the Z boson is electrically neutral. These bosons couple to a universal weak charge. Since W and Z bosons are heavy, the weak interaction is limited to a very short range. All the gauge bosons have spin 1.

In the electroweak unification, the W boson is a triplet of the weak isospin from the $SU(2)$ gauge group. The singlet state from the weak hypercharge group $U(1)$ is called B_0 boson. As outlined above, we neither observe W_0 nor B_0 in nature, the W_0 cannot be identified with the Z , because of the mass difference. Instead, the spontaneous symmetry breaking in the electroweak sector caused by the Higgs mechanism produces the observable states Z and γ . The mixing is defined by

$$\begin{pmatrix} \gamma \\ Z \end{pmatrix} = \begin{pmatrix} \cos \theta_W & \sin \theta_W \\ -\sin \theta_W & \cos \theta_W \end{pmatrix} \begin{pmatrix} B_0 \\ W_0 \end{pmatrix}, \quad (3)$$

where θ_W is the Weinberg angle whose value needs to be measured in experiment. The mass of the Z is then related to the mass of the W by

$$m_Z = \frac{m_W}{\cos \theta_W}. \quad (4)$$

The interactions have different conservation laws which can be attributed to the properties of the exchanged bosons. For example, since neither photons nor gluons carry electric charge, the electric charge is conserved in these interactions, not necessarily in weak interactions, though, since the W boson carries electric charge.

There is only one particle missing to complete the Standard Model, this is the Higgs boson, which was discovered in 2012. It is responsible for giving mass to the otherwise massless vector bosons via the Higgs mechanism, a spontaneous symmetry breaking of the underlying local symmetry.

For all fermions, antiparticles exist with the same properties but an opposite value of the electric charge.

The Standard Model is a gauge field theory which is invariant under local gauge transformations. Its underlying symmetry is $SU(3) \times SU(2) \times U(1)$. The $SU(3)$ part is described by Quantum Chromodynamics, which is the theory of strong interactions. $SU(2) \times U(1)$ acts on the electroweak sector, which gives, after mixing, the photon, the W and the Z bosons. $SU(2)$ groups leptons and quarks into doublets and singlets. Particles in doublets are called left-handed, the ones in singlets are called right-handed.

1.2 Supersymmetry

Though being a very successful theory, the Standard Model has a few problems which cannot be explained in its framework. One of these issues is the hierarchy problem. The Higgs mass receives radiative corrections from every particle that couples directly to it. The particles don't even need to couple directly to the Higgs, even indirect couplings via gauge interactions lead to massive corrections. They depend quadratically on the ultraviolet cutoff scale Λ_{UV} , the energy scale at which the Standard Model stops being valid and new physics take over. For example, a scalar with Yukawa coupling λ_S leads to a correction at first order of the squared Higgs mass parameter m_H^2 by

$$\Delta m_H^2 = \frac{\lambda_S}{16\pi^2} \Lambda_{UV}^2. \quad (5)$$

The correction from a fermion with Yukawa coupling λ_f has a similar form,

$$\Delta m_H^2 = -\frac{|\lambda_f|^2}{8\pi^2} \Lambda_{UV}^2 . \quad (6)$$

Note the negative sign, which is due to the spin-statistics theorem and fermions having antisymmetric wave functions.

In order to balance the Higgs mass to be of the order of 10^2 GeV, either the cutoff scale needs to be small or the radiative corrections need to cancel. A small cutoff scale leads to the prediction of new particles at this scale, otherwise it is not clear why the Standard Model should stop being valid. Since the Standard Model has proven to be valid up to higher energies than the Higgs mass, the cutoff scale is assumed to be large, maybe even at the Planck scale, i.e. at the order of 10^{19} GeV. At these energies, the Standard Model necessarily will break down due to increasing influence of quantum gravitation. The small Higgs mass can then be explained by a cancellation of the radiative corrections. These cancellations can happen through a very fine tuning of the parameters involved but it is not clear what the underlying principle of these exact cancellations is.

One option without the need of a fine tuning is to introduce two scalars for each fermion and a fermion for each boson. Since left- and right-handed particles have different gauge transformations in the Standard Model, they must have their own complex scalar partner, so a fermion has indeed two scalar partners, a left-handed one and a right-handed one. Furthermore, if the Yukawa couplings are the same, i.e. $\lambda_S = |\lambda_f|^2$, the cancellations of the radiative corrections happen naturally, as can be seen by looking at Equations 5 and 6, making the theory independent of the cutoff scale.

The theory that exploits this idea is called Supersymmetry (SUSY), since it relates fermions to bosons and vice versa. Scalar SUSY particles are named after their Standard Model counterparts, by prepending an “s”, for scalar. This leads to sfermions and squarks, in particular, there are selectrons, staus, supers or stops. We denote them with an additional tilde over the Standard Model notion, e.g. a selectron is denoted as \tilde{e} . More precisely, a left-handed selectron is denoted by \tilde{e}_L and a right-handed one by \tilde{e}_R . It is important to keep in mind that the index L or R cannot describe the handedness of the selectron, since it has spin 0, but that of its Standard Model counterpart.

The SUSY fermions on the other hand carry the names of the Standard Model partners appended with an “ino”. Gauge bosons become gauginos, e.g. gluinos, winos, binos or higgsinos. In SUSY, there need to be at least two supermultiplets for the Higgs, the supermultiplet (H_u^+, H_u^0) give mass to the up-type quarks, while (H_d^0, H_d^-) give mass to the down-type quarks and to the charged leptons. The Standard Model Higgs is a linear combination of H_u^0 and H_d^0 . Taking into account effects from electroweak symmetry breaking in the Standard Model and supersymmetry breaking, the aforementioned particles are not the physical eigenstates, but are mixed. Mixed charged gauginos are called charginos and the mixed neutral gauginos neutralinos, they are denoted by $\tilde{\chi}^\pm$ and $\tilde{\chi}^0$, respectively.

SUSY cannot be an exact theory of nature, since its predicted particles would have been observed already but for phenomenological reasons, none of the Standard Model particles can be a SUSY partner of another Standard Model particle, i.e. no SUSY particle has been observed to date. A symmetry breaking mechanism must therefore be at work to raise the masses of the SUSY particles. The nature of this mechanism is not known but it is clear that the Yukawa couplings cannot be altered, since otherwise $\lambda_S \neq |\lambda_f|^2$ and we end up again with a hierarchy problem. Therefore we can split the Lagrangian \mathcal{L} into

$$\mathcal{L} = \mathcal{L}_{SUSY} + \mathcal{L}_{SOFT} , \quad (7)$$

with \mathcal{L}_{SUSY} being the exact SUSY Lagrangian, which contains all gauge and Yukawa interactions and \mathcal{L}_{SOFT} contains the symmetry breaking parameters. While \mathcal{L}_{SUSY} is already mostly defined by Standard Model parameters, it is our ignorance of \mathcal{L}_{SOFT} that leads to the many open questions and free parameters in the SUSY theory.

These free parameters lead to various SUSY flavours. The minimal extension to the Standard Model is called Minimal Supersymmetric Standard Model (MSSM). It possesses 105 independent parameters, additional to the 19 parameters of the Standard Model. To reduce the amount of parameters, some assumptions are made and subsets of the MSSM are introduced. These subsets are chosen such, that searches are simplified but still general enough, examples are minimal super gravity models (mSUGRA) or phenomenological Minimal Supersymmetric Standard Models (pMSSM). Even more reduced to only two parameters are so called “simplified models”, in which searches can be generalized to more realistic SUSY models. I will conduct a SUSY search in simplified models and pMSSMs, they are introduced in Section 4.2.

In the MSSM, baryon numbers and lepton numbers are not conserved, as a consequence the proton would not be stable. To preserve the proton from decaying, conservation of R -parity R_P is introduced. It is defined as

$$R_P = (-1)^{3(B+L)+2s}, \quad (8)$$

where B is the baryon number, L the lepton number and s the spin. All Standard Model particles have $R_P = 1$ and all SUSY particles have $R_P = -1$. As a consequence, every vertex needs to have an even number of SUSY particles. Hence, if R -parity is conserved, the lightest SUSY particle (LSP) is stable.

Furthermore, SUSY would not just solve the hierarchy problem, but could also be a step towards a unified theory of particle interactions. The running coupling constants need to be modified at the energy scale where SUSY particles enter and the three Standard Model gauge couplings can unify at an energy close to the Planck scale. Moreover, SUSY provides a natural dark matter candidate, a hypothesized particle which would explain the gravitational dynamics we see in the Universe and should make up approximately one quarter of the energy density in the Universe. For this to be the case, the LSP needs to be massive, stable and only weakly interacting. Neutralinos make up excellent dark matter candidates and are usually considered as LSP’s.

2 The ATLAS experiment at the Large Hadron Collider

In this section I present the Large Hadron Collider and the ATLAS experiment with its detector. I'm not going into much detail about either but will only give a brief overview, since both subjects have been covered in great detail in many publications before. For a comprehensive overview of the ATLAS detector, see e.g. [19].

Section 2.3 deals with the reconstruction of physics objects, i.e. translating the measurements from the detector into physical entities and Section 2.4 deals with the ATLAS trigger system and data acquisition.

2.1 The Large Hadron Collider

The Large Hadron Collider (LHC) [20] is a proton-proton accelerator with a design energy of 7 TeV per beam, operating at the European Organization for Nuclear Research (CERN), the world's largest particle physics laboratory, situated near Geneva, Switzerland.

In 2010 and 2011, the LHC operated at an energy of 3.5 TeV per beam and in 2012 this energy was raised to 4 TeV. This holds for protons, but also lead ions are accelerated with the LHC. The energy reached per nucleus in 2012 is 2.76 TeV, while the design energy is 5.5 TeV per nucleon. To accelerate particles to such high energies, a whole complex of accelerators is needed.

As a proton source, a bottle of hydrogen is used. The hydrogen atoms are stripped off their electrons and the resulting charged particles can be accelerated in electric fields and channelled by magnetic fields. The first accelerator in the CERN accelerator complex is a linear accelerator. In the case of accelerated protons, this is Linac 2, for lead ions, this is Linac 3. Linear accelerators use radiofrequency cavities to accelerate charged particles. These conductors are charged positively and negatively in turns, alternatively pushing and pulling charged particles in one direction. At the end of Linac 2, the protons have a kinetic energy of 50 MeV and enter the Proton Synchrotron Booster.

The proton particles are then further accelerated to energies of 1.4 GeV and are then injected into the Proton Synchrotron. Lead ions, on the other hand, take the route via Low Energy Ion Ring, before they are injected into the Proton Synchrotron.

The Proton Synchrotron is a very versatile machine, in its existence of over 50 years, it accelerated not just protons and lead ions, but also electrons, positrons, antiprotons, alpha particles and oxygen or sulphur nuclei. Protons destined for the LHC, will leave the Proton Synchrotron at an energy of 25 GeV and are now injected into the Super Proton Synchrotron, the second-largest machine in CERN's accelerator complex. In 1983, the W and the Z boson were discovered at the Super Proton Synchrotron, back then operating as a proton-antiproton accelerator. Nowadays, the Super Proton Synchrotron is not the last stage in the journey of a proton, instead it will be transferred to the LHC at an energy of 450 GeV.

The LHC is the most powerful particle accelerator ever built. It has a circumference of 26.659 km and is at a mean depth of roughly 100 meter below surface. In 2012, the protons were accelerated to 4 TeV, before they were brought to collision at one of the collision points. Figure 1 shows the whole CERN accelerator complex.

When talking about the LHC, the high centre-of-mass energy of 8 TeV is mentioned often, but as important as a high centre-of-mass energy is also a high luminosity, which translates to a high event rate. The luminosity \mathcal{L} is measured in $\text{cm}^{-2}\text{s}^{-1}$, the design luminosity of the LHC is $\mathcal{L} = 10^{34} \text{ cm}^{-2}\text{s}^{-1}$. To not carry around large numbers, one translates this usually into inverse barns, where $1 \text{ b} = 10^{-24} \text{ cm}^2$. Therefore we have for

CERN's Accelerator Complex

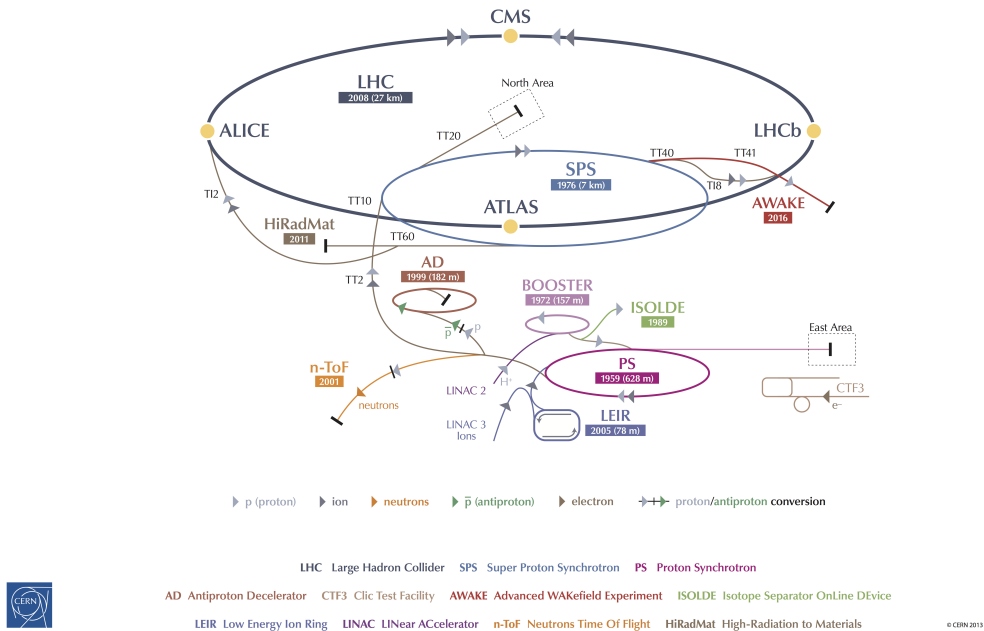


Figure 1: Schematic overview of the accelerator complex at CERN [21]. Shown are accelerators, in case of synchrotrons their circumferences, year of construction, and the four large LHC experiments ALICE, ATLAS, CMS and LHCb. Sizes not to scale.

the design luminosity $\mathcal{L} = 10 \text{ nb}^{-1}\text{s}^{-1}$, i.e. at design luminosity, the LHC delivers a luminosity of 10 nb^{-1} every second.

When analyzing data, one uses a large dataset, sometimes accumulated over many years. One is then interested in the integrated luminosity, which is given by

$$L = \int \mathcal{L} dt . \quad (9)$$

Sometimes, one refers to the integrated luminosity L simply as luminosity.

A barn is a unit used for cross-sections. When giving the luminosity in inverse barns, the expected event count can simply be determined by using the cross-section σ of the process in question

$$N = \sigma L . \quad (10)$$

The integrated luminosity delivered by the LHC, recorded by ATLAS and certified as good quality, i.e. when all detector parts of ATLAS were running at nominal conditions, is shown in Figure 2.

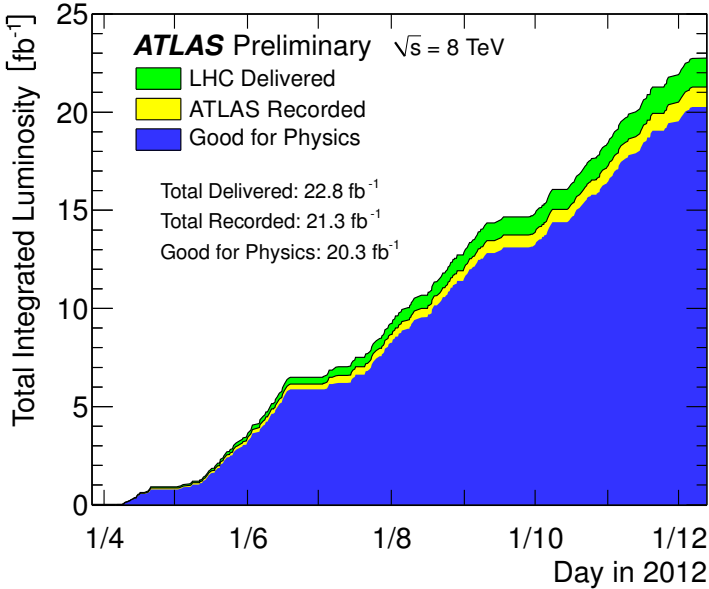


Figure 2: Cumulative luminosity as a function of the date in 2012. Green is collision data delivered by the LHC, yellow the collision data recorded by the ATLAS detector and blue the collision data which is certified as good quality by all detector subsystems.

Particles are accelerated in bunches and accelerators are filled in steps. First the Proton Synchrotron Booster is filled with bunches of protons. During the filling the magnetic field stays constant. Once it has reached the maximum number of bunches, the particles are accelerated and the magnetic field is ramped up. When the particles reach the designated energy, they get passed on to the next stage and the filling starts again. A schematic view of this process is shown in Figure 3.

A complete LHC fill consists of 2808 bunches, each with roughly $1.1 \cdot 10^{11}$ protons. A bunch is usually a few centimeters long and about 1 mm wide, at the collision points it is squeezed to $16 \mu\text{m}$ to enhance the chance of a collision and therefore the luminosity. The

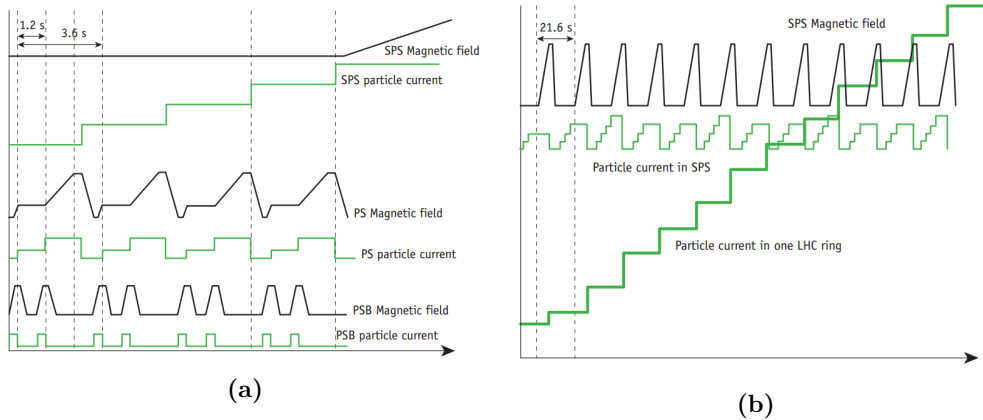


Figure 3: Scheme of filling, magnetic field and particle current in Proton Synchrotron Booster (PSB), Proton Synchrotron (PS), Super Proton Synchrotron (SPS) and LHC, as published in [22]. Green lines are the particle current, black lines the magnetic field. (a) is a zoomed in version of (b).

filling of the LHC takes less than 5 minutes per beam, accelerating them to 4 TeV takes less than 20 minutes, a stable beam can therefore be achieved within 30 minutes and it lasts for several hours before it is dumped.

Collisions take place at four designated spots, where four different detectors get as much information from the collision products as possible: These are the two multi-purpose detectors ATLAS [19, 23] and CMS [24, 25], as well as a detector optimized for lead ion collisions called ALICE [26, 27] and last but not least LHCb [28, 29], a forward detector designed to study flavour physics, especially b hadrons. Smaller experiments like TOTEM [30, 31], LHCf [32] and MoEDAL [33, 34] are also using LHC collisions.

2.2 The ATLAS detector

The ATLAS detector is a general-purpose experiment to measure known (Standard Model) processes with more precision, and to find new particles. A huge success of the experiment was the discovery of a Higgs boson [35], together with CMS [36]. To carry out high precision measurements and identify new particles, a large detector is needed.

ATLAS is the largest detector at the LHC, it is 44 m long and has a diameter of 25 m. Figure 4 shows a schematic view of the ATLAS detector.

The coordinate system used in ATLAS is a right-handed one with the origin in the nominal interaction point. The x -axis points in direction to the centre of the LHC, the y -axis points upwards and the z -axis is a tangent to the beampipe. Usually one uses cylindrical coordinates where ϕ is defined as the azimuthal angle around the z -axis in the x - y -plane and the polar angle θ is the angle from the z -axis. Instead of θ , often the pseudorapidity η is used, which is defined as

$$\eta = -\ln \left(\tan \left(\frac{\theta}{2} \right) \right). \quad (11)$$

The difference in pseudorapidity of two particles is independent of Lorentz-boosts along the beam axis.

In the next section I will briefly go through the different detectors that make up the complete ATLAS detector, we will start inside and take the same path as a particle that

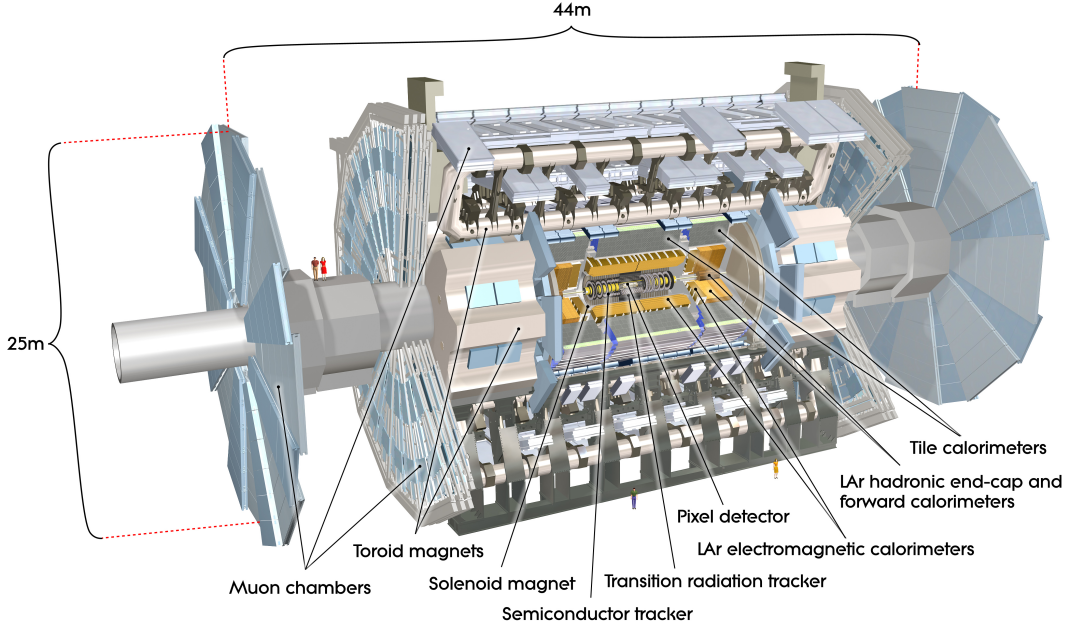


Figure 4: Schematic view of the ATLAS detector [37] and its subsystems.

is created at the collision point and crosses the detector. The first detector is the inner detector, it consists of the pixel detector, the semiconductor tracker and the transition radiation tracker. Then, an overview over the calorimeters, i.e. the liquid Argon electromagnetic calorimeters and the tile calorimeters is given. Finally, the muon chambers are discussed. In Section 3, the insertable b -layer is presented. It is a fourth layer which will be inserted into the present pixel detector during the long shutdown, i.e. during the writing of this thesis. Since I tested optical readout components for this additional layer, it is presented in its own section in more detail.

The inner detector The pixel detector, the semiconductor tracker and the transition radiation tracker make up the inner detector, the first material a particle crosses - not counting the beampipe - when emerging from the interaction point. Figure 5 shows a schematic view of the whole inner detector. The inner detector has a length of 6.2 m and a diameter of 2.1 m.

The pixel detector is depicted in Figure 6, its main goal is high-precision tracking, this is achieved by a very high granularity of the pixels as close to the interaction point as possible. The ability to find short-lived particles, like b -hadrons is mostly determined by the pixel detectors ability to separate different vertices. Three barrels and three disks on each side (endcaps) make up the pixel detector. The innermost barrel layer is called b -layer. Modules are overlapping to give hermetic coverage on the acceptance. A fourth layer even closer to the collision point is inserted during the writing of this thesis. The insertable b -layer (IBL) is subject of Section 3. On my authorship task, I worked in the IBL group, testing optical readout devices which are used in the near future to read out data from the IBL.

The semiconductor tracker (SCT) consists of silicon microstrips and mostly contributes to momentum measurements, impact parameters and vertex positions. The

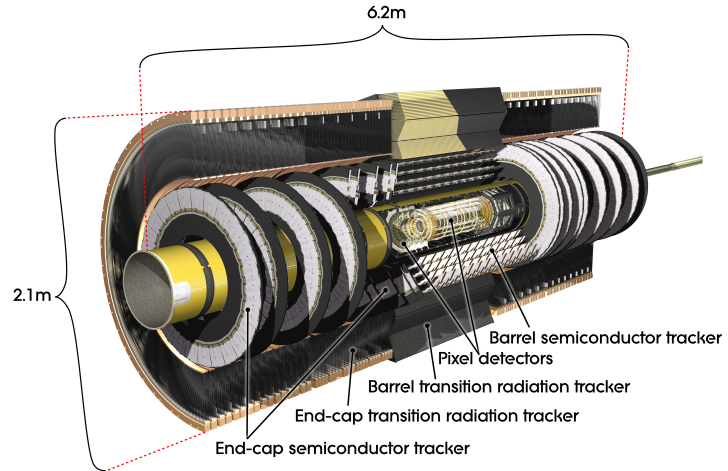


Figure 5: Schematic view of the inner detector, consisting of (from inside out) pixel detector (see Figure 6), semiconductor tracker and transition radiation tracker [38].

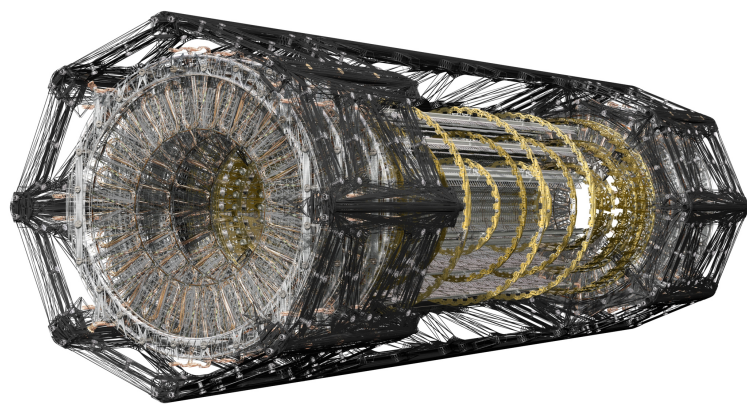


Figure 6: Schematic view of the pixel detector [39].

transition radiation tracker (TRT) is a straw detector that can operate at very high rates due to the small diameter of the straws. Charged particles ionize the gas inside the straws and the released charges are collected. The straws are aligned parallel to the beampipe in the barrel and radially pointing to the beampipe in the endcap.

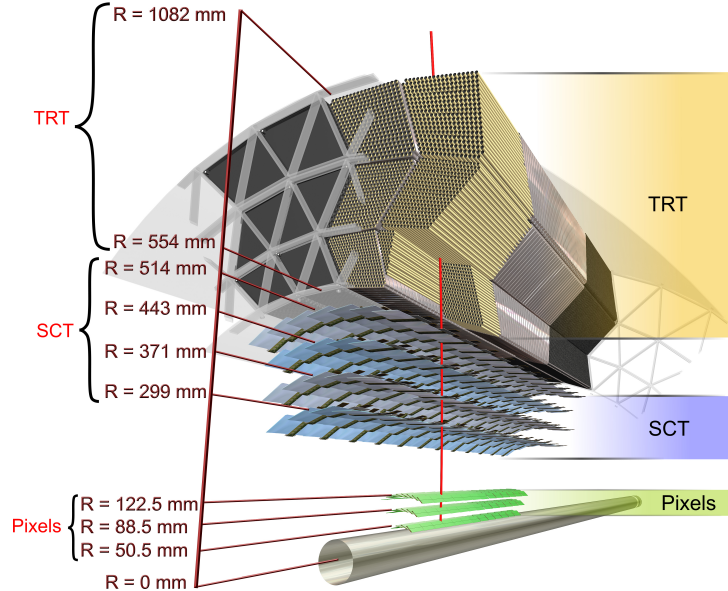


Figure 7: Schematic view of the different layers of the inner detector. Pixels are part of the pixel detector, SCT stands for semiconductor tracker and TRT for transition radiation tracker. The tube at the bottom is the beampipe. R is the distance from the centre of the beampipe, the designated interaction axis [38].

A schematic view of the different layers of pixel detector, SCT and TRT is shown in Figure 7.

Around the inner detector, a solenoid provides a magnetic field that bends charged particles and allows for momentum measurements. The central solenoid consists of a flat superconducting cable with an aluminium stabiliser. It provides a magnetic field of 2 T.

The calorimeters The calorimeters are next to the inner detector. They are divided into two detectors, an electromagnetic calorimeter absorbing electrons and photons by the electromagnetic interaction, and a hadronic calorimeter, absorbing hadrons by the strong interaction. The absorbed particles deposit their energy in the calorimeter cells by undergoing multiple interactions with the calorimeter material. In this process, the energy of the particles is measured.

High energetic electrons and photons are absorbed in the electromagnetic calorimeter mainly by pair production and bremsstrahlung, producing additional particles that undergo the same interactions. A cascading avalanche of particles is produced:

an electromagnetic shower. Eventually, the particles are soft enough to lose their remaining energy by ionization and excitation.

Both calorimeters are sampling calorimeters, i.e. the material that produces the particle shower is distinct from the one that absorbs it. The materials alternate, as absorber lead is used, the active medium to facilitate showers is liquid argon. The accordion geometry of the calorimeters provide full ϕ symmetry and are segmented longitudinally into three layers, called strips, middle and back. In the barrel region with $|\eta| < 1.8$ the energy measurement is improved by introducing a presampler where particles already start showering before entering the calorimeter.

The hadronic calorimeter uses plastic scintillators as active material and plates of steel as absorber in the barrel, while the endcap uses copper as absorber material and the active medium is liquid argon.

High energetic particles are supposed to leave all their energy within the calorimeters and not punch-through to the muon chambers. 22 radiation lengths in the barrel and 24 radiation lengths in the endcap ensure that the complete energy of these particles is deposited in the calorimeters.

A schematic view of the calorimeter system is shown in Figure 8.

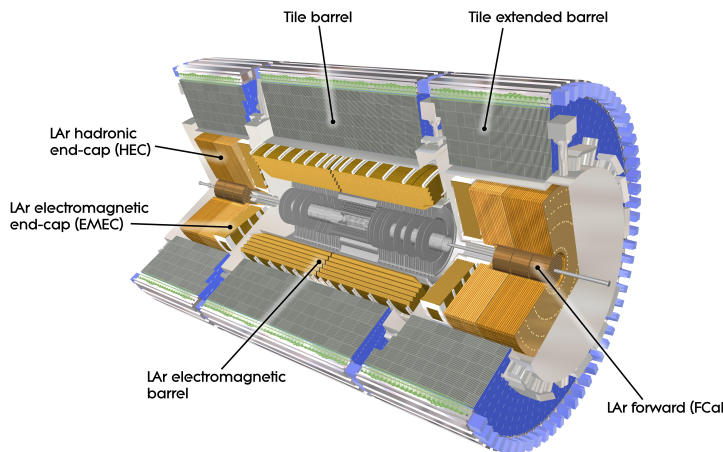


Figure 8: Schematic view of the calorimeters [40].

The muon chambers The muon spectrometers, often called muon chambers, are the outermost detector subsystem of ATLAS. Omitting only weakly interacting particles like neutrinos and a hypothesized LSP, only muons are supposed to reach this part of the detector. Other particles can punch-through and will be wrongly reconstructed as muons, too, but these objects are removed offline in a process called overlap removal (see Section 4.6).

The muon chambers can be seen in Figure 9. The momentum and the charge of the muons is determined by measuring the radius of their trajectories due to the magnetic field generated by the endcap toroids and the barrel toroid. The magnetic field on these superconductors is 4 T, but inhomogeneous over the detector volume, especially in the barrel endcap transition region. It is continuously monitored by 1800 Hall sensors distributed throughout the spectrometer volume.

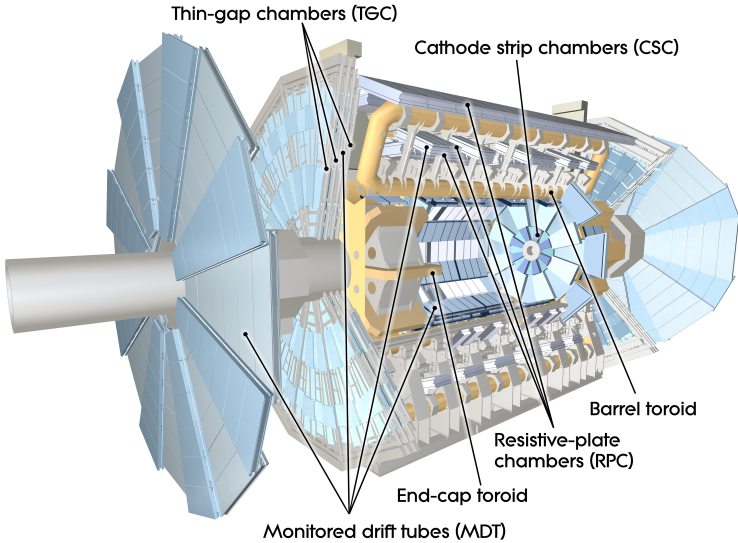


Figure 9: Schematic view of the muon chambers [41].

2.3 Reconstruction

In this section, the reconstruction of the physics objects will be discussed.

Electrons A track in the inner detector and an electromagnetic shower in the electromagnetic calorimeter are the signature of electrons. The reconstruction of these objects is done with an algorithm called sliding-window clustering [42]. Three steps are performed in this algorithm: tower building, precluster (seed) finding and cluster filling.

For tower building, the electromagnetic calorimeter is divided in $\eta - \phi$ space by varying r , the energy of all cells within $\Delta\eta \times \Delta\phi = 0.025 \times 0.025$ is summed up into the tower energy. A precluster is formed, if a local maximum in transverse energy is found which is required to be larger than 3 GeV.

Starting from these preclusters, the cluster filling is performed by taking all cells from the middle layer, the strips, the presampler and the back.

An alternative to the sliding-window algorithm is given by the topological clustering algorithm: cells with a significant signal to noise ratio are grouped to clusters and from these seeds the objects are reconstructed.

Depending on the analysis, different qualities are required for the electrons. They are selected as loose, medium or tight. The tight selection has a good background rejection from e.g. jets, but also some real electrons are not tagged as tight. The other selections, on the other hand, have less background rejection power. The use of the different selections will be picked up again in Section 4.6, where the objects for the analysis at hand will be defined.

The details of the cuts are outlined in [43]. A loose electron selection cuts on the detector acceptance, i.e. $|\eta| < 2.47$, ratio of the transverse energy in the hadronic calorimeter over the electromagnetic cluster and geometries of the shower. A medium selection contains the loose selection and additionally cuts on the shower width, ratio of the energy deposits and includes track quality cuts by e.g. requesting at least one

hit in the pixel detector and a track matching. The tight selection adds further cuts on track quality and track matching and rejects electron candidates matching to reconstructed photon conversions.

The efficiencies in a $Z \rightarrow ee$ sample with $E_T > 20$ GeV are measured to be 94.32 %, 90.00 % and 71.59 % for the loose, medium and tight selections, respectively.

Muons A muon leaves tracks in the inner detector and in the muon spectrometer. Attempting to reconstruct the full muon trajectory can be obtained in various ways [44]. The *Muonboy* reconstruction uses the muon spectrometer only, tracks are extrapolated to the beampipe. *MuTag* uses reconstructed tracks in the inner detector and searches for nearby hits of the extrapolated trajectory in the muon spectrometer. Finally, *STACO* statistically combines the *Muonboy* hits in the spectrometer and tracks reconstructed in the inner detector.

STACO muons have the highest purity, in two regions there are acceptance losses, though: At $\eta \approx 0$, the muon spectrometer is only partially equipped, in order to provide space for inner detector and calorimeter services. In the transition region between barrel and endcap, where $1.1 < \eta < 1.3$, only one layer of muon chambers were present during data taking up to 2012. Meanwhile, additional muon chambers have been installed [45].

The *MuTag* and the *STACO* reconstruction algorithms are combined, leading to an overall good efficiency except at $\eta \approx 0$. To enhance the efficiency also in this region, another algorithm is defined: If a track in the inner detector can be associated to an energy deposit in the calorimeter as expected from a minimum ionizing particle, it is identified as a muon. This algorithm has the lowest purity, but recovers the acceptance loss where $\eta < 0.1$. These three reconstruction algorithms together lead to an overall efficiency of $\approx 98\%$ over the whole detector volume.

Jets Quarks and gluons are known not to exist in unbound states. If a quark or a gluon dashes out of the interaction point, the hadronization process will create additional particles by the strong interaction. A narrow cone of hadrons and other particles produced in this process is called a jet.

Jets are reconstructed using the anti- k_t algorithm [46] with a radius parameter of $\Delta R = \sqrt{(\Delta\phi)^2 + (\Delta\eta)^2} = 0.4$. The reconstruction is similar to the case of the electrons, a calorimeter tower is built in the hadronic calorimeter with the dimensions $\Delta\eta \times \Delta\phi = 0.1 \times 0.1$ [47] and the same procedure as for electrons is carried out to reconstruct jets. The sliding-window algorithm is used as well as topological clusters.

The jet reconstruction efficiency is above 99 % over a wide kinematic range. For low p_T jets, the efficiency is smaller though. For a jet with $p_T = 25$ GeV, the reconstruction efficiency is $\approx 96\%$.

Taus The lifetime of a tau is too short to reach the detector material. Leptonically decaying taus are reconstructed as the leptons they have decayed to, hadronically decayed taus are reconstructed as jets at first order, but can be reconstructed to taus by a multivariate analysis boosted decision tree [48]. The hadronic tau identification optimization was performed on QCD di-jet and $Z \rightarrow ee$ background samples.

Loose taus reach a signal efficiency of $\approx 60\%$ while the tight tau efficiency is of the order of $\approx 35\%$.

E_T^{miss} The momentum of a parton inside a proton is described by parton distribution functions. These are defined as probability densities finding a particle in a state with a particular longitudinal momentum. Since we don't know what fraction of the total momentum is carried by the parton involved in the high energy interaction, the longitudinal momentum is not known. However, the transversal momentum must be close to 0, i.e. vectorially adding all transverse momenta of the event in question gives 0:

$$\sum \vec{p}_T^{\text{all}} = \vec{0}, \quad (12)$$

where the sum is to be made over all objects, detected or not. In practice, though, there are particles that, in general, do not interact with the detector and therefore leave it undetected. To account for these undetected particles, we introduce a correction factor called \vec{p}_T^{miss} . If we sum over all *reconstructed* objects, we have

$$\sum \vec{p}_T^{\text{reco}} + \vec{p}_T^{\text{miss}} = \vec{0}. \quad (13)$$

Its magnitude is then, in a slightly sloppy expression coming from $E = |\vec{p}|$ for massless particles, called missing transverse energy, E_T^{miss}

$$E_T^{\text{miss}} = |\vec{p}_T^{\text{miss}}|. \quad (14)$$

Calculating E_T^{miss} at first order is done by summing up all energy deposits in the calorimeter cells. However, muons only deposit a small fraction of their energy in the calorimeters. A more sensible way of defining E_T^{miss} takes into account reconstructed objects by

$$E_T^{\text{miss}} = \sqrt{\sum_{i=x,y} (E_i^{\text{miss}})^2} \quad (15)$$

$$= \sqrt{\sum_{i=x,y} \left(E_i^e + E_i^\gamma + E_i^{\text{jets}} + E_i^\mu + E_i^{\text{cluster}} \right)^2}, \quad (16)$$

where E^e is the energy associated with reconstructed electrons, E^γ the one from reconstructed photons, E^{jets} the one from reconstructed jets, E^μ the one from reconstructed muons and E^{cluster} the low energy calorimeter deposits e.g. from soft jets or pileup [49].

Photons Photons are not used in this analysis. They are showering in the electromagnetic calorimeter much like electrons but without leaving a track in the inner detector [50]. A tight selection still reaches an efficiency of $\approx 85\%$.

2.4 Trigger and data acquisition

The rate of events produced by the LHC is far too high to be recorded by ATLAS, most data is never stored on disk. To decide if an event shall be stored, a three-level trigger system is implemented to search for interesting objects in an event. Each trigger level refines the decisions made at the previous level.

The first level trigger L1 needs to make a decision if the event shall be stored or not within $2.5\mu s$, reducing the event rate from 40 MHz to about 75 kHz. It has only access to a limited amount of the total detector information: Muons are identified in trigger chambers, calorimeter objects are reconstructed with a reduced granularity. If the L1

trigger identifies an interesting object, e.g. a high p_T object, the event is passed to the level two trigger L2 and the η and ϕ coordinates, where the interesting object is found is marked as Region-of-Interest (RoI). Multiple RoI's can be defined by the L1. RoI data includes also information on the type of feature identified and the criterion why the event passed that trigger stage.

The second level trigger L2 uses the fully reconstructed objects but only over the RoI's, approximately 2 % of the total event data is available to the L2. The processing time is about 40 ms, the event rate needs to be reduced to ≈ 3.5 kHz.

The final stage of the three level trigger system is called event filter, the even rate is reduced to roughly 200 Hz. While the first two trigger levels are hardware implementations, the event filter relies on software algorithms. The average processing time of an event is of the order of four seconds. Selected events are then transferred to permanent storage at the CERN computer centre. The data transmission is controlled by the data acquisition system.

3 IBL

For run 1, which took place between 2009 and 2012, the pixel detector consisted of 3 layers. During the long shutdown in 2013 and 2014, an additional layer is inserted inside the innermost layer, called insertable b -layer (IBL) [51].

The reasons for installing an additional layer are manifold: The radiation on the present innermost layer of the pixel detector, the b -layer, is enormous. Front-end readout chips will eventually die and cannot be replaced. By adding an additional layer, these inevitable failures are compensated. In addition, for a higher luminosity and a higher event pileup, more information is needed to correctly reconstruct tracks, the IBL introduces redundancy. Moreover, since it will be closer to the interaction point, it will provide enhanced leverage, which is important especially for b -jet tagging and high precision vertexing.

Since there is not enough space for an additional layer between the present beampipe and the b -layer, the beampipe needs to be replaced with a smaller one. The inner radius of the new beampipe will shrink from 29 mm to 25 mm. The additional space gained is enough to install the IBL. Figure 10 shows the present pixel detector with the present beampipe as well as the new beampipe with the IBL mounted on it.

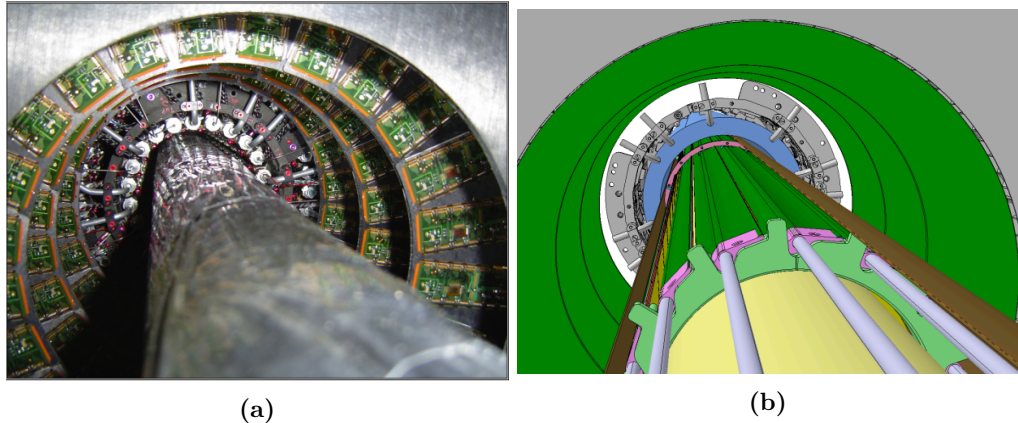


Figure 10: Installation of the IBL. (a) shows the present pixel detector and beampipe; (b) shows a schematic view of the present pixel detector without present beampipe and the new beampipe with the IBL mounted on it.

Some of the prerequisites for a successful operation of the IBL will be radiation hard technology, since it is the innermost layer where radiation is the hardest. Material needs to be minimized by simultaneously having a small radiation length. Last but not least, the front-end chips are required to have a higher active area. A cross-section view of the IBL is shown in Figure 11.

The IBL will introduce an updated readout technology, in particular new optical readout components are needed. The requirements on the receiver plugins are outlined in Section 3.1. The experimental setup to carry out tests is presented in Section 3.2.

Commercial parallel fiber optic receivers with 12 channels exist, they seem to fit the need but have to be tested for reliability, low frequency and input sensitivity. The name of these components is SNAP12.

LHCb is already using around 600 of these components from Agilent. In the four years the SNAP12's were used in the LHCb detector, they never reported a failure [53], hence the reliability is proven. Nonetheless, the SNAP12 components were also put into a climate chamber at 85° C and at 85% relative humidity. According to industrial standards, a stress

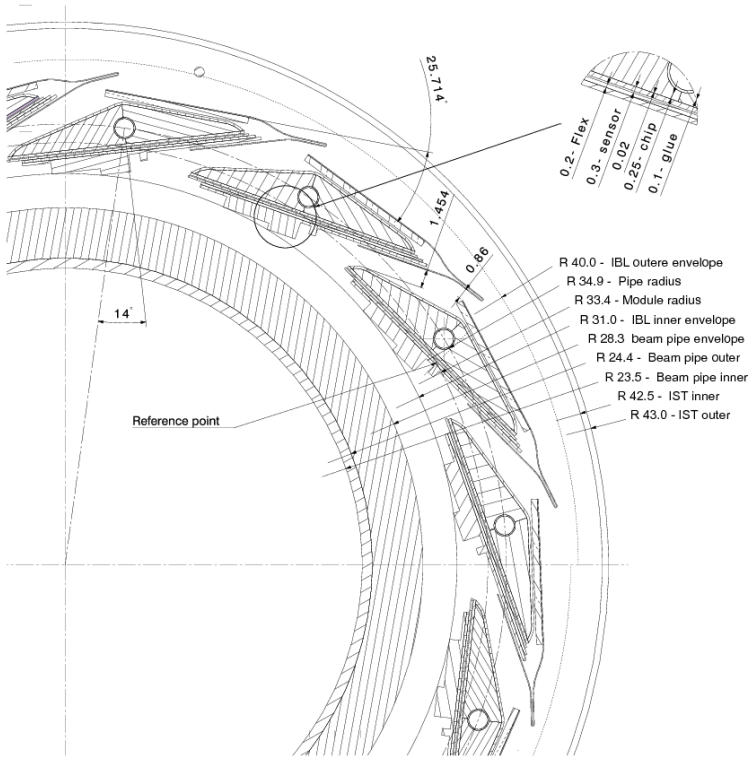


Figure 11: Partial cross-section view through the IBL and its staves [52].

test at these conditions for 1000 hours, corresponds to normal usage of 10 years. Two Rx from Avago and two Rx from Tyco were tested for 1000 hours, additionally, two Rx from Avago and two Rx from Tyco were tested for another 500 hours. After this stress test, all Rx's have been tested again. Not a single channel failed, proving these components to be very reliable.

The SNAP12's are to be mounted on the back of crate (BOC) card, which takes care of the signal processing and transfers signals to the Read Out Driver (ROD), the front card in the crate, see Figure 12. As the BOC receives signals at a rate of 160 Mbit/s, the SNAP12 should operate at a frequency of 160 MHz. This is a rather low frequency for these optical readout components. The question addressed in chapter 3.3 is, if the SNAP12's are able to deliver reliable results at this low frequency.

At the beginning it was not clear how much optical power the SNAP12 readout (Rx) will receive. In chapter 3.4 a measurement is outlined, to determine in which interval the input power has to be in order for the SNAP12 to deliver a stable signal.

Different suppliers of SNAP12's exist. We test the products from Avago, Tyco Electronics and Reflex Photonics¹. See Figure 13 for a SNAP12 specimen of each supplier.

3.1 Rx requirements

In the final setup the optical signal will be sent from an optoboard just outside the detector to the BOC, where the signal will be read out by a SNAP12 device. Figure 12 shows the situation for the pixel detector, which is similar to the one of the IBL. The modules in Figure 12 are part of the detector, the module control chip (MCC) is the interface

¹The SNAP12's used by LHCb are from Agilent. They are the same as the ones from Avago.

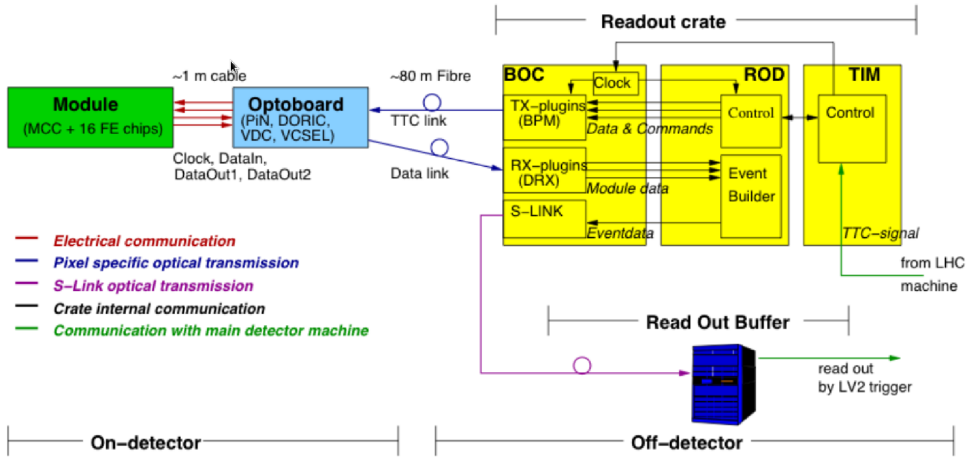


Figure 12: The ATLAS readout chain. Abbreviations explained in the text.

between front-end (FE) chips and readout. On-detector, the data is first transmitted to an optoboard, where the electrical signal is converted into an optical signal. The optical transmission of the signal does not suffer from potential differences or cross-cable talking. The optoboards are equipped with one 8-way PiN diode array for the electronic communication. For transmitting optical signals, a vertical-cavity surface-emitting laser (VCSEL) and the VCSEL driver chip (VDC) are used, the receiving part of the optical signals is taken care of by digital opto-receiver integrated circuits (DORIC). The Tx- and Rx-plugins are to be exchanged with SNAP12 devices for the IBL readout. The plugins used for the pixel detector reported several failures well before their expected lifetime [54].

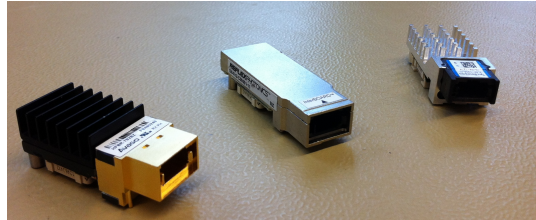


Figure 13: SNAP12's from different manufacturers: (from left to right) Avago, Reflex Photonics, Tyco Electronics.

The data coming from the optoboard will be 8bit-10bit (8b10b) encoded, assuring a DC-balanced signal with at least 2 edges per 10 bit and the transmission of 5 equal bits in sequence at maximum. As the SNAP12 is known to be able to read a fast signal, a problem might only arise when the frequency is too low. With a 160 Mbit/s data stream and a worst case scenario of 5 bits at the same value, we have a transition at least at the frequency of 32 MHz. The SNAP12 specifications sheet [55] lists a maximum modulation data rate of 2.72 Gbit/s, while no minimum data rate is specified. The supplier specific data sheet from Avago [56] lists a maximum sampling rate per channel of 2.7 Gbd and “a lower cut off frequency near 100 kHz”. The data sheet from Reflex Photonics [57] on the other hand states “a lower cut-off frequency of 175 kHz” in the text but a low frequency cut-off of 150 Mbit/s in a table. Last but not least Tyco Electronics does not offer a data sheet but lists a data rate of 2.700 Gbit/s as highlight of the product on their website [58], not listing any limits.

The data sheets indicate that a SNAP12 should run without problems at a data rate of 160 Mbit/s. In Section 3.3 the low frequency behaviour of the SNAP12's are examined.

The question about the input sensitivity and input saturation is a more subtle one, as while testing it was not clear what power the optoboards will output. The SNAP12 agreement [55] specifies the average optical input power between -16 dBm and -2 dBm. Both data sheets from Avago and from Reflex Photonics have the same specifications. Section 3.4 explains the measurement of the input sensitivity in detail.

3.2 Experimental setup

The central part of the experimental setup is the mezzanine board, manufactured at the Bergische Universität Wuppertal. It has an FMC connector where the signals can directly be driven (see Figure 14). To measure the lower frequency cut-off a signal generator is used. It is connected to the FMC connector via SMA cable, where it is internally routed to the SNAP12 Transmitter. The signal is then looped back to the Rx on the same board. It is read out with an oscilloscope connected to the FMC connector.

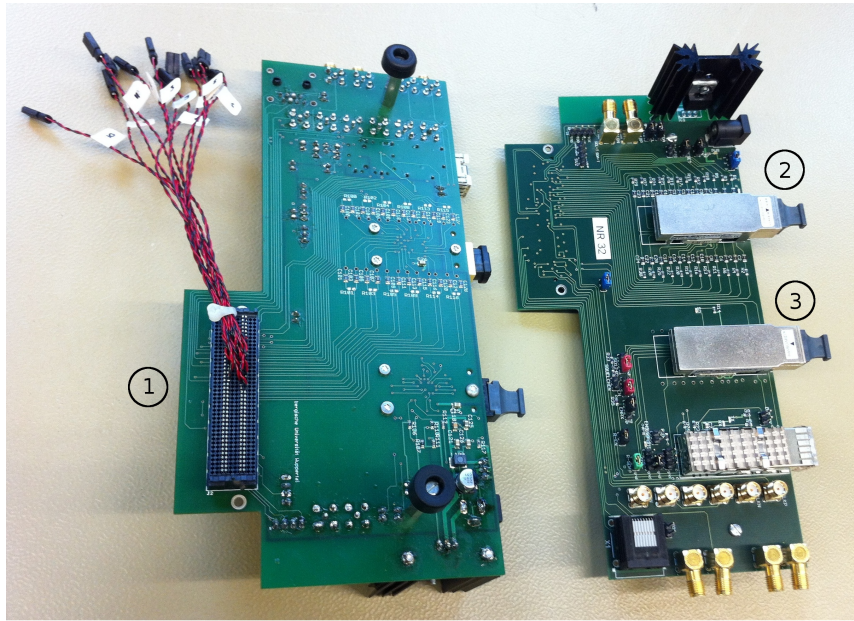


Figure 14: Mezzanine board with FMC connector (1) and two slots for a SNAP12 Tx (2) and a SNAP12 Rx (3), respectively.

For the input sensitivity and saturation measurement, the Tx could not be used, as it converts the electrical signal always to the same optical power, not taking into account the input current, as long as it is over a certain threshold. For this measurement a so called USB Jig [59], manufactured at Cambridge University, is used (see Figure 15). This tool can be connected via USB cable to a computer which can steer the output power of the mounted VCSEL. However, the output power on the VCSEL has to be calibrated first. For this purpose, an optical fanout cable is connecting the USB Jig and the oscilloscope via an optical probe. When connecting the optical cable to the Rx, the voltage can be measured via FMC connector just as before.

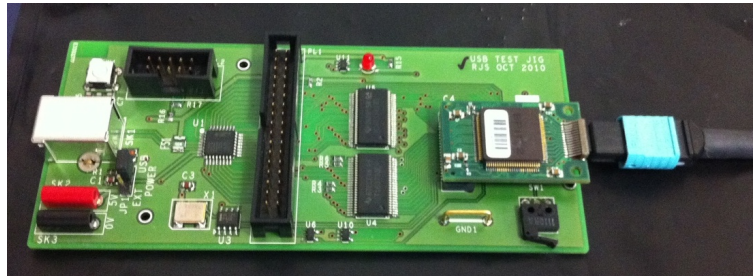


Figure 15: USB Jig with VCSEL mounted on the right side and plugged in optical fibre.

3.3 Low Frequency tests

To measure the frequency the signal generator is used to send a step signal at different frequencies. Figure 16 shows the input signal of the signal generator directly routed to the oscilloscope as the pink step function and the blue signal as the same signal but processed by the Rx. Figure 16a is the signal at 300 kHz, Figure 16b at 10 kHz. It is obvious that a transfer rate at 10 kHz would not be possible with this setup, while the test at 300 kHz shows good results. Higher frequencies were also tested, all of them delivered a stable signal similar to the one in Figure 16a. Therefore it is no problem to run the Rx at 160 Mbit/s. Since the problematic frequency of 10 kHz is very low compared to the operation frequency, this measurement was carried out only in a qualitative way. All the SNAP12's from different manufacturers behaved equally well.

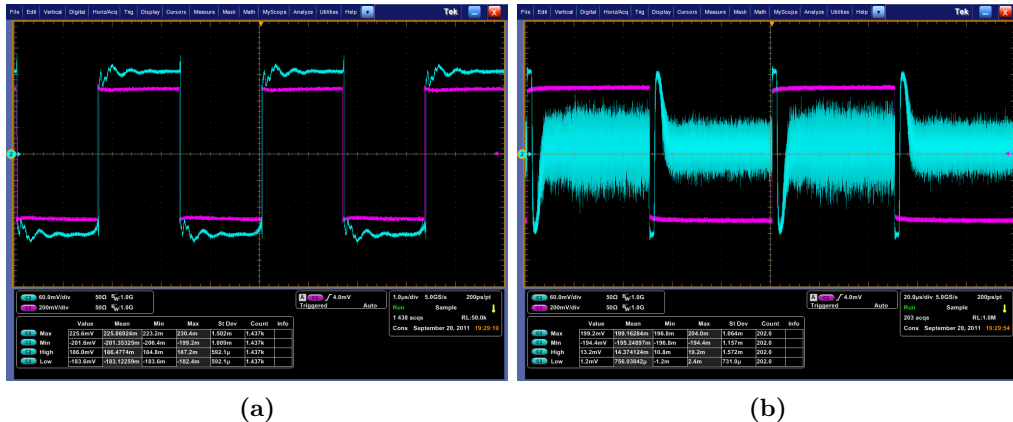


Figure 16: Input signal (pink) and output signal (blue) after routing it via a SNAP12 device at 300 kHz (a) and at 10 kHz (b).

3.4 Input sensitivity

To change the optical power on the fibre the USB Jig is used (see Figure 15). We can control it via a USB cable and a dedicated software. Possible inputs are numbers between 0 and 255 but it is not a priori clear how those numbers translate to a physical meaningful quantity, so the power on the cable has to be measured first to calibrate the USB Jig output. The measurement is shown in Figure 17. A SNAP12 device has 12 channels, but channels 0, 1, 10 and 11 are not driven by the USB Jig. Channels 3, 7 and 9 are not used

because of failures on the old VCSEL that is used. Looking at the 5 remaining channels we observe results that show the same behaviour for all channels, though the exact values differ for every channel. The difference in the inclination of the slope in Figure 17 may have several origins: It is known that some channels on old VCSELs slowly stop operating after some time [54]. But also the mounting of the ST connector of the fibre to the VCSEL may cause such differences as it is highly sensitive to its alignment. A proper alignment is not possible due to a missing leading device on the USB Jig.

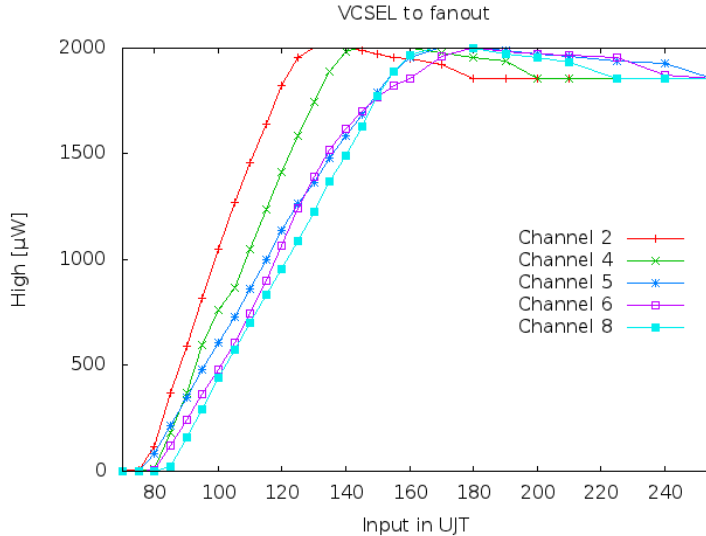


Figure 17: Amplitude of each channel with respect to the input value in the USB Jig Tool (UJT).

Looking at the curves in Figure 17, we see that we have a linear inclination up to almost 2 mW before it saturates. It is the optical probe that saturates, not the optical power on the fibre. This has been confirmed by using a selfmade attenuator. It is assumed that the optical power on the fibre rises linearly up to the input value of 255 on the USB Jig software.

The measured curve is fitted by a linear function as can be seen in Figure 18. The fit is done for every curve separately. This leads to a linear function for each channel. The channel is denoted by a subscript:

$$f_{2,fit}(x) = 43x - 3256 , \quad (17)$$

$$f_{4,fit}(x) = 34x - 2677 , \quad (18)$$

$$f_{5,fit}(x) = 24x - 1830 , \quad (19)$$

$$f_{6,fit}(x) = 28x - 2328 , \quad (20)$$

$$f_{8,fit}(x) = 27x - 2233 . \quad (21)$$

The measured quantity is the optical power which reaches the oscilloscope, this may slightly differ from the power that reaches the Rx due to different cabling. The insertion loss (IL) introduced from the fanout cable which connects the USB Jig with the oscilloscope has to be corrected and replaced by the insertion loss introduced by the optical fibre which connects the USB Jig with the Rx. The values are given by the manufacturer of the fibres and can be seen in Table 1.

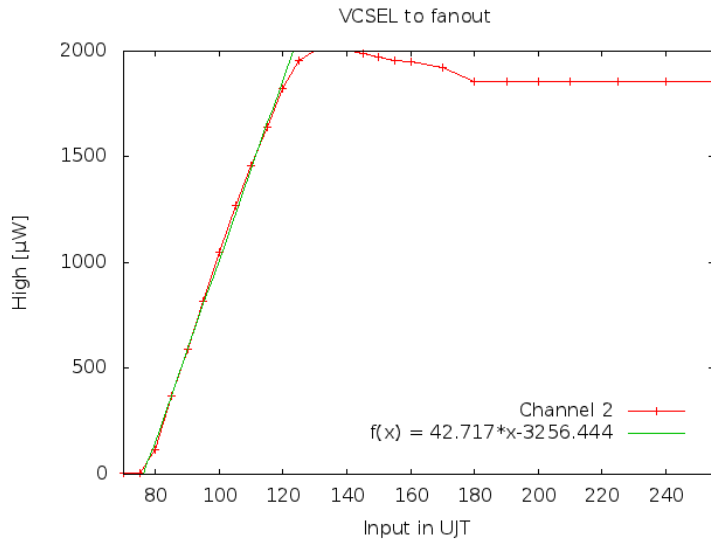


Figure 18: Amplitude of channel 2 with respect to the input value in the USB Jig Tool (UJT) and linear fit.

	IL _{fibre}	IL _{fanout}
Channel 2	0.18	0.25
Channel 4	0.08	0.23
Channel 5	0.09	0.10
Channel 6	0.12	0.14
Channel 8	0.11	0.23

Table 1: Insertion loss (IL) of the different cables used.

The fitted function is also corrected by a conversion factor of the optical probe with respect to the wavelength. The conversion function $c(\lambda)$ happens to be 1 for the used wavelength at 800 nm. The corrected function which describes the power at the Rx is now calculated as

$$f_k(x) = f_{k,fit} \cdot \frac{e^{-\text{IL}_{\text{fibre}}}}{e^{-\text{IL}_{\text{fanout}}} \cdot c(\lambda)}, \quad (22)$$

where k is the number of the channel, i.e. either 2, 4, 5, 6 or 8. The corrected linear fit functions are

$$f_2(x) = 41x - 3018, \quad (23)$$

$$f_4(x) = 36x - 2655, \quad (24)$$

$$f_5(x) = 21x - 1437, \quad (25)$$

$$f_6(x) = 23x - 1654, \quad (26)$$

$$f_8(x) = 20x - 1489. \quad (27)$$

Now we can measure the output voltage on the Rx by means of the input parameter of the USB Jig and translate this input parameter into a physically meaningful quantity with the functions calculated above. The results can be seen in Figures 19 (Avago), 20 (Reflex Photonics) and 21 (Tyco Electronics).

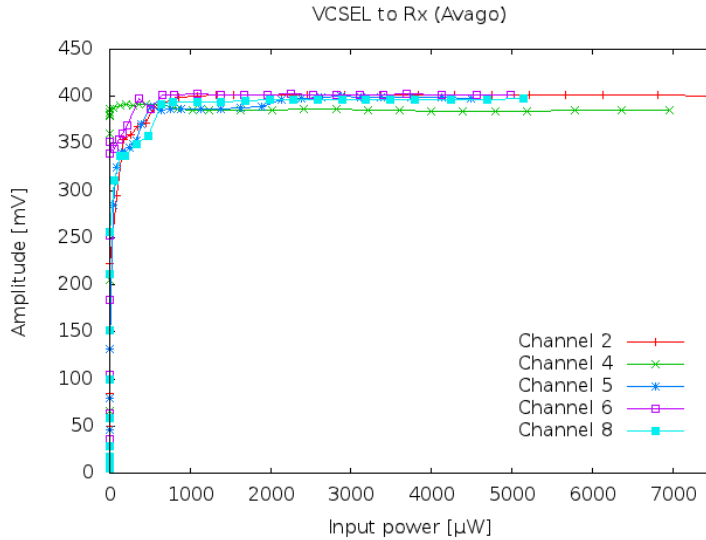


Figure 19: Amplitude of electrical output after conversion from an optical signal by a SNAP12 device (Avago)

Although the error bars in this measurement are assumed to be rather large and a complete analysis with error estimation has not been carried out, a general behaviour of the SNAP12 from Reflex Photonics becomes apparent: It cannot handle signals with high input powers. This behaviour may be only due to different heat conducting and may be corrected by mounting a proper heatsink. The SNAP12's from Avago and Tyco Electronics come with integrated heatsinks. As the other two SNAP12's show good results, the device from Refles Photonics is omitted of the decision process.

Due to good test results and availability, the SNAP12's from AVAGO are chosen and built into the detector readout of the IBL.

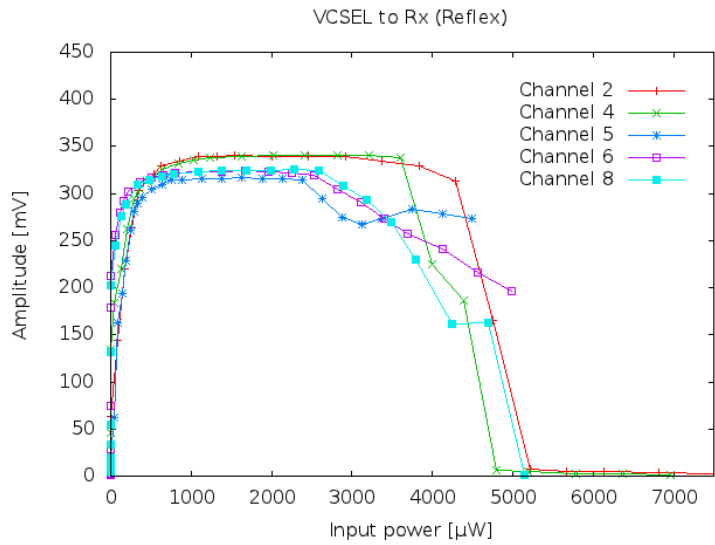


Figure 20: Amplitude of electrical output after conversion from an optical signal by a SNAP12 device (Reflex Photonics)

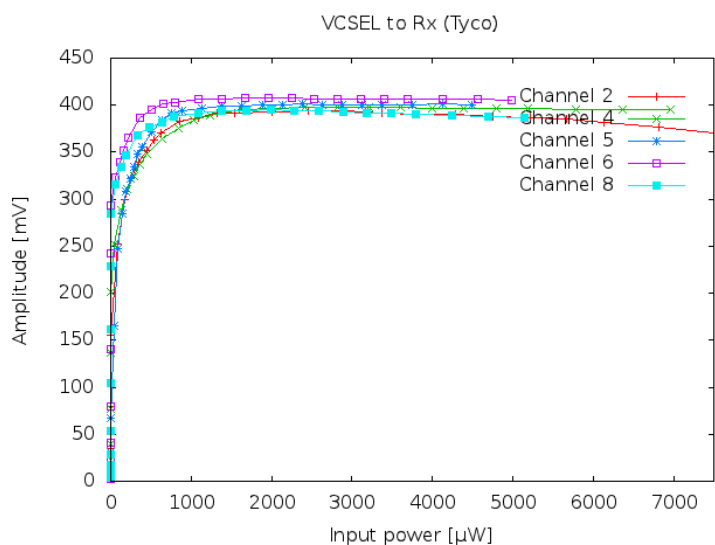


Figure 21: Amplitude of electrical output after conversion from an optical signal by a SNAP12 device (Tyco Electronics)

4 Search for electroweakly produced supersymmetry

This section outlines the analysis, where I performed the binning and the optimization of one of the signal regions and carried out the statistical interpretation. For a detailed overview about my contributions, see page 8f. The search was published on arXiv and JHEP [2] with the title “Search for supersymmetry in events with three leptons and missing transverse momentum in 20.3 fb^{-1} pp collisions at $\sqrt{s} = 8 \text{ TeV}$ with the ATLAS detector”. This section is an introduction to the analysis: it motivates the analysis, introduces the SUSY models studied, presents the backgrounds involved, describes object definitions and basic event selection and gives a brief overview of our main background estimation method, the Matrix Method. It follows mainly the supporting material of [2] which can be found in [60].

My two main contributions to this paper was the development of a new statistical method to analyze many signal regions contemporaneously and the statistical interpretation of the results. These two contributions I will outline here in detail. The optimization and the binning of one of the signal regions is described in Section 5. Validation of the background modeling is described in Section 6 and the observation of events in data in the signal region is summarized in Section 7. The statistical interpretation of the results, is first summarized in general in Chapter 8 and then explained for the analysis at hand in Section 9.

4.1 Motivation

As any SUSY model has a large number of degrees of freedom, so could SUSY appear in a large variety of different final states. Naturalness asks for SUSY particle masses to be below 1 TeV, looking at Figure 22, we see that many experimental search results from ATLAS constrain the gluino \tilde{g} and squark \tilde{q} masses to be above $\approx 1 \text{ TeV}$. Since these lower limits hold only for colored sparticles, we can still save naturalness by requesting \tilde{g} and \tilde{q} masses to be high, but electroweak sparticle masses, like chargino $\tilde{\chi}_1^\pm$ and neutralino $\tilde{\chi}_2^0$ masses to be $< 1 \text{ TeV}$.

At a hadron collider like the LHC, dominant processes include colored particles. Figure 23 shows that the associated $\tilde{\chi}_1^\pm$ and $\tilde{\chi}_2^0$ production cross-section is two to four order of magnitudes below a typical cross-section for colored sparticles. The cross-sections shown in Figure 23 were calculated with PROSPINO [61]. More details about SUSY production cross-sections can be found in [62, 63, 64]. However, assuming naturalness and henceforth SUSY particle masses $\lesssim 1 \text{ TeV}$ and since colored sparticles are largely excluded up to $\approx 1 \text{ TeV}$, the production of electroweak SUSY particles has a good chance of becoming a dominant process at the LHC.

Multilepton final states have an excellent potential to distinguish electroweakly produced SUSY particles from the Standard Model background. Requesting three leptons and a moderate amount of E_T^{miss} , suppress the overwhelming QCD background present at a hadron collider, leaving mainly WZ , $t\bar{t}$ and some other more rare processes. A detailed discussion of all Standard Model backgrounds considered can be found in Sections 4.3 and 4.4.

4.2 SUSY models

In my analysis I studied nine different SUSY models, which can be divided into two different categories. The five phenomenological Minimal Supersymmetric Standard Models

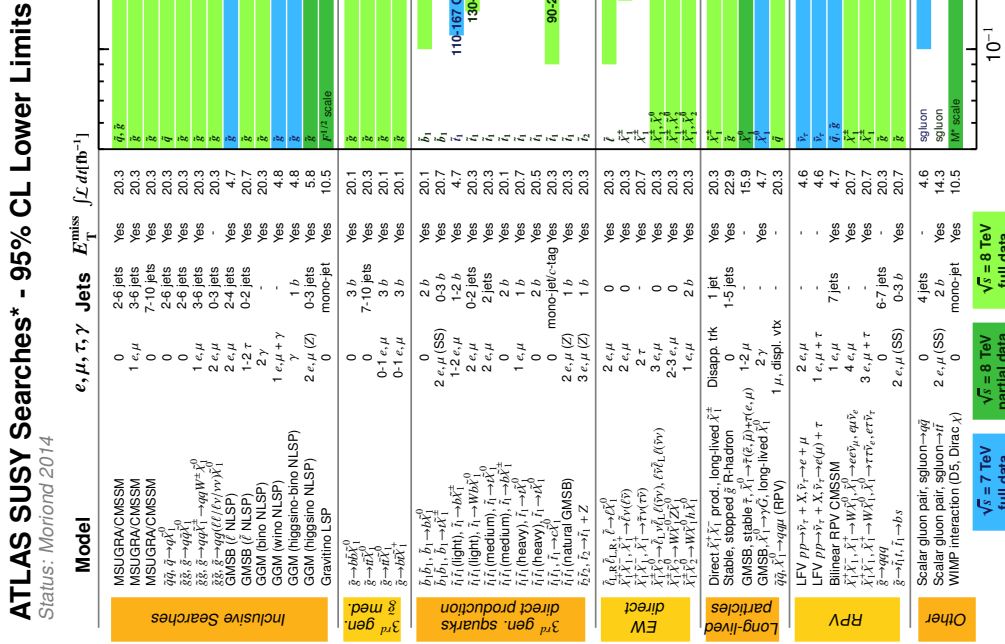


Figure 22: 95 % confidence level lower limits on various SUSY particle masses in different models. Some assumptions are made for the SUSY specific parameters, to come up with these lower limits, nonetheless it can be seen that the limits on colored particles are higher in general than the ones on electroweak particles. Naturalness asks for SUSY particles at $\lesssim 1$ TeV. This summary plot includes the results described in this thesis, which are the two EW direct (direct electroweak production of SUSY) limits with three leptons at 700 GeV and 420 GeV, respectively.

misses scale [TeV]

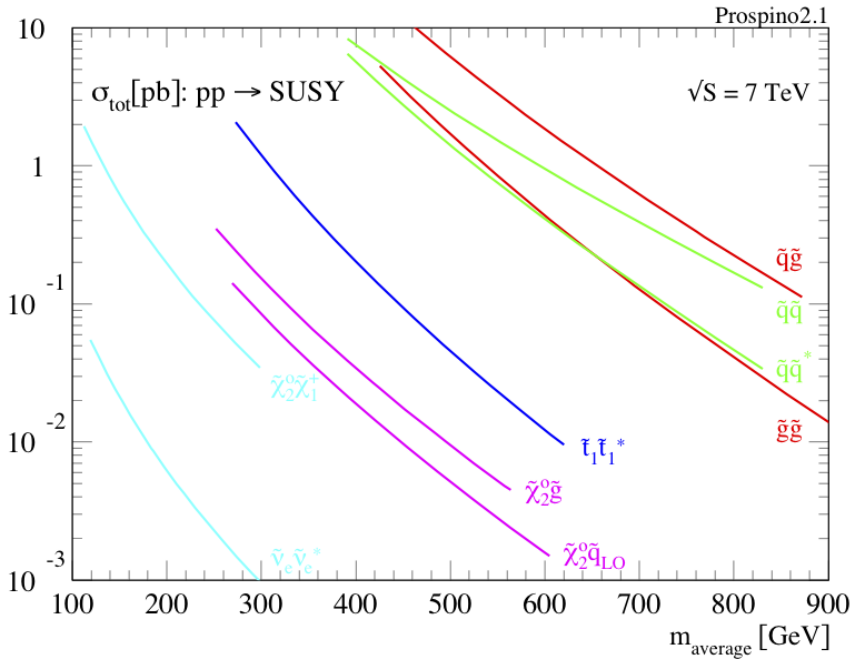


Figure 23: Cross sections for producing SUSY particles in pp collisions at $\sqrt{s} = 7$ TeV computed with PROSPINO. The cross-sections at $\sqrt{s} = 8$ TeV look similar.

(pMSSM) are full-fledged SUSY models which could be realized in nature. Its many possible SUSY processes makes exclusion limits difficult to generalize to other SUSY models. On the other hand, the 4 simplified models are not full SUSY models and will not be realized in nature due to their many simplifications. But in case they are excluded, the exclusion limits could be more easily adapted by theorists to their favorite models. All models are described below.

pMSSM A pMSSM is characterized by 19 free parameters. In pMSSMs, the first and second generation sfermions are set as degenerate, but to further constrain the model and reduce the parameter space, we also set the third generation sfermions as degenerate (except for the stau). Moreover we want the colored sparticles to be heavy and to make things not unnecessarily complicated, we only care about right-handed sleptons, therefore we set all squark masses, the left-handed sleptons and the gluino mass parameter M_3 to 3 TeV. Setting $m_A = 125$ GeV and setting the 3 trilinear couplings to tune the Standard Model-like Higgs to 125 GeV with mixing in the stop sector, we end up with only six parameters:

- The right-handed selectron and smuon masses, $m_{\tilde{e},R} = m_{\tilde{\mu},R}$
- The right-handed stau mass, $m_{\tilde{\tau},R}$
- The ratio of the vacuum expectation values of the two Higgs fields, $\tan \beta$
- The bino mass parameter, M_1
- The wino mass parameter, M_2
- The higgsino mass parameter, μ

Now we choose different values for these six parameters to generate five grids, the two parameters M_2 and μ are always given in a range, leading to a two-dimensional

plane of SUSY models, in which we will set exclusion limit contours, if no excess in data is observed. In the models that we call “DGemt” (for Direct Gaugino with light selectron, smuon and stau), the slepton masses are degenerate and small, leading to a variety of different final states. Three models are distinguished by the bino mass parameter M_1 . The higher this parameter, the smaller the sensitivity in final states with three leptons. In the “DGstau” (for Directo Gaugino with light stau), only the stau is light, while the selectron and the smuon are heavy, leading to an enhanced sensitivity in tau final states. Finally, in the “DGnoslep” (for Direct Gaugino with no light sleptons), all sleptons are heavy and decays via Standard Model particles like W , Z or Higgs dominate.

All distinctive parameters of the 5 pMSSMs are summarized as follows:

DGemt100

- $m_{\tilde{e},R} = m_{\tilde{\mu},R} = m_{\tilde{\tau},R} = \frac{1}{2} (m_{\tilde{\chi}_1^0} + m_{\tilde{\chi}_2^0})$
- $\tan \beta = 6$
- $M_1 = 100$ GeV
- $100 \text{ GeV} < M_2 < 700 \text{ GeV}$
- $100 \text{ GeV} < \mu < 700 \text{ GeV}$

DGemt140

- $m_{\tilde{e},R} = m_{\tilde{\mu},R} = m_{\tilde{\tau},R} = \frac{1}{2} (m_{\tilde{\chi}_1^0} + m_{\tilde{\chi}_2^0})$
- $\tan \beta = 6$
- $M_1 = 140$ GeV
- $100 \text{ GeV} < M_2 < 700 \text{ GeV}$
- $100 \text{ GeV} < \mu < 700 \text{ GeV}$

DGemt250

- $m_{\tilde{e},R} = m_{\tilde{\mu},R} = m_{\tilde{\tau},R} = \frac{1}{2} (m_{\tilde{\chi}_1^0} + m_{\tilde{\chi}_2^0})$
- $\tan \beta = 6$
- $M_1 = 250$ GeV
- $100 \text{ GeV} < M_2 < 500 \text{ GeV}$
- $100 \text{ GeV} < \mu < 500 \text{ GeV}$

DGstau75

- $m_{\tilde{e},R} = m_{\tilde{\mu},R} = 3 \text{ TeV}$
- $m_{\tilde{\tau},R} = \frac{1}{2} (m_{\tilde{\chi}_1^0} + m_{\tilde{\chi}_2^0})$
- $\tan \beta = 50$
- $M_1 = 75$ GeV
- $100 \text{ GeV} < M_2 < 600 \text{ GeV}$
- $100 \text{ GeV} < \mu < 600 \text{ GeV}$

DGnoslep

- $m_{\tilde{e},R} = m_{\tilde{\mu},R} = m_{\tilde{\tau},R} = 3 \text{ TeV}$
- $\tan \beta = 10$
- $M_1 = 50$ GeV
- $100 \text{ GeV} < M_2 < 500 \text{ GeV}; \text{ asymptotic point at } M_2 = 3000 \text{ GeV}$
- $100 \text{ GeV} < \mu < 500 \text{ GeV}; \text{ asymptotic point at } \mu = 3000 \text{ GeV}$

Simplified models The simplified models considered in this analysis address only $\tilde{\chi}_1^\pm \tilde{\chi}_2^0$ associated production. $\tilde{\chi}_1^\pm$ and $\tilde{\chi}_2^0$ are assumed to be degenerate. They are wino-like while the LSP $\tilde{\chi}_1^0$ is bino-like, this way the $\tilde{\chi}_1^\pm \tilde{\chi}_2^0$ production cross-section is the largest among the direct electroweakino processes. Assumptions are also made on certain slepton masses, all the other masses are set to be heavy; they are not taken into account.

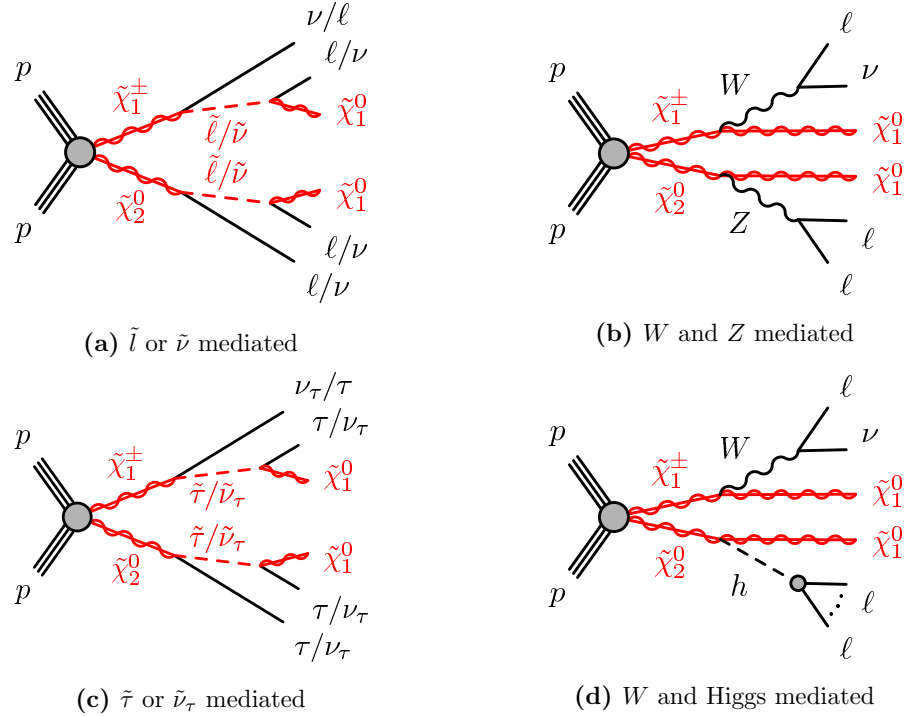


Figure 24: The Feynman diagrams for the four $\tilde{\chi}_1^\pm \tilde{\chi}_2^0$ simplified models. $\tilde{\chi}_1^\pm$ and $\tilde{\chi}_2^0$ are always degenerate. The dashed line in (d) depicts the inclusion of decays via intermediate particles, like $\tau\tau$, WW or ZZ .

$\tilde{\ell}_L$ mediated The left-handed sleptons are considered light and degenerate, the $\tilde{\chi}_1^\pm \tilde{\chi}_2^0$ decay happens via intermediate $\tilde{\ell}_L$ as depicted in Figure 24a. The $\tilde{\ell}_L$ masses are set to $m_{\tilde{\ell},L} = \frac{1}{2}(m_{\tilde{\chi}_1^0} + m_{\tilde{\chi}_2^0})$. The branching ratio of the $\tilde{\chi}_1^\pm$ into $\tilde{\ell}\tilde{\nu}_L$ and into $\tilde{\ell}_L\nu$, as well as the branching ratio of the $\tilde{\chi}_2^0$ into $\tilde{\ell}\tilde{\ell}_L$ and into $\tilde{\nu}_L\nu$ are all set to 0.5.

WZ mediated All slepton masses are heavy, the branching ratio of the charginos and neutralinos to the WZ gauge bosons is 1. The Feynman diagram for this simplified model can be seen in Figure 24b.

$\tilde{\tau}_L$ mediated In the $\tilde{\tau}_L$ mediated simplified model, \tilde{e} and $\tilde{\mu}$ are heavy, but $\tilde{\tau}$ and $\tilde{\nu}_\tau$ are set to $m_{\tilde{\tau}} = m_{\tilde{\nu}_\tau} = \frac{1}{2}(m_{\tilde{\chi}_1^0} + m_{\tilde{\chi}_2^0})$. The branching ratio of the $\tilde{\chi}_1^\pm$ into $\tilde{\tau}\tilde{\nu}_\tau$ and into $\tilde{\tau}\nu_\tau$ and of the $\tilde{\chi}_2^0$ into $\tau\tilde{\tau}$ and into $\nu_\tau\tilde{\nu}_\tau$ are all set to 0.5. The Feynman diagram of the decay via $\tilde{\tau}_L$ can be seen in Figure 24c.

Wh mediated In the Wh mediated simplified model, the slepton masses are all heavy. The $\tilde{\chi}_1^\pm$ decay always to a W and the $\tilde{\chi}_2^0$ always to a Higgs boson.

The Higgs mass is assumed to be 125 GeV. It can decay to $\ell\ell$ via $\tau\tau$, WW or ZZ as depicted in Figure 24d, where the various decay chains of the Higgs are illustrated with three dots.

The cross-sections of the four simplified models can be seen in Figure 25.

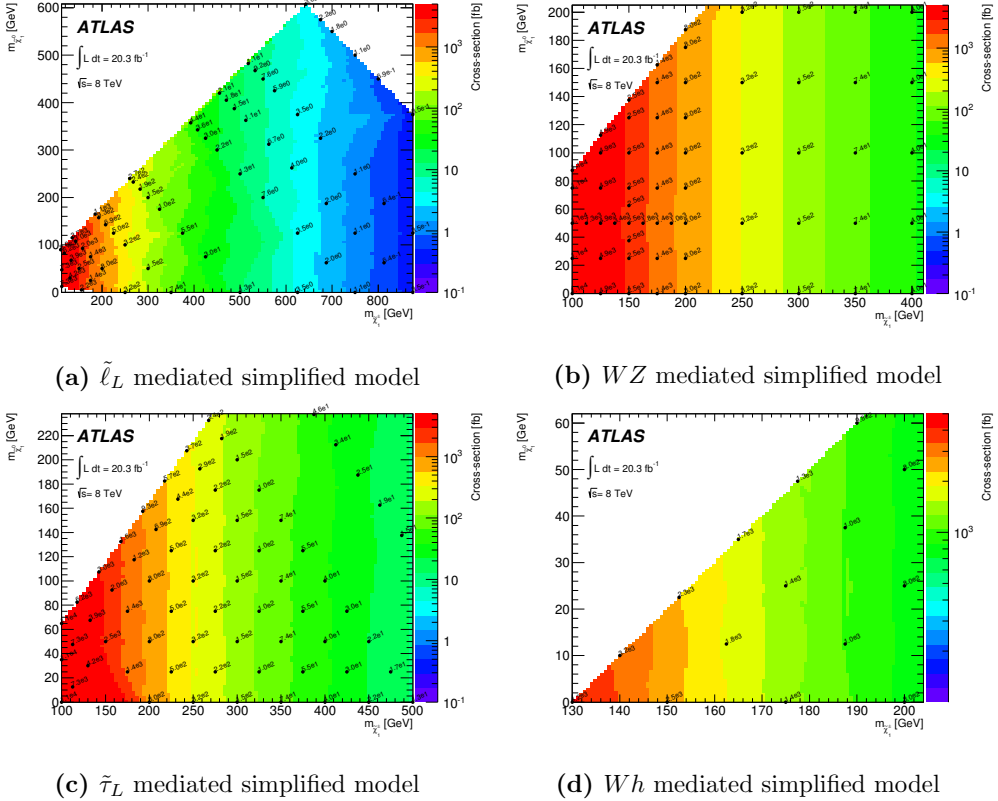


Figure 25: The cross-sections of the four simplified models, given in fb. The figures also show the granularity of the grid.

4.3 Irreducible background

Several Standard Model processes can lead to a multilepton final state. We distinguish between irreducible and reducible processes. A process is called irreducible, when all three leptons are prompt and genuinely isolated, i.e. coming from a W , Z or Higgs decay.

Reducible background has at least one lepton that is non-prompt or not genuinely isolated. It could originate either from a semi-leptonic decay of a b or c quark, from mis-identified light flavour jets or from conversion leptons from photon radiation.

Irreducible background processes with three leptons in the final state are divided into WZ , ZZ , top + V (where V is either W or Z), VVV (sometimes called tribosons) and processes including Higgs. Irreducible background processes are derived purely from Monte Carlo.

Reducible backgrounds with possibly noticeable contributions in a three lepton final state are $t\bar{t}$, single t , $V + \text{jets}$ and $V + \gamma$. These processes are described in Section 4.4. Ultimately, they are measured in data with the Matrix Method as described in Section 4.7.

All background processes and the Monte Carlo generators used are briefly described in the following paragraphs. The cross-sections shown in the tables below are leading order (LO) in perturbation theory, the k -factors to derive the next to leading order (NLO) cross-sections are given if available, it holds that $\sigma_{NLO} = k \cdot \sigma_{LO}$. On certain samples, filters are applied to reduce the size of the samples. These filters are explained in the text. The filter efficiencies are given in the tables. The filter efficiency is defined as ratio of the number of events passing a generator filter cut over the total number of events. The total integrated luminosities of the samples are also given in the tables, all samples are normalized to the same luminosity given by the delivered data of the experiment.

All Monte Carlo samples used in this analysis are produced using the ATLAS Underlying Event Tune 2B based detector simulation [65]. Different combinations of generators are used for the background. They are described in the following section. As PDF set, CT10 [66] is used for MC@NLO and Powheg samples, while ALPGEN and MADGRAPH were generated using CTEQ6L1. The signal samples are generated with HERWIG++ [67] using CTEQ6L1.

WZ Figure 26 shows diagrams of possible contributions of the WZ background to a final state with 3 leptons and E_T^{miss} . Both gauge bosons can be off-shell. Instead of a Z , there could also be a (possibly off-shell) γ , in Figure 26 this is depicted by Z/γ^* , for simplicity I will refer to this background process always as WZ , omitting the fact that the Z boson could also be a photon.

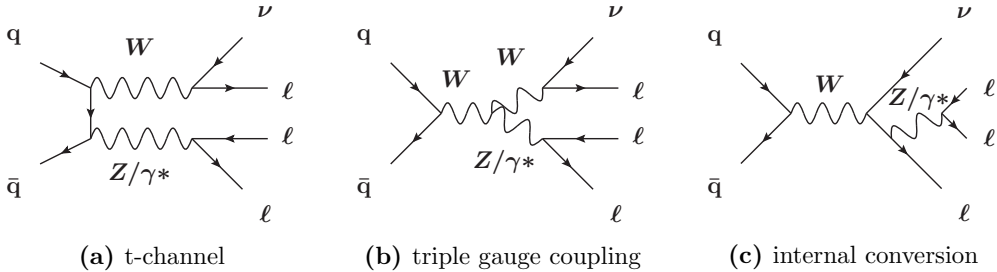


Figure 26: Diagrams contributing to the WZ background with a final state of 3 leptons and E_T^{miss} .

In most regions considered in this analysis, WZ is the most important irreducible background. Simulated processes are generated with the NLO generator Powheg [68], showering is done with Pythia8 [69]. Leptonic decays of the gauge bosons are enforced to increase efficiency, the branching ratios are incorporated into the LO cross-sections. On generator level a filter is applied to request two leptons, either electrons or muons (e/μ filter in Table 2) or to request any two charged leptons ($e/\mu/\tau$ filter). In these filters, the transverse momentum of the light lepton is required to be $p_t^{e,\mu} > 5$ GeV, while the transverse momentum of the hadronically decaying τ is required to be $p_t^{\tau} > 15$ GeV. A filter is also applied to request $m_Z > 4$ GeV. A possible overlap between samples has been taken into account and has been included in the filter efficiencies. Table 2 show the LO cross-sections, the k -factors, the filter efficiencies and the integrated luminosities of the WZ samples.² The WZ samples are normalized to the cross-sections obtained from *Monte Carlo for Fem-*

²The Powheg WZ samples carry the wrong filename and unfortunately, this is propagated to many analyses. The W^+ and W^- labels are mixed up. The signs in Table 2 are correct.

tobarn (*MCFM*), a program to calculate cross-sections for various femtobarn-level processes at hadron-hadron colliders [70, 71].

The difference in Table 2 in the cross-sections in spite of lepton universality comes from different mass windows in which the invariant mass of the same flavour opposite sign lepton pair is required to be. This cuts away a different amount of the overwhelming Drell Yan background at low γ^* invariant masses. After reconstruction and requesting a p_T of the lepton in the GeV range, this effect cancels.

In previous rounds of this analysis, the WZ background has been simultaneously fitted in a WZ enriched control region and in the signal region. Fit results have always shown that WZ is excellently described by Monte Carlo, for simplicity this method is subsequently dropped in this round and WZ is now - as any other irreducible background - taken directly from Monte Carlo. A normalization factor to the luminosity of the LHC data is applied.

Process (ID)	σ [pb]	k -factor	filter efficiency	$\int \mathcal{L} dt$ [fb^{-1}]
$WZ (e^+ \bar{\nu}_e e^+ e^-) [e/\mu] (129477)$	1.41	1.122	0.29	408.6
$WZ (e^+ \bar{\nu}_e \mu^+ \mu^-) [e/\mu] (129478)$	0.94	1.122	0.35	512.6
$WZ (e^+ \bar{\nu}_e \tau^+ \tau^-) [e/\mu] (129479)$	0.17	1.122	0.17	2325.6
$WZ (\mu^+ \bar{\nu}_\mu e^+ e^-) [e/\mu] (129480)$	1.40	1.122	0.29	412.4
$WZ (\mu^+ \bar{\nu}_\mu \mu^+ \mu^-) [e/\mu] (129481)$	0.95	1.122	0.35	505.4
$WZ (\mu^+ \bar{\nu}_\mu \tau^+ \tau^-) [e/\mu] (129482)$	0.17	1.122	0.17	2300.6
$WZ (\tau^+ \bar{\nu}_\tau e^+ e^-) [e/\mu] (129483)$	1.40	1.122	0.14	336.2
$WZ (\tau^+ \bar{\nu}_\tau \mu^+ \mu^-) [e/\mu] (129484)$	0.94	1.122	0.18	395.5
$WZ (\tau^+ \bar{\nu}_\tau \tau^+ \tau^-) [e/\mu] (129485)$	0.17	1.122	0.06	1683.5
$WZ (e^- \nu_e e^+ e^-) [e/\mu] (129486)$	0.98	1.144	0.30	570.7
$WZ (e^- \nu_e \mu^+ \mu^-) [e/\mu] (129487)$	0.64	1.144	0.35	736.3
$WZ (e^- \nu_e \tau^+ \tau^-) [e/\mu] (129488)$	0.11	1.144	0.16	3697.9
$WZ (\mu^- \nu_\mu e^+ e^-) [e/\mu] (129489)$	0.94	1.144	0.30	596.2
$WZ (\mu^- \nu_\mu \mu^+ \mu^-) [e/\mu] (129490)$	0.65	1.144	0.35	722.8
$WZ (\mu^- \nu_\mu \tau^+ \tau^-) [e/\mu] (129491)$	0.11	1.144	0.16	3685.5
$WZ (\tau^- \nu_\tau e^+ e^-) [e/\mu] (129492)$	0.94	1.144	0.15	479.5
$WZ (\tau^- \nu_\tau \mu^+ \mu^-) [e/\mu] (129493)$	0.64	1.144	0.19	557.2
$WZ (\tau^- \nu_\tau \tau^+ \tau^-) [e/\mu] (129494)$	0.11	1.144	0.06	2648.3
$WZ (e^+ \bar{\nu}_e \tau^+ \tau^-) [e/\mu/\tau] (179385)$	0.17	1.122	0.163	2382.4
$WZ (\mu^+ \bar{\nu}_\mu \tau^+ \tau^-) [e/\mu/\tau] (179386)$	0.17	1.122	0.164	2367.0
$WZ (\tau^+ \bar{\nu}_\tau e^+ e^-) [e/\mu/\tau] (179387)$	1.40	1.122	0.053	228.2
$WZ (\tau^+ \bar{\nu}_\tau \mu^+ \mu^-) [e/\mu/\tau] (179388)$	0.94	1.122	0.058	309.5
$WZ (\tau^+ \bar{\nu}_\tau \tau^+ \tau^-) [e/\mu/\tau] (179389)$	0.17	1.122	0.198	498.1
$WZ (e^- \nu_e \tau^+ \tau^-) [e/\mu/\tau] (179390)$	0.11	1.144	0.151	3912.0
$WZ (\mu^- \nu_\mu \tau^+ \tau^-) [e/\mu/\tau] (179391)$	0.11	1.144	0.152	3882.4
$WZ (\tau^- \nu_\tau e^+ e^-) [e/\mu/\tau] (179392)$	0.94	1.144	0.057	310.5
$WZ (\tau^- \nu_\tau \mu^+ \mu^-) [e/\mu/\tau] (179393)$	0.64	1.144	0.066	396.4
$WZ (\tau^- \nu_\tau \tau^+ \tau^-) [e/\mu/\tau] (179394)$	0.11	1.144	0.183	819.7

Table 2: WZ samples used in this analysis. Given are the LO cross-sections, the k -factors, the filter efficiencies and the integrated luminosities per sample. The leptons in the square brackets indicate the applied Powheg filter. All samples are generated with Powheg and showered with Pythia8.

The production cross-section of the WZ process at the LHC has been measured with the ATLAS detector for both a centre-of-mass energy of $\sqrt{s} = 7$ TeV [72] and

$\sqrt{s} = 8$ TeV [73]. Both measurements have shown good agreement with the Standard Model expectation.

ZZ The second important diboson background is ZZ . When both Z 's decay into charged leptons, usually all four leptons fall into the acceptance of the detector. But they could also be outside the fiducial volume, be mismeasured as a jet or be too soft to be detected (especially if it's a τ). This leads to a final state with three or even less leptons. Another possibility leading to such a final state is, when one Z decays to τ 's and subsequently one τ decays hadronically and is not reconstructed as a τ . ZZ production can happen via quark or gluon fusion, the corresponding Feynman diagrams are depicted in Figure 27.

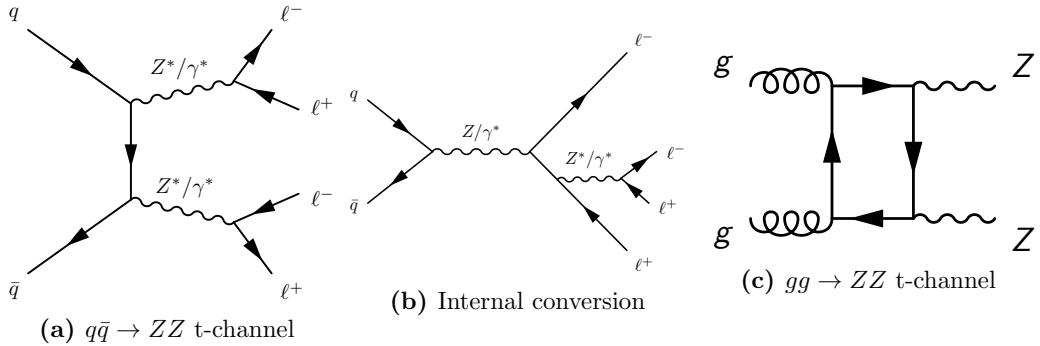


Figure 27: Diagrams contributing to the ZZ production. Not shown are u-channel diagrams.

The samples used are shown in Table 3. For the ZZ 's produced via quark annihilation, **Powheg** is used as a generator with the same filters applied as for WZ while **Pythia8** is used for showering. ZZ events produced via gluon fusion are generated without filter using **JIMMY** [74].

The ZZ production cross-section at the LHC has been measured with the ATLAS detector for centre-of-mass energies of $\sqrt{s} = 7$ TeV [75, 76] and also $\sqrt{s} = 8$ TeV [77, 78]. All measurements show good agreement with the Standard Model expectation.

top + V The top + V background consists mostly of $t\bar{t}$ and either a W or a Z , but single top together with a Z contributes as well. A top quark almost always decays to Wb , the subsequent immediate decay of the W bosons can lead to a final state with two leptons (see Figure 28). The mesons formed by the b quarks can decay leptonically as well, but being non-prompt, $t\bar{t}$ is a reducible process. However, if accompanied by a vector boson, this can become a proper irreducible process. For simplicity all samples are assumed to be irreducible, it has been shown that the effect is small.

The samples used are listed in Table 4. They have been produced with **ALPGEN** [79], except for top + Z and $t\bar{t} + WW$ where at the time of the analysis was carried out no samples from **ALPGEN** were available, henceforth **MADGRAPH** [80] has been used. In any way, **Pythia8** was used for the fragmentation and for the hadronisation. The choice of **ALPGEN** over **MADGRAPH** lies in the more general simulation of the Z boson: While in **MADGRAPH** the Z is always on-shell, in **ALPGEN** the Z mass considered is between 5 GeV and 8 TeV.

The V in these samples has to be understood as $V + \text{jets}$.

Process (ID)	σ [pb]	k -factor	filter efficiency	$\int \mathcal{L} dt$ [fb^{-1}]
ZZ ($4e$) [e/μ] (126937)	0.08	1	0.91	15767.9
ZZ ($2e2\mu$) [e/μ] (126938)	0.18	1	0.83	11018.7
ZZ ($2e2\tau$) [e/μ] (126939)	0.18	1	0.58	10760.7
ZZ (4μ) [e/μ] (126940)	0.08	1	0.91	15680.7
ZZ ($2\mu2\tau$) [e/μ] (126941)	0.18	1	0.59	10669.5
ZZ (4τ) [e/μ] (126942)	0.08	1	0.11	36813.5
ZZ ($2e2\tau$) [$e/\mu/\tau$] (178411)	0.18	1	0.084	7487.0
ZZ ($2\mu2\tau$) [$e/\mu/\tau$] (178412)	0.18	1	0.082	7627.3
ZZ (4τ) [$e/\mu/\tau$] (178413)	0.08	1	0.324	12045.4
$gg2ZZ$ ($4e$) (116601)	$1.54 \cdot 10^{-3}$	1	1	58631.9
$gg2ZZ$ (4μ) (116602)	$1.54 \cdot 10^{-3}$	1	1	58631.9
$gg2ZZ$ ($2e2\mu/2e2\tau/2\mu2\tau$) (179396)	2.79×10^{-3}	1	0.95594	26246.0

Table 3: ZZ samples used in this analysis. Given are the LO cross-sections, the k -factors, the filter efficiencies and the integrated luminosities per sample. The leptons in the square brackets indicate the applied **Powheg** filter. All samples are generated with **Powheg** and showered with **Pythia8**, except the $gg2ZZ$ samples which are generated with **JIMMY**.

Process	σ [pb]	k -factor	$\int \mathcal{L} dt$ [fb^{-1}]
$t\bar{t} + W(\ell\nu)$ Np0 (174233)	$2.7 \cdot 10^{-2}$	1.255	443.4
$t\bar{t} + W(\ell\nu)$ Np1 (174234)	$1.8 \cdot 10^{-2}$	1.255	443.0
$t\bar{t} + W(\ell\nu)$ Np2 (174235)	$9.5 \cdot 10^{-3}$	1.255	421.0
$t\bar{t} + W(\ell\nu)$ Np3+ (174236)	$6.5 \cdot 10^{-3}$	1.255	366.1
$t\bar{t} + W(qq)$ Np0 (174238)	$5.4 \cdot 10^{-2}$	1.255	440.1
$t\bar{t} + W(qq)$ Np1 (174239)	$3.7 \cdot 10^{-2}$	1.255	432.9
$t\bar{t} + W(qq)$ Np2 (174240)	$1.9 \cdot 10^{-2}$	1.255	415.5
$t\bar{t} + W(qq)$ Np3+ (174241)	$1.3 \cdot 10^{-2}$	1.255	390.4
$t\bar{t} + Z(\nu\nu)$ Np0 (174243)	$1.1 \cdot 10^{-2}$	1.277	740.0
$t\bar{t} + Z(\nu\nu)$ Np1 (174244)	$1.0 \cdot 10^{-2}$	1.277	390.0
$t\bar{t} + Z(\nu\nu)$ Np2 (174245)	$6.9 \cdot 10^{-3}$	1.277	226.0
$t\bar{t} + Z(\nu\nu)$ Np3+ (174246)	$5.0 \cdot 10^{-3}$	1.277	236.3
$t\bar{t} + Z(\ell\ell)$ Np0 (174248)	$7.9 \cdot 10^{-3}$	1.277	496.6
$t\bar{t} + Z(\ell\ell)$ Np1 (174249)	$7.7 \cdot 10^{-3}$	1.277	511.7
$t\bar{t} + Z(\ell\ell)$ Np2 (174250)	$5.3 \cdot 10^{-3}$	1.277	443.8
$t\bar{t} + Z(\ell\ell)$ Np3+ (174251)	$4.0 \cdot 10^{-3}$	1.277	393.7
top + $Z(\ell\ell)$ Wt -channel (179991)	$4.1 \cdot 10^{-3}$	1	24212.8
top + $Z(\ell\ell)$ st -channel (179992)	$30.0 \cdot 10^{-2}$	1	3214.4
$t\bar{t} + WW$ (119583)	$9.19 \cdot 10^{-4}$	1.34	10880

Table 4: top + V samples used in this analysis. Given are the LO cross-sections, the k -factors and the integrated luminosities per sample. All top + V samples are generated with **ALPGEN**, the top + Z and the $t\bar{t} + WW$ samples are generated with **MADGRAPH**. Np gives the number of partons.

VVV Processes with three gauge bosons (tribosons) are rather rare at the LHC. Nonetheless, they can account for a substantial source of background in some signal regions. Simulated tribosons samples are WWW , ZWW and ZZZ (see Table 5). In a tribosons event, for every W that is replaced by a Z , the cross-section goes substantially down. The ZZW process is small enough and can be safely ignored, it was not added as at the time the analysis was carried out, this sample was missing. The contribution from ZZZ can be neglected as well but since there exists an official sample, it was used for completeness.

The tribosons samples are generated with **MADGRAPH** at LO in QCD, the k -factor is taken from [81]. Showering is done with **Pythia8**.

Process	σ [fb]	k -factor	$\int \mathcal{L} dt$ [fb $^{-1}$]
WWW (167006)	5.10	1.5	6533
ZWW (167007)	1.55	1.5	21500
ZZZ (167008)	0.33	1.5	101000

Table 5: Tribosons samples used in this analysis. Given are the LO cross-sections, the k -factors and the integrated luminosities per sample.

Higgs A Higgs boson with an assumed mass of $m_h = 125$ GeV has become a visible background in three lepton signal regions. Higgs decays to $\tau\tau$, WW^* and ZZ^* producing leptons are considered. These are expected to be the most important sources of Higgs background. Five production mechanisms are included: Gluon fusion (ggF), vector boson fusion (VBF), associated Wh production, associated Zh production and associated $t\bar{t} + h$ production. Not all combinations of Higgs production and decays are considered, a summary of the samples used can be found in Table 6.

The Higgs decays do not all produce an irreducible three lepton final state, but for simplicity, all of them are treated as such.

4.4 Reducible Background

This section describes the reducible background samples used in this analysis. Some of the simulated Monte Carlo samples have a relatively low integrated luminosity, but since they are ultimately measured in data by the Matrix Method (see Section 4.7), this is not crucial.

$t\bar{t}$ This is by far the most important reducible background in almost all our regions. The two decaying top quarks provide two leptons and two b -quarks, the latter have a good chance to decay leptonically and be misidentified as prompt leptons, see Figure 28 for a Feynman diagram of a $t\bar{t}$ decay. To suppress this background, all signal regions veto events with b -tagged jets.

The $t\bar{t}$ sample used is generated with **Powheg**, showered with **Pythia8**. A filter excludes events when both W bosons decay hadronically to reduce the size of the sample. The characteristics of this sample is summarized in Table 7.

single t Single top provides a small background in regions requesting three leptons, since only one prompt and genuinely isolated lepton is present, but due to its high production cross-section at the LHC, it can become substantial. As we will learn in Section 4.7 about the estimation of the reducible background with the Matrix

Process	Higgs decay	σ [pb]	filter efficiency	$\int \mathcal{L} dt$ [fb $^{-1}$]
ggF (161005)		$4.41 \cdot 10^{-1}$	0.491	2311
VBF (161055)		$3.56 \cdot 10^{-2}$	0.507	16600
WH (161105)	$H \rightarrow WW^* -> \ell\nu\ell\nu$	$1.50 \cdot 10^{-1}$	0.105	1270
ZH (161155)		$8.90 \cdot 10^{-3}$	1.000	2250
$t\bar{t} + h$ (161305)	$H \rightarrow WW^*$	$2.80 \cdot 10^{-2}$	1.000	6700
ggF (160655)		$4.67 \cdot 10^{-2}$	0.446	2400
VBF (160705)		$3.77 \cdot 10^{-3}$	0.446	17800
WH (160755)	$H \rightarrow ZZ^* -> \ell\ell\nu\nu$	$1.67 \cdot 10^{-3}$	0.446	26900
ZH (160805)		$1.04 \cdot 10^{-2}$	0.040	48000
$t\bar{t} + h$ (169072)	$H \rightarrow ZZ^*$	$3.44 \cdot 10^{-3}$	1.000	29100
ggF (160155)		$5.26 \cdot 10^{-3}$	1.000	37000
VBF (160205)		$4.25 \cdot 10^{-4}$	1.000	460000
WH (160255)	$H \rightarrow ZZ^* -> 4\ell$	$1.88 \cdot 10^{-4}$	1.000	520000
ZH (160305)		$1.04 \cdot 10^{-2}$	0.010	780000
WH (160505)	$H \rightarrow ZZ^* -> \ell\ell q\bar{q}$	$1.84 \cdot 10^{-2}$	0.141	7700
ZH (160555)		$1.04 \cdot 10^{-2}$	0.141	13600
ZH (161675)	$H \rightarrow \tau^{lep}\tau^{lep}$	$2.49 \cdot 10^{-2}$	0.124	160000
ttH (161708)		$8.23 \cdot 10^{-3}$	0.124	29400
ZH (161686)	$H \rightarrow \tau^{lep}\tau^{had}$	$2.49 \cdot 10^{-2}$	0.456	44000
ttH (161719)		$8.23 \cdot 10^{-3}$	0.456	8000
ZH (161697)	$H \rightarrow \tau^{had}\tau^{had}$	$2.49 \cdot 10^{-2}$	0.420	47800
ttH (161730)		$8.23 \cdot 10^{-3}$	0.420	8700
ZH (167418)	$H \rightarrow \mu\mu$	$8.67 \cdot 10^{-5}$	1.00	346000

Table 6: Higgs samples used in this analysis. Given are the cross-sections, the filter efficiencies and the integrated luminosities per sample. The gluon fusion and the vector boson fusion samples are generated with **Powheg** and showered with **Pythia8**, all other samples are generated and showered with **Pythia8**. The cross-sections are calculated at NNLO QCD and NLO electroweak precision, except for $pp \rightarrow t\bar{t} + h$, which is calculated at NLO QCD precision [82].

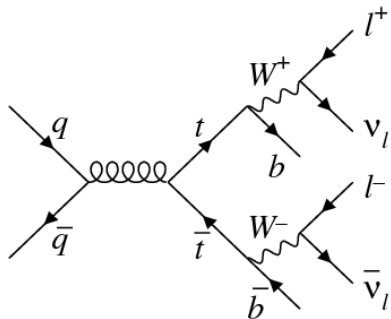


Figure 28: Feynman diagram of $t\bar{t}$ production with subsequent decay into a final state with two charged leptons and two b quarks. The leading diagram at the LHC involves gluon fusion rather than $q\bar{q}$ annihilation.

Process	σ [pb]	k -factor	filter efficiency	$\int \mathcal{L} dt$ [fb $^{-1}$]
$t\bar{t}$ (117050)	252.89	1	0.54	545.6

Table 7: $t\bar{t}$ sample used in this analysis. Given is the LO cross-section, the k -factor, the filter efficiency and the integrated luminosity of the sample. It was generated with **Powheg**, showered with **Pythia8**. The filter requests at least one leptonically decaying W boson.

Method, events with one isolated and prompt lepton and two non-signal leptons do occur. Generators used for single top are **AcerMC** and **MC@NLO** [83], fragmentation and hadronisation are performed with **HERWIG** [84], using **JIMMY** for the underlying event. The samples are summarized in Table 8.

Process	σ [pb]	k -factor	$\int \mathcal{L} dt$ [fb $^{-1}$]
Wt MC@NLO (108346)	20.66	1.08	78.9
t -channel $e\nu$ AcerMC (117360)	8.60	1.10	31.6
t -channel $\mu\nu$ AcerMC (117361)	8.60	1.1	31.6
t -channel $\tau\nu$ AcerMC (117362)	8.60	1.1	31.6
s -channel $e\nu$ MC@NLO (108343)	0.56	1.07	278.9
s -channel $\mu\nu$ MC@NLO (108344)	0.56	1.07	278.9
s -channel $\tau\nu$ MC@NLO (108345)	0.56	1.07	278.7

Table 8: Single top samples used in this analysis. Given are the LO cross-sections, the k -factors and the integrated luminosities per sample. For all samples, **HERWIG** is used for fragmentation and hadronisation while **JIMMY** is used for the underlying event.

$V + \text{jets}$ $V + \text{jets}$ consists of $Z + \text{jets}$, $W + \text{jets}$ and $\gamma^* + \text{jets}$, but for simplicity I will omit the γ^* . When talking about $Z + \text{jets}$, $Z/\gamma^* + \text{jets}$ is meant. $Z + \text{jets}$ is - besides $t\bar{t}$ - the other large contribution to our reducible background. In Figure 29 one of many $Z + \text{jets}$ production is illustrated.

$Z + \text{jets}$ samples are generated with **ALPGEN**, while **Pythia** is used the showering. The Z is requested to decay leptonically, its mass is $60 \text{ GeV} < M_Z < 2 \text{ TeV}$ and $30 \text{ GeV} < M_Z < 2 \text{ TeV}$ if the jets are b -tagged jets. Additional samples generated by **ALPGEN** and showered by **JIMMY** are produced to cover the mass range $10 \text{ GeV} < M_Z < 60 \text{ GeV}$. Overlapping events in these samples have been removed. A list of all samples can be found in Table 9.

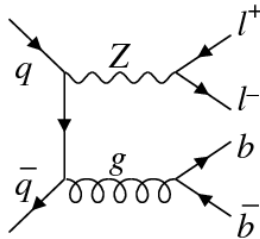


Figure 29: One of many diagrams that contribute to $Z + \text{jets}$ events.

Process	σ [pb]	$\int \mathcal{L} dt$ [fb $^{-1}$]	Process	σ [pb]	$\int \mathcal{L} dt$ [fb $^{-1}$]
$Z + \text{jets}$ (low mass)			$Z + \text{jets}$ (low mass)		
(ee+Np0) (117650)	848.29	7.8	(ee+Np0) (146830)	4154.56	0.2
(ee+Np1) (117651)	207.21	6.4	(ee+Np1) (146831)	129.99	2.3
(ee+Np2) (117652)	69.44	5.8	(ee+Np2) (146832)	63.05	7.5
(ee+Np3) (117653)	18.36	6.0	(ee+Np3) (146833)	13.50	10.7
(ee+Np4) (117654)	4.64	6.5	(ee+Np4) (146834)	3.09	11.7
(ee+Np5) (117655)	1.42	7.1	(ee+Np5) (146835)	0.83	96.2
($\mu\mu$ +Np0) (117660)	848.31	7.8	($\mu\mu$ +Np0) (146840)	4154.44	0.2
($\mu\mu$ +Np1) (117661)	207.46	6.4	($\mu\mu$ +Np1) (146841)	129.93	2.3
($\mu\mu$ +Np2) (117662)	69.39	5.8	($\mu\mu$ +Np2) (146842)	63.01	7.5
($\mu\mu$ +Np3) (117663)	18.40	6.0	($\mu\mu$ +Np3) (146843)	13.43	10.8
($\mu\mu$ +Np4) (117664)	4.61	6.5	($\mu\mu$ +Np4) (146844)	3.11	11.7
($\mu\mu$ +Np5) (117665)	1.41	7.1	($\mu\mu$ +Np5) (146845)	0.83	96.2
($\tau\tau$ +Np0) (117670)	848.24	7.8	($\tau\tau$ +Np0) (146850)	4154.44	0.2
($\tau\tau$ +Np1) (117671)	207.48	6.4	($\tau\tau$ +Np1) (146851)	129.92	2.3
($\tau\tau$ +Np2) (117672)	69.18	5.9	($\tau\tau$ +Np2) (146852)	63.00	7.5
($\tau\tau$ +Np3) (117673)	18.30	6.0	($\tau\tau$ +Np3) (146853)	13.53	10.7
($\tau\tau$ +Np4) (117674)	4.66	6.4	($\tau\tau$ +Np4) (146854)	3.10	70.5
($\tau\tau$ +Np5) (117675)	1.39	7.2	($\tau\tau$ +Np5) (146855)	0.83	96.6
$Z + bb$			$Z + cc$		
(ee+Np0) (110817)	9.49	15.8	(ee+Np0) (110805)	17.83	33.9
(ee+Np1) (110818)	3.82	21.0	(ee+Np1) (110806)	8.51	30.5
(ee+Np2) (110819)	1.34	33.5	(ee+Np2) (110807)	3.58	30.7
(ee+Np3) (110820)	0.58	7.8	(ee+Np3) (110808)	1.39	28.8
($\mu\mu$ +Np0) (110821)	9.49	15.8	($\mu\mu$ +Np0) (110809)	17.84	33.6
($\mu\mu$ +Np1) (110822)	3.79	21.1	($\mu\mu$ +Np1) (110810)	8.49	31.2
($\mu\mu$ +Np2) (110823)	1.35	33.5	($\mu\mu$ +Np2) (110811)	3.58	32.2
($\mu\mu$ +Np3) (110824)	0.60	8.3	($\mu\mu$ +Np3) (110812)	1.39	28.9
($\tau\tau$ +Np0) (110825)	9.48	15.8	($\tau\tau$ +Np0) (110813)	17.84	33.6
($\tau\tau$ +Np1) (110826)	3.81	21.0	($\tau\tau$ +Np1) (110814)	8.50	31.2
($\tau\tau$ +Np2) (110827)	1.35	33.3	($\tau\tau$ +Np2) (110815)	3.59	32.1
($\tau\tau$ +Np3) (110828)	0.58	8.6	($\tau\tau$ +Np3) (110816)	1.38	29.0
$W + \text{jets}$			$W + c / W + cc / W + bb$		
(e ν +Np0) (117680)	9300.36	0.4	(Np0) (126601)	867.46	7.5
(e ν +Np1) (117681)	2047.68	1.2	(Np1) (126602)	313.46	6.6
(e ν +Np2) (117682)	619.05	6.1	(Np2) (126603)	81.88	6.4
(e ν +Np3) (117683)	167.62	6.0	(Np3) (126604)	18.77	5.9
(e ν +Np4) (117684)	42.63	5.9	(Np4) (126605)	5.43	3.7
(e ν +Np5) (117685)	12.99	5.4			
($\mu\nu$ +Np0) (117690)	9296.48	0.4	(Np0) (126606)	163.53	7.8
($\mu\nu$ +Np1) (117691)	2049.06	1.2	(Np1) (126607)	164.23	6.4
($\mu\nu$ +Np2) (117692)	618.67	6.1	(Np2) (126608)	92.31	5.7
($\mu\nu$ +Np3) (117693)	167.44	6.0	(Np3) (126609)	41.07	4.1
($\mu\nu$ +Np4) (117694)	42.67	6.0			
($\mu\nu$ +Np5) (117695)	13.05	5.0	(Np0) (110801)	59.73	8.0
($\tau\nu$ +Np0) (117700)	9299.11	0.4	(Np1) (110802)	52.05	6.9
($\tau\nu$ +Np1) (117701)	2050.20	1.2	(Np2) (110803)	27.06	6.5
($\tau\nu$ +Np2) (117702)	618.64	6.1	(Np3) (110804)	14.32	3.5
($\tau\nu$ +Np3) (117703)	167.43	6.0			
($\tau\nu$ +Np4) (117704)	42.59	5.9			
($\tau\nu$ +Np5) (117705)	13.19	4.9			

Table 9: $V + \text{jets}$ samples used in this analysis. Given are the NNLO cross-sections and the integrated luminosities per sample. Np gives the number of partons.

$V + \gamma$ The $V + \gamma$ samples used are listed in Table 10. They are generated with **Sherpa**, the gauge boson is enforced to decay leptonically.

Process (ID)	σ [pb]	$\int \mathcal{L} dt$ [fb $^{-1}$]
$W\gamma (e\nu)$ Sherpa (126739)	163.11	11.0
$W\gamma (\mu\nu)$ Sherpa (126742)	162.74	11.0
$W\gamma (\tau\nu)$ Sherpa (126856)	162.00	11.0
$Z\gamma (ee)$ Sherpa (145161)	32.26	37.1
$Z\gamma (\mu\mu)$ Sherpa (145162)	32.32	37.1
$Z\gamma (\tau\tau)$ Sherpa (126854)	32.33	30.9

Table 10: $V + \gamma$ samples used in this analysis. Given are the LO cross-sections and the integrated luminosities per sample.

Other backgrounds like $W + \text{jets}$ or QCD have been checked and are not a noteworthy contribution to a final state with three leptons.

4.5 Preselection

Before finding a suitable region to search for a SUSY signal, a preselection has to be carried out to ensure that only qualitatively immaculate events pass the selection. The preselection consists of a Good Runs List (GRL) cut, a trigger cut and further quality cuts. These cuts are described below.

GRL The Good Runs List is used for reporting which parts of beam and detector operated at which conditions. Data used for this analysis was recorded in 2012 by ATLAS and satisfied the GRL for which LHC declared stable beam and ATLAS operated at nominal conditions. The data collected in this period corresponds to a total integrated luminosity of (20.3 ± 0.57) fb $^{-1}$.

Trigger The ATLAS Trigger system is described in Section 2.4. Triggers used in this analysis consist of single isolated lepton triggers and double lepton triggers. For an event to be considered, it needs to pass any of these triggers. A summary of the triggers can be found in Table 11. A trigger count as passed, when the corresponding trigger has been fired, a trigger matching lepton has been identified and is within $\Delta R = \sqrt{(\Delta\phi)^2 + (\Delta\eta)^2} < 0.15$ of the relevant trigger object and when the trigger matching lepton has an offline threshold as given in Table 11. The offline threshold has been introduced to avoid the turn-on curve of the trigger efficiency and to ensure the lepton is on the plateau, where a trigger efficiency can effectively be measured. Overlap between triggers have been removed.

Since our τ object definition is looser as the one used by hadronic τ triggers, no τ triggers are used, to not bias the efficiencies and fake rates.

To derive the trigger efficiencies, a Z mass tag and probe method is used. In this method, two leptons that form a same flavour opposite sign pair and are within 10 GeV of the Z mass are selected. The one passing the single isolated lepton trigger is the tagged lepton, the other the probed lepton. The probed lepton is tested against the di-lepton trigger. The efficiencies derived in data and in Monte Carlo are in good agreement, a conservative systematic uncertainty of 5 % is applied to account for the largest differences seen between the trigger in data and its simulation.

Trigger efficiencies in the plateau are typically between 80 % and 100 % for electrons and 60 % to 80 % for muons, depending on the topology of the event. For an event with three leptons, the trigger efficiency is close to 100 %, going down to ≈ 80 % for $1\mu 2\tau$ events.

Trigger	Detail	offline threshold [GeV]
Single Isolated e	EF_e24vhi_medium1	25
Single Isolated μ	EF_mu24i_tight	25
Double e	EF_2e12Tvh_loose1 EF_e24vh_medium1_e7_medium1	14,14 25,10
Double μ	EF_2mu13 EF_mu18_tight_mu8_EFFS	14,14 18,10
Combined $e\mu$	EF_e12Tvh_medium1_mu8 EF_mu18_tight_e7_medium1	14,10 18,10

Table 11: Triggers used in this analysis. Offline threshold is a cut applied on the p_T of the lepton passing the trigger to avoid the turn-on curve and ensure the lepton is on the plateau of the trigger efficiency.

Quality cuts Quality cuts are applied to all events in all analysis before the selection takes place. Those quality cuts veto events, where certain instrumental effects have been observed and a reconstruction of the event is likely to be faulty. A list of the quality cuts can be found in [60]. The quality cuts are common to all analysis and comply with the official recommendation from the ATLAS SUSY Working Group for release 17 of the ATLAS software and release 00-03-04 of SUSYTOOLS. At the time of the analysis, release 17 was the latest release of the ATLAS software for physics use, later releases are targeting at functionality to process xAOD’s, a common data format still in development [85]. SUSYTOOLS-00-03-04 was released for physics use in July 2013, later releases did not affect our analysis with one exception: The b-tagging calibration changed in release 00-03-06, but studies have shown that our analysis would be affected by this update at the sub percent level so it was decided to drop.

4.6 Object definition

For all objects, a baseline and a signal object is defined. A signal object is always a baseline object with additional requirements, the details of the selections are described below. A genuine three lepton event has exactly three baseline and exactly three signal leptons. A veto on additional baseline-only leptons ensures orthogonality to other final states which might define their signal objects differently, while the object defintion for baseline objects must be consistent with other SUSY analyses, to facilitate for a possible combination.

The distinction between baseline and signal objects will be picked up again in Section 4.7, since the Matrix Method is using both baseline and signal objects.

All objects are subject to an overlap removal before defining them as baseline objects. The details of the overlap removal are described below.

Baseline electrons To select baseline electrons, the medium++ recommendation from the EGamma group is applied, see [86] for details. The efficiency of this selection is ≈ 85 %. Additional requirements are:

- $p_T > 10$ GeV after the electron p_T has been smeared in Monte Carlo to reproduce resolution effects of the calorimeters.
- Cluster pseudorapidity $|\eta^{cl}| < 2.47$ to account for fiducial volume of detector.
- Pass EGamma algorithm optimised for high p_T electrons.
- Don't cross regions connected to dead optical transmitters.
- Separated from other baseline electrons or muons by $\Delta R > 0.3$.
- Pass overlap removal scheme (see at the end of this section).

Signal electrons A series of quality cuts are applied as outlined in [86] under the tight++ criterion. Baseline electrons that are passing this selection and the additional requirements listed below are called signal electrons. The additional requirements are:

- $\frac{|d_0|}{\sigma(d_0)} < 5$, where d_0 is the transversal impact parameter, the distance between the point of closest approach of a track and primary vertex in the (x, y) plane. σ denotes the standard deviation. This cut is introduced to suppress $t\bar{t}$, since non-prompt leptons originating from a b -meson decay often exceed this value as studies have shown.
- $|z_0 \sin(\theta)| < 0.4$ mm, where z_0 is the longitudinal impact parameter, defined as the z position of the track at the point of closest approach to the primary vertex. This cut has been introduced to suppress $t\bar{t}$ as well.
- $\frac{p_{T,\text{cone}30}}{p_T} < 0.16$, where $p_{T,\text{cone}30}$ is the transverse momentum of all other tracks within a cone $\Delta R < 0.3$ around the electron track. This is the first isolation criterion.
- $\frac{p_{T,\text{cone}30}^{\text{corrected}}}{p_T} < 0.18$, where $p_{T,\text{cone}30}^{\text{corrected}}$ is the corrected $p_{T,\text{cone}30}$, where the correction term is given by $A \cdot n_{\text{vert}}$, where A is 20.15 MeV for data and 17.94 MeV for Monte Carlo and N_{vert} is the number of vertices with at least 5 tracks. This is the second isolation criterion.

Baseline muons All muons are reconstructed by statistically combining tracks from the inner detector with tracks from the muon spectrometer (*STACO* muons, see also Section 2.3). Before the combination, the p_T 's from the simulated muons are smeared to simulate instrumental effects of the detector. Quality requirement for the baseline muons is loose, as defined by the Muon Combined Performance Group [87]. Additional requirements are:

- $p_T > 10$ GeV after smearing in Monte Carlo.
- Pseudorapidity $|\eta| < 2.5$.
- Several hit requirements in the inner detector.
- Separated from other baseline electrons or muons by $\Delta R > 0.3$.
- Pass overlap removal scheme (see at the end of this section).

Signal muons For a baseline muon to become a signal muon, it needs to pass the additional requirements:

- $\frac{|d_0|}{\sigma(d_0)} < 3$ to suppress background from $t\bar{t}$.
- $|z_0 \sin(\theta)| < 1$ mm.

- $\frac{p_{T,\text{cone}30}^{\text{corrected}}}{p_T} < 0.12$ where $p_{T,\text{cone}30}^{\text{corrected}}$ is defined as is the case for electrons but with $A = 10.98$ MeV for data and $A = 6.27$ MeV for Monte Carlo.

Baseline taus When talking about taus, only hadronically decayed taus are meant. Leptonically decaying taus are reconstructed as the light leptons they decayed to. Baseline taus are reconstructed via signal jets defined below. To distinguish taus from QCD jets, a boosted decision tree algorithm is used for the reconstruction [48], achieving an efficiency of $\approx 50\%$. Requirements for a baseline tau are:

- $p_T > 20$ GeV.
- $|\eta| < 2.5$.
- 1 or 3 associated tracks.
- $q = \pm 1$.
- Pass overlap removal scheme (see at the end of this section).

Signal taus A signal tau is simply a baseline tau with the additional requirement that it needs to pass the medium tau identification.

Jets This analysis uses jets directly only by vetoing b -tagged jets, but also via the reconstruction of hadronically decaying taus and the overlap removal a dependency on the jet selection can enter in regions without any direct jet requirements. The anti- k_T jet algorithm with $\Delta R = 0.4$ is used to reconstruct jets [46]. Baseline jets have $p_T > 20$ GeV and pseudorapidity $|\eta| < 4.5$. For signal jets the requirement on the pseudorapidity is reduced to $|\eta| < 2.5$. For jets with $p_T < 50$ GeV and $|\eta| < 2.4$, an additional cut of $\text{JVF} > 0.5$ is required, where JVF is the Jet Vertex Fraction, a quantity which measures the probability that a jet originated from a particular vertex. Jet selection based on this discriminant is shown to be insensitive to the contributions from simultaneous uncorrelated soft collisions that occur during pile-up [88]. Additional cuts on jet properties are required to suppress instrumental background.

Jets containing b -hadrons are called b -tagged jets. They are signal jets which pass the MV1 algorithm, a neural network based algorithm that uses different b -tagging algorithms as input [89]. The efficiency of the average b -tagging efficiency is $\approx 80\%$.

E_T^{miss} The missing transverse energy E_T^{miss} is introduced in Section 2.3. E_T^{miss} is an excellent experimental signature for R-parity conserving SUSY models, since a stable LSP would lead to a sizable E_T^{miss} , while in the Standard Model, only neutrinos leave the detector undetected. This analysis requires rather moderate cuts on E_T^{miss} , since requesting three leptons is already a strong discriminator between background and signal, therefore also low E_T^{miss} scenarios are considered, which are favored by compressed scenarios, i.e. scenarios where the mass difference between $\tilde{\chi}_1^\pm$ and $\tilde{\chi}_1^0$ are rather small, henceforth leading only to low E_T^{miss} .

Overlap removal All objects are subject to an overlap removal, to qualify them as baseline objects. A single physical object can be reconstructed by several algorithms, leading to more than one reconstructed objects. This “overlap” constitutes itself that the objects are close by to each other in terms of $\Delta R = \sqrt{(\Delta\phi)^2 + (\Delta\eta)^2}$.

Deciding in which order the different steps of the overlap removal are performed is not straight-forward. The ordering chosen in this analysis is very similar to most

other SUSY analysis, an effort to harmonize all of them is on-going. The different steps of the overlap removal and its ordering can be found in Table 12.

Step	Objects involved	Removed object	ΔR
1	2 electrons	lower p_T electron	< 0.05
2	electron & jet	jet	< 0.2
3	electron & tau	tau	< 0.2
4	muon & tau	tau	< 0.2
5	electron & jet	electron	< 0.4
6	muon & jet	muon	< 0.4
7	electron & muon	both	< 0.01
8	2 muons	both	< 0.05
9	SFOS	both	< 12 GeV
10	signal tau & jet	jet	< 0.2

Step	Remove ...
1	... duplicated electrons with different clusters but shared tracks
2	... duplicated electrons in jet container
3	... duplicated electrons in tau container
4	... duplicated muons in tau container
5	... electrons within jets
6	... muons within jets
7	... muons undergoing bremsstrahlung
8	... muons with shared tracks
9	... lepton pairs from low mass decays
10	... duplicated taus in jet container

Table 12: Different steps of the overlap removal. Steps at the top are performed first. SFOS stands for same flavour opposite sign lepton pair.

4.7 Matrix Method

The irreducible background is taken from Monte Carlo. The reducible background, on the other hand, is estimated with the Matrix Method. The Matrix Method is described here only very briefly, for more information see [60].

The Matrix Method is used to estimate the reducible background, i.e. background where at least one lepton is non-prompt or not genuinely isolated, in the following called fake³, as opposed to real leptons, which are prompt and genuinely isolated.

Leptons are classified as real (R) or fake (F), but also depending on their reconstruction quality as tight (T) and loose but not tight (L). A lepton is called tight when it is classified as signal lepton, a loose but not tight lepton is a baseline lepton that fails the criterion for becoming a signal lepton. Both the selections for baseline and signal leptons are outlined in Section 4.6.

³The term fake lepton is misleading, fake leptons can be real leptons but coming from an non-prompt decay. A proper term for fake leptons would be “fake or non-prompt leptons”, for simplicity I will just call them fake.

The probability that a real lepton is tight is given by its real lepton identification efficiency ϵ ,

$$N_T = \epsilon \cdot N_R , \quad (28)$$

where N_T denotes the number of events with a lepton that is classified as tight and N_R the number of events with a real lepton. Similarly, N_L is the number of events with a loose lepton failing the tight criterion and N_F is the number of events with a fake lepton.

The probability that a fake lepton is tight is given by its fake rate f ,

$$N_T = f \cdot N_F . \quad (29)$$

Subsequently, the probabilities for identifying a real lepton as loose but not tight, and a fake lepton as loose but not tight are given by

$$N_L = (1 - \epsilon) \cdot N_R \text{ and} \quad (30)$$

$$N_L = (1 - f) \cdot N_F . \quad (31)$$

This holds for events with one lepton in question. It is generalized to events with three leptons, but assuming that the leading lepton is always real, which according to Monte Carlo studies is the case for more than 95 % of the events. Hence, we describe only the second leading and third leading lepton with the Matrix Method. As described above, we count the number of events, but now using two indexes, to describe the quality of the second leading lepton (first index) and the quality of the third leading lepton (second index). This then leads to a 4×4 matrix equation

$$\begin{pmatrix} N_{TT} \\ N_{TL} \\ N_{LT} \\ N_{LL} \end{pmatrix} = M \cdot \begin{pmatrix} N_{RR} \\ N_{RF} \\ N_{FR} \\ N_{FF} \end{pmatrix} , \quad (32)$$

with

$$M = \begin{pmatrix} \epsilon_1 \epsilon_2 & \epsilon_1 f_2 & f_1 \epsilon_2 & f_1 f_2 \\ \epsilon_1 (1 - \epsilon_2) & \epsilon_1 (1 - f_2) & f_1 (1 - \epsilon_2) & f_1 (1 - f_2) \\ (1 - \epsilon_1) \epsilon_2 & (1 - \epsilon_1) f_2 & (1 - f_1) \epsilon_2 & (1 - f_1) f_2 \\ (1 - \epsilon_1) (1 - \epsilon_2) & (1 - \epsilon_1) (1 - f_2) & (1 - f_1) (1 - \epsilon_2) & (1 - f_1) (1 - f_2) \end{pmatrix} , \quad (33)$$

where ϵ_1 and f_1 correspond to the real efficiency and the fake rate of the second leading lepton and ϵ_2 and f_2 to the one of the third leading lepton.

Ultimately we are interested in the contribution of the reducible background in a three lepton final state. Since we are only selecting tight leptons, we are looking for the contamination of at least one fake lepton getting selected. Using Equation (32), this is given by

$$N_{Fake \rightarrow TT} = \epsilon_1 f_2 \cdot N_{RF} + f_1 \epsilon_2 \cdot N_{FR} + f_1 f_2 \cdot N_{FF} \quad (34)$$

To apply Equation (34), the real efficiency ϵ and the fake rate f have to be measured.

The real efficiency ϵ is measured per flavour in data and corrected by a scale factor which is given as the ratio of the efficiency measured in data over the efficiency measured in Monte Carlo. The scale factor has been measured to be consistent with 1. The measurement is binned in p_T , $|\eta|$ and the number of vertices to account for possible dependencies. Since no significant dependency on these variables has been found, the binning

has been dropped. The measurement itself is carried out with a tag-and-probe method in a dedicated $Z \rightarrow ll$ control region, using the full 8 TeV dataset.

The measurement of the fake rate f is a bit more elaborate, since f depends on the type of the fake candidate (heavy flavour, light flavour or conversion) and on its originating process. As a consequence, fake rates measured in one region are not directly applicable to another region, since the composition of the processes may change. The fake rates are obtained per type and per process but in the end a weighted averaged fake rate is used, given by

$$f_{\text{region}}^{\ell} = \sum_{i,j} (sf^i \times R_{\text{region}}^{ij} \times f^{ij}) . \quad (35)$$

The index i runs over the fake types, i.e. light flavour, heavy flavour and conversion, and j is the index of the originating process, i.e. top, $Z + \text{jets}$, $V + \gamma$ and diboson processes. sf^i is the scale factor described above, assumed to be independent of the process category j ; R_{region}^{ij} the fraction of type i originating from process j in a certain region and f^{ij} the fake rate of type i from process j .

5 Binning the signal region

Signal regions are signal enriched regions in parameter space where an expected SUSY signal can be distinguished from the otherwise overwhelming Standard Model background. In this section I describe the optimization of the signal region and its binning. Binning the signal region here means to cut it in multiple smaller regions, all of them orthogonal and altogether cover the complete signal region. The newly established regions are called bins. They will be statistically combined in the end. The binning of the signal region with the optimization process is my major, new contribution to the field.

The optimization on the signal grids is outlined in Section 5.1, the basic selection used before binning the region is described in Section 5.2. In Section 5.3 the variables used to bin the signal region are presented and in Section 5.4 the approach itself is outlined. Section 5.5 describes in detail the optimization of the cuts to maximize the sensitivity of the binned signal region. Section 5.6 explains the $3\ell Z$ veto and Section 5.7 gives a detailed breakdown of the expected signal region events in every bin.

The signal region I will be talking about is called SR0 τ_a in [2] and [60]. I will call it just *the* signal region, since this thesis focus mainly on this region. There are other regions defined. For completeness I define them in Section 5.8. For the final results, I combine my bins with the signal regions defined in 5.8.

Sections 5.9 and 5.10 describe the systematic uncertainties on the Standard Model background and show acceptance and efficiency.

5.1 Signal grid optimization

I considered 9 different signal grids, as outlined in Section 4.2. An optimization on all of them would be laborious and complex, since a signal region per SUSY process would need to be defined. For the $\tilde{\ell}_L$ mediated simplified model, one signal region might suffice, but for the WZ mediated simplified model, different physics for different mass parameters is expected. For example, if $m_{\tilde{\chi}_1^\pm} - m_{\tilde{\chi}_1^0} \gg m_Z$, high energetic on-shell gauge bosons and high energetic LSP's are expected (see Figure 24b for a Feynman diagram of this process), a good signal region therefore would cut at e.g. high E_T^{miss} and/or high lepton p_T 's. But for $m_{\tilde{\chi}_1^\pm} - m_{\tilde{\chi}_1^0} \ll m_Z$ (sometimes referred to as “compressed scenarios”), the gauge bosons would be highly off-shell decaying to soft leptons and soft LSP's, a cut on high E_T^{miss} or high lepton p_T 's would cut away most of the signal. The situation is even more tricky for $m_{\tilde{\chi}_1^\pm} - m_{\tilde{\chi}_1^0} \approx m_Z$, the signal will decay via on-shell gauge bosons, making the distinction between signal and background extremely difficult. Using one signal region in this grid, a poor sensitivity would be achieved.

The situation with the difficult WZ like region can be illustrated with a history of the exclusion contours in this grid, all data collected with the ATLAS detector at the LHC. In Figure 30, the three published exclusion contours that I made for earlier analyses can be seen. Figure 30a used collected data corresponding to 4.7 fb^{-1} at $\sqrt{s} = 7 \text{ TeV}$ [5], Figure 30b is the exclusion contour corresponding to 13.0 fb^{-1} at $\sqrt{s} = 8 \text{ TeV}$ [6] and Figure 30c was carried out with the full 8 TeV dataset corresponding to 20.7 fb^{-1} [8]⁴.

In Figure 30a and Figure 30b, two signal regions have been used, both requesting events with a same flavour opposite sign pair but one not more than 10 GeV away from

⁴The full 8 TeV dataset was preliminarily analyzed to correspond to 20.7 fb^{-1} , a subsequent more detailed analysis estimated the total luminosity to be 20.3 fb^{-1} , the uncertainty on the luminosity was reduced from 3.6 % to 2.8 %. Analysis published before spring 2013 quote a luminosity of 20.7 fb^{-1} , later published analyses quote a luminosity of 20.3 fb^{-1} .

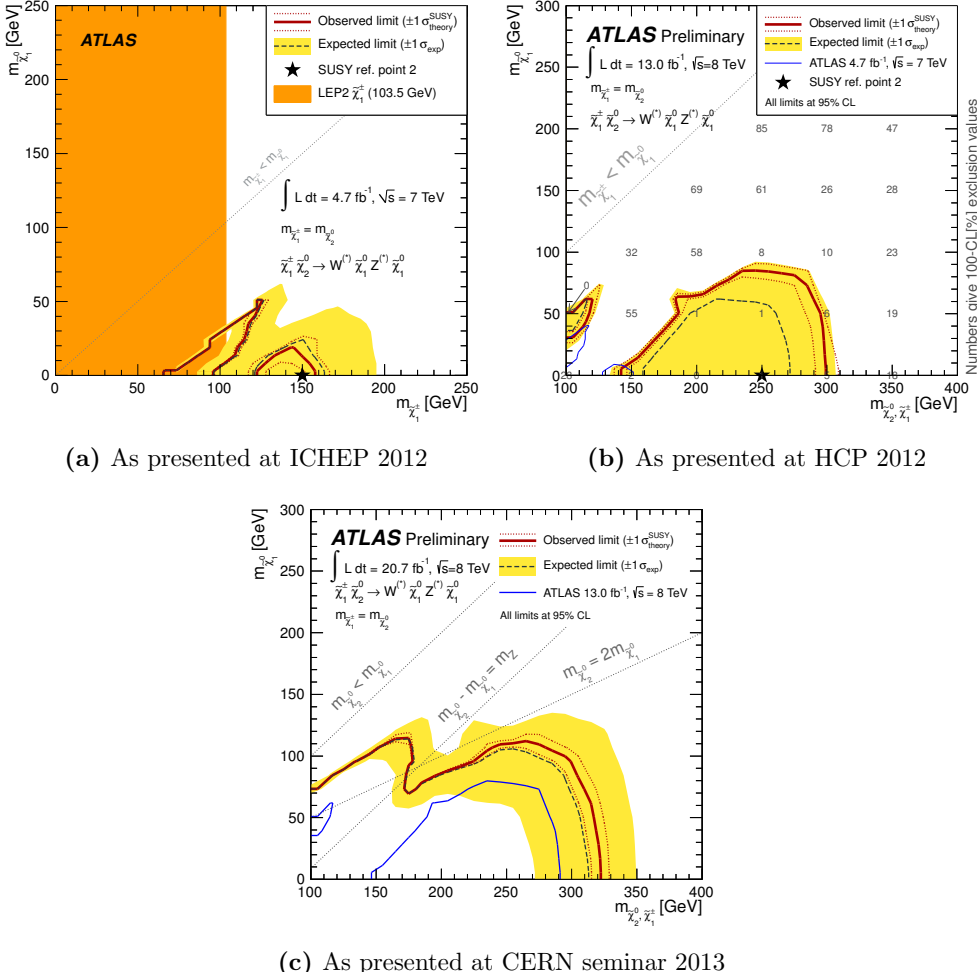


Figure 30: Different exclusion contours for the WZ mediated simplified model as presented at different physics conferences. Exclusion is at the 95 % confidence level. The yellow band around the expected limit shows the $\pm 1\sigma$ variations of the expected limit. Both expected and observed exclusion limits include all uncertainties except theoretical signal uncertainties. The dotted lines around the observed exclusion limit correspond to the $\pm 1\sigma$ variations of these theoretical uncertainties on the signal cross-section. Linear interpolation is used to account for the discrete nature of the signal grids.

the Z mass, while the other vetoing on-shell Z 's. Further cuts on E_T^{miss} , m_T (see Section 5.3 for a definition), p_T and the number of b -tagged jets have been imposed. The exclusion contour is clearly distinct in two regions, one in the region where $m_{\tilde{\chi}_1^\pm} - m_{\tilde{\chi}_1^0} > m_Z$ and one where $m_{\tilde{\chi}_1^\pm} - m_{\tilde{\chi}_1^0} < m_Z$. In Figure 30c, 6 orthogonal signal regions have been defined, which I statistically combined to get the resulting exclusion contours. Even with 6 signal regions, the difficult WZ -like region with $m_{\tilde{\chi}_1^\pm} - m_{\tilde{\chi}_1^0} \approx m_Z$ is clearly visible.

The optimization of 6 different signal regions is laborious. Considering that these 6 regions only target one specific grid and that the physics in the pMSSMs is even more complex, I searched for a more general way to maximize sensitivity in the most grids possible.

Since the SUSY models considered give rise to a rich variety of different physics processes and many possible final states, a general approach with many signal regions covering the largest possible parameter space is needed. These thoughts led me to the idea to take the whole parameter space after a basic selection and cut it in different regions (subsequently this procedure is called binning). The basic selection applied before the binning is described in the next section.

This approach is very general and leads to a good sensitivity in many different SUSY models, even if the signal regions have not been optimized for them. A pure optimization on a single grid may lead to a good sensitivity in this specific SUSY model, but it is very unlikely that this particular model is realized in nature due to the many parameters that are not known *a priori*. Therefore, a more general approach to scan for a wide range of different SUSY signals can cover a wider range of possible SUSY models. The downside of the binning approach is that with many bins, the discovery potential is smaller. When looking into many different bins, an upward fluctuation in observed data events is more likely to happen by pure chance (this is known as look-elsewhere effect). This has to be taken into account when calculating a global discovery p -value and in the very likely case that the SUSY signal will not be spread over the whole parameter space, the discovery sensitivity of the binned approach will be smaller than the one of a single signal region targeting this SUSY process. However, where SUSY is hiding is not known and many searches have been carefully carried out without seeing a signal anywhere. Therefore, even when having a smaller discovery potential, a scan of the whole parameter space makes sense to identify possibly interesting region. If such regions are found, a subsequent analysis can then concentrate on such regions with less general, but more specialized regions, enhancing again the discovery potential and reducing the look-elsewhere effect.

The signal region optimization, though fairly general, will still be applied to a certain grid. The pMSSM grids are not taken into account in this optimization, since these models are rather specific. The simplified models, on the other hand, are very general and make little assumptions on SUSY parameters while still describing a possible (though not complete) SUSY signal.

As a baseline selection for the binned signal region, three leptons are requested, while additional τ 's are vetoed. This selection has enough statistics to make a meaningful binning feasible. For the grids to be used as optimization benchmark, the WZ and ℓ_L mediated simplified models are used. The $\tilde{\tau}_L$ mediated simplified model will decay predominantly via τ 's, signal regions vetoing additional τ 's will therefore not have a good sensitivity. The Wh grid with its rich possible final states, on the other hand would be a valid choice, but since the Standard Model Higgs couples predominantly to heavier particles, a signal region with *light* leptons is not favored. The two remaining simplified models, the WZ mediated and the $\tilde{\ell}_L$ mediated are signal models where a great sensitivity in a pure light lepton signal region can be expected. Therefore, these two models are chosen to optimize

the signal region.

5.2 Basic selection

Before the signal region optimization is carried out, some basic selection cuts are applied. After removing events that do not pass the preselection outlined in Section 4.5, exactly three light baseline and exactly three light signal leptons have been requested, while events with additional τ 's are vetoed. Events with additional baseline leptons are vetoed to guarantee orthogonality with other analysis working groups looking at different final states and simplify a combination at a later stage. Additionally a same flavour opposite sign lepton pair is required, an $E_T^{\text{miss}} > 50 \text{ GeV}$ cut has been applied and all events with b -tagged jets have been vetoed. For the other signal regions that veto same flavour opposite sign lepton pairs or request at least one tau, see Section 5.8 or [2] for more details. The cut on E_T^{miss} at 50 GeV is moderate, to not lose sensitivity to compressed scenarios but to leave some room for validation regions. Finally, b -tagged events have been discarded to suppress background from $t\bar{t}$, while our signal does not give rise to large b -jet multiplicities. The totality of all events passing this loose selection is called signal region, but see Section 5.6 for an additional event veto on certain events in certain bins.

5.3 Discriminating variables

After the basic selection, the remaining region is binned into an a priori unknown number of bins. The variables used are

E_T^{miss} Missing transverse energy is an excellent discriminator for SUSY events. Since only neutrinos are not detected by ATLAS, a high E_T^{miss} is an indicator of an unknown process. See Section 4.6 for a definition of E_T^{miss} .

m_{SFOS} SFOS stands for same flavour opposite sign lepton pair, m_{SFOS} is the invariant mass of this lepton pair. If combinatorics allow for more than one such pair, the one with its mass closest to the Z mass is chosen. Since a same flavour opposite sign lepton pair is requested, m_{SFOS} is well defined for every event in the signal region. This variable mimics the mass of the Z boson.

m_T The transverse mass is defined as the invariant mass transverse to the beam direction formed by the third lepton - the one not forming m_{SFOS} - and E_T^{miss}

$$m_T = \sqrt{2 \cdot E_{T,l} \cdot E_T^{\text{miss}} (1 - \cos(\phi))}, \quad (36)$$

where ϕ is the angle between the third lepton and the transverse momentum \vec{p}_T^{miss} . This variable mimics the transverse part of the reconstructed W boson mass.

Other variables like the scalar sum of all lepton p_T 's, called L_T , the transverse scalar sum of all objects (without E_T^{miss}), S_T , or the transverse scalar sum of all objects including E_T^{miss} , called the effective mass m_{eff} , were also considered. Since E_T^{miss} , m_{SFOS} and m_T have responded well to the optimizations and already have previously proven to be good discriminator between background and signal [8], these variables have not been used in the final optimization process.

In the use of other variables there is a potential to improve the binning method. This has been omitted since a good set of variables have already been found and the binning method implies many open statistical questions whose feasibility first had to be proven.

A possible study could involve lepton p_T 's, jet properties, angles between objects or more sophisticated quantities, like e.g. the razor [90]. Important is that the variables used are not only strong discriminators from signal and background, but also that they are not overly correlated.

In the beginning, more than just the three variables were considered: A first approach was to split the region in two, where one region has a Z request (typically called the Z window) and the other a Z veto. A Z request means $|m_{\text{SFOS}} - m_Z| < 10 \text{ GeV}$ and a Z veto $|m_{\text{SFOS}} - m_Z| > 10 \text{ GeV}$. A rationalization for this approach is the number of background events inside the Z window, which is much larger than outside. Inside the Z window, a finer binning could be realised, while outside one could work with a coarser binning. The two regions were then further divided into three bins in m_T , three bins in L_T and four bins in E_T^{miss} . This led to $2 \cdot 3 \cdot 3 \cdot 4 = 72$ bins. A quick calculation of the expected CL_s (see Section 8.4) values showed great improvement with respect to the signal regions used in the three lepton analysis for the last publication [8]. The calculation of the expected CL_s values has to be taken with a grain of salt, since all the statistical subtleties with the binning method were omitted. Nevertheless, this brief study showed the potential of a binned signal region. It also revealed a few difficulties that one had to be aware of, which subsequently lead to a limit on the number of bins considered in this round.

Since a finer binning leads to an enhanced sensitivity, why not let the number of bins go towards infinity? What limits the number of bins? There are a few limitations:

The Matrix Method (see Section 4.7) is used to determine the reducible background contribution from data in every bin separately, many bins increase the workload and at some point low statistics will become an issue.

The more bins, the more CPU intensive the calculation of the CL_s values becomes. Moreover, finer binning leads to less populated bins, if the number of expected background events in certain bins is below a certain threshold, the approximation of the asymptotic formulae (see Section 8.5 and [91]) would not be valid anymore, a calculation with Monte Carlo pseudo-experiments becomes necessary. Such calculations is very time intensive, even on distributed computing systems.

These are technical limitations, but also conceptual limitations to an all too fine binning can be made. Ultimately, this leads to very low event multiplicities, the uncertainty due to limited Monte Carlo statistics would become comparable and even bigger as the event multiplicity itself. At some point the expectations are governed by limitations of the Monte Carlo statistics and fluctuations. No meaningful statement could be made about the probability of the observed data. A large local p -value would even be expected to observe by pure fluctuations.

These considerations lead to the limitation of 20 to 30 bins. In the end, 20 bins are used. But this is by no means the limit, a subsequent analysis could enhance this number.

5.4 Binning approach

Having chosen 3 variables to do the binning, there are still many options how to proceed. At first a binning in m_{SFOS} is conducted as follows:

$$\begin{aligned} 12 < m_{\text{SFOS}} < & 40 \\ 40 < m_{\text{SFOS}} < & 60 \\ 60 < m_{\text{SFOS}} < & 81.2 \\ 81.2 < m_{\text{SFOS}} < & 101.2 \\ 101.2 < m_{\text{SFOS}} < & \infty \end{aligned},$$

where all values are in GeV.

The reason why $m_{\text{SFOS}} > 12 \text{ GeV}$ always, is due to the overlap removal (see Table 12) where same flavour opposite sign lepton pairs with $m_{\text{SFOS}} < 12 \text{ GeV}$ are removed. A possible signal would drown in the overwhelming Drell-Yan background in this region. Although, if the SUSY spectrum is very compressed, the signal might hide exactly in the low m_{SFOS} region. A general approach like the binning will hardly be successful in such a case, a more sophisticated signal region, optimized for low mass differences then is advisable.

The binning in m_{SFOS} outlined above has been proven strong in earlier signal region optimizations (see [8]). The fourth bin is the Z window. From now on this binning in m_{SFOS} is fixed and will not be subject to optimizations. The background distribution in m_{SFOS} with the basic cuts outlined in Section 5.2 applied, is shown in Figure 31. Since the signal region binning optimization is done purely in Monte Carlo, all the figures about the optimization of the signal region contain purely Monte Carlo simulated events.

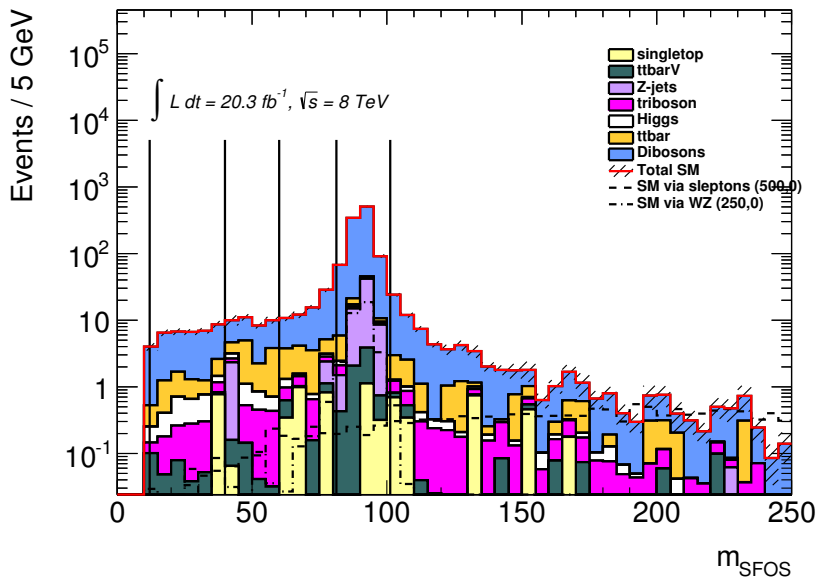


Figure 31: Background distribution in m_{SFOS} from Monte Carlo after a basic three lepton selection. Vertical black lines indicate bin edges. Two exemplary signal distributions are also shown.

The binning in m_{SFOS} leads to 5 slices in the parameter space. With one cut in m_T and one cut in E_T^{miss} we end up with a total of $5 \cdot 2 \cdot 2 = 20$ bins. These cuts can be carried out in different ways, as depicted in Figure 32. Consider only one slice in m_{SFOS} , now we could chose exactly one value in E_T^{miss} and exactly one value in m_T , this gives four bins, as shown in Figure 32a.

But one could also consider a more general approach, depicted in Figure 32b and Figure 32c, where only one cut is chosen in either E_T^{miss} or in m_T , but two in the other variable, one for the low E_T^{miss}/m_T region, and one for the high E_T^{miss}/m_T region. This is how the signal region optimization is conducted in the end. The method shown in Figure 32a is a special case of this method.

One could also consider another method to cut one m_{SFOS} slice into four bins, as depicted in Figure 32d, where the region is cut into two parts and the subsequent cuts

are only applied in one half of the region. This way of binning the signal region is in analogy with multivariate techniques, and is not considered during this round of signal region optimization.

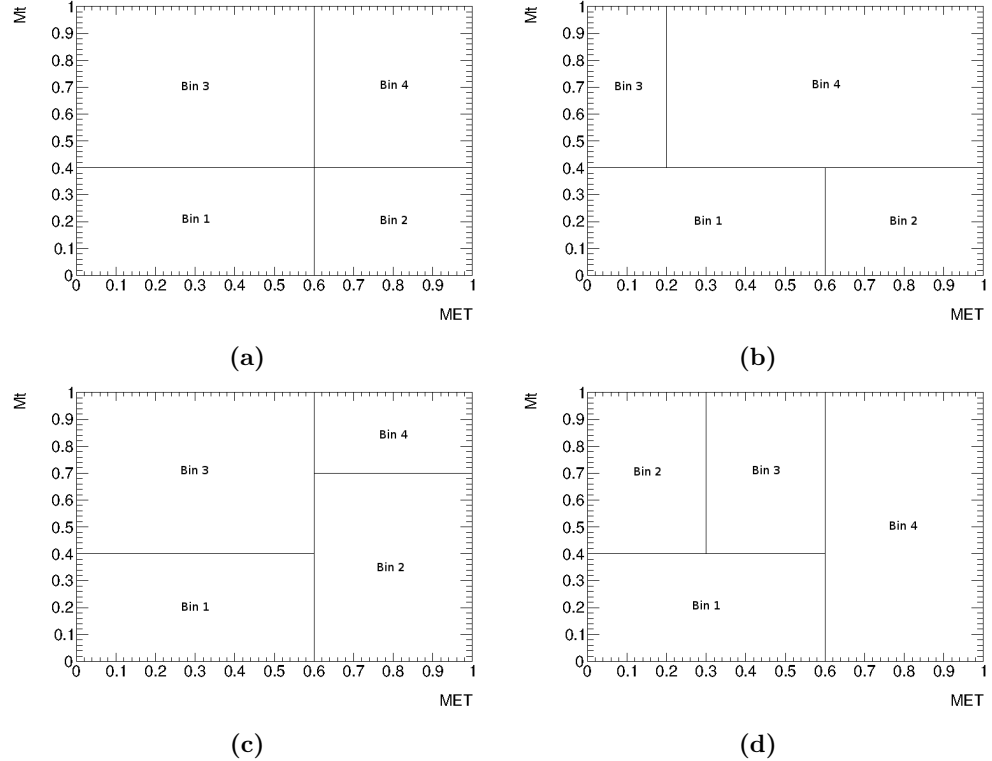


Figure 32: Different possibilities how a binning with one cut in m_T and one cut in E_T^{miss} inside an m_{SFOS} slice could be conducted. The axes are in arbitrary units.

5.5 Signal region optimization

In Section 5.1 it is outlined that the signal region optimization will be performed in the $\tilde{\ell}_L$ mediated simplified model and on the WZ mediated simplified model. A quick study to determine which m_{SFOS} slice has a good sensitivity in which grid showed, that the $\tilde{\ell}_L$ mediated simplified model has a good response to the high m_{SFOS} and high m_T masses and also to a high E_T^{miss} . Heavy sleptons produce copious events with high values for these parameters, while the backgrounds in these regions are rather low. The $m_{\text{SFOS}} > 101.2$ GeV slice proved to be much more sensitive than any other m_{SFOS} slice.

In the WZ mediated simplified model on the other hand, the SUSY particles decay via intermediate gauge bosons. Sensitivity in $m_{\text{SFOS}} > m_Z$ is not expected. All the other slices showed good sensitivity in particular parts of the grid space, the low m_{SFOS} slice for compressed scenarios close to the diagonal, the higher m_{SFOS} slices gradually moving towards a larger mass splitting with finally the m_{SFOS} slice in the Z window being very sensitive to the bulk region where $m_{\tilde{\chi}_1^\pm} \gg m_{\tilde{\chi}_1^0}$.

This mutual exclusiveness of sensitivity in the m_{SFOS} slices proved convenient for the signal region optimization: While the $m_{\text{SFOS}} > 101.2$ GeV slice is solely optimized in the $\tilde{\ell}_L$ mediated simplified model, all the other m_{SFOS} slices are optimized on the WZ

mediated simplified model.

With the optimization of the signal region, one means finding a global maximum for the sensitivity. This has been done with a scan of different binnings in a m_{SFOS} slice, i.e. a scan of the possible signal region cuts on E_T^{miss} and m_T , while keeping the m_{SFOS} cuts constant.

While optimizing the binned signal region, I realized that using the standard approach with the Z_N formula, which is defined below, is not adequate. With this method, only one bin at a time can be optimized, a combination is possible only very roughly and I decided that this rough approximation is not good enough. Hence I had to find another way of optimizing the binned signal region, for that I used a likelihood ratio approach, where a combination of regions can be achieved by multiplying their respective Poissonian terms.

In the next few paragraphs I will first describe the standard Z_N approach for optimizing signal regions and then show why its approximation is not good enough. After that I will introduce the likelihood ratio and explain why this approach leads to more accurate results. Then I outline the optimization process as it is carried out. I will not further use the Z_N formula.

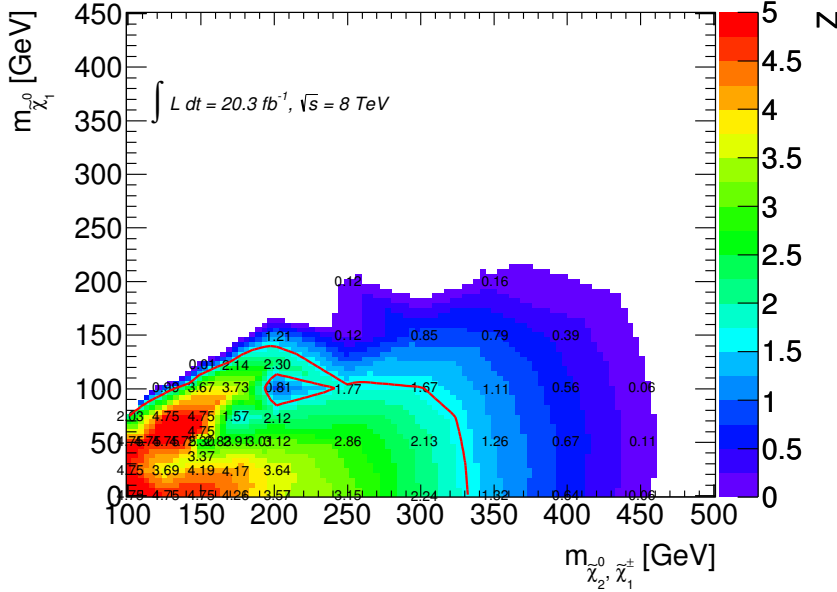
The significance of the sensitivity Z_N is the deviation from a background hypothesis in Gaussian standard deviation equivalents (see [92]). Z_N is defined as

$$Z_N = \sqrt{2}\text{erf}^{-1}(1 - 2p) = \Phi^{-1}(1 - p) , \quad (37)$$

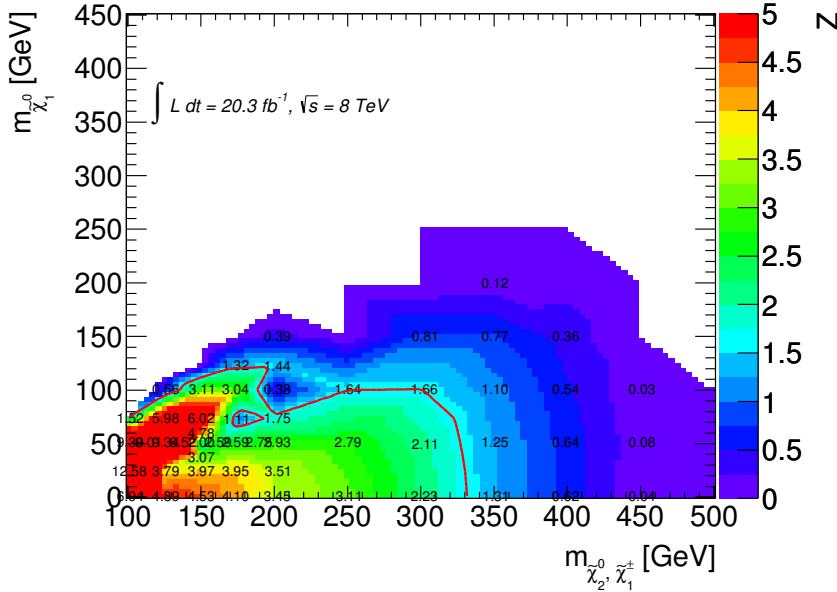
where erf^{-1} is the error function and p is the expected p -value for a given number of background events, signal events and an uncertainty on the number of background events. It is usually chosen to be 30 % or 50 %. The error function comes into play as the quantile (inverse) cumulative distribution function of the standard normal (Gaussian) distribution, denoted as Φ^{-1} . See Chapter 8 for a more detailed discussion of p -values, distributions or quantiles. This method has the advantage of being conceptually and computationally straight forward, omitting all the details and difficulties that a full-fledged profiled likelihood method would involve.

However, there are two fundamental weaknesses to this method: First, it cannot incorporate systematic uncertainties. Since, at this stage, this is only an optimization study and systematic uncertainties are not expected to differ largely over different regions in parameter space and therefore the incorporation of systematic uncertainties should not alter the conclusions, this flaw can be ignored. Second, it cannot easily combine different regions. While straight-forward in a likelihood approach, where additional Poissonian terms can be added by multiplication in the likelihood formula, this is not possible in the Z_N approach. A way to overcome this, is by adding the significances derived with Formula (37) in quadrature. This is an approximation and its validity is not clear. In order to validate this method, a comparison between a full-fledged profile likelihood calculation and the approximation using the Z_N formula (37) and combining the regions by adding them in quadrature is carried out.

The result is not conclusive: on the one hand, the exclusion shapes at $Z_N \approx 1.64\sigma$, which corresponds to an exclusion at the 95 % confidence level, are well reproduced. But looking at particular significances, they do not agree very well over the whole grid, as can be seen in Figure 33. In the bulk region, where $m_{\tilde{\chi}_1^\pm} \gg m_{\tilde{\chi}_1^0}$, the significances do agree pretty well, this is the region which is mainly driven by one bin. But in the difficult WZ like region, where $m_{\tilde{\chi}_1^\pm} - m_{\tilde{\chi}_1^0} \approx m_Z$, where many different regions add to the sensitivity, the significances are not well reproduced. At some points, they differ even by a factor of 2 or more.



(a)



(b)

Figure 33: A comparison of a full-fledged profile likelihood calculation of the significances (a) and one by using the approximative Z_N formula (37) and combining the different regions by adding them in quadrature (b) in the WZ mediated simplified model. (a) is exact, (b) is the approximation of which its validity is tested. In (a), no significance goes above 4.75. This is only due to a technical limitation. Wherever a significance of $Z = 4.75$ is reported, this should read as $Z \geq 4.75$.

For these reasons, the method using the Z_N formula (37) is not sufficient to do a full signal grid optimization, it is merely used in the end as a validation. Instead, the profile likelihood method using asymptotic formulae [91] is adopted, the same method used to calculate the final exclusion limits.

In a profile likelihood fit, the combination of different regions can be implemented by multiplying their respective Poissonian terms in the likelihood L , i.e.

$$L(\mu) = \prod_{i=1}^N \frac{(\mu s_i + b_i)^{n_i}}{n_i!} e^{-(\mu s_i + b_i)}, \quad (38)$$

where i is the index of a region, N the number of different regions, μ the signal strength, s_i the number of expected signal events, b_i the number of expected background events and n_i the number of observed events in region i . During optimization, the number of observed events is set to the number of expected events, to not bias the selection. Then the setup which maximizes the likelihood (38) defines the optimal choice of the binning. A more detailed discussion about the profile likelihood method is given in Chapter 8.

The disadvantage of using this method is clear: it is CPU intensive. In order to minimize CPU time, systematic uncertainties are omitted during the optimization process.

To get the optimal values for the cuts on E_T^{miss} and m_T , a scan on all possible combinations has been performed and the significances of the combination of the resulting four bins are compared. For the first four m_{SFOS} slices and the optimization on the WZ mediated simplified model, the cuts considered are at $E_T^{\text{miss}} \in [75, 90, 105, 120, 135]$ GeV and $m_T \in [80, 110, 140, 170]$ GeV. Table 13 shows an example to further clarify how the scanning is performed.

First, the m_T cut at 80 GeV is fixed, the E_T^{miss} cut for the low m_T bin is fixed at 75 GeV, and the E_T^{miss} cut for the high m_T bin is varied and set to all five values defined above. Then the E_T^{miss} cut for the low m_T bin is raised to 90 GeV and the E_T^{miss} cut for the high m_T bin is varied again over all predefined values. This corresponds to the first column in Table 13. After all possible combinations of E_T^{miss} have been applied at an m_T cut at 80 GeV, the m_T cut is raised to 110 GeV, and E_T^{miss} went through all possible combinations again. This corresponds to the second column in Table 13.

Once all these combinations are analyzed, the E_T^{miss} cut is fixed first and all combinations of the two m_T cuts are processed. This corresponds to columns three and four in Table 13.

With this scanning, there is some overlap, which has been removed during optimization but not in Table 13, since it would only confuse the reader.

Let us count the number of different binnings that are analyzed during this scan: The number of different E_T^{miss} cuts is 5. For the m_T cut, we considered 4 different values. If we have only one m_T cut, but two E_T^{miss} cuts, then there are $4 \cdot 5 \cdot 5 = 100$ different binnings. If there's only one E_T^{miss} cut but two m_T cuts, then we have $5 \cdot 4 \cdot 4 = 80$ possibilities. But some of these are counted twice, namely when the cut on both sides is at the same value, e.g. when we cut m_T at 80 GeV, lower E_T^{miss} cut at 75 GeV and higher E_T^{miss} cut at 75 GeV, then it is the same as having one E_T^{miss} cut at 75 GeV and the lower m_T cut at 80 GeV and the higher m_T cut at 80 GeV. Double-counted are $5 \cdot 4 = 20$ binnings, removing them gives a total of $100 + 80 - 20 = 160$ binnings that are analyzed. But this is only for one m_{SFOS} slice. The first four m_{SFOS} slices all used the same cut values defined above. In the last one, where $m_{\text{SFOS}} > 101.2$ GeV, the only one being optimized in the $\tilde{\ell}_L$ mediated simplified model, $E_T^{\text{miss}} \in [110, 130, 150, 170, 190, 210]$ GeV and $m_T \in [100, 120, 140, 160, 180]$ GeV are considered. $6 \cdot 6 \cdot 5 + 6 \cdot 6 \cdot 5 - 6 \cdot 5 = 300$ different combinations are possible in this m_{SFOS} slice. All in all, a total number of $4 \cdot 160 + 300 = 940$ different binnings are

m_T	E_T^{miss}	m_T	E_T^{miss}		m_T	E_T^{miss}	m_T	E_T^{miss}
0 – 80	50 – 75	0 – 110	50 – 75		0 – 80	50 – 75	0 – 80	50 – 90
	75 – ∞		75 – ∞		80 – ∞		80 – ∞	
80 – ∞	50 – 75	110 – ∞	50 – 75		0 – 80	75 – ∞	0 – 80	90 – ∞
	75 – ∞		75 – ∞		80 – ∞		80 – ∞	
0 – 80	50 – 75	0 – 110	50 – 75		0 – 80	50 – 75	0 – 80	50 – 90
	75 – ∞		75 – ∞		80 – ∞		80 – ∞	
80 – ∞	50 – 90	110 – ∞	50 – 90		0 – 110	75 – ∞	0 – 110	90 – ∞
	90 – ∞		90 – ∞		110 – ∞		110 – ∞	
0 – 80	50 – 75	0 – 110	50 – 75		0 – 80	50 – 75	0 – 80	50 – 90
	75 – ∞		75 – ∞		80 – ∞		80 – ∞	
80 – ∞	50 – 105	110 – ∞	50 – 105		0 – 140	75 – ∞	0 – 140	90 – ∞
	105 – ∞		105 – ∞		140 – ∞		140 – ∞	
:		:		...	:		:	
0 – 80	50 – 90	0 – 110	50 – 90		0 – 110	50 – 75	0 – 110	50 – 90
	90 – ∞		90 – ∞		110 – ∞		110 – ∞	
80 – ∞	50 – 75	110 – ∞	50 – 75		0 – 80	75 – ∞	0 – 80	90 – ∞
	75 – ∞		75 – ∞		80 – ∞		80 – ∞	
0 – 80	50 – 90	0 – 110	50 – 90		0 – 110	50 – 75	0 – 110	50 – 90
	90 – ∞		90 – ∞		110 – ∞		110 – ∞	
80 – ∞	50 – 90	110 – ∞	50 – 90		0 – 110	75 – ∞	0 – 110	90 – ∞
	90 – ∞		90 – ∞		110 – ∞		110 – ∞	
0 – 80	50 – 90	0 – 110	50 – 90		0 – 110	50 – 75	0 – 110	50 – 90
	90 – ∞		90 – ∞		110 – ∞		110 – ∞	
80 – ∞	50 – 105	110 – ∞	50 – 105		0 – 140	75 – ∞	0 – 140	90 – ∞
	105 – ∞		105 – ∞		140 – ∞		140 – ∞	
:		:			:		:	

Table 13: Example of different binnings that are analyzed during signal region optimization scan. Table is best read from top down. Overlapping combinations have not been removed in this Table but during optimization process.

analyzed⁵. Taking into account, the number of signal points, more than 75 000 different likelihoods have been evaluated.

There are many different approaches how the best binning out of the analyzed ones can be chosen. One might define the strongest binning such, that the exclusion contour at the 95 % confidence level is extended the most. But this would only work for an expected exclusion. The approach adopted here is averaging all significances over the whole grid and choosing the one which gives the best average sensitivity. This would not push the exclusion contour, but the excluded upper-limits on the model cross-section, a more important quantity for theorist than the exclusion contour of a simplified model.

A limitation is set on the minimum number of expected background events per bin, this is set to be $\gtrsim 1$ event, because once uncertainties are added, the significance of such bins with very low event multiplicities go severely down. An exception has been made where $m_{\text{SFOS}} > 101.2 \text{ GeV}$, since these bins have proven to be highly more sensitive in the $\tilde{\ell}_L$ mediated simplified model than other bins.

The resulting bins that proved to be most sensitive within the given outline described above can be seen in Table 14. The bins are numbered from 1 to 20 for further reference.

m_{SFOS}	m_T	E_T^{miss}	$3\ell Z$ veto	SR bin
12 – 40	0 – 80	50 – 90	yes	1
		90 – ∞		2
	80 – ∞	50 – 75		3
		75 – ∞		4
40 – 60	0 – 80	50 – 75		5
		75 – ∞		6
	80 – ∞	50 – 135		7
		135 – ∞		8
60 – 81.2	0 – 80	50 – 75	yes	9
		80 – ∞		10
	0 – 110	75 – ∞		11
		110 – ∞		12
81.2 – 101.2	0 – 110	50 – 90	yes	13
		90 – ∞		14
	110 – ∞	50 – 135		15
		135 – ∞		16
101.2 – ∞	0 – 180	50 – 210	yes	17
		180 – ∞		18
	0 – 120	210 – ∞		19
		120 – ∞		20

Table 14: Summary of the bins in m_{SFOS} , m_T , and E_T^{miss} . The $3\ell Z$ veto is described in 5.6. All units are in GeV.

The E_T^{miss} and m_T distributions of these bins can be seen in Figures 34 and 35.

5.6 The $3\ell Z$ veto

While looking at data to Monte Carlo comparison in validation regions (see Section 6.1), it became apparent, that the $Z + \text{jets}$ component with $Z \rightarrow \ell\ell\ell$, where one ℓ is a converted photon from final state radiation is poorly modelled in Monte Carlo. But since these

⁵I do not show these 940 plots for obvious reasons

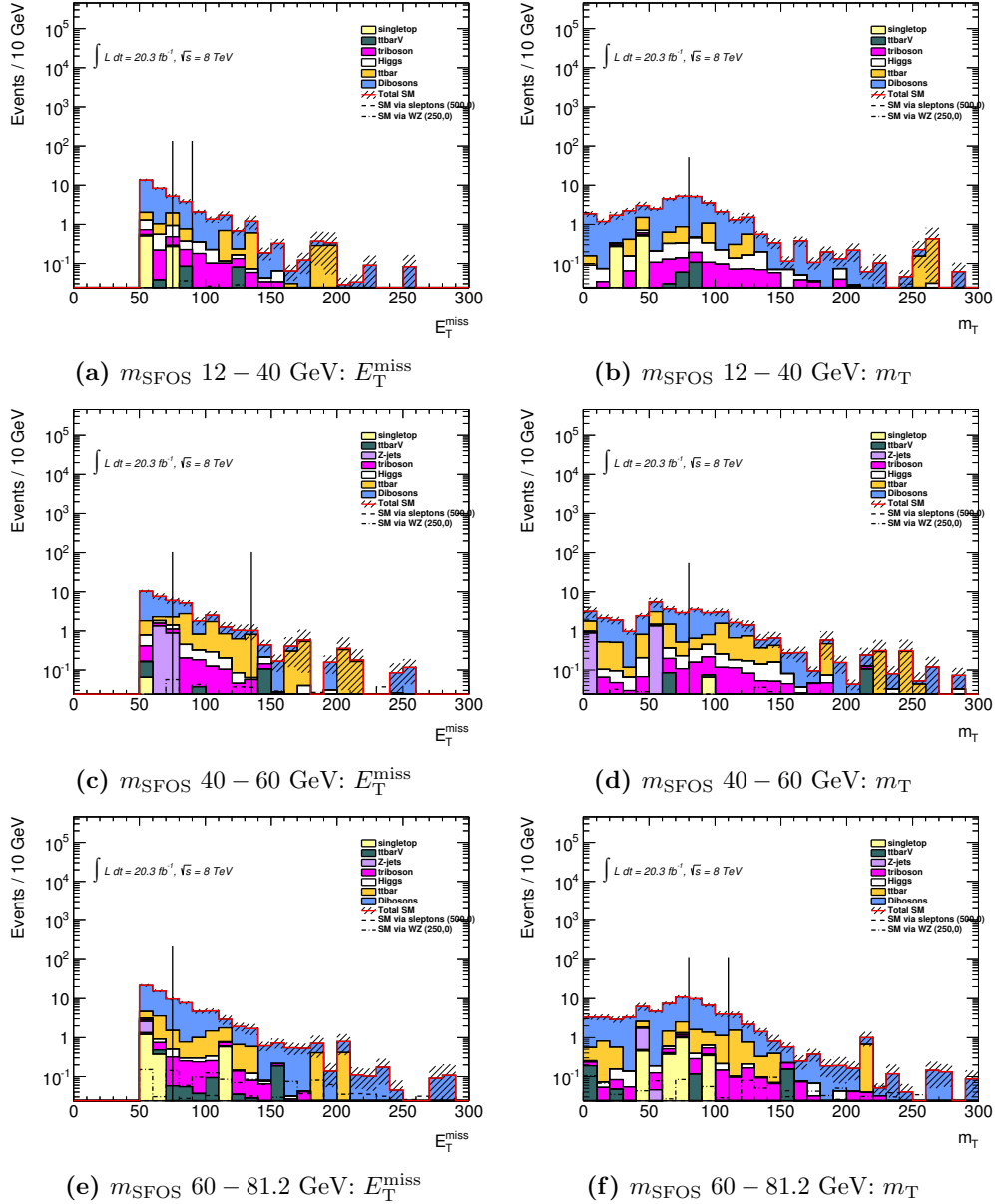


Figure 34: The $E_{\text{T}}^{\text{miss}}$ and m_{T} distributions for the first three m_{SFOS} bins. The vertical black lines indicate bin edges.

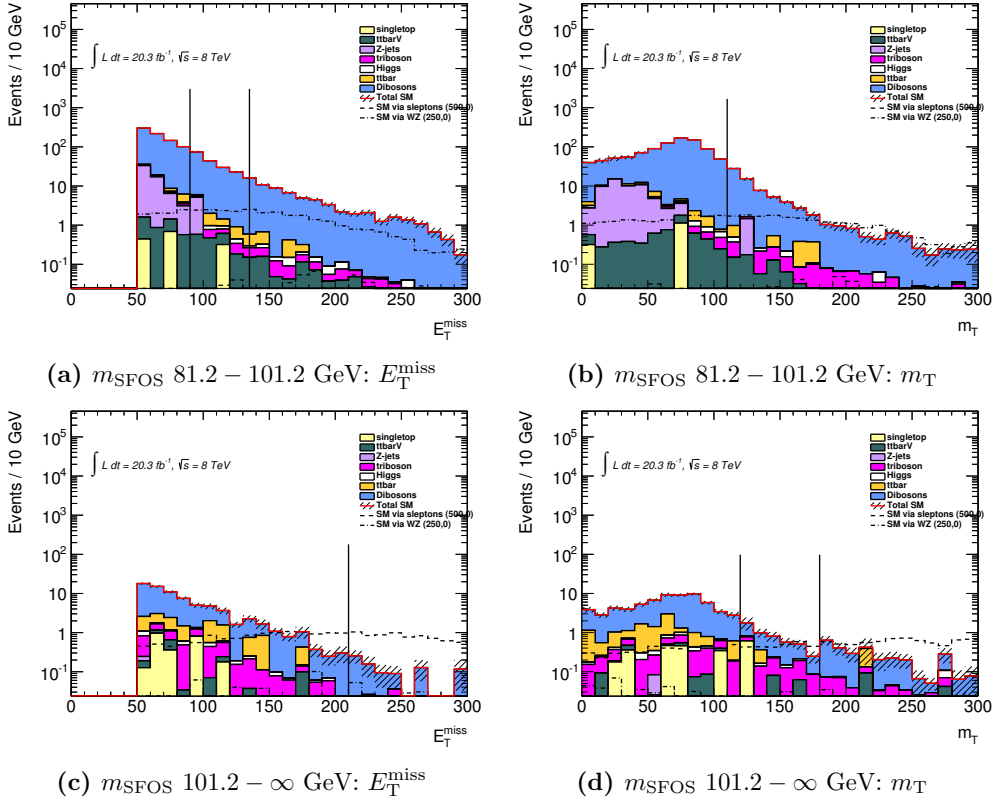


Figure 35: The E_T^{miss} and m_T distributions for the last two m_{SFOS} bins. The vertical black lines indicate bin edges.

events do not produce a high E_T^{miss} signature, they are relevant at most in the low E_T^{miss} regions. In the validation regions these events are rejected for a better test of the modelling of other, more relevant backgrounds, i.e. if the invariant mass of the 3 light leptons lies within 10 GeV of the Z mass, the event is rejected. This is denoted as the $3\ell Z$ veto. For consistency, the $3\ell Z$ veto is also considered in the signal regions. But a drop of sensitivity is observed, hence it is tested if $Z + \text{jets}$ really is a background in the binned signal region, since it should only appear in low E_T^{miss} regions.

As can be seen in Figures 36 - 40, only bins 5, 9 and 13 have a relevant contribution of $Z + \text{jets}$ inside the Z window, thus the $3\ell Z$ veto is only applied in these bins.

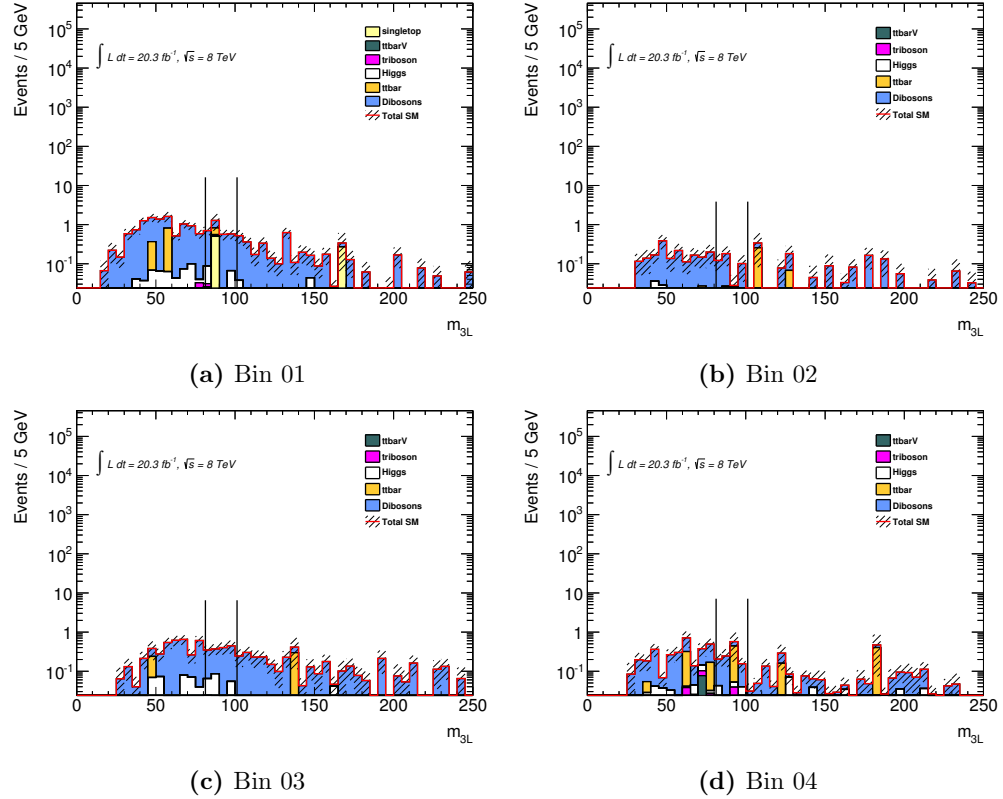


Figure 36: $m_{3\ell}$ distributions for $m_{\text{SFOS}} \in [12, 40]$ GeV. The Z window is indicated by vertical black lines. No contribution of $Z + \text{jets}$ is seen in the Z window.

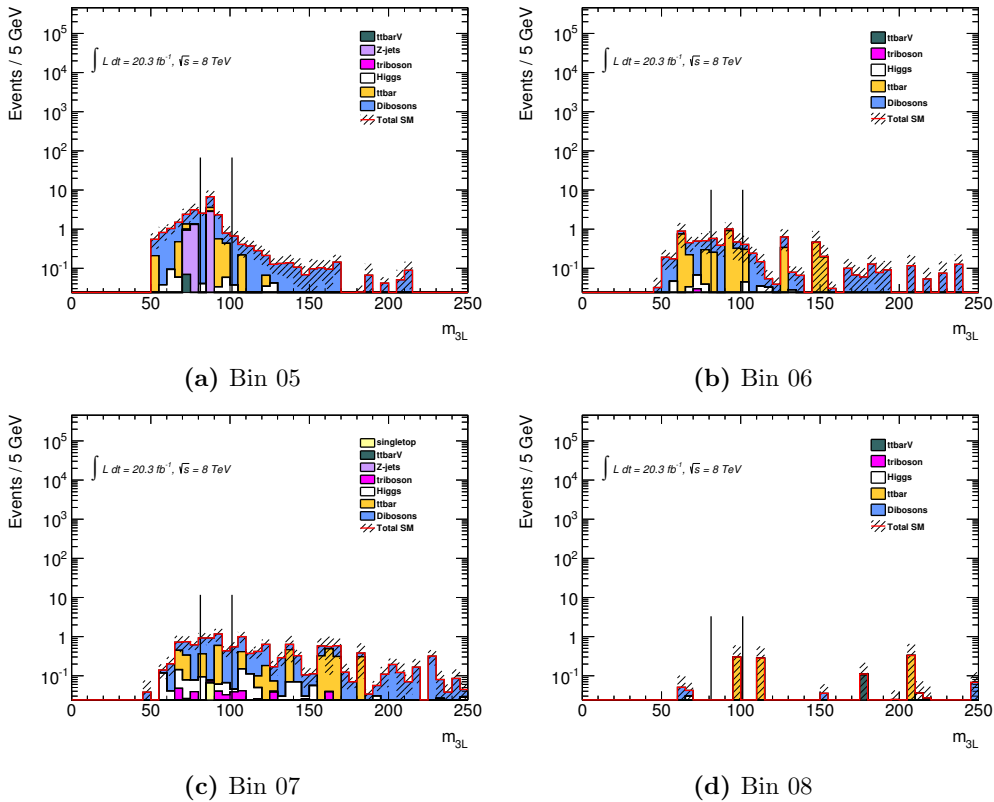


Figure 37: $m_{3\ell}$ distributions for $m_{\text{SFOS}} \in [40, 60]$ GeV. The Z window is indicated by vertical black lines. Bin 05 (a) shows a contribution of $Z + \text{jets}$ within the Z window.

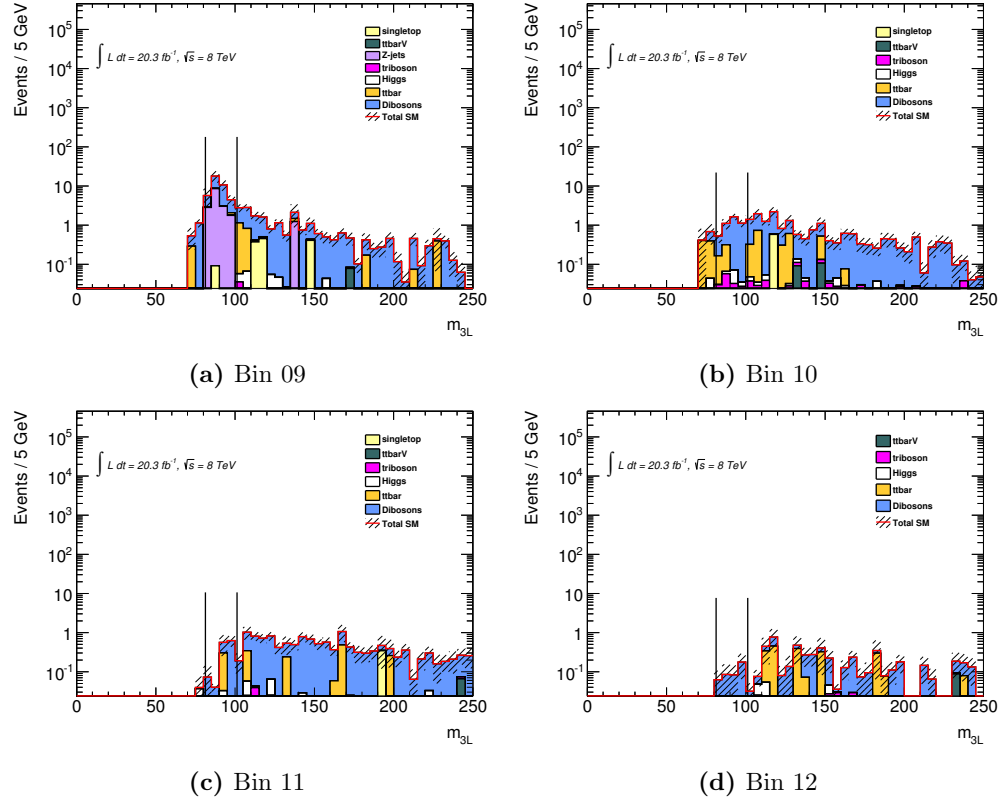


Figure 38: $m_{3\ell}$ distributions for $m_{\text{SFOS}} \in [60, 81.2]$ GeV. The Z window is indicated by vertical black lines. Bin 09 (a) shows a contribution of $Z + \text{jets}$ within the Z window.

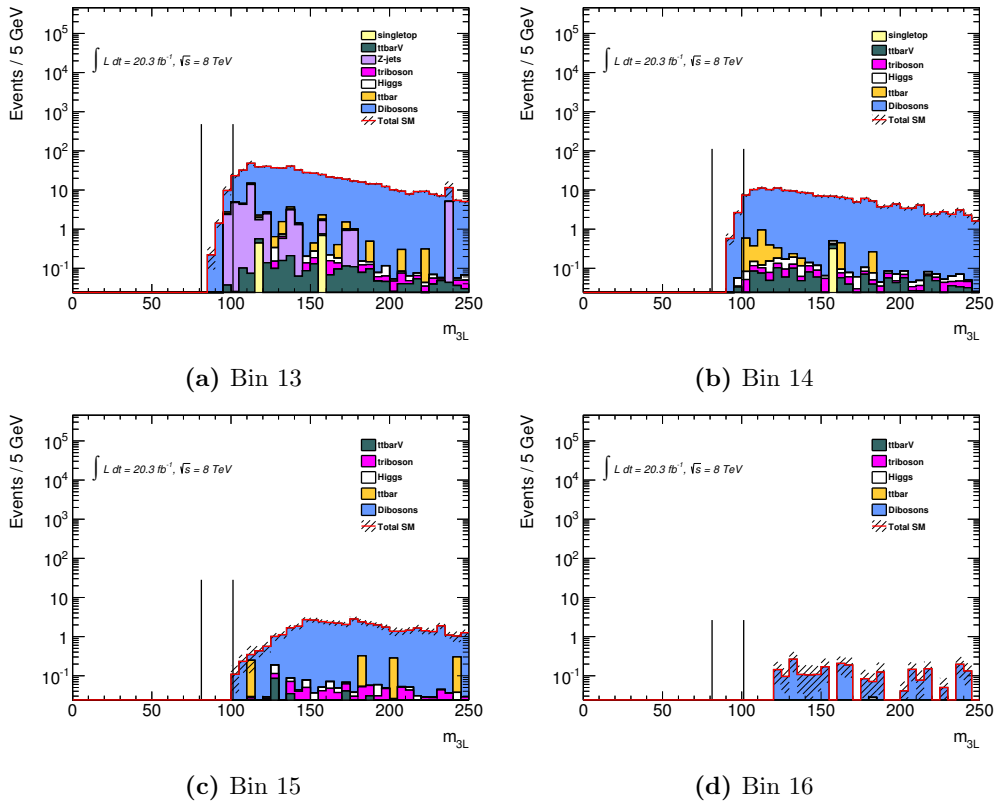


Figure 39: $m_{3\ell}$ distributions for $m_{\text{SFOS}} \in [81.2, 101.2]$ GeV. The Z window is indicated by vertical black lines. Bin 13 (a) shows a contribution of $Z + \text{jets}$ within the Z window.

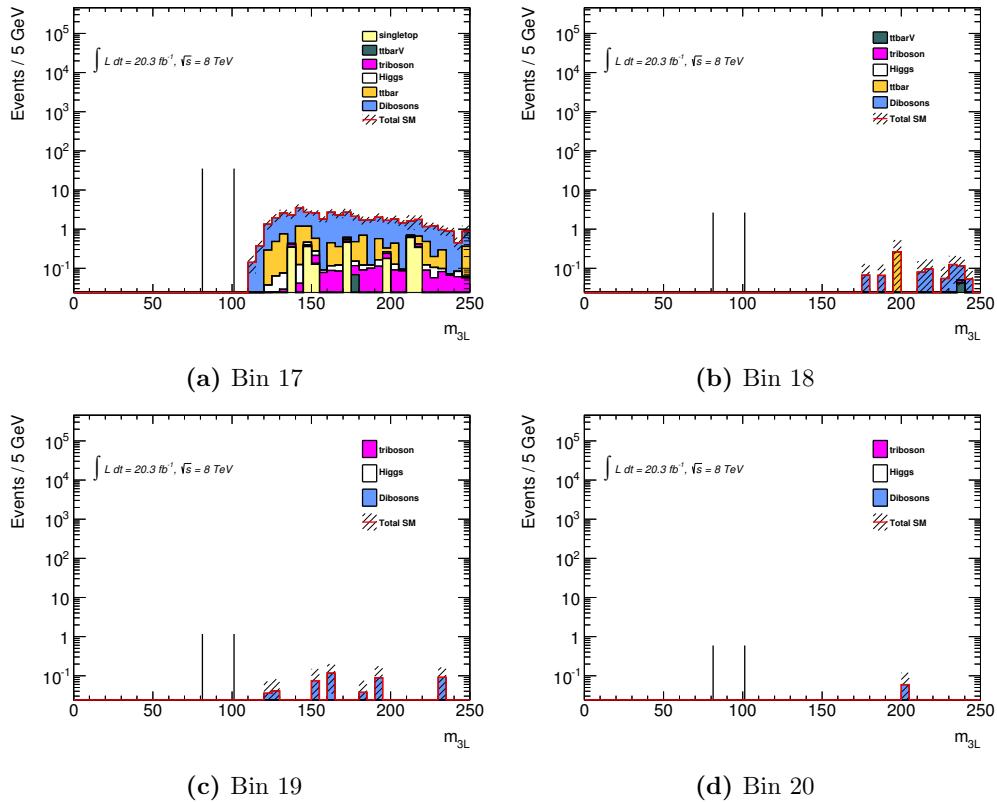


Figure 40: $m_{3\ell}$ distributions for $m_{\text{SFOS}} \in [101.2, \infty] \text{ GeV}$. The Z window is indicated by vertical black lines. As m_{SFOS} is already above the Z window, no contribution of $Z + \text{jets}$ is possible within the Z window.

5.7 Signal region breakdown

A breakdown of the expected events purely from Monte Carlo is given in Tables 15 - 19. The final estimate, where the reducible background is estimated with the Matrix Method is given in Table 25 in Section 7. Figures 41 and 42 show the total signal yield in all 20 bins together for all grid points of the WZ and the $\tilde{\ell}_L$ mediated simplified model. Also shown are the expected significance by combining these bins statistically in all signal points. A breakdown of the signal yields and the significances by each bin separately is reported in Appendix A

m_{SFOS} [GeV] m_T [GeV] E_T^{miss} [GeV]	12 – 40			
	0 – 80		80 – ∞	
	50 – 90	90 – ∞	50 – 75	75 – ∞
WZ	13.24±0.60	2.98±0.26	7.76±0.45	4.49±0.31
ZZ	1.41±0.04	0.12±0.01	0.40±0.02	0.20±0.02
top + V	0.14±0.03	0.07±0.01	0.03±0.01	0.14±0.03
tribosons	0.33±0.03	0.10±0.01	0.19±0.02	0.57±0.04
Higgs	0.66±0.02	0.15±0.01	0.64±0.03	0.46±0.02
Σ SM irreducible	15.78±0.61	3.41±0.26	9.03±0.45	5.85±0.31
$t\bar{t}$	1.31±0.39	0.65±0.32	0.47±0.33	1.94±0.65
single t	0.77±0.55	0.00±0.00	0.00±0.00	0.00±0.00
WW	0.10±0.05	0.03±0.02	0.02±0.02	0.02±0.02
Z + jets	0.00±0.00	0.00±0.00	0.00±0.00	0.00±0.00
V +gamma	0.16±0.09	0.00±0.00	0.04±0.04	0.00±0.00
Σ SM reducible	2.35±0.68	0.68±0.32	0.53±0.33	1.97±0.65
Σ SM	18.13±0.91	4.09±0.42	9.55±0.56	7.81±0.72

Table 15: Numbers of expected background events splitted by contributions for the 4 bins where $12 < m_{\text{SFOS}} < 40$ GeV. All estimates are taken purely from Monte Carlo. Uncertainties are from limited Monte Carlo statistics only.

m_{SFOS} [GeV] m_T [GeV] E_T^{miss} [GeV]	40 – 60			
	0 – 80		80 – ∞	
	50 – 75	75 – ∞	50 – 135	135 – ∞
WZ	6.31±0.38	3.74±0.27	7.61±0.39	0.30±0.06
ZZ	1.55±0.04	0.25±0.02	0.55±0.03	0.01±0.00
top + V	0.11±0.04	0.05±0.01	0.04±0.01	0.11±0.05
tribosons	0.26±0.02	0.24±0.02	0.88±0.05	0.13±0.02
Higgs	0.36±0.02	0.33±0.02	0.98±0.05	0.13±0.02
Σ SM irreducible	8.59±0.39	4.61±0.28	10.05±0.40	0.69±0.08
$t\bar{t}$	1.20±0.40	4.08±0.94	3.58±0.92	0.93±0.46
single t	0.00±0.00	0.00±0.00	0.07±0.05	0.00±0.00
WW	0.16±0.06	0.05±0.03	0.35±0.12	0.00±0.00
Z + jets	2.16±1.25	0.00±0.00	0.00±0.00	0.00±0.00
V +gamma	1.52±0.33	0.30±0.14	1.12±0.26	0.00±0.00
Σ SM reducible	5.05±1.35	4.43±0.95	5.11±0.97	0.93±0.46
Σ SM	13.63±1.41	9.04±0.99	15.17±1.05	1.62±0.47

Table 16: Numbers of expected background events splitted by contributions for the 4 bins where $40 < m_{\text{SFOS}} < 60$ GeV. All estimates are taken purely from Monte Carlo. Uncertainties are from limited Monte Carlo statistics only.

	m_{SFOS} [GeV]	60 – 81.2			
		0 – 80		80 – ∞	
		m_T [GeV]	E_T^{miss} [GeV]	0 – 110	110 – ∞
WZ	16.19±0.74	13.09±0.63	19.49±0.80	3.68±0.35	
ZZ	1.43±0.04	0.60±0.03	0.65±0.03	0.14±0.01	
top + V	0.16±0.03	0.12±0.03	0.41±0.05	0.12±0.03	
tribosons	0.23±0.02	0.40±0.03	0.59±0.03	0.61±0.04	
Higgs	0.32±0.02	0.22±0.01	0.28±0.01	0.12±0.01	
Σ SM irreducible	18.32±0.74	14.44±0.63	21.43±0.81	4.66±0.35	
$t\bar{t}$	2.69±0.75	1.96±0.62	3.51±0.91	2.07±0.62	
single t	1.23±0.71	0.35±0.35	0.58±0.58	0.00±0.00	
WW	0.10±0.06	0.08±0.05	0.17±0.10	0.05±0.04	
Z + jets	1.26±0.89	0.00±0.00	0.00±0.00	0.00±0.00	
V +gamma	1.39±0.27	0.50±0.19	0.40±0.09	0.16±0.16	
Σ SM reducible	6.66±1.39	2.88±0.74	4.66±1.09	2.28±0.65	
Σ SM	24.98±1.57	17.31±0.97	26.09±1.35	6.95±0.73	

Table 17: Numbers of expected background events splitted by contributions for the 4 bins where $60 < m_{\text{SFOS}} < 81.2$ GeV. All estimates are taken purely from Monte Carlo. Uncertainties are from limited Monte Carlo statistics only.

	m_{SFOS} [GeV]	81.2 – 101.2			
		0 – 110		110 – ∞	
		m_T [GeV]	E_T^{miss} [GeV]	50 – 90	90 – ∞
WZ	612.54±4.79	207.04±2.77	58.34±1.37	3.87±0.39	
ZZ	28.86±0.19	5.54±0.09	3.49±0.06	0.12±0.01	
top + V	2.92±0.12	2.00±0.08	0.67±0.05	0.08±0.01	
tribosons	1.32±0.04	0.80±0.03	1.01±0.04	0.33±0.02	
Higgs	2.17±0.03	0.98±0.02	0.31±0.01	0.03±0.00	
Σ SM irreducible	647.82±4.80	216.36±2.78	63.83±1.37	4.43±0.39	
$t\bar{t}$	4.86±1.01	2.85±0.69	1.30±0.49	0.11±0.08	
single t	1.12±0.56	0.32±0.32	0.00±0.00	0.00±0.00	
WW	0.23±0.09	0.07±0.07	0.00±0.00	0.02±0.02	
Z + jets	53.85±10.18	0.00±0.00	5.84±4.13	0.00±0.00	
V +gamma	5.61±0.51	0.00±0.00	0.90±0.34	0.00±0.00	
Σ SM reducible	65.67±10.26	3.24±0.76	8.04±4.17	0.13±0.08	
Σ SM	713.49±11.32	219.60±2.88	71.86±4.39	4.57±0.40	

Table 18: Numbers of expected background events splitted by contributions for the 4 bins where $81.2 < m_{\text{SFOS}} < 101.2$ GeV. All estimates are taken purely from Monte Carlo. Uncertainties are from limited Monte Carlo statistics only.

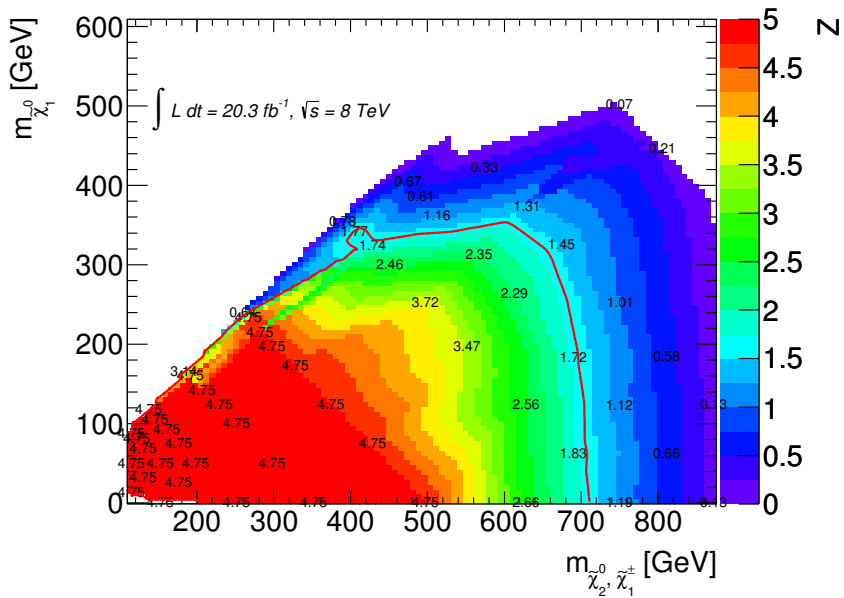
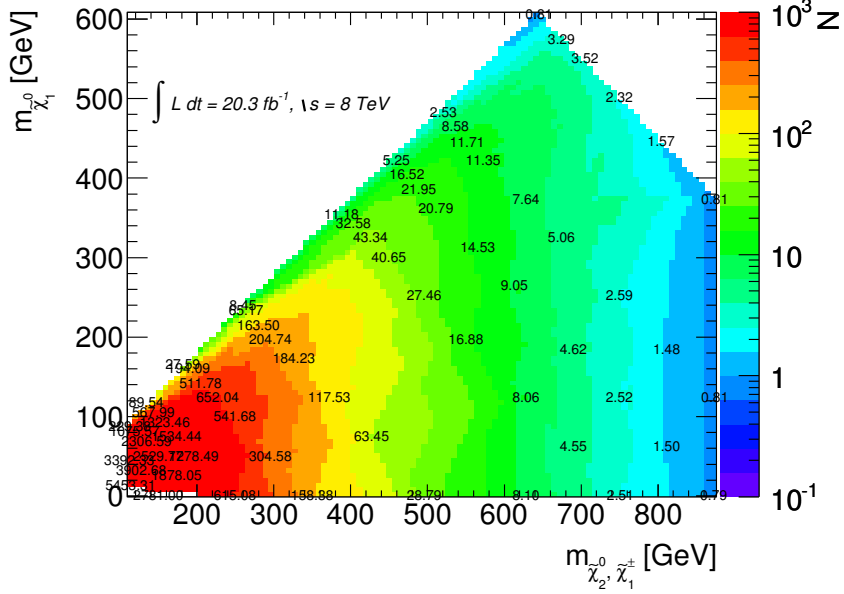
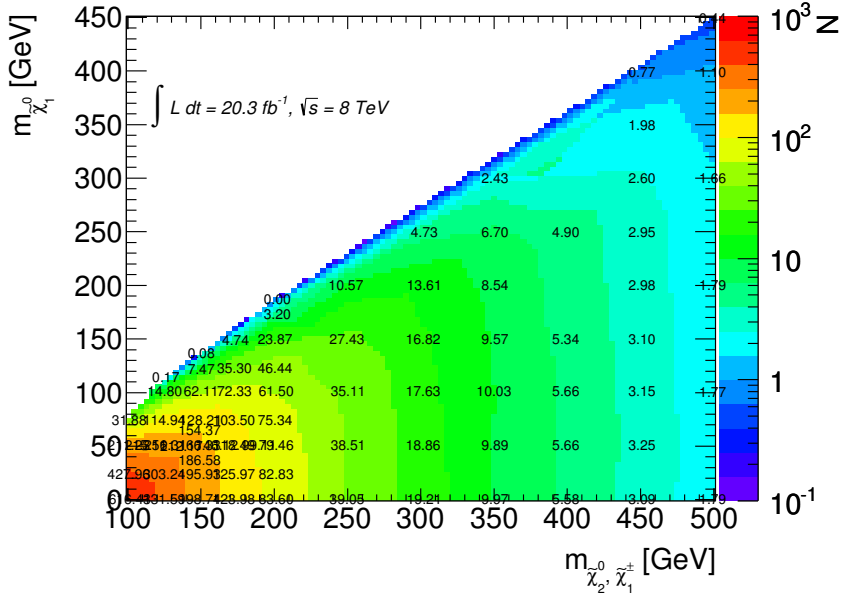
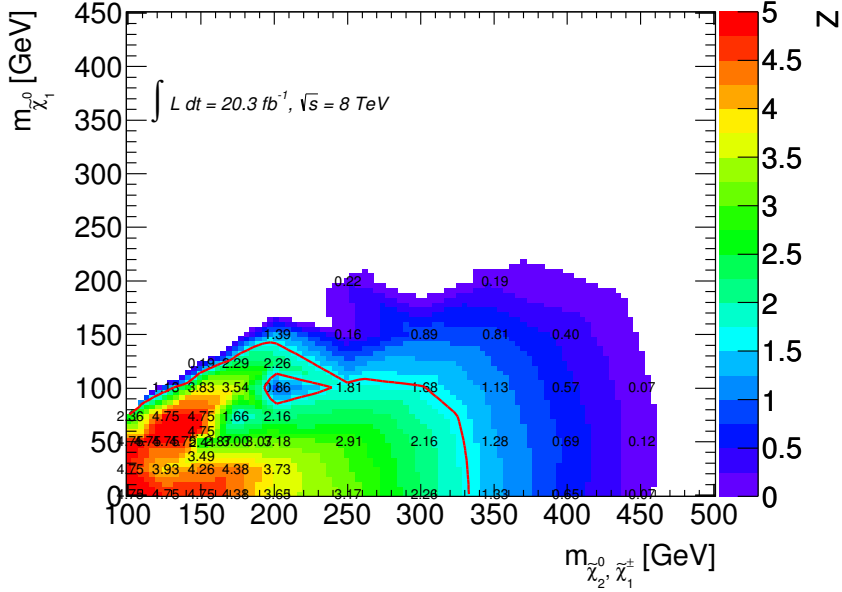


Figure 41: Expected number of signal events for the whole signal region, i.e. all 20 bins summed up and expected significances for the statistical combination of the 20 bins in the $\tilde{\ell}_L$ mediated simplified model. All numbers are estimated with Monte Carlo only. The red line indicates exclusion at the 95 % confidence level $\approx 1.64\sigma$.



(a) $\Sigma_{\text{bin}01}^{\text{bin}20}$ Signal event yields



(b) Expected significance

Figure 42: Expected number of signal events for the whole signal region, i.e. all 20 bins summed up and expected significances for the statistical combination of the 20 bins in the WZ mediated simplified model. All numbers are estimated with Monte Carlo only. The red line indicates exclusion at the 95 % confidence level $\approx 1.64\sigma$.

m_{SFOS} [GeV]	$101.2 - \infty$			
m_T [GeV]	0 – 180	180 – ∞	0 – 120	120 – ∞
E_T^{miss} [GeV]	50 – 210		210 – ∞	
WZ	50.41 ± 1.28	2.33 ± 0.29	0.92 ± 0.17	0.11 ± 0.06
ZZ	2.43 ± 0.06	0.08 ± 0.01	0.02 ± 0.01	0.01 ± 0.00
top + V	0.77 ± 0.08	0.15 ± 0.04	0.00 ± 0.00	0.01 ± 0.01
tribosons	3.22 ± 0.08	0.54 ± 0.03	0.08 ± 0.01	0.07 ± 0.01
Higgs	0.95 ± 0.04	0.05 ± 0.01	0.01 ± 0.00	0.00 ± 0.00
Σ SM irreducible	57.78 ± 1.29	3.14 ± 0.29	1.03 ± 0.17	0.21 ± 0.06
$t\bar{t}$	8.57 ± 1.28	0.26 ± 0.26	0.00 ± 0.00	0.00 ± 0.00
single t	2.41 ± 0.85	0.00 ± 0.00	0.00 ± 0.00	0.00 ± 0.00
WW	0.23 ± 0.08	0.00 ± 0.00	0.00 ± 0.00	0.04 ± 0.04
$Z + \text{jets}$	0.06 ± 0.06	0.00 ± 0.00	0.00 ± 0.00	0.00 ± 0.00
$V + \text{gamma}$	1.86 ± 0.37	0.00 ± 0.00	0.00 ± 0.00	0.00 ± 0.00
Σ SM reducible	13.14 ± 1.58	0.26 ± 0.26	0.00 ± 0.00	0.04 ± 0.04
Σ SM	70.91 ± 2.04	3.40 ± 0.39	1.03 ± 0.17	0.25 ± 0.07

Table 19: Numbers of expected background events splitted by contributions for the 4 bins where $101.2 < m_{\text{SFOS}} < \infty$ GeV. All estimates are taken purely from Monte Carlo. Uncertainties are from limited Monte Carlo statistics only.

5.8 Other signal regions

In [2] and [60], other signal regions are defined. They are presented in Table 20, but are not further discussed. Some of them are used in the exclusion limit contours, where they are statistically combined with the 20 bins. In the WZ and $\tilde{\ell}_L$ mediated simplified models, where the binned signal region is optimized on, the other signal region add practically no additional sensitivity.

5.9 Systematic uncertainties

The different sources of systematic uncertainties are described. A graphical representation of each systematic uncertainty in each bin can be found in Appendix B. All systematic uncertainties are treated as correlated between regions and samples if not noted otherwise.

Monte Carlo statistics Since Monte Carlo statistics is limited, it is a source of a systematic uncertainty. This uncertainty is usually one of the leading ones, especially for samples with low Monte Carlo statistics (top + V) or for tight bins (bin 19 and 20). This uncertainty is for irreducible and reducible background equally important. It is treated as uncorrelated among regions and samples.

Electron scale factor uncertainty The ratio between the data efficiency measurements and the Monte Carlo predictions is called scale factor. A p_T and η dependent scale factor is applied to all leptons passing object selection and overlap removal. This introduces an uncertainty on the electron scale factor, it is generally rather small.

Electron energy scale: Z scale uncertainty The electron energy scale calibration is performed in-situ using $Z \rightarrow ee$ decays. To study the linearity of the electron energy scale, $J/\Psi \rightarrow ee$ decays are used. Alternatively, the ratio E/p , where the energy E is measured in the electromagnetic calorimeter and the momentum p is measured in the inner detector is exploited. This technique gives access to $W \rightarrow e\nu$ with larger statistics but it depends on the calibration of the inner detector [93].

SR	SR0 τ b	SR1 τ	SR2 τ a	SR2 τ b
ℓ flavour/sign	$\ell^\pm \ell^\pm \ell'^\mp$	$\tau^\pm \ell^\mp \ell^\mp$	$\tau\tau\ell$	$\tau^\pm \tau^\mp \ell$
Z boson	–	veto (ee)	–	–
b -jet	veto	veto	veto	veto
E_T^{miss}	> 50	> 50	> 50	> 60
m_{T2} max	–	–	> 100	–
$p_T^{2^{\text{nd}}\ell}$	–	> 30	–	–
$p_T^{3^{\text{rd}}\ell}$	> 20	–	–	–
$\min(\Delta\phi(\ell^\pm, \ell^\mp))$	≤ 1.0	–	–	–
$\sum p_T^\ell$	–	> 70	–	–
$\sum p_T^\tau$	–	–	–	> 110
$m_{\ell\tau}$	–	< 120	–	–
$m_{\tau\tau}$	–	–	–	70–120

Table 20: The other signal regions defined in [2] and [60]. All signal regions shown here are orthogonal to the binned signal region by either selecting at least one τ (SR1 τ , SR2 τ a and SR2 τ b) or by vetoing a same flavour opposite sign lepton pair (SR0 τ b). Except SR2 τ a and SR2 τ b, all signal regions are also orthogonal to each other.

The electron energy scale uncertainty is split in four uncorrelated components. The first component is associated to the Z scale, uncertainties arise due to limited statistics, a possible bias of the fit method and differences that arise in the choice of the generator.

Electron energy scale: Presampler scale uncertainty A presampler is installed in front of the electromagnetic calorimeter below a pseudorapidity of $|\eta| < 1.8$. It corrects for the energy loss upstream, which depends on the pseudorapidity and is due to other detectors and detector material. This 1.1 cm thin layer of liquid Argon introduces a systematic uncertainty on the presampler energy scale for particles with $|\eta| < 1.8$. Since the fraction of energy deposited in the presampler decreases with higher electron energies, it is only relevant for low- p_T electrons.

Electron energy scale: Material uncertainty Electrons interact with additional material in front of the electromagnetic calorimeter. Such additional material can be other detectors, cables, coils or cryostats. The imperfect knowledge of this additional material affects the measurement of the electron energies. This energy lost is corrected in the $Z \rightarrow ee$ measurements, but it does not account for a possible p_T dependence, since the p_T 's from the decaying Z will be peaked around 40 GeV. Low- p_T electrons are affected more severely by this effect, hence the systematic uncertainty for low- p_T electrons will be more relevant.

Electron energy scale: Low- p_T uncertainty The $Z \rightarrow ee$ calibration method is verified for low- p_T electrons by performing the electron energy scale calibration also on $J/\Psi \rightarrow ee$ decays. The agreement is very good, nonetheless, an additional uncertainty of 1 % for electrons with $p_T = 10$ GeV, decreasing linearly to 0 % for electrons with $p_T = 20$ GeV is added.

Electron energy resolution Test-beam measurements are used to calibrate the electromagnetic calorimeter. Transferring the test-beam results to the ATLAS detector

introduces an uncertainty on its resolution: 3 % in the central region and 5 % in the forward region.

Electron reconstruction efficiency Electron reconstruction efficiency is p_T and η dependent and generally higher for low- p_T electrons. The uncertainty on the efficiency is also much larger in the forward calorimeters [93], nonetheless this uncertainty is rather small in this analysis.

Muon inner detector track p resolution To measure the muon energy scale, $Z \rightarrow \mu\mu$, $J/\Psi \rightarrow \mu\mu$ and $\Upsilon \rightarrow \mu\mu$ decays are used. The systematic uncertainty on the muon energy scale depends on p_T and η and is measured to be in the order of $\approx 0.1\%$ [45].

Muon spectrometer track p resolution Measured in the same manner as in the inner detector, the uncertainty on the muon energy scale in the spectrometer is a bit larger but still a very small systematic uncertainty in this analysis [45].

Muon reconstruction efficiency The muon reconstruction efficiency in data compared to Monte Carlo simulations shows very good agreement for muons coming from a Z decay and somewhat less good agreement for low- p_T muons coming from a J/Ψ decay. A systematic uncertainty between 0.2 % and 2 % is applied to correct for uncertainties in the reconstruction efficiency [45].

Tau reconstruction efficiency To measure the reconstruction efficiencies of taus, a tag-and-probe selection of events with $Z \rightarrow \tau_{lep}\tau_{had}$ where the leptonically decaying τ_{lep} is tagged and then the search for the probe from the hadronically decaying τ_{had} is performed. The measurement was also carried out on $W \rightarrow \tau_{had}\nu_\tau$ decays. The resulting systematic uncertainty is in the order of 3 % [94]. For the binned signal region which vetoes taus, this uncertainty is of course always zero.

Tau energy scale Since taus are decaying inside the beampipe, jets are effectively measured in the detectors. As such, the jet energy scale can be used to retrieve the energy of the tau, but since the tau decays mostly into pions, a more accurate answer about the tau energy can be given by measuring its own energy scale. The associated systematic uncertainty is usually below 3 % for 1-prong taus, and below 4 % for multi-prong taus with a peak of $\approx 7.5\%$ for multi-prong taus in the transition region of barrel and endcap at $1.3 < |\eta| < 1.6$, due to the large amount of dead material [95].

Jet energy scale Using test-beam measurements, the energy scale measured by the electromagnetic and the hadronic calorimeters is established. This procedure accounts well for electrons and photons, but not for jets, since the calorimeter response to hadrons is lower than to electrons or photons and due to reconstruction inefficiencies [96]. This is a large systematic uncertainty and important for e.g. a top cross-section measurement. Since we are using jets only as a component in E_T^{miss} , in the overlap removal (see Section 4.6) and the veto of b -tagged jets, this uncertainty is not as crucial for us.

The Jet Energy Scale can have many different sources, to account for a possible p_T dependence, it was treated as uncorrelated between different regions in previous analyses, but since 20 bins would introduce 20 nuisance parameters for the Jet Energy Scale alone, this idea was dropped. Instead the profiling of the nuisance parameter for different binning in the Jet Energy scale was carried out as described in [97].

Since no overprofiling was observed in any binning, a single nuisance parameter was used in the end, fully correlating the Jet Energy Scale over all regions and samples. For the same reason, the jet energy scale was not split up in components, as is the case for the electron energy scale.

Jet energy resolution The energy resolution of jets in Monte Carlo is smeared to account for possible detector inaccuracies in data. Since the exact resolution is not known, this leads to a systematic uncertainty. For the Jet Energy Resolution, the same thing about its correlations hold as for the Jet Energy Scale: since no region dependence was observed, only one nuisance parameter was used to describe this systematic uncertainty.

Jet vertex fraction uncertainty Using tracking and vertexing information, a discriminant called Jet Vertex Fraction is defined which described the probability that a jet originated from a particular vertex. Since a cut on this discriminant is applied, a systematic uncertainty is introduced. This uncertainty is very small across all bins.

b-tagging uncertainty Jets with at least one b quark are tagged as b -jets. Its uncertainty is rather small, only playing a role in top enriched samples such as top + V .

c-tagging uncertainty The flavour tagging algorithm tags jets as b -jets, c -jets (jets with at least one c quark but no b quark) or l -jets (light jets without b or c quark). c -jets are not considered in this analysis, but a b -jet that is wrongly tagged as c -jet will still alter the selection since b -tagged jets are vetoed in the signal regions and requested in some validation regions. This uncertainty is always very small.

l -tagging uncertainty Similar to the c -tagging uncertainty, a systematic uncertainty is applied to the light jet tagging algorithm. This uncertainty is even smaller than the one on c -tagging.

E_T^{miss} energy scale The energy scale uncertainties on the physics objects needs to be propagated to the E_T^{miss} . Additionally, so called soft terms need to be considered as well. Soft terms are contributions from cell out and soft jets, where cell out are energy cell deposits that do not correspond to any reconstructed object (e.g. pile-up) and soft jets are jets with $p_T < 20$ GeV. These soft terms have been studied in events without jets with $p_T > 20$ GeV. Though this systematic uncertainty has many contributions, it remains rather small.

E_T^{miss} energy resolution Similar as for the E_T^{miss} energy scale uncertainty which takes into account all energy scale uncertainties from physics objects and cell deposits that enter the E_T^{miss} , the resolution uncertainty on the E_T^{miss} is derived. The resulting uncertainty is of the same order as the E_T^{miss} energy scale uncertainty.

Luminosity The systematic uncertainty on the luminosity for the 8 TeV dataset is reported to be 2.8 % [98, 99].

Trigger The trigger simulation has been studied in $Z + \text{jets}$ events and a systematic uncertainty of 5 % is applied, see also Section 4.5.

Pile-up The scale factors to weight Monte Carlo events in order to take into account the harsh pile-up conditions at the LHC introduce another systematic uncertainty.

Generator Different Monte Carlo generators are compared for WZ , ZZ and $t\bar{t} + V$. The Powheg + Pythia8 baseline samples for the dibosons are checked against MC@NLO + HERWIG. Comparison to parton shower Pythia6 is also carried out. The ALPGEN $t\bar{t} + V$ samples are compared with MADGRAPH.

The alternative Monte Carlo generators are normalized to the baseline generators at the three lepton level, i.e. the generator uncertainties describe only differences in acceptance, not in cross-sections or parton distribution functions. Additional cuts may be applied to match generator cuts.

The generator uncertainty is calculated as $\sigma_{\text{TOT}} = \sqrt{\sigma_{\text{SYST}}^2 + \sigma_{\text{STAT}}^2}$, where σ_{SYST} is the difference of the number of events observed in the two generators and σ_{STAT} is the statistical uncertainty of the alternative generator *only*, to not double-count the statistical uncertainty of the baseline generator. The generator uncertainty is then symmetrized.

The size of the generator uncertainty depends on the region, but is usually the largest systematic uncertainty. It is correlated among all regions but not among samples.

Cross-section The uncertainty on Monte Carlo cross-sections is measured to be 7 % for WZ [73], 5 % for ZZ [77], 30 % for $t\bar{t} + V$ [100, 101] and a conservative estimate of 100 % is assumed for the tribosons background. For the associated production of Vh and Higgs production via vector boson fusion, a systematic uncertainty of 20 % is applied, while the $t\bar{t} + h$ samples and the gluon fusion Higgs production have an uncertainty of 100 % [82]. This systematic is one of the leading systematic uncertainties in this analysis. All cross-section uncertainties are uncorrelated between samples, but correlated in different regions.

PDF The uncertainty on the parton distribution functions for a basic three leptons selection is already taken into account in the cross-section uncertainties. Only a deviation from the basic 3 lepton selection due to signal region selection is considered here. The uncertainties are calculated using the full eigenset of the CT10 PDF set for WZ and ZZ , no additional uncertainty is applied for other samples. The PDF uncertainty is correlated among regions but not among samples.

The total experimental uncertainty, not including Monte Carlo statistics is shown in Figures 43 and 44 for the most sensitive regions.

5.10 Acceptance & Efficiency

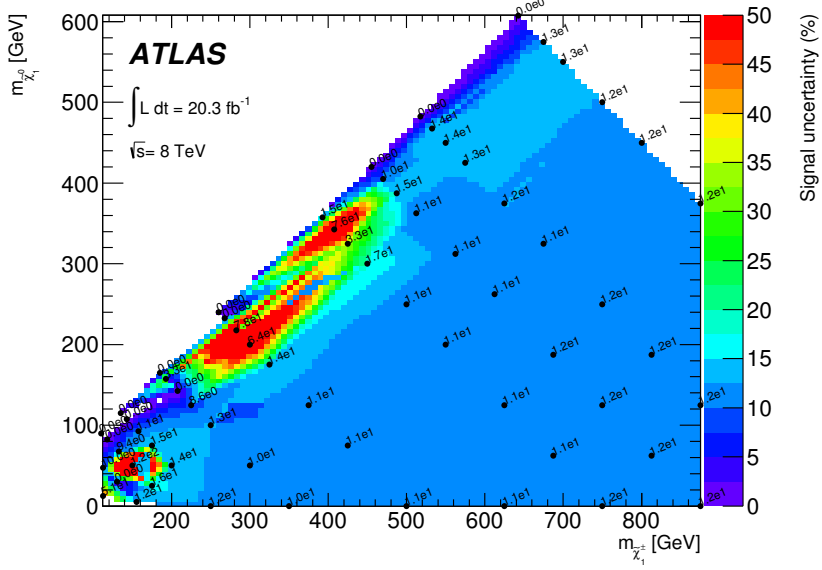
Acceptance (Acc) and Efficiency (Eff) are defined as follows. Truth Monte Carlo simulated events are generated events before detector simulation, reconstructed Monte Carlo is after detector simulation and corresponding inefficiencies.

$$\text{Acc} = \frac{N_{\text{SR,Truth}}}{N_{\text{Sample,Truth}}} , \quad (39)$$

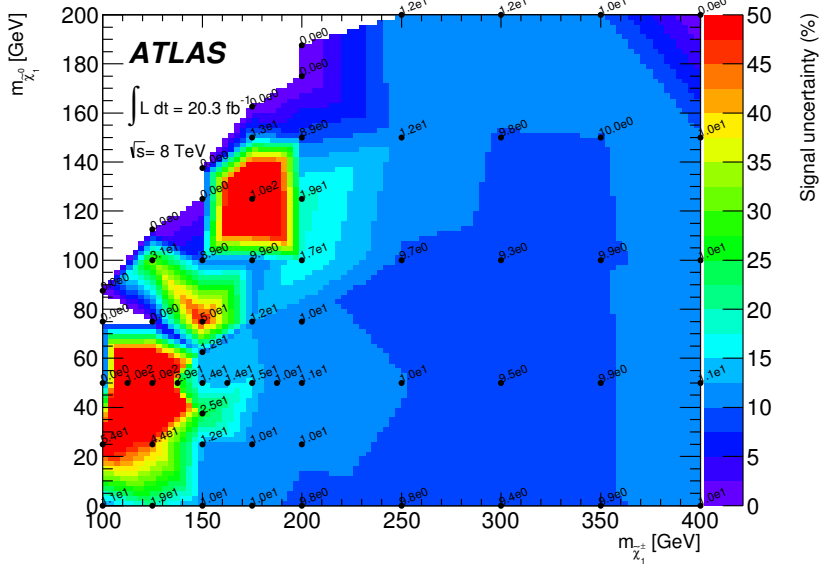
$$\text{Eff} = \frac{N_{\text{SR,Reco}}}{N_{\text{SR,Truth}}} , \quad (40)$$

where

- $N_{\text{SR,Truth}}$: The number of events passing a certain signal region selection in truth Monte Carlo.

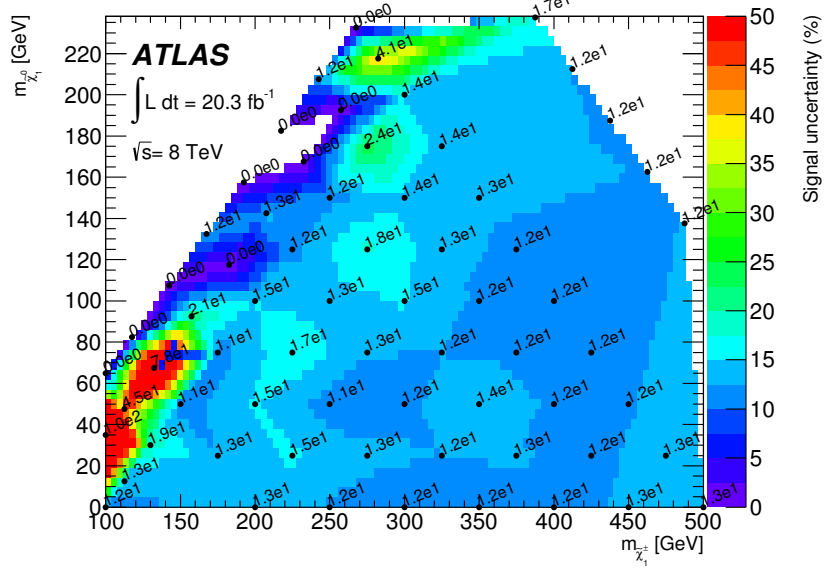


(a) $\tilde{\ell}_L$ mediated simplified model

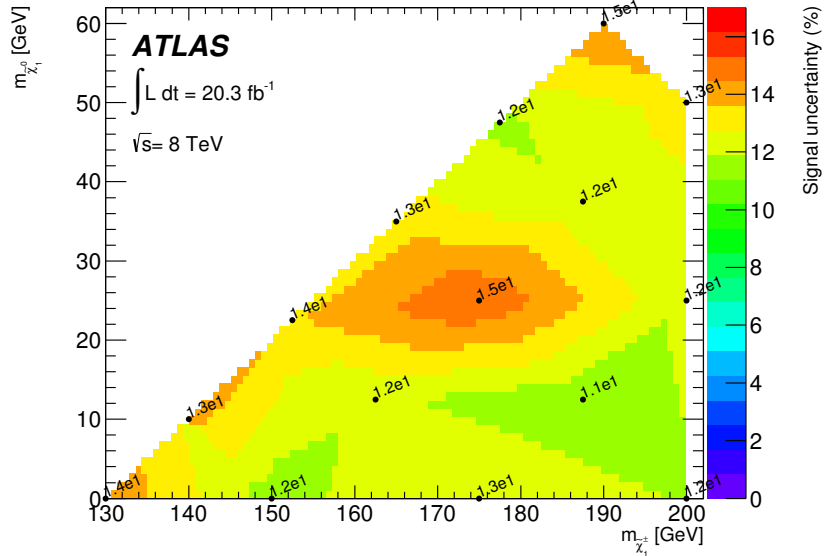


(b) WZ mediated simplified model

Figure 43: Total experimental uncertainty, not including Monte Carlo statistics for the most sensitive regions, i.e. bin 20 for the $\tilde{\ell}_L$ mediated and bin 16 for the WZ mediated simplified model.



(a) $\tilde{\tau}_L$ mediated simplified model



(b) Wh mediated simplified model

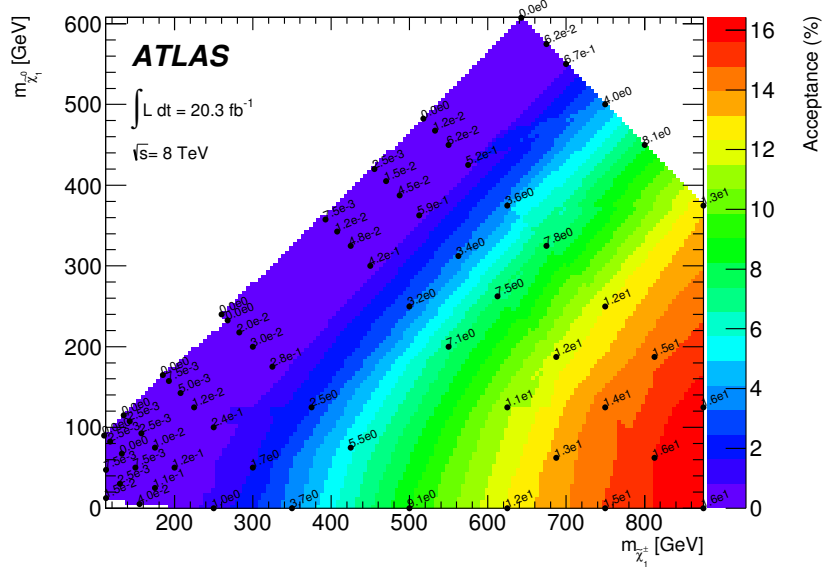
Figure 44: Total experimental uncertainty, not including Monte Carlo statistics for the most sensitive regions, i.e. SR2 τ a for the $\tilde{\tau}_L$ mediated and SR2 τ b for the Wh mediated simplified model.

- $N_{\text{Sample},\text{Truth}}$: The number of events in the complete sample in truth Monte Carlo.
- $N_{\text{SR},\text{Reco}}$: The number of events passing a certain signal region selection in reconstructed Monte Carlo.

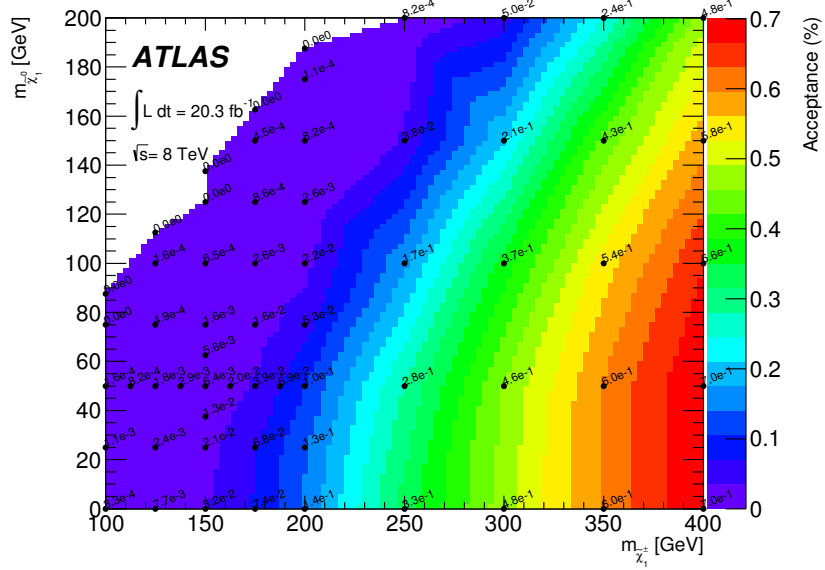
Acceptance times efficiency gives

$$\text{Acc} \cdot \text{Eff} = \frac{N_{\text{SR},\text{Reco}}}{N_{\text{Sample},\text{Truth}}} \quad (41)$$

The acceptance for the most sensitive regions in the simplified models is given in Figures 45 and 46 and the efficiency for the same regions is given in Figures 47 and 48.

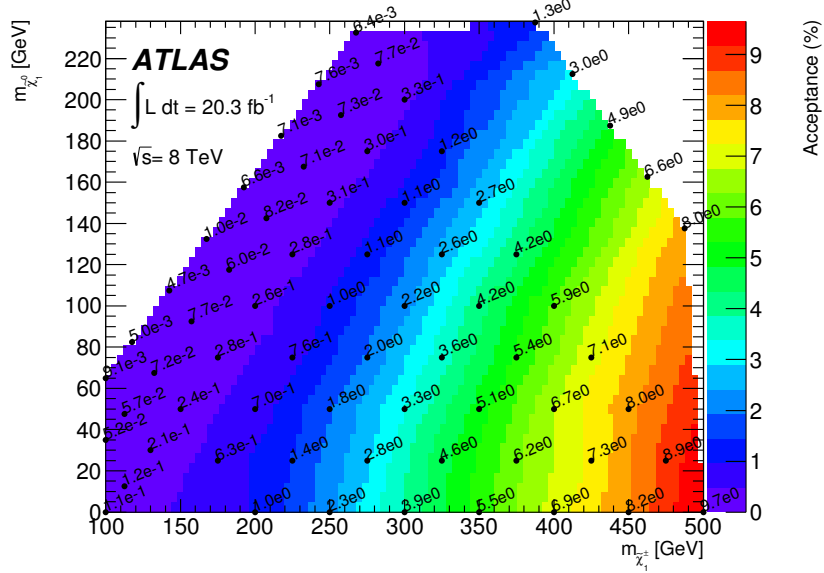


(a) $\tilde{\ell}_L$ mediated simplified model

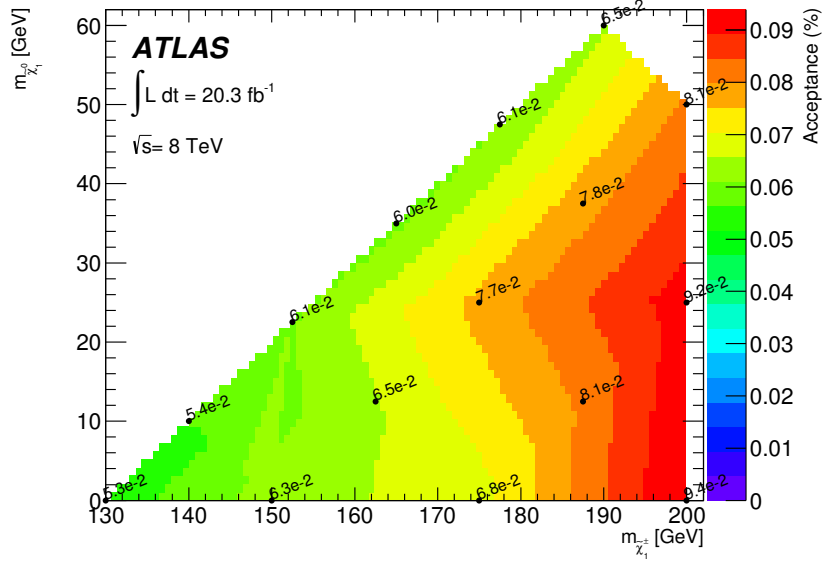


(b) WZ mediated simplified model

Figure 45: Acceptance in the most sensitive regions, i.e. bin 20 for the $\tilde{\ell}_L$ mediated, bin 16 for the WZ mediated simplified model.

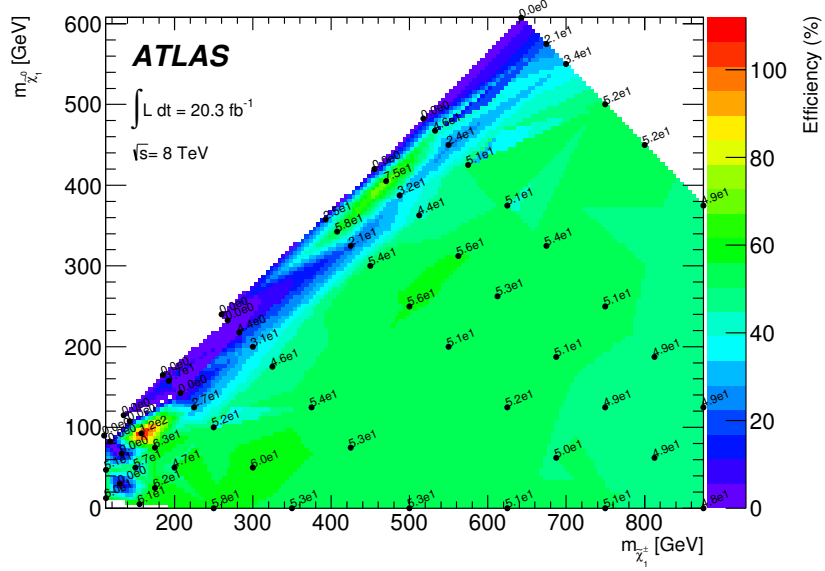


(a) $\tilde{\tau}_L$ mediated simplified model

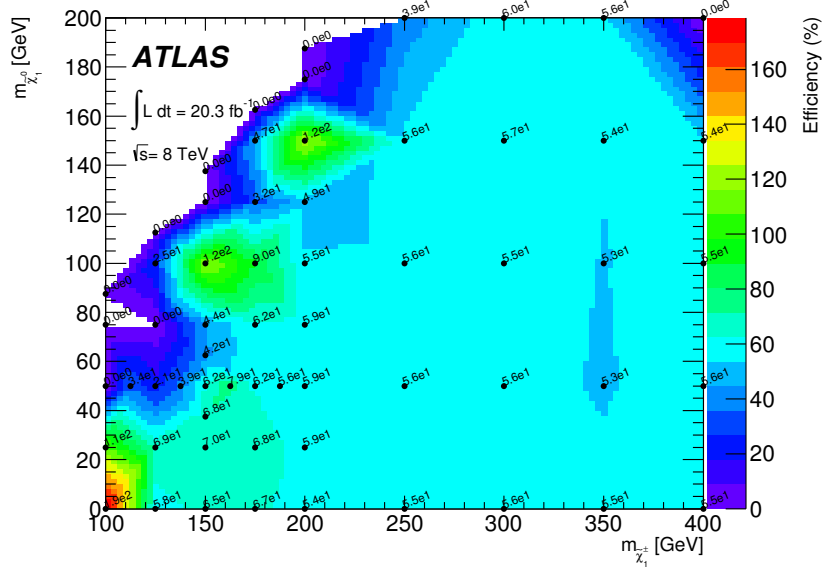


(b) Wh mediated simplified model

Figure 46: Acceptance in the most sensitive regions, i.e. SR2 τ a for the $\tilde{\tau}_L$ mediated and SR2 τ b for the Wh mediated simplified model.

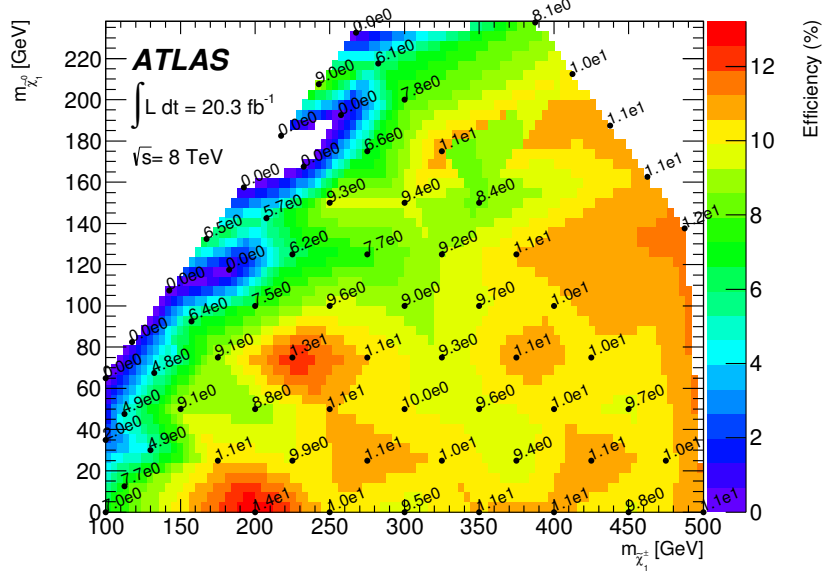


(a) $\tilde{\ell}_L$ mediated simplified model

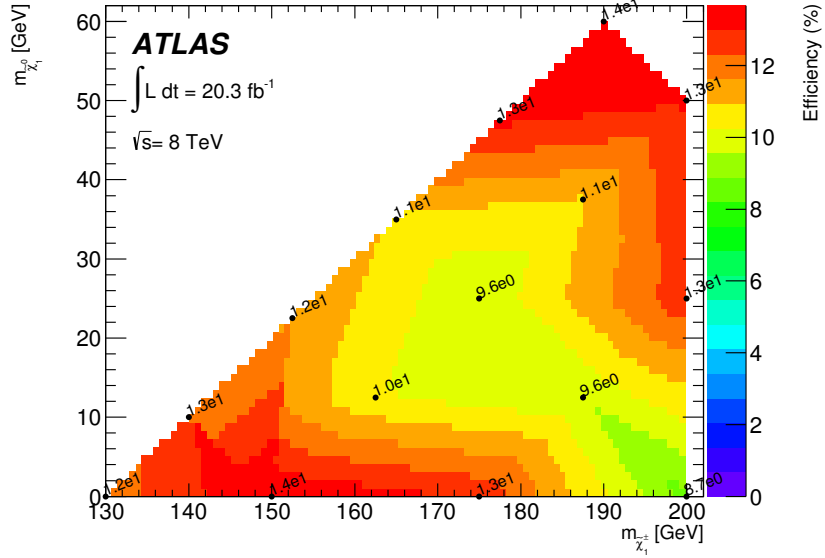


(b) WZ mediated simplified model

Figure 47: Efficiency in the most sensitive regions, i.e. bin 20 for the $\tilde{\ell}_L$ mediated, bin 16 for the WZ mediated simplified model.



(a) $\tilde{\tau}_L$ mediated simplified model



(b) Wh mediated simplified model

Figure 48: Efficiency in the most sensitive regions, i.e. SR2 τ a for the $\tilde{\tau}_L$ mediated and SR2 τ b for the Wh mediated simplified model.

6 Validation of background modeling

Before looking at the data in the signal region, the modeling of the background is validated in dedicated validation regions, which sole purpose is to confirm the agreement of the expected kinematic distributions with the ones seen in data. They do not enter in the signal region fit, as opposed to control regions⁶. If the agreement between background model and data is not sufficiently good, the cause for the disagreement must be found before the analysis can carry on and look at data in the signal region. The data in the signal region is blinded until the analysis is in its final form. No alterations are to be made after looking at data, in order to not bias the analysis.

The regions used to validate the background modeling are described in Section 6.1. A possible signal contamination is discussed in Section 6.2.

6.1 Validation regions

In order to validate the background model, different regions have been defined where the agreement between predicted background and events in data is compared. It is crucial that these validation regions do not have a large contribution from the signal, since otherwise agreement would not be seen if a signal is present. Moreover, validation regions should not be too different from the signal regions, since ultimately, we want to understand our background modeling in these regions. They are therefore defined by either requesting a b -tagged jet or E_T^{miss} between 35 GeV and 50 GeV. Since all regions veto b -tagged jets and have a $E_T^{\text{miss}} > 50$ GeV cut, one of these requests is sufficient to ensure orthogonality with any signal region. The restriction to E_T^{miss} between 35 and 50 GeV, rather than going down to 0 GeV, arises because of a known bad performance of the Matrix Method for $E_T^{\text{miss}} < 35$ GeV. Since this E_T^{miss} region is far away from any signal region, this does not cause a threat in understanding the background.

The defined validation regions are shown in Table 21⁷. The naming convention is as follows: VR stands for validation region, 0τ stands for a selection with exactly 3 light leptons and no taus, while noZ and Z, respectively, stand for a Z boson veto (“noZ”) or Z boson request (“Z”). The Z boson request is always a request of a same flavour opposite sign lepton pair less than 10 GeV away from the Z mass, while a veto does not just veto events with a same flavour opposite sign lepton pair in the Z window, but also a $3\ell Z$ veto as defined in section 5.6.

	VR0 τ noZa	VR0 τ Za	VR0 τ noZb	VR0 τ Zb
Z boson	$m_{\text{SFOS}} \& m_{3\ell}$ veto	request	$m_{\text{SFOS}} \& m_{3\ell}$ veto	request
E_T^{miss}	35–50	35–50	> 50	> 50
b -tagged jets	–	–	1	1
Target process	$WZ^*, Z^*Z^*, Z^* + \text{jets}$	$WZ, Z + \text{jets}$	$t\bar{t}$	WZ

Table 21: Summary of the selection requirements for the validation regions. All units are in GeV. Z^* stands for an off-shell Z. The binned validation region VR0 τ b is not in this table.

⁶This notation is widely used in ATLAS but not universal. Some analyses call regions that are used for background estimates (control region) normalization region and regions that are only used to validate the background model (validation regions) control region. Other notations might exist.

⁷In [2], 9 validation regions have been defined. I’m showing only the five light lepton validation regions here, since the other four (two regions with two light leptons and one tau and two regions with one light lepton and two taus) are not used to validate background modeling in the binned signal region, which requests three light leptons only and no taus.

The “a” regions ($\text{VR0}\tau\text{noZa}$ and $\text{VR0}\tau\text{Za}$) are adjacent to the binned signal region by requesting $35 < E_{\text{T}}^{\text{miss}} < 50$ GeV, while in the “b” regions ($\text{VR0}\tau\text{noZb}$ and $\text{VR0}\tau\text{Zb}$), orthogonality is ensured by requesting exactly 1 b -tagged jet.

Originally, the request of one b -tagged jet was inclusive. This lead to an excess in $\text{VR0}\tau\text{noZb}$. Analyzing distributions it became apparent, that the events with at least two b -tagged jets were responsible for the excess. The distribution of the number of b -tagged jets can be seen in Figure 49. The source of this excess is still unknown. A group has been created to investigate this excess [102]. Since the excess is only visible in regions with at least two b -tagged jets, they are too distinct from our signal region, where no b -tagged jets are allowed, therefore the validation regions were redefined by requesting *exactly* one b -tagged jet, rather than an inclusive selection.

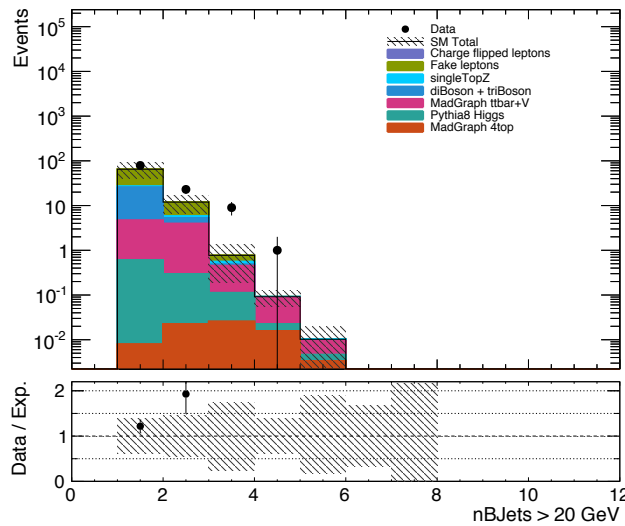


Figure 49: The observed excess in the distribution of number of b -tagged jets in the $\text{VR0}\tau\text{noZb}$ region where at least one b -tagged jet is requested. As opposed to the validation region ultimately used in this analysis, where exactly one b -tagged jet is requested. The excess is especially visible in the bin with three b -tagged jets.

A binned validation region, called $\text{VR0}\tau\text{b}$, was also defined. These bins are defined exactly as the binned signal region, but with a request of exactly one b -tagged jet. The statistics in these regions is rather low. Due to large statistical uncertainties they are not well suited for a data to Monte Carlo comparison. But the reason for defining this region was not to validate the background modeling - which was done with the other validation regions - but rather to validate the binned signal region approach. The stability of the Matrix Method predictions were tested and compared to pure Monte Carlo predictions. This validation region was also used to perform a profiled likelihood fit with all systematic uncertainties over all 20 bins to guarantee the stability of the fits and to study the effects of a multi-bin fit on the profiled quantities. Results of these studies can be found in [60].

The breakdown of all event multiplicities for all components as well as the data counts and CL_b values for the non-binned validation regions is given in Table 22, while Table 23 is only showing the total Standard Model background, events in data and the CL_b values. The CL_b is explained in Section 8.4.

While there’s perfect agreement in $\text{VR0}\tau\text{Za}$, the other validation regions show a slight overfluctuation, but overall good agreement is observed.

Region	VR0 τ noZa	VR0 τ Za	VR0 τ noZb	VR0 τ Zb
WZ	91^{+12}_{-12}	471^{+47}_{-47}	$10.5^{+1.8}_{-2.0}$	58^{+7}_{-7}
ZZ	19^{+4}_{-4}	48^{+7}_{-7}	$0.62^{+0.12}_{-0.12}$	$2.6^{+0.4}_{-0.4}$
top + V	$3.211^{+1.010}_{-0.970}$	$10.1^{+2.3}_{-2.2}$	$9.5^{+3.1}_{-3.1}$	18^{+4}_{-4}
VVV	$1.9^{+1.9}_{-1.9}$	$0.7^{+0.7}_{-0.7}$	$0.35^{+0.36}_{-0.36}$	$0.18^{+0.18}_{-0.18}$
Higgs	$2.7^{+1.3}_{-1.3}$	$2.7^{+1.5}_{-1.5}$	$1.5^{+1.0}_{-1.0}$	$0.71^{+0.29}_{-0.29}$
Reducible	73^{+20}_{-17}	261^{+70}_{-63}	47^{+15}_{-13}	19^{+5}_{-5}
Σ SM	191^{+24}_{-22}	794^{+86}_{-80}	69^{+15}_{-14}	98^{+10}_{-10}
Data	228	792	79	110
CL_b	0.90	0.49	0.72	0.79

Table 22: Data and background yields in the validation regions, except the binned validation region. Irreducible background components are derived purely from Monte Carlo; reducible components have been computed with the Matrix Method. Uncertainties are statistical and systematic.

For the binned validation region, the observed data count and the Standard Model expectation can be seen in Figure 50. The agreement in most bins is very good, bin 12 shows the largest deviation from expectation. While 2.8 ± 0.8 events are expected, 8 events are observed, which corresponds to a CL_b value of 0.96. Taking into account the look-elsewhere effect, such a deviation is not unexpected when looking at many different regions.

Figures 51 - 58 show the distributions in the four non-binned validation regions. The distributions for every bin in the binned validation region VR0 τ b can be found in Appendix C.

Sample	Σ SM	Data	CL_b
VR0 τ b bin 01	$6.1^{+1.9}_{-1.8}$	6	0.49
VR0 τ b bin 02	$3.412^{+1.031}_{-0.987}$	2	0.28
VR0 τ b bin 03	$2.3^{+0.7}_{-0.7}$	3	0.63
VR0 τ b bin 04	$3.9^{+1.2}_{-1.1}$	4	0.51
VR0 τ b bin 05	$4.9^{+1.5}_{-1.4}$	5	0.51
VR0 τ b bin 06	$6.4^{+2.0}_{-1.9}$	2	0.09
VR0 τ b bin 07	$8.1^{+2.4}_{-2.2}$	9	0.59
VR0 τ b bin 08	$1.0^{+0.5}_{-0.5}$	2	0.72
VR0 τ b bin 09	$6.6^{+1.7}_{-1.6}$	4	0.22
VR0 τ b bin 10	$2.5^{+0.7}_{-0.7}$	2	0.40
VR0 τ b bin 11	$9.7^{+2.3}_{-2.2}$	12	0.70
VR0 τ b bin 12	$2.8^{+0.8}_{-0.8}$	8	0.96
VR0 τ b bin 13	60^{+7}_{-6}	67	0.74
VR0 τ b bin 14	28^{+4}_{-4}	30	0.61
VR0 τ b bin 15	$7.7^{+1.6}_{-1.5}$	11	0.80
VR0 τ b bin 16	$1.3^{+0.8}_{-0.5}$	0	0.20
VR0 τ b bin 17	21^{+4}_{-4}	26	0.77
VR0 τ b bin 18	$1.0^{+0.5}_{-0.5}$	2	0.72
VR0 τ b bin 19	$0.28^{+0.25}_{-0.15}$	0	0.37
VR0 τ b bin 20	$0.31^{+0.28}_{-0.30}$	0	0.41

Table 23: Data and background yields in the binned validation region. Irreducible background components are derived purely from Monte Carlo; reducible components have been computed with the Matrix Method. Uncertainties are statistical and systematic. Only the total Standard Model background Σ SM is shown, not the separate contributions.

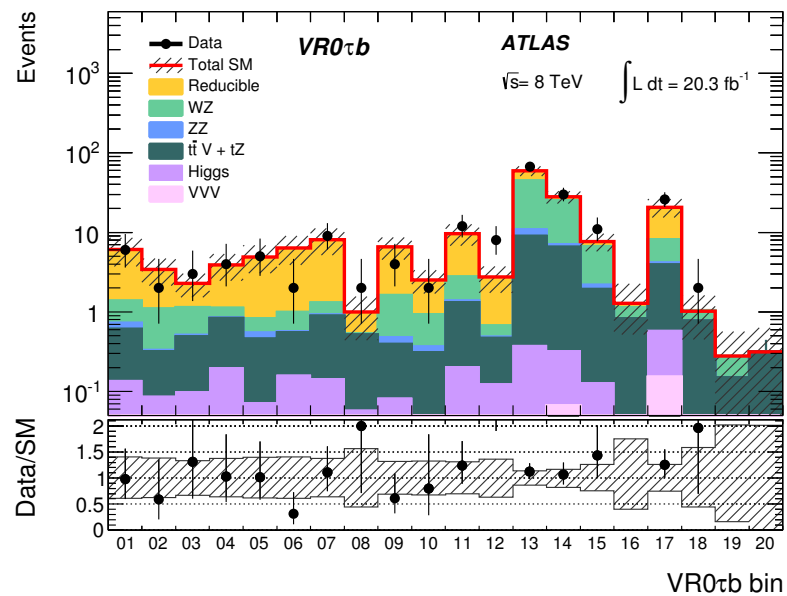


Figure 50: Number of observed and expected events in all bins of the binned validation region. Uncertainty bands include statistical and systematic uncertainties.

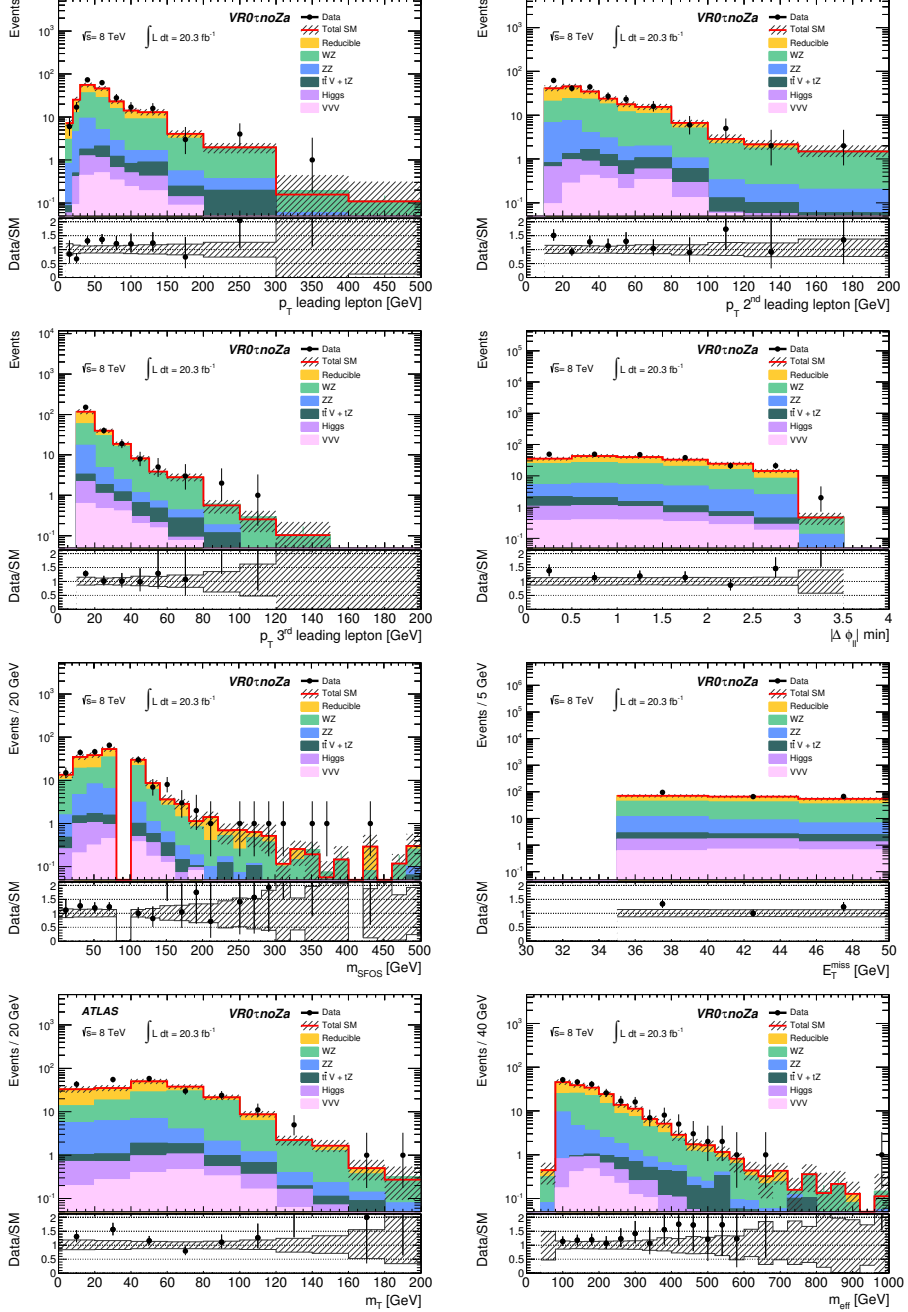


Figure 51: Distributions in VR0 τ noZa. Uncertainty bands include statistical and systematic uncertainties.

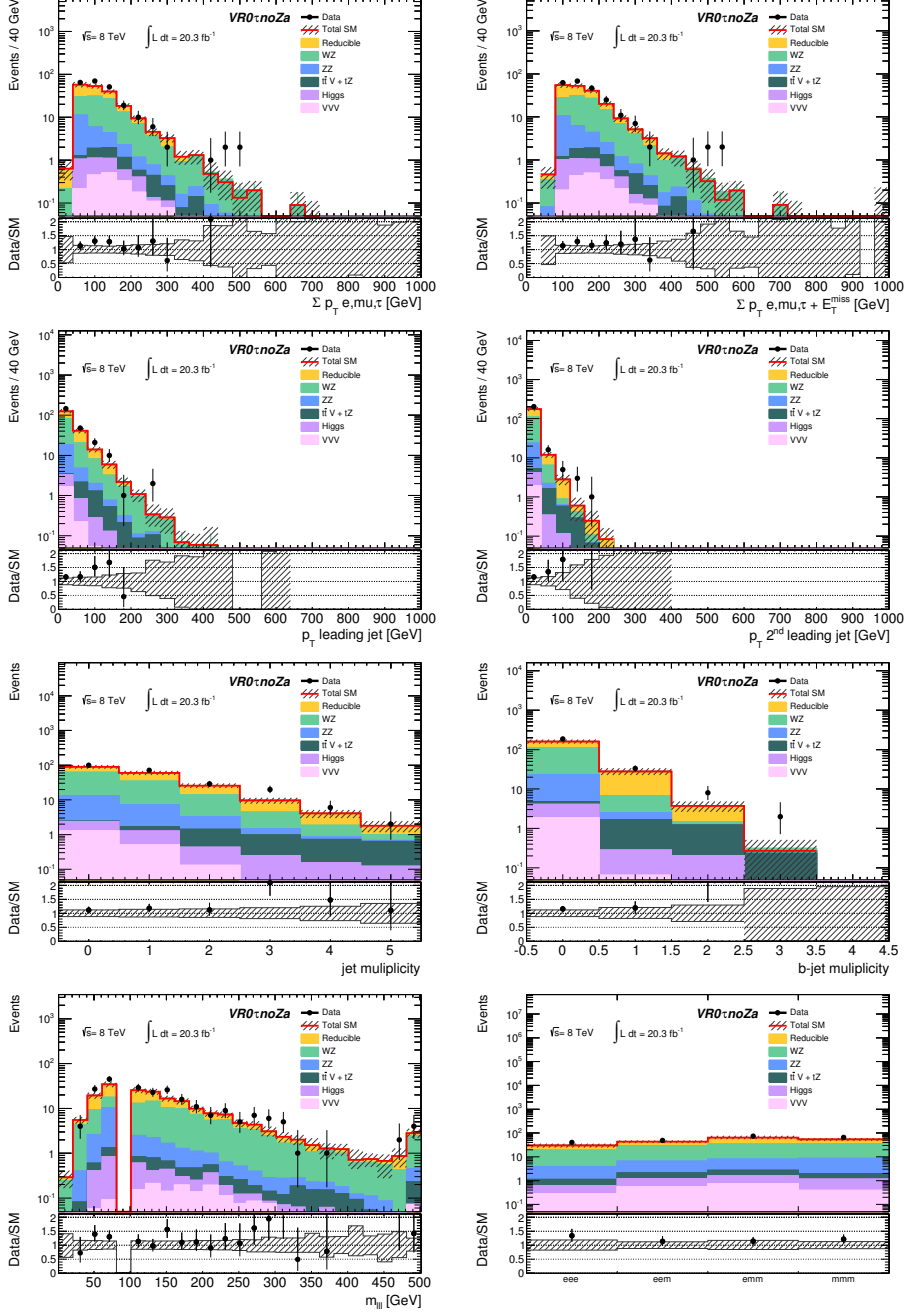


Figure 52: Distributions (continued) in VR0 τ :noZa. Uncertainty bands include statistical and systematic uncertainties.

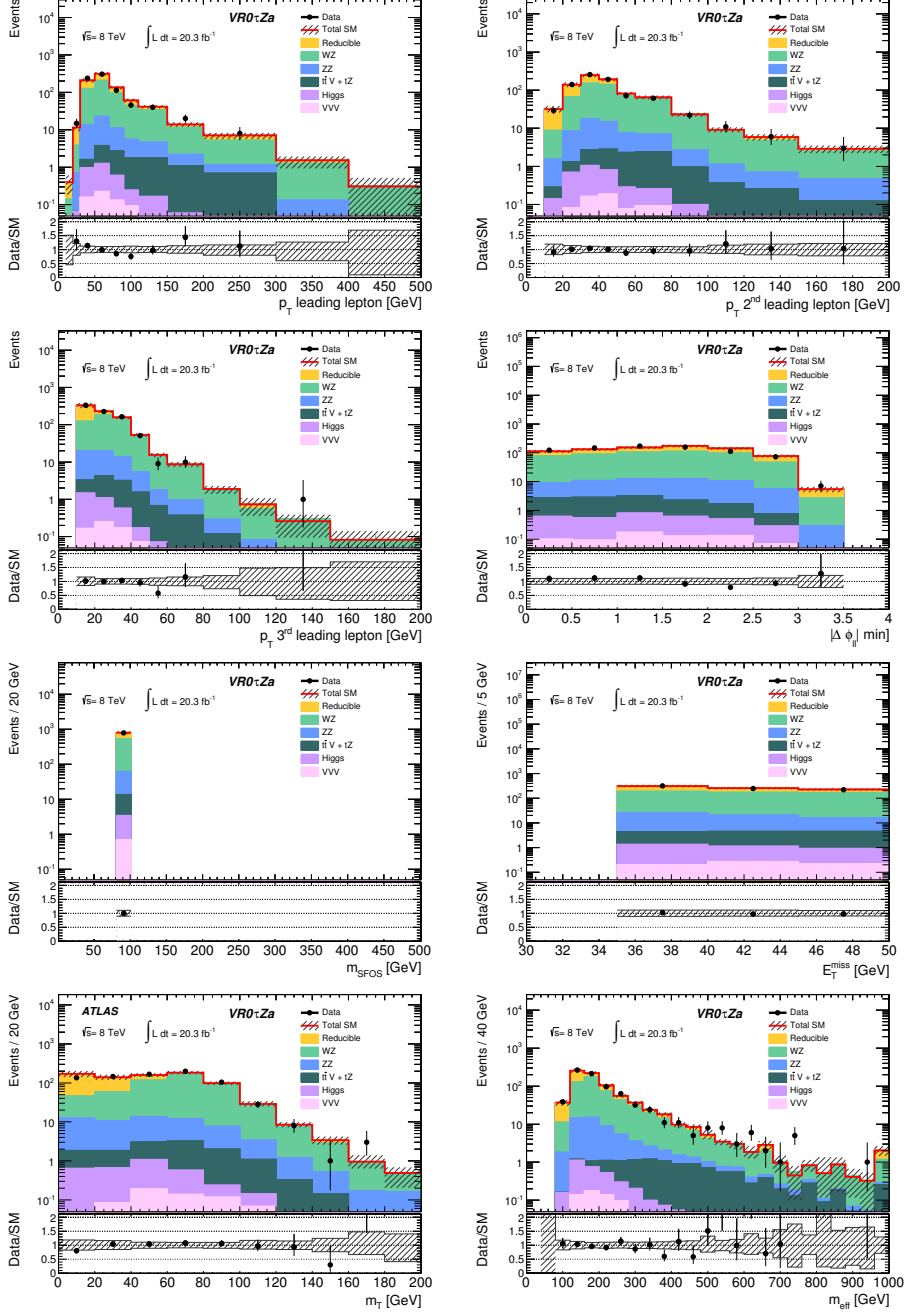


Figure 53: Distributions in VR0 τ Za. Uncertainty bands include statistical and systematic uncertainties.

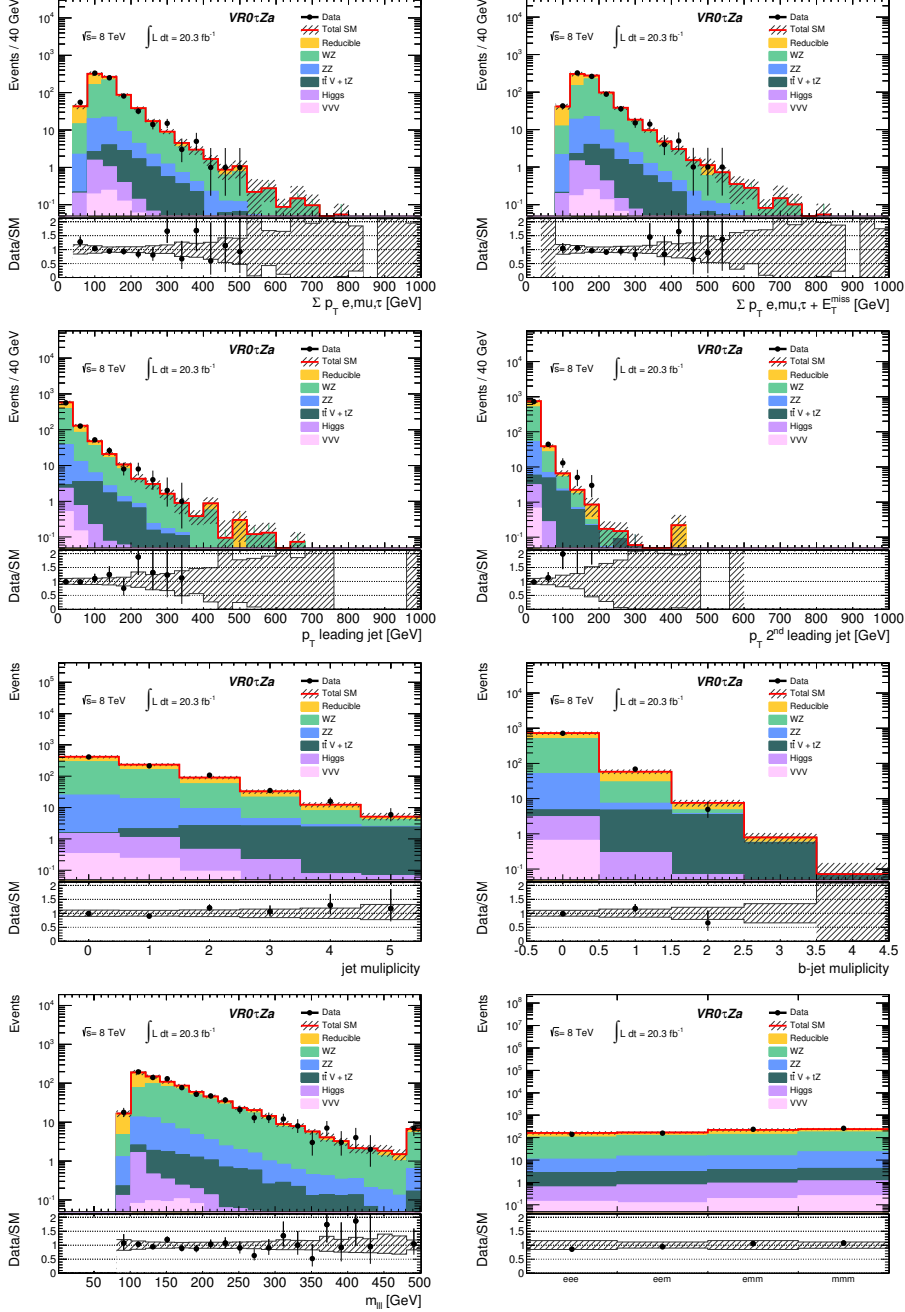


Figure 54: Distributions (continued) in VR0 τ Za. Uncertainty bands include statistical and systematic uncertainties.

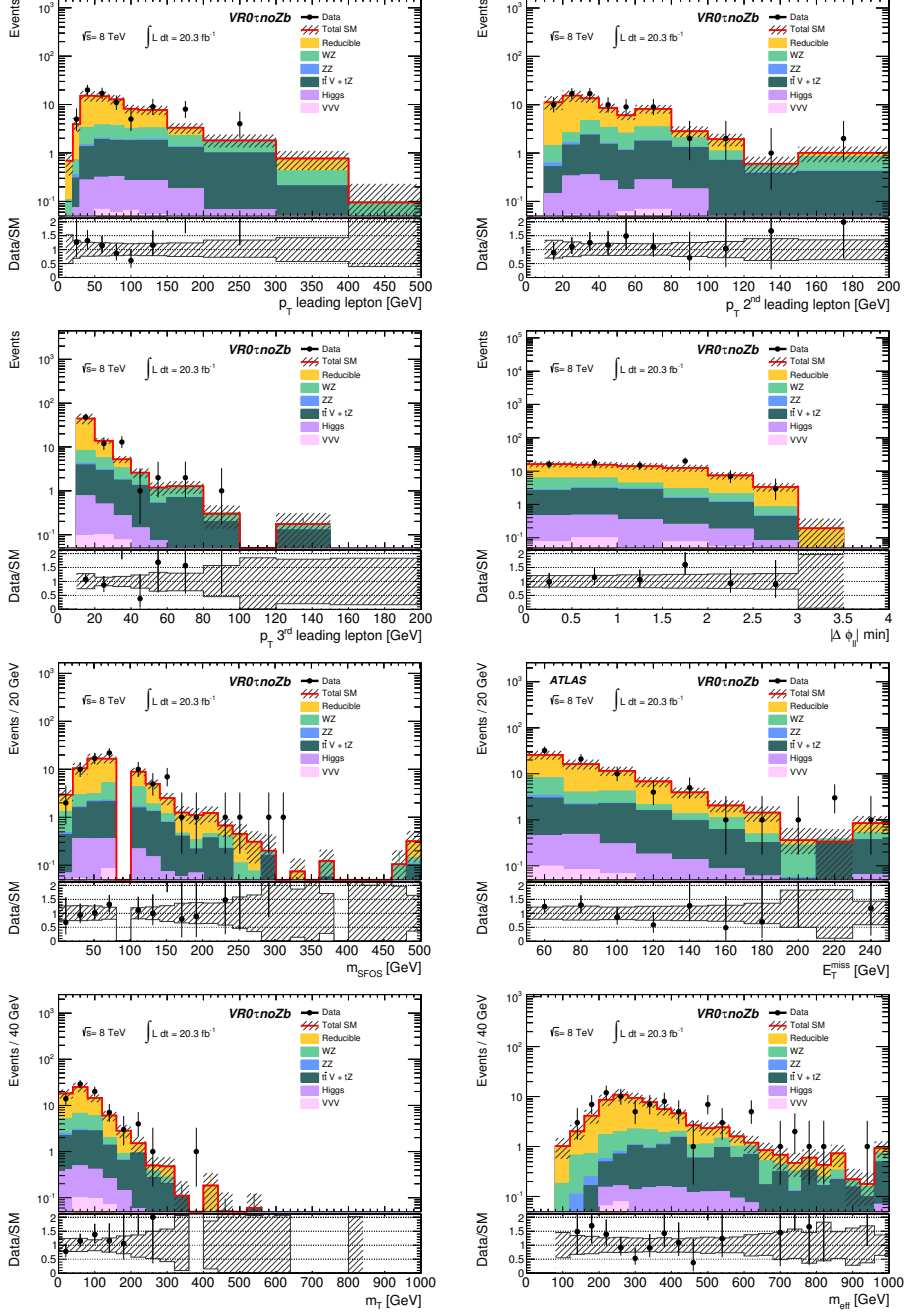


Figure 55: Distributions in VR0 τ noZb. Uncertainty bands include statistical and systematic uncertainties.

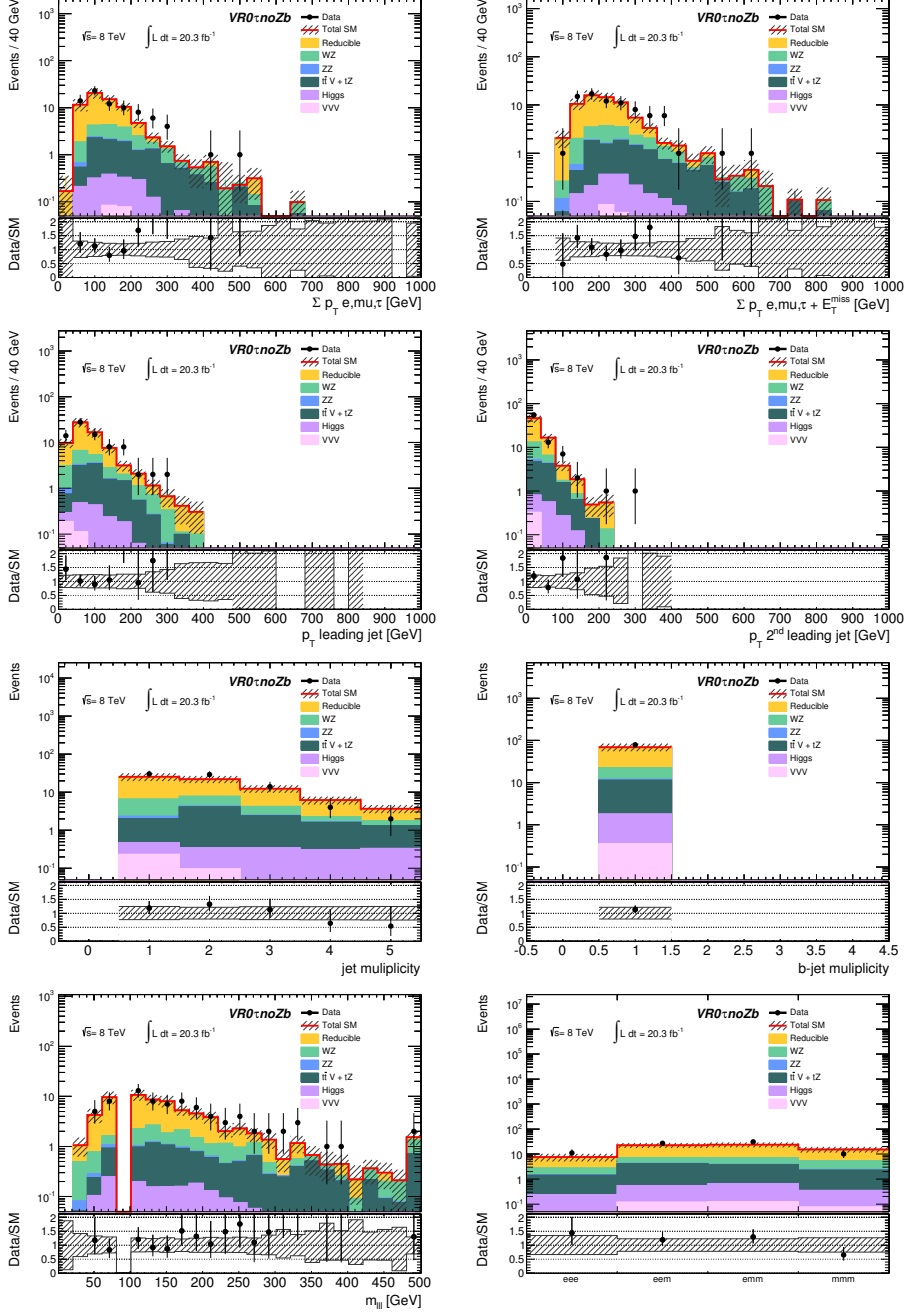


Figure 56: Distributions (continued) in VR0 τ noZb. Uncertainty bands include statistical and systematic uncertainties.

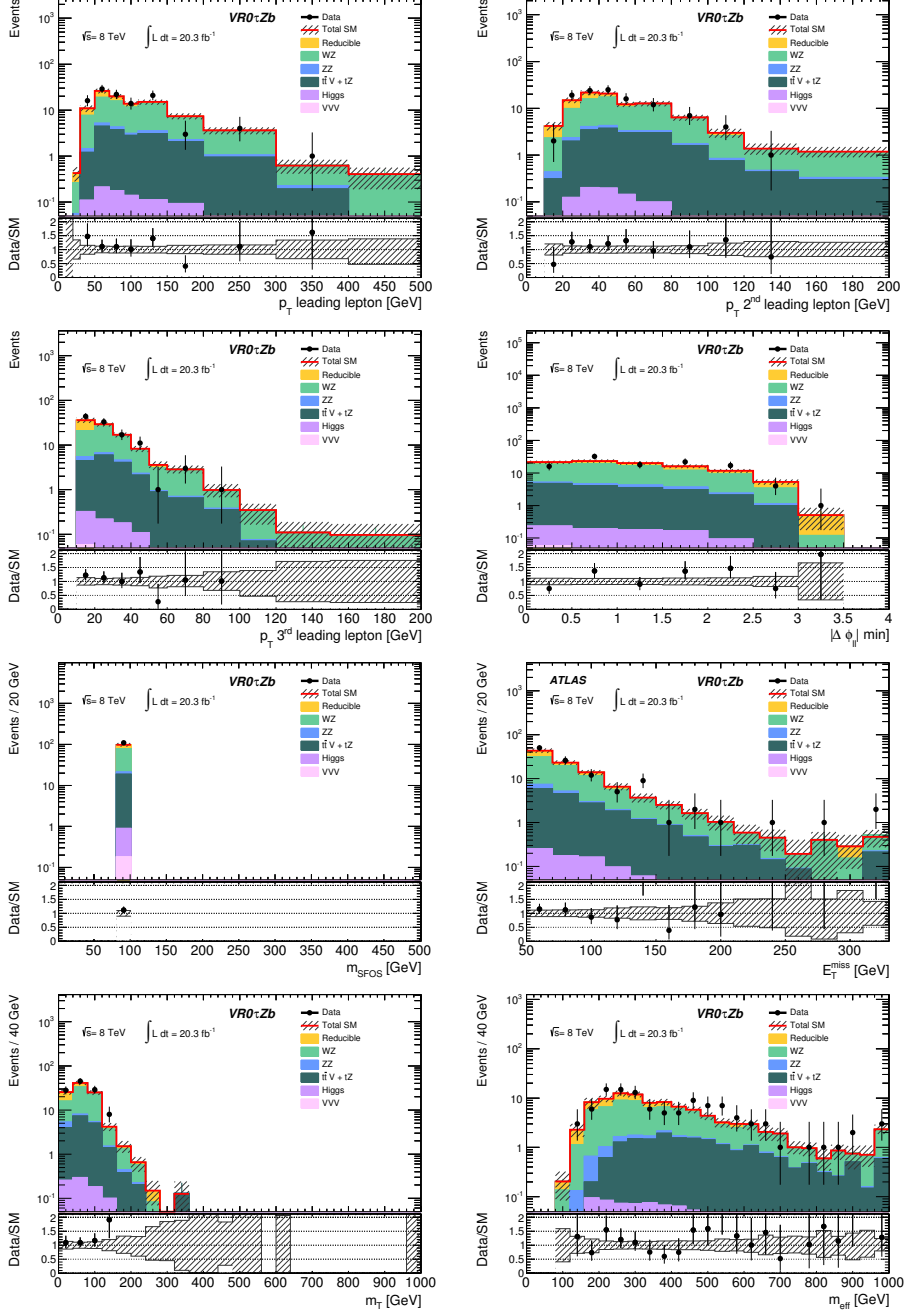


Figure 57: Distributions in VR0 τ Zb. Uncertainty bands include statistical and systematic uncertainties.

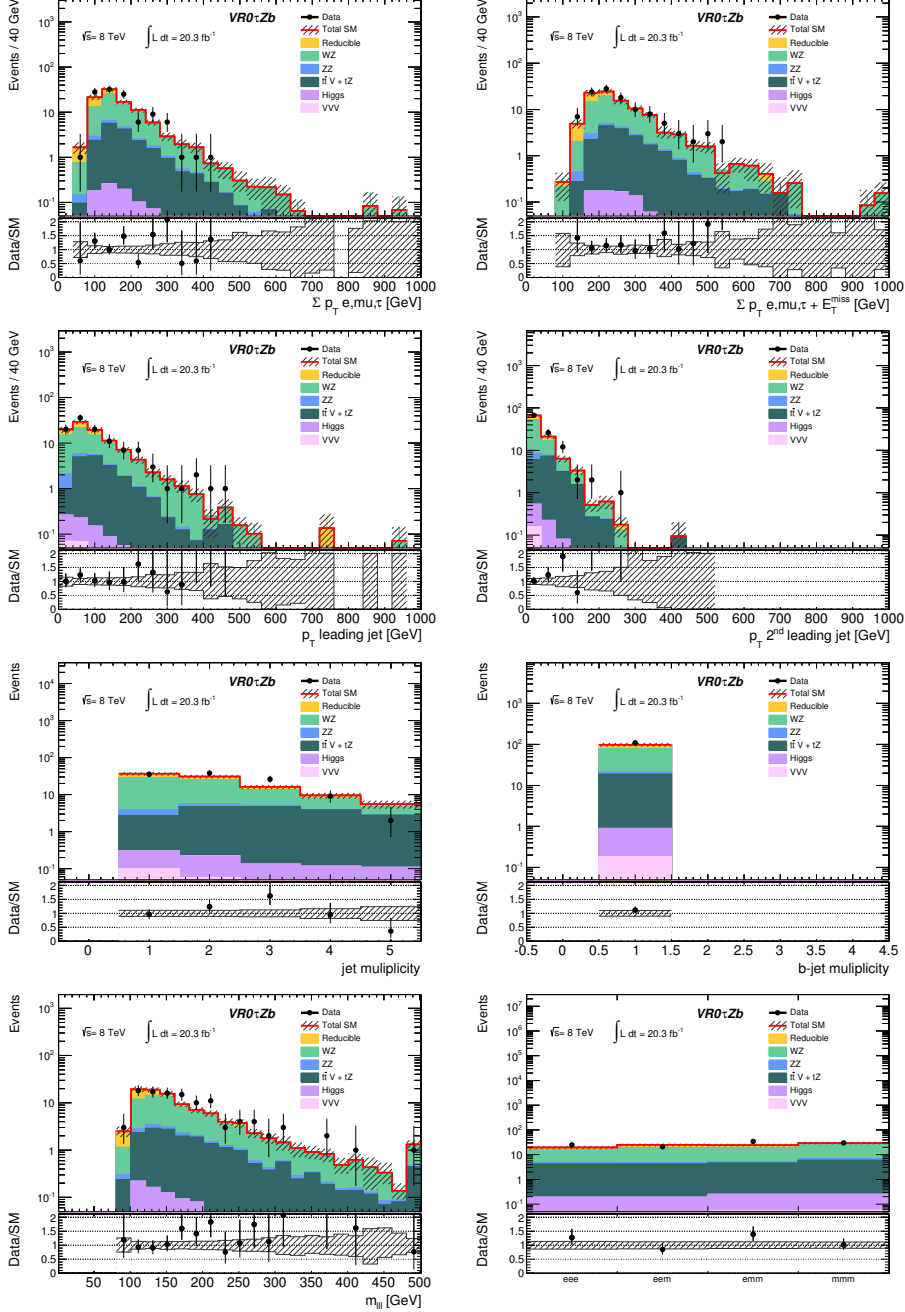


Figure 58: Distributions (continued) in VR0 τ Zb. Uncertainty bands include statistical and systematic uncertainties.

6.2 Signal contamination

Validating the background model makes only sense in regions where no signal is expected. In Figure 59, the signal contamination in the validation regions can be seen. Only the validation regions with the highest signal contamination are shown. It is generally very low, except for some low mass points. These points are already excluded and if a signal at these low masses would be present, it would have already been found in LHC data.

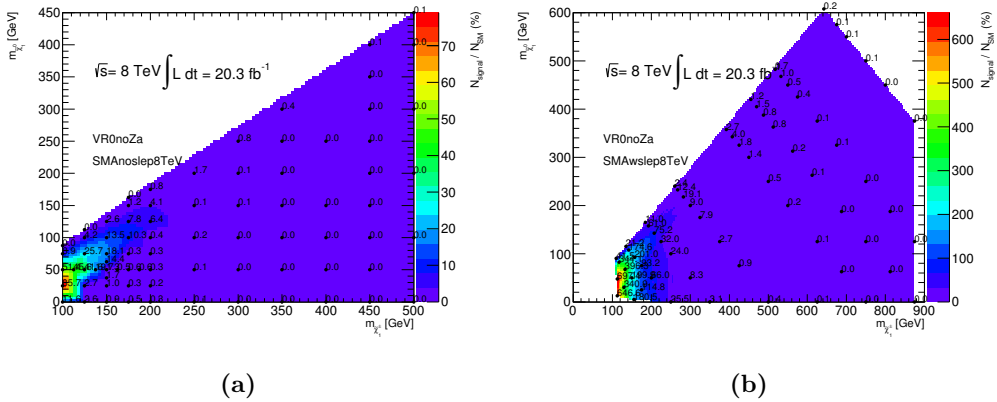


Figure 59: Signal contamination in the validation regions; only the simplified models in combination with the validation regions with the largest signal contamination are shown. (a) is the signal contamination from the WZ mediated simplified model in VR0 τ noZa, (b) is the signal contamination from the $\tilde{\ell}_L$ mediated simplified model in VR0 τ noZa.

Since the agreement between expected background and data in all validation regions is good, the background is expected to be understood, not just in these regions, but also in the adjacent signal regions. Therefore we turn our attention now to data in the signal region.

7 Events in the signal region

This chapter presents the expected and observed number of events in the signal region. No significant excess over the Standard Model has been observed. The expected irreducible background for every component in every bin can be seen in Table 24, the expected reducible background per bin, the total expected background per bin and the observed data events in every bin is shown in Table 25.

Bin	WZ	ZZ	$top + V$	VVV	Higgs	Σ Irreducible
01	$13.2^{+3.4}_{-3.2}$	$1.4^{+0.6}_{-0.5}$	$0.14^{+0.05}_{-0.05}$	$0.33^{+0.33}_{-0.33}$	$0.66^{+0.26}_{-0.26}$	$15.8^{+3.6}_{-3.4}$
02	$3.0^{+1.4}_{-1.4}$	$0.12^{+0.06}_{-0.06}$	$0.07^{+0.04}_{-0.04}$	$0.0982^{+0.1015}_{-0.1016}$	$0.15^{+0.08}_{-0.08}$	$3.4^{+1.4}_{-1.4}$
03	$7.8^{+1.6}_{-1.6}$	$0.40^{+0.14}_{-0.14}$	$0.035^{+0.046}_{-0.047}$	$0.19^{+0.19}_{-0.19}$	$0.64^{+0.22}_{-0.22}$	$9.0^{+1.7}_{-1.7}$
04	$4.5^{+1.1}_{-1.0}$	$0.20^{+0.18}_{-0.18}$	$0.14^{+0.13}_{-0.13}$	$0.6^{+0.6}_{-0.6}$	$0.46^{+0.18}_{-0.17}$	$5.9^{+1.3}_{-1.3}$
05	$6.3^{+1.6}_{-1.6}$	$1.5^{+0.5}_{-0.5}$	$0.11^{+0.08}_{-0.08}$	$0.26^{+0.27}_{-0.27}$	$0.36^{+0.14}_{-0.15}$	$8.6^{+1.8}_{-1.8}$
06	$3.7^{+1.6}_{-1.6}$	$0.25^{+0.14}_{-0.11}$	$0.047^{+0.022}_{-0.021}$	$0.24^{+0.24}_{-0.24}$	$0.33^{+0.13}_{-0.12}$	$4.6^{+1.7}_{-1.6}$
07	$7.6^{+1.3}_{-1.3}$	$0.55^{+0.16}_{-0.14}$	$0.04^{+0.15}_{-0.15}$	$0.9^{+0.9}_{-0.9}$	$0.98^{+0.29}_{-0.30}$	$10.1^{+1.7}_{-1.7}$
08	$0.30^{+0.25}_{-0.24}$	$0.012^{+0.008}_{-0.007}$	$0.12^{+0.13}_{-0.13}$	$0.13^{+0.14}_{-0.14}$	$0.13^{+0.06}_{-0.06}$	$0.69^{+0.32}_{-0.31}$
09	$16.2^{+3.2}_{-3.1}$	$1.43^{+0.32}_{-0.28}$	$0.16^{+0.09}_{-0.12}$	$0.23^{+0.24}_{-0.23}$	$0.32^{+0.11}_{-0.11}$	$18.3^{+3.3}_{-3.1}$
10	$13.1^{+2.5}_{-2.6}$	$0.60^{+0.12}_{-0.13}$	$0.12^{+0.10}_{-0.10}$	$0.4^{+0.4}_{-0.4}$	$0.22^{+0.10}_{-0.11}$	$14.4^{+2.6}_{-2.7}$
11	19^{+4}_{-4}	$0.7^{+1.2}_{-1.2}$	$0.41^{+0.24}_{-0.22}$	$0.6^{+0.6}_{-0.6}$	$0.28^{+0.12}_{-0.12}$	21^{+4}_{-4}
12	$3.7^{+1.2}_{-1.2}$	$0.14^{+0.09}_{-0.09}$	$0.12^{+0.11}_{-0.11}$	$0.6^{+0.6}_{-0.6}$	$0.12^{+0.06}_{-0.06}$	$4.7^{+1.4}_{-1.4}$
13	613^{+65}_{-64}	29^{+4}_{-4}	$2.9^{+0.7}_{-0.6}$	$1.3^{+1.3}_{-1.3}$	$2.2^{+0.7}_{-0.7}$	648^{+67}_{-66}
14	207^{+33}_{-32}	$5.5^{+1.5}_{-1.5}$	$2.0^{+0.7}_{-0.6}$	$0.8^{+0.8}_{-0.8}$	$0.98^{+0.20}_{-0.20}$	216^{+33}_{-33}
15	58^{+12}_{-13}	$3.5^{+1.1}_{-1.0}$	$0.67^{+0.29}_{-0.28}$	$1.0^{+1.0}_{-1.0}$	$0.31^{+0.11}_{-0.11}$	64^{+13}_{-13}
16	$3.9^{+1.6}_{-1.4}$	$0.12^{+0.08}_{-0.07}$	$0.08^{+0.10}_{-0.10}$	$0.33^{+0.33}_{-0.33}$	$0.033^{+0.018}_{-0.018}$	$4.4^{+1.7}_{-1.5}$
17	50^{+7}_{-6}	$2.4^{+0.7}_{-0.6}$	$0.8^{+0.5}_{-0.5}$	$3.2^{+3.2}_{-3.2}$	$0.95^{+0.29}_{-0.29}$	58^{+8}_{-7}
18	$2.3^{+1.3}_{-1.3}$	$0.08^{+0.04}_{-0.04}$	$0.15^{+0.16}_{-0.16}$	$0.5^{+0.5}_{-0.5}$	$0.05^{+0.04}_{-0.04}$	$3.1^{+1.4}_{-1.4}$
19	$0.9^{+0.4}_{-0.4}$	$0.021^{+0.019}_{-0.019}$	$0.0023^{+0.0032}_{-0.0019}$	$0.08^{+0.08}_{-0.08}$	$0.007^{+0.006}_{-0.006}$	$1.0^{+0.4}_{-0.4}$
20	$0.12^{+0.11}_{-0.11}$	$0.009^{+0.009}_{-0.009}$	$0.012^{+0.016}_{-0.016}$	$0.07^{+0.08}_{-0.07}$	$0.0009^{+0.0004}_{-0.0004}$	$0.21^{+0.14}_{-0.14}$

Table 24: Total irreducible background in the binned signal region. All components are derived purely from Monte Carlo. Uncertainties are statistical and systematic.

As can be seen in Table 25, no significant excess over the expected Standard Model background has been observed, although there are some bins with overfluctuations, most noteworthy bin 1, where 23 ± 4 events are expected, but 36 have been observed. This corresponds to a CL_b value of 0.96. Since we are looking at many bins, overfluctuations are expected by statistical fluctuations.

A graphical representation of Table 25 showing the number of expected and observed events including statistical and systematic uncertainties is shown in Figure 60. Figure 61 shows the E_T^{miss} , the m_T , the m_{SFOS} distributions in all 20 bins of the signal region joined together. Additionally the breakdown of lepton flavours is also shown. All distributions per bin are shown in Appendix D.

Bin	Irreducible	Reducible	Σ SM	Data	CL_b
01	$15.8^{+3.6}_{-3.4}$	$6.7^{+2.4}_{-2.4}$	23^{+4}_{-4}	36	0.96
02	$3.4^{+1.4}_{-1.4}$	$0.8^{+0.4}_{-0.4}$	$4.2^{+1.5}_{-1.5}$	5	0.60
03	$9.0^{+1.7}_{-1.7}$	$1.6^{+0.7}_{-0.6}$	$10.6^{+1.8}_{-1.8}$	9	0.35
04	$5.9^{+1.3}_{-1.3}$	$2.656^{+1.043}_{-0.988}$	$8.5^{+1.7}_{-1.6}$	9	0.55
05	$8.6^{+1.8}_{-1.8}$	$4.3^{+1.6}_{-1.4}$	$12.9^{+2.4}_{-2.3}$	11	0.34
06	$4.6^{+1.7}_{-1.6}$	$2.0^{+0.8}_{-0.8}$	$6.6^{+1.9}_{-1.8}$	13	0.93
07	$10.1^{+1.7}_{-1.7}$	$4.0^{+1.5}_{-1.4}$	$14.1^{+2.2}_{-2.2}$	15	0.58
08	$0.69^{+0.32}_{-0.31}$	$0.40^{+0.27}_{-0.26}$	$1.1^{+0.4}_{-0.4}$	1	0.47
09	$18.3^{+3.3}_{-3.1}$	$4.1^{+1.3}_{-1.2}$	$22.4^{+3.6}_{-3.4}$	28	0.80
10	$14.4^{+2.6}_{-2.7}$	$1.9^{+0.9}_{-0.8}$	$16.4^{+2.8}_{-2.8}$	24	0.91
11	21^{+4}_{-4}	$5.7^{+2.1}_{-1.9}$	27^{+5}_{-5}	29	0.60
12	$4.7^{+1.4}_{-1.4}$	$0.9^{+0.5}_{-0.4}$	$5.5^{+1.5}_{-1.4}$	8	0.77
13	648^{+67}_{-66}	68^{+21}_{-19}	715^{+70}_{-68}	714	0.49
14	216^{+33}_{-33}	$2.2^{+1.9}_{-2.0}$	219^{+33}_{-33}	214	0.45
15	64^{+13}_{-13}	$1.2^{+0.6}_{-0.6}$	65^{+13}_{-13}	63	0.45
16	$4.4^{+1.7}_{-1.5}$	$0.14^{+0.25}_{-0.27}$	$4.6^{+1.7}_{-1.5}$	3	0.31
17	58^{+8}_{-7}	$11.3^{+3.5}_{-3.2}$	69^{+9}_{-8}	60	0.22
18	$3.1^{+1.4}_{-1.4}$	$0.27^{+0.20}_{-0.20}$	$3.4^{+1.4}_{-1.4}$	1	0.22
19	$1.0^{+0.4}_{-0.4}$	$0.17^{+0.16}_{-0.15}$	$1.2^{+0.4}_{-0.4}$	0	0.20
20	$0.21^{+0.14}_{-0.14}$	$0.08^{+0.11}_{-0.10}$	$0.29^{+0.18}_{-0.17}$	0	0.37

Table 25: Expected Standard Model background and observed number of events in data in the binned signal region. Irreducible background components are derived purely from Monte Carlo, the numbers split up in components are shown in Table 24. Reducible background is computed with the Matrix Method. Uncertainties are statistical and systematic. A graphical representation of this table is given in Figure 60.

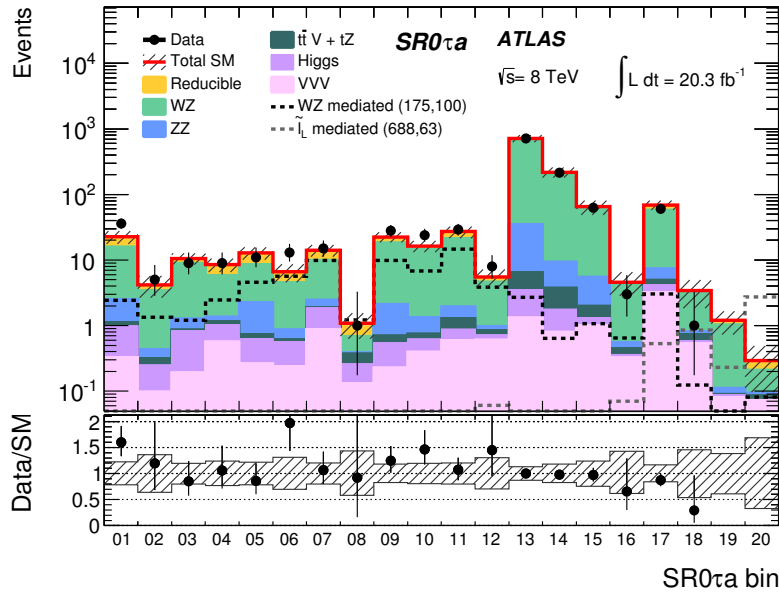


Figure 60: Number of expected and observed events in each bin of the binned signal region.

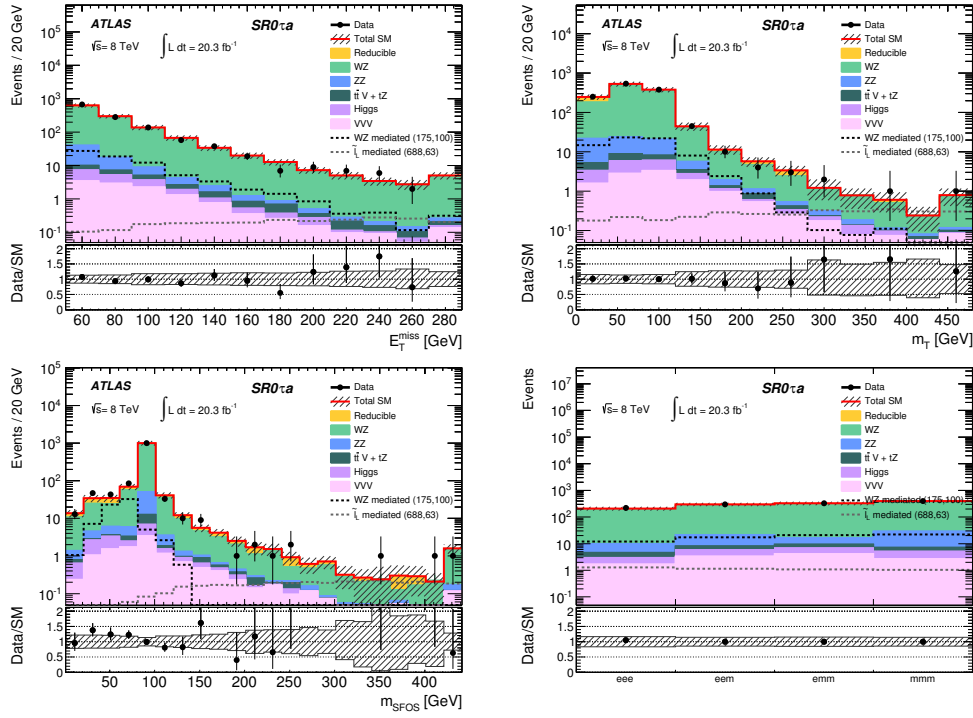


Figure 61: Distributions in the 20 bins of the binned signal region joined together. The uncertainties are statistical and systematic.

8 Statistical Test

Most analyses in ATLAS use a profile log likelihood ratio method to statistically interpret their observations. This method is briefly described here before the statistical interpretation of the analysis at hand is carried out and exclusion limits are set in Chapter 9. Mainly I will follow [91, 92, 103, 104, 105, 106, 107].

In Section 8.1, I introduce the important notion of a *p*-value. Section 8.2 deals with likelihoods in general and Section 8.3 introduces the test statistic that is used in this analysis. The CL_s method, which is used to set limits only on SUSY signals one actually has sensitivity to, is described in Section 8.4. The sampling distributions of the test statistic together with the asymptotic formulae used to approximate these sampling distributions are discussed in Section 8.5. Finally Section 8.6 describes the use of the “Asimov dataset” to get the expected sensitivity of an experiment.

8.1 *p*-values

We define the *p*-value as the probability of an experiment to get a certain outcome or one that is more extreme as the one that was observed, i.e. the *p*-value is calculated as the integral over the probability density function, integrated from the observed value till infinity,

$$p = \int_{t_{obs}}^{\infty} f(t) dt , \quad (42)$$

where t is the test statistic which is to be defined later. For now we can think of the test statistic as being the number of observed events in a given signal region (the integral then needs to be replaced by a sum since only integer numbers are allowed). Later we will need a more sophisticated test statistic to be able to incorporate systematic uncertainties.

Now we define the null hypothesis H_0 which is tested against the alternative hypothesis H_1 . Later, when we calculate discovery *p*-values and limits on the visible cross-section, H_0 will be the Standard Model (i.e. for a given region the number of expected background events b) and H_1 will be the hypothesis that additional to the Standard Model, a signal exists which leads to an enhanced event multiplicity in the region under investigation. The signal model is not further defined.

If no excess over the Standard Model has been observed, limits are set. The role of the null hypothesis H_0 and the alternative hypothesis H_1 are exchanged. H_0 is the Standard Model with the specific SUSY model and H_1 is the Standard Model only. The goal is always to reject H_0 .

When one rejects H_0 to exclude SUSY models, a *p*-value of less than 5% is usually required, though different standards can be applied. We then say the particular model is excluded at the 95% confidence level. For a discovery a much more stringent confidence level is required. This can be interpreted as introducing a Bayesian degree of belief: Because the Standard Model has withstood many tests, its degree of belief to be true (even if it’s just an effective theory) is much higher than any SUSY theory which signal we haven’t observed yet. To reject the Standard Model and claim discovery, a confidence level of $1 - 2.87 \cdot 10^{-7}$ is needed. The $2.87 \cdot 10^{-7}$ comes from the number of standard deviations in a Gaussian distributed variable. A significance of $Z = 5\sigma$ corresponds to a *p*-value of $2.87 \cdot 10^{-7}$, i.e. to claim discovery, a “ 5σ effect” needs to be observed. The agreement to call a 5σ deviation from the expected value a discovery is arbitrary but established. Other fields use different definitions. The high value protects us from statistical fluctuations, but it does not protect us from wrong assumptions like underestimated systematic effects.

Another important significance threshold is at $Z = 3\sigma$, which is called “evidence”. $Z = 3\sigma$ corresponds to a p -value of $1.35 \cdot 10^{-3}$. On the other hand, to exclude a SUSY signal model, we defined above the 95 % confidence level as sufficient, this corresponds to a significance of $Z = 1.64\sigma$. Figure 62 shows a standard normally distributed variable with a one-sided p -value of 95 %.

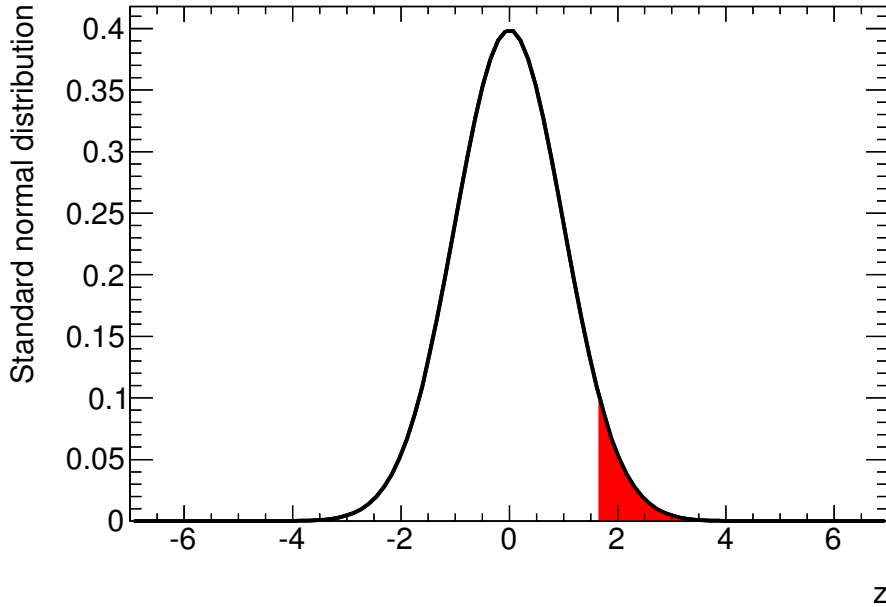


Figure 62: A standard normal distribution (= a Gaussian distribution with mean $\mu = 0$ and standard deviation $\sigma = 1$). The filled area corresponds to a p -value of 5 %.

Note that these values hold for one-sided p -values⁸ as in high energy physics this is what one is interested in, since a signal enhances the event multiplicity but does not decrease it. This is not always the case, e.g. neutrino oscillations.

Close connected to the p -value of a probability density function is the cumulative distribution function $F(t_{obs})$. It describes the probability, that a random variable will be found at a value less than or equal to the observed value of the test statistic t_{obs} ,

$$F(t_{obs}) = \int_{-\infty}^{t_{obs}} f(t) dt . \quad (43)$$

The cumulative distribution function of the standard normal distribution carries a special symbol: $\Phi(t)$. Since the integral over the whole probability density function must be 1, we can rewrite the p -value of a standard normally distributed variable as

$$p = 1 - \Phi(Z) , \quad (44)$$

and hence

$$Z = \Phi^{-1}(1 - p) . \quad (45)$$

The inverse of the cumulative distribution function - in the case of a standard normal distribution this is Φ^{-1} - is also called the quantile.

⁸For example, the two-sided p -value of a 95 % confidence level is at $Z = 1.96\sigma$. For symmetry reason, $Z = 1.64\sigma$ would correspond to a p -value of 2.5 %.

8.2 The likelihood function

For every bin in our signal region, we have

$$E[n_i] = \mu s_i + b_i , \quad (46)$$

where $i \in [1, 2, \dots, N]$ is the number of bins, $E[n_i]$ is the expectation value in bin i , s_i is the number of expected signal events in bin i , b_i is the number of expected background events in bin i and μ is a parameter called signal strength. The signal strength is our parameter of interest. If $\mu = 0$, we are dealing with the background-only hypothesis, while $\mu = 1$ corresponds to the nominal signal hypothesis.

Since an event either is in a signal region or not, we can use a binomial distribution to quantify the likelihood of our data. As the probability of an event to lie in a signal region is very small and we are looking at a big sample of events, we can simplify the approach by using a Poissonian distribution, rather than a binomial distribution. Hence we can construct the likelihood as a product of one Poissonian per bin

$$L(\mu) = \prod_{i=1}^N \frac{(\mu s_i + b_i)^{n_i}}{n_i!} e^{-(\mu s_i + b_i)} . \quad (47)$$

Now we could maximize this likelihood function to determine the signal strength μ . But we haven't accounted for any systematic uncertainties yet, before we continue, we have to incorporate them into our likelihood.

In a profiled likelihood method, the systematic uncertainties enter the likelihood as nuisance parameters. They are measured, but not known a priori and are fitted at the same time as the likelihood is minimized. That means that the measurement itself is used to determine the systematic uncertainties. A possible over- or underestimation of systematic uncertainties can be corrected this way. If the observation agrees well with the expectation, the systematic uncertainties get fitted below the input uncertainties. On the other hand, if a signal is present, the excess in observation is first attributed to a systematic effect; large systematic uncertainties will eat up the observed signal. The measurement and handling of systematic uncertainties in a profiled likelihood fit is a vast subject, it is described in great detail in e.g. [97].

We assume the nuisance parameters to be Gaussian distributed. This is partly a guess and partly legitimated by the central limit theorem. We denote the entirety of them as θ and multiply Gaussian terms to Equation (47), the likelihood then becomes $L(\mu, \theta)$. Note, that all the expected background yields b_i in Equation (47) are nuisance parameters as well, not so the signal yields s_i , though, since these are parametrized via the signal strength μ and this parameter is the one we are interested in.

Now we construct the likelihood ratio $\lambda(\mu)$

$$\lambda(\mu) = \frac{L\left(\mu, \hat{\theta}(\mu)\right)}{L\left(\hat{\mu}, \hat{\theta}\right)} . \quad (48)$$

$\hat{\mu}$ and $\hat{\theta}$ are the maximum likelihood estimators, they are chosen such, that the likelihood $L(\mu, \theta)$ becomes maximal. $L\left(\hat{\mu}, \hat{\theta}\right)$ is called the unconditional maximum likelihood. $\hat{\theta}$ on the other hand is the maximum likelihood estimator for a given μ . $L\left(\mu, \hat{\theta}(\mu)\right)$ is called the conditional maximum likelihood.

Consequently, $0 \leq \lambda(\mu) \leq 1$ with $\lambda(\mu)$ close to 1 indicating good agreement between observed and hypothesized value of μ , which is either $\mu = 0$ for discovery, $\mu = 1$ for exclusion and a variable μ for upper limits.

Before we look at the definition of our test statistic, we will modify the likelihood ratio to correct for one shortcoming: Consider a large underfluctuation, the unconditional maximum likelihood estimator $\hat{\mu}$ will be smaller than 0 and the likelihood ratio (48) will become small, indicating disagreement between hypothesis and data. While this is true, there has certainly no new signal been observed, since we require signals with $\mu > 0$. Again, this is not necessarily true for all cases, destructive interference or neutrino oscillations predict a signal with $\mu < 0$. But in our case we are only interested in $\mu > 0$ and large underfluctuations are either statistical flukes or indicate a problem in the background modeling. However, it is certainly not the signal we are looking for. Therefore we constrain $\hat{\mu} > 0$ and redefine the likelihood ratio as

$$\tilde{\lambda}(\mu) = \begin{cases} \frac{L(\mu, \hat{\theta}(\mu))}{L(\hat{\mu}, \hat{\theta})} & \hat{\mu} \geq 0 \\ \frac{L(\mu, \hat{\theta}(\mu))}{L(\mu=0, \hat{\theta}(\mu=0))} & \hat{\mu} < 0 \end{cases} . \quad (49)$$

8.3 Test statistic

A test statistic is a scalar quantity that incorporates measurements in possibly more than one channels and can also include systematic uncertainties. Using a test statistic, we will have a one-dimensional distribution, irrespective of the number of search channels and parameters. The test statistic we use, the likelihood ratio, is the most powerful available, according to the Neyman-Pearson Lemma. However, this does not hold when adding systematic uncertainties, but it's still the best guess of the most powerful test we have.

For reasons that become more clear later (see Section 8.5), we define the test statistic \tilde{t}_μ as

$$\tilde{t}_\mu = -2 \ln \tilde{\lambda}(\mu) , \quad (50)$$

where the tilde on \tilde{t}_μ indicates the use of $\tilde{\lambda}(\mu)$, i.e. the likelihood ratio (49) with protection against underfluctuations.

\tilde{t}_μ can be any positive number with $\tilde{t}_\mu = 0$ indicating perfect agreement between data and hypothesis. The level of disagreement between them can be quantified with

$$p_\mu = \int_{\tilde{t}_{\mu,obs}}^{\infty} f(\tilde{t}_\mu | \mu) d\tilde{t}_\mu , \quad (51)$$

where $f(\tilde{t}_\mu | \mu)$ is the probability density function of \tilde{t}_μ for a given μ and $\tilde{t}_{\mu,obs}$ is the value of the test statistic observed in data. But Equation (51) looks exactly as Equation (42), so the disagreement is given by a p -value of the test statistic distribution. This corresponds to Figure 62 with the sole exception that the test statistic will not be normally distributed.

When looking for a signal in a signal region, one first enters “discovery mode”, i.e. defining the Standard Model as null hypothesis by setting $\mu = 0$. The discovery test statistic has a special notation, $\tilde{q}_0 = \tilde{t}_0$, it is given by Equations (49) and (50) as

$$\tilde{q}_0 = -2 \ln \tilde{\lambda}(\mu = 0) = \begin{cases} -2 \ln \frac{L(\mu=0, \hat{\theta}(\mu=0))}{L(\hat{\mu}, \hat{\theta})} & \hat{\mu} \geq 0 \\ 0 & \hat{\mu} < 0 \end{cases} . \quad (52)$$

If an overfluctuation has been observed, one can quote a one-sided discovery p -value

$$p_0 = \int_{\tilde{q}_{0,obs}}^{\infty} f(\tilde{q}_0|\mu=0) d\tilde{q}_0 . \quad (53)$$

If no significant excess over the Standard Model background has been observed, null and alternative hypothesis are switched and μ is set to 1. Hence, $b+s$ becomes the expectation value of the null hypothesis which one tries to reject. The test statistic \tilde{q}_1 in this case is defined as

$$\tilde{q}_1 = \begin{cases} -2 \ln \frac{L(\mu=1, \hat{\theta}(\mu=1))}{L(\mu=0, \hat{\theta}(\mu=0))} & \hat{\mu} < 0 \\ -2 \ln \frac{L(\mu=1, \hat{\theta}(\mu=1))}{L(\hat{\mu}, \hat{\theta})} & 0 \leq \hat{\mu} \leq 1 \\ 0 & \hat{\mu} > 1 . \end{cases} \quad (54)$$

Here we are not only protecting the test statistic from underfluctuation ($\hat{\mu} < 0$), but also from going $\hat{\mu} > 1$, since we want to set an upper limit on the signal model in question, and while $\hat{\mu} > 1$ does indeed show a disagreement between hypothesis and data, we certainly don't want to exclude a model because it is producing an event rate which is too high.

The p -value in the case of exclusion is set as in Equation (53), with \tilde{q}_1 replacing \tilde{q}_0 everywhere,

$$p_1 = \int_{\tilde{q}_{1,obs}}^{\infty} f(\tilde{q}_1|\mu=1) d\tilde{q}_1 . \quad (55)$$

Once we have exclusion limits, we can also set an upper limit on the signal strength parameter μ . This is similar to the exclusion mode, except that μ is not fixed, but rather allowed to float and the goal is to find μ_{up} which corresponds to an exclusion at the 95 % confidence level. Hence the null hypothesis is the distribution under the expected event rate given by $b + \mu s$. The test statistic is similar to the exclusion case (54),

$$\tilde{q}_\mu = \begin{cases} -2 \ln \frac{L(\mu, \hat{\theta}(\mu))}{L(\mu=0, \hat{\theta}(\mu=0))} & \hat{\mu} < 0 \\ -2 \ln \frac{L(\mu, \hat{\theta}(\mu))}{L(\hat{\mu}, \hat{\theta})} & 0 \leq \hat{\mu} \leq \mu \\ 0 & \hat{\mu} > \mu . \end{cases} \quad (56)$$

Note, Equation (54) is a special case of (56) with $\mu = 1$.

As usual, the p -value of \tilde{q}_μ is given by

$$p_\mu = \int_{\tilde{q}_{\mu,obs}}^{\infty} f(\tilde{q}_\mu|\mu) d\tilde{q}_\mu , \quad (57)$$

and μ_{up} is found by requesting

$$p_{\mu_{up}} = \int_{\tilde{q}_{\mu_{up},obs}}^{\infty} f(\tilde{q}_{\mu_{up}}|\mu_{up}) d\tilde{q}_{\mu_{up}} = 0.05 . \quad (58)$$

8.4 CL_s

I first define the components used to construct the CL_s and then describe its merits. For more details, see [104] and [105].

The CL_s method is only used to exclude signal models. For discovery we simply look at the p -value under the assumption of the background-only hypothesis. For simplicity we will from now on only look at the exclusion test statistic \tilde{q}_1 defined in (54). The case for upper limits, where μ is variable and need to be determined by searching for a specific p -value, is handled in a similar way.

We first define the CL_b as the probability of the test statistic \tilde{q}_1 to be larger than the observed value of \tilde{q}_1 given a distribution of b only in data, i.e. under the background-only hypothesis,

$$\text{CL}_b = \int_{\tilde{q}_{1,obs}}^{\infty} f(\tilde{q}_1|b) d\tilde{q}_1 . \quad (59)$$

One has to be careful with the notation: In the test statistic, μ is equal to 1, since we are in exclusion mode and the null hypothesis is $s + b$. On the other hand, in the distribution in data which we simulate with Monte Carlo pseudo-experiments or using asymptotic formulae (see Section 8.5), μ is set to 0, since we assume the Standard Model hypothesis without additional signal to be true, i.e. $\mu s + b = b$.

The CL_{s+b} is defined the same way but under the assumption of a distribution of $s + b$ in data, i.e. under the nominal signal hypothesis

$$\text{CL}_{s+b} = \int_{\tilde{q}_{1,obs}}^{\infty} f(\tilde{q}_1|s + b) d\tilde{q}_1 . \quad (60)$$

Here we have $\mu = 1$ for both the hypothesis being tested and the assumed value in the distribution of the data.

Note that the definitions of CL_{s+b} and CL_b differ in the literature. While [91] defines the p -value of CL_b only as integral from $-\infty$ to \tilde{q}_{obs} , [105] defines both CL_{s+b} and CL_b as integral from $-\infty$ to \tilde{q}_{obs} , but with a test statistic that increases for more signal-like outcomes of the experiment. Here, I use the test statistic as defined in [91], i.e. one that decreases for more signal-like data. Taking this into account, CL_{s+b} and CL_b are defined the same way as in [105].⁹

CL stands for confidence level, but if one wants to exclude a signal at the 95 % confidence level, one tests for $\text{CL}_{s+b} < 0.05$, so the confidence level is given by $1 - \text{CL}_{s+b}$.

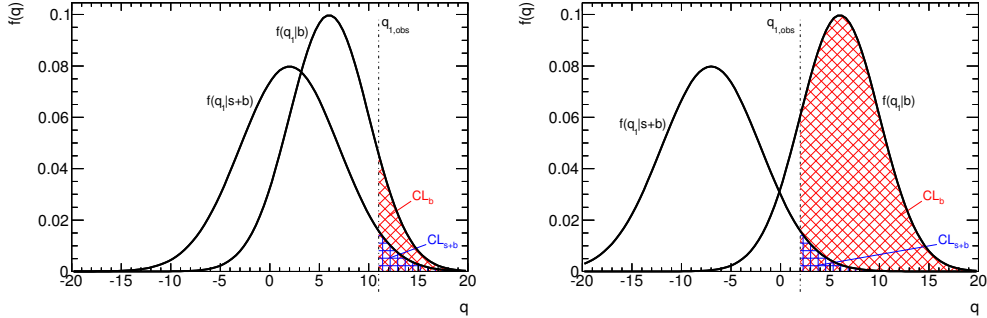
CL_s is then defined as

$$\text{CL}_s = \frac{\text{CL}_{s+b}}{\text{CL}_b} . \quad (61)$$

Even when CL_s carries a CL in its name, it is not a confidence level, nor is it a p -value, but a ratio of p -values.

Using the CL_s method is conservative in the sense that we do not exclude models to which we don't have sensitivity to. Looking at Equation (61), the denominator is always smaller than 1, i.e. the CL_s is always larger than the CL_{s+b} . Figure 63 shows two plots with each two exemplary distributions: background-only and background plus nominal signal hypotheses. In both cases, the $\text{CL}_{s+b} < 5\%$, thus, both signal models would be excluded when looking only at this p -value. In Figure 63a, the background-only hypothesis is not too different from the nominal signal hypothesis. The CL_s method gives a penalty to signal models one has no or not much sensitivity to. Since in this case the CL_b is small, too, the signal model would not be excluded with the CL_s method. In Figure 63b, on the other hand, the probability density functions of the background-only and the nominal signal model are well separated, the CL_b value is close to 1, and the penalty by the CL_s method is small enough to still exclude the model.

⁹Tables 22, 23 and 25 on the other hand, use the definition of CL_b as in [91].



(a) Distributions with low sensitivity to the signal.
(b) Distributions with good sensitivity to the signal.

Figure 63: Exemplary distributions with different separations between the background-only and the background + signal hypotheses. (a) has a small separation between these two hypotheses and therefore a low sensitivity to the signal. (b) has a larger separation between these two hypotheses and therefore a higher sensitivity to the signal. Note that the test statistic has a smaller value for more signal-like data.

8.5 Sampling distributions

Now that we have defined our test statistic for the three different use cases, we would like to calculate the p -values given in Equations (53), (55) and (57). For this we need the sampling distributions $f(\tilde{q}_\mu | \mu')$, where μ is the test statistic and μ' - which can but doesn't have to be the same as μ - is the distribution in data.

To get the sampling distributions, one can run an ensemble of Monte Carlo pseudo-experiments, or more informally: throwing toys. This does always work, but can take up a huge amount of CPU time (see also Section 9.5). It is desirable to have a computationally more light weight solution to compute these distributions, especially for sensitivity studies. Approximative formulae exist for sufficiently large data sample sizes [91]. In this approximation, the sampling distribution follows a chi-square distribution mixed with a delta distribution at zero. The approximation is sometimes also called asymptotic formula, or asymptotic limit.

When using the discovery test statistic (52), the cumulative distribution function (43) becomes¹⁰

$$F_{(\tilde{q}_0 | \mu')}(\tilde{q}_{0,obs}) = \Phi \left(\sqrt{\tilde{q}_{0,obs}} - \frac{\mu'}{\sigma} \right), \quad (62)$$

where σ is the standard deviation of $\hat{\mu}$, it can be estimated by using a special, artificial data set called “Asimov data set” (see Section 8.6). Using (44) and (45), we get

$$Z_0 = \Phi^{-1}(1-p) = \sqrt{\tilde{q}_{0,obs}} - \frac{\mu'}{\sigma}, \quad (63)$$

and in the usual case of no signal present in data the simple formula

$$Z_0 = \sqrt{\tilde{q}_{0,obs}}. \quad (64)$$

The subscript in Z_0 indicates $\mu = 0$.

¹⁰My notation differs here from [91], where this result was taken from, to clearly distinguish between random variable and argument of the cumulative distribution function.

Using the exclusion test statistic (54), where we replace $\tilde{\lambda}(\mu)$ from Equation (48) with $\lambda(\mu)$ (49) for simplicity, and subsequently writing q_1 instead of \tilde{q}_1 , we get for the cumulative distribution function

$$F_{(q_1|\mu')}(q_{1,obs}) = \Phi\left(\sqrt{q_{1,obs}} - \frac{1-\mu'}{\sigma}\right). \quad (65)$$

and hence, using again (44) and (45)

$$Z = \sqrt{q_{1,obs}} - \frac{1-\mu'}{\sigma}. \quad (66)$$

Setting $\mu' = 1$ gives the significance of the CL_{s+b}

$$Z_{CL_{s+b}} = \sqrt{q_{1,obs}}, \quad (67)$$

and with $\mu' = 1$ we get the significance of the CL_b

$$Z_{CL_b} = \sqrt{q_{1,obs}} - \frac{1}{\sigma}. \quad (68)$$

The case for the test statistic \tilde{q}_1 and the one for upper limits (56) is similar but more cluttered. It can be looked up in [91].

All these results are approximations and only valid in the asymptotic limit of a large sample. The goodness of the approximation is not only dependent of the number of expected events, but also on the value of the test statistic. This can be seen in Figure 64, which is taken from [91].

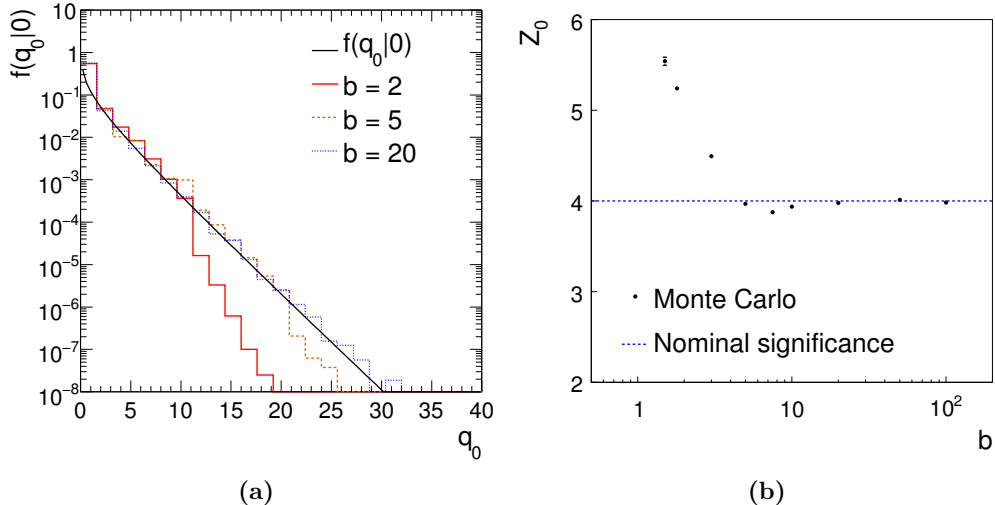


Figure 64: Comparisons for the asymptotic limit formula and Monte Carlo pseudo-experiments. Only the discovery test statistic (52) with no signal present in data is shown. (a) shows the probability density function $f(q_0|0)$ for three different values of b and the curve from the asymptotic limit as a function of q_0 . (b) shows the discovery significance Z_0 from Equation (64) with a fixed asymptotic value of $Z_0 = \sqrt{q_{0,obs}} = 4$ and derived with Monte Carlo pseudo-experiments as a function of b .

As can be seen in Figure 64a, the distribution from Monte Carlo pseudo-experiments falls off more quickly, than the asymptotic formula, the integral of the tail is therefore

overestimated in the asymptotic limit, leading to a conservative estimation of the discovery significance. A closer look at Figure 64b reveals that this is indeed true for most of the background values, but roughly between 5 and 10 background events, the asymptotic formula is even too aggressive, although not by much. When $b \geq 4$, the accuracy is better than 10 %.

For the exclusion test statistic, the situation is the other way round, since null and alternative hypotheses are exchanged, i.e. asymptotic exclusion limits will be more aggressive. This can also be seen in our comparison of exclusion limit contours derived with pseudo-experiments and with the asymptotic formulae in Figure 94.

In practice it's not always easy to assess if the asymptotic formula is good enough or Monte Carlo pseudo-experiments need to be run, which are computationally expensive. So in general one wants to prevent it and use asymptotic formulae. Best practice is to compare pseudo-experiments results with asymptotic results and decide on a case by case basis. Usually, a background expectation of $b \geq 2$ has a good chance to be close enough to the true value and asymptotic results can be used. There's a tendency in ATLAS to also use asymptotic results for lower background estimates. For a discovery p -value, this gives a conservative result, but for exclusion limit contours, the result will be too aggressive. I advocate the use of asymptotic results also for lower values of b as long as one can show that the differences are not too large and it is clearly stated in the publication that the asymptotic approximation has been used. This subject is discussed in more detail in Section 9.5.

8.6 Expected values and the Asimov dataset

So far we have only discussed how to achieve observed limits, but usually one also wants to quote an expected sensitivity. For discovery, one would like to know the expected p -value, given the nominal signal hypothesis is true and in the case of exclusion, one is interested in the CL_s under the background-only hypothesis.

The expected sensitivity is given by taking the median of the test statistic of the alternative hypothesis and taking the p -value of the null hypothesis test statistics¹¹. For example, to find the expected discovery p -value, one plots $f(\tilde{q}_0|0)$, the probability density function of the discovery test statistic under the assumption of no signal and $f(\tilde{q}_0|1)$, the probability density function of the discovery test statistic under the nominal signal assumption. Then one has to find $\text{med}[\tilde{q}_0|1]$, the median value of $f(\tilde{q}_0|1)$, and calculate the discovery p -value

$$p_0 = \int_{\text{med}[\tilde{q}_0|1]}^{\infty} f(\tilde{q}_0|\mu=0) d\tilde{q}_0 = 1 - F_{(\tilde{q}_0|0)}(\text{med}[\tilde{q}_0|1]) , \quad (69)$$

where $F_{(\tilde{q}_0|0)}(\text{med}[\tilde{q}_0|1])$ denotes the cumulative distribution function of $f(\tilde{q}_0|\mu=0)$ evaluated at $\text{med}[\tilde{q}_0|1]$. Figure 65 depicts the situation.

When using Monte Carlo pseudo-experiments to derive the observed limit, getting the expected limit is straight-forward by the procedure described above. Again: this is computationally expensive and should be avoided. When using asymptotic formulae, we can plug in Equation (62) and use Equation (63) and get for the median (expected) discovery significance $Z_{0,\text{exp}}$

$$Z_{0,\text{exp}} = \sqrt{\text{med}[\tilde{q}_0|1]} \quad (70)$$

¹¹At this point I feel obliged to emphasize that the expected sensitivity is given by the median of \tilde{q}_μ , assuming an alternative $\mu' \neq \mu$ and *not*, as often assumed, by setting the observed number of events to the expected number of events.

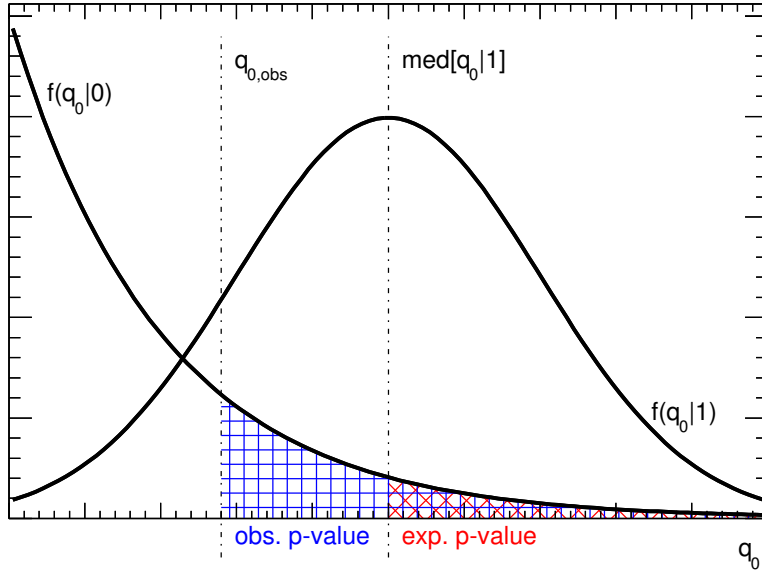


Figure 65: Illustration of observed and expected discovery p -value.

But how do we derive $\text{med}[\tilde{q}_0|1]$, the median of $f(\tilde{q}_0|1)$? Looking at its cumulative distribution function (62), we see that it depends on σ of $\hat{\mu}$, i.e. we need an approximation for σ .

The approximation of σ is achieved by introducing a special, artificial dataset called “Asimov dataset”. The “Asimov dataset” is chosen such, that when one uses it to evaluate the estimators for all parameters, one obtains the true parameter values. For the simple case of a Poissonian likelihood, as in (47), the “Asimov dataset” is given by $n = \mu's + b$. The “Asimov dataset” is the dataset that shows no statistical fluctuations, see Figure 66.

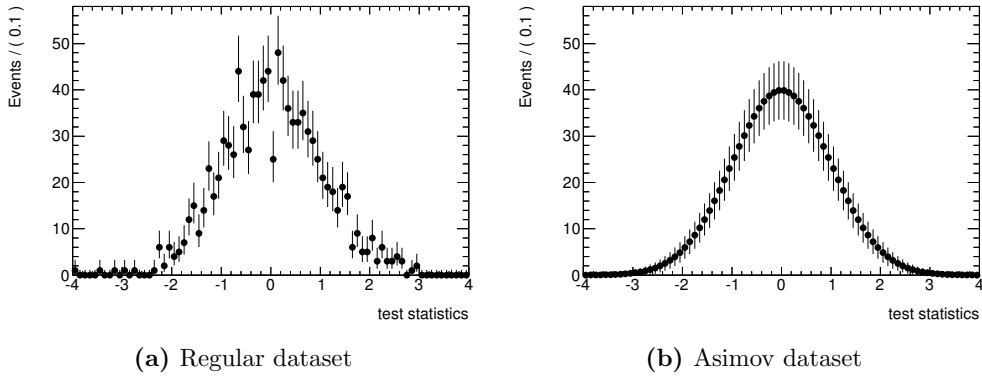


Figure 66: A regular dataset (a) and the “Asimov dataset” (b) for 1000 events standard normally distributed. The “Asimov dataset” shows no fluctuations.

Using the “Asimov dataset”, Equation (70) becomes [91]

$$Z_{0,\text{exp}} = \sqrt{\tilde{q}_{0,A}} , \quad (71)$$

where $\tilde{q}_{0,A}$ stands for the test statistic evaluated with the “Asimov dataset”, for the expected exclusion significance one finds in a similar manner

$$Z_{1,exp} = \sqrt{\tilde{q}_{1,A}} . \quad (72)$$

The $\pm 1\sigma$ error bands on the expectation values are found by shifting the integration boundary in (69) from $\text{med}[\tilde{q}_0|1]$ to $\text{med}[\tilde{q}_0|1] \pm 1\sigma$.

To get familiar with the “Asimov dataset”, we can look at an example deriving the discovery significance using the likelihood in (47), with (64) and for simplicity assuming $\hat{\mu} > 0$ we get

$$Z_0 = \sqrt{\tilde{q}_{0,obs}} = \sqrt{-2 \ln \left(\frac{L(0)}{L(\hat{\mu})} \right)} . \quad (73)$$

But the maximum likelihood estimator $\hat{\mu}$ for a likelihood consisting of a single Poissonian is trivially given by $\hat{\mu}s + b = n$, we then get

$$Z_0 = \sqrt{2 \left(n \ln \left(\frac{n}{b} \right) + b - n \right)} . \quad (74)$$

To get the expected discovery significance, we plug in the “Asimov dataset” which is $n = \mu's + b$, and assuming the nominal signal model, i.e. $\mu' = 1$

$$Z_{0,exp} = \sqrt{\tilde{q}_{0,A}} = \sqrt{2 \left((s + b) \ln \left(1 + \frac{s}{b} \right) - s \right)} = \frac{s}{\sqrt{b}} \left(1 + \mathcal{O} \left(\frac{s}{b} \right) \right) , \quad (75)$$

so we get the often used estimation for the expected significance of s/\sqrt{b} , which is only valid for small values of s/b , though.

9 Statistical Interpretation

In this chapter we apply the methods outlined in Chapter 8. Section 9.1 reports the discovery p -values of the bins. Since no significant excess has been observed, exclusion limit contours are set in Section 9.2. Upper limits on model cross-sections are given in Section 9.3 and results of the profile likelihood fit are shown in Section 9.4. Finally, in Section 9.5 the use of asymptotic formulae vs. pseudo-experiments is discussed and some advice is given how to handle a situation, where it's not clear if asymptotic formulae can be used or not.

For all results in this chapter, HistFitter-00-00-33 [13] is used.

9.1 Discovery p -value

As reported in Table 25, no bin has shown a significant excess over the expected Standard Model background. In Table 26 the p -values are shown. If the bin has an overfluctuation, the significance of the overfluctuation is shown too. Results are derived with Monte Carlo pseudo-experiments.

Bin 1 has the largest overfluctuation, expecting 23 ± 4 events, but 36 observed. The discovery p -value is 0.015, identical to a discovery significance of 2.16σ . The overfluctuation is substantial, but when looking at 20 bins, an overfluctuation like this becomes quite likely due to the look-elsewhere effect. To better estimate the degree of excess we observe in this bin, we could calculate the global p -value by taking into account the look-elsewhere effect, as opposed to just quote the local p -value. This was not done, since the observation was not strong enough. Nonetheless, it is quite remarkable that all overfluctuations happen to be in bins with low numbers, corresponding to a low value of m_{SFOS} , targeting compressed scenarios.

Since no significant excess is observed, exclusion limits are set.

9.2 Exclusion limits

Exclusion limits on the visible cross-section are shown in Table 27, every model that produces more events after acceptance and efficiency is excluded at the 95 % confidence level.

The exclusion limits are derived using the full combination of all signal regions, that is the 20 bins of SR0 τ a, SR0 τ b, SR1 τ and either SR2 τ a or SR2 τ b, since the last two are not orthogonal with respect to each other. Figures 67 and 68 show the exclusion limit contours of the simplified models, while Figures 69, 70 and 71 show the exclusion limit contours of the pMSSMs. For all exclusion contours except the Wh mediated simplified model, the statistical combination of SR0 τ a, SR0 τ b, SR1 τ and SR2 τ a is used. For the Wh mediated simplified model, the statistical combination of SR0 τ a, SR0 τ b, SR1 τ and SR2 τ b is used.

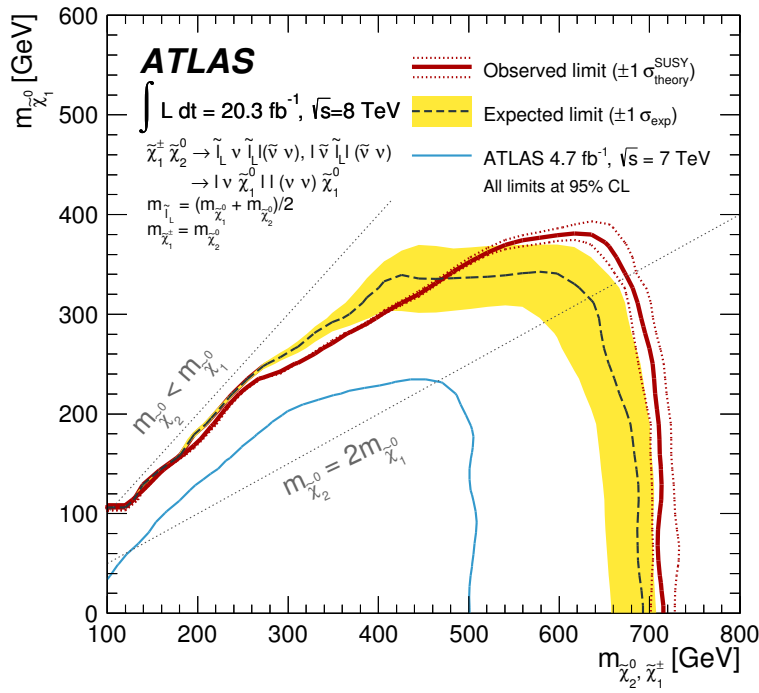
For all exclusion limit contours shown in Figures 67, 68, 69, 70 and 71, the yellow band around the expected limit shows the $\pm 1\sigma$ variations of the expected limit. Both expected and observed exclusion limits include all uncertainties except theoretical signal uncertainties. The dotted lines around the observed exclusion limit correspond to the $\pm 1\sigma$ variations of the theoretical uncertainties on the signal cross-section. If shown, the blue contours correspond to the 7 TeV limits from the ATLAS three-lepton analysis [5]. Linear interpolation is used to account for the discrete nature of the signal grids. 100 000 pseudo-experiments are used per signal grid point.

Bin	N_{exp}	N_{obs}	p_0	$Z[\sigma]$
01	$23^{+4.0}_{-4.0}$	36	0.015	2.16
02	$4.2^{+1.5}_{-1.5}$	5	0.35	0.38
03	$10.6^{+1.8}_{-1.8}$	9	0.50	–
04	$8.5^{+1.7}_{-1.6}$	9	0.40	0.26
05	$12.9^{+2.4}_{-2.3}$	11	0.50	–
06	$6.6^{+1.9}_{-1.8}$	13	0.028	1.91
07	$14.1^{+2.2}_{-2.2}$	15	0.37	0.33
08	$1.1^{+0.4}_{-0.4}$	1	0.50	–
09	$22.4^{+3.6}_{-3.4}$	28	0.13	1.12
10	$16.4^{+2.8}_{-2.8}$	24	0.068	1.50
11	$27^{+5.0}_{-5.0}$	29	0.39	0.28
12	$5.5^{+1.5}_{-1.4}$	8	0.21	0.82
13	$715^{+70.0}_{-68.0}$	714	0.50	–
14	$219^{+33.0}_{-33.0}$	214	0.50	–
15	$65^{+13.0}_{-13.0}$	63	0.50	–
16	$4.6^{+1.7}_{-1.5}$	3	0.50	–
17	$69^{+9.0}_{-8.0}$	60	0.50	–
18	$3.4^{+1.4}_{-1.4}$	1	0.50	–
19	$1.2^{+0.4}_{-0.4}$	0	0.50	–
20	$0.29^{+0.18}_{-0.17}$	0	0.50	–

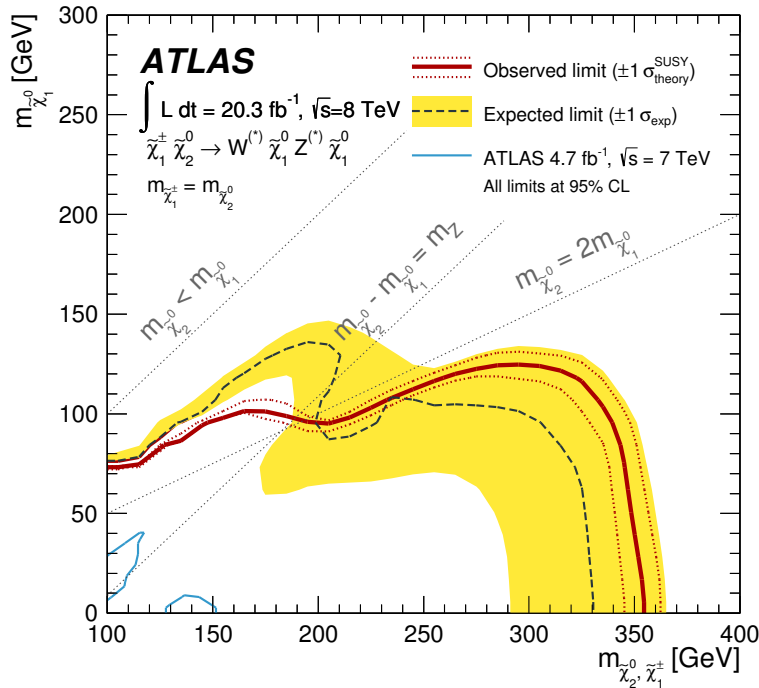
Table 26: Discovery p -value of each bin and in case of an overfluctuation the significance in σ 's. Using the definition of a one-sided p -value, the probability density function is capped and every underfluctuation has a p -value of 0.5. 100 000 pseudo-experiments have been run for each bin with an overfluctuation. The number of expected (N_{exp}) and the number of observed events (N_{obs}) are also given.

Bin	N_{exp}	N_{obs}	S_{exp}^{95}	S_{obs}^{95}
01	$23.^{+4.0}_{-4.0}$	36	$14.1^{+5.6}_{-3.6}$	26.8
02	$4.2^{+1.5}_{-1.5}$	5	$6.2^{+2.5}_{-1.7}$	6.9
03	$10.6^{+1.8}_{-1.8}$	9	$8.4^{+3.1}_{-2.3}$	7.3
04	$8.5^{+1.7}_{-1.6}$	9	$7.7^{+3.1}_{-2.1}$	8.4
05	$12.9^{+2.4}_{-2.3}$	11	$9.0^{+3.6}_{-2.5}$	7.9
06	$6.6^{+1.9}_{-1.8}$	13	$8.0^{+3.2}_{-1.9}$	14.4
07	$14.1^{+2.2}_{-2.2}$	15	$9.6^{+3.9}_{-2.5}$	10.8
08	$1.1^{+0.4}_{-0.4}$	1	$3.7^{+1.5}_{-0.9}$	3.7
09	$22.4^{+3.6}_{-3.4}$	28	$12.7^{+4.9}_{-3.5}$	18.0
10	$16.4^{+2.8}_{-2.8}$	24	$11.3^{+4.5}_{-3.1}$	18.3
11	$27.^{+5.0}_{-5.0}$	29	$13.8^{+5.4}_{-3.7}$	15.3
12	$5.5^{+1.5}_{-1.4}$	8	$6.9^{+2.9}_{-1.7}$	9.2
13	$715.^{+70.0}_{-68.0}$	714	133^{+46}_{-36}	133
14	$219.^{+33.0}_{-33.0}$	214	66^{+24}_{-18}	65
15	$65.^{+13.0}_{-13.0}$	63	$28.6^{+10.1}_{-7.2}$	27.6
16	$4.6^{+1.7}_{-1.5}$	3	$5.9^{+2.6}_{-1.5}$	5.2
17	$69.^{+9.0}_{-8.0}$	60	$21.4^{+8.2}_{-5.6}$	18.8
18	$3.4^{+1.4}_{-1.4}$	1	$4.8^{+2.0}_{-1.1}$	3.7
19	$1.2^{+0.4}_{-0.4}$	0	$3.71^{+1.35}_{-0.70}$	3.01
20	$0.29^{+0.18}_{-0.17}$	0	$3.00^{+0.83}_{-0.00}$	3.00

Table 27: Observed and expected number of signal events excluded at the 95 % confidence level. All results derived with Monte Carlo pseudo-experiments. 50 000 pseudo-experiments have been run per bin. The number of expected (N_{exp}) and the number of observed events (N_{obs}) are also given.

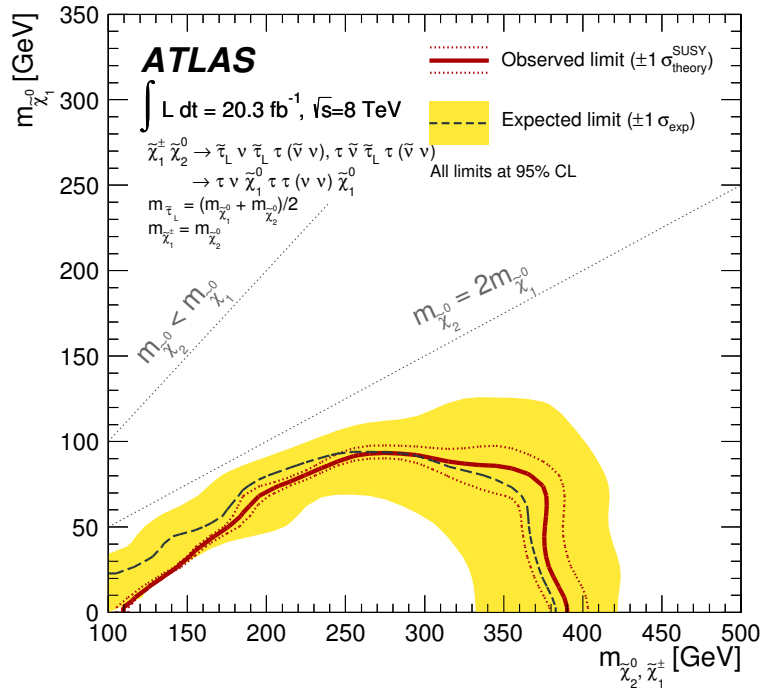


(a) $\tilde{\ell}_L$ -mediated simplified model

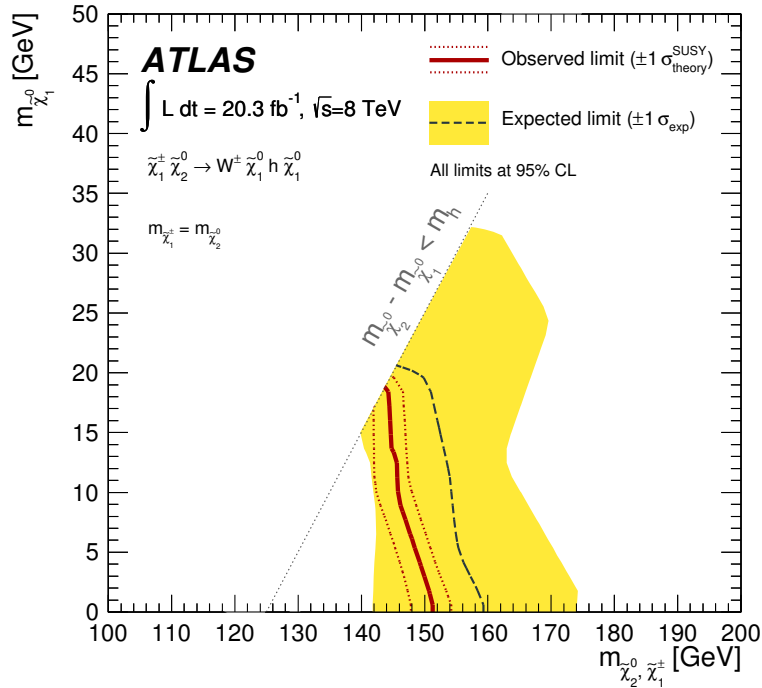


(b) WZ -mediated simplified model

Figure 67: Observed and expected exclusion limit contours at the 95 % confidence level. (a) is the $\tilde{\ell}_L$ mediated and (b) the WZ mediated simplified model.

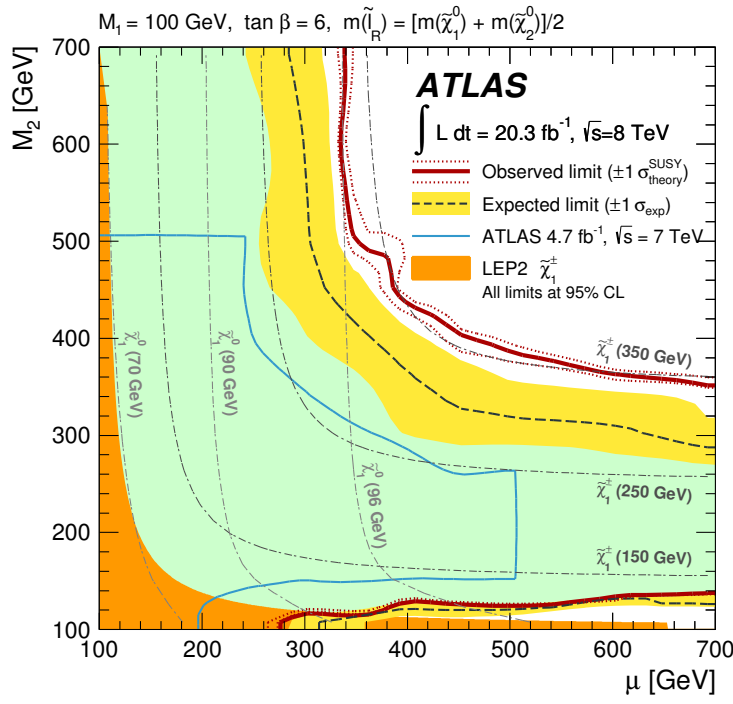


(a) $\tilde{\tau}_L$ -mediated simplified model

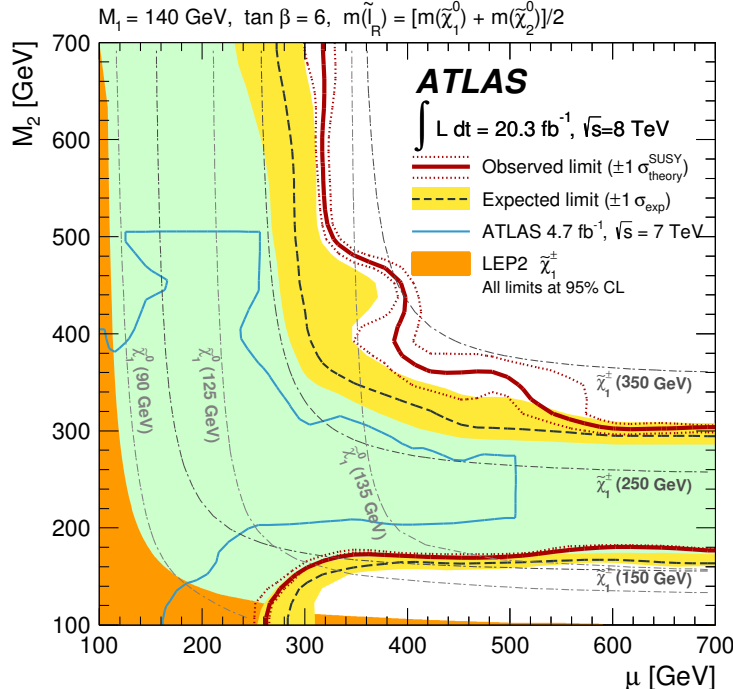


(b) Wh -mediated simplified model

Figure 68: Observed and expected exclusion limit contours at the 95 % confidence level. (a) is the $\tilde{\tau}_L$ mediated and (b) the Wh mediated simplified model.

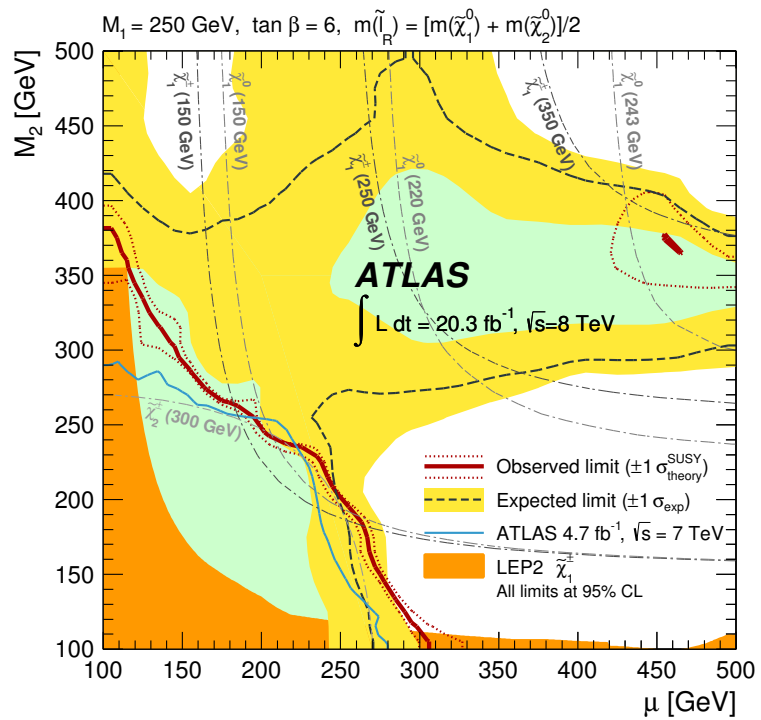


(a) pMSSM $\tilde{\ell}_R$, $M_1=100$ GeV



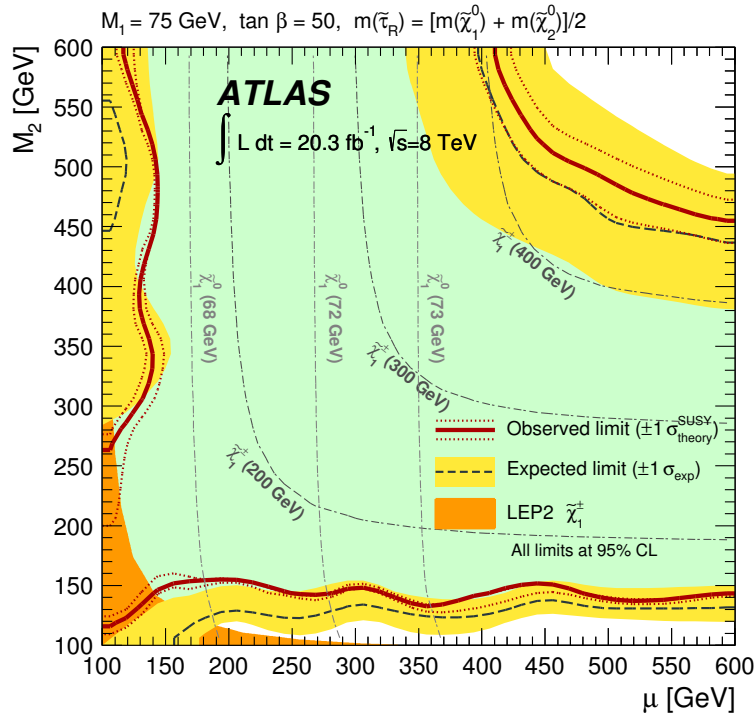
(b) pMSSM $\tilde{\ell}_R$, $M_1=140$ GeV

Figure 69: Observed and expected exclusion limit contours at the 95 % confidence level in the pMSSMs with light sleptons. (a) is with $M_1 = 100$ GeV, (b) is with $M_1 = 140$ GeV.

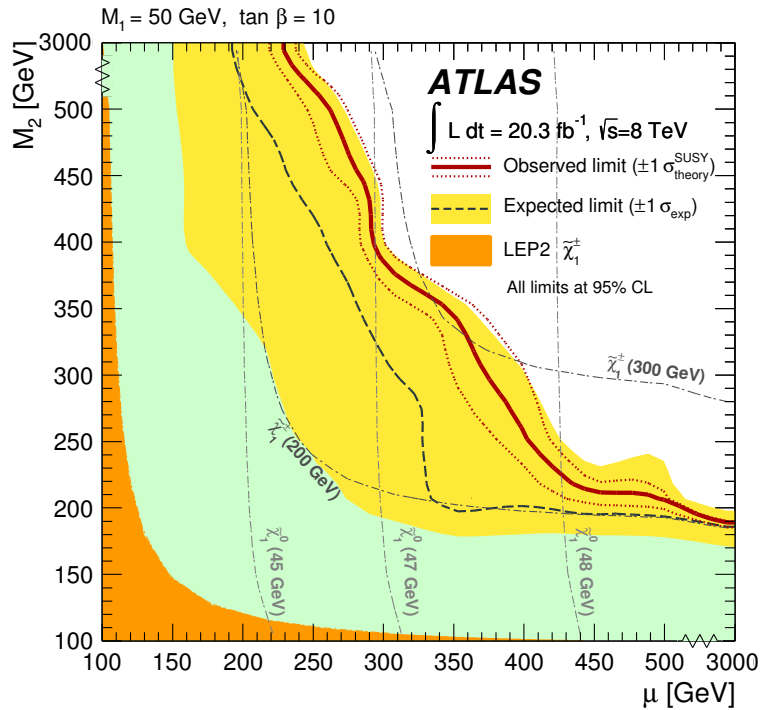


(a) pMSSM \tilde{l}_R , $M_1=250$ GeV

Figure 70: Observed and expected exclusion limit contours at the 95 % confidence level in the pMSSMs with light sleptons and $M_1 = 250$ GeV.



(a) pMSSM $\tilde{\tau}_R$, $M_1=75$ GeV



(b) pMSSM no $\tilde{\ell}$, $M_1=50$ GeV

Figure 71: Observed and expected exclusion limit contours at the 95 % confidence level in the pMSSMs. (a) is the staus model and (b) the model without sleptons.

The expected and observed CL_s values are shown in Figures 72 to 80. All CL_s values separately per bin for the $\tilde{\ell}_L$ and the WZ mediated simplified model can be found in Appendix E. The plots in this appendix give a feeling how much each bin adds to the total sensitivity. Especially for the WZ mediated simplified model, Figures 163 - 168 show nicely how almost every bin plays a role in enhancing the sensitivity in the WZ like region. Moreover, the expected CL_s values in the figures in Appendix E can be compared to the sensitivities in Appendix A. Based on the figures in Appendix A the signal region optimization (see Section 5.1) was carried out. The agreement between these two appendixes is good, proving that the signal region optimization was carried out on solid ground and firm assumptions.

The binning of the signal region was optimized in the $\tilde{\ell}_L$ and the WZ mediated simplified model, we can compare the results of the binned signal region to the one obtained with the same dataset, but different signal regions [8]. The six signal regions used in the previous round have also been optimized on these grids, so a comparison is justified. In Figure 81, we can see that the binned signal region performs generally stronger than the six distinct signal regions. The observed exclusion limit is weaker in the compressed scenarios, due to the overfluctuations seen in the bins with low m_{SFOS} . The expected limit is much stronger, especially in the WZ mediated simplified model. In the $\tilde{\ell}_L$ mediated simplified model, there's a dip where the previous six signal regions perform better.

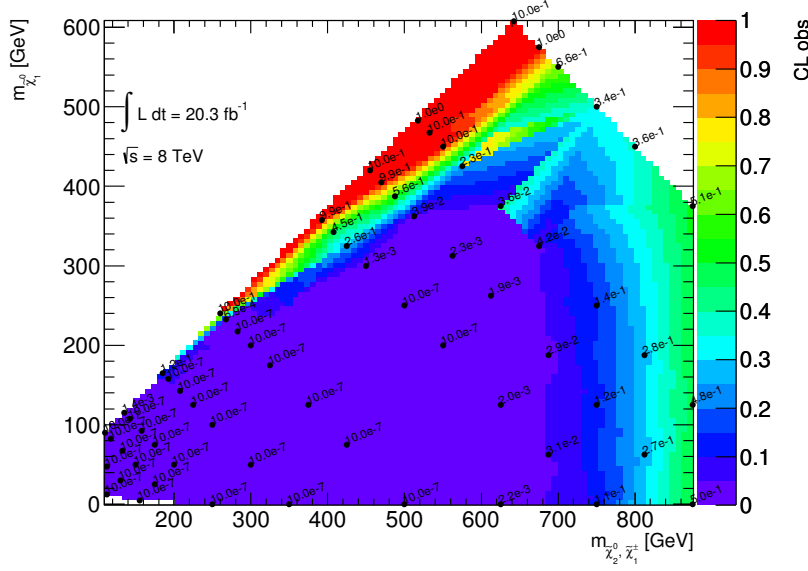
The binned signal region has also been used for a combination with a two lepton final state [3] for the WZ mediated simplified model and for the pMSSM with $M_1 = 250$ GeV, for the other SUSY models, the combination would not have lead to a substantial improvement, since the three lepton exclusion limits alone are much stronger than the two lepton ones. The exclusion limit contours of the combination can be seen in Figure 82.

A SUSY signal coming from these simplified models was also searched for by CMS [108]. Their exclusion limit contours in the $\tilde{\ell}_L$ mediated and the WZ mediated simplified models are shown in Figure 83. In these exclusions, search results from two and three lepton final states are combined. Comparing my exclusion limit contour for the $\tilde{\ell}_L$ mediated simplified model in Figure 67a with the one from CMS in Figure 83a, we see that both exclusion contours are comparable. While my exclusion extends a bit further into the high mass region, the CMS exclusion gets a bit closer to the diagonal.

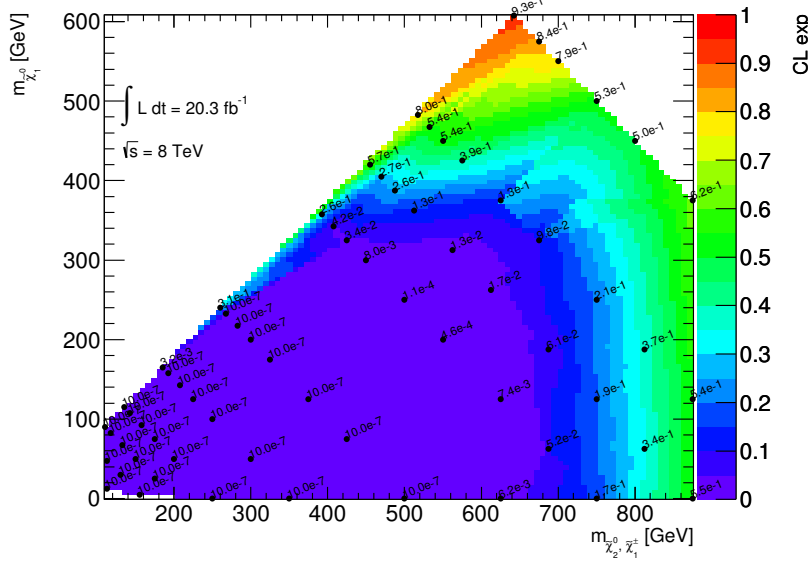
The situation is different for the WZ mediated simplified model. Comparing for both analyses the combined two and three lepton final state searches, i.e. Figure 82a with 83b, we see that my exclusion limit is much stronger. It extends to roughly 425 GeV on the x-axis, while CMS has only an observed exclusion of 280 GeV. The large difference in exclusion can partially be explained by a large overfluctuation that CMS sees in their data. But even comparing the expected exclusion limit, my result is still more than 30 GeV stronger. In the region where the signal resembles WZ , a stronger limit of roughly 80 GeV is set by me.

A direct comparison of my results with the ones from CMS is shown in Figure 84. Since at the time of writing this thesis there were no HEPData available from the CMS paper, the CMS exclusion limit contours in Figure 84 are drawn by hand. For the official results, consult Figure 83.

There is one more thing I'd like to discuss in the exclusion limit contours in Figures 69, 70 and 71: the LEP limit. In many publications (e.g. the predecessor paper for this analysis [5], see also Figure 30a), the LEP limit is quoted as limit on the $\tilde{\chi}_1^\pm$ mass of 103.5 GeV. This is not quite correct. The LEP limit is a function of $\Delta m = m_{\tilde{\chi}_1^\pm} - m_{\tilde{\chi}_1^0}$ and is shown in Figure 85a. As can be seen, the limit is indeed at 103.5 GeV for $\Delta m \lesssim 0.15$ GeV or $\Delta m \gtrsim 3$ GeV, but in between the limit goes down to a minimum of 92 GeV.

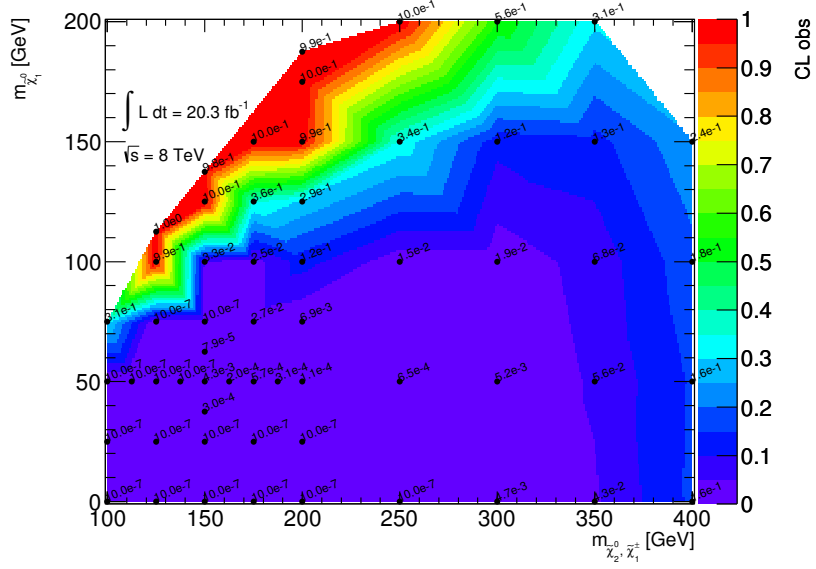


(a) Observed CL_s

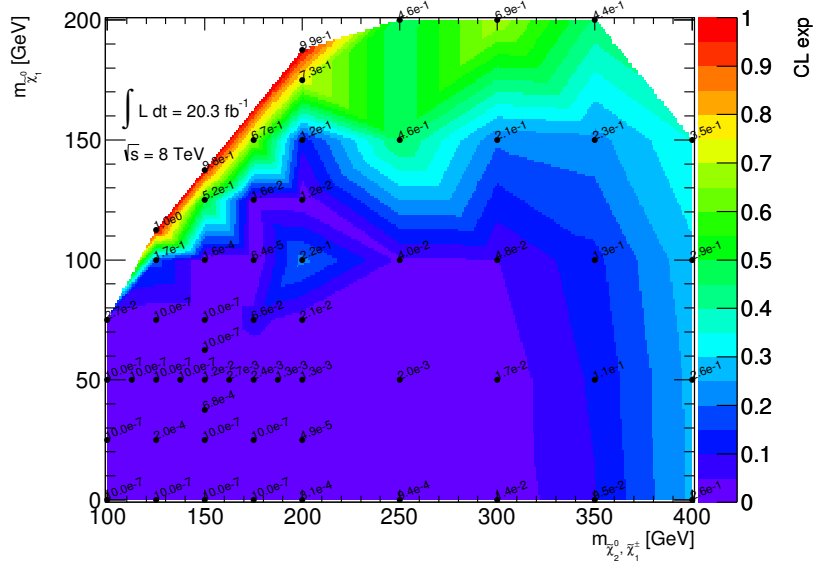


(b) Expected CL_s

Figure 72: Observed (a) and expected (b) CL_s at each grid point for the $\tilde{\ell}_L$ mediated simplified model. Exclusion is at $CL_s < 5\%$.

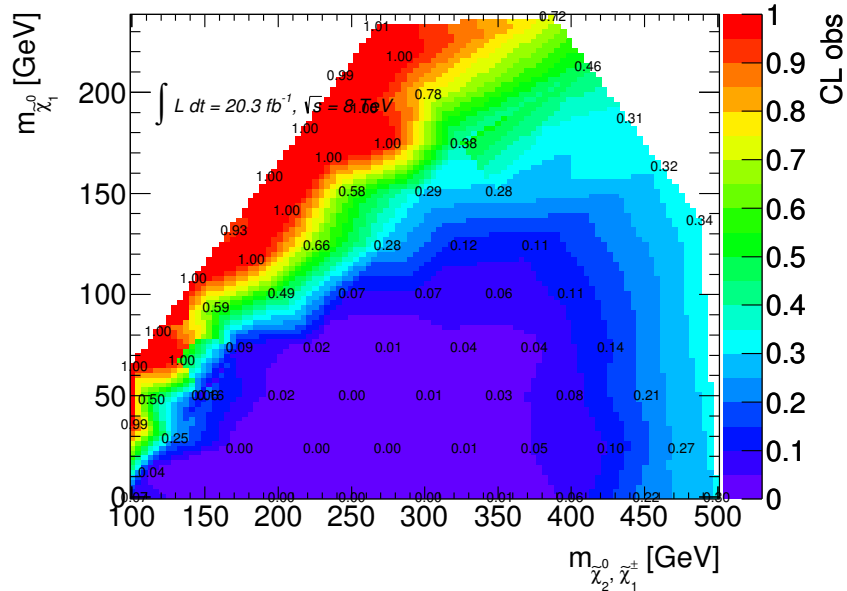


(a) Observed CL_s

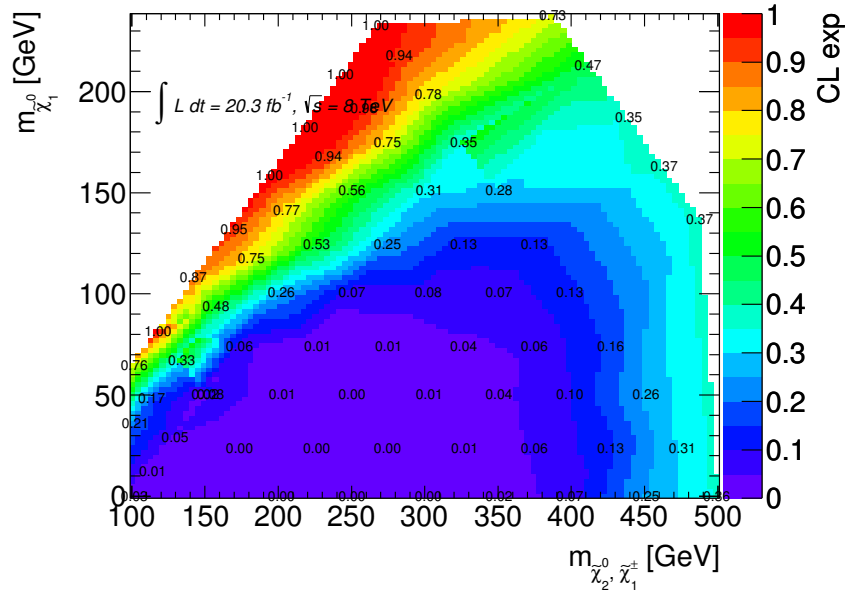


(b) Expected CL_s

Figure 73: Observed (a) and expected (b) CL_s at each grid point for the WZ mediated simplified model. Exclusion is at $CL_s < 5\%$.

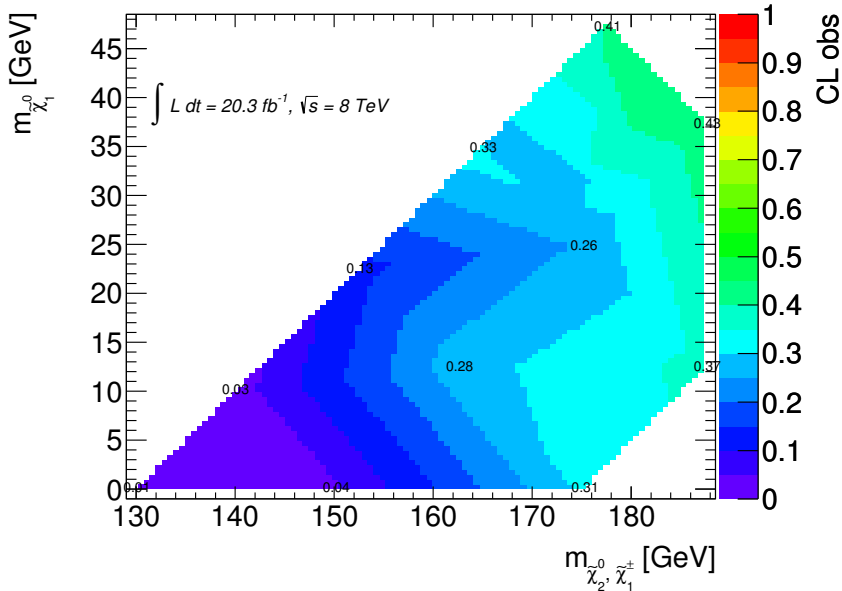


(a) Observed CL_s

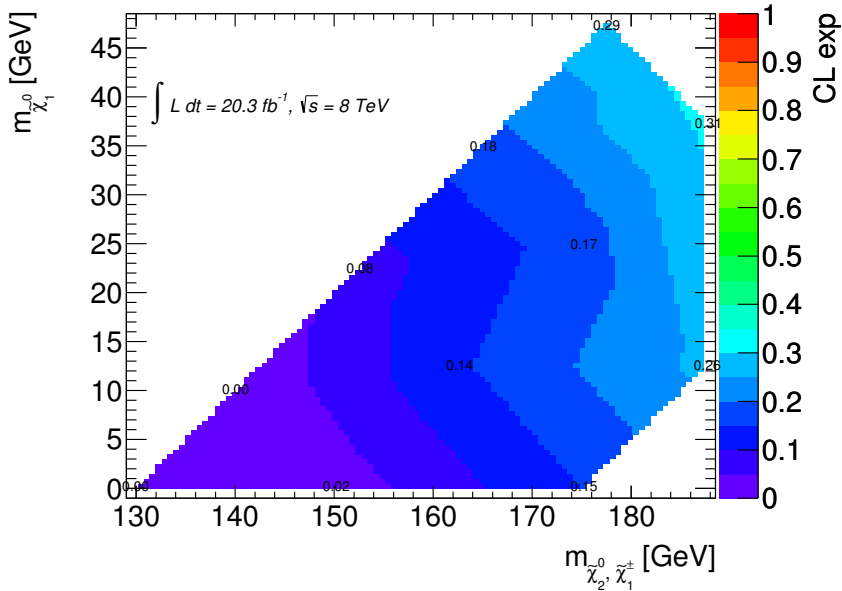


(b) Expected CL_s

Figure 74: Observed (a) and expected (b) CL_s at each grid point for the $\tilde{\tau}_L$ mediated simplified model. Exclusion is at $CL_s < 5\%$.

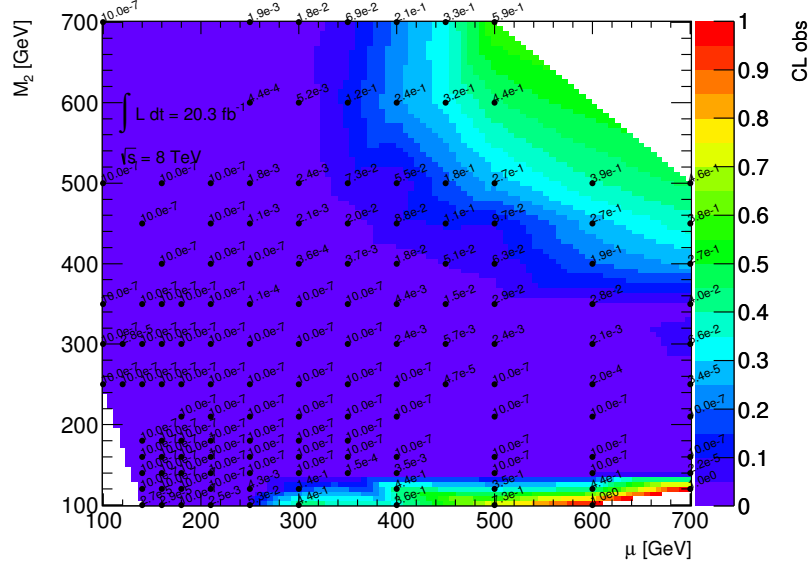


(a) Observed CL_s

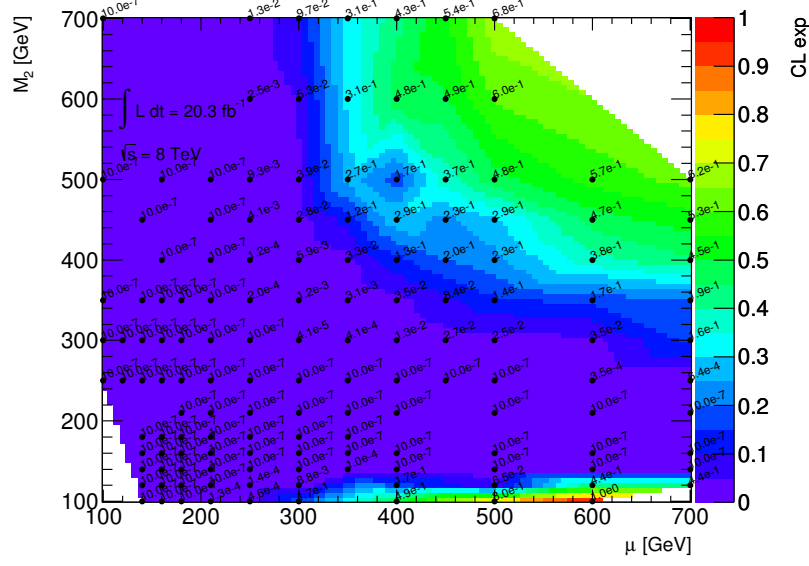


(b) Expected CL_s

Figure 75: Observed (a) and expected (b) CL_s at each grid point for the Wh mediated simplified model. Exclusion is at $CL_s < 5\%$.

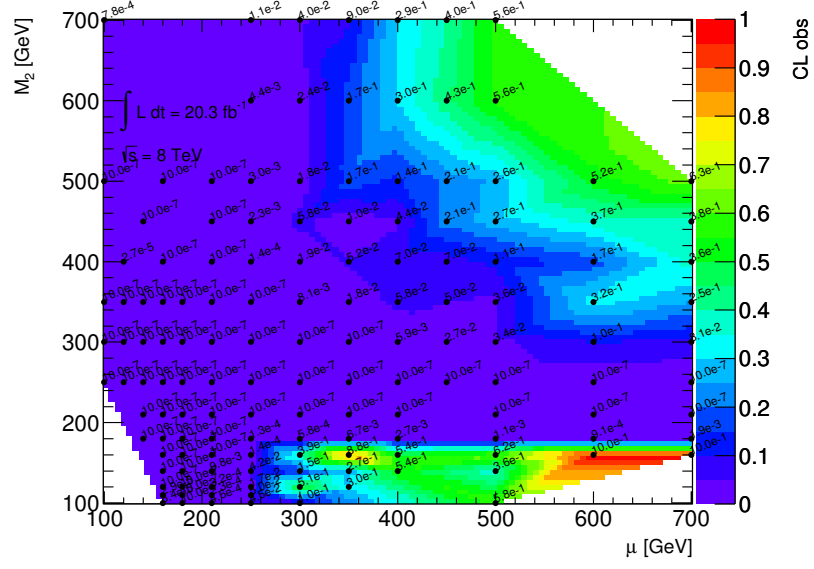


(a) Observed CL_s

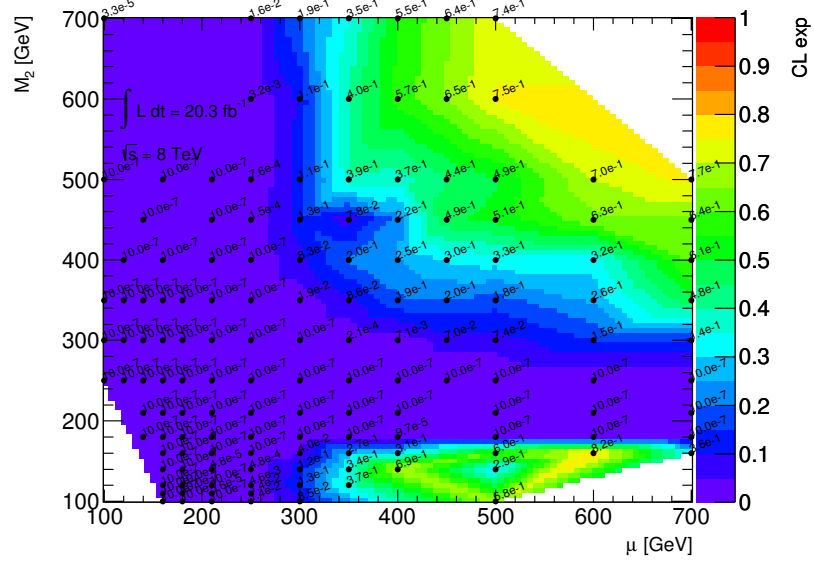


(b) Expected CL_s

Figure 76: Observed (a) and expected (b) CL_s at each grid point for the pMSSMs with $\tan \beta = 6$ and $M_1 = 100$ GeV. Exclusion is at $CL_s < 5\%$.

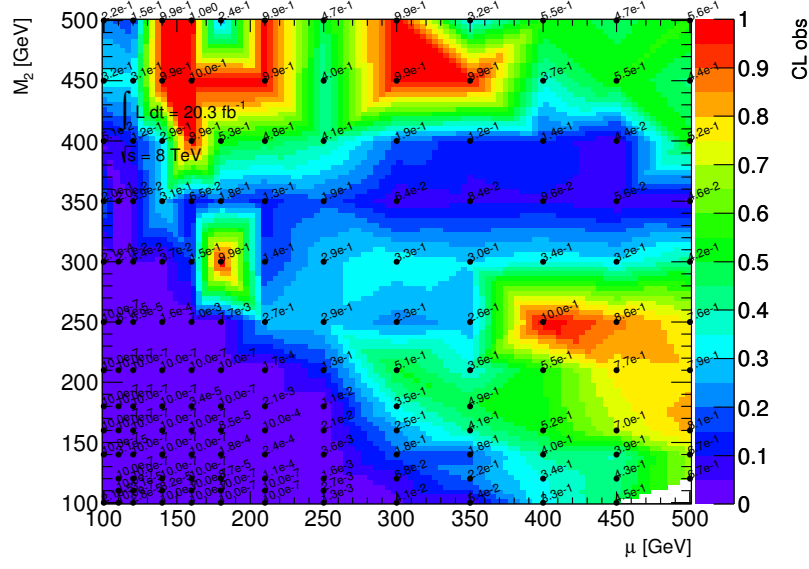


(a) Observed CL_s

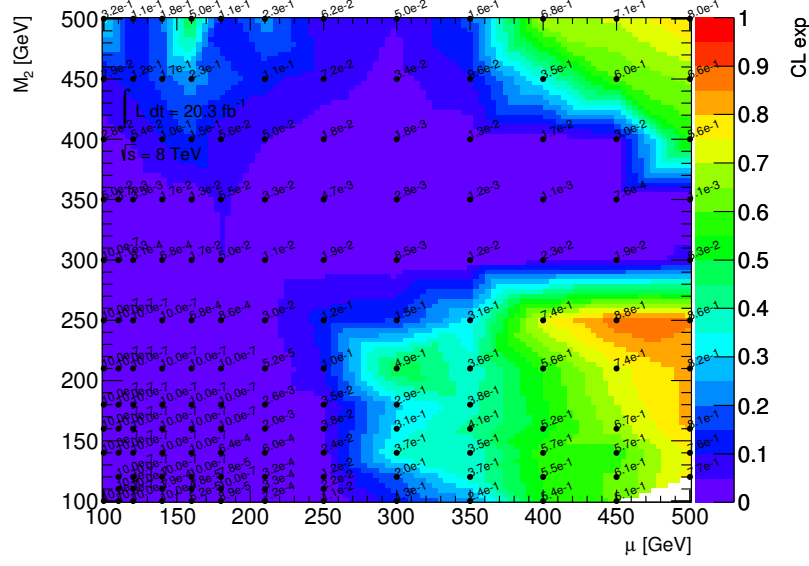


(b) Expected CL_s

Figure 77: Observed (a) and expected (b) CL_s at each grid point for the pMSSMs with $\tan \beta = 6$ and $M_1 = 140$ GeV. Exclusion is at $CL_s < 5\%$.

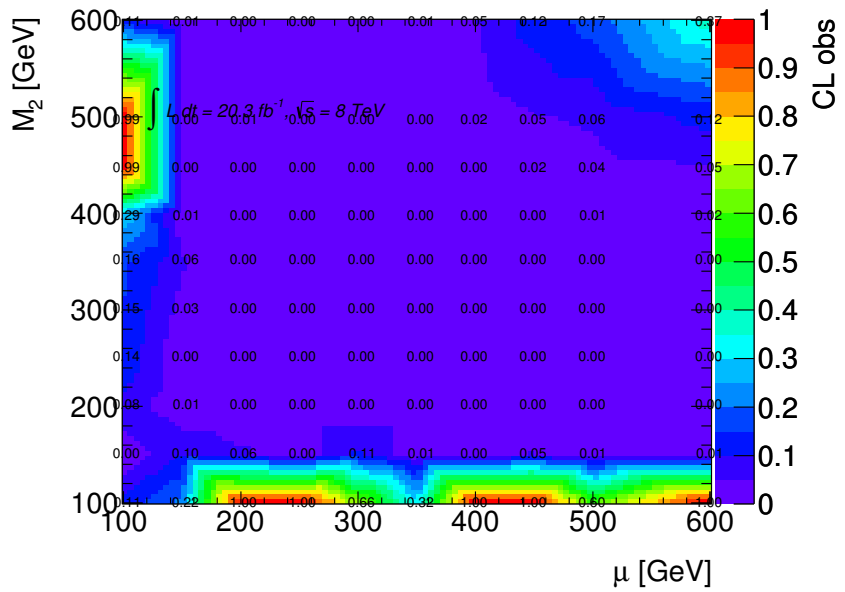


(a) Observed CL_s

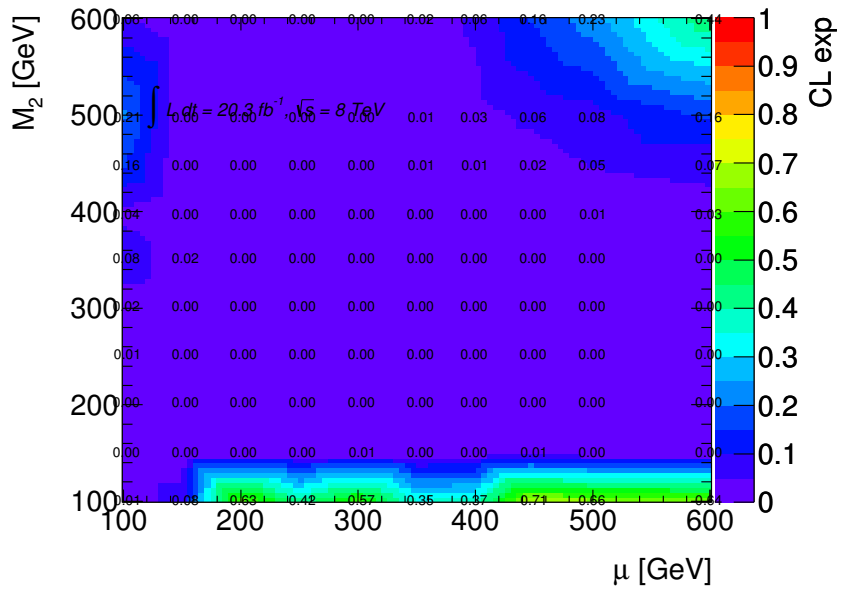


(b) Expected CL_s

Figure 78: Observed (a) and expected (b) CL_s at each grid point for the pMSSMs with $\tan \beta = 6$ and $M_1 = 250$ GeV. Exclusion is at CL_s < 5 %.

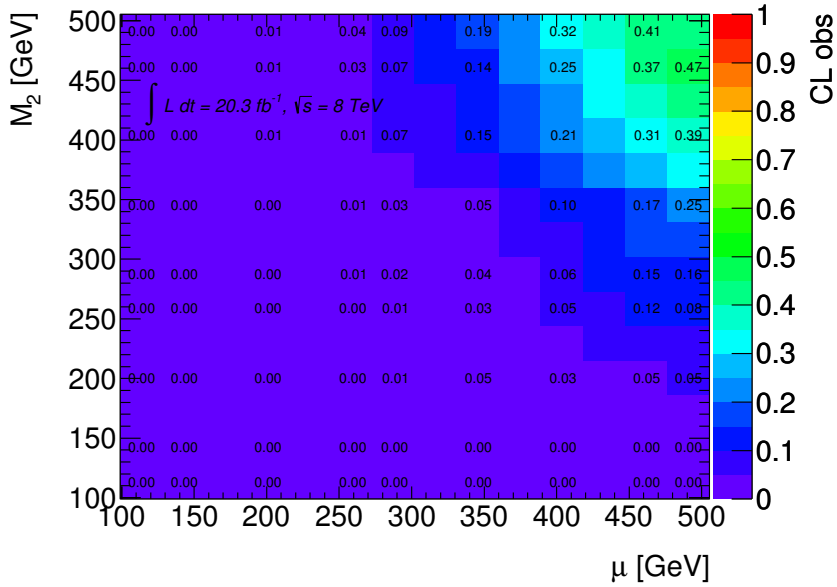


(a) Observed CL_s

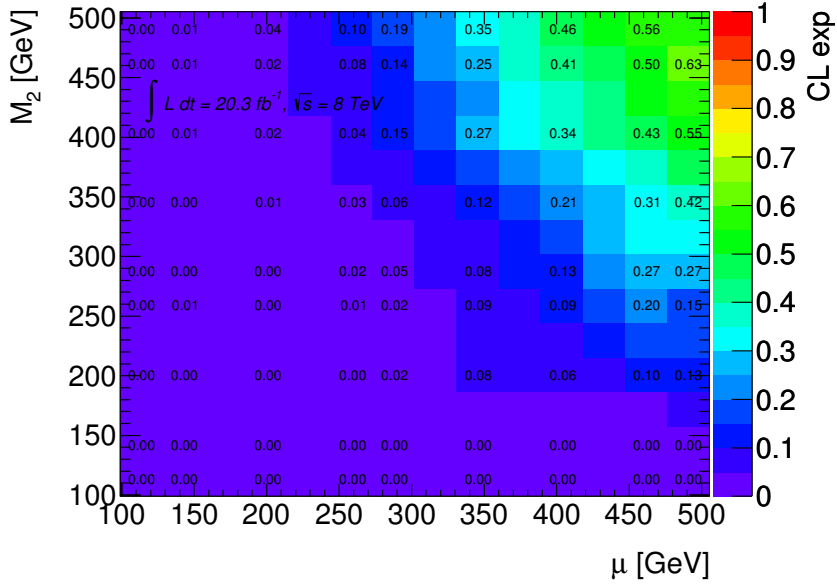


(b) Expected CL_s

Figure 79: Observed (a) and expected (b) CL_s at each grid point for the pMSSMs with $\tan \beta = 50$ and $M_1 = 75$ GeV. Exclusion is at $CL_s < 5\%$.

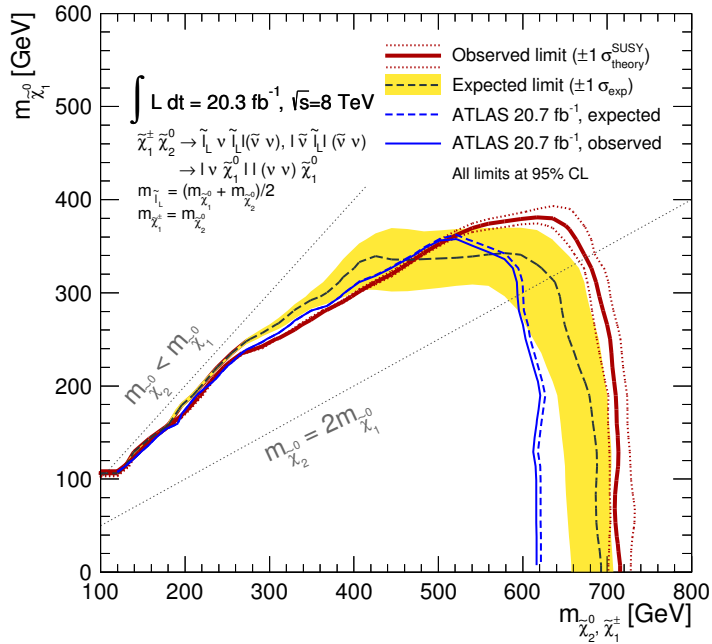


(a) Observed CL_s

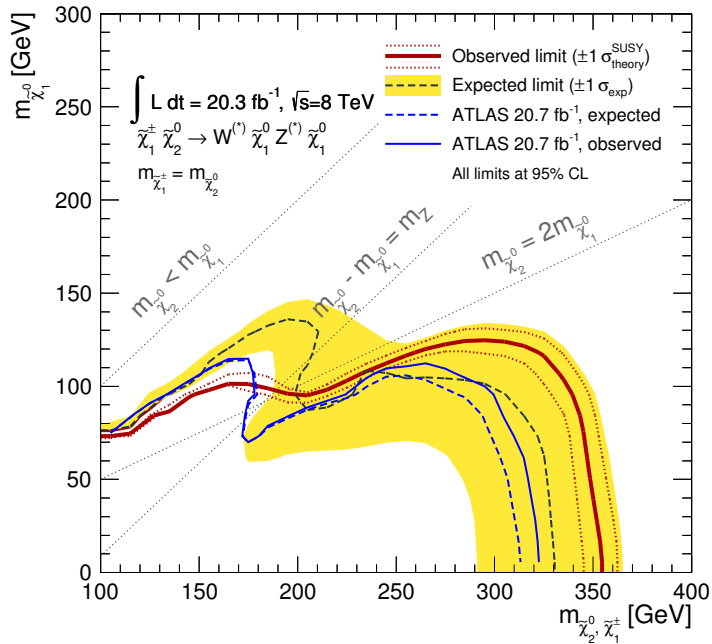


(b) Expected CL_s

Figure 80: Observed (a) and expected (b) CL_s at each grid point for the pMSSMs with $\tan \beta = 10$ and $M_1 = 50$ GeV. Exclusion is at $CL_s < 5\%$.

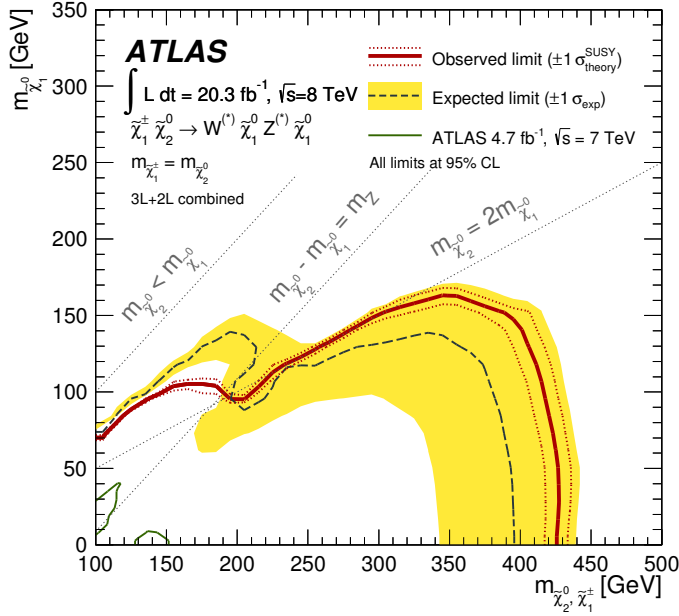


(a) $\tilde{\ell}_L$ mediated simplified model

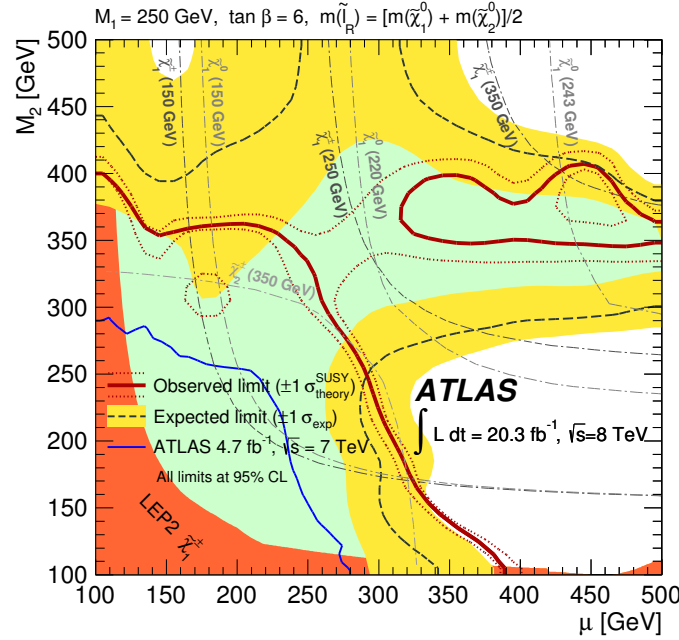


(b) WZ mediated simplified model

Figure 81: Comparing the exclusion limit contours of the conference note published in March 2013 [8] and the paper published in March 2014 [2]. Both use the full 8 TeV dataset (but see footnote on page 53), both analyses use signal regions that were optimized on these grids. From [8], the nominal expected and observed are shown. [8] used six signal regions, while [2] uses the binned signal region.

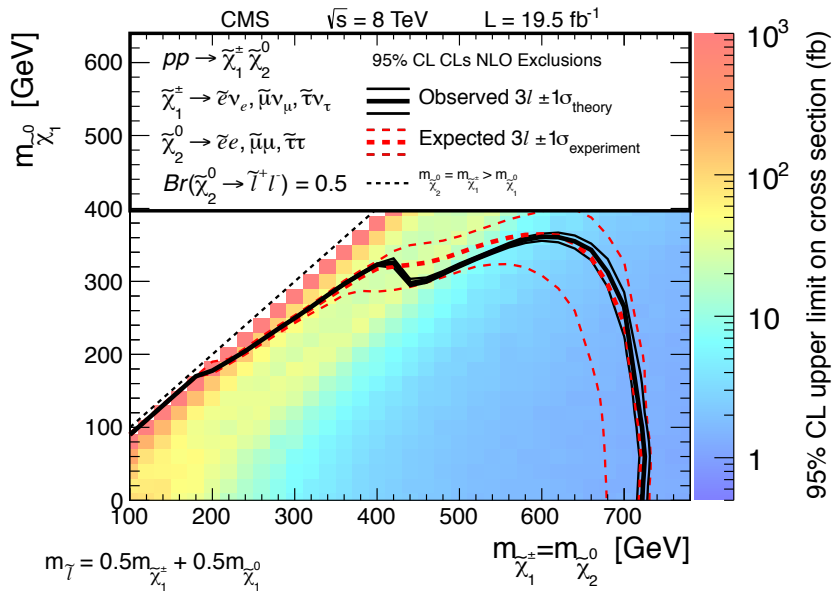


(a)

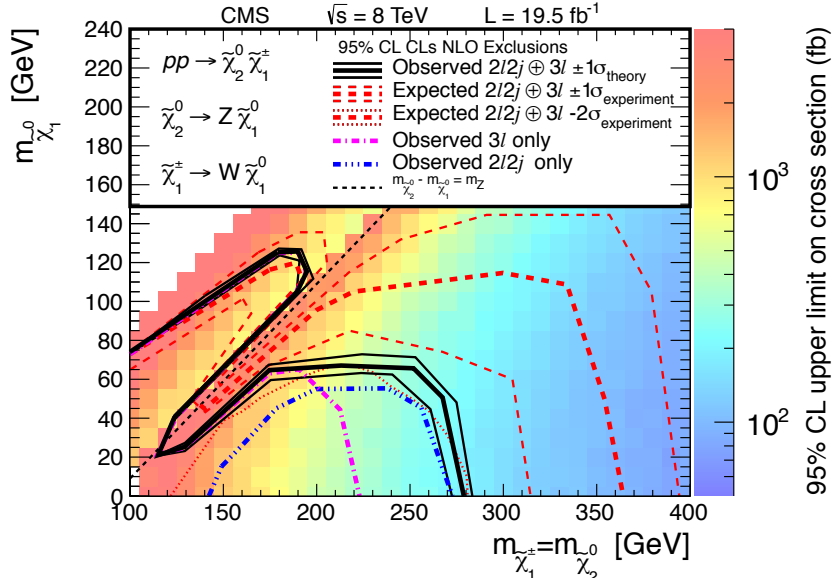


(b)

Figure 82: Observed and expected exclusion contours at the 95 % confidence level for the two and three leptons final state combination in the WZ mediated simplified model (a) and the pMSSM with $M_1 = 250$ GeV (b). The exclusion limits are published in [3]. The green contour in (a) corresponds to the 7 TeV limit of the three lepton search, the blue contour in (b) corresponds to the 7 TeV two and three lepton combined search [5]. Asymptotic formulae are used for these results, as opposed to Figures 67 and 70.

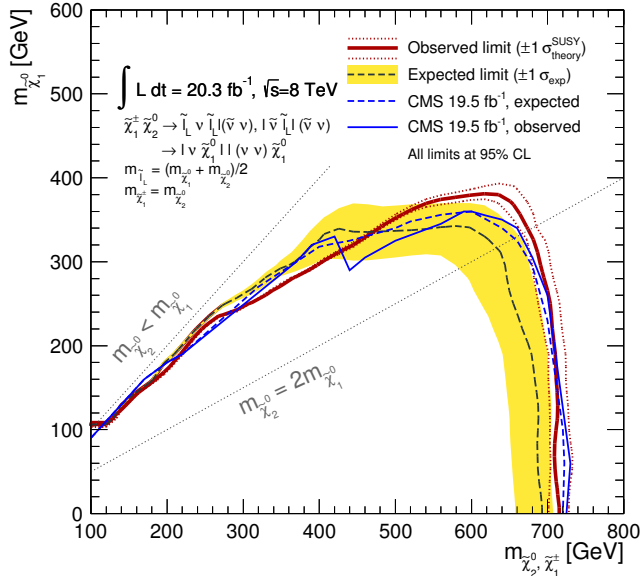


(a)

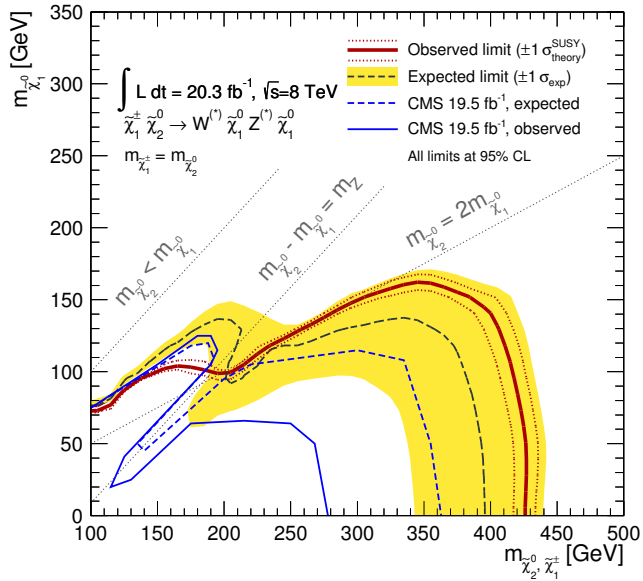


(b)

Figure 83: Exclusion limit contours in the $\tilde{\ell}_L$ mediated simplified model (a) and the WZ mediated simplified model (b) as published in [108].



(a)



(b)

Figure 84: Comparing my exclusion limit contours with the ones from CMS as published in [108]. The CMS results are drawn by hand and may not be 100 % accurate, see Figure 83 for the official results. (a) is the \tilde{l}_L mediated simplified model. The results are comparable, but CMS published a combination of two searches. One search in a final state with two leptons and one search in a final state with three leptons. I only used data in a final state with three leptons. (b) is the WZ mediated simplified model. Both analyses use a combination of two and three lepton final state searches. In this grid, the usage of the binned signal region pays out, my exclusion contour is much stronger, especially in the WZ like region.

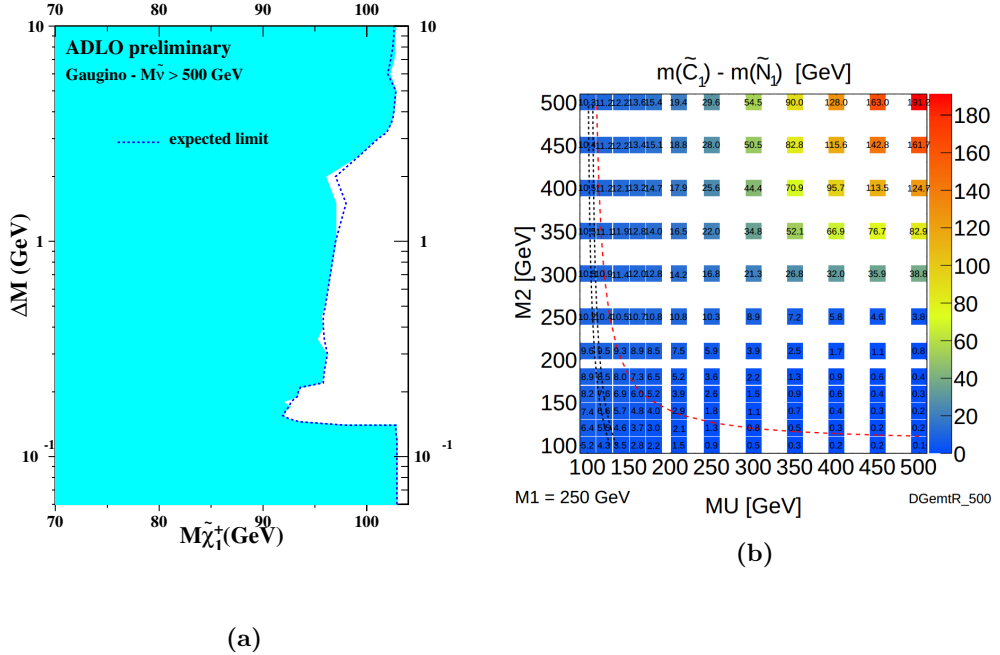


Figure 85: Limit derived as a combination of different detectors at the LEP accelerator at CERN. The limit is set on the $\tilde{\chi}_1^\pm$ masses as a function of $\Delta m = m_{\tilde{\chi}_1^\pm} - m_{\tilde{\chi}_1^0}$ (a). Δm in the pMSSM with $M_1 = 250$ GeV (b).

In order to set the true LEP limit, we need to know Δm in the grid. As an example the pMSSM with $M_1 = 250$ GeV is shown in Figure 85b and indeed Δm drops below 3 GeV in the lower right part of the signal grid, where the $\tilde{\chi}_1^\pm$ mass is near ≈ 100 GeV. As a consequence, the LEP limit in Figure 70 has some irregularities in this region. For this reason, the mass is removed here from the LEP limit in the legend, as it has not a constant value.

9.3 Upper limits on the model cross-sections

For the simplified models, limits have also been set on the model cross-section. For this, the test statistic from Equation (56) was used and the signal strength parameter μ was varied until the model predicting $\mu \cdot s$ events was excluded at the 95 % confidence level. The standard approach is to first estimate the excluded μ asymptotically and then take several values of μ and interpolate between them to get the excluded μ . A graphical representation of this procedure trying 10 different values of μ is shown in Figure 86. All figures of the μ scans for deriving the upper limit on model cross-sections are shown in Appendix F.

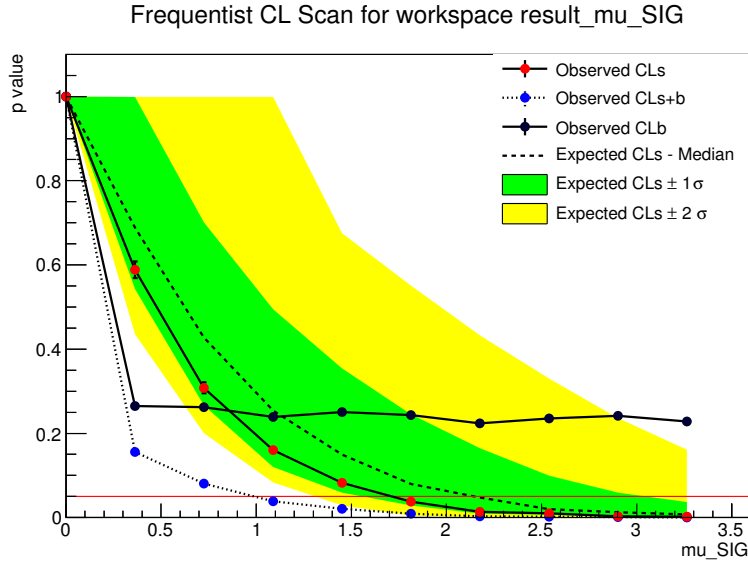


Figure 86: Upper limit scan for varying μ . 10 different values for μ have been tried. The dashed line is the expected CL_s including 1σ and 2σ uncertainty band. The observed CL_s are the red dots, as ratio between the blue dots (CL_{s+b}) and the black dots (CL_b). The uncertainties on the observed CL_s are also shown but usually too small to spot. Once the observed CL_s goes below the predefined value of 0.05, the excluded value of μ at the 95 % confidence level is found with linear interpolation. 10 000 pseudo-experiments are run for each point.

Running $10 \cdot 10 000$ pseudo-experiments can take a considerable amount of time, moreover the guessing of the μ range is sometimes not optimal, if the observed CL_s will already fall at low μ below the 0.05 line, the resolution due to the interpolation will be only rough and the approximation is poor. On the other hand, if the last tried value for μ is still above 0.05, the line needs to be extrapolated and the approximation might be poor again.

Therefore a more efficient approach was developed. For this, two grids were evaluated twice with the conventional method, once with asymptotic formulae and once with pseudo-experiments. Two such plots can be seen in Figure 87, this specific point shows the expected behaviour, namely that the result from pseudo-experiments (Figure 87b) is more conservative than the one from asymptotic formulae (Figure 87a). This is the case most of the time, but not necessarily always, as described in Section 8.5.

Evaluating the ratio between the μ_{asym} derived by using asymptotic formulae and μ_{toys} derived with Monte Carlo pseudo-experiments, one finds for the more than 100 evaluated

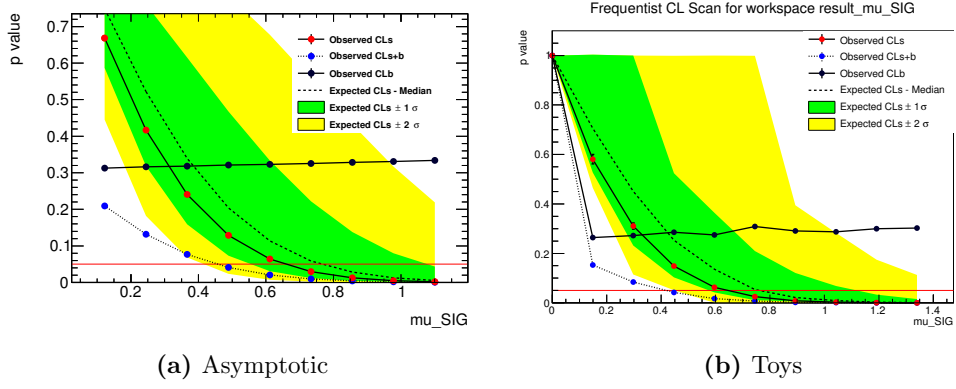


Figure 87: Upper limit scan for the WZ mediated point with $m_{\tilde{\chi}_1^\pm} = 150$ GeV and $m_{\tilde{\chi}_1^0} = 50$ GeV. In (a) asymptotic formulae have been used, in (b) $10 \cdot 10\,000$ Monte Carlo pseudo-experiments have been used.

models that always $\mu_{toys}/\mu_{asym} \in [0.99, 1.38]$. Thus, the value of μ_{toys} is usually between $0.99 \cdot \mu_{asym}$ and $1.38 \cdot \mu_{asym}$.

Now instead of trying 10 different values for μ , I just ran 3 different ones, with μ_{toys} set to $0.99 \cdot \mu_{asym}$, $1.22 \cdot \mu_{asym}$ and $1.45 \cdot \mu_{asym}$. The value of 1.45 is a conservative estimate with a certain safety margin. The result of this scan can be seen in Figure 88a. Linear interpolation between the CL_s values is used in this figure, but looking at Figure 86, this is not justified. To get a better approximation of the excluded μ , a second scan has been carried out. To emphasize that the μ derived in Figure 88a is only an intermediate approximation to μ , we call it $\mu_{toys,est.}$, as opposed to μ_{toys} or simply μ , which is our final result. To get μ_{toys} , we set μ again to 3 different values, once at $0.9 \cdot \mu_{toys,est.}$, $1.0 \cdot \mu_{toys,est.}$ and $1.1 \cdot \mu_{toys,est.}$. The result of this scan can be seen in Figure 88b.

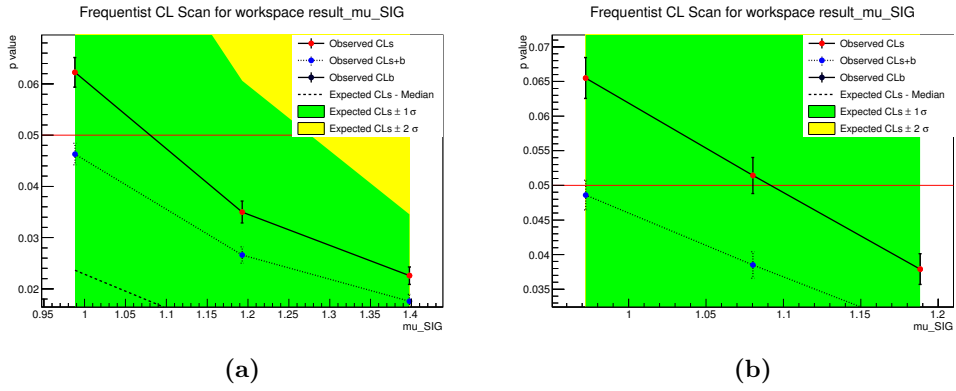


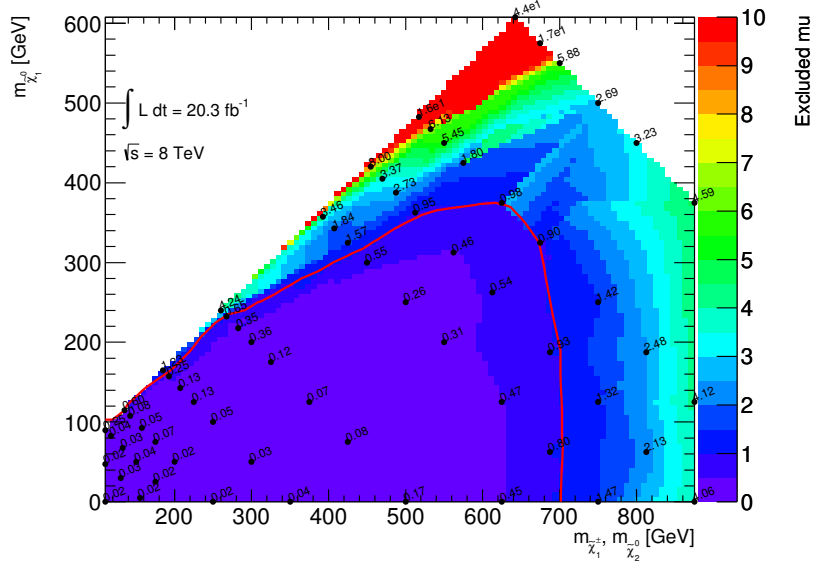
Figure 88: Upper limit scan for the $\tilde{\tau}_L$ mediated point with $m_{\tilde{\chi}_1^\pm} = 150$ GeV and $m_{\tilde{\chi}_1^0} = 50$ GeV. In (a) the values for μ are set to $0.99 \cdot \mu_{asym}$, $1.22 \cdot \mu_{asym}$ and $1.45 \cdot \mu_{asym}$. In (b) the values for μ are set to $0.9 \cdot \mu_{toys,est.}$, $1.0 \cdot \mu_{toys,est.}$ and $1.1 \cdot \mu_{toys,est.}$, where $\mu_{toys,est.}$ is the approximation from (a). For all points, $10 \cdot 10000$ Monte Carlo pseudo-experiments have been used.

When using the improved method for scanning the μ , we run $6 \cdot 10\,000$ Monte Carlo pseudo-experiments, as opposed to $10 \cdot 10\,000$ in the old method. This does not seem like a big gain, but another benefit - on a technical level - is, that the jobs can easily be split.

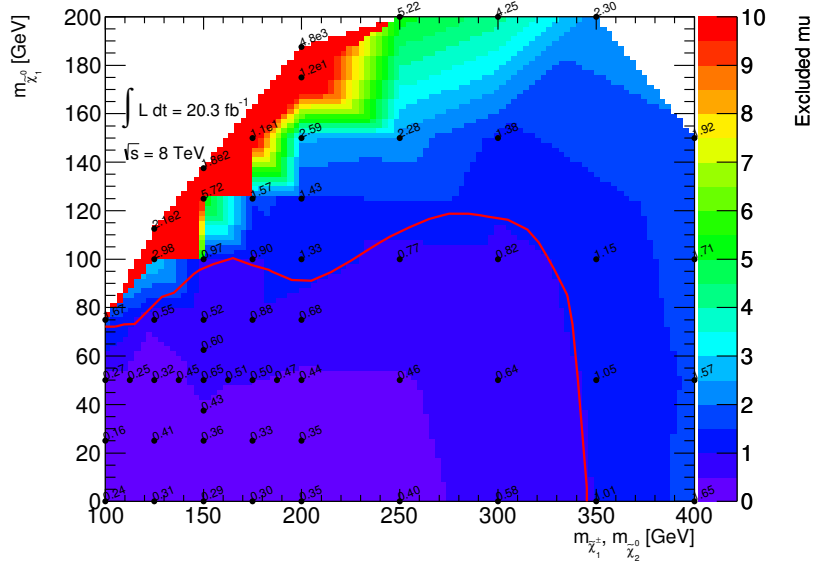
Before we had $10 \cdot 10\,000$ pseudo-experiments, if the μ lies outside the scanned range, one would need to redo the whole scanning. For the new method we run first $3 \cdot 10\,000$ pseudo-experiments and then again $3 \cdot 10\,000$, if μ happens to be somewhere else than expected, one can already intervene after $3 \cdot 10\,000$ pseudo-experiments. Moreover, the new method provides a much improved resolution, in fact in Figure 88b, the error bar of the middle observed CL_s touches the p -value of 0.05, so to increase the resolution, one would need to run more pseudo-experiments. The resolution of the old method is already improved with the first approximation, by using only 30 % of the pseudo-experiments.

The result from the upper limit scans are shown in Figures 89 to 92. Figures 89 and 90 show the excluded signal strengths μ at which an exclusion at the 95 % confidence level is reached, multiplying these numbers with the model cross-section, branching ratios and filter efficiencies, we get the excluded model cross-sections, which are shown in Figures 91 and 92. Several of these points have been cross-checked to validate the results.

Again we can compare the results of the binned signal region with the six signal regions used in the previous analysis [8]. Figure 93 show the results from the previous round, using the same dataset. Comparing this to Figures 91a and 91b, we see that the upper limits from the binned signal region are smaller in most of the points, putting stronger limits on the excluded model cross-sections.

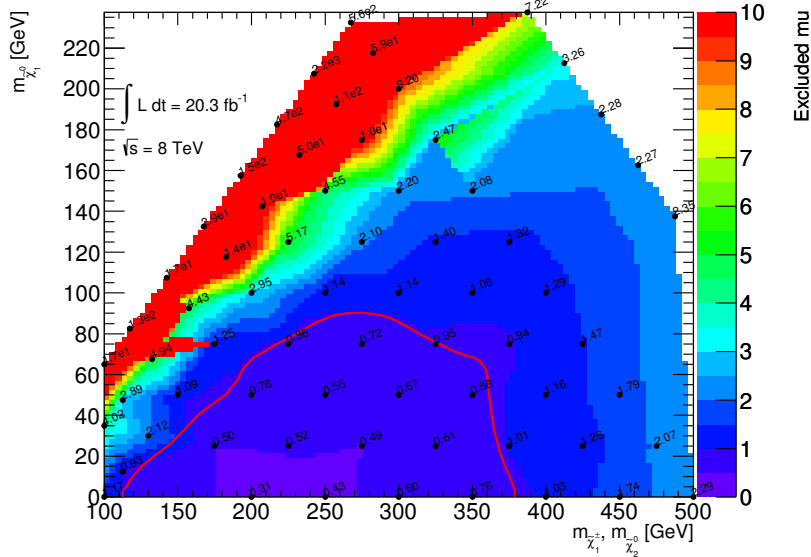


(a) $\tilde{\ell}_L$ mediated simplified model

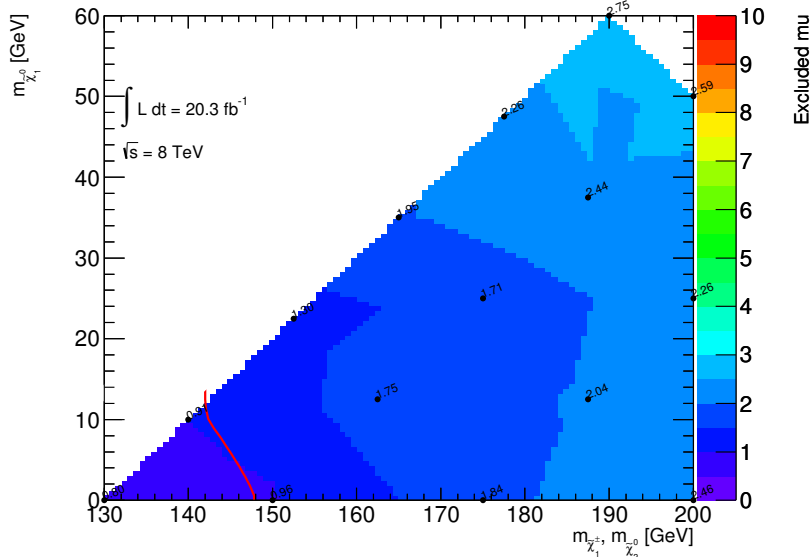


(b) WZ mediated simplified model

Figure 89: The excluded signal strength μ from the upper limit scan. The values for μ in the test statistic \tilde{q}_μ are the ones that are excluded at the 95 % confidence level.

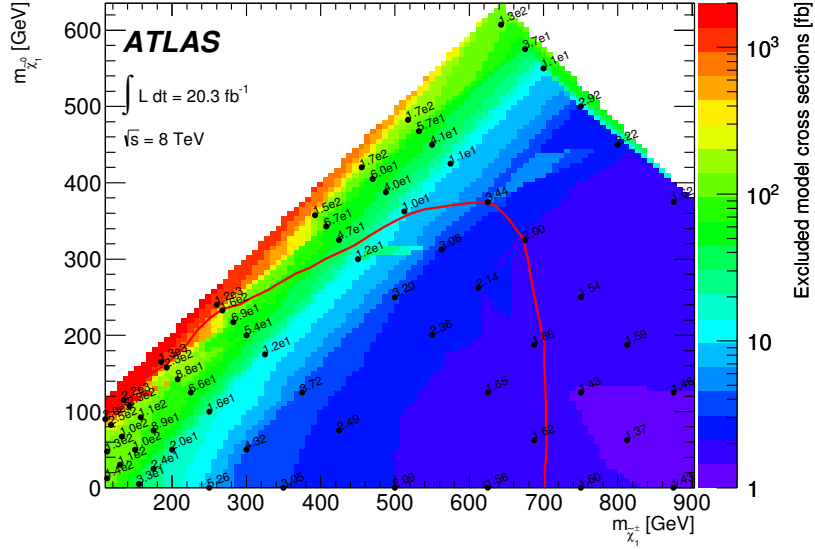


(a) $\tilde{\tau}_L$ mediated simplified model

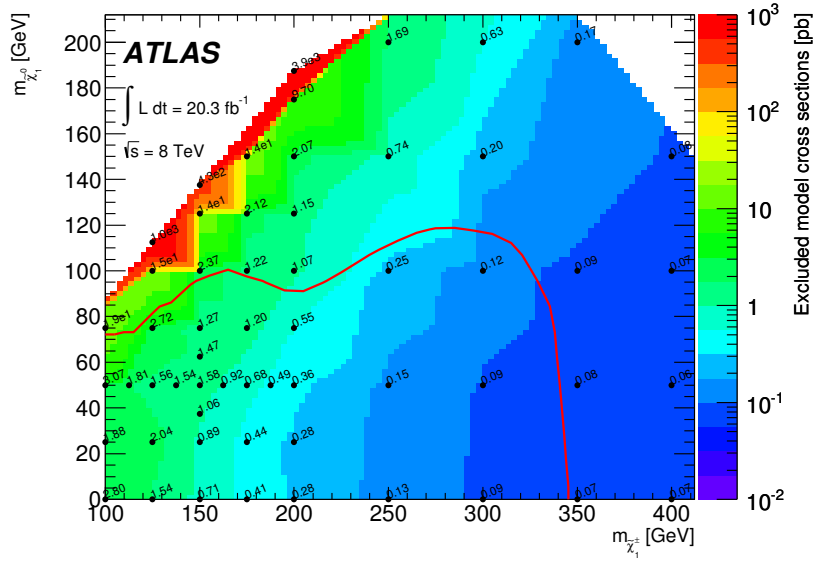


(b) *Wh* mediated simplified model

Figure 90: The excluded signal strength μ from the upper limit scan. The values for μ in the test statistic \tilde{q}_μ are the ones that are excluded at the 95 % confidence level.

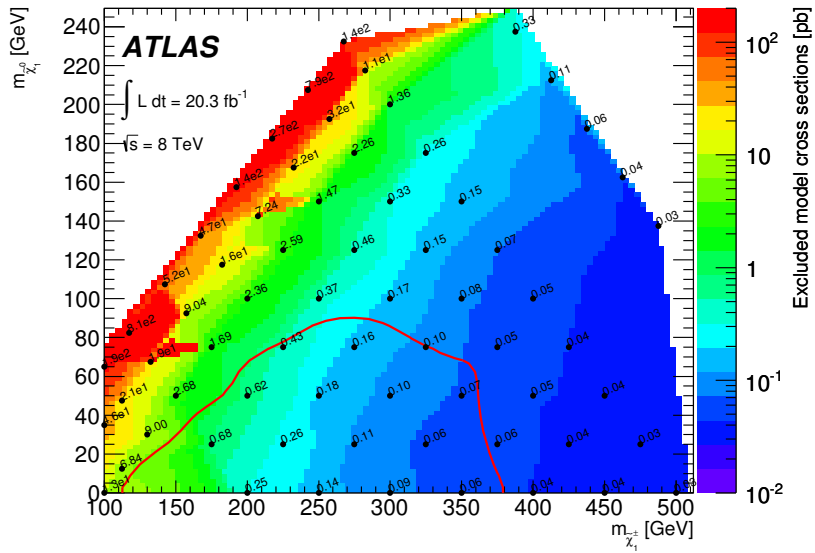


(a) $\tilde{\ell}_L$ mediated simplified model

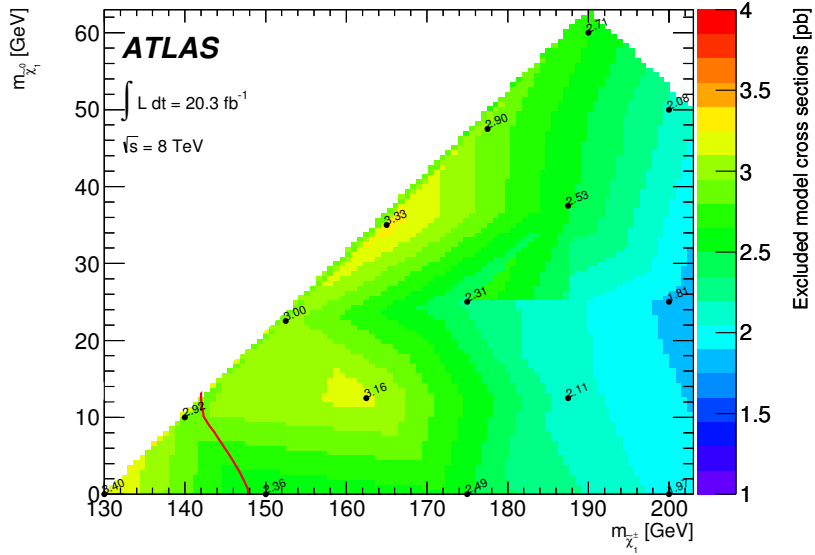


(b) WZ mediated simplified model

Figure 91: The excluded model cross-sections at the 95% confidence level from the upper limit scan. Cross-sections are in fb for the $\tilde{\ell}_L$ mediated simplified model and in pb for the WZ mediated simplified model.

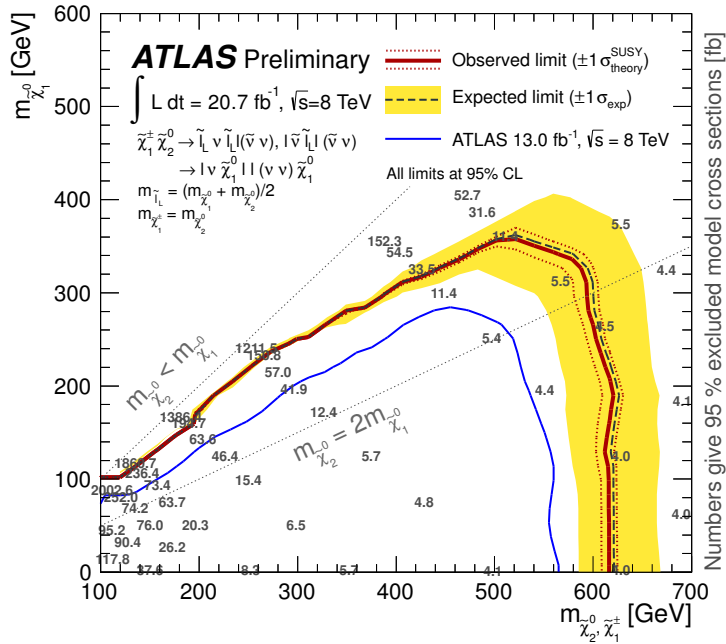


(a) $\tilde{\tau}_L$ mediated simplified model

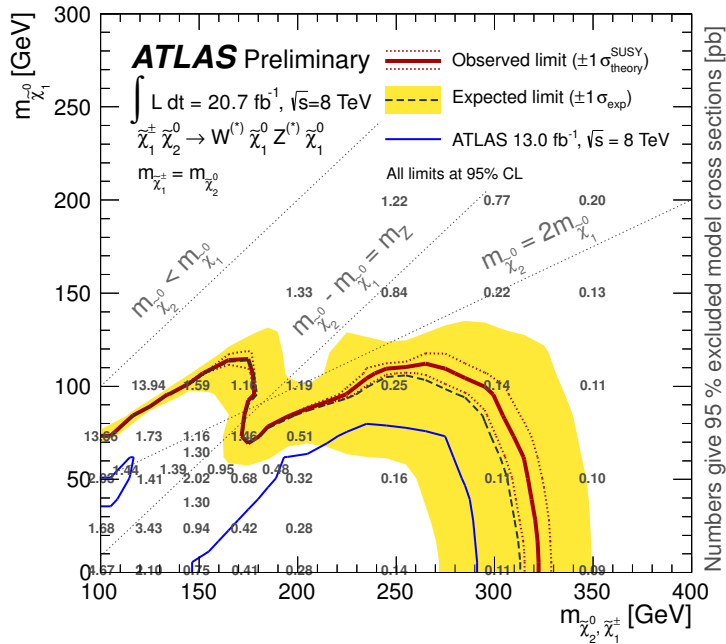


(b) Wh mediated simplified model

Figure 92: The excluded model cross-sections at the 95% confidence level from the upper limit scan. Cross-sections are in pb.



(a) \tilde{l}_L mediated simplified model



(b) WZ mediated simplified model

Figure 93: The excluded model cross-sections at the 95% confidence level from the conference note published in March 2013 [8]. Both analyses use the full 8 TeV dataset (but see footnote on page 53), both analyses use signal regions that were optimized on these grids. [8] used six signal regions, while [2] uses the binned signal region.

9.4 Fit results

The signal strength μ and the nuisance parameters θ are fit to data, as outlined in Section 8.2. Its best fit values or more precisely: the maximum likelihood estimators $\hat{\mu}$ and $\hat{\theta}$ are shown in the following tables.

Tables 28 - 30 show the results of the background only exclusion fit of the 20 bins, together with SR0 τ b, SR1 τ and SR2 τ a, which is used for most of the signal models. The tables show the number of events before fitting and the number of events after the simultaneous fit of the 23 regions. The errors shown in these tables are systematic and statistical, for technical reason the errors shown are symmetrized. The following tables show only the background only fit.

Bin	01	02	03	04	05
Observed events	36	5	9	9	11
Fitted SM events	26.18 ± 2.33	4.75 ± 0.78	10.79 ± 1.05	9.00 ± 1.03	13.86 ± 1.49
Fitted WZ events	14.52 ± 1.59	3.35 ± 0.74	7.76 ± 0.86	4.50 ± 0.51	6.37 ± 0.77
Fitted ZZ events	1.42 ± 0.55	0.12 ± 0.06	0.38 ± 0.13	0.20 ± 0.17	1.43 ± 0.49
Fitted ttbarV events	0.14 ± 0.03	0.06 ± 0.03	$0.03^{+0.04}_{-0.03}$	0.13 ± 0.09	0.10 ± 0.03
Fitted tribosons events	$0.12^{+0.22}_{-0.12}$	$0.03^{+0.06}_{-0.03}$	$0.07^{+0.12}_{-0.07}$	$0.20^{+0.37}_{-0.20}$	$0.09^{+0.17}_{-0.09}$
Fitted Higgs events	0.70 ± 0.25	0.15 ± 0.06	0.65 ± 0.18	0.46 ± 0.14	0.35 ± 0.13
Fitted fake events	9.29 ± 2.16	1.04 ± 0.28	1.91 ± 0.46	3.53 ± 0.87	5.51 ± 1.28
MC exp. SM events	22.52 ± 4.20	4.19 ± 1.46	10.58 ± 1.78	8.50 ± 1.63	12.85 ± 2.31
MC exp. WZ events	13.24 ± 3.29	2.98 ± 1.37	7.76 ± 1.57	4.49 ± 1.01	6.31 ± 1.51
MC exp. ZZ events	1.41 ± 0.56	0.12 ± 0.06	0.40 ± 0.14	0.20 ± 0.18	1.55 ± 0.52
MC exp. ttbarV events	0.14 ± 0.04	0.07 ± 0.04	$0.03^{+0.04}_{-0.03}$	0.14 ± 0.10	0.11 ± 0.04
MC exp. tribosons events	$0.33^{+0.33}_{-0.33}$	$0.10^{+0.10}_{-0.10}$	$0.19^{+0.19}_{-0.19}$	$0.57^{+0.57}_{-0.57}$	$0.26^{+0.26}_{-0.26}$
MC exp. Higgs events	0.66 ± 0.25	0.15 ± 0.06	0.64 ± 0.19	0.46 ± 0.15	0.36 ± 0.13
MC exp. fake events	6.74 ± 2.10	0.78 ± 0.27	1.55 ± 0.46	2.66 ± 0.88	4.26 ± 1.29
Bin	06	07	08	09	10
Observed events	13	15	1	28	24
Fitted SM events	8.03 ± 1.06	14.77 ± 1.43	1.15 ± 0.33	24.10 ± 2.02	17.48 ± 1.39
Fitted WZ events	4.49 ± 0.90	7.58 ± 0.68	0.37 ± 0.15	16.92 ± 1.94	13.78 ± 1.29
Fitted ZZ events	0.25 ± 0.12	0.54 ± 0.13	0.01 ± 0.00	1.41 ± 0.31	0.59 ± 0.12
Fitted ttbarV events	0.05 ± 0.02	$0.03^{+0.09}_{-0.03}$	0.10 ± 0.07	0.13 ± 0.07	0.12 ± 0.07
Fitted tribosons events	$0.09^{+0.17}_{-0.09}$	$0.31^{+0.57}_{-0.31}$	$0.04^{+0.08}_{-0.04}$	$0.08^{+0.15}_{-0.08}$	$0.14^{+0.27}_{-0.14}$
Fitted Higgs events	0.37 ± 0.12	0.98 ± 0.26	0.13 ± 0.05	0.32 ± 0.09	0.23 ± 0.07
Fitted fake events	2.79 ± 0.71	5.34 ± 1.29	0.49 ± 0.19	5.24 ± 1.03	2.62 ± 0.72
MC exp. SM events	6.60 ± 1.84	14.06 ± 2.20	1.08 ± 0.42	22.43 ± 3.42	16.37 ± 2.75
MC exp. WZ events	3.74 ± 1.59	7.61 ± 1.24	0.30 ± 0.24	16.19 ± 3.08	13.09 ± 2.53
MC exp. ZZ events	0.25 ± 0.12	0.55 ± 0.15	0.01 ± 0.00	1.43 ± 0.30	0.60 ± 0.12
MC exp. ttbarV events	0.05 ± 0.02	$0.04^{+0.10}_{-0.04}$	0.11 ± 0.08	0.16 ± 0.07	0.12 ± 0.08
MC exp. tribosons events	$0.24^{+0.24}_{-0.24}$	0.88 ± 0.88	$0.13^{+0.14}_{-0.13}$	$0.23^{+0.23}_{-0.23}$	$0.40^{+0.40}_{-0.40}$
MC exp. Higgs events	0.33 ± 0.11	0.98 ± 0.27	0.13 ± 0.05	0.32 ± 0.09	0.22 ± 0.07
MC exp. fake events	1.99 ± 0.69	4.01 ± 1.31	0.39 ± 0.18	4.11 ± 1.04	1.93 ± 0.65

Table 28: Background only fit results of the simultaneous fit of the 20 bins, SR0 τ b, SR1 τ and SR2 τ a. This table shows the first 10 bins. Errors shown are statistical plus systematic, but symmetrized.

Bin	11	12	13	14	15
Observed events	29	8	714	214	63
Fitted SM events	29.01 ± 1.93	5.83 ± 0.76	719.18 ± 22.52	220.88 ± 10.55	63.14 ± 5.51
Fitted WZ events	19.87 ± 1.62	4.00 ± 0.62	597.11 ± 26.70	208.59 ± 11.32	57.00 ± 5.35
Fitted ZZ events	$0.69^{+0.91}_{-0.69}$	0.14 ± 0.08	28.11 ± 3.78	5.49 ± 1.38	3.33 ± 0.94
Fitted ttbarV events	0.39 ± 0.17	0.11 ± 0.06	2.87 ± 0.55	1.91 ± 0.59	0.61 ± 0.24
Fitted tribosons events	$0.21^{+0.39}_{-0.21}$	$0.21^{+0.40}_{-0.21}$	$0.46^{+0.86}_{-0.46}$	$0.28^{+0.52}_{-0.28}$	$0.35^{+0.65}_{-0.35}$
Fitted Higgs events	0.27 ± 0.09	0.12 ± 0.03	2.19 ± 0.64	0.98 ± 0.17	0.30 ± 0.08
Fitted fake events	7.58 ± 1.81	1.24 ± 0.38	88.43 ± 19.38	3.63 ± 2.34	1.54 ± 0.38
MC exp. SM events	27.11 ± 4.26	5.51 ± 1.42	715.44 ± 68.54	218.61 ± 32.76	65.02 ± 12.97
MC exp. WZ events	19.49 ± 3.50	3.68 ± 1.14	612.54 ± 63.80	207.04 ± 32.29	58.34 ± 12.49
MC exp. ZZ events	$0.65^{+0.94}_{-0.65}$	0.14 ± 0.08	28.86 ± 4.12	5.54 ± 1.45	3.49 ± 1.04
MC exp. ttbarV events	0.41 ± 0.19	0.12 ± 0.06	2.92 ± 0.59	2.00 ± 0.64	0.67 ± 0.27
MC exp. tribosons events	0.59 ± 0.59	$0.61^{+0.61}_{-0.61}$	1.32 ± 1.32	0.80 ± 0.80	1.01 ± 1.01
MC exp. Higgs events	0.28 ± 0.10	0.12 ± 0.03	2.17 ± 0.65	0.98 ± 0.18	0.31 ± 0.08
MC exp. fake events	5.68 ± 1.82	0.85 ± 0.35	67.63 ± 19.44	2.24 ± 1.69	1.20 ± 0.38
Bin	16	17	18	19	20
Observed events	3	60	1	0	0
Fitted SM events	4.65 ± 0.77	68.40 ± 3.10	3.23 ± 0.76	1.15 ± 0.32	0.29 ± 0.14
Fitted WZ events	4.12 ± 0.73	48.84 ± 2.31	2.52 ± 0.69	0.90 ± 0.28	0.14 ± 0.08
Fitted ZZ events	0.11 ± 0.07	2.34 ± 0.60	0.08 ± 0.04	0.02 ± 0.02	0.01 ± 0.01
Fitted ttbarV events	$0.08^{+0.08}_{-0.08}$	0.70 ± 0.45	0.13 ± 0.11	0.00 ± 0.00	$0.01^{+0.01}_{-0.01}$
Fitted tribosons events	$0.11^{+0.21}_{-0.11}$	$1.13^{+2.09}_{-1.13}$	$0.18^{+0.33}_{-0.18}$	$0.03^{+0.05}_{-0.03}$	$0.02^{+0.05}_{-0.02}$
Fitted Higgs events	0.03 ± 0.01	0.97 ± 0.25	0.05 ± 0.01	0.01 ± 0.00	0.00 ± 0.00
Fitted fake events	0.19 ± 0.09	14.43 ± 3.00	0.28 ± 0.05	0.20 ± 0.09	0.10 ± 0.08
MC exp. SM events	4.57 ± 1.49	69.08 ± 7.91	3.42 ± 1.43	1.20 ± 0.43	0.29 ± 0.17
MC exp. WZ events	3.87 ± 1.39	50.41 ± 6.04	2.33 ± 1.27	0.92 ± 0.38	0.11 ± 0.10
MC exp. ZZ events	0.12 ± 0.07	2.43 ± 0.65	0.08 ± 0.04	0.02 ± 0.02	0.01 ± 0.01
MC exp. ttbarV events	$0.08^{+0.10}_{-0.08}$	0.77 ± 0.49	0.15 ± 0.13	0.00 ± 0.00	$0.01^{+0.01}_{-0.01}$
MC exp. tribosons events	$0.33^{+0.33}_{-0.33}$	3.22 ± 3.21	$0.54^{+0.54}_{-0.54}$	$0.08^{+0.08}_{-0.08}$	$0.07^{+0.08}_{-0.07}$
MC exp. Higgs events	0.03 ± 0.01	0.95 ± 0.26	0.05 ± 0.02	0.01 ± 0.00	0.00 ± 0.00
MC exp. fake events	0.14 ± 0.11	11.30 ± 3.13	0.27 ± 0.04	0.17 ± 0.08	0.08 ± 0.07

Table 29: Background only fit results of the simultaneous fit of the 20 bins, SR0 τ b, SR1 τ and SR2 τ a. This table shows the last 10 bins. Errors shown are statistical plus systematic, but symmetrized.

Bin	SR0 τ b	SR1 τ	SR2 τ a
Observed events	3	13	6
Fitted SM events	3.21 ± 0.72	9.95 ± 0.80	6.88 ± 0.73
Fitted WZ events	0.68 ± 0.10	4.63 ± 0.40	1.56 ± 0.23
Fitted ZZ events	0.03 ± 0.01	0.36 ± 0.07	0.05 ± 0.01
Fitted ttbarV events	$0.14^{+0.21}_{-0.14}$	$0.14^{+0.14}_{-0.14}$	$0.21^{+0.24}_{-0.21}$
Fitted tribosons events	$0.35^{+0.64}_{-0.35}$	$0.18^{+0.34}_{-0.18}$	$0.03^{+0.05}_{-0.03}$
Fitted Higgs events	0.49 ± 0.15	0.29 ± 0.07	0.02 ± 0.01
Fitted fake events	1.53 ± 0.18	4.35 ± 0.30	5.02 ± 0.49
MC exp. SM events	3.84 ± 1.13	10.27 ± 1.05	6.95 ± 0.79
MC exp. WZ events	0.68 ± 0.13	4.64 ± 0.59	1.51 ± 0.32
MC exp. ZZ events	0.03 ± 0.01	0.36 ± 0.08	0.05 ± 0.01
MC exp. ttbarV events	$0.17^{+0.24}_{-0.17}$	0.16 ± 0.15	$0.21^{+0.24}_{-0.21}$
MC exp. tribosons events	$1.00^{+1.00}_{-1.00}$	0.51 ± 0.51	$0.09^{+0.09}_{-0.09}$
MC exp. Higgs events	0.49 ± 0.15	0.28 ± 0.07	0.02 ± 0.01
MC exp. fake events	1.48 ± 0.18	4.32 ± 0.30	5.06 ± 0.50

Table 30: Background only fit results of the simultaneous fit of the 20 bins, SR0 τ b, SR1 τ and SR2 τ a. This table shows SR0 τ b, SR1 τ and SR2 τ a. Errors shown are statistical plus systematic, but symmetrized.

9.5 Asymptotic limits vs. pseudo-experiments

All results in this section are derived with Monte Carlo pseudo-experiments. Using asymptotic formulae would highly simplify the derivation of the results. A comparison of results with asymptotic formulae and with pseudo-experiments for the discovery p -values is shown in Table 31.

Bin	N_{exp}	N_{obs}	asymptotic		toys	
			p_0	$Z[\sigma]$	p_0	$Z[\sigma]$
01	$23^{+4.0}_{-4.0}$	36	0.024	1.98	0.015	2.16
02	$4.2^{+1.5}_{-1.5}$	5	0.38	0.31	0.35	0.38
03	$10.6^{+1.8}_{-1.8}$	9	0.50	—	0.50	—
04	$8.5^{+1.7}_{-1.6}$	9	0.44	0.15	0.40	0.26
05	$12.9^{+2.4}_{-2.3}$	11	0.50	—	0.50	—
06	$6.6^{+1.9}_{-1.8}$	13	0.039	1.76	0.028	1.91
07	$14.1^{+2.2}_{-2.2}$	15	0.41	0.22	0.37	0.33
08	$1.1^{+0.4}_{-0.4}$	1	0.50	—	0.50	—
09	$22.4^{+3.6}_{-3.4}$	28	0.18	0.92	0.13	1.12
10	$16.4^{+2.8}_{-2.8}$	24	0.075	1.44	0.068	1.50
11	$27^{+5.0}_{-5.0}$	29	0.39	0.29	0.39	0.28
12	$5.5^{+1.5}_{-1.4}$	8	0.20	0.83	0.21	0.82
13	$715^{+70.0}_{-68.0}$	714	0.50	—	0.50	—
14	$219^{+33.0}_{-33.0}$	214	0.50	—	0.50	—
15	$65^{+13.0}_{-13.0}$	63	0.50	—	0.50	—
16	$4.6^{+1.7}_{-1.5}$	3	0.50	—	0.50	—
17	$69^{+9.0}_{-8.0}$	60	0.50	—	0.50	—
18	$3.4^{+1.4}_{-1.4}$	1	0.50	—	0.50	—
19	$1.2^{+0.4}_{-0.4}$	0	0.50	—	0.50	—
20	$0.29^{+0.18}_{-0.17}$	0	0.50	—	0.50	—

Table 31: Discovery p -value of each bin and in case of an overfluctuation the significance in σ 's. Using the definition of a one-sided p -value, the probability density function is capped and every underfluctuation has a p -value of 0.5. Asymptotic and pseudo-experiments results are given, “asymptotic” refers to asymptotic formulae introduced in Section 8.5, “toys” refers to an ensemble of Monte Carlo pseudo-experiments. The official result is the one from the pseudo-experiments. 100 000 pseudo-experiments have been run for each bin with an overfluctuation.

The differences between results derived with asymptotic formulae and with pseudo-experiments show the expected behaviour: they are usually small, but larger for bins with larger deviations from the expected number of events and the results from the pseudo-experiments are more aggressive. To get a feeling how this translates to exclusion contours and if pseudo-experiments are needed, a comparison has been made on one grid first. The

$\tilde{\ell}_L$ mediated simplified model has been chosen for this comparison, since it is mainly driven by bin 20 and this bin has the lowest number of expected event. Asymptotic formulae deviate from pseudo-experiments results mostly for bins with low background expectations.

A comparison of observed CL_s values is shown in Figure 94. The differences are - not unexpected - quite substantial in this model, especially at high $\tilde{\chi}_1^\pm$ masses. Therefore it was decided to run pseudo-experiments on all models, also for the exclusion contours and the upper limits on model cross-sections.

In order to not suffer from statistical fluctuations, one has to decide how many Monte Carlo pseudo-experiments to run. Extensive tests checking against convergence have been made. The convergence criterion being as follows: 10 000 pseudo-experiments has been defined as a “set”. After every set, the observed and expected CL_s values have been noted with an accuracy of three digits after decimal. If they agree with each other three times in a row, the convergence criterion has been met, e.g. if after 30 000, 40 000 and 50 000 pseudo experiments, the observed and the expected CL_s are 0.123, convergence is reached. At most, 100 000 pseudo-experiments were run¹². The study has shown, that most points do not converge according to this definition after 100 000 pseudo-experiments, therefore the convergence criterion was dropped and 100 000 pseudo-experiments have been run always. In the end, some exclusion contours were smoothed and by this the possible statistical fluctuations of the pseudo-experiments have been washed out, a subsequent test has shown that 50 000 pseudo-experiments would have led to the same result as 100 000.

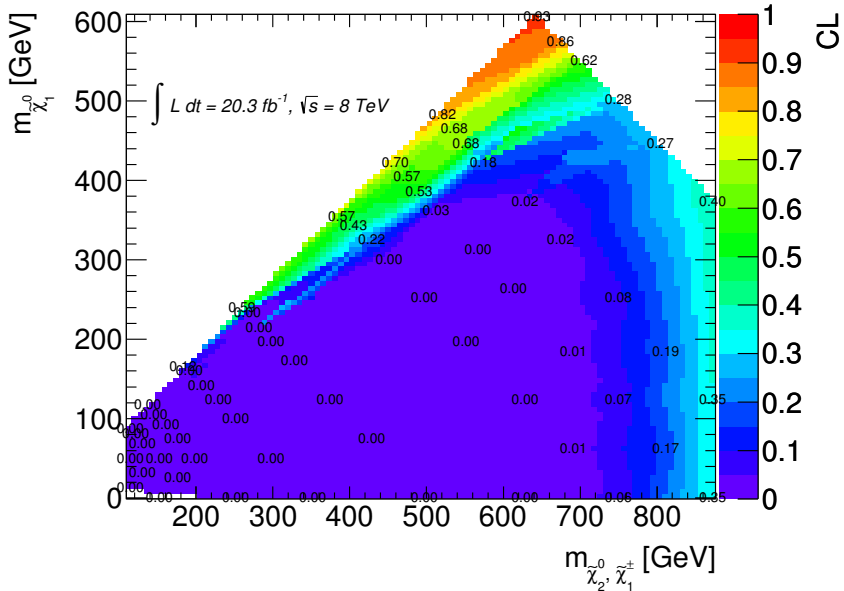
For the discovery p -values, 100 000 pseudo-experiments were run in each bin with an overfluctuation, i.e. $9 \cdot 100 000$ pseudo-experiments, for the visible cross-section, $20 \cdot 50 000$. The exclusion contours have ≈ 850 modeled signal points, for an exclusion contour, every point has to be run 3 times (nominal and $\pm 1\sigma$ variation on the theoretical uncertainty on the signal), giving a total of $850 \cdot 3 \cdot 100 000 = 250 000 000$ pseudo-experiments. Moreover, for the simplified model, with ≈ 200 generated signal points, the upperlimit on the model cross-sections had to be run. Since this is a scan in μ and ≈ 6 different values of μ were tested while every fixed value of μ required 10 000 pseudo-experiments, an additional $200 \cdot 6 \cdot 10 000 = 12 000 000$ pseudo-experiments had to be calculated. Running on ≈ 1500 cores in parallel, this still took ≈ 1 month¹³, not including time needed for scripting and debugging. Time that could be spent more meaningful.

Based on this experience, my suggestions for using asymptotic formulae vs. Monte Carlo pseudo-experiments is as follows:

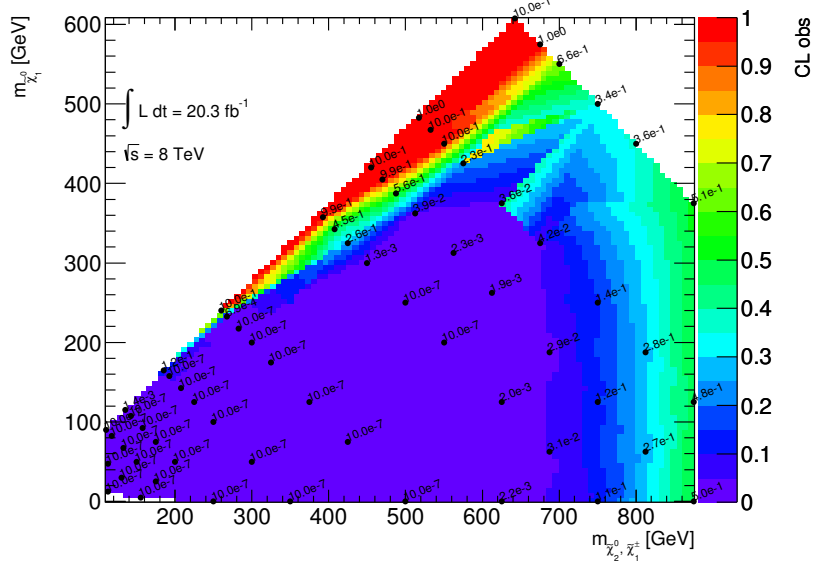
1. Try to use asymptotic formulae presented in Section 8.5. If background expectation in at least one region is $\lesssim 2$ events, you might make some checks, to estimate the differences, if the background expectation in at least one region is $\lesssim 1$ event, you have to run pseudo-experiments. It might be worth considering avoiding such tight regions from the beginning, if they do not add a huge boost to the sensitivity. Spending a month optimizing the background estimation or systematic uncertainties, might more than compensate the loss in sensitivity by choosing a less tight region. Moreover, a month spent on understanding the physics processes and the detector is better spent than running millions of pseudo-experiments.

¹²This convergence criterion has a major flaw: Since we are using significances Z for the interpolation in exclusion contours, one should also make the convergence criterion dependent on the significance, rather than on the CL_s . Nonetheless, the study has not been repeated, since the convergence criteria was ultimately not used.

¹³The time needed to run pseudo-experiments is highly dependent on the complexity of the likelihood function. The likelihood function used here consists of 23 Poissonian terms (for the 23 regions fitted simultaneously) and ≈ 50 Gaussian terms (for the ≈ 50 nuisance parameters from the systematic uncertainties); fitting an easier setup will take much less time



(a) Asymptotic formulae



(b) Pseudo-experiments

Figure 94: Observed CL_s values derived with asymptotic formulae (a) and with Monte Carlo pseudo-experiments (b).

2. If such a tight region is present and pseudo-experiments need to be run, check first if this region adds sensitivity to all your signals. If not, remove this region from the likelihood for those signals where it does not enhance the sensitivity and derive those results with asymptotic formulae. If some results are derived with pseudo-experiments and some of them are derived with asymptotic formulae, clearly state this in the publication.
3. Running pseudo-experiments for discovery p -values and visible cross-sections should not be too time consuming. The exclusion contours and the upper limits on the model cross-section, on the other hand, can easily require weeks to run, always depending on the complexity of the setup, the number of Monte Carlos to generate and cores available. For the exclusion contours, define *beforehand* if you want to smooth the models. If so, less pseudo-experiments will be needed to derive a stable result, not suffering from statistical fluctuations. Depending on the complexity of the setup, 20 000 to 30 000 should suffice, if the exclusion contour is smoothed. Otherwise 30 000 to 50 000 are recommended.
4. Split jobs in small batches of pseudo-experiments, e.g. 10 000. If a job crashes, one loses only the small batch of pseudo-experiments, not the full bulk. Moreover, batch-systems work well with small but repetitive jobs, calculating all 100 000 pseudo-experiments in one job only caused problems on our batch-system.
5. Introducing a convergence criterion as outlined above is not worthwhile. The convergence criterion will add an overhead in scripting, debugging and processing, moreover a meaningful convergence criterion needs to be discussed and agreed upon and if jobs of pseudo-experiments are split, communication between different jobs need to be set up.
6. Test your batch-system well ahead!

Finally, I'd like to discuss the presentation of exclusion contours with the theory band around the observed exclusion line: The recommendation from ATLAS and CMS is to remove the nuisance parameters for the theoretical signal uncertainties from the likelihood fit but evaluate the exclusion limits three times: once at the nominal signal cross-section and once each for $\pm 1\sigma$ on the signal cross-section where the uncertainty is coming from the theoretical signal uncertainties (pdf and scales) [109]. While clearly beneficial for theorists to have this information at hand, it means effectively tripling the number of pseudo-experiments that need to be run. There must be a less time consuming way to present this information. This recommendation should be revisited.

Conclusions

While being a PhD student at the Laboratory for High Energy Physics (LHEP) at the Albert Einstein Center for Fundamental Physics (AEC), I worked on two different projects on the ATLAS experiment. During the first part, I studied commercial optical receivers to assess if they are suitable to be used with the new insertable b -layer. The second part of my term as PhD student I analyzed collision data with the scientific objective of finding a supersymmetric (SUSY) signal.

The insertable b -layer will introduce a new readout technology. In particular, new optical components were planned to be adopted. I tested them for reliability, low frequency behaviour and response to input sensitivity. The reliability test I conducted in a climate chamber at 85° C and 85% relative humidity. At these conditions, electric components age rapidly. None of the channels showed any malfunctions. Hence the reliability should not be an issue.

The optical receivers are designed to operate at a frequency of 2.7 GHz. For ATLAS the frequency needed is 160 MHz, so I tested the optical receivers at these low frequencies. I showed that the optical receivers can cope with the low frequency of 160 MHz without any problems. Only at even lower frequencies around 300 kHz the receivers started to lose signals.

In the final setup, the optical signals are transmitted from the detector to the optical readout components via optoboard. The exact optical power transmitted by the opto-board was not known at time of testing. Therefore, a scan of different optical powers was made to set limits on the minimal and maximal optical power to be transmitted by the optoboard. An interesting behaviour was observed during these tests, where the optical receivers of three different suppliers were tested. While all products had a minimal optical power lower than 1 mW, two of them did not show any instabilities at high powers tested up to 7 mW. But the device of one supplier became highly unreliable already at input powers of around 2 mW. I subsequently excluded these from the list of possible devices. The other two products did pass all tests and I proposed the usage of either one of these two components. One of them is produced by AVAGO and is currently being installed in the readout electronics of the detector. It will be used to readout data from the insertable b -layer as soon as ATLAS will start to operate again in 2015.

For the part of my work on the physics data analysis I focused on the search for electroweakly produced SUSY particles in a multi lepton final state. I started with setting up a simultaneous fit of the most important background, WZ , and in the statistical interpretation of the results in a SUSY search in final states with exactly three leptons [5], published in August 2012. In the following publication of the same SUSY search [6], I again contributed to the simultaneous fit method, but taking over the lead in the statistical interpretation of the search results. At the same time, I statistically interpreted a similar SUSY search, but with four leptons in the final state [7]. Both searches were published in November 2012. While carrying out the statistical interpretation of these analyses, I built up a package of scripts to facilitate the statistical analysis [11, 12]. These scripts have also been adopted by another part of the ATLAS collaboration, namely the group that searches for SUSY signals in a final state with two leptons.

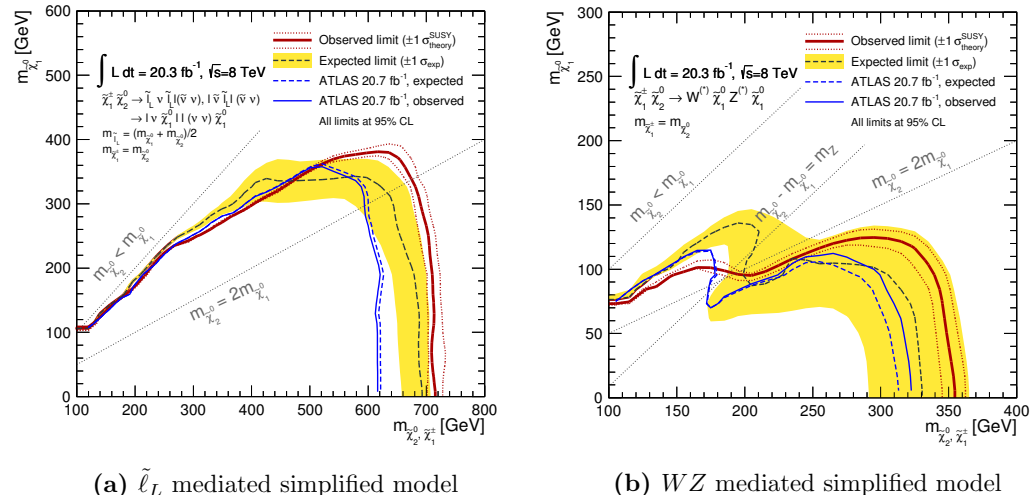
While working on these publications and the statistical interpretation of a SUSY signal that, due to its kinematics, is difficult to distinguish from the Standard Model background, I came up with the idea of generalizing the approach with the signal regions. Instead of using one signal region with a sensitivity in only a small part of the SUSY parameter space, I intended to use a large signal region in a final state of three light leptons and

subdivide it into smaller regions. Using a large signal region broadens the sensitivity to different SUSY models, while subdividing this region into smaller regions - called binning the signal region - maximizes its sensitivity.

The optimization of such a binned signal region has proven not to be possible in the standardized way. Therefore, I had to develop a more general solution how to optimize multiple regions at once. Instead of using a formula to determine the sensitivity of one region, which cannot combine multiple regions, I used a profile likelihood approach to find a combination of signal regions that maximizes the sensitivity.

Due to short timescale, the implementation of the binned signal region could not be finalized for the next search, which was published in March 2013. In these publications I again carried out the statistical interpretation in both SUSY searches with three leptons [8] and four leptons [9] in their final states.

The following SUSY search in a final state with three leptons [2] is the main subject of this thesis. The analysis is published in a paper on arXiv and JHEP. For this analysis, I guided the optimization of the tau signal regions, carried out the complete statistical interpretation and provided most of the figures and tables for the final publication. But my main contribution to this publication was the binning of the light lepton signal region into 20 bins using three distinct variables. These variables are the same flavour opposite sign lepton pair invariant mass m_{SFOS} , the absolute value of the missing transverse momentum E_T^{miss} and the transverse mass from the remaining lepton not used for m_{SFOS} and E_T^{miss} . The binning led to more stringent exclusion limit contours and excluded upper limits on the model cross-sections. The improvement over former results using the same dataset is shown in the figure below.



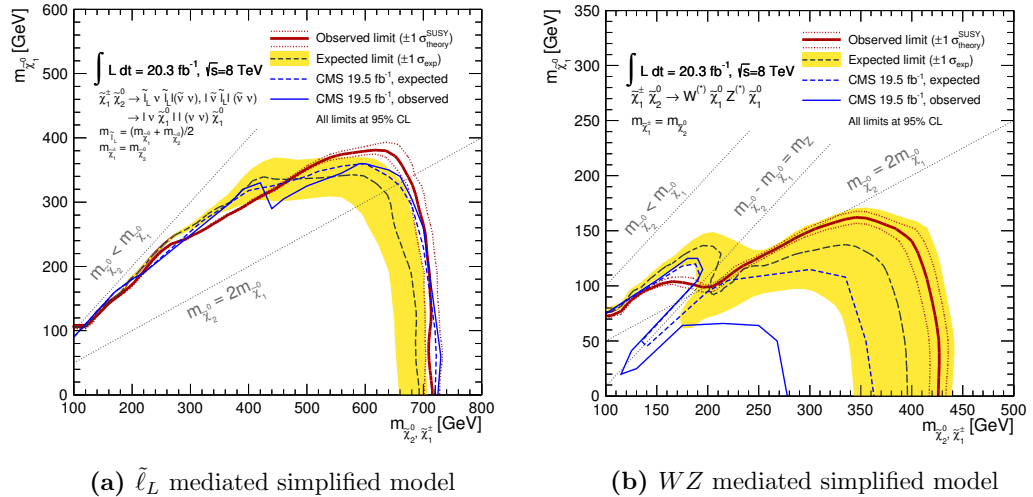
This figure compares the exclusion limit contours of the conference note published in March 2013 [8] and the paper published in March 2014 [2]. For both publications I interpreted the results statistically, but only in the latter I optimized the signal region. Both use the full 8 TeV dataset and both analyses use signal regions that were optimized on these grids. From [8], the nominal expected and observed are shown. [8] used six signal regions, while [2] uses my binned signal region.

The improvement is substantial: in the $\tilde{\ell}_L$ mediated simplified model, for low $\tilde{\chi}_1^0$ masses, the expected improvement at the 95 % confidence level is about 70 GeV, while the observed improvement is even 100 GeV. For the WZ mediated simplified model, again at low $\tilde{\chi}_1^0$

masses, the expected improvement is about 20 GeV and the observed improvement is more than 30 GeV. For the part in the parameter space where $m_{\tilde{\chi}_2^0} - m_{\tilde{\chi}_1^0} < m_Z$, the expected improvement is about 30 GeV, but the observed exclusion limit is partially weaker. This is due to overfluctuations in data in many bins contributing to the sensitivity of this region. It is interesting to note, that many overfluctuations in my binned signal region could be explained by SUSY having a compressed spectrum. This is an interesting area to look further for SUSY signals, once the Large Hadron Collider (LHC) is producing data again.

My binned signal region has also been used in a combination with another search for SUSY in a final state with exactly two leptons [3]. The results have also been presented in the CERN courier journal [4].

CMS, the other multi-purpose experiment at the LHC, has published results of a multi-lepton search as well [108]. They set limits in exactly the same signal grids as I do. They combine signal regions from final states requesting two and three leptons, while a combination of my binned signal region with a signal region from a two lepton final state is only carried out in the WZ mediated signal grid. A comparison of both observed and expected exclusion contours is shown in the figure below. The exclusion contours from CMS are drawn by hand.



(a) $\tilde{\ell}_L$ mediated simplified model

(b) WZ mediated simplified model

In the $\tilde{\ell}_L$ mediated simplified model, the observed exclusion is comparable. The expected exclusion from CMS, on the other hand, is stronger by about 20 to 30 GeV for high $\tilde{\chi}_1^\pm$ masses. This can be explained by the additional use of two lepton final state signal regions by CMS. Comparing the WZ mediated simplified model, where both analyses have a combined result of two different final states, my exclusion contour is much stronger. For high $\tilde{\chi}_1^\pm$ masses, the expected exclusion is stronger by about 30 GeV, while the observed one even reaches almost 150 GeV. But also in the WZ like region, my exclusion results are much stronger.

My method of binning the signal region is general. It can be easily applied to other final states as well. Even a generalization to other non-SUSY signals is possible, but would only make sense if the signal searched for has a set of unknown parameters. Given that large amounts of data and simulated events are available, my method could also be applied outside ATLAS, even outside collider experiments.

Many improvements to my approach with the binned signal region are thinkable, but their feasibility would need to be studied first. Possible improvements might be:

- Instead of 20 bins, one could think of using more bins. Naively one might think, the more bins one introduces, the more information about the parameter space is available and the more stringent limits can be set. There are several caveats to this line of thought. The background modeling in many bins will be difficult, data-driven techniques but also limited Monte Carlo generated events will run into low statistics regime and statistical fluctuations will govern the background modeling in the bins. Moreover, due to the look-elsewhere effect, the discovery potential will go severely down when introducing many bins, large overfluctuations are expected by pure chance. To detect a SUSY signal in such a setting will be extremely difficult. Nonetheless, the number of bins can be adjusted, for example the bins with m_{SFOS} close to the Z mass, where a large amount of events is available and low statistics is not an issue, can be further divided into more bins.
- I used three discriminating variables. There's a huge potential in using other variables to discriminate signal from background. The use of m_{SFOS} , E_T^{miss} and m_T was mainly motivated since these variables have already been proven to be strong discriminators. Other variables include lepton flavours, different combinations of well known variables or angular distributions. Moreover, theorists suggested to change our definition of the m_{SFOS} variable [110].
- As baseline signal region, where the binning was carried out, the parameter space was chosen to be as large as possible, only the part with $m_{\text{SFOS}} < 12 \text{ GeV}$, $E_T^{\text{miss}} < 50 \text{ GeV}$ and events with b -tagged jets were removed. If the parameter space is extended below m_{SFOS} of 12 GeV and below E_T^{miss} of 50 GeV, the sensitivity to SUSY signals close to the diagonal could be enhanced, since these are characterized with small values of m_{SFOS} and E_T^{miss} . But one might also think of choosing a smaller baseline signal region and concentrate only on a subset of the phase space, e.g. compressed scenarios.

SUSY may not have been found in the first run of the LHC and the parameter space where natural SUSY exists is getting narrower. But even in the exclusion limits I presented above there is still some space for a SUSY signal, most notably for compressed scenarios, i.e. close to the diagonal where $m_{\tilde{\chi}_2^0} = m_{\tilde{\chi}_1^0}$. These scenarios are difficult to detect since the mass splitting of $\tilde{\chi}_2^0$ and $\tilde{\chi}_1^\pm$ to $\tilde{\chi}_1^0$ is small and not much phase space for a decay of $\tilde{\chi}_2^0$ and $\tilde{\chi}_1^\pm$ is available. Hence, both $\tilde{\chi}_2^0$ and $\tilde{\chi}_1^\pm$ will become long-lived and maybe decay only outside the detector. In this case, while $\tilde{\chi}_1^\pm$ will generate a track in the inner detector and shower in the hadronic calorimeter, the $\tilde{\chi}_2^0$ will escape the detector volume undetected. Even when those particles are short-lived and decay within the beampipe, the resulting leptons will be soft. A qualitatively good reconstruction of the leptons will be more difficult, hence a loss in efficiency is expected. This could also explain why ATLAS hasn't observed a SUSY signal yet. Such signals have to be tackled with different strategies than those used in my analysis. One should consider lowering the p_T thresholds of the reconstructed leptons. Lowering these will enhance the acceptance but also raise systematic uncertainties. Another problem arises from the fact that events with only soft leptons are not recognized as interesting by the ATLAS trigger logic and it will not be recorded. This problem could be overcome by taking advantage of a jet from initial state radiation, which causes a trigger to fire. These are certainly things to look at for future analyses, and one does not even need to wait for new data to carry them out.

Even when no compressed scenario SUSY signals are found and the exclusion contours of the simplified models in question are excluded further to about 1 TeV, there still cannot be a conclusion drawn that no natural SUSY exists. In the simplified models considered, many assumptions are made. For example, branching ratios involving SUSY particles are set to one, although they could be smaller. Realistic models will have different cross-sections and it is not unlikely that a SUSY signal with low masses exists but has not been found yet. At this point the collaboration between theorist and experimentalist becomes necessary. It is the duty of the theorists to inform us on which SUSY signals are still realistic. We experimentalists, on the other hand, should consider simplified models that can be adapted to the more likely SUSY scenarios by the theorists. Interpreting the search results in realistic SUSY models like the (phenomenological) minimal SUSY Standard Model - (p)MSSM - might be a nice add-on to an analysis, but should not be the main focus of a search. Optimizations should never be carried out on MSSM models, since one would be too specific and become only sensitive to one small subset of theories. The chances that one of them is realized in nature are slim. Simplified models are the perfect tool to study SUSY signals, as I have learned by feedback and discussions I had with theorists.

When taking the binning of the signal region one step further, one might end up with a multivariate analysis. A multivariate analysis is highly specialized and will always reach a higher sensitivity than a simple cut and count analysis. Hence, the exclusion contours shown in the figure above can be extended with the same data by using a multivariate analysis. Multivariate analyses exist already in different flavours, the methods are well developed and tested, such an analysis could be carried out with less work than what I had to invest for the binned signal region. However, I do not propose the use of a multivariate analysis in SUSY. In SUSY, we do not expect the signal to be of the sort of the simplified model that we study, instead we look for a signal that resembles similar dynamics to the model studied, where “similar” is not even clearly defined. In the end we don’t know where SUSY hides. The simplified models we interpret our results in are merely tools to optimize our searches and to document our progress. The optimization part should not be overstressed, though. It is not the goal to optimize only on this particular model, but rather on a whole family of different models. My method is fairly general, since I look at a large phase space, many different SUSY signals could be detected. A multivariate analysis, on the other hand, would mainly be sensitive to the model it was optimized on.

Being general can also be looked at as a weakness of the method. Since I basically look for a SUSY signal in a large part of the phase space with three leptons in the final state, overfluctuations by pure chance are expected. The discovery potential of such a method is weakened, since one has to take into account the look-elsewhere effect. But so far, no SUSY signal has been observed and since SUSY can explain such vast possibilities of signatures, one needs to look everywhere to find possible traces of a SUSY signature, even when reducing the discovery potential. Once one might have spotted a region in phase space where SUSY has an enhanced probability of hiding, one can narrow the search and concentrate on this region and again maximize the discovery potential. Finding such a favoured region in phase space can happen by theoretical considerations or experimental hints from previous searches.

My binned signal region discovered exactly such a hint in the phase space region close to the diagonal, where compressed scenarios are present. In my results, I showed a discrepancy between expectation and observation of roughly 2σ in the bins with low invariant masses from same flavour opposite sign pairs. This is an interesting fluctuation,

but one should also keep in mind that this is only a local p -value, without corrections from the look-elsewhere effect. Nonetheless, it is a very promising region and a clear sign that low-mass SUSY is far from excluded. Once ATLAS is collecting data again, close attention should be paid to this region.

Acknowledgements

I thank Prof. Dr. Antonio Ereditato for giving me the opportunity to do PhD studies at the Albert Einstein Center for Fundamental Physics at the University of Bern. I thank Dr. Jamie Boyd for accepting to be external referee and co-examiner. Also I thank Prof. Dr. Thomas Becher for being the examiner of this thesis.

A special thank you to Prof. Dr. Michele Weber for the careful review of this thesis and for the help and support throughout my term as a student. Knowing that I can call you at any time of the day, any day of the week, was very important to me.

For helping me getting started in the broad ATLAS experiment, I'm in debt to PD Dr. Hans Peter Beck, Dr. Sigve Haug, Dr. Lucian Ancu and Dr. Alberto Cervelli. Thank you for the many fruitful discussions we had and for the many feedback I got from you, be it about my work, about my presentations or about mistakes I made. This feedback is always very valuable to me. I also thank Dr. Gianfranco Sciacca, who supports the computer cluster at the Laboratory for High Energy Physics in Bern and made it continuing working, no matter how much I hammered it.

I would also like to thank all my other colleagues at the Laboratory for High Energy Physics, be it fellow students or people from the workshops. Special thank to Dr. Tobias Kruker and Lukas Marti, two fellow students with whom I discussed many crazy ideas - some of them even made it into a publication - and who really made me enjoying to be a physicist in the ATLAS experiment. Too bad you guys are leaving the field.

Also I would like to acknowledge the help and collaboration of many people from the ATLAS experiment outside the University of Bern. Thanks to Dr. Tobias Flick, who helped me getting started in the hardware work of the insertable b -layer. In the multilepton analysis group, I thank all the fellow analyzers who gave me helpful feedback and explained many things to me. To emphasize I'd like the acknowledgement of the editors I worked with: Dr. Anadi Canepa, Dr. Christina Potter and Dr. Zoltan Gecse.

A very warm thank you goes to my family and my friends. They did not always have it easy with me, but did always support me. Especially I would like to mention my mother, she never stopped believing in me.

Last but not least, I thank Jasna, my girlfriend, for being the person you are.

Appendix A Signal region event yields and sensitivities

This appendix shows all signal event multiplicities and derived sensitivities in all 20 bins. To derive the sensitivity, HistFitter [13] was used, no systematic uncertainties are included and the background modeling comes solely from Monte Carlo. Figures 97 - 101 show the $\tilde{\ell}_L$ mediated simplified model, Figures 102 - 106 show the WZ mediated simplified model.

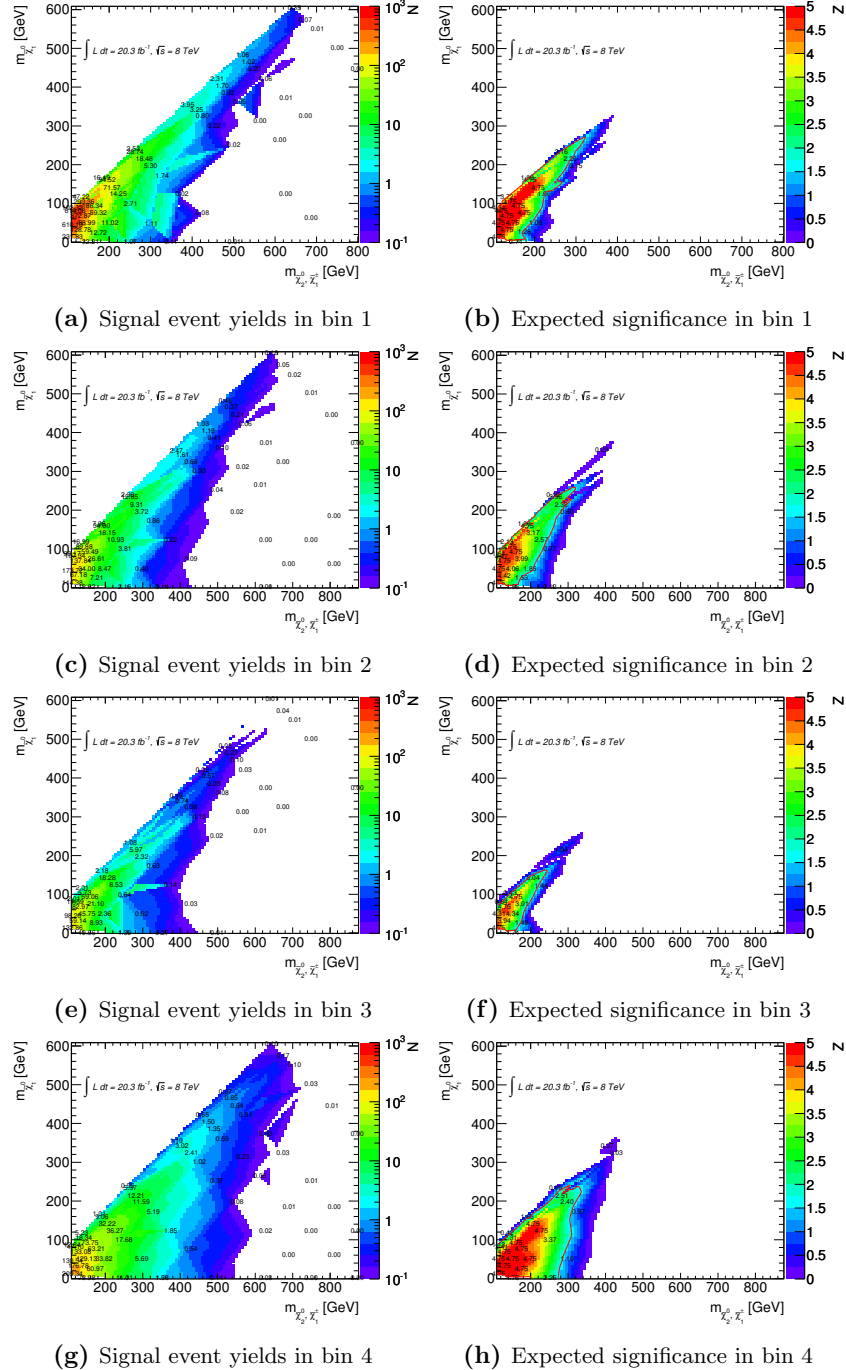


Figure 97: Expected number of signal events and expected significances in the four bins where $m_{\text{SFOS}} \in [12, 40]$ GeV for the $\tilde{\ell}_L$ mediated simplified model

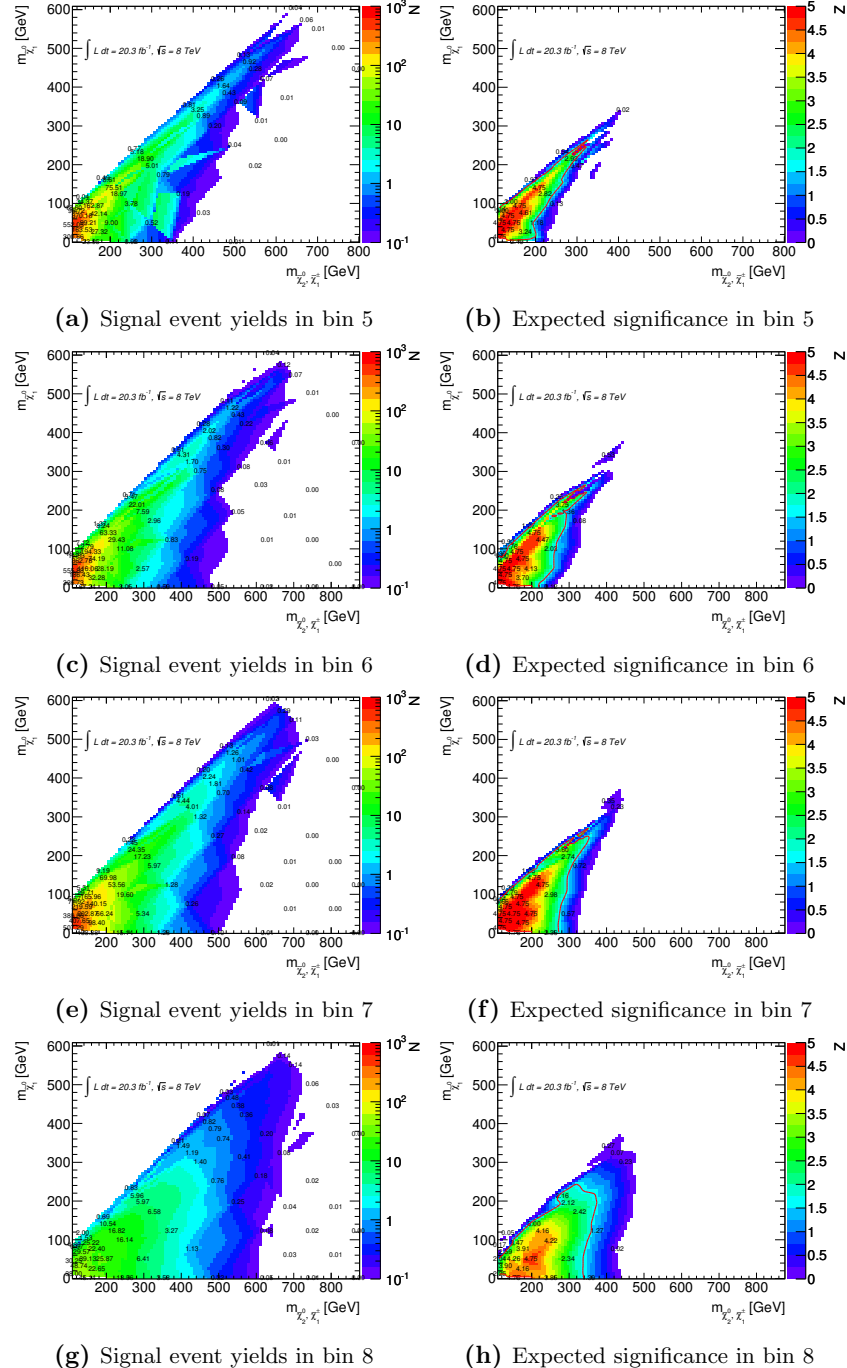


Figure 98: Expected number of signal events and expected significances in the four bins where $m_{\text{SFOS}} \in [40, 60] \text{ GeV}$ for the ℓ_L mediated simplified model

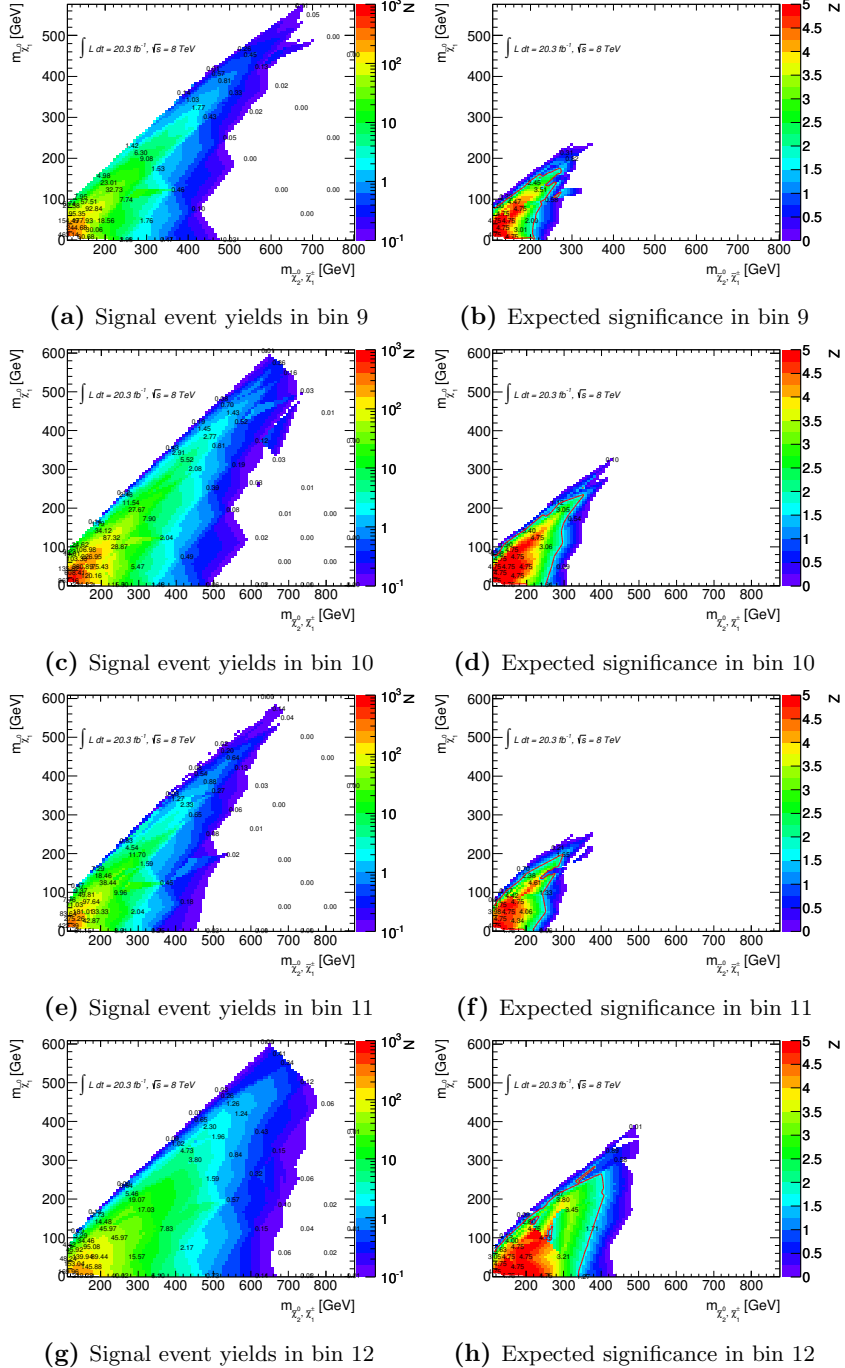


Figure 99: Expected number of signal events and expected significances in the four bins where $m_{\text{SFOS}} \in [60, 81.2]$ GeV for the $\tilde{\ell}_L$ mediated simplified model

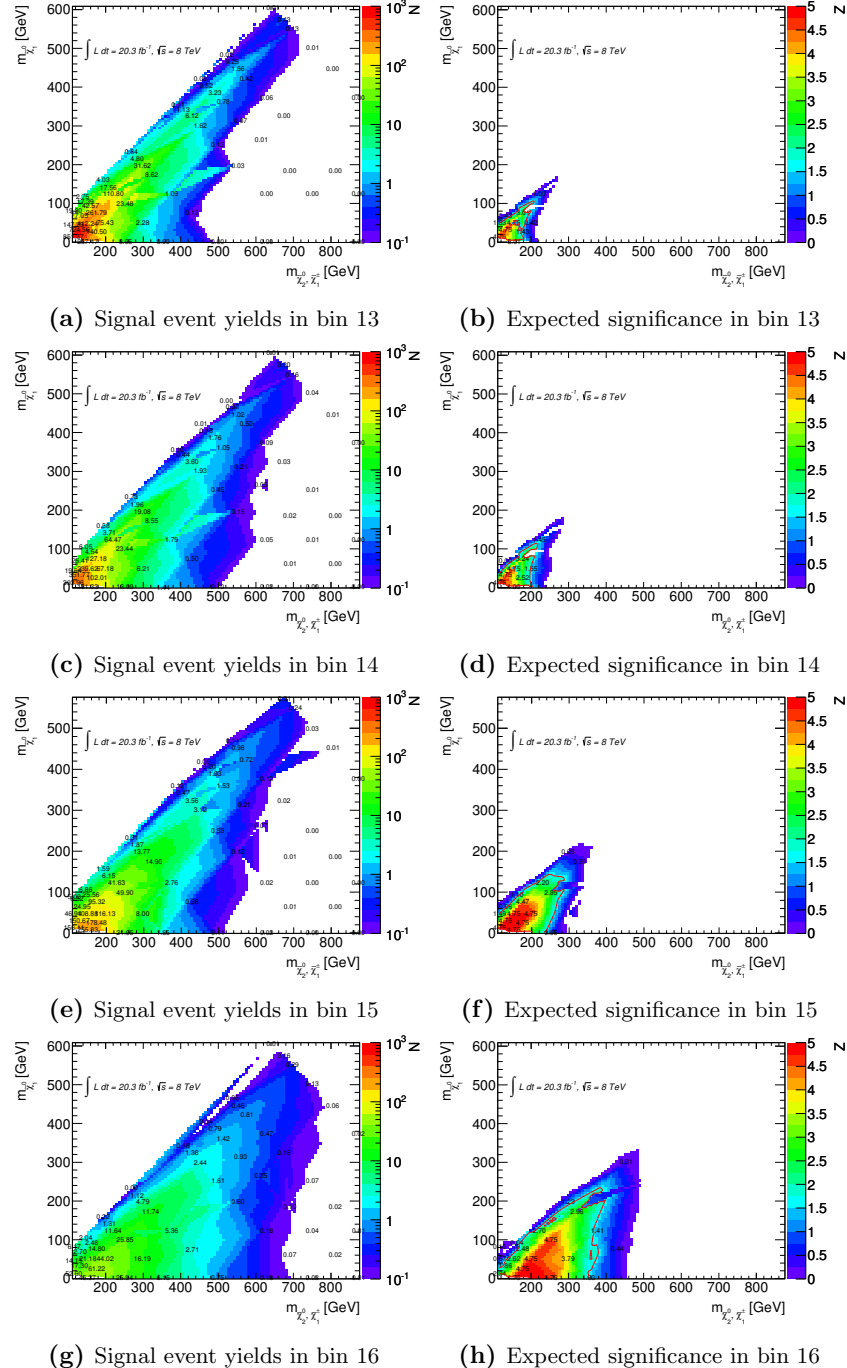


Figure 100: Expected number of signal events and expected significances in the four bins where $m_{\text{SFOS}} \in [81.2, 101.2] \text{ GeV}$ for the ℓ_L mediated simplified model

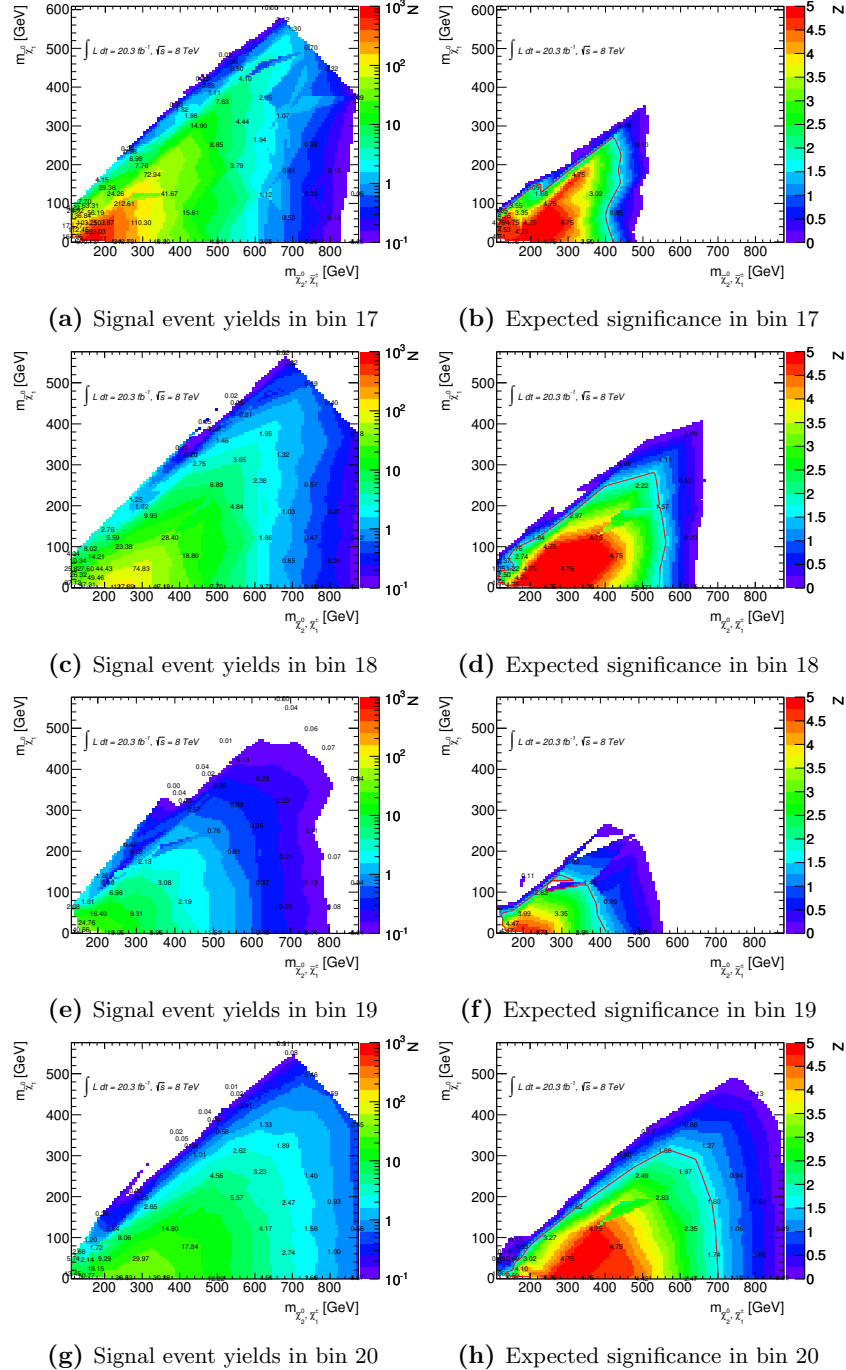


Figure 101: Expected number of signal events and expected significances in the four bins where $m_{\text{SFOS}} \in [101.2, \infty]$ GeV for the ℓ_L mediated simplified model

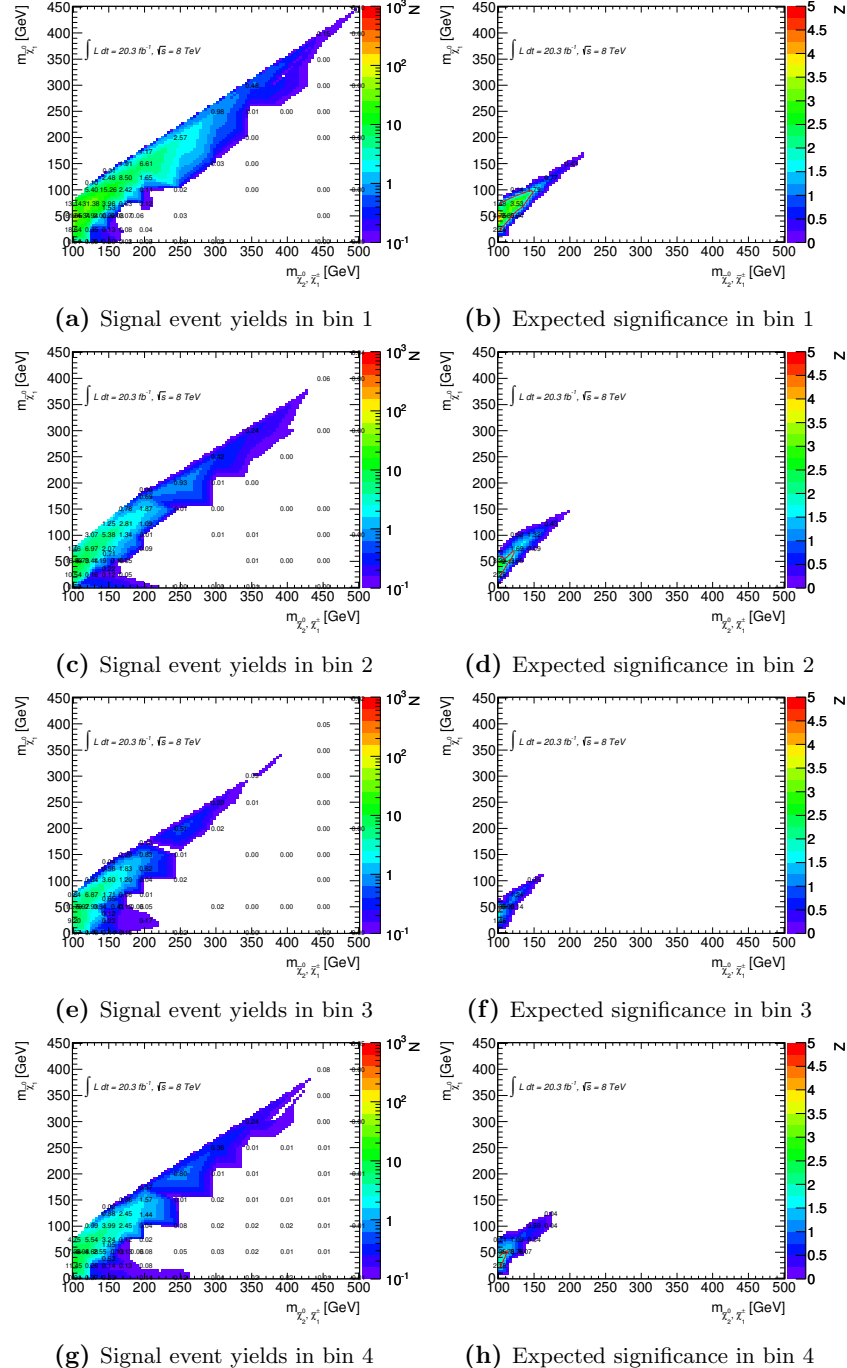


Figure 102: Expected number of signal events and expected significances in the four bins where $m_{\text{SFOS}} \in [12, 40] \text{ GeV}$ for the WZ mediated simplified model

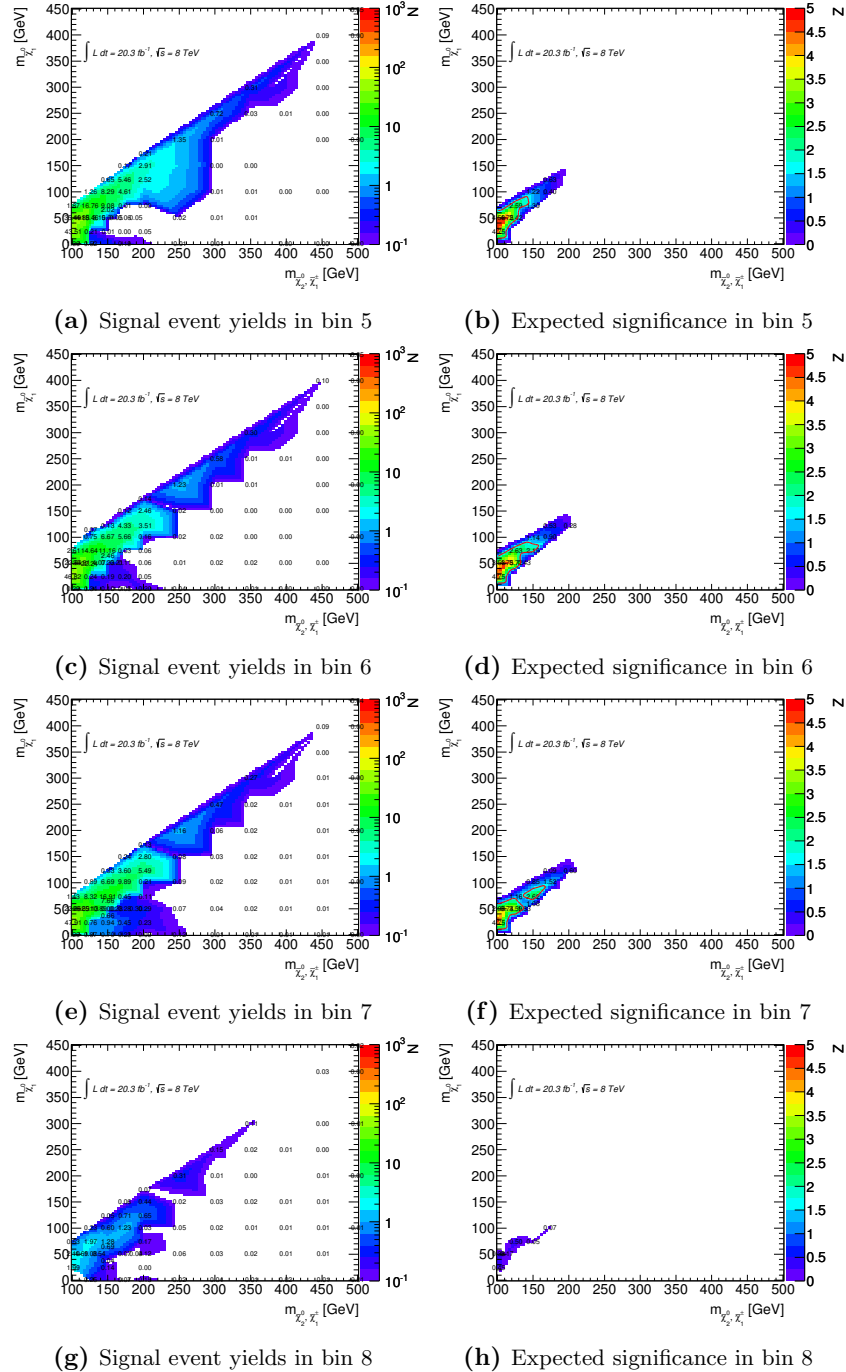


Figure 103: Expected number of signal events and expected significances in the four bins where $m_{\text{SFOS}} \in [40, 60] \text{ GeV}$ for the WZ mediated simplified model

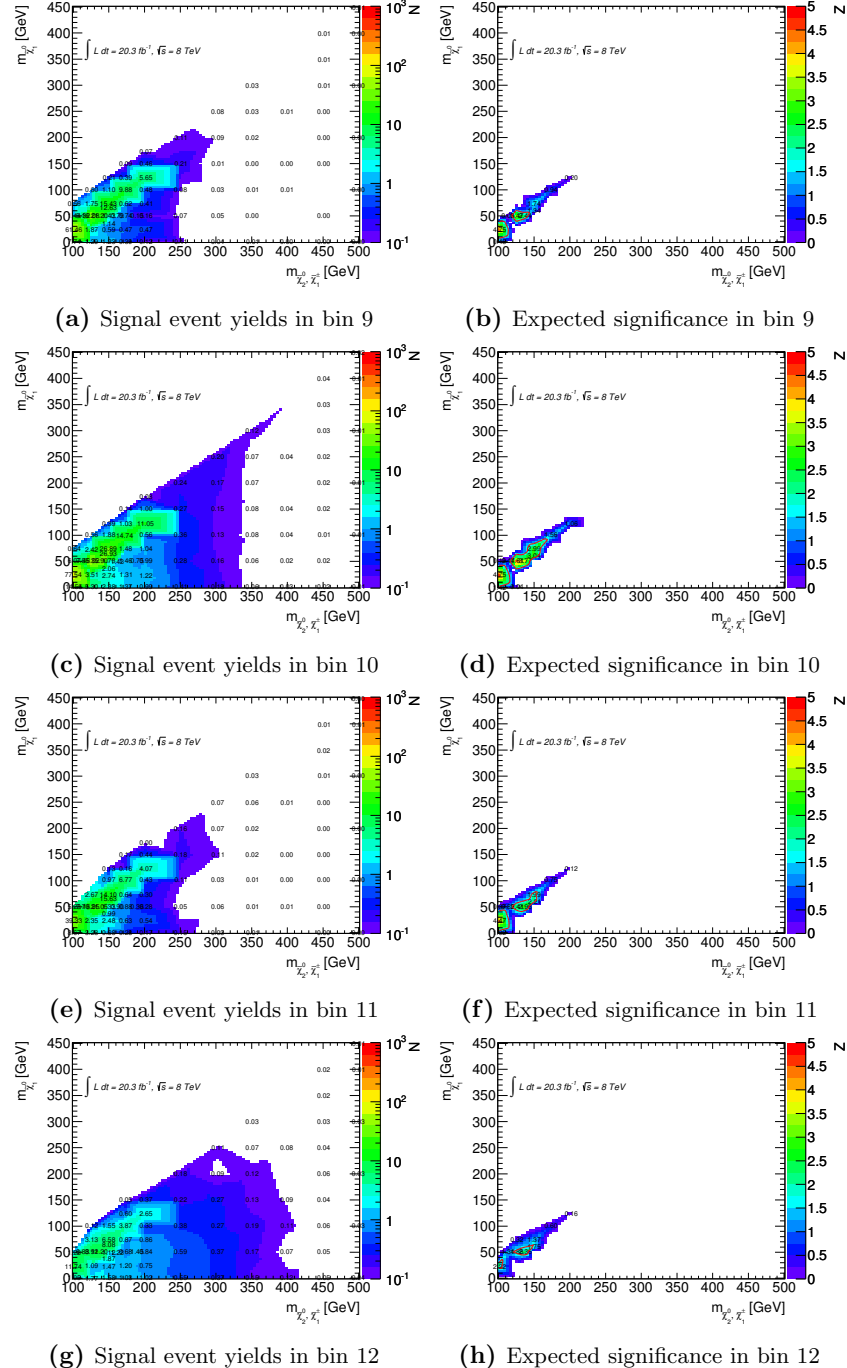


Figure 104: Expected number of signal events and expected significances in the four bins where $m_{\text{SFOS}} \in [60, 81.2]$ GeV for the WZ mediated simplified model

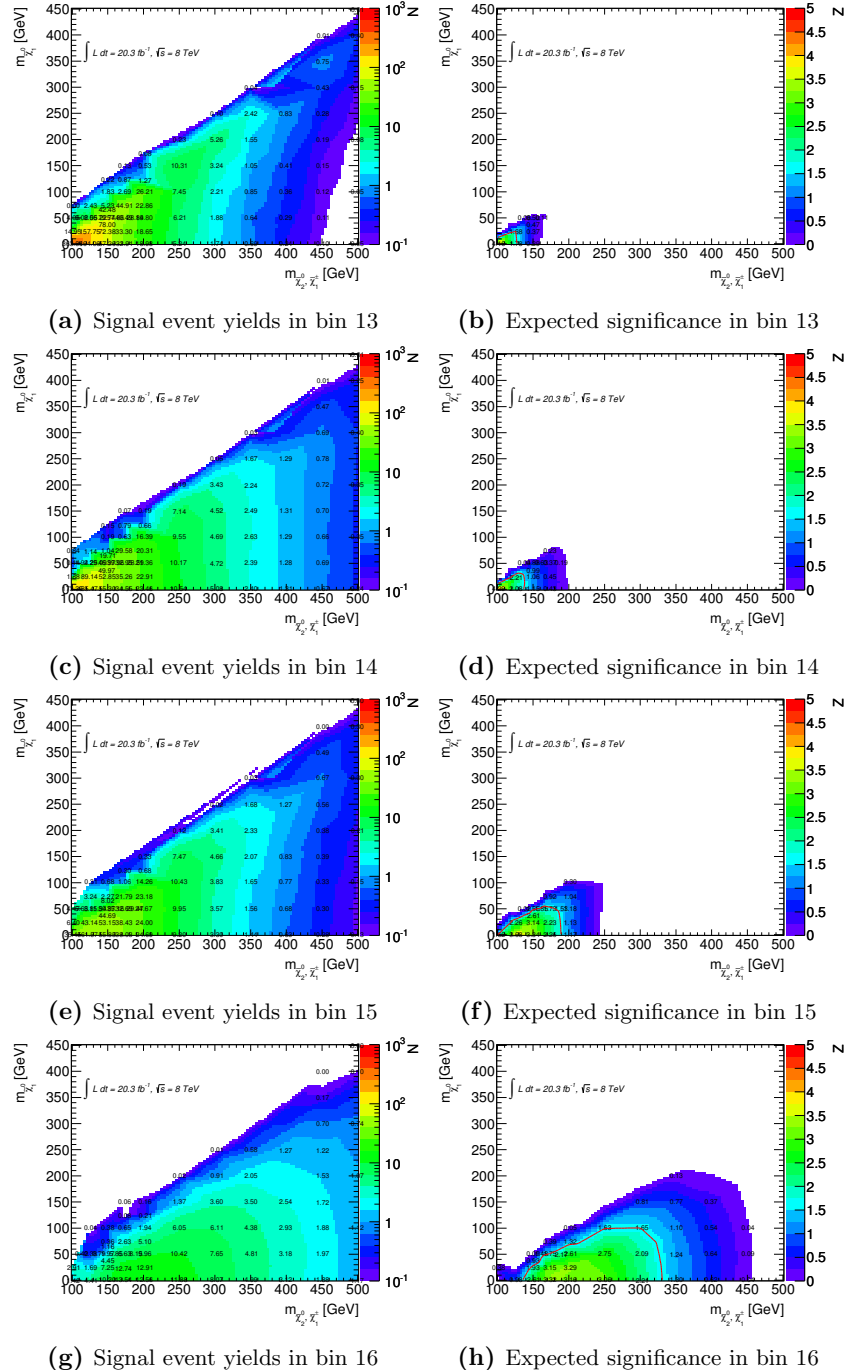


Figure 105: Expected number of signal events and expected significances in the four bins where $m_{\text{SFOS}} \in [81.2, 101.2] \text{ GeV}$ for the WZ mediated simplified model

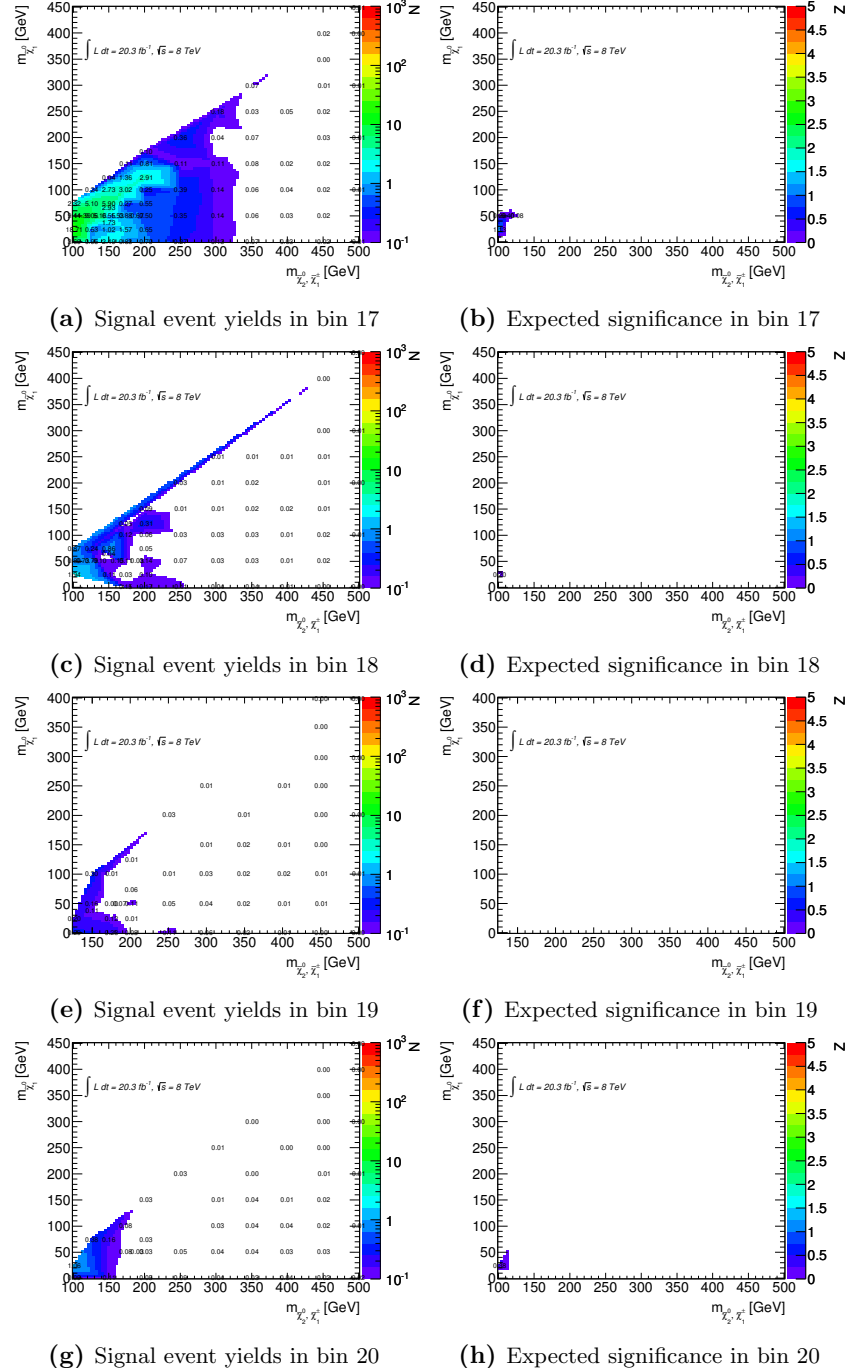


Figure 106: Expected number of signal events and expected significances in the four bins where $m_{\text{SFOS}} \in [101.2, \infty]$ GeV for the WZ mediated simplified model

Appendix B Systematic uncertainties

An overview of the systematic uncertainties is given in Section 5.9. In this appendix, the systematic uncertainties in each bin are graphically represented in Figures 107 - 116. The abbreviations in these figures are:

Total The total uncertainty in each bin (red) and per sample. The different sources of uncertainties are added in quadrature for uncorrelated systematic uncertainties and added linearly for correlated systematics. The cross-section, the PDF and the generator uncertainties are treated as correlated between regions but uncorrelated between background processes. All other uncertainties are treated as correlated between regions and between samples, except the uncertainty from limited Monte Carlo statistics which is not correlated. Due to technical limitations, a systematic uncertainty is always treated as either fully correlated or fully uncorrelated.

MC Stat Monte Carlo statistics

MM Stat Matrix Method statistics

JES Jet energy scale

JER Jet energy resolution

JVF Jet vertex fraction

ESF Electron identification efficiency (electron scale factors)

MEFF Muon identification efficiency

BJET b -tagging

CJET c -tagging

BMISTAGJET l -tagging (b -mistagging)

TauID SF Tau identification efficiency

EES low Electron energy scale for low- p_T electrons

EES mat Electron energy scale due to additional material

EES ps Electron energy scale in presampler

EES Z Electron energy scale due to $Z \rightarrow ee$ measurement

EER Electron energy resolution

MID Muon track resolution in inner detector

MMS Muon track resolution in muon spectrometer

TES Tau energy scale

Scale ST E_T^{miss} energy scale

Reso ST E_T^{miss} energy resolution

Lumi Luminosity

MM elec eff Matrix Method electron real efficiency

MM muon eff Matrix Method muon real efficiency

MM tau eff Matrix Method tau real efficiency

MM elec fr Matrix Method electron fake rate

MM muon fr Matrix Method muon fake rate

MM tau fr Matrix Method tau fake rate

TIDSF Tau identification scale factor

TES Tau scale factor

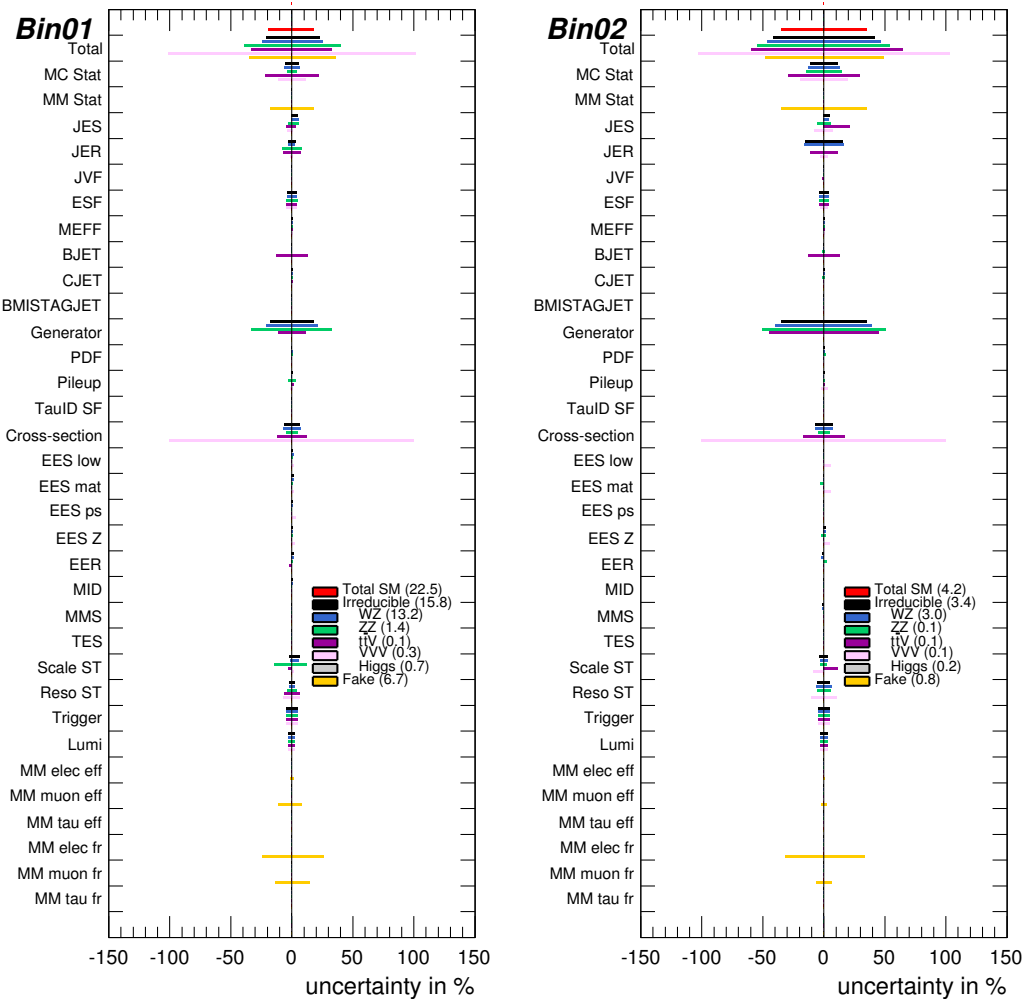


Figure 107: Systematic uncertainties in bin 1 and 2 of the signal region. The abbreviations are given in the text.

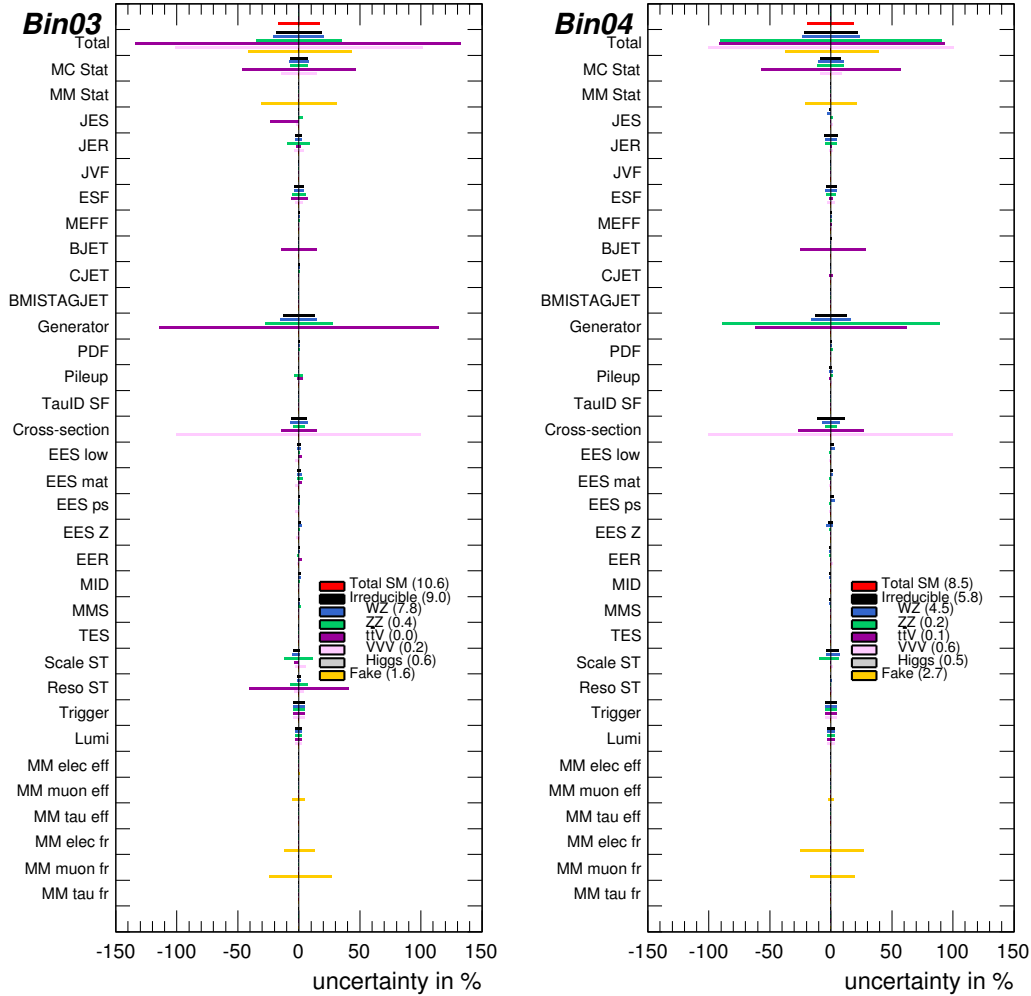


Figure 108: Systematic uncertainties in bin 3 and 4 of the signal region. The abbreviations are given in the text.

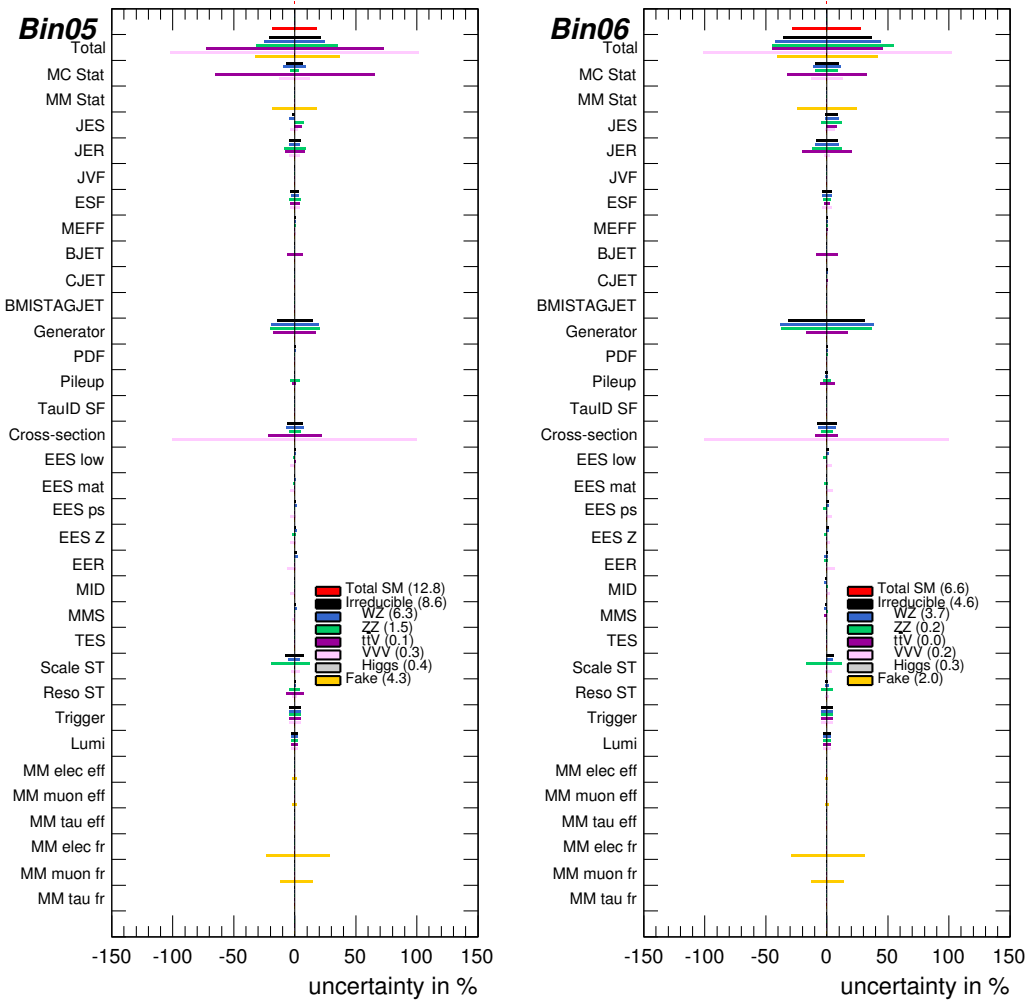


Figure 109: Systematic uncertainties in bin 5 and 6 of the signal region. The abbreviations are given in the text.

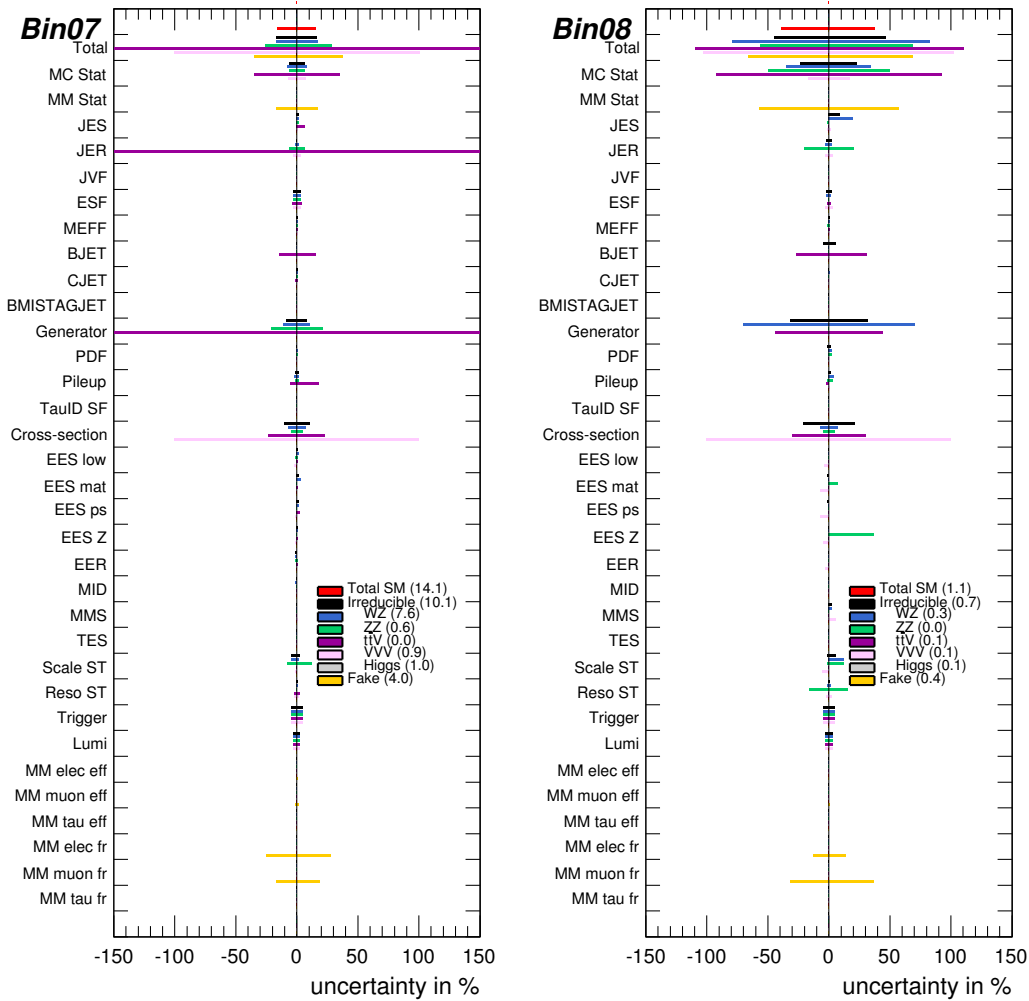


Figure 110: Systematic uncertainties in bin 7 and 8 of the signal region. The abbreviations are given in the text.

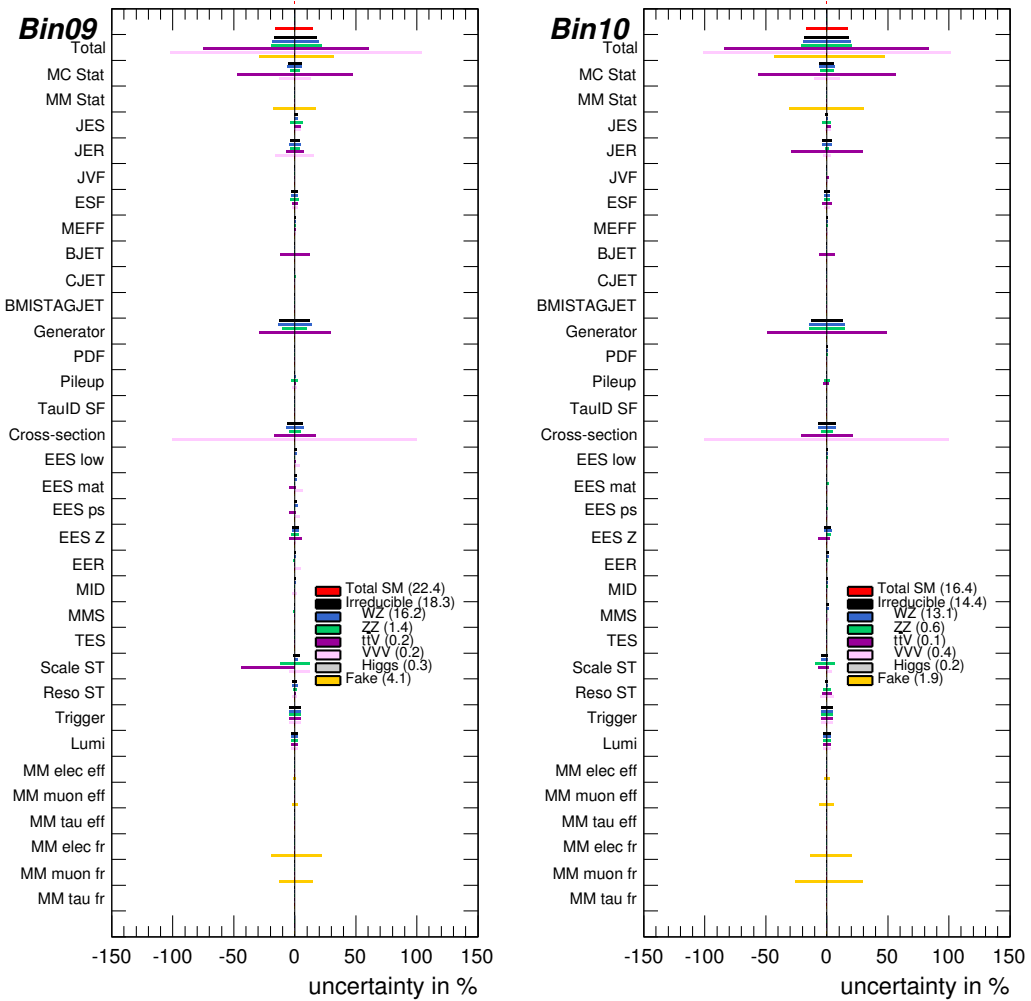


Figure 111: Systematic uncertainties in bin 9 and 10 of the signal region. The abbreviations are given in the text.

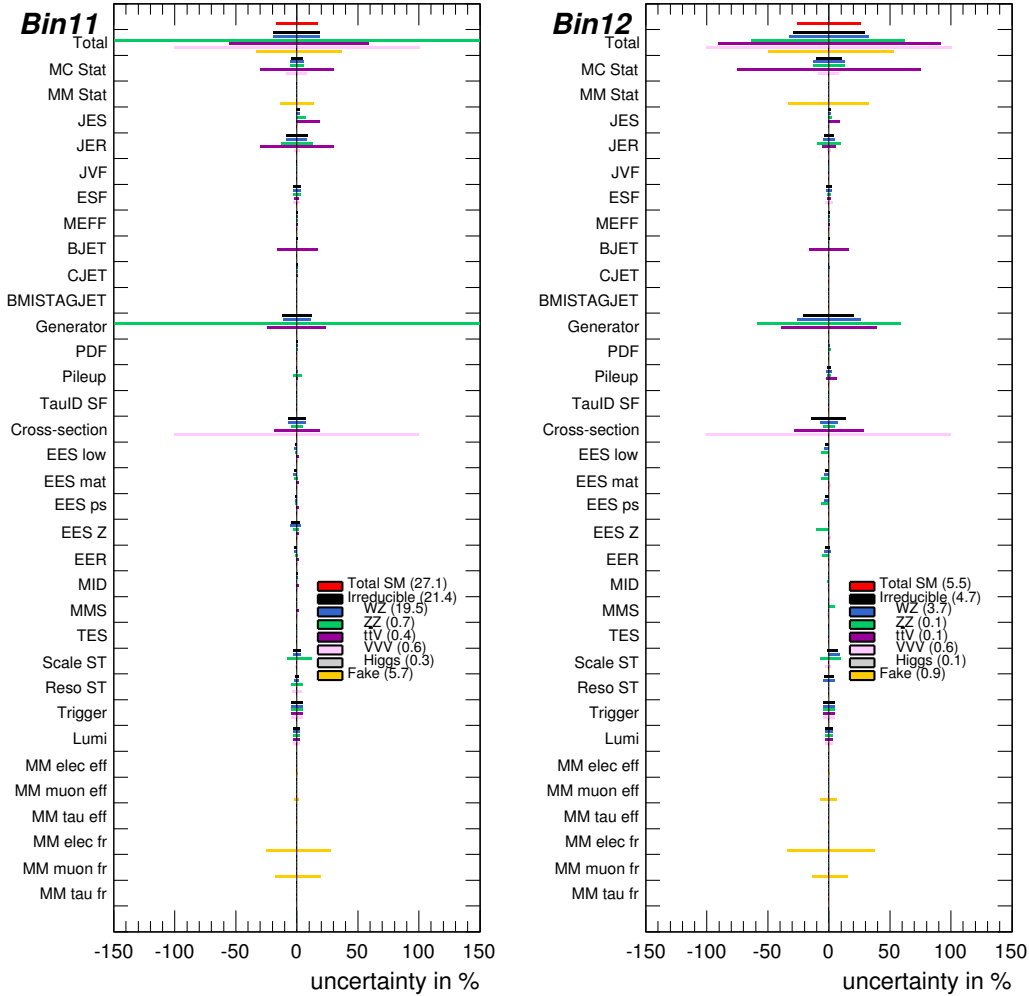


Figure 112: Systematic uncertainties in bin 11 and 12 of the signal region. The abbreviations are given in the text.

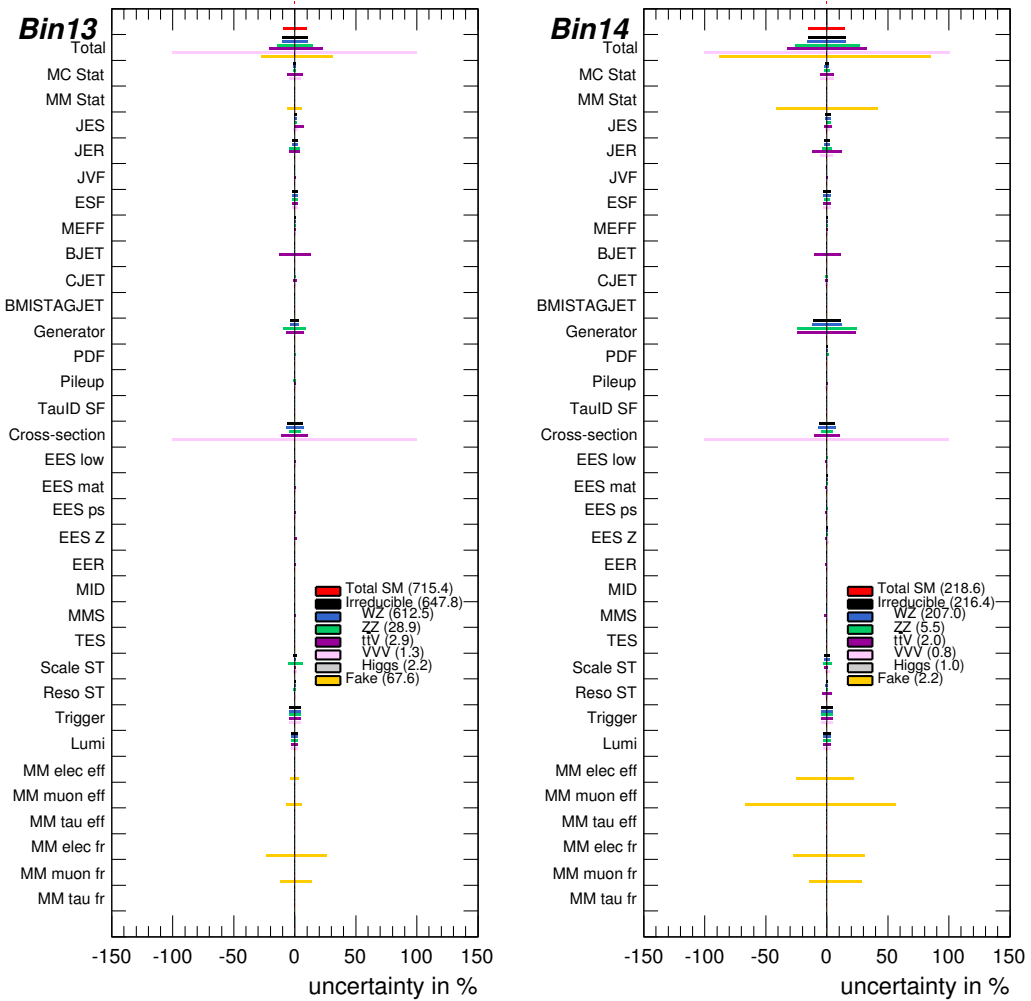


Figure 113: Systematic uncertainties in bin 13 and 14 of the signal region. The abbreviations are given in the text.

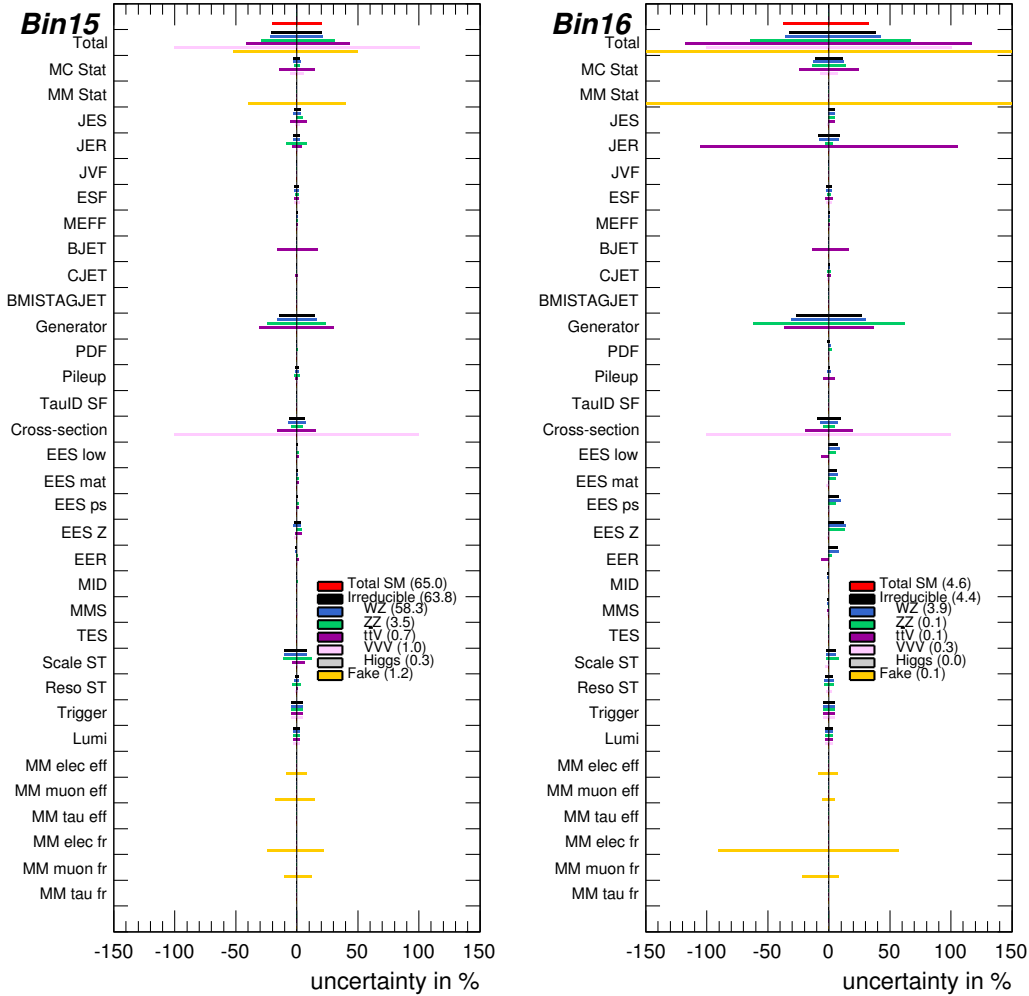


Figure 114: Systematic uncertainties in bin 15 and 16 of the signal region. The abbreviations are given in the text.

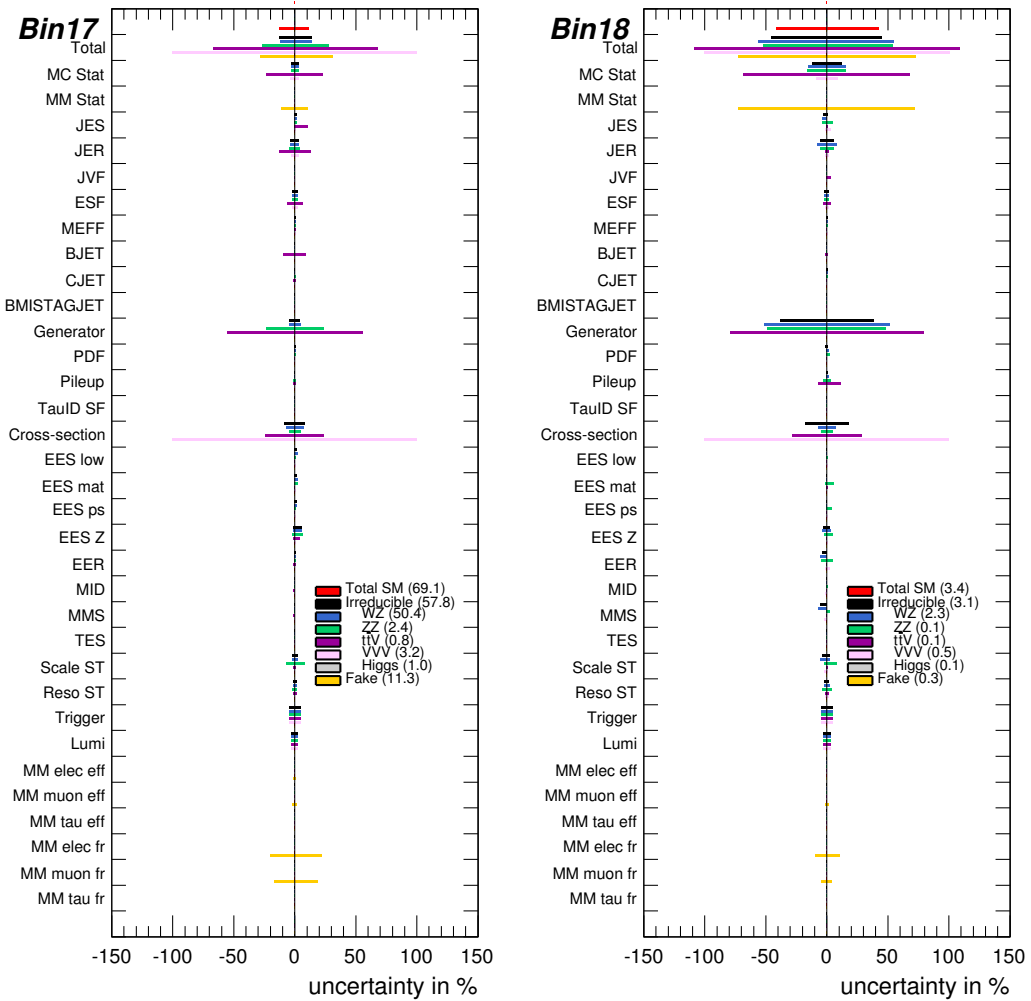


Figure 115: Systematic uncertainties in bin 17 and 18 of the signal region. The abbreviations are given in the text.

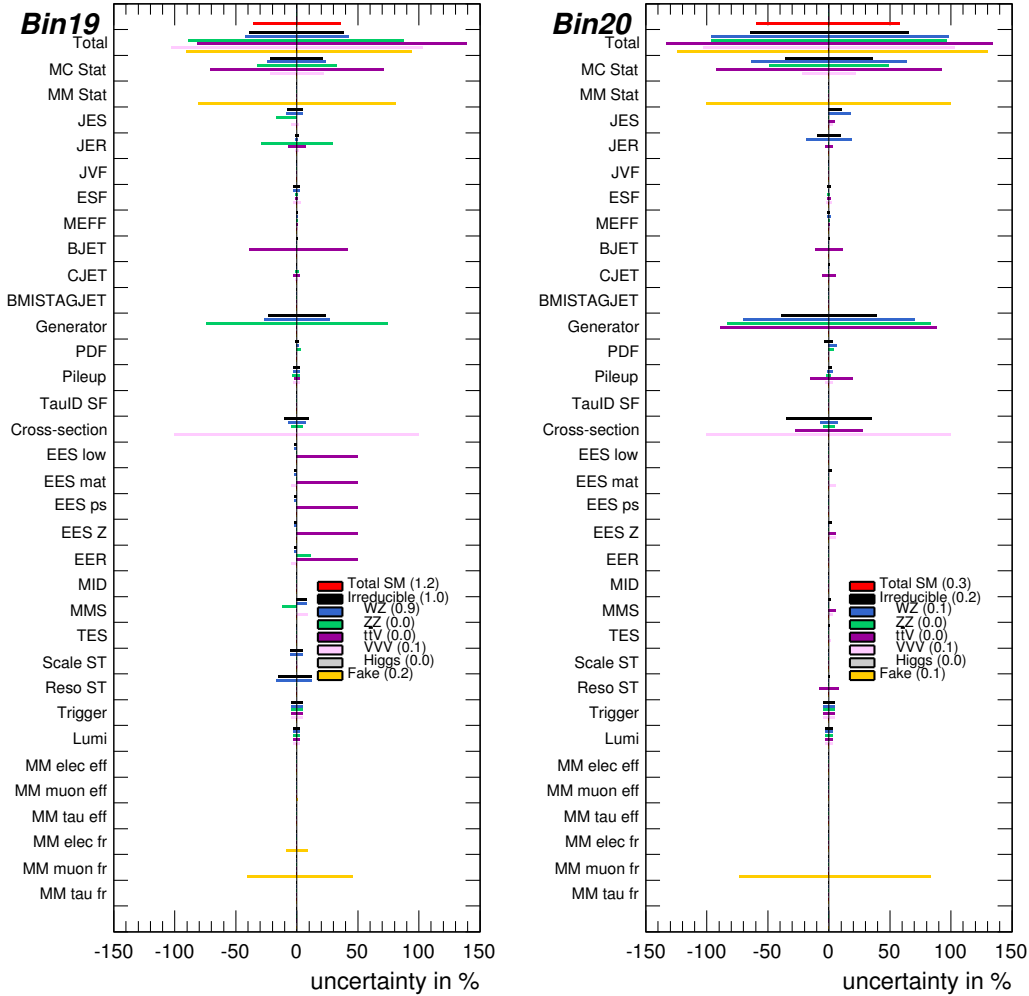


Figure 116: Systematic uncertainties in bin 19 and 20 of the signal region. The abbreviations are given in the text.

Appendix C Distributions in VR0 τ b-binned

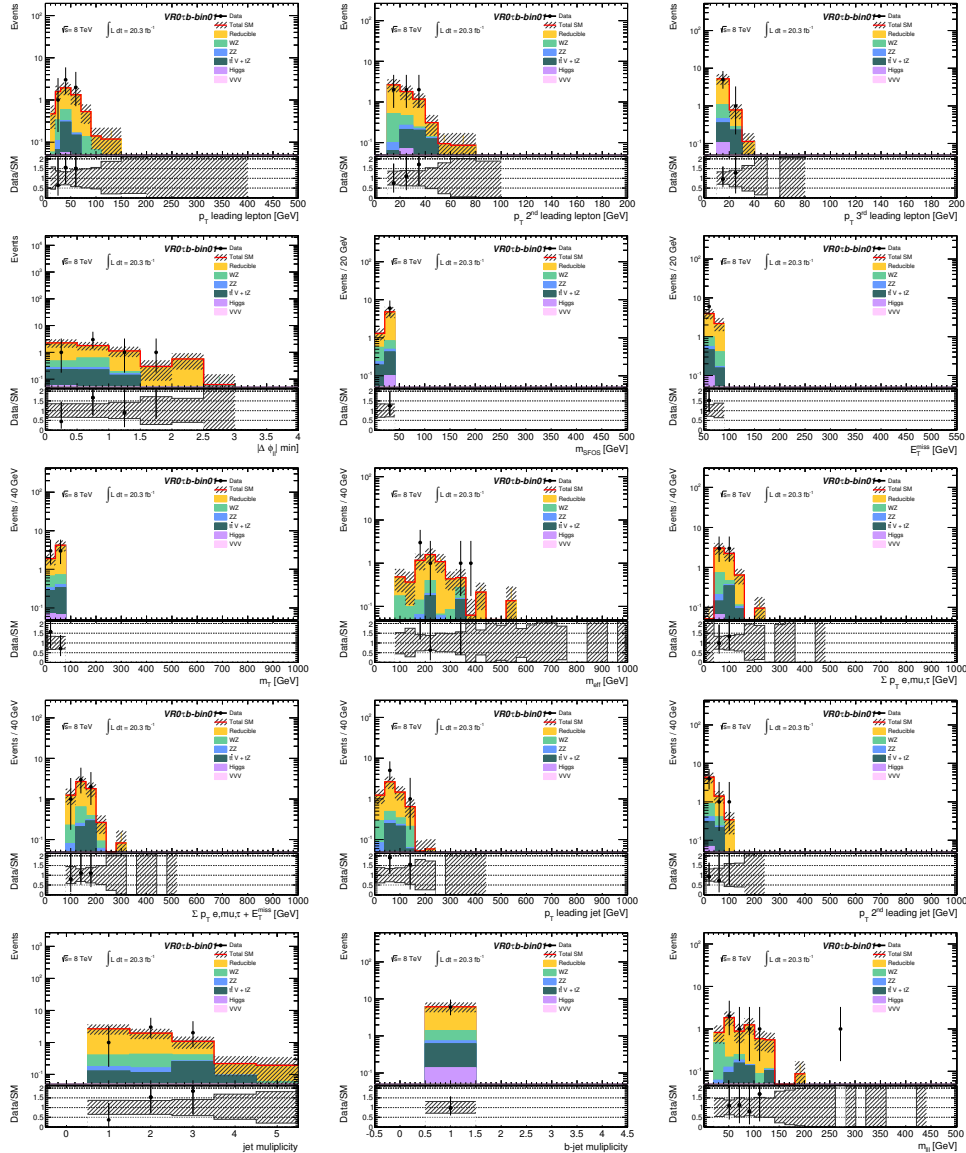


Figure 117: Distributions in VR0 τ b-bin1. The uncertainties are statistical and systematic.

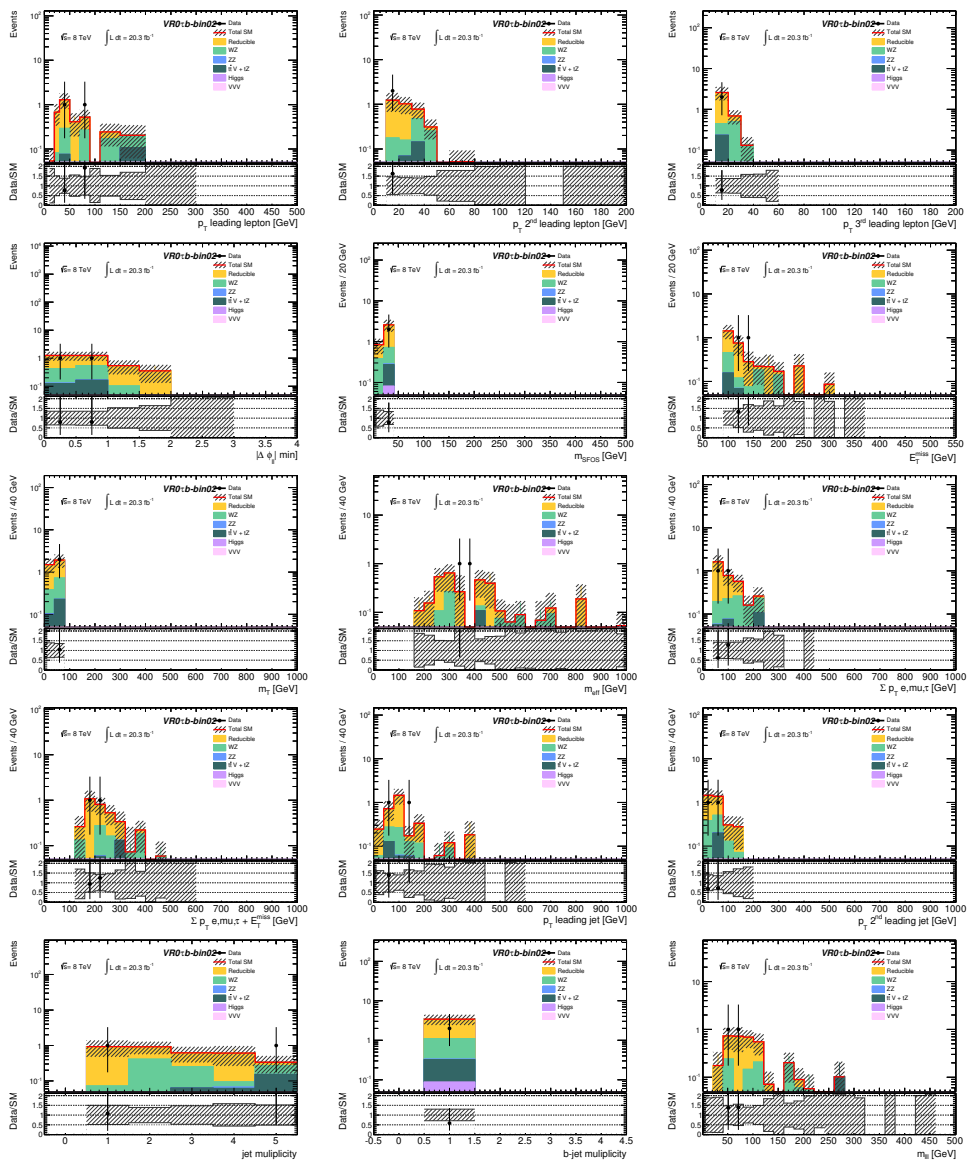


Figure 118: Distributions in VR0 τ b-bin2. The uncertainties are statistical and systematic.

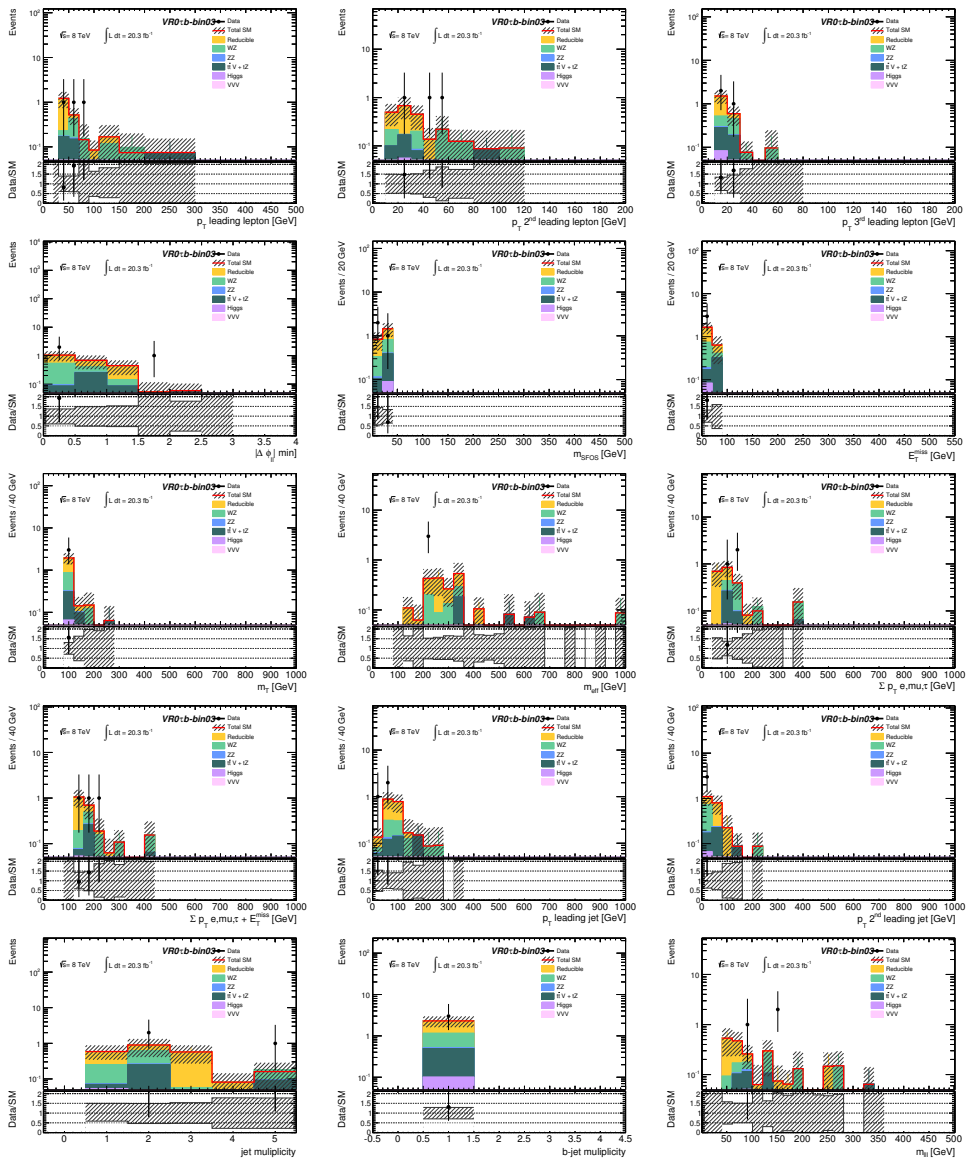


Figure 119: Distributions in VR0 τ b-bin3. The uncertainties are statistical and systematic.

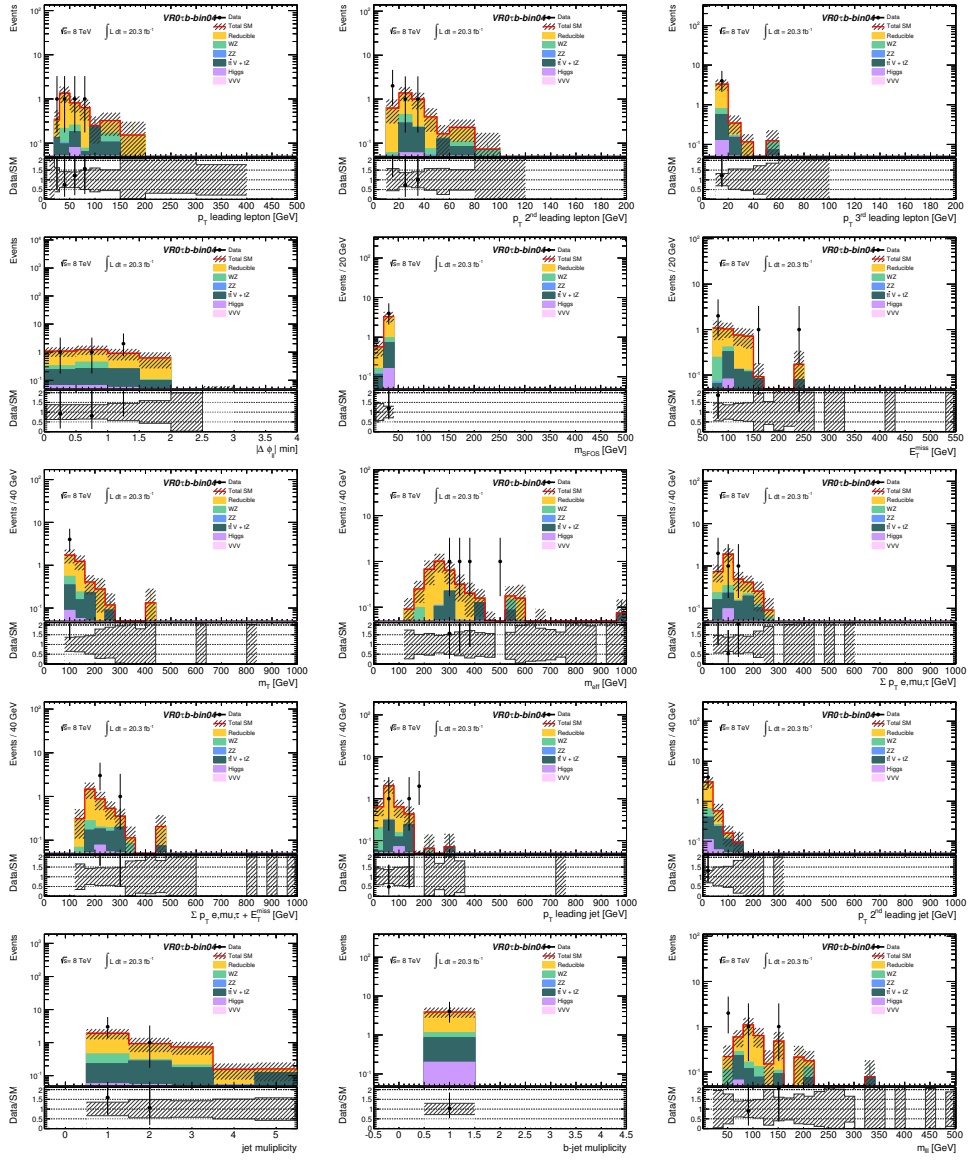


Figure 120: Distributions in VR0 τ b-bin4. The uncertainties are statistical and systematic.

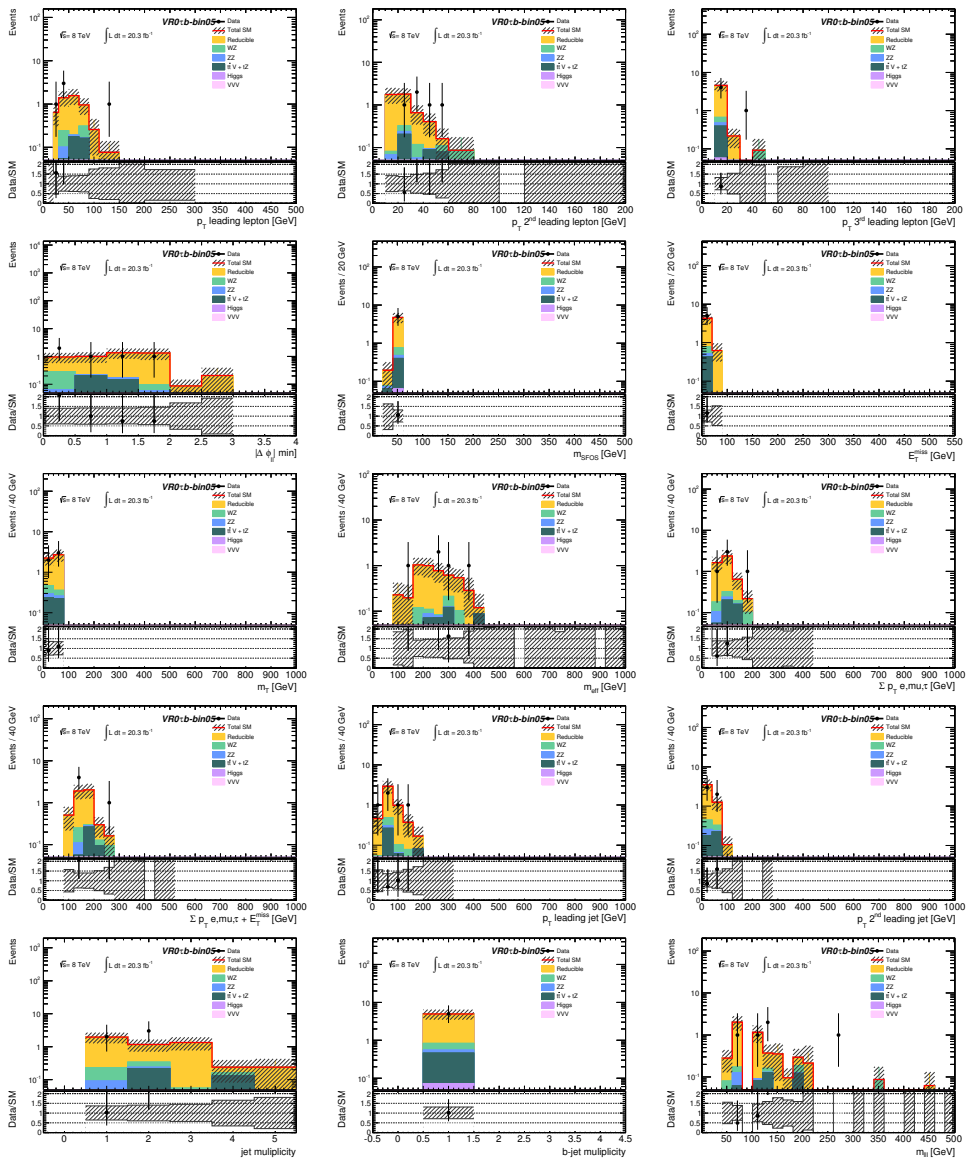


Figure 121: Distributions in VR0 τ b-bin5. The uncertainties are statistical and systematic.

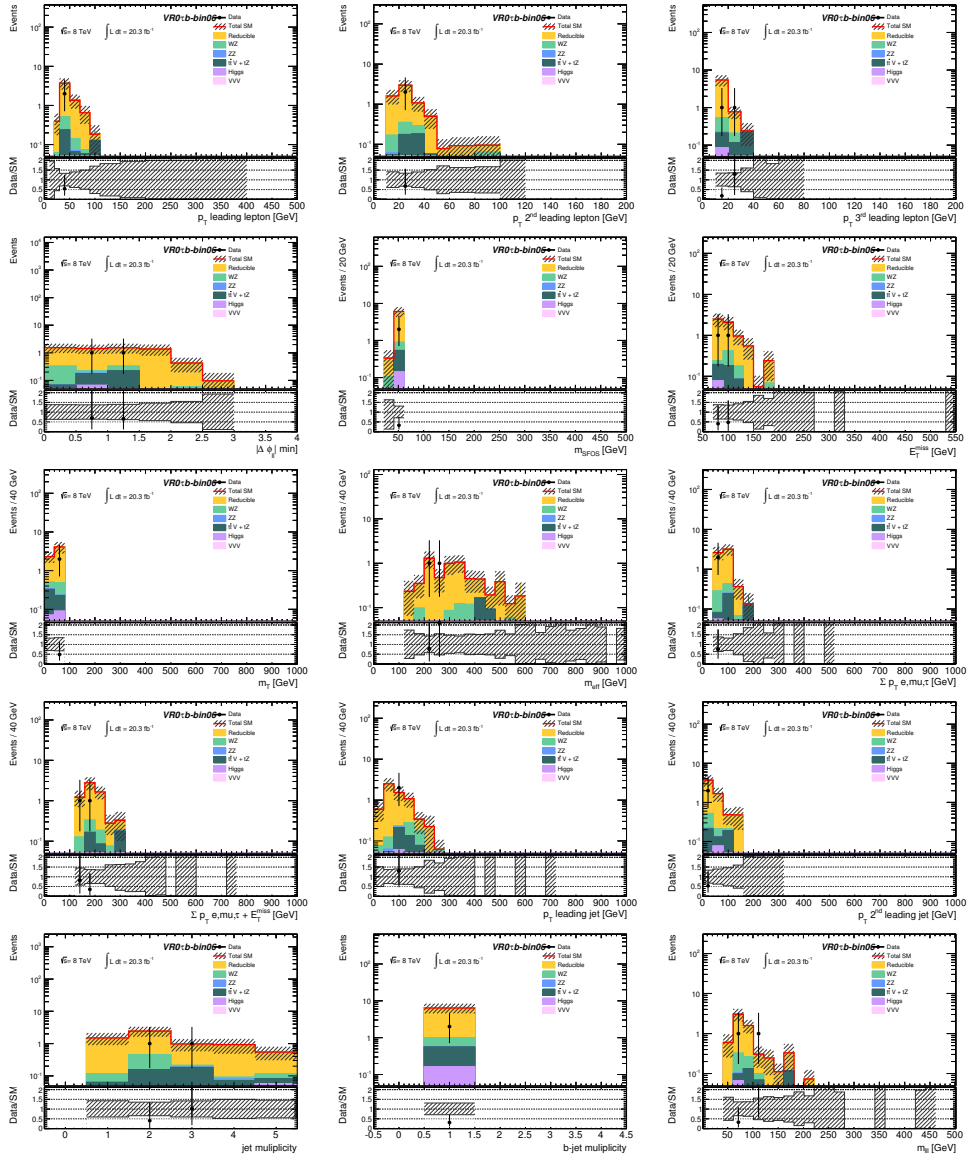


Figure 122: Distributions in VR0 τ b-bin6. The uncertainties are statistical and systematic.

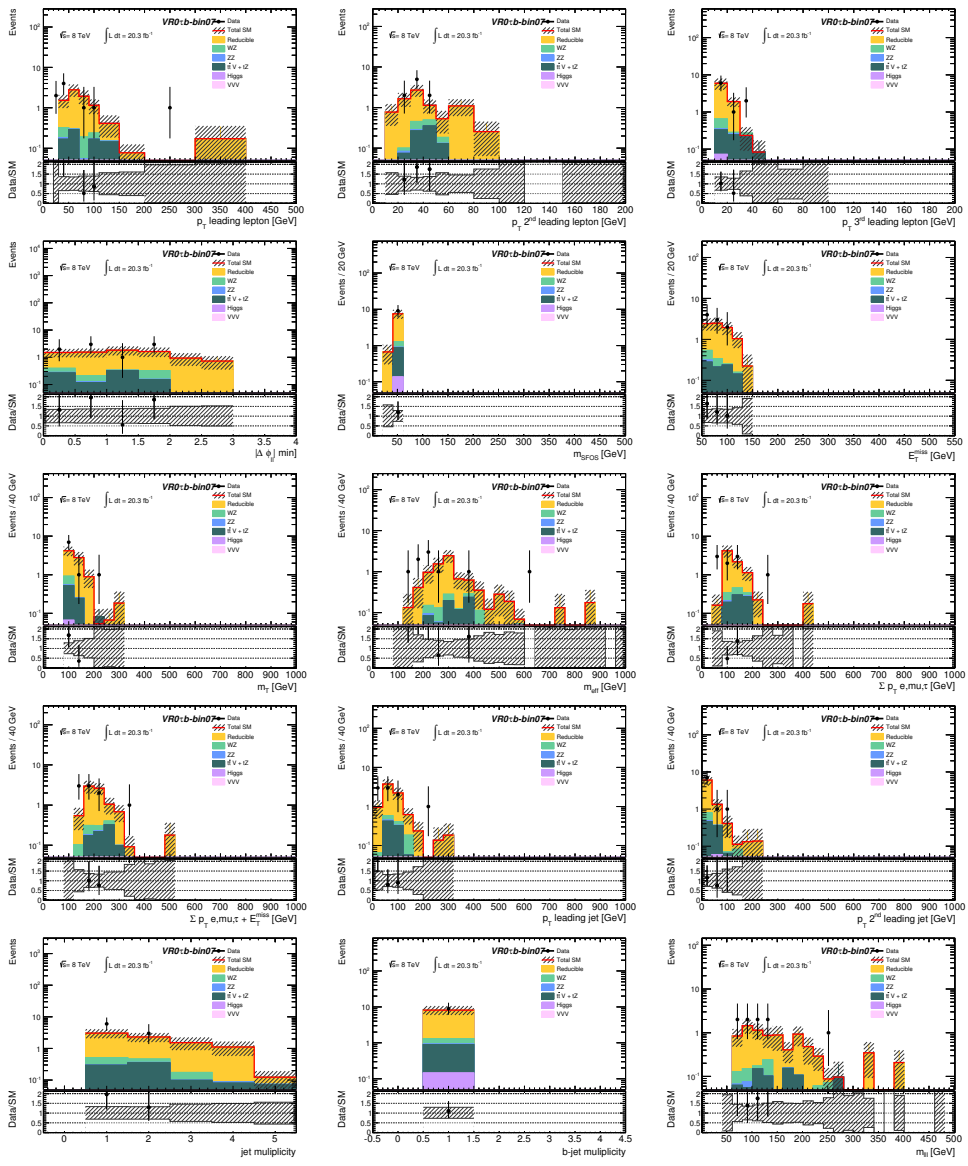


Figure 123: Distributions in VR0 τ b-bin7. The uncertainties are statistical and systematic.

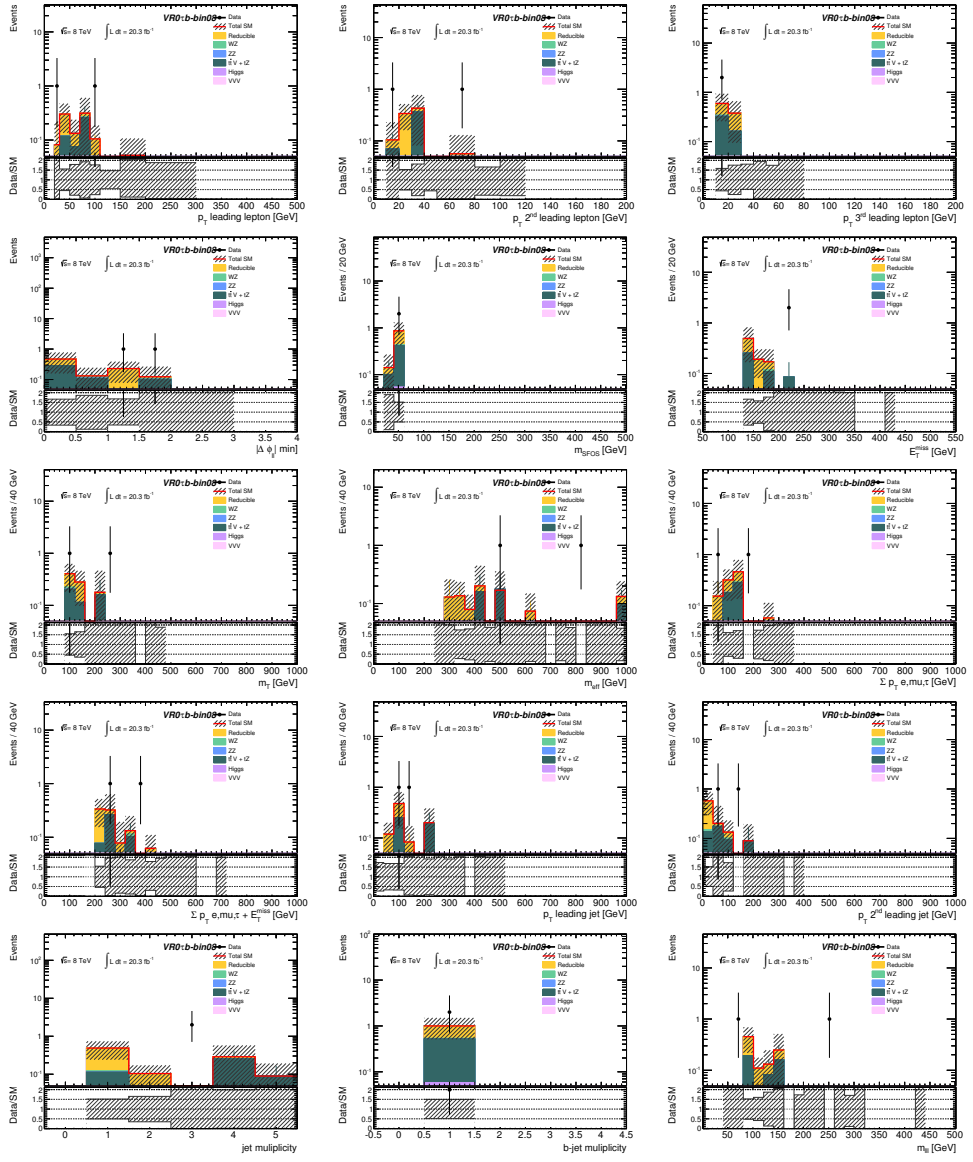


Figure 124: Distributions in VR0 τ b-bin8. The uncertainties are statistical and systematic.

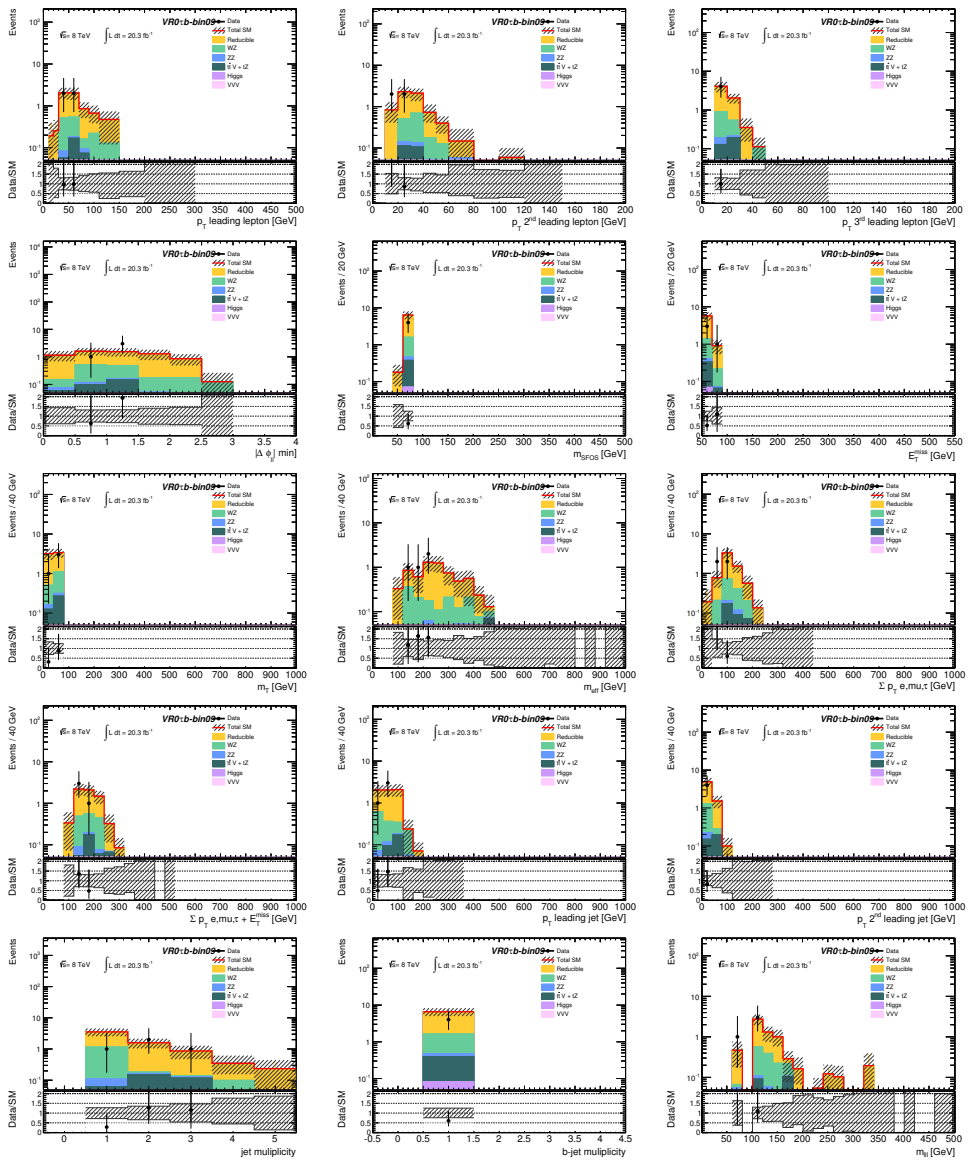


Figure 125: Distributions in VR0 τ b-bin9. The uncertainties are statistical and systematic.

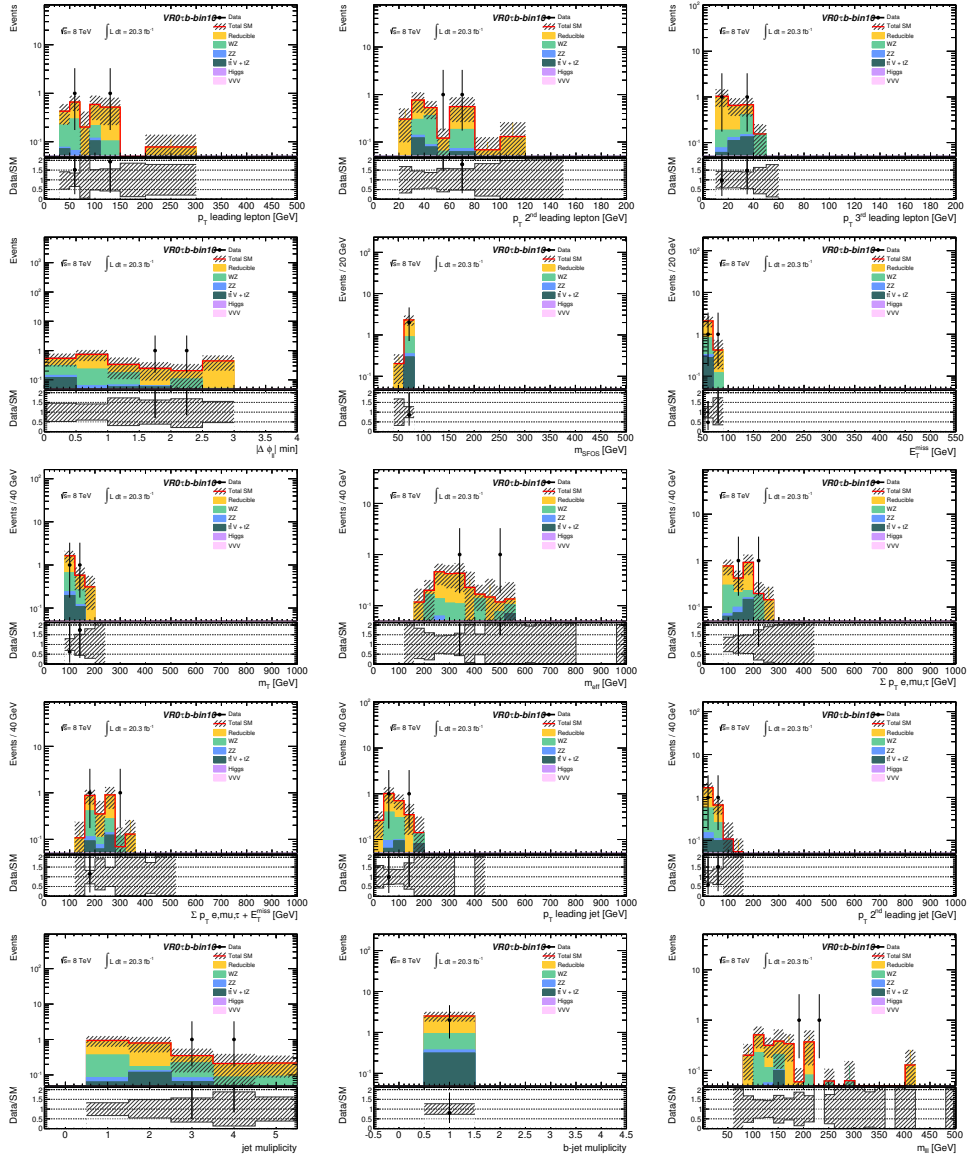


Figure 126: Distributions in VR0 τ -bin10. The uncertainties are statistical and systematic.

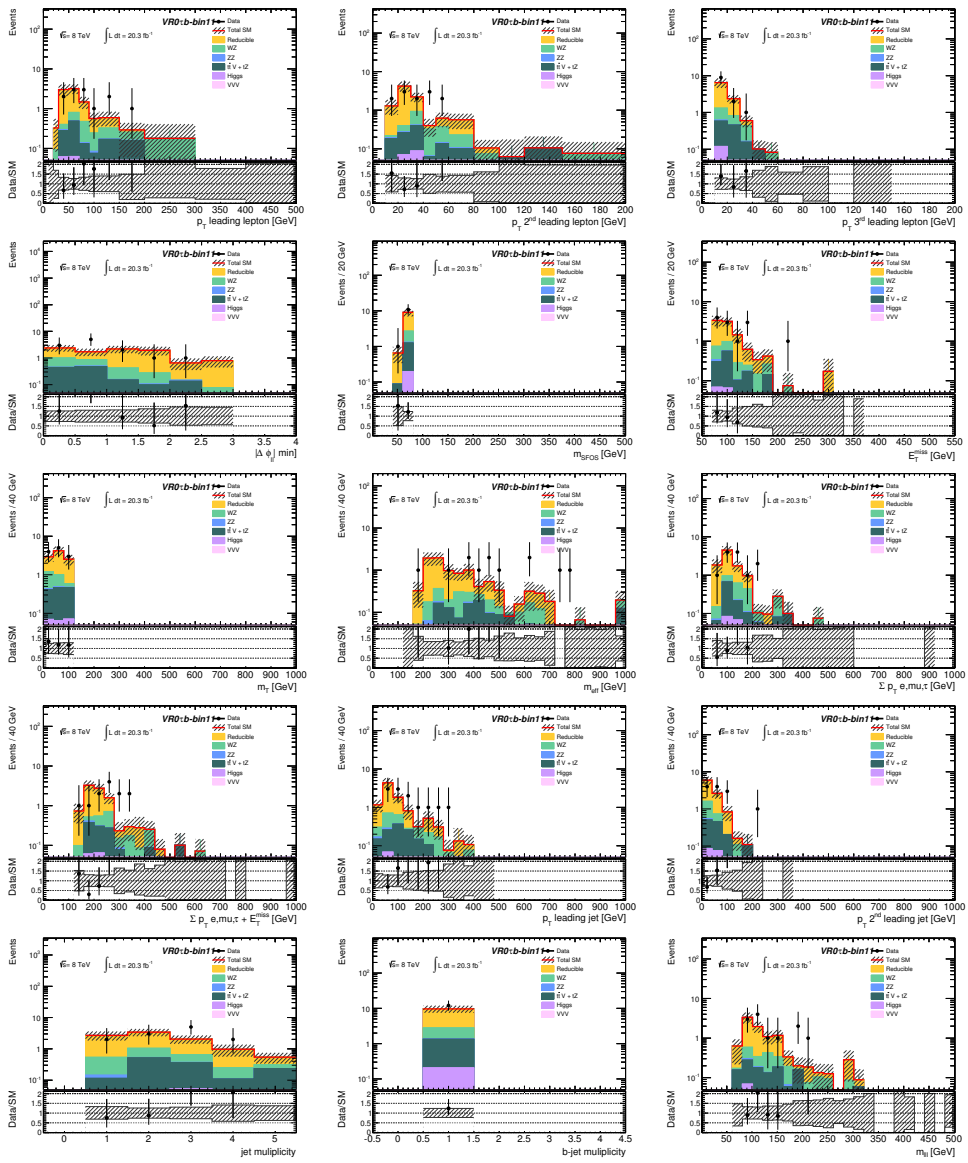


Figure 127: Distributions in VR0 τ -bin11. The uncertainties are statistical and systematic.

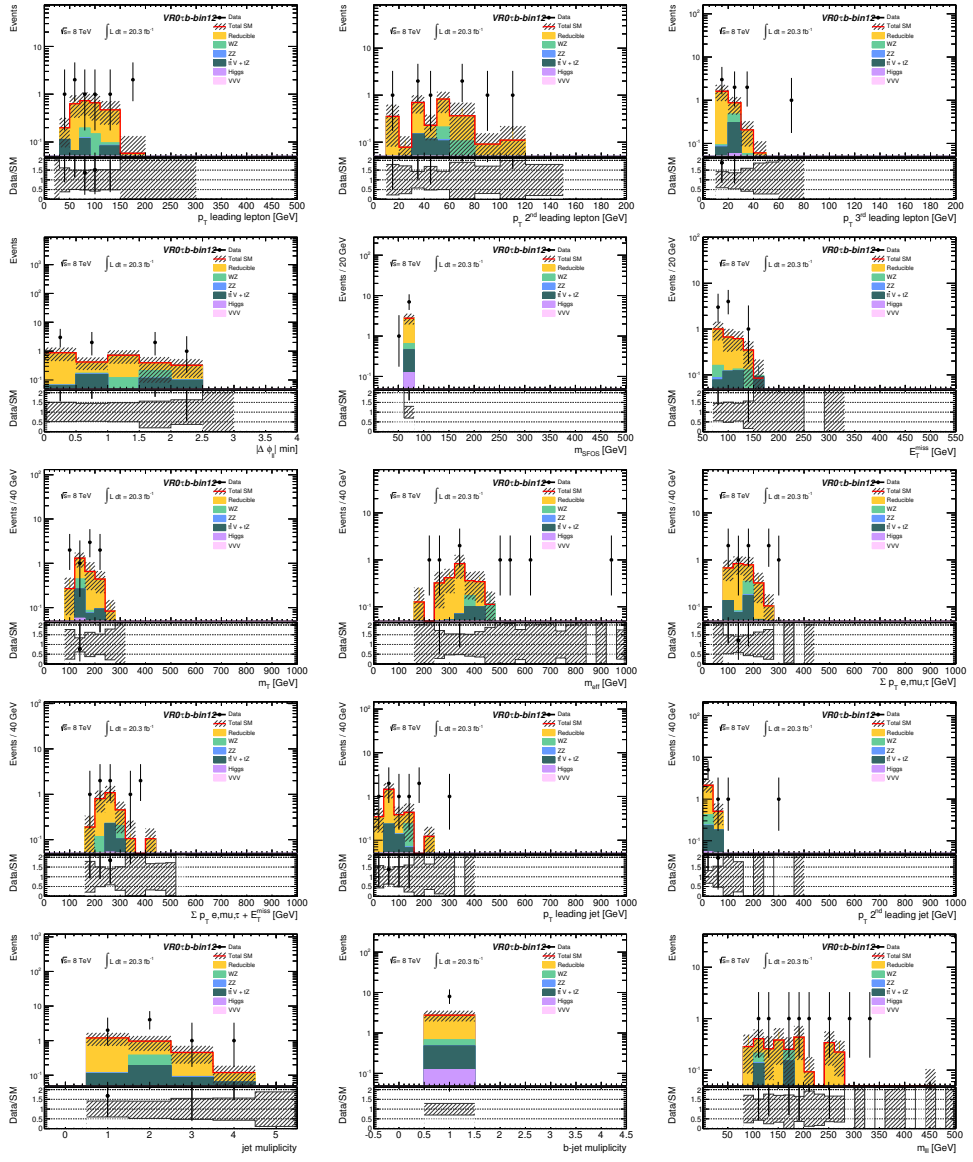


Figure 128: Distributions in VR0 τ b-bin12. The uncertainties are statistical and systematic.

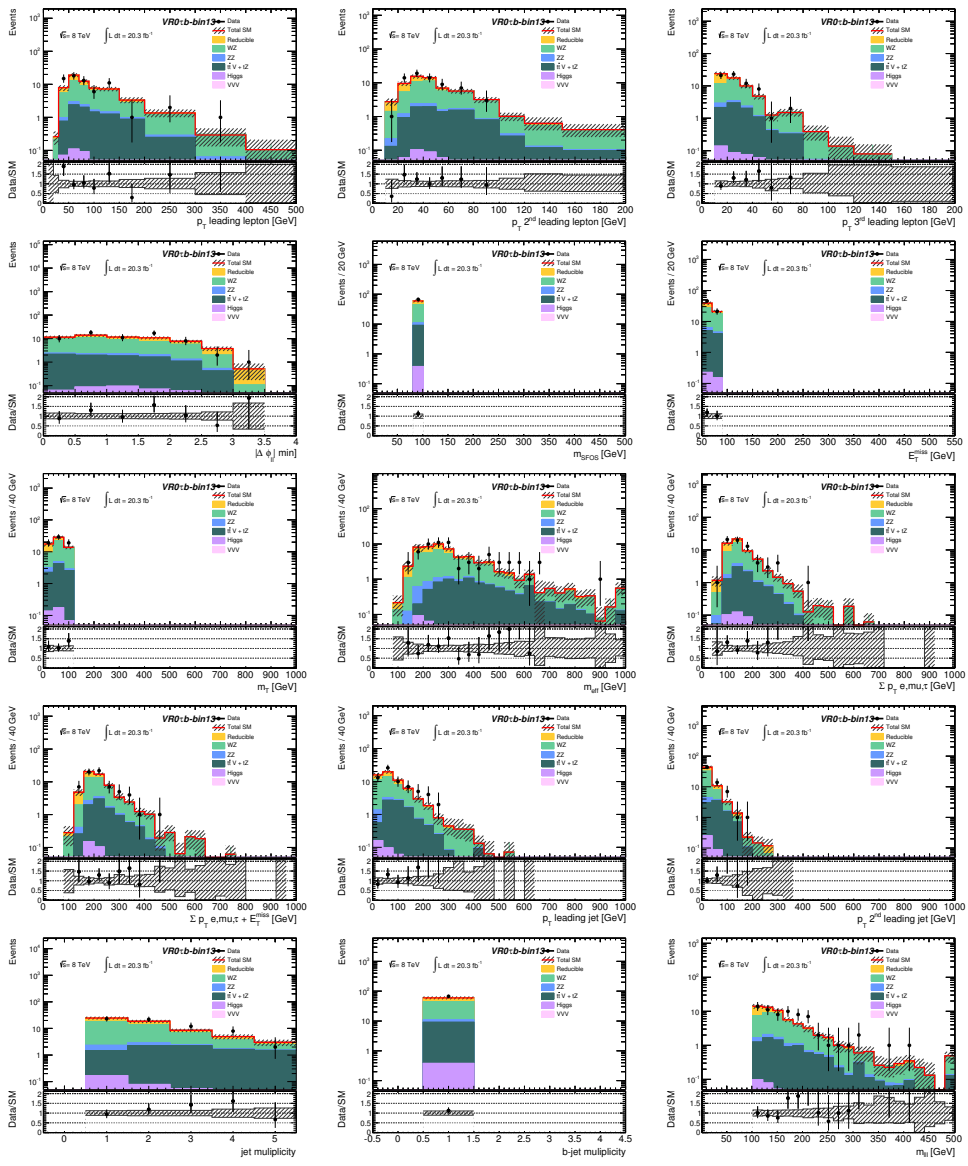


Figure 129: Distributions in VR0 τ -bin13. The uncertainties are statistical and systematic.

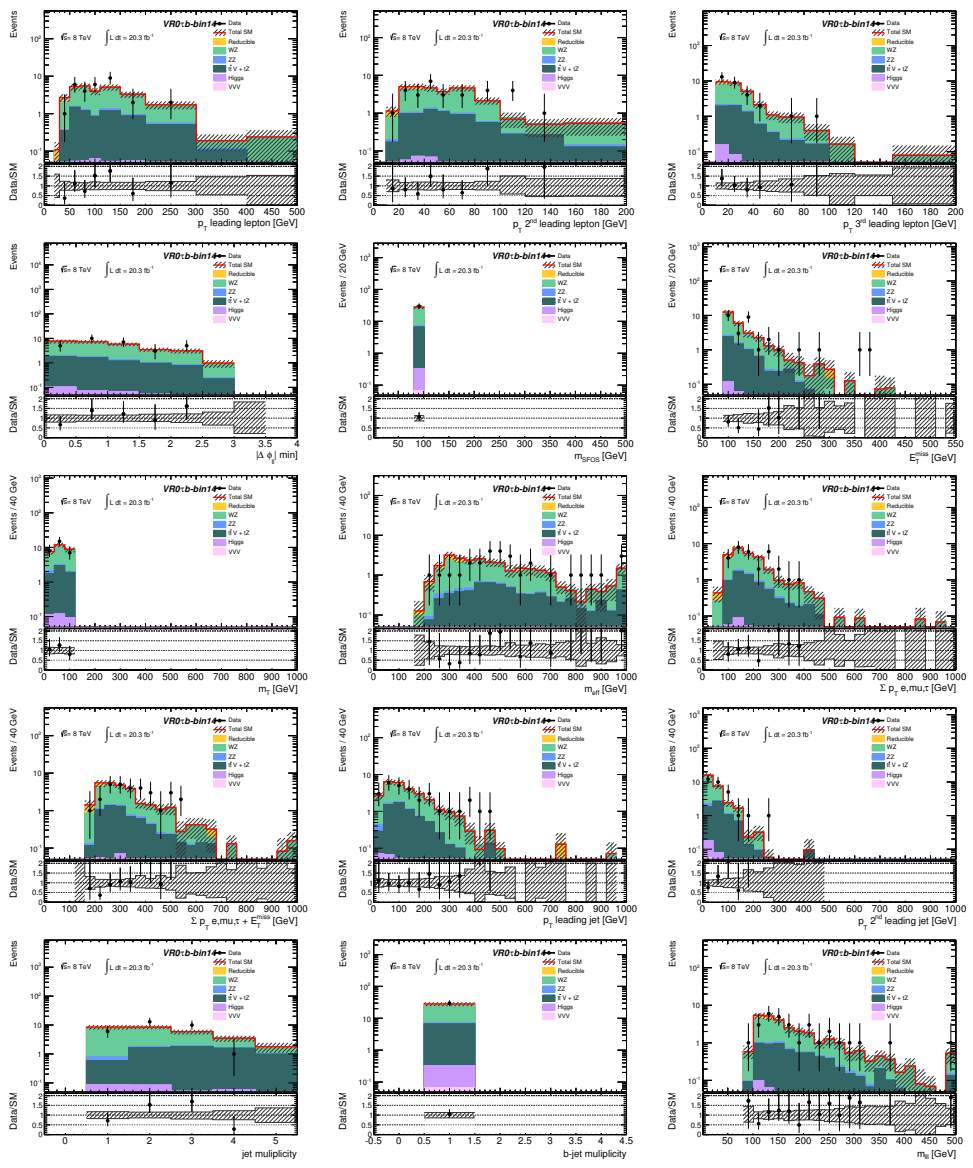


Figure 130: Distributions in VR0 τ -bin14. The uncertainties are statistical and systematic.

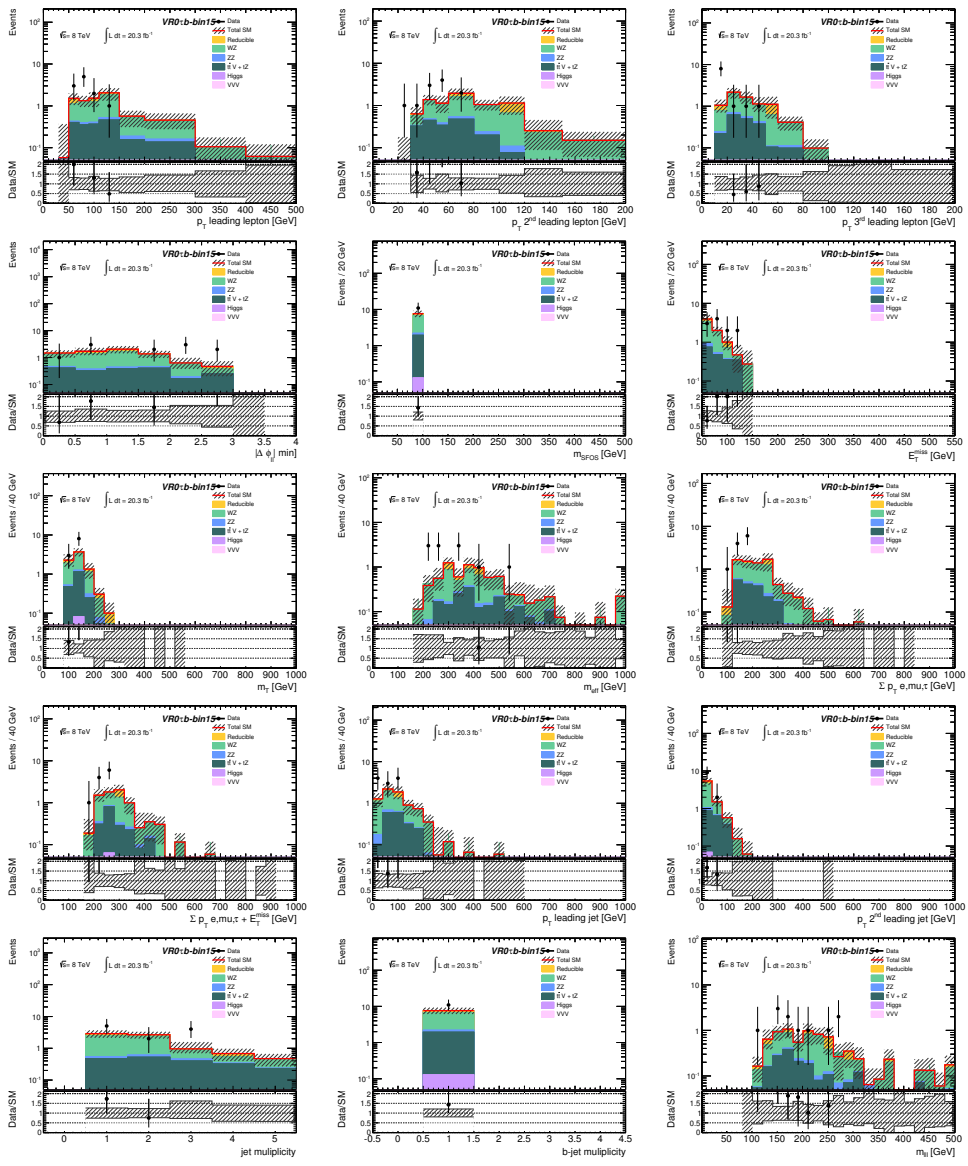


Figure 131: Distributions in VR0 τ -bin15. The uncertainties are statistical and systematic.

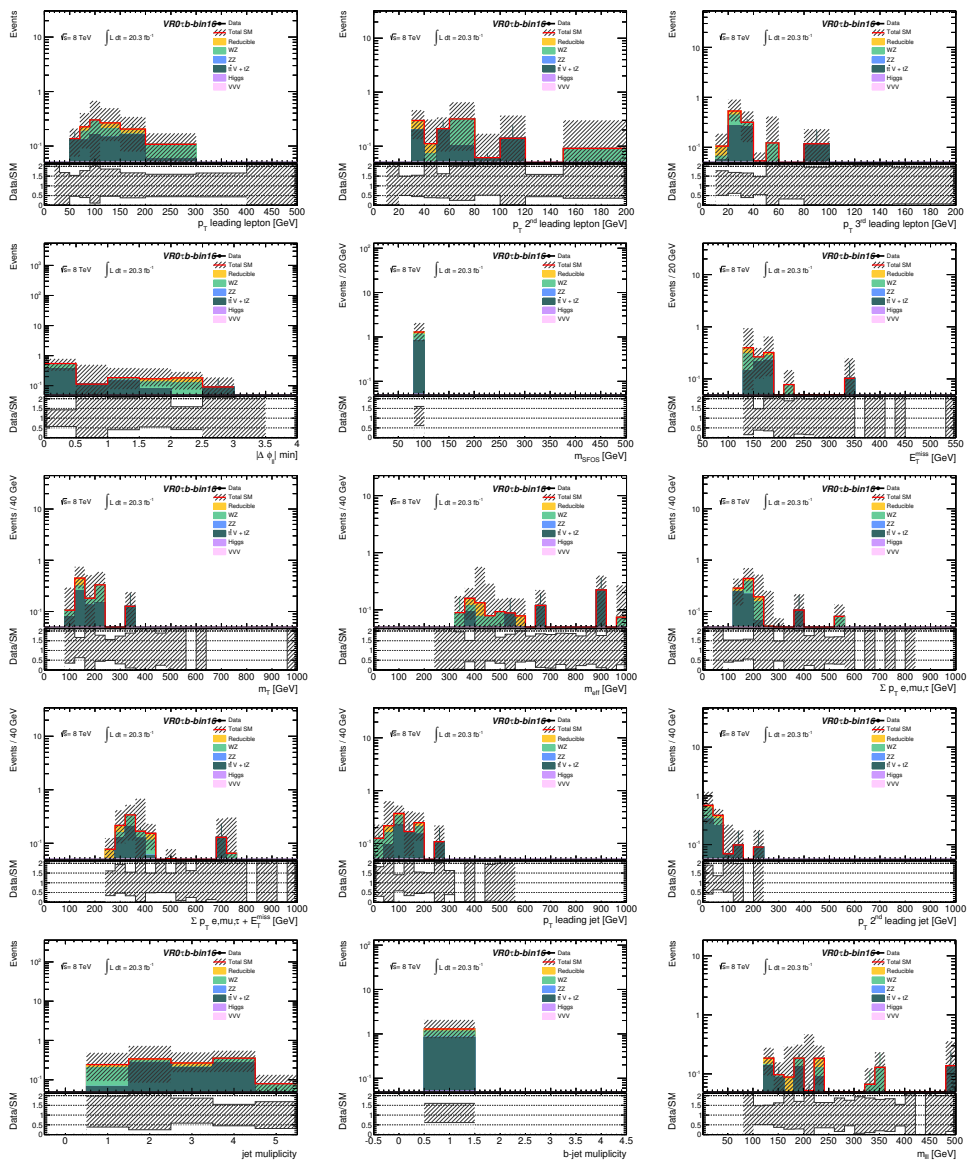


Figure 132: Distributions in VR0 τ b-bin16. The uncertainties are statistical and systematic.

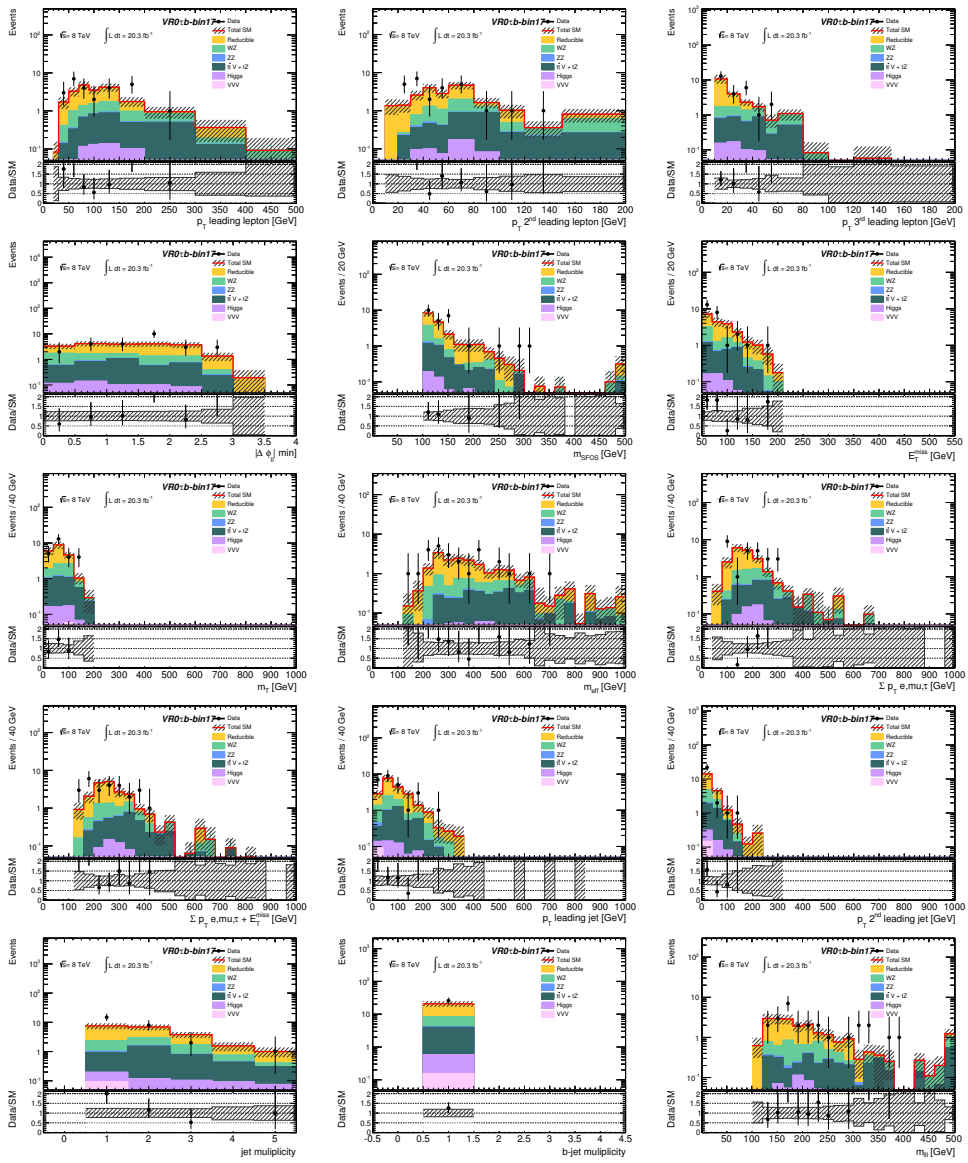


Figure 133: Distributions in VR0 τ -bin17. The uncertainties are statistical and systematic.

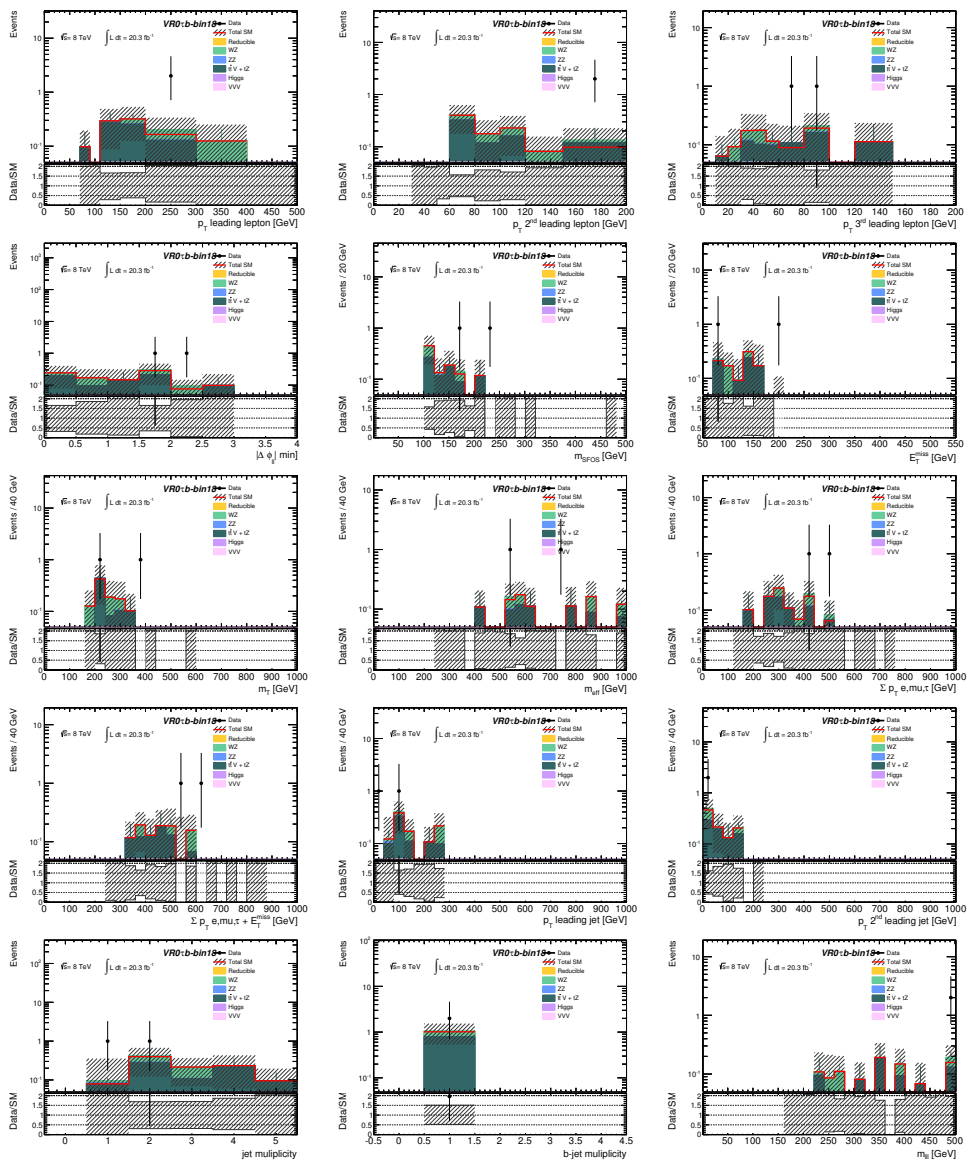


Figure 134: Distributions in VR0 τ b-bin18. The uncertainties are statistical and systematic.

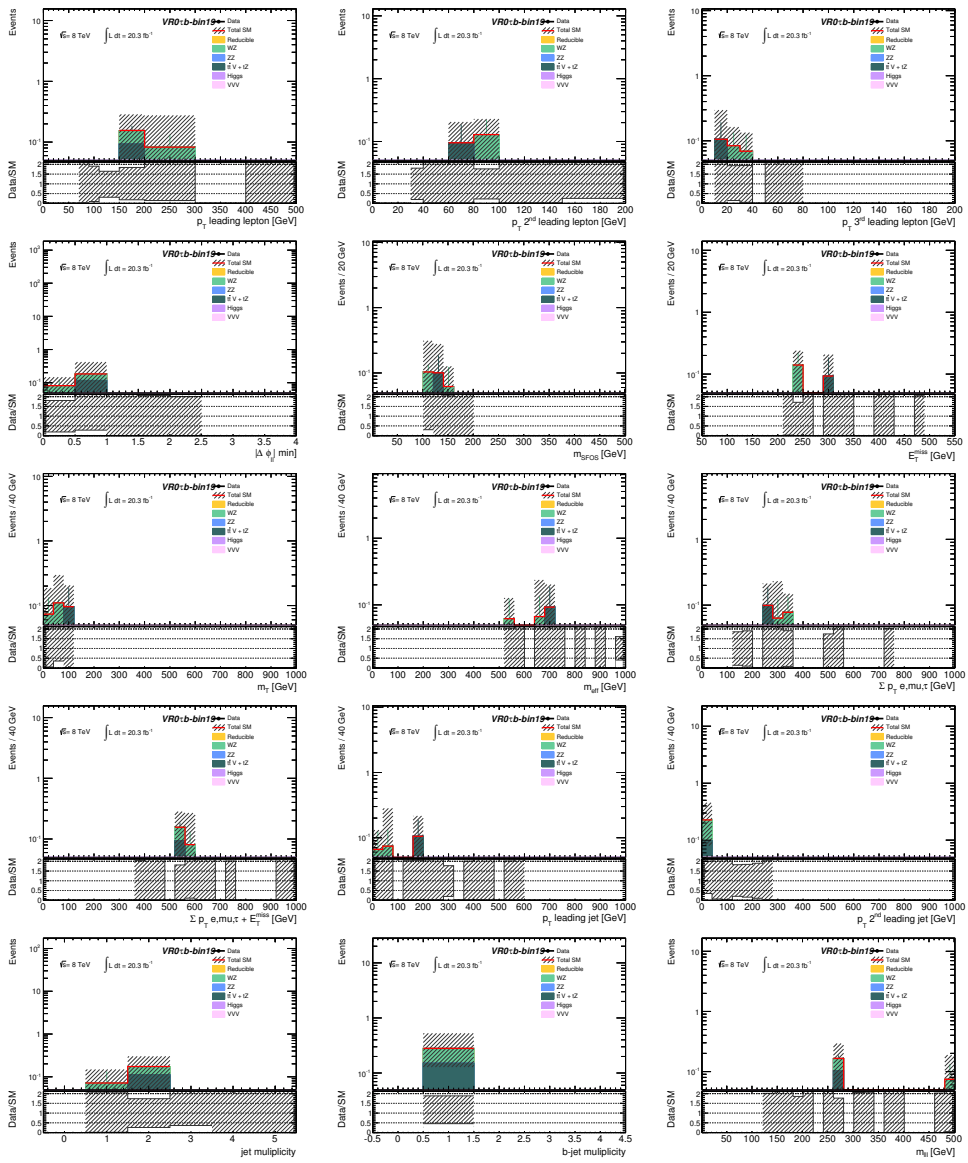


Figure 135: Distributions in VR0 τ -bin19. The uncertainties are statistical and systematic.

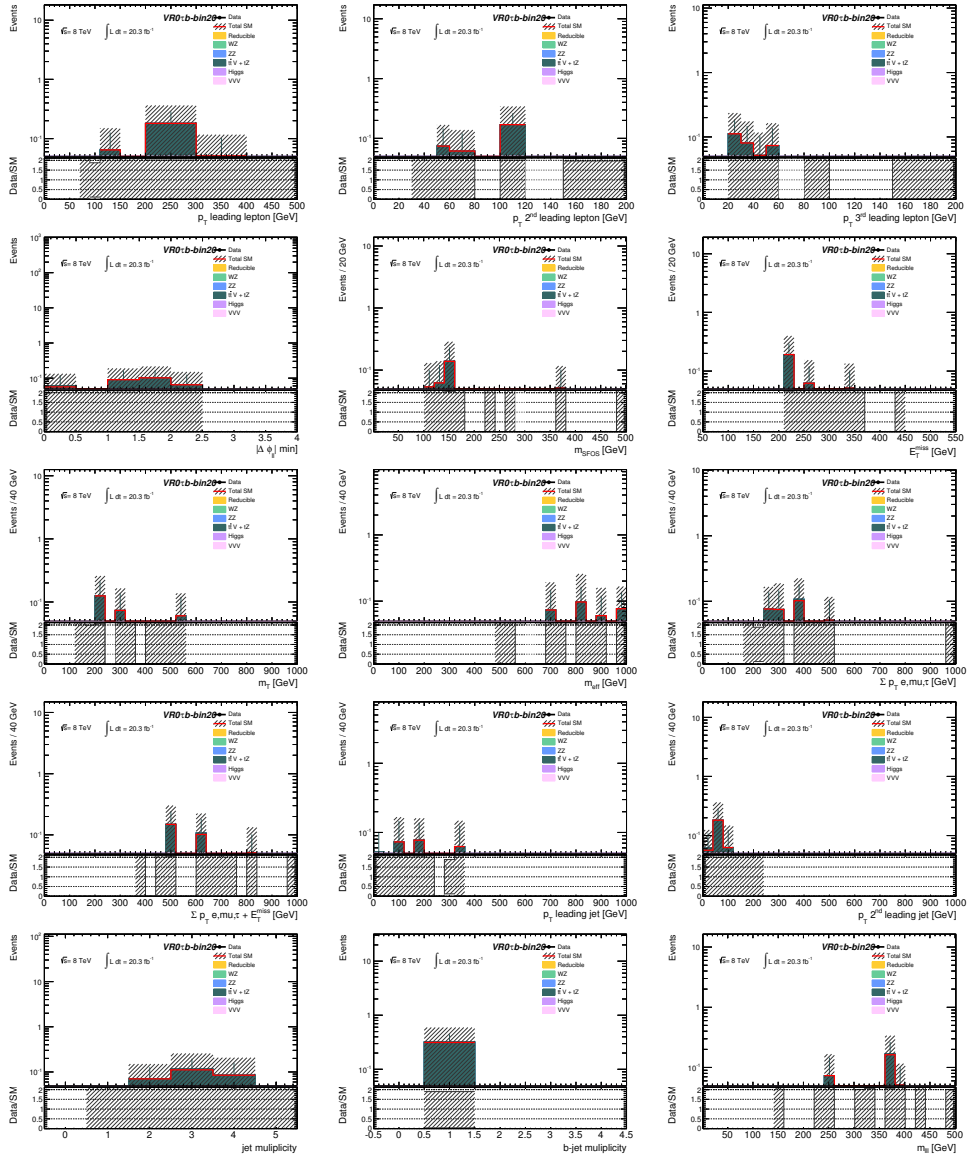


Figure 136: Distributions in VR0 τ -bin20. The uncertainties are statistical and systematic.

Appendix D Distributions in binned signal region

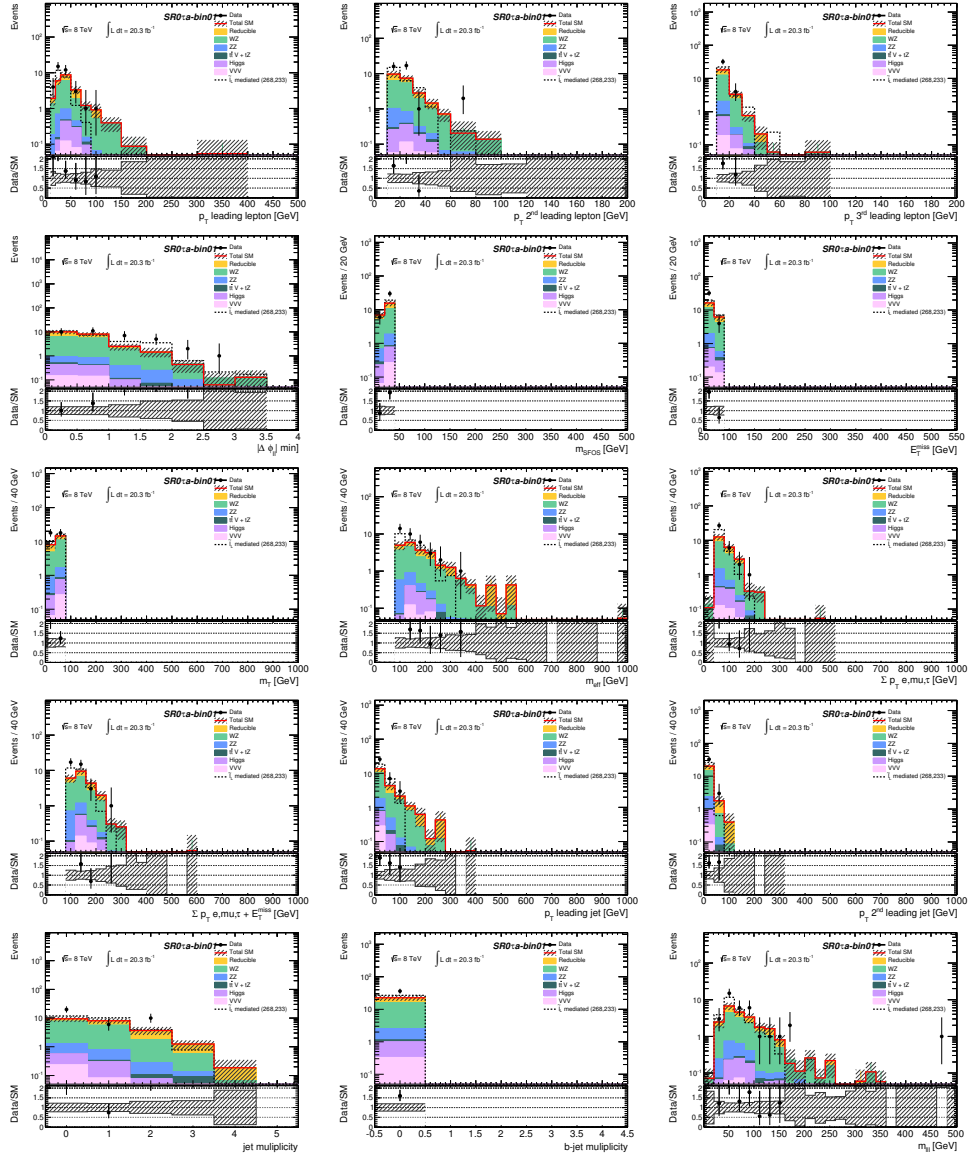


Figure 137: Distributions in bin 1. The uncertainties are statistical and systematic.

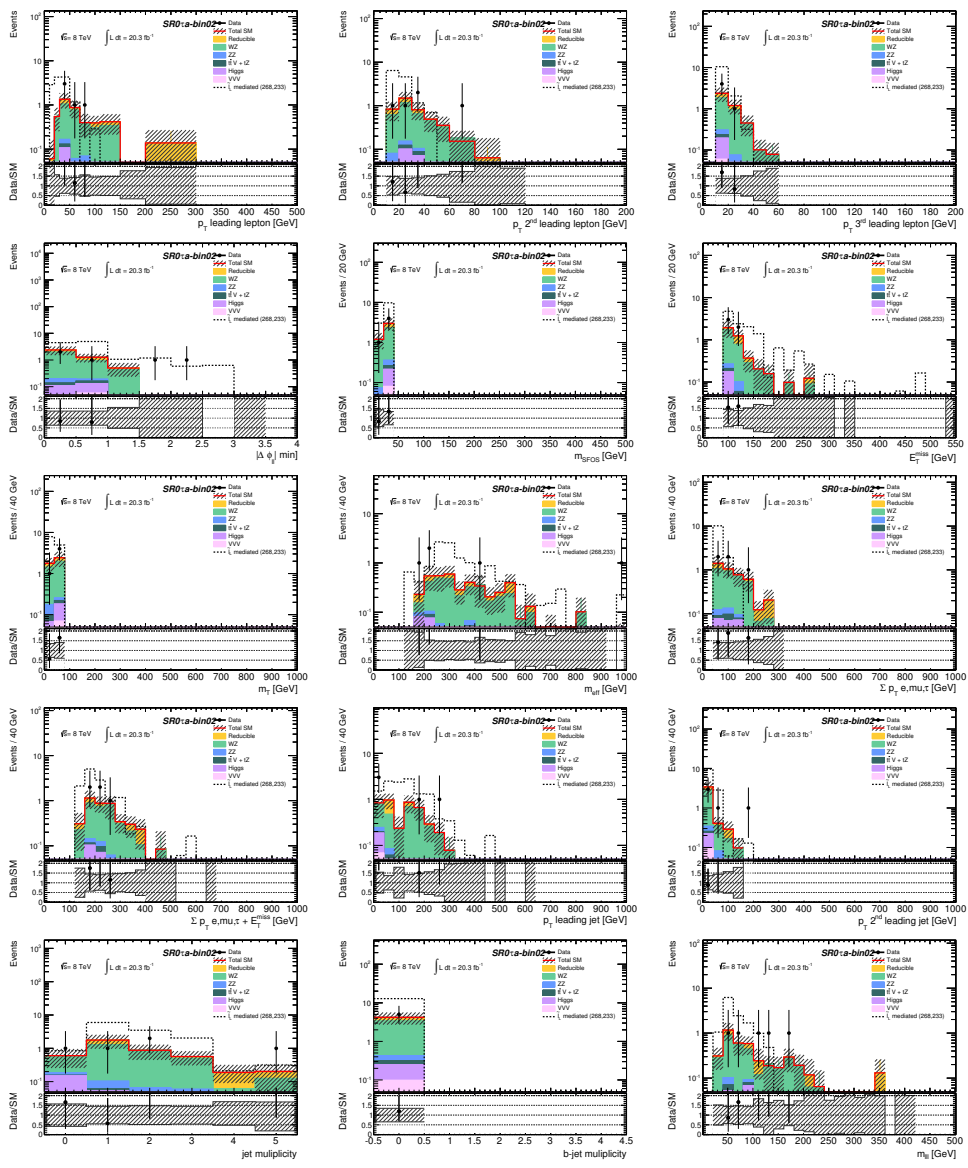


Figure 138: Distributions in bin 2. The uncertainties are statistical and systematic.

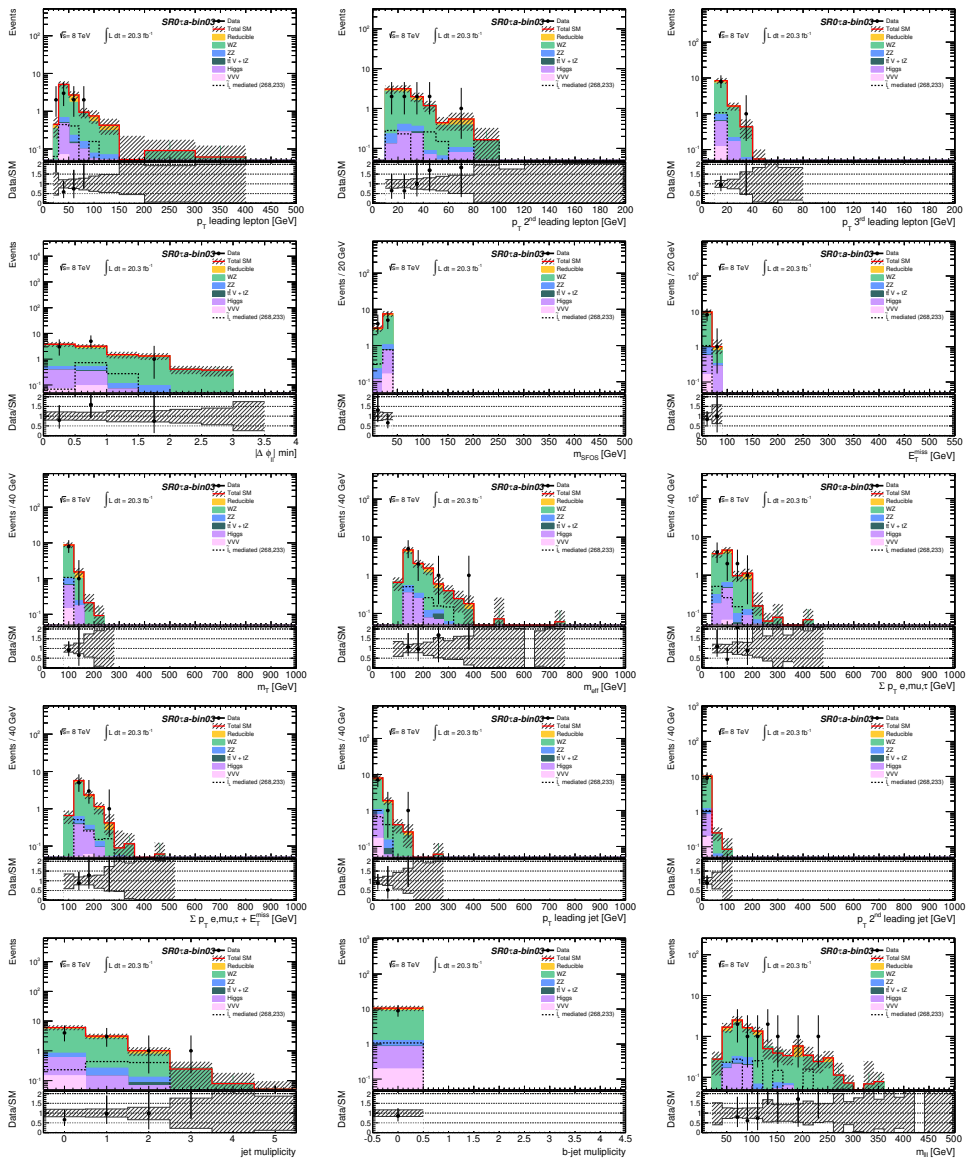


Figure 139: Distributions in bin 3. The uncertainties are statistical and systematic.

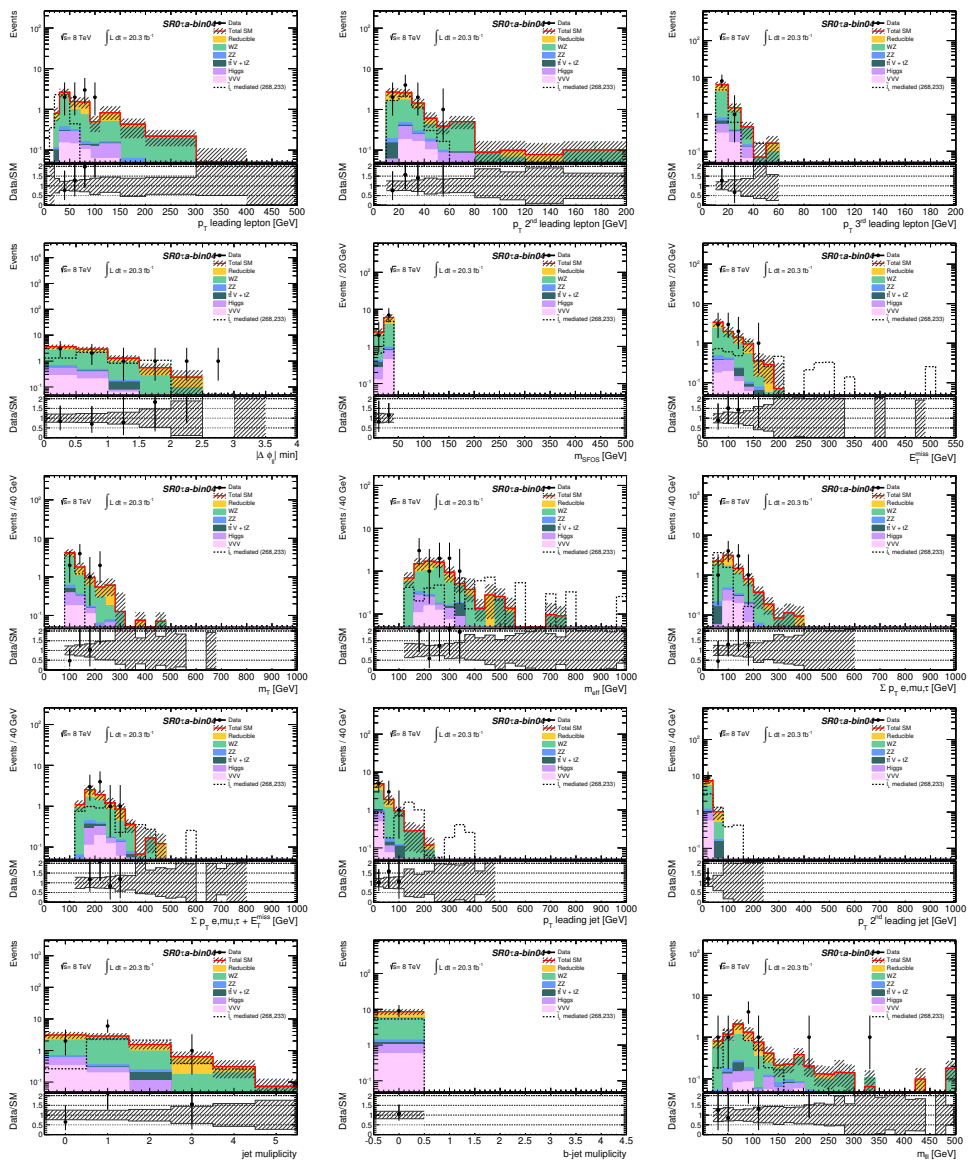


Figure 140: Distributions in bin 4. The uncertainties are statistical and systematic.

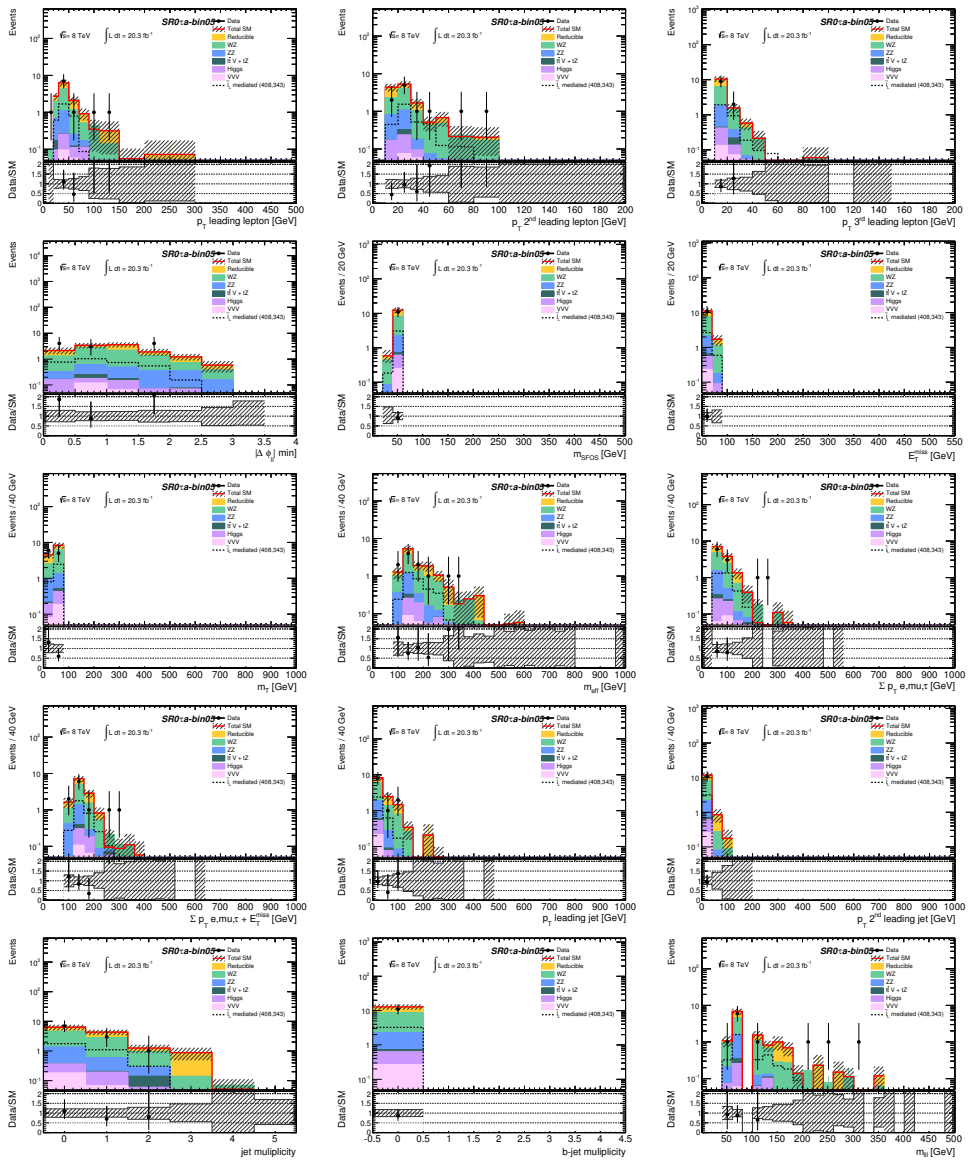


Figure 141: Distributions in bin 5. The uncertainties are statistical and systematic.

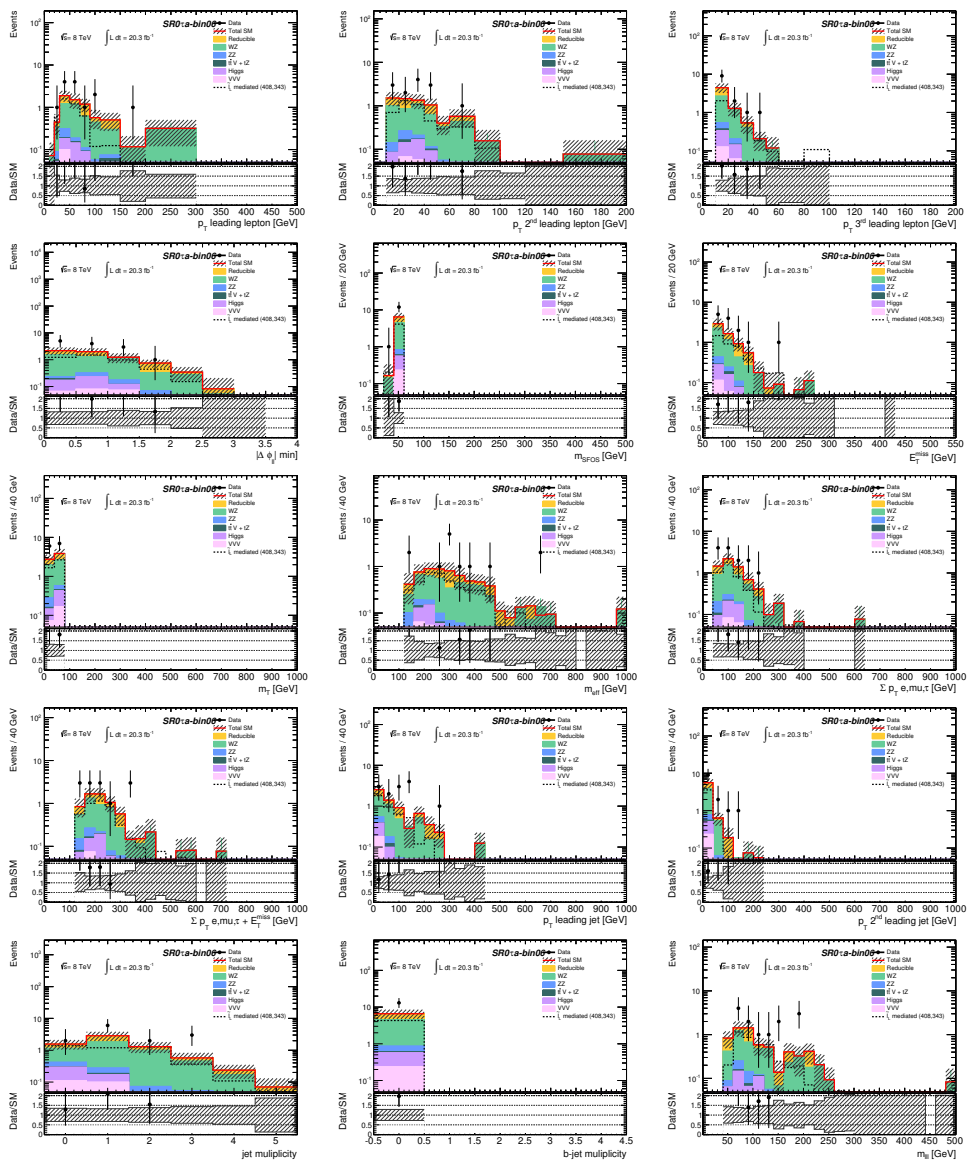


Figure 142: Distributions in bin 6. The uncertainties are statistical and systematic.

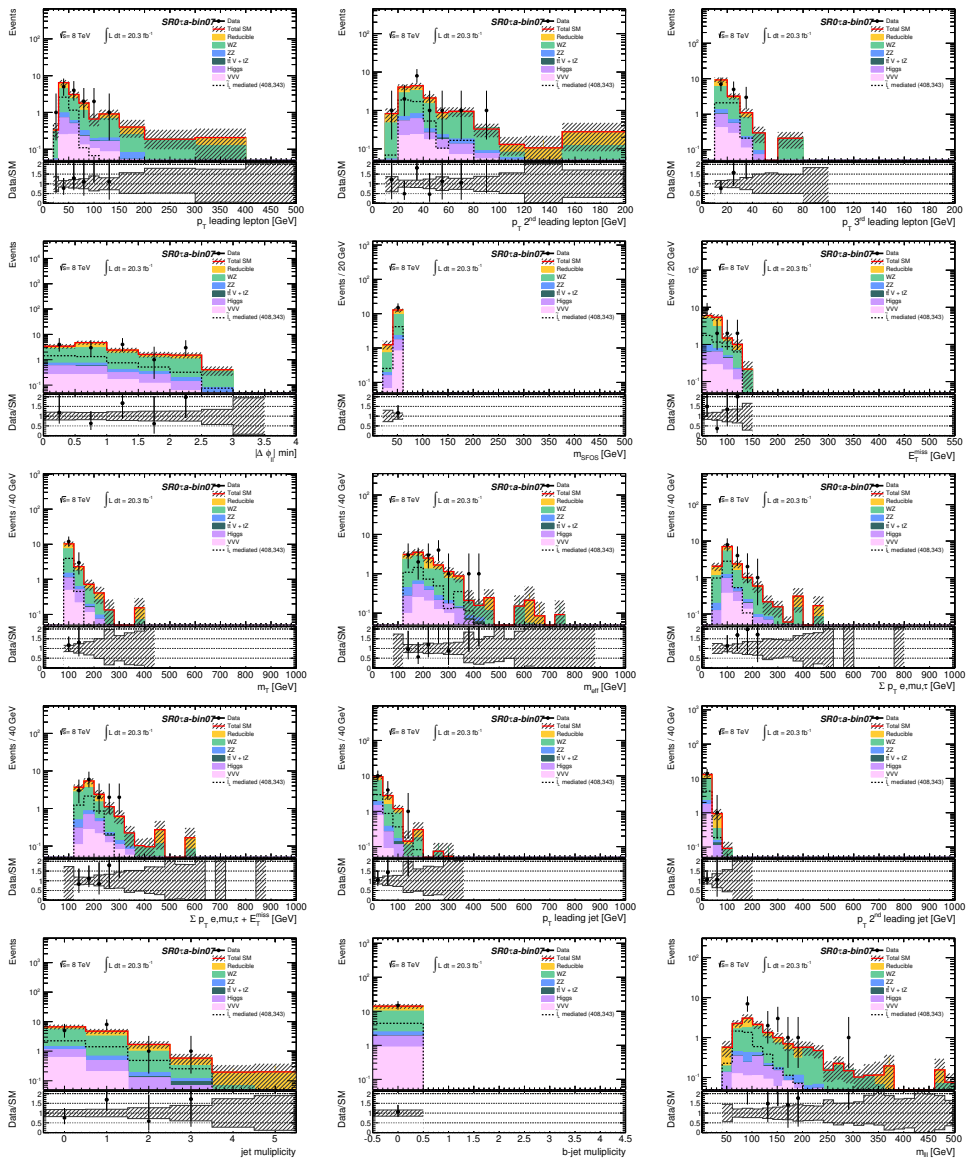


Figure 143: Distributions in bin 7. The uncertainties are statistical and systematic.

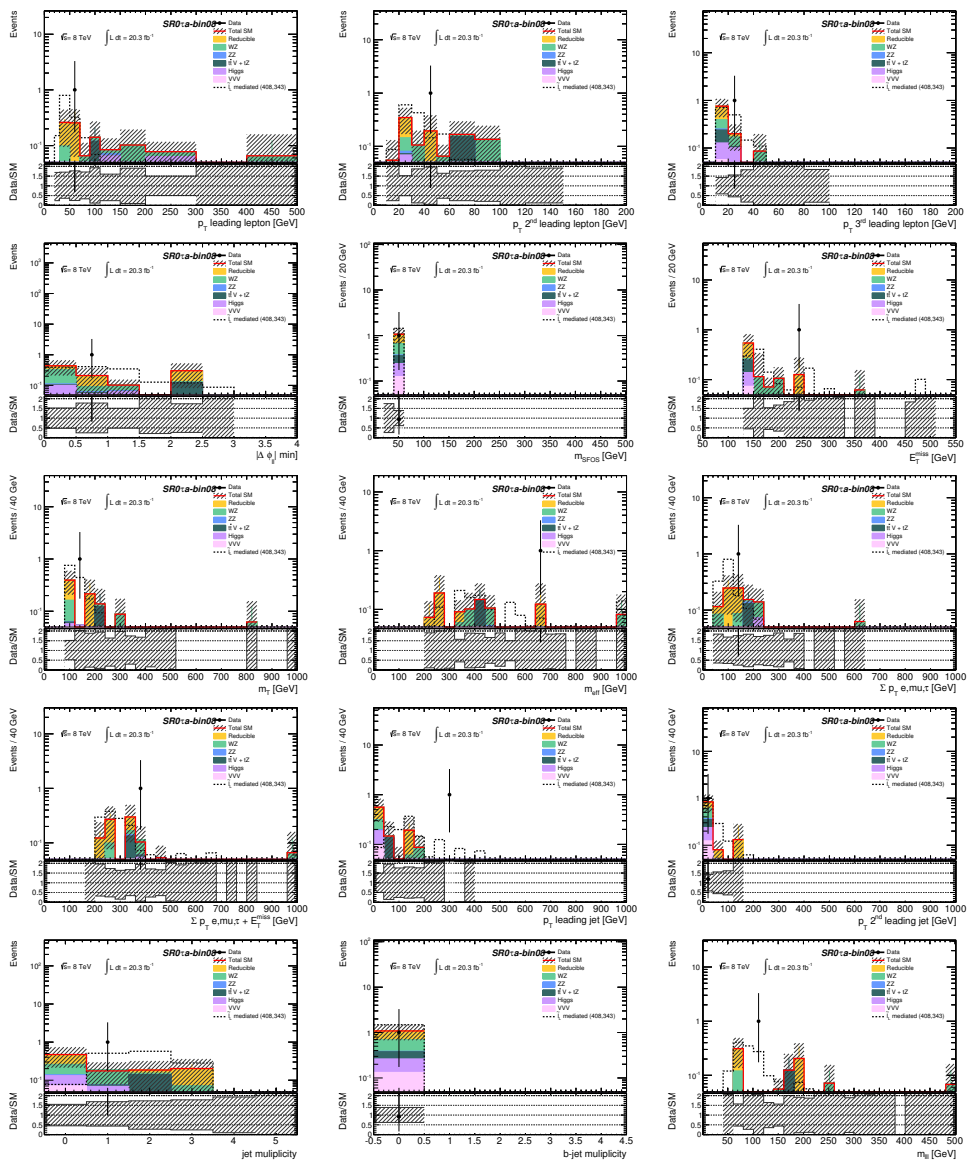


Figure 144: Distributions in bin 8. The uncertainties are statistical and systematic.

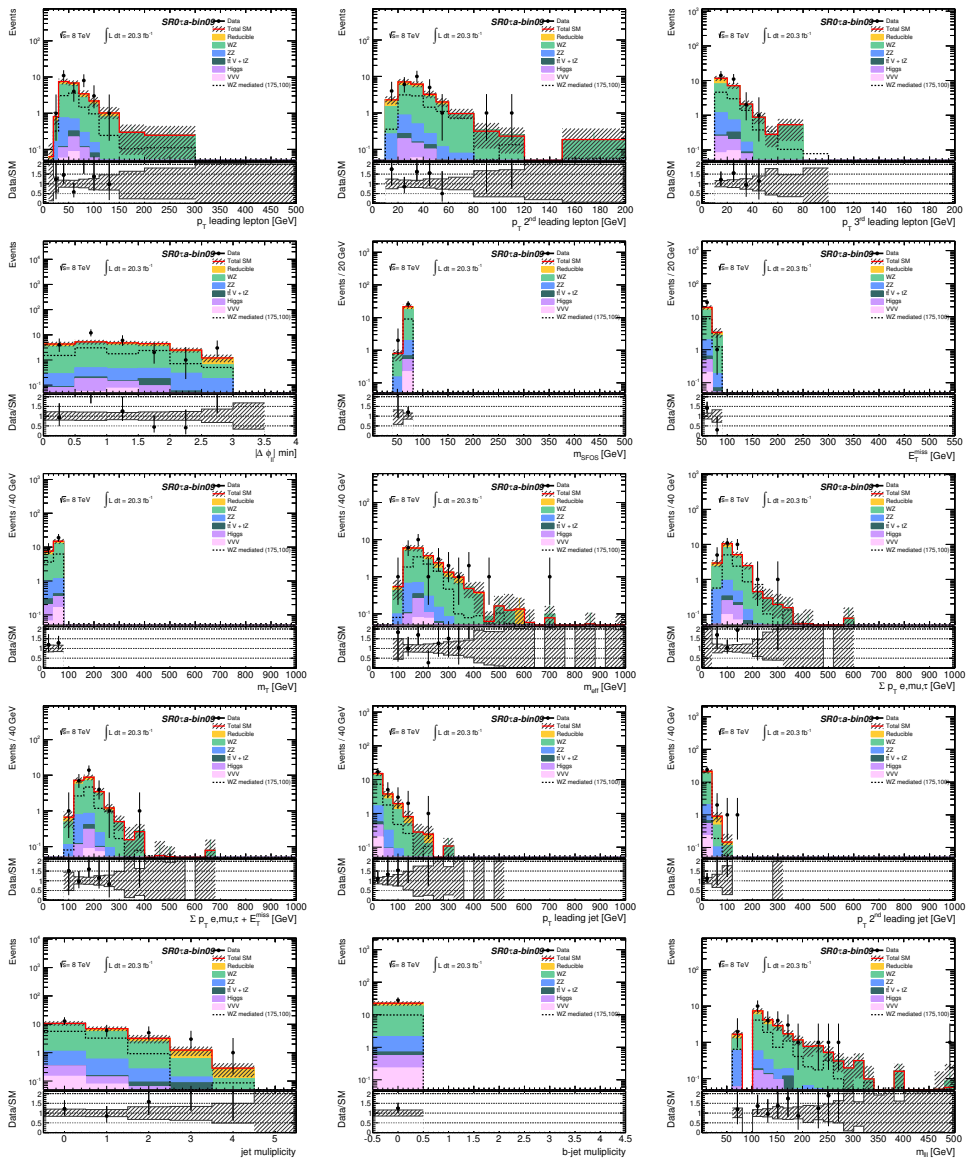


Figure 145: Distributions in bin 9. The uncertainties are statistical and systematic.

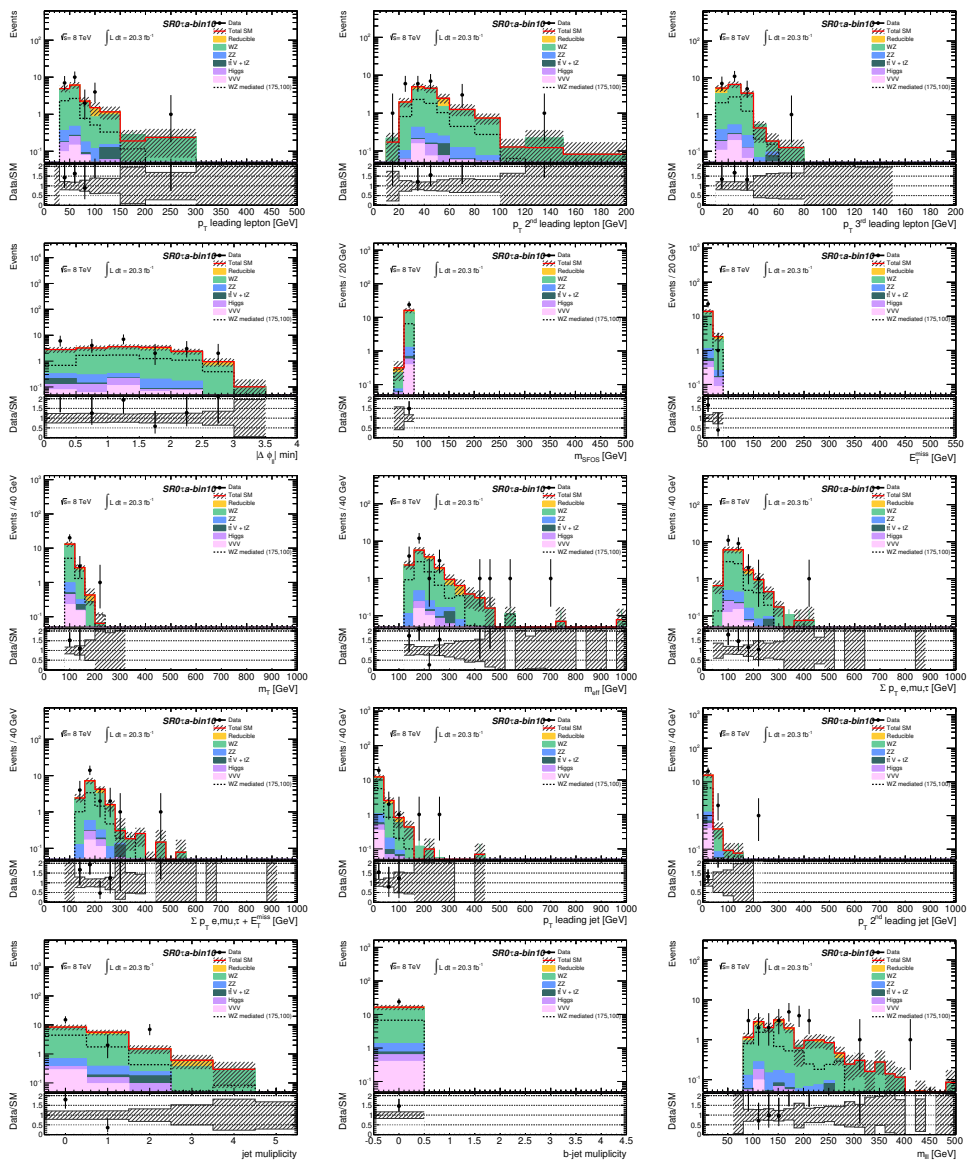


Figure 146: Distributions in bin 10. The uncertainties are statistical and systematic.

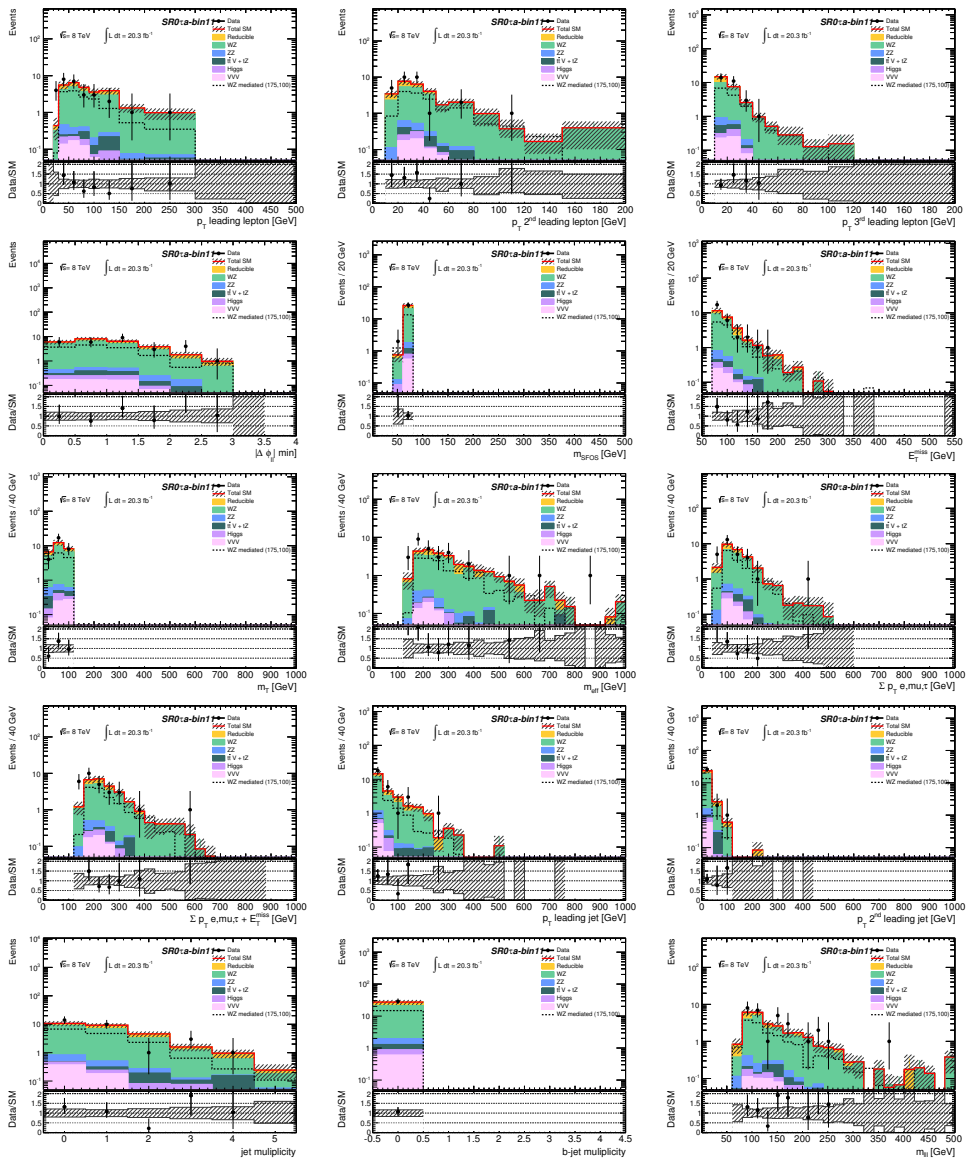


Figure 147: Distributions in bin 11. The uncertainties are statistical and systematic.

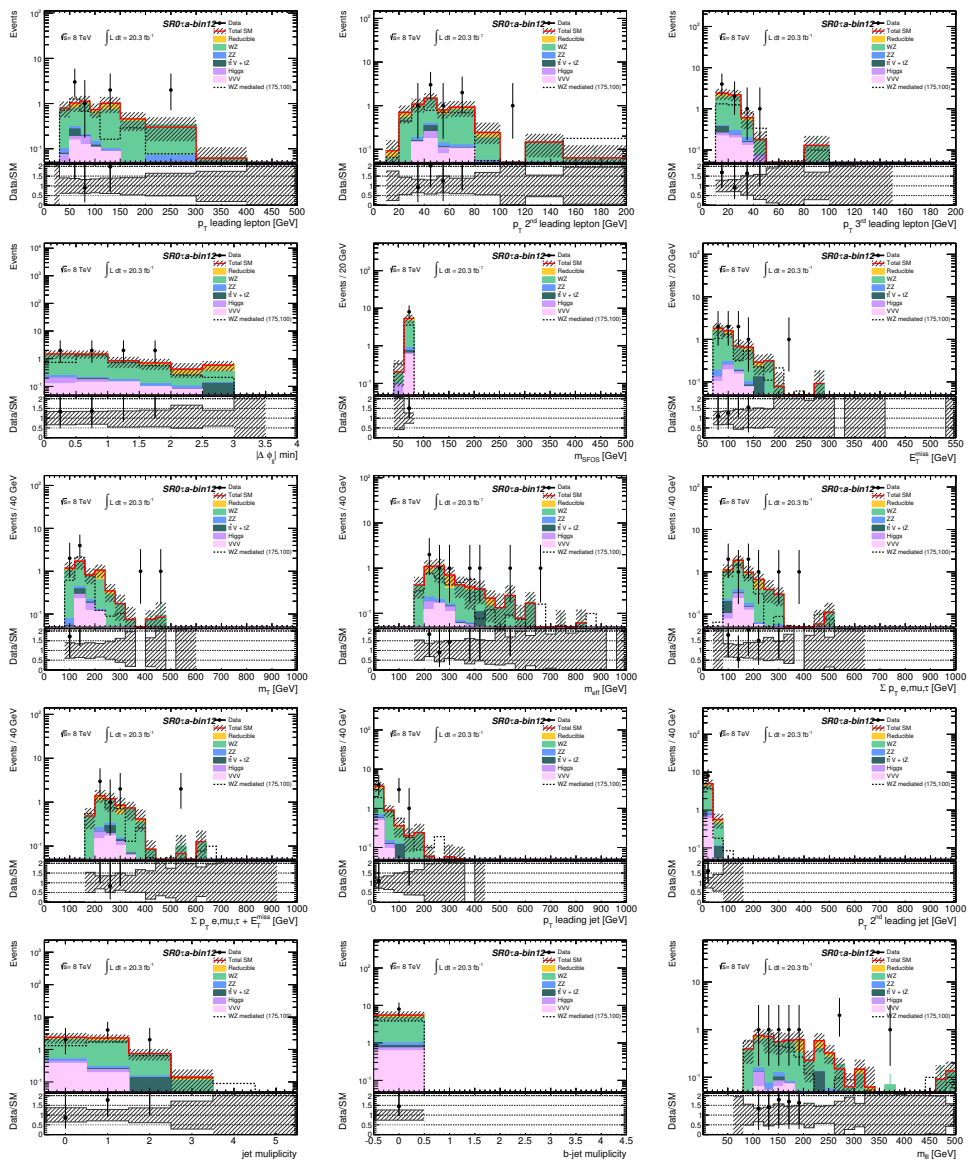


Figure 148: Distributions in bin 12. The uncertainties are statistical and systematic.

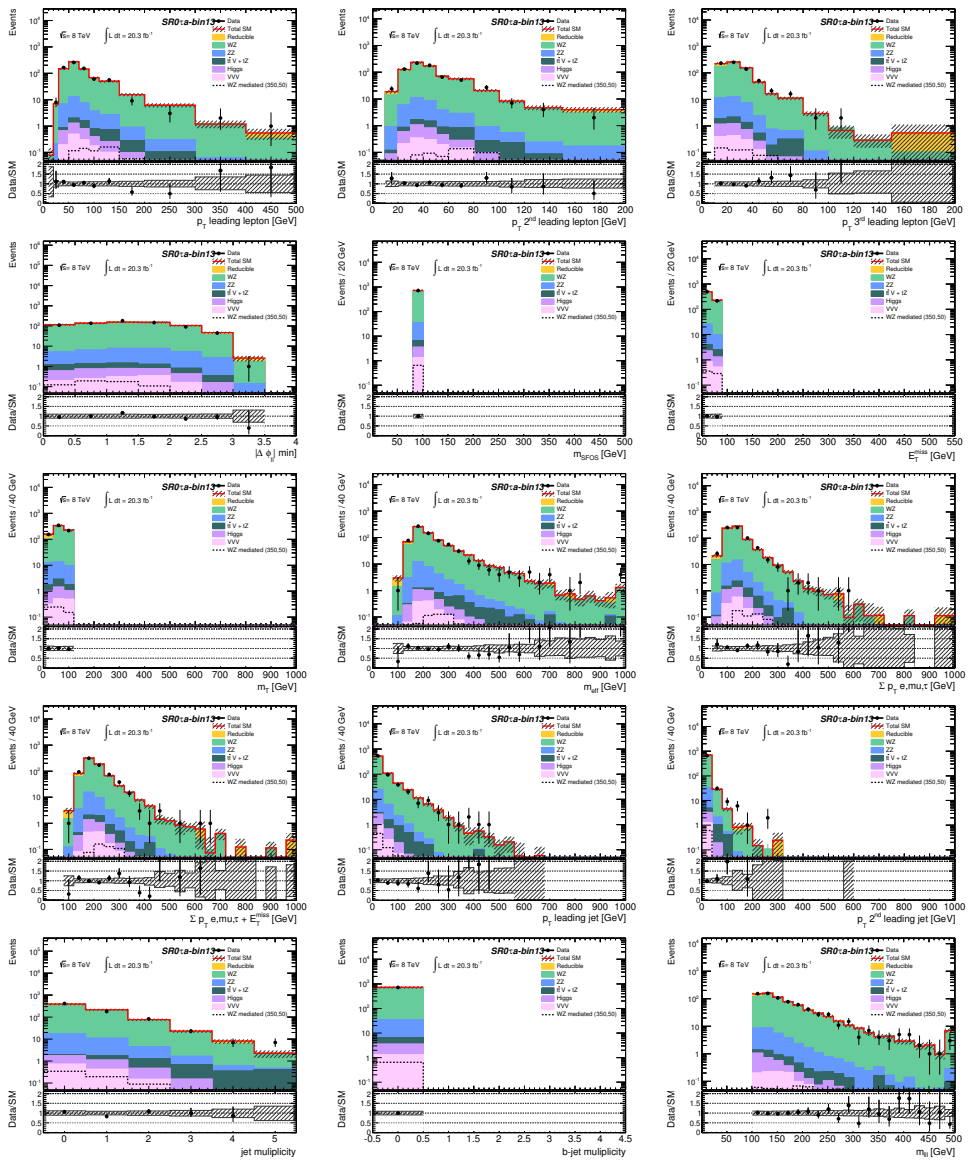


Figure 149: Distributions in bin 13. The uncertainties are statistical and systematic.

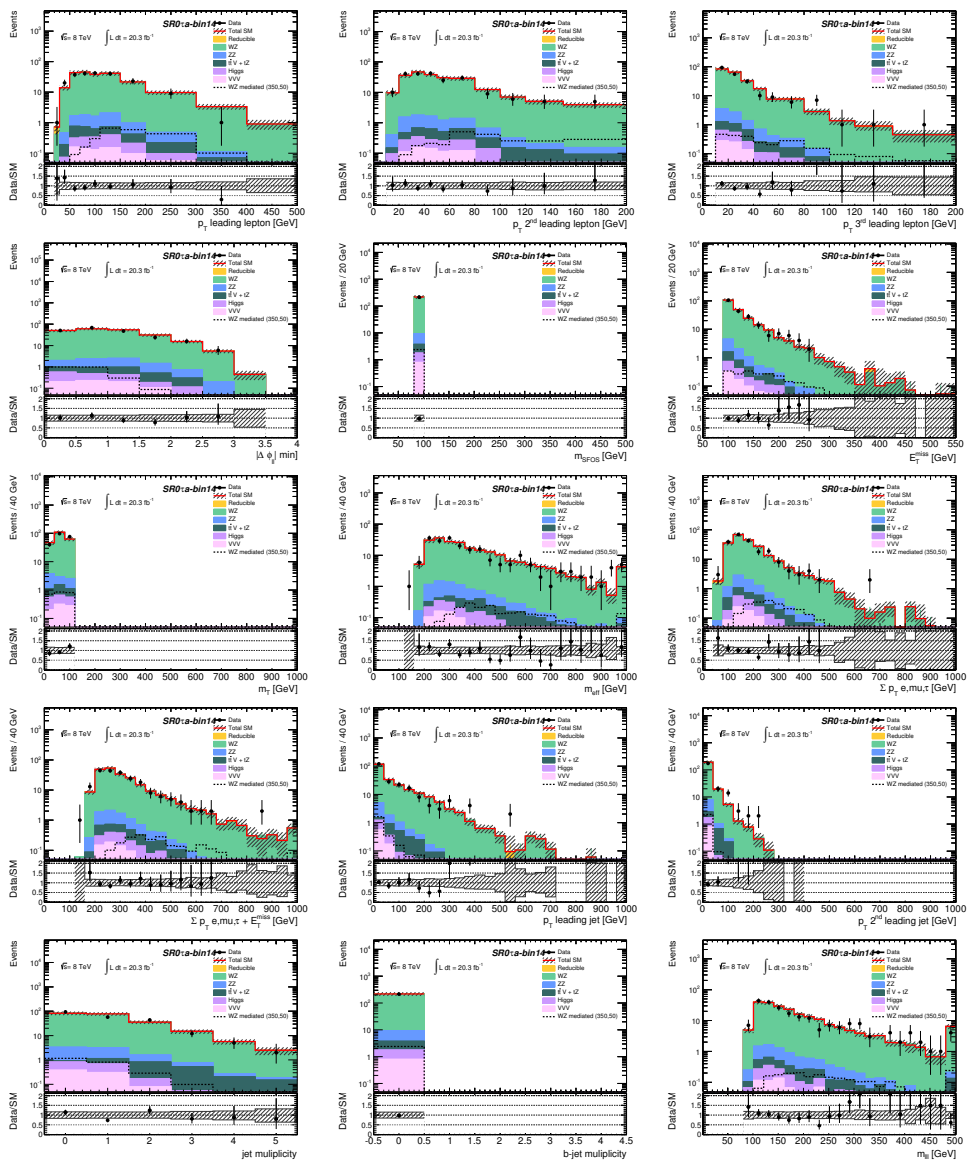


Figure 150: Distributions in bin 14. The uncertainties are statistical and systematic.

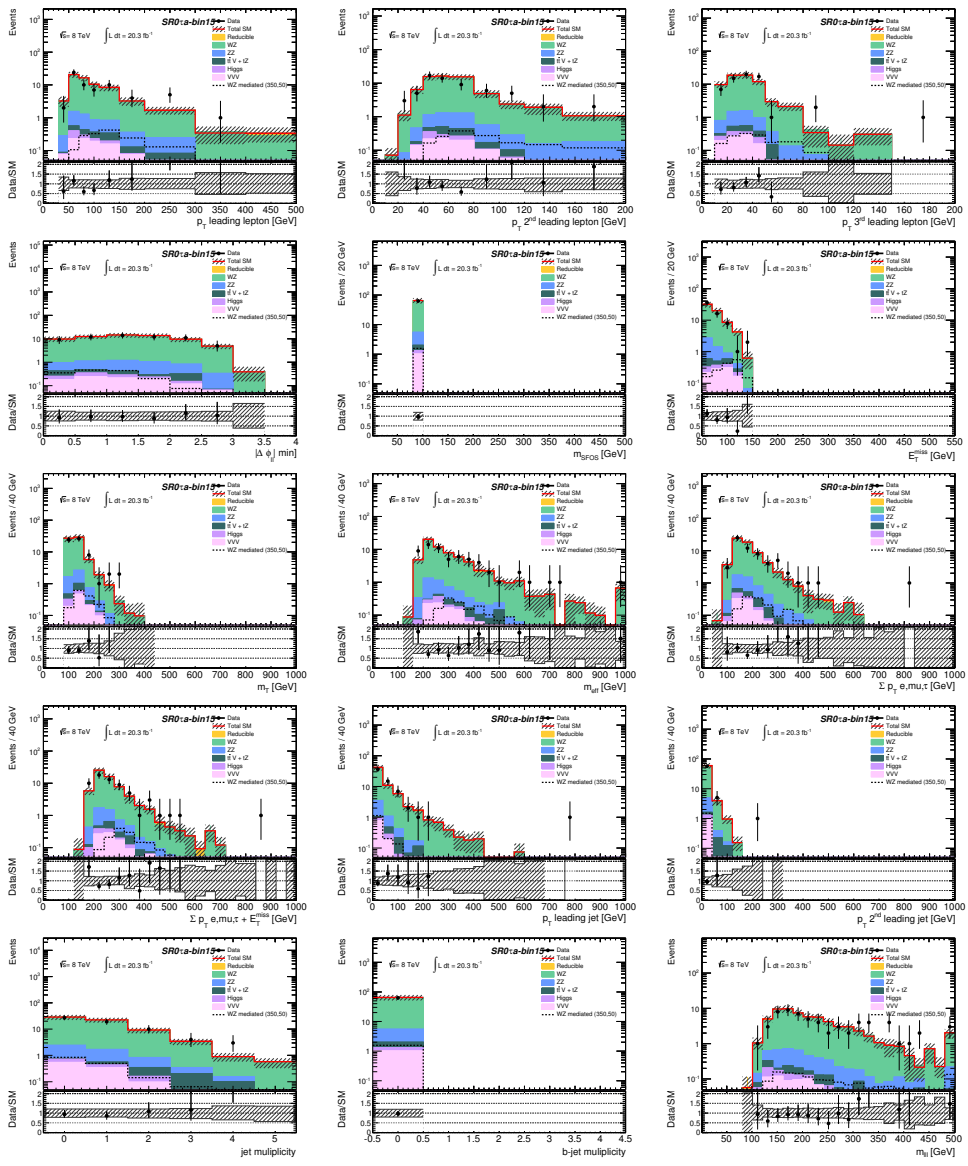


Figure 151: Distributions in bin 15. The uncertainties are statistical and systematic.

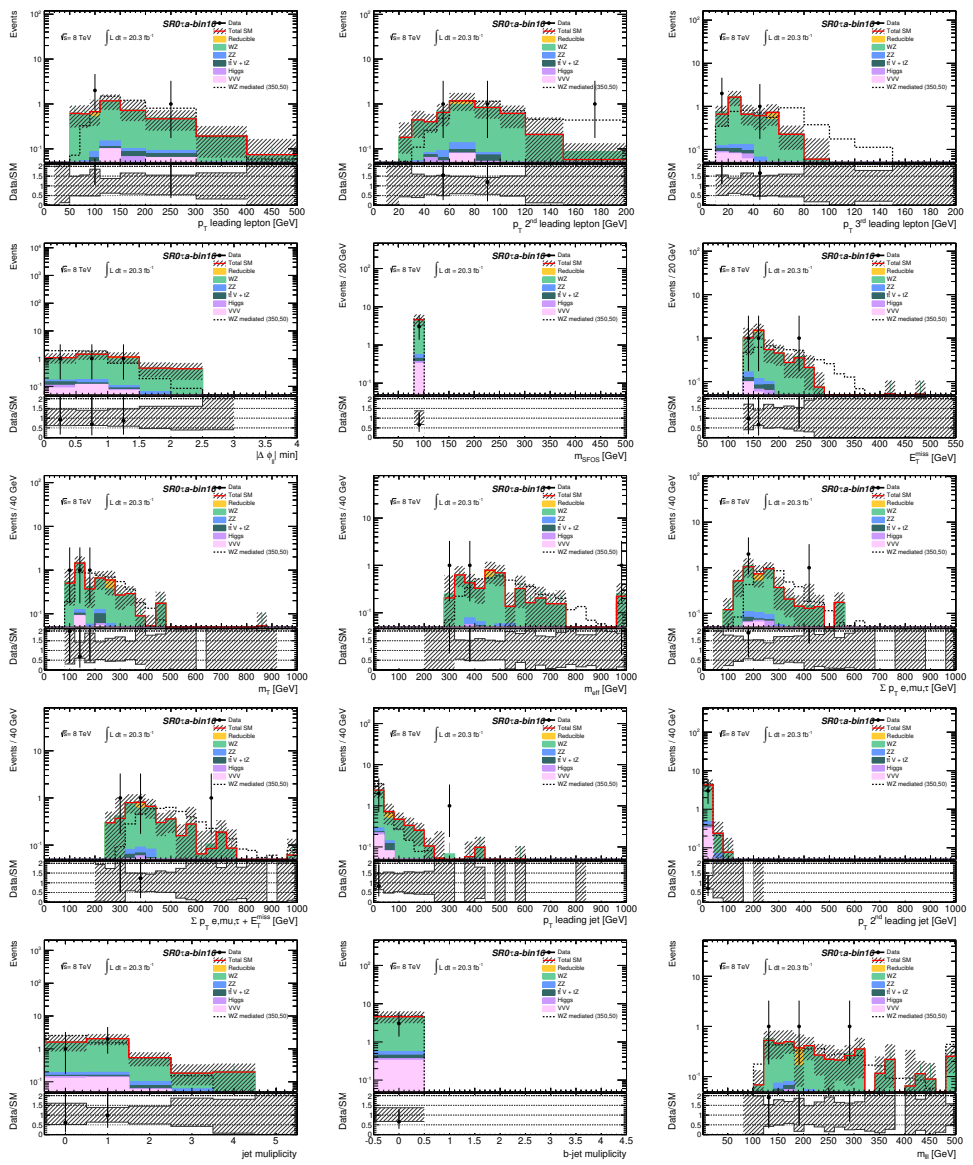


Figure 152: Distributions in bin 16. The uncertainties are statistical and systematic.

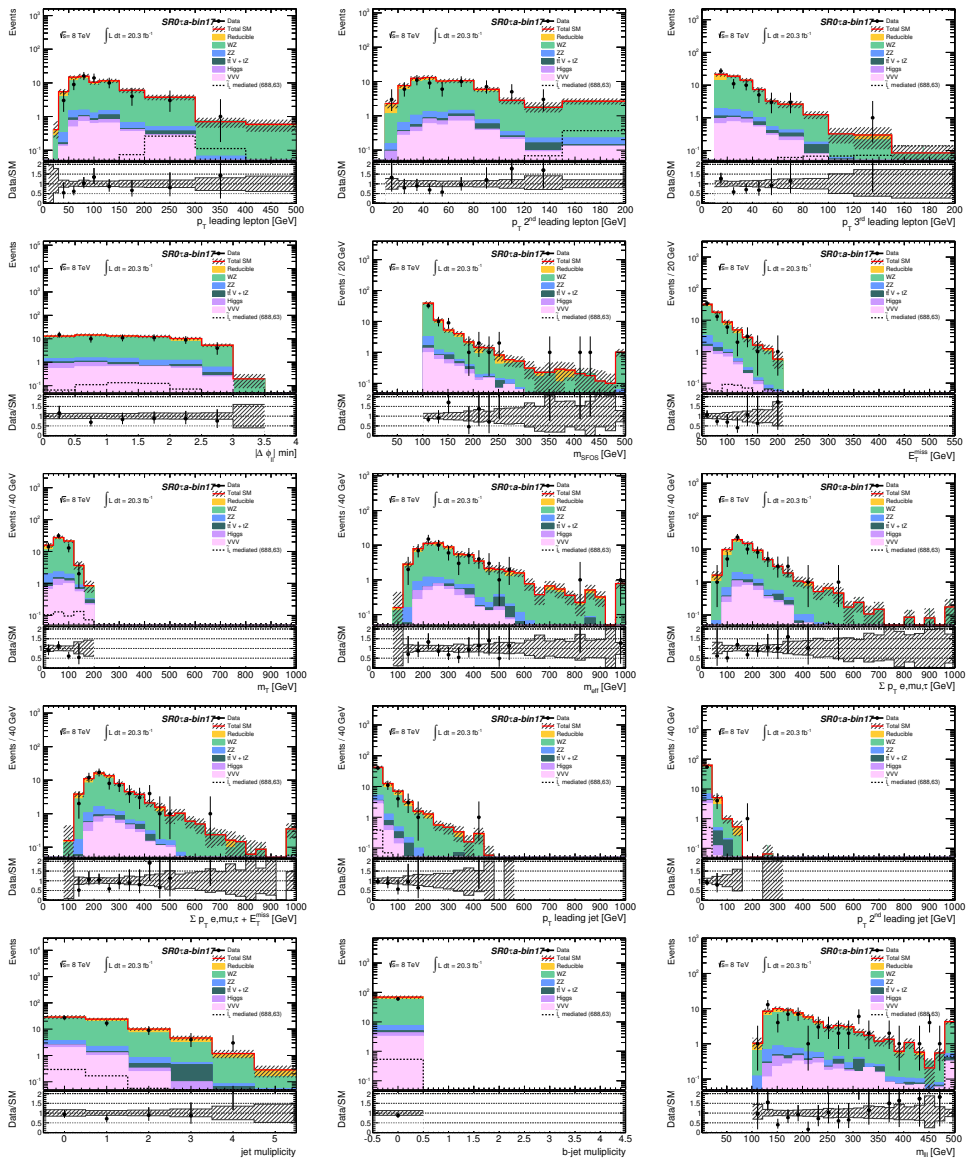


Figure 153: Distributions in bin 17. The uncertainties are statistical and systematic.

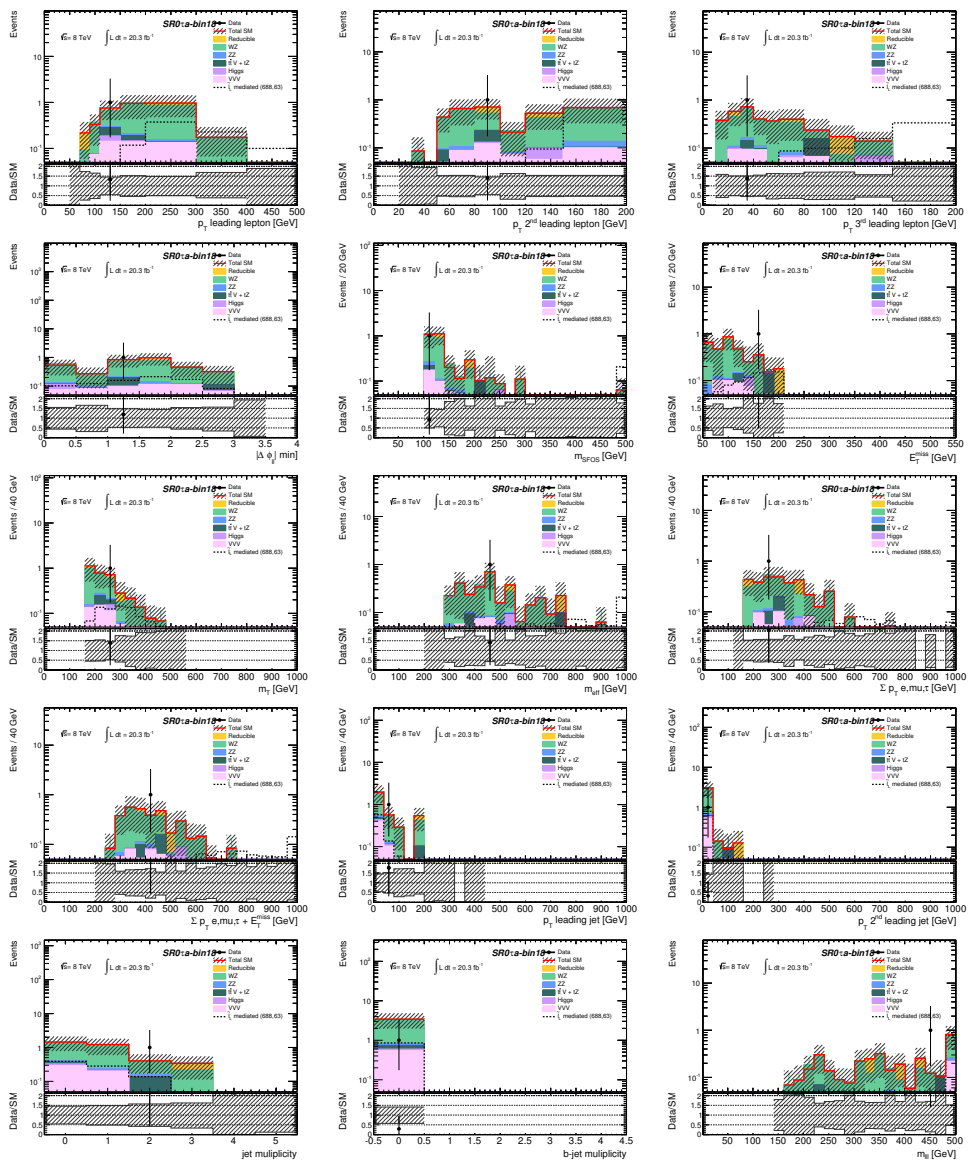


Figure 154: Distributions in bin 18. The uncertainties are statistical and systematic.

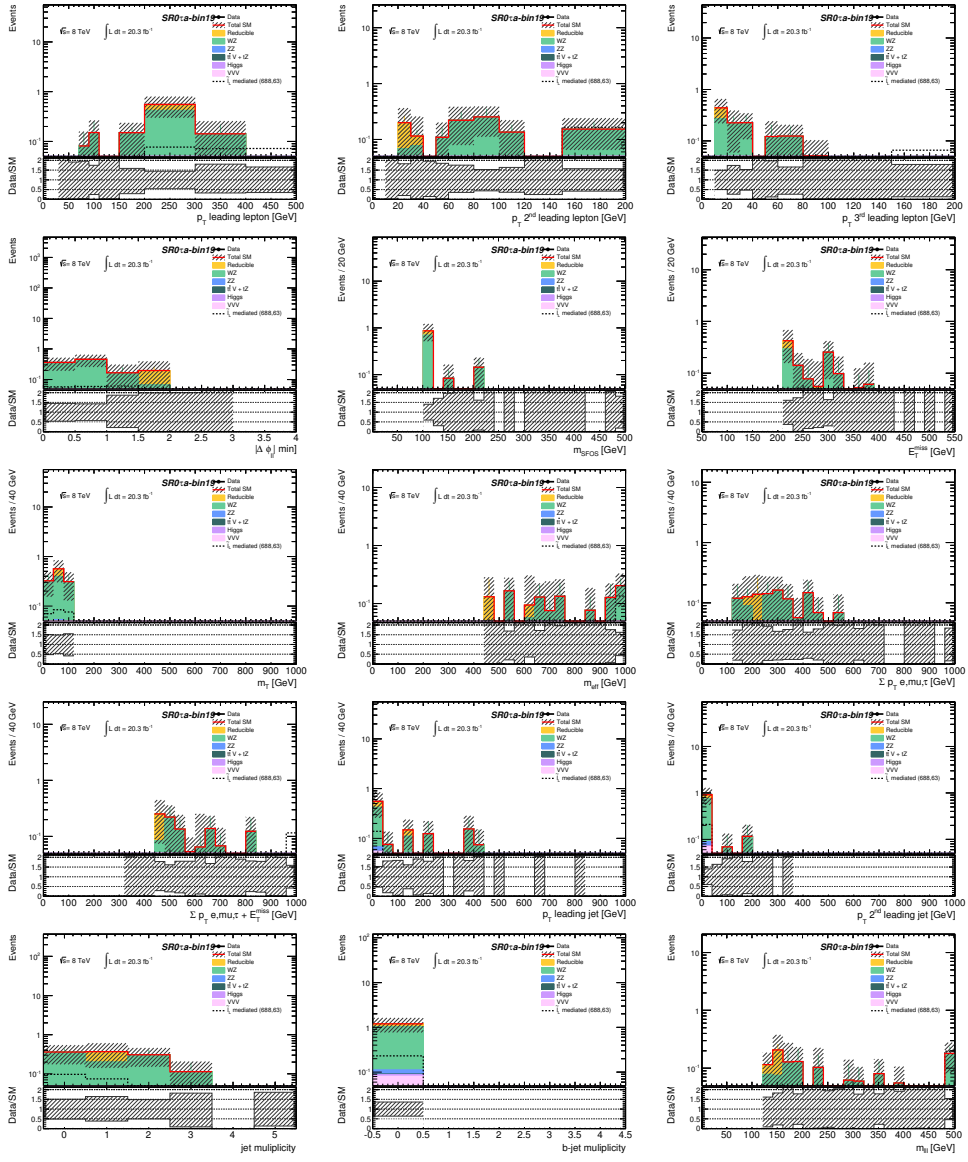


Figure 155: Distributions in bin 19. The uncertainties are statistical and systematic.

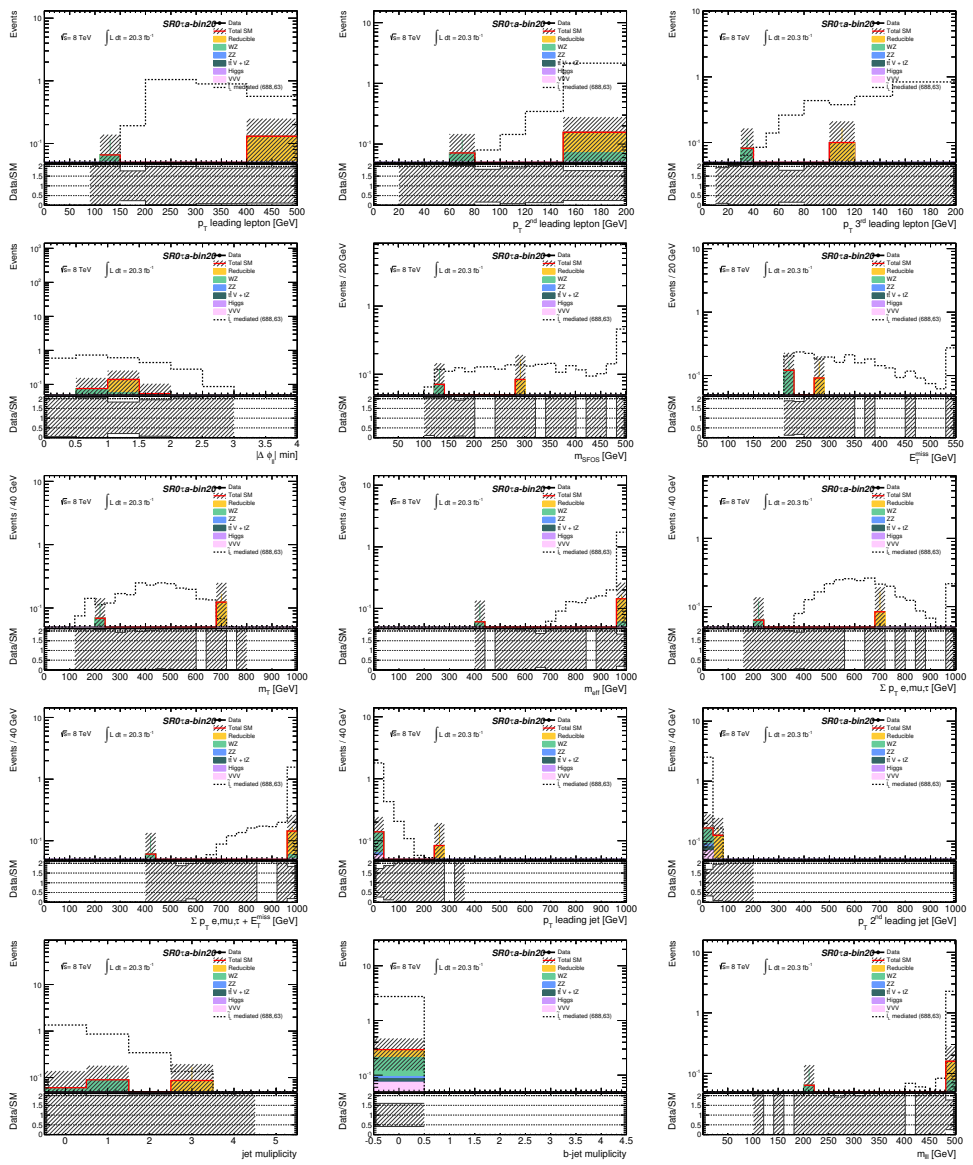


Figure 156: Distributions in bin 20. The uncertainties are statistical and systematic.

Appendix E CL_s per bin

The CL_s values are shown here for each bin separately. Figures 157 - 162 show the $\tilde{\ell}_L$ mediated simplified model, figures 163 - 168 show WZ mediated simplified model. All CL_s values are derived with asymptotic formulae.

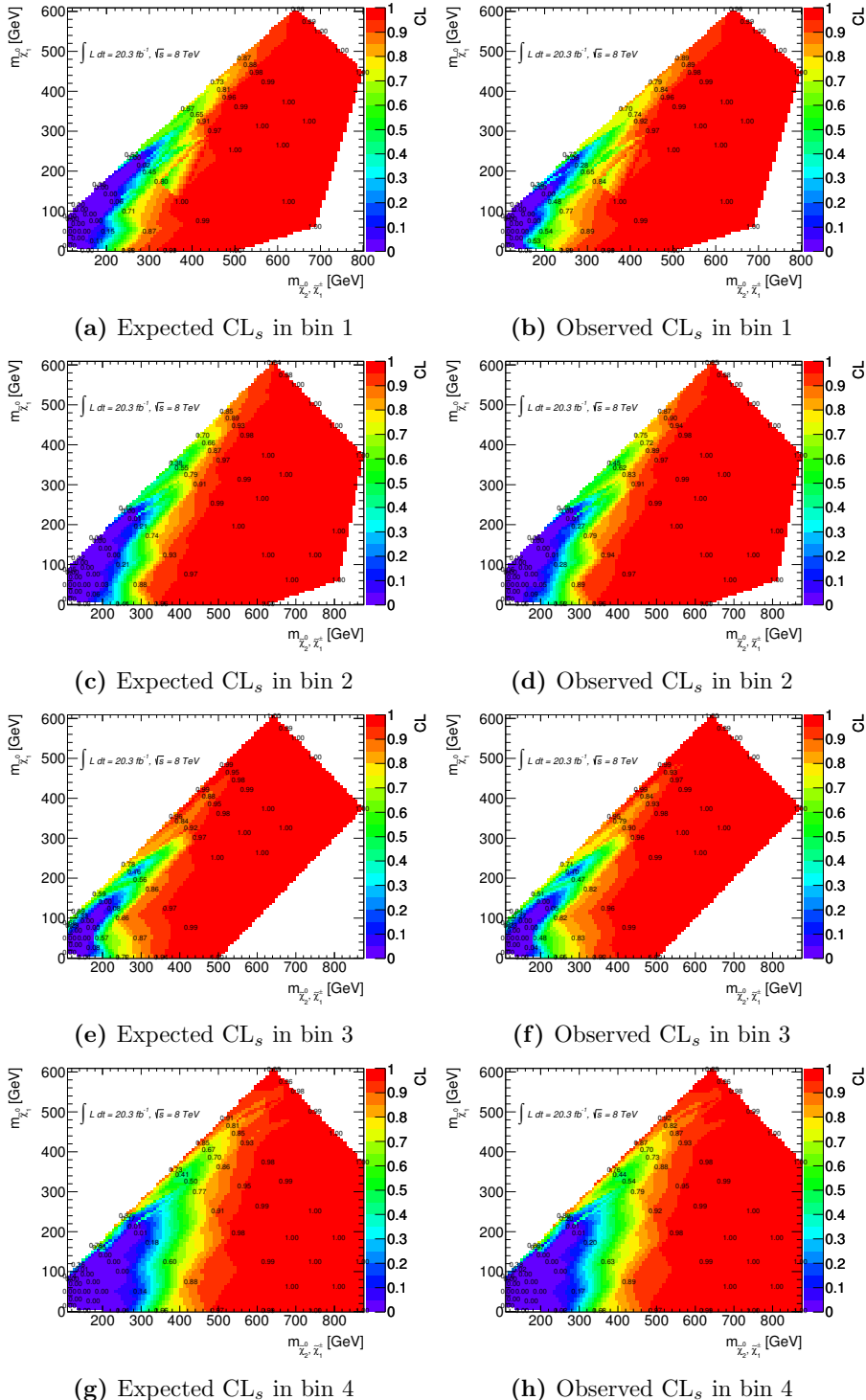


Figure 157: Expected (left) and observed (right) CL_s values for the $\tilde{\ell}_L$ mediated simplified model in the four bins where $m_{\text{SFOS}} \in [12, 40] \text{ GeV}$.

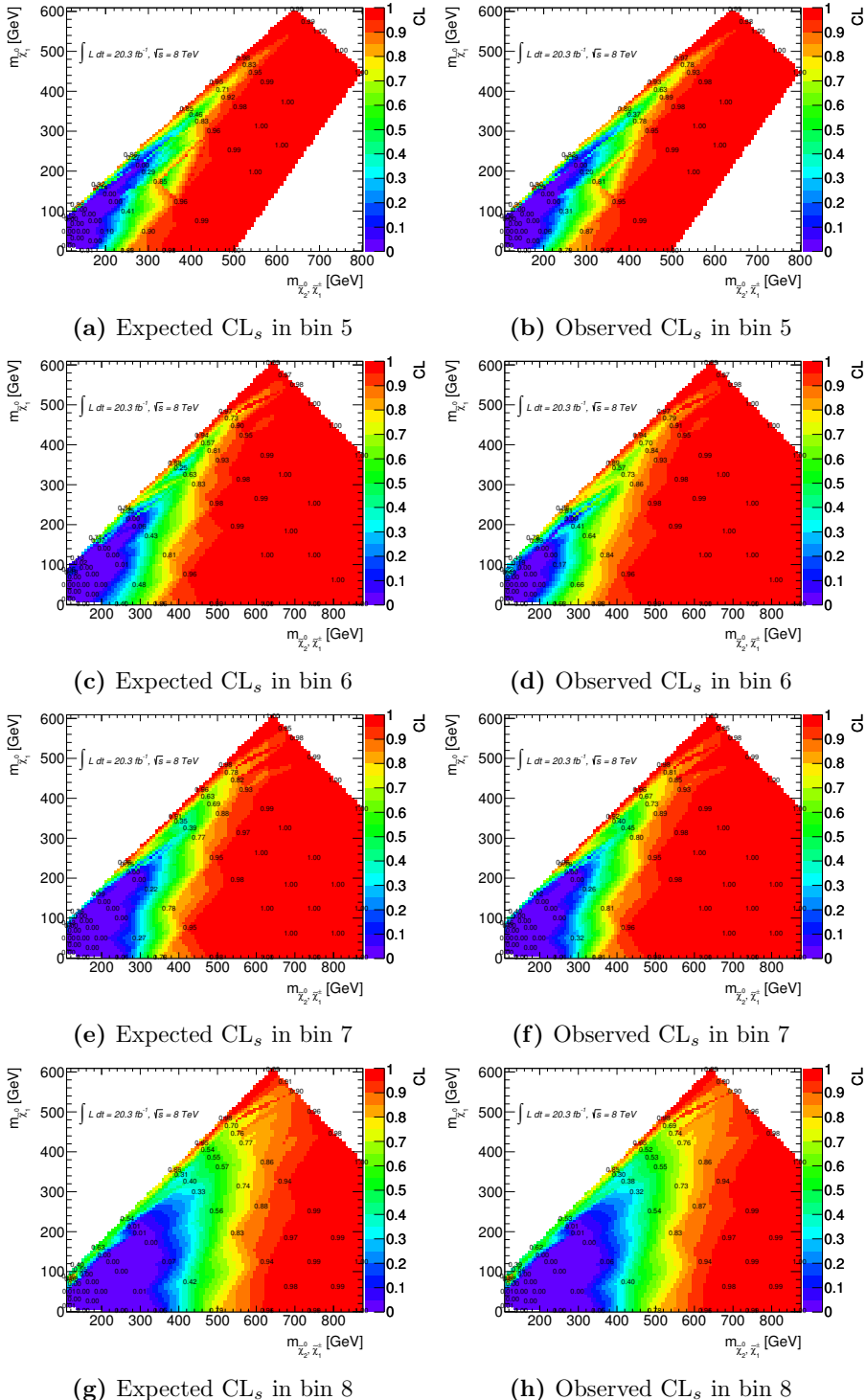


Figure 158: Expected (left) and observed (right) CL_s values for the $\tilde{\ell}_L$ mediated simplified model in the four bins where $m_{\text{SFOS}} \in [40, 60]$ GeV.

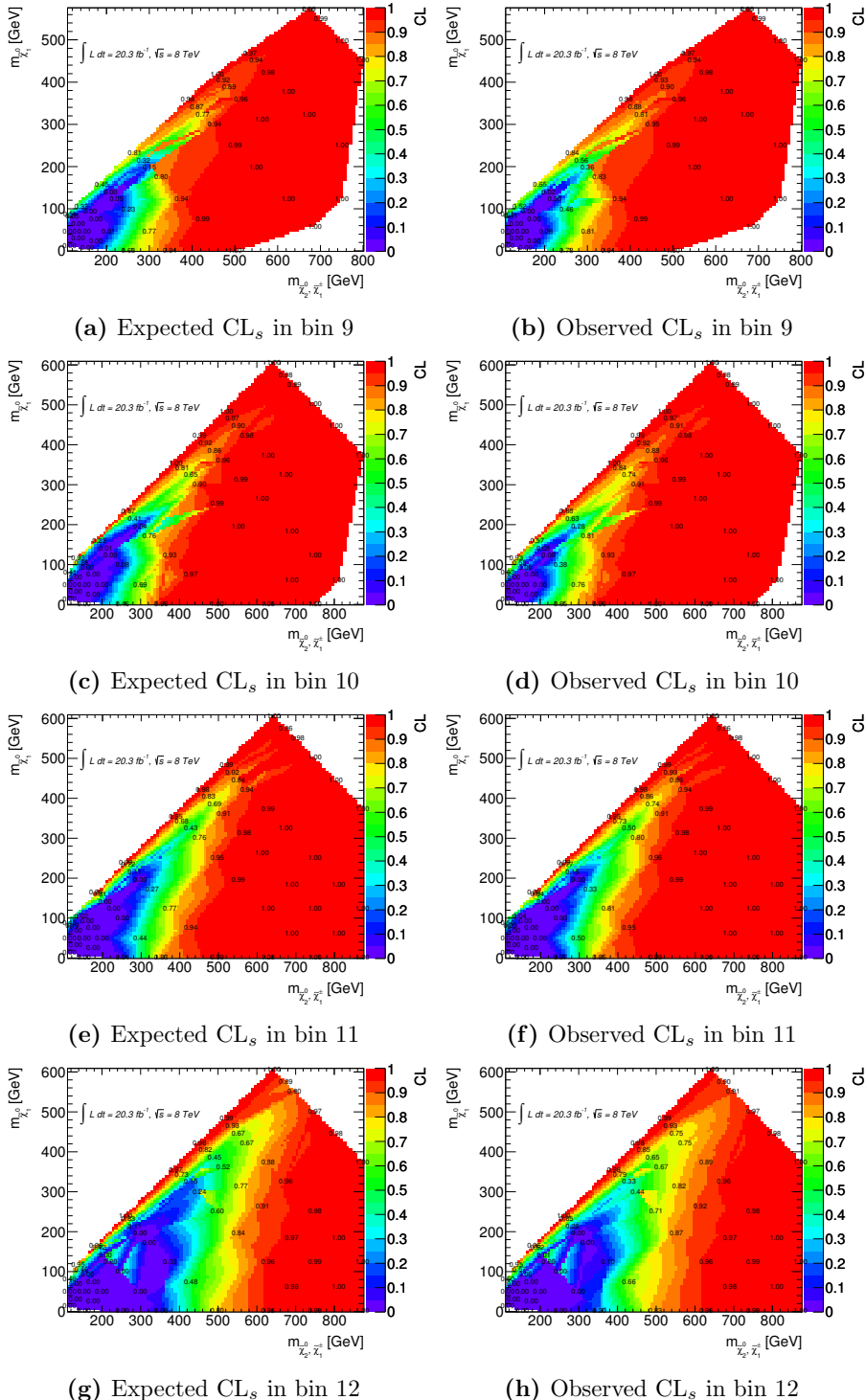


Figure 159: Expected (left) and observed (right) CL_s values for the $\tilde{\ell}_L$ mediated simplified model in the four bins where $m_{\text{SFOS}} \in [60, 81.2]$ GeV.

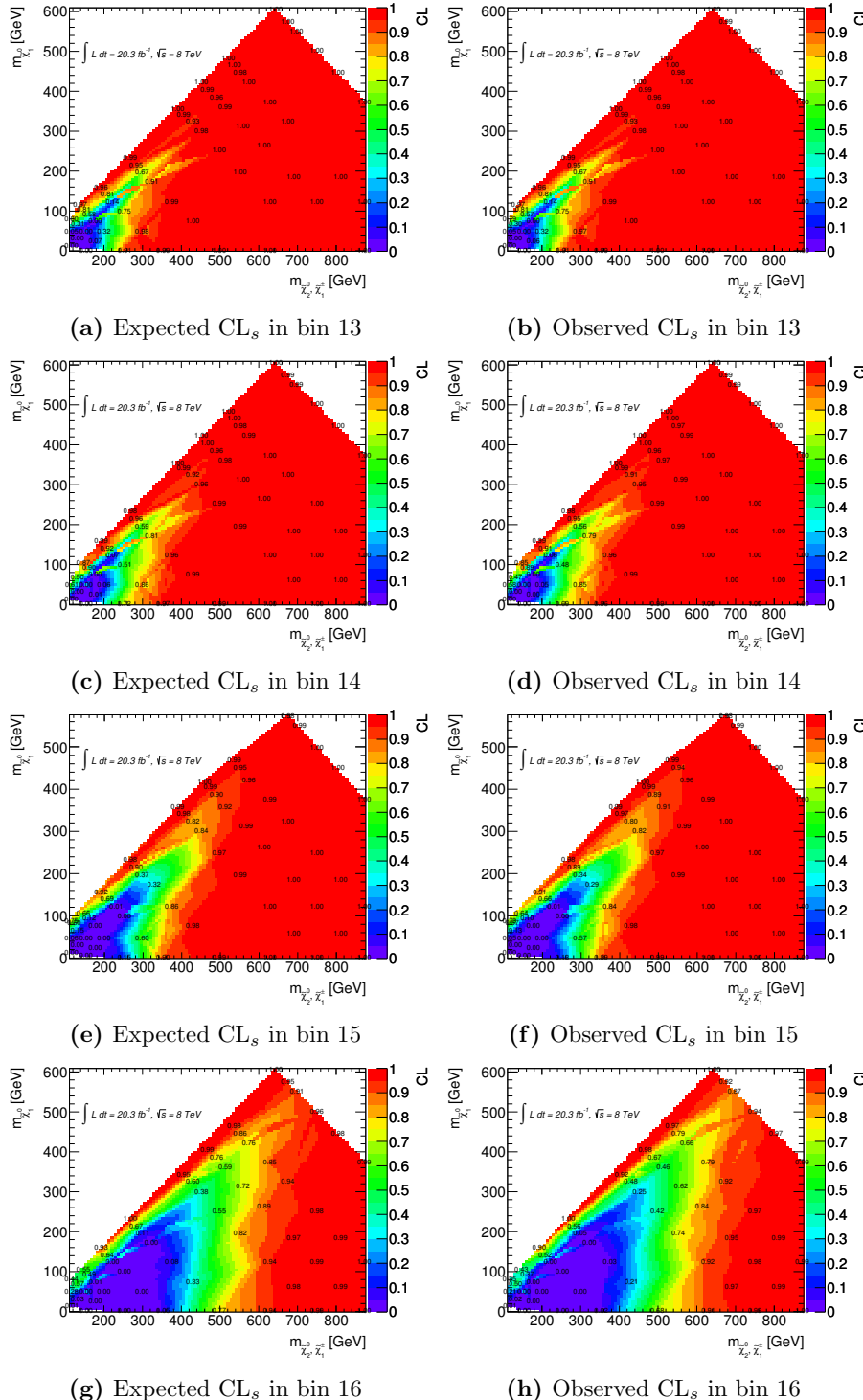


Figure 160: Expected (left) and observed (right) CL_s values for the $\tilde{\ell}_L$ mediated simplified model in the four bins where $m_{\text{SFOS}} \in [81.2, 101.2]$ GeV.

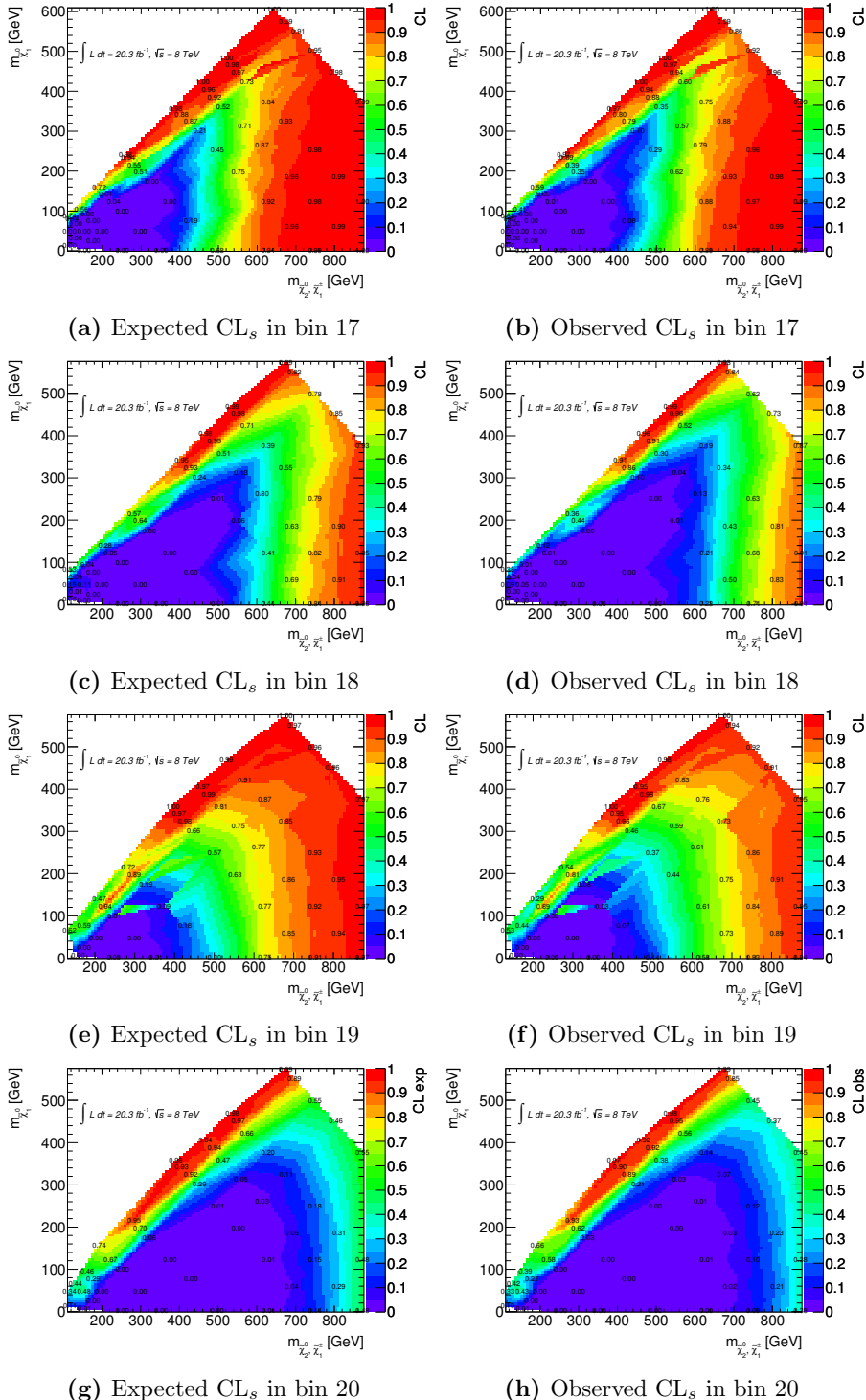


Figure 161: Expected (left) and observed (right) CL_s values for the $\tilde{\ell}_L$ mediated simplified model in the four bins where $m_{\text{SFOS}} \in [81.2, \infty]$ GeV.

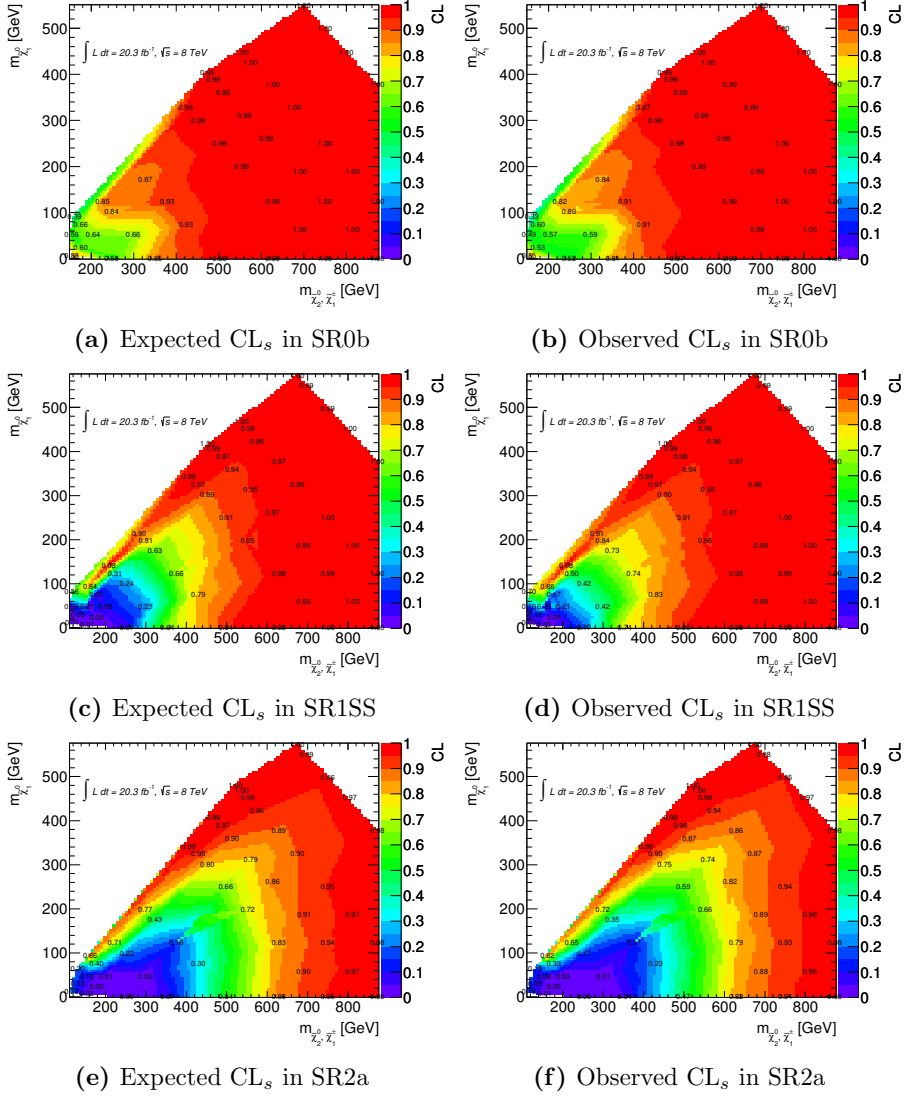


Figure 162: Expected (left) and observed (right) CL_s values for the \tilde{l}_L mediated simplified model in the unbinned signal regions.

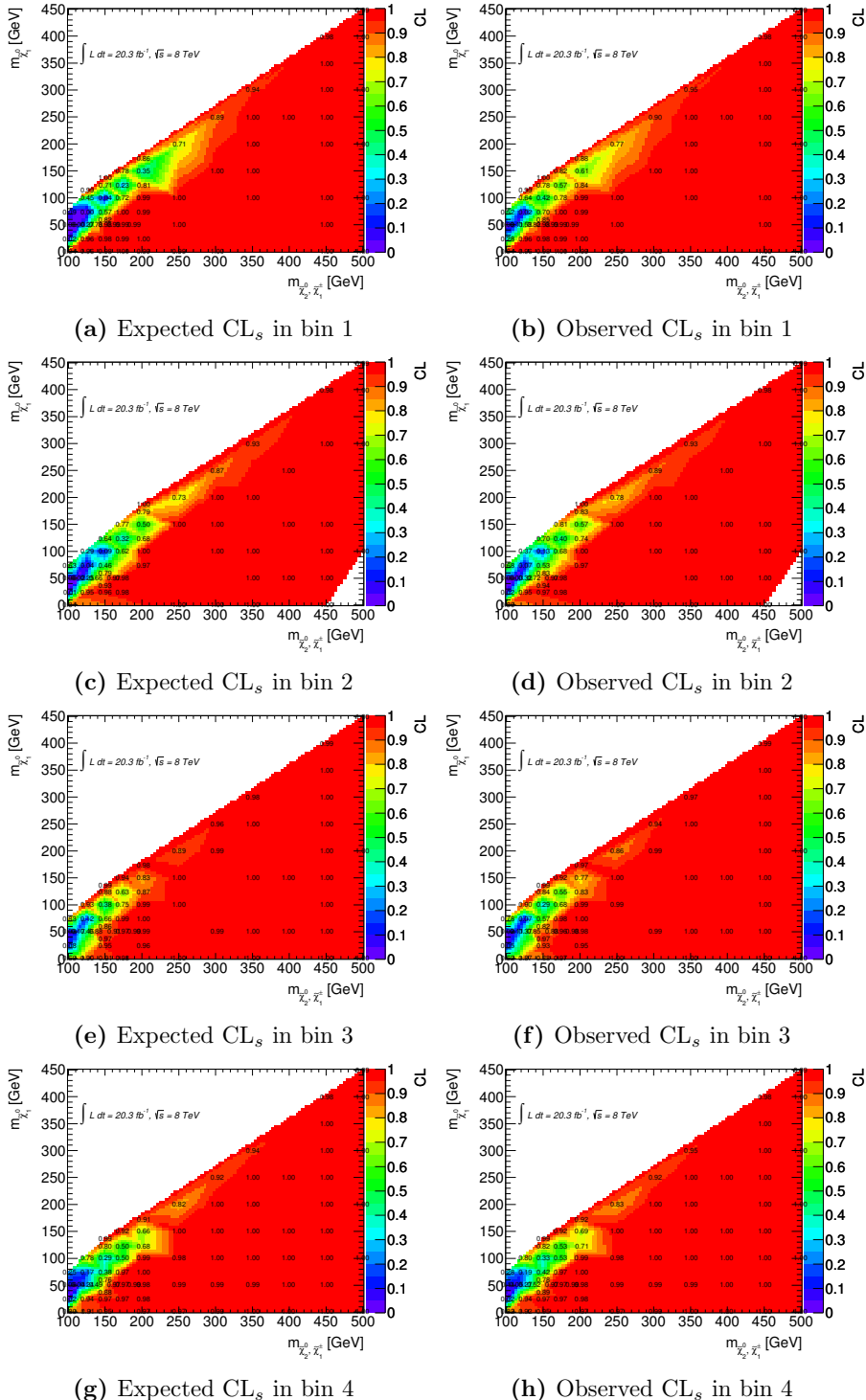


Figure 163: Expected (left) and observed (right) CL_s values for the WZ mediated simplified model in the four bins where $m_{\text{SFOS}} \in [12, 40] \text{ GeV}$.

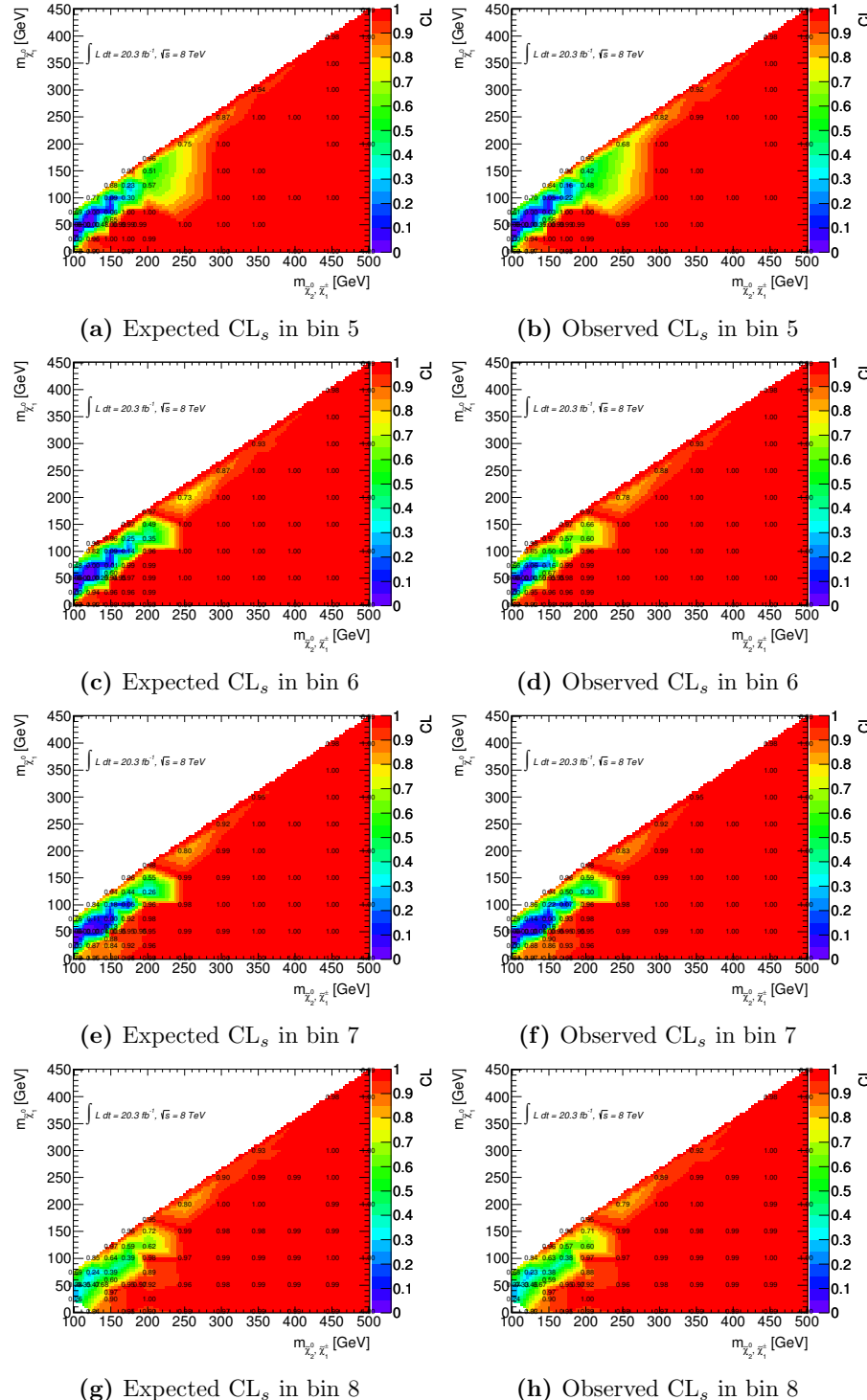


Figure 164: Expected (left) and observed (right) CL_s values for the WZ mediated simplified model in the four bins where $m_{\text{SFOS}} \in [40, 60]$ GeV.

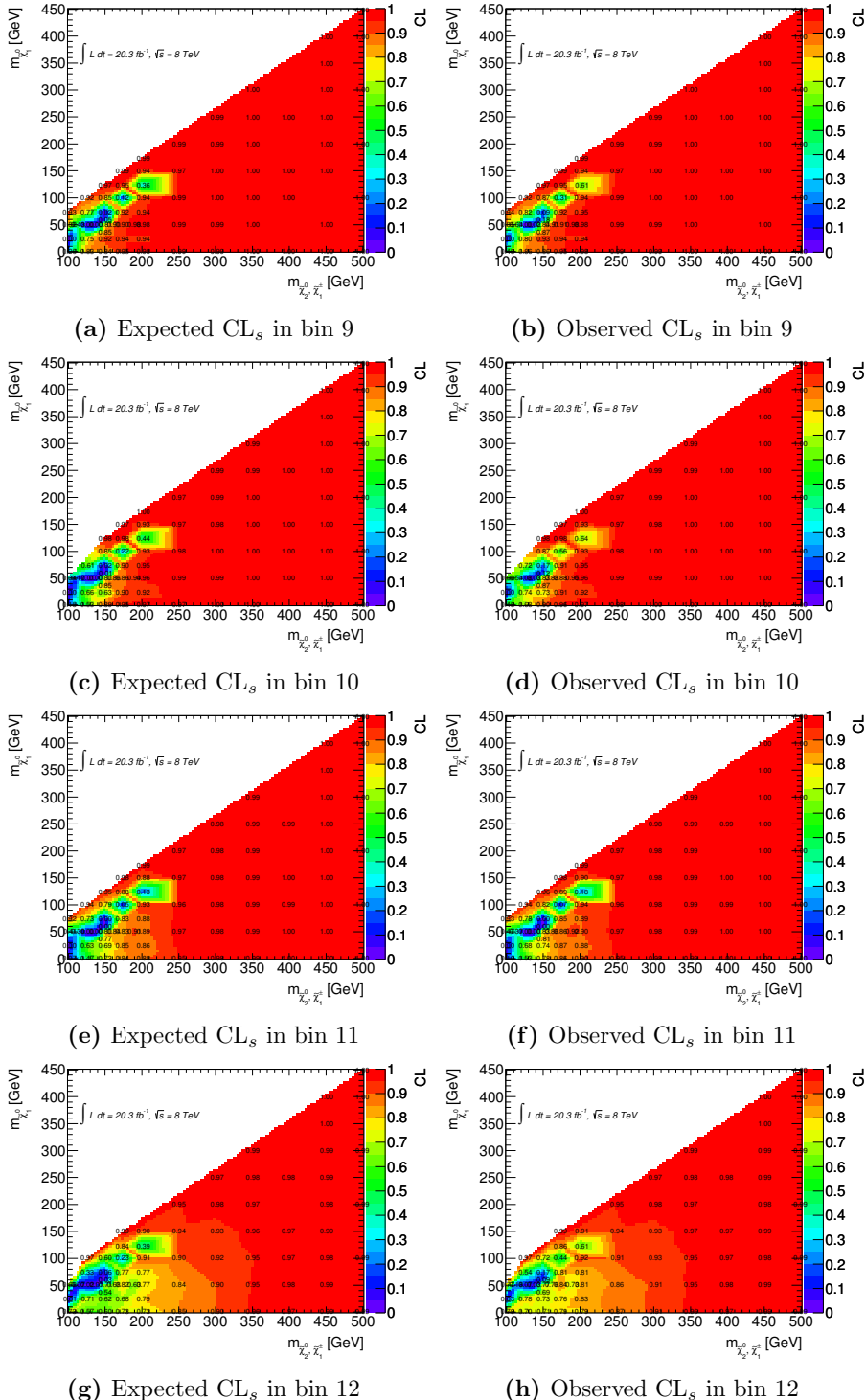


Figure 165: Expected (left) and observed (right) CL_s values for the WZ mediated simplified model in the four bins where $m_{\text{SFOS}} \in [60, 81.2]$ GeV.

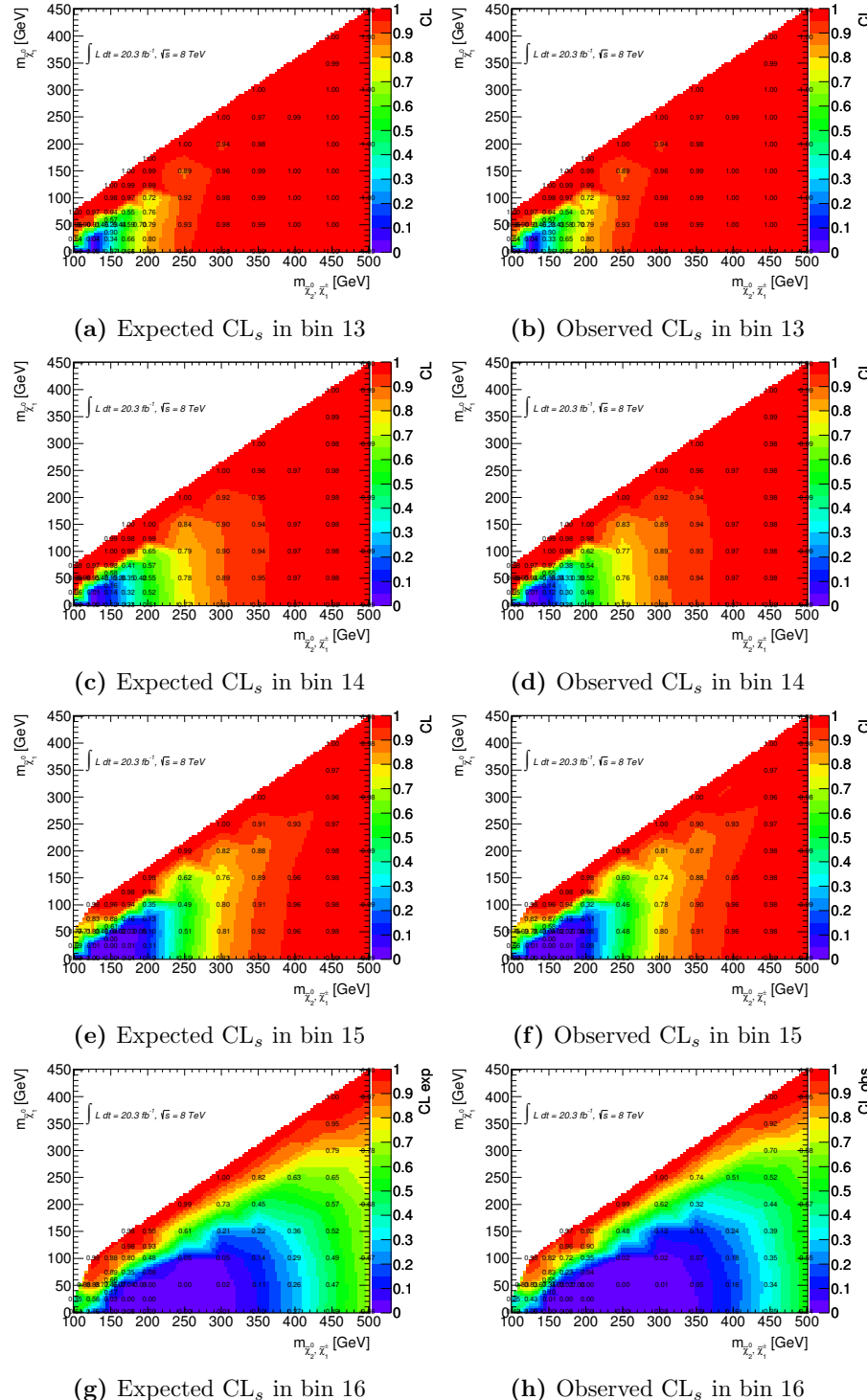


Figure 166: Expected (left) and observed (right) CL_s values for the WZ mediated simplified model in the four bins where $m_{\text{SFOS}} \in [81.2, 101.2]$ GeV.

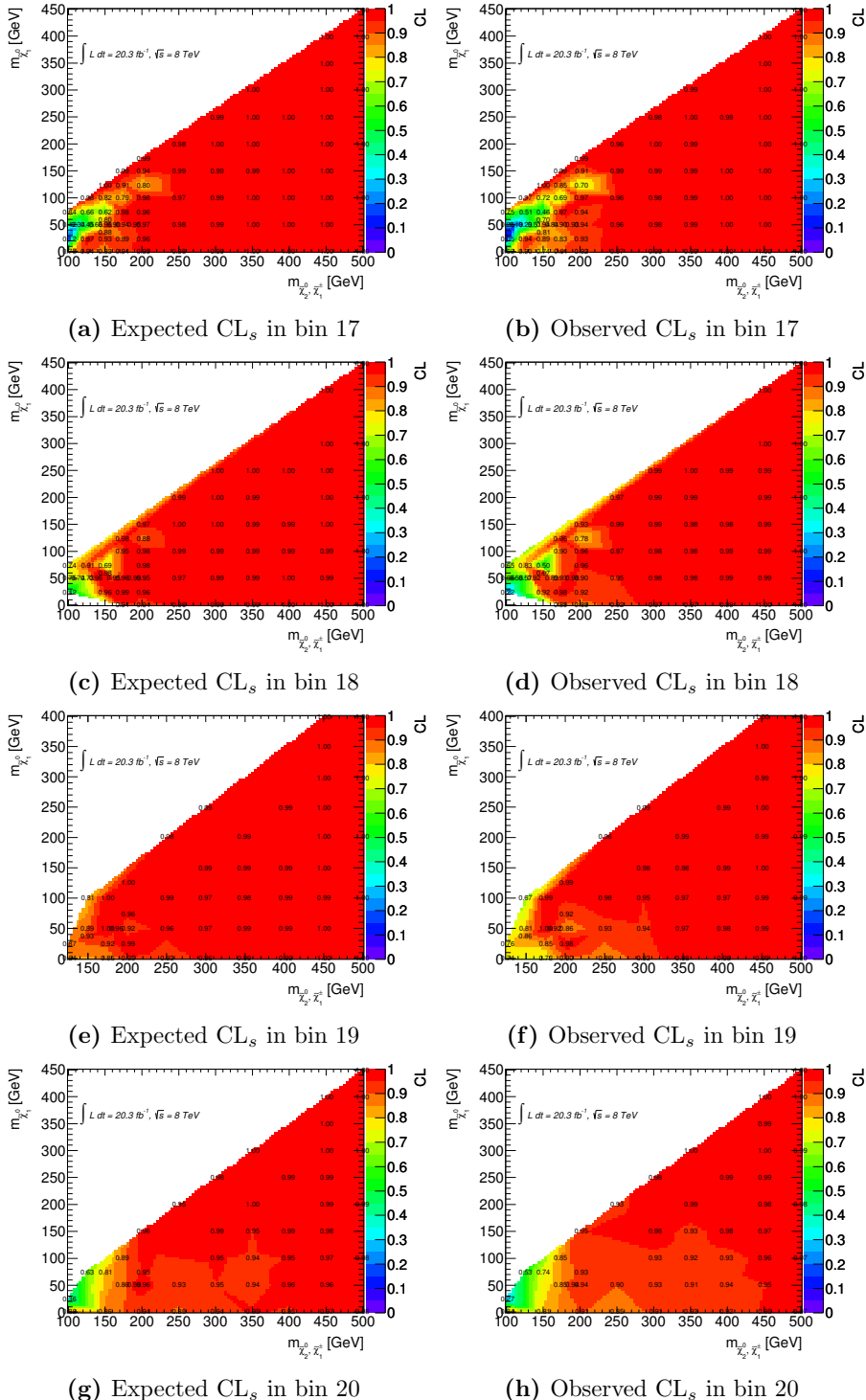


Figure 167: Expected (left) and observed (right) CL_s values for the WZ mediated simplified model in the four bins where $m_{\text{SFOS}} \in [101.2, \infty]$ GeV.

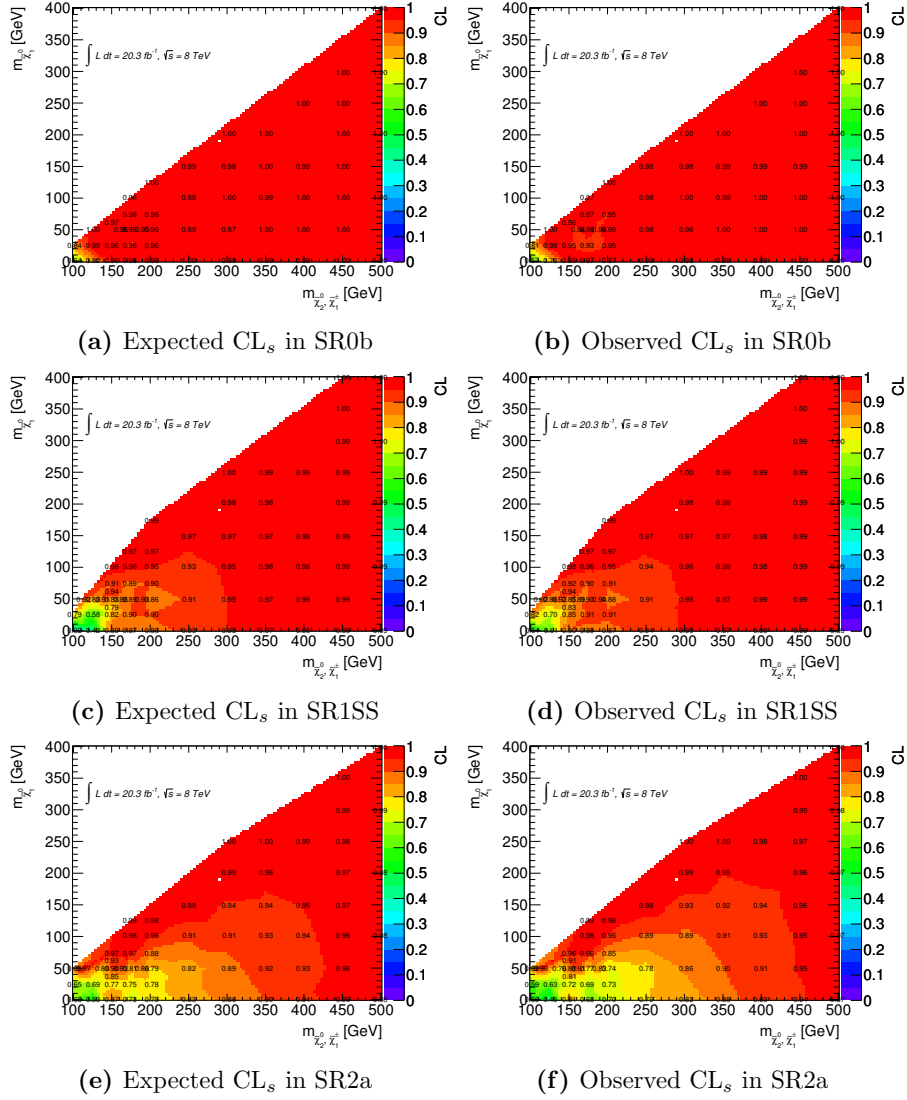


Figure 168: Expected (left) and observed (right) CL_s values for the WZ mediated simplified model in the unbinned signal regions.

Appendix F Upper limit on model cross-section scans in μ

The following figures show the scan in μ to derive the upperlimit on model cross-sections. The model is said to be excluded for the value of μ at which the CL_s falls below 0.05. Figures 178 - 185 show the WZ mediated simplified model, Figures 169 - 177 show the $\tilde{\ell}_L$ mediated simplified model.

Most of the upper limits are derived with the old method, a few (see e.g. Figure 173f) are also calculated with the new method. See Section 9.3 for a discussion of the two methods.

As always, to not blow up this thesis, only the WZ and the $\tilde{\ell}_L$ mediated simplified models are shown.

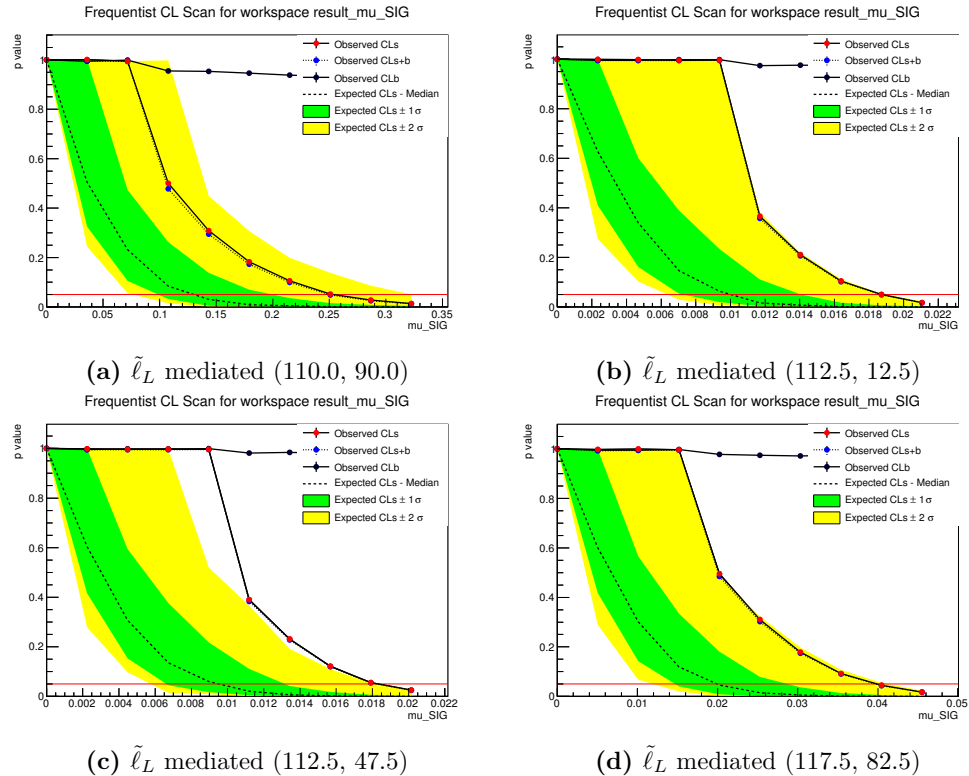


Figure 169: Scan for different values of μ for upper limits on model cross-sections. The numbers in parentheses are $(m_{\tilde{\chi}_1^\pm}, m_{\tilde{\chi}_1^0})$

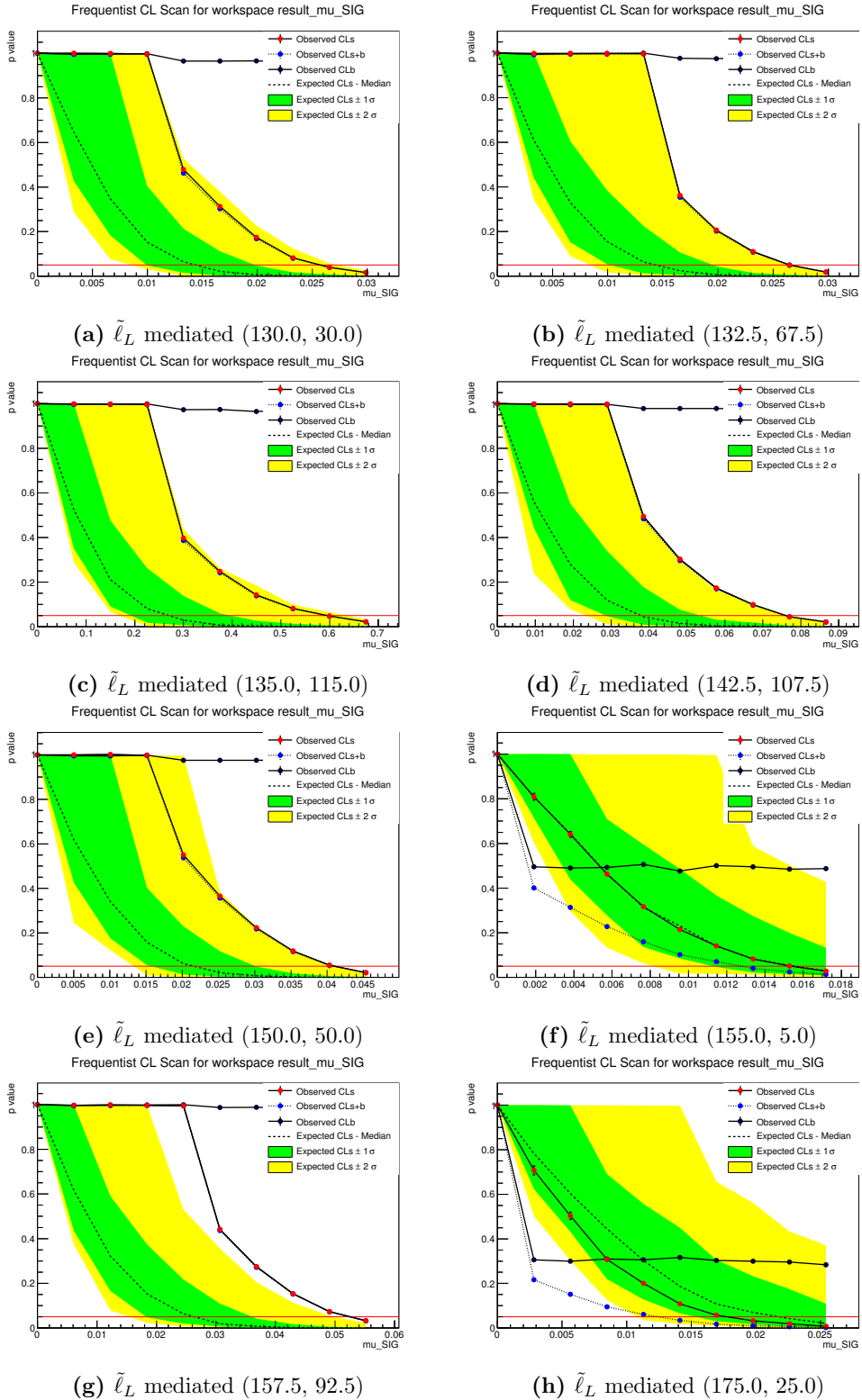


Figure 170: Scan for different values of μ for upper limits on model cross-sections. The numbers in parentheses are $(m_{\tilde{\chi}_1^\pm}, m_{\tilde{\chi}_1^0})$

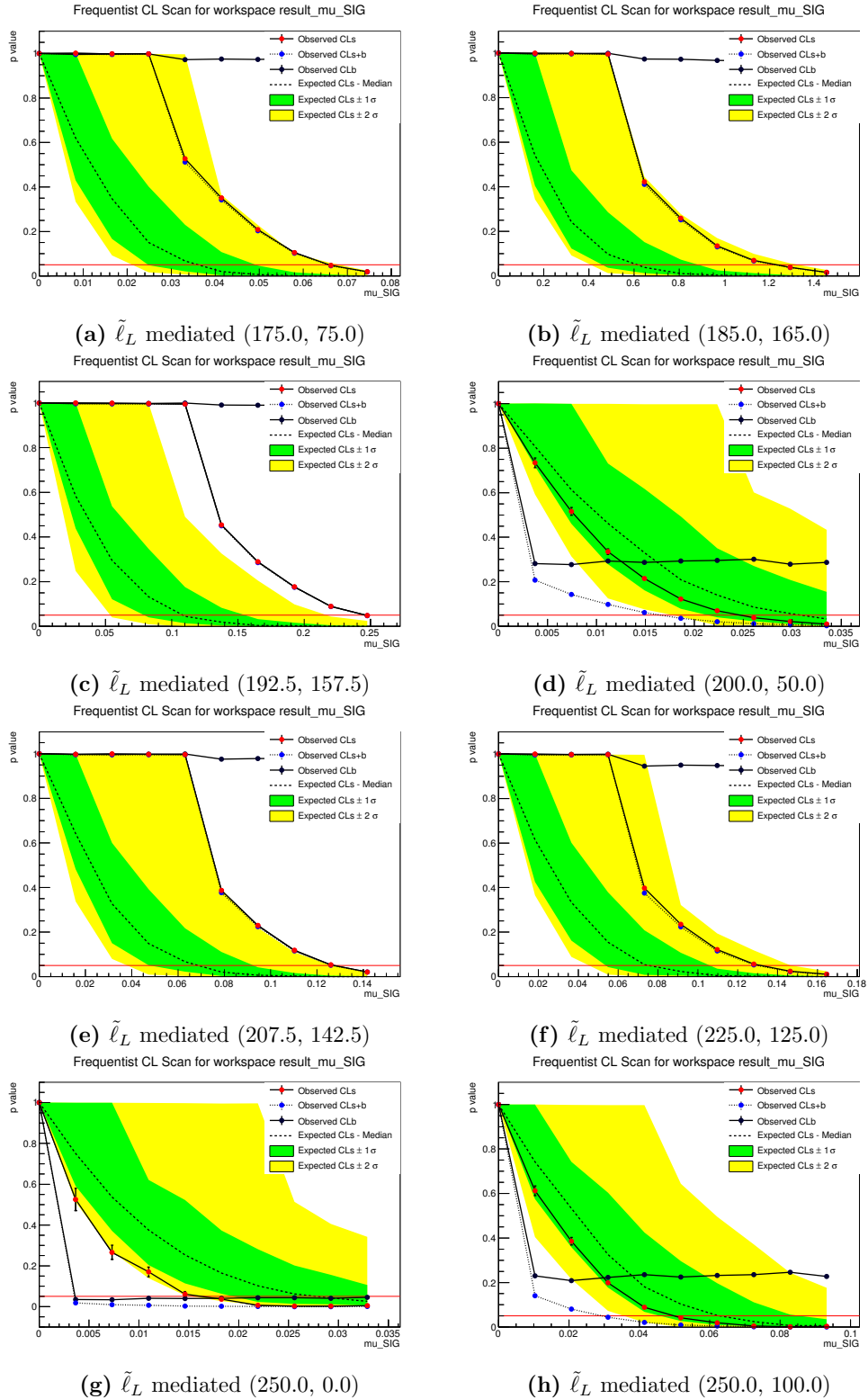


Figure 171: Scan for different values of μ for upper limits on model cross-sections. The numbers in parentheses are $(m_{\tilde{\chi}_1^\pm}, m_{\tilde{\chi}_1^0})$.

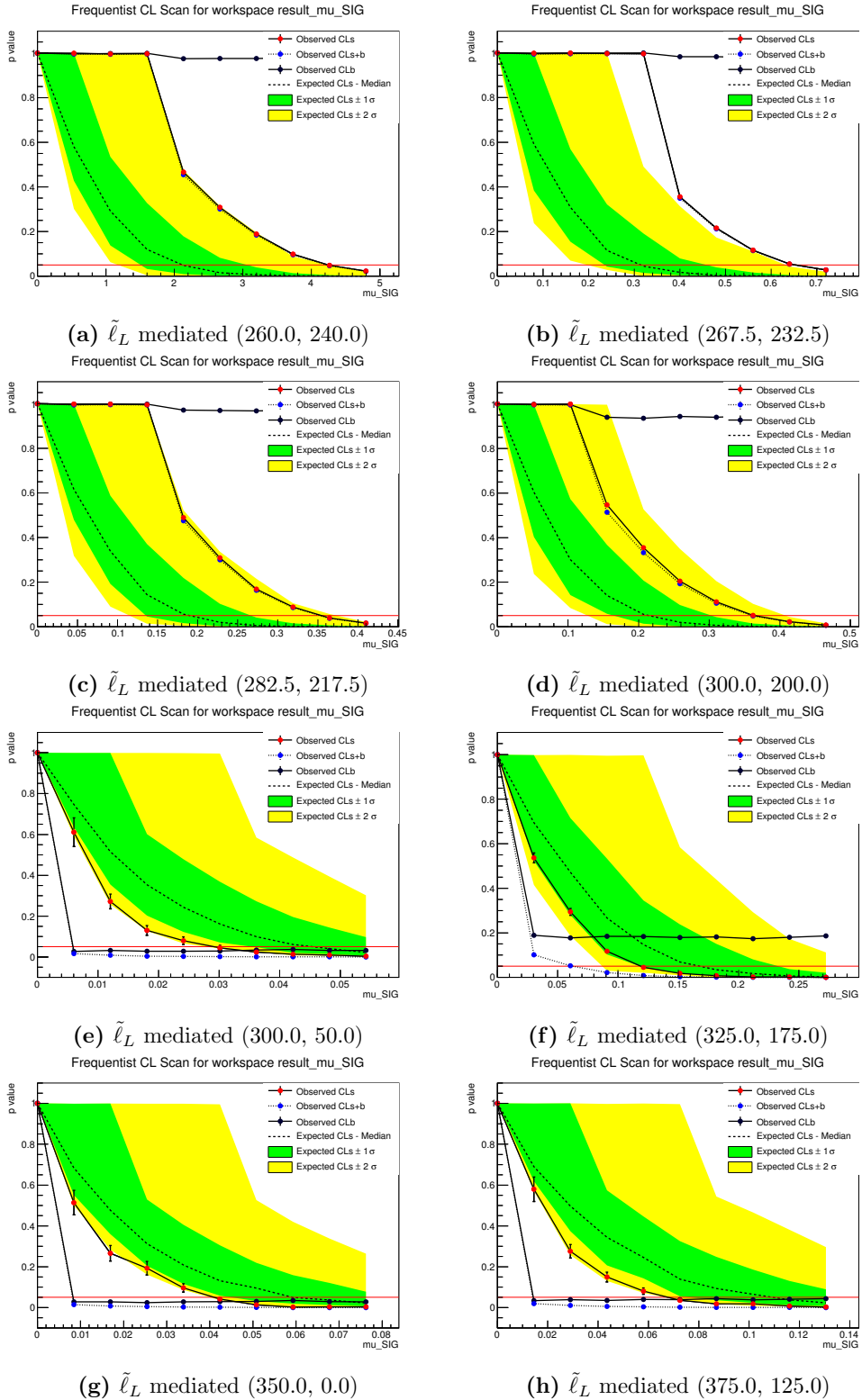


Figure 172: Scan for different values of μ for upper limits on model cross-sections. The numbers in parentheses are $(m_{\tilde{\chi}_1^\pm}, m_{\tilde{\chi}_1^0})$

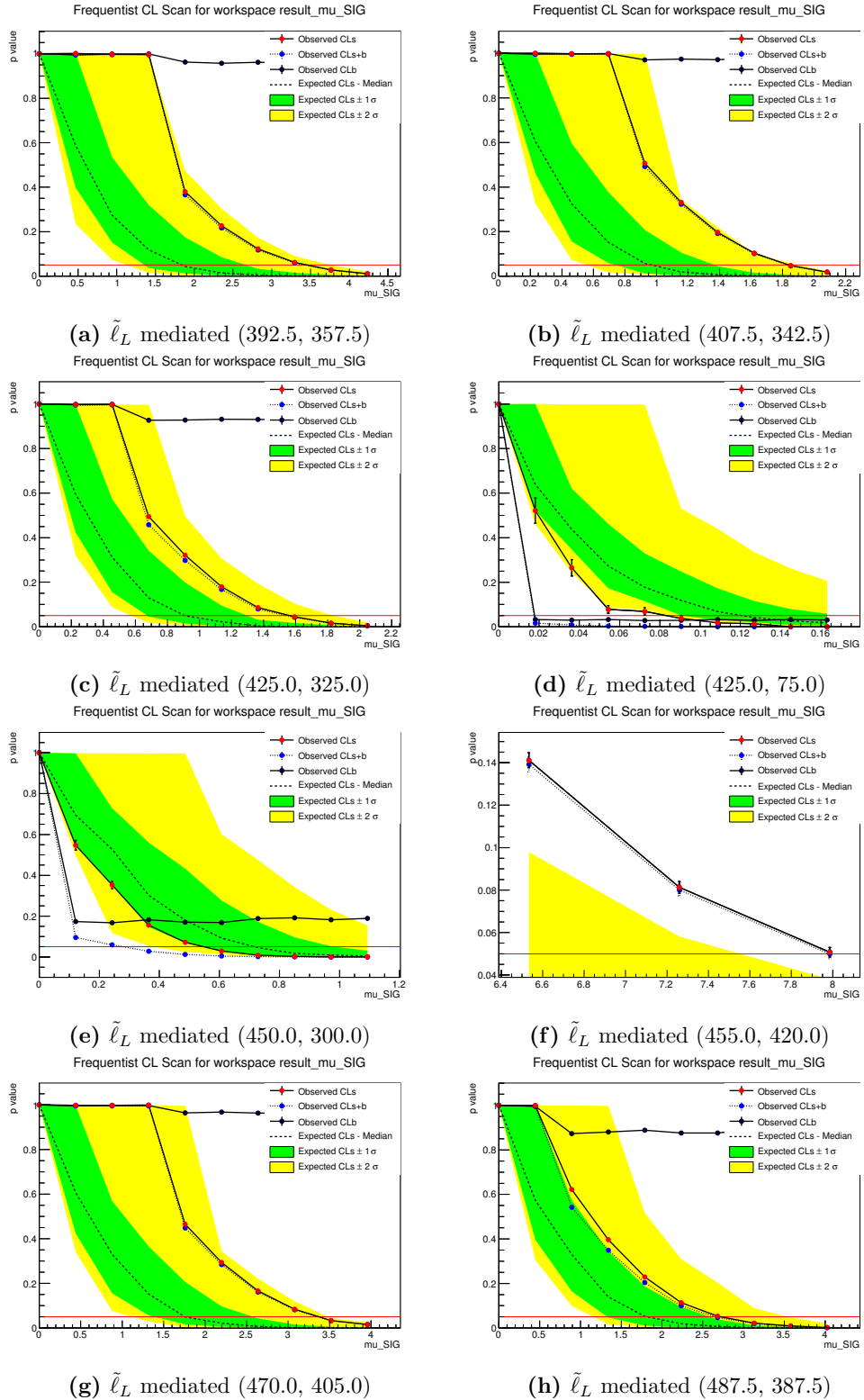


Figure 173: Scan for different values of μ for upper limits on model cross-sections. The numbers in parentheses are $(m_{\tilde{\chi}_1^\pm}, m_{\tilde{\chi}_1^0})$

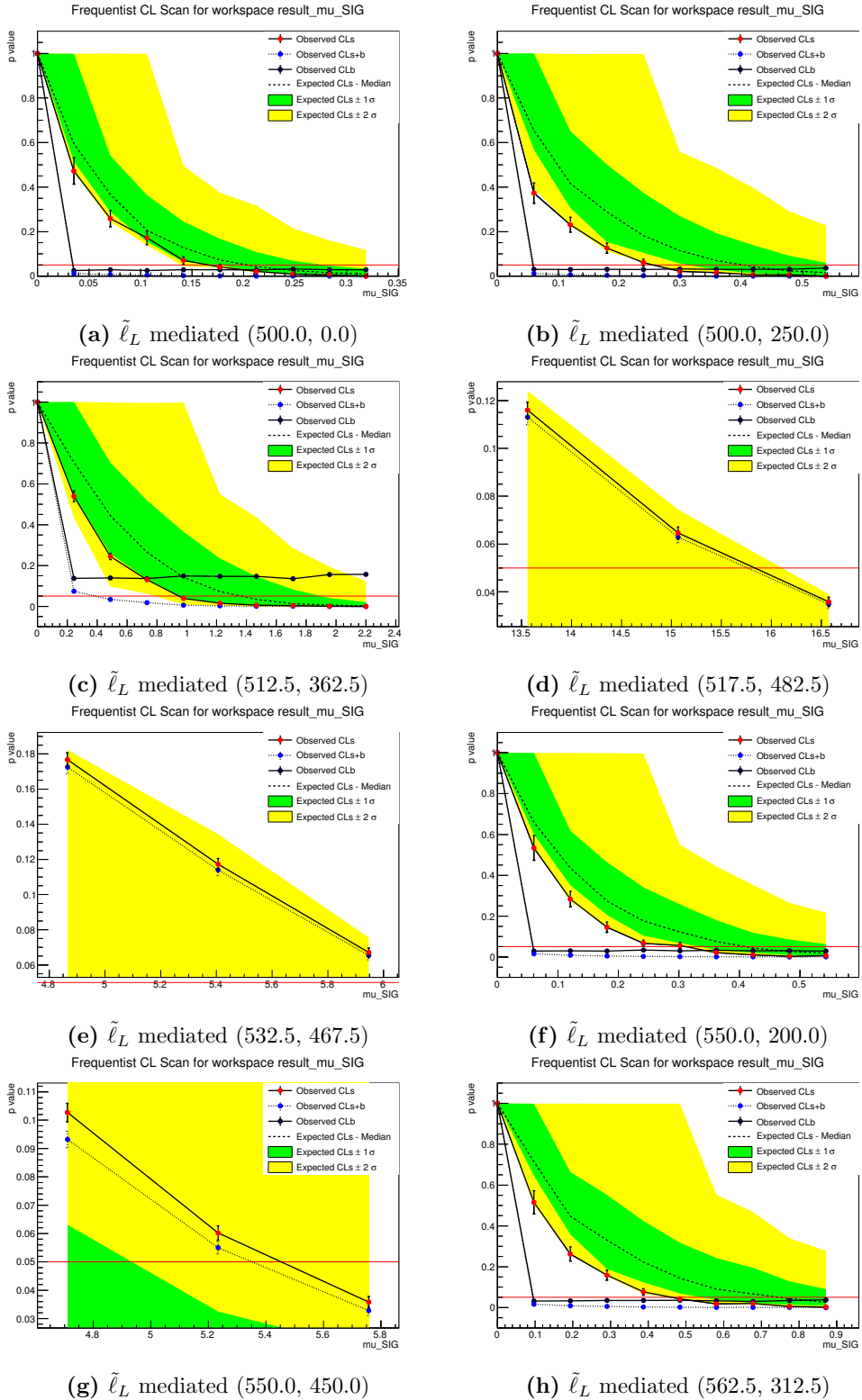


Figure 174: Scan for different values of μ for upper limits on model cross-sections. The numbers in parentheses are $(m_{\tilde{\chi}_1^\pm}, m_{\tilde{\chi}_1^0})$

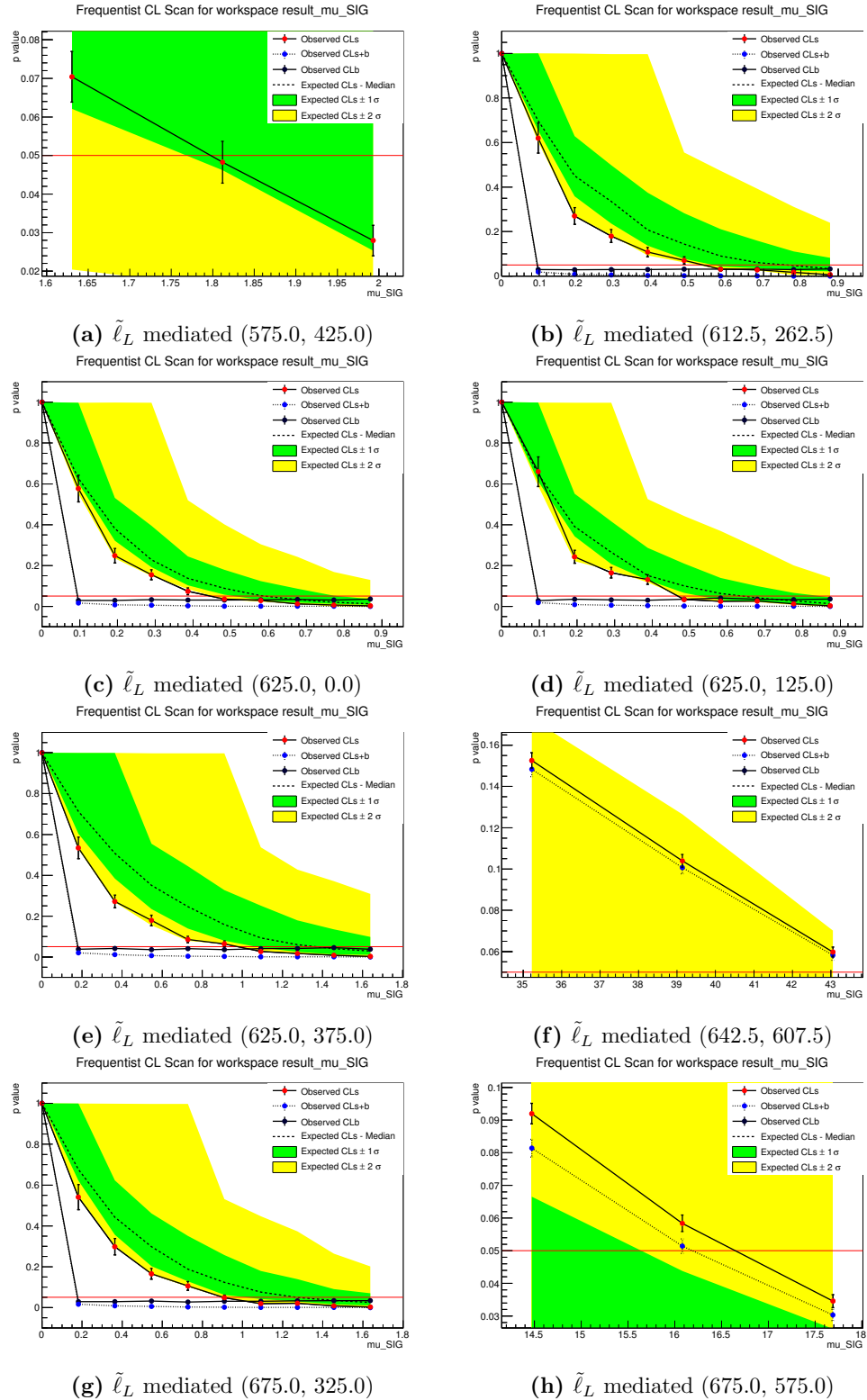


Figure 175: Scan for different values of μ for upper limits on model cross-sections. The numbers in parentheses are $(m_{\tilde{\chi}_1^\pm}, m_{\tilde{\chi}_1^0})$

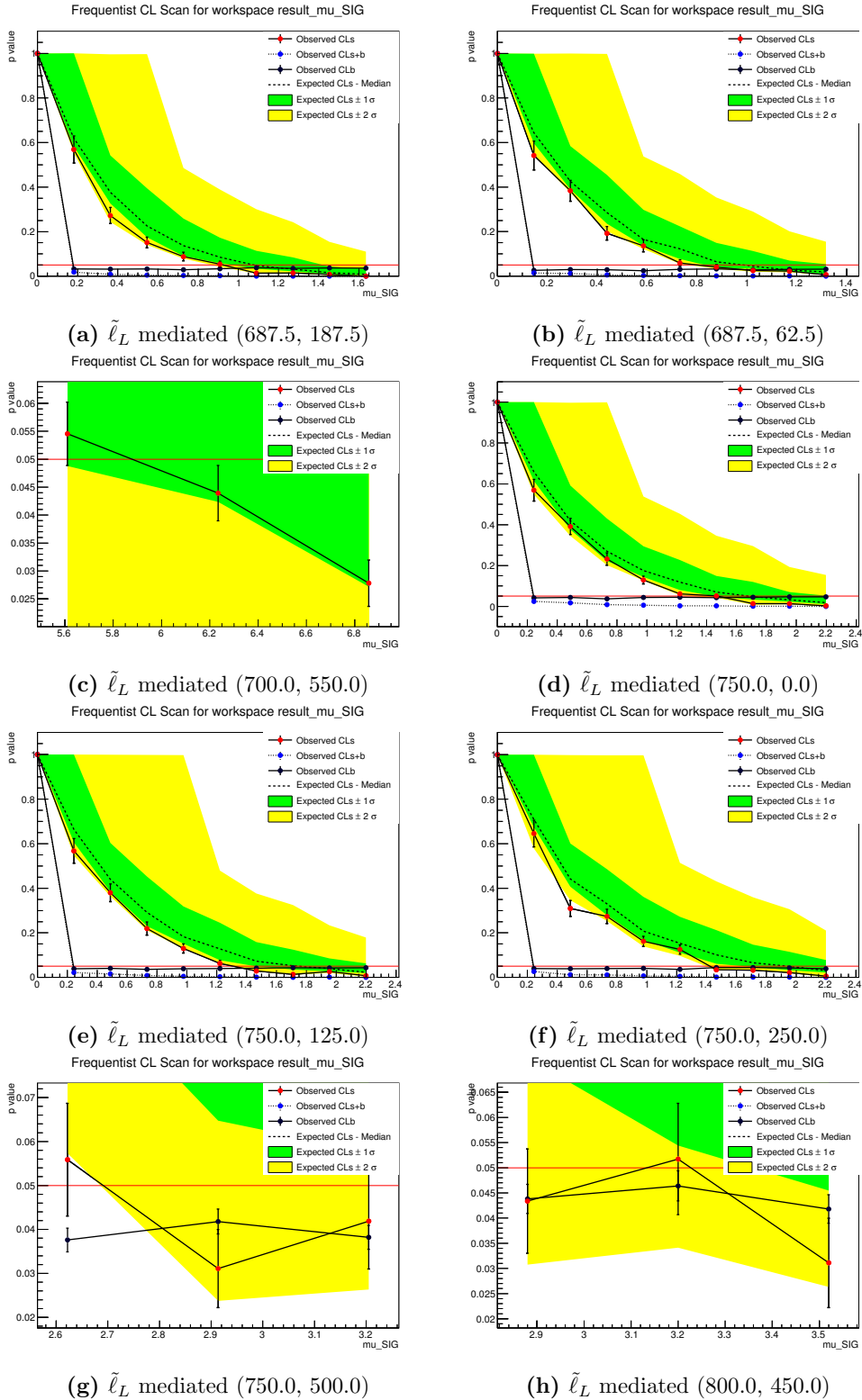


Figure 176: Scan for different values of μ for upper limits on model cross-sections. The numbers in parentheses are $(m_{\tilde{\chi}_1^\pm}, m_{\tilde{\chi}_1^0})$

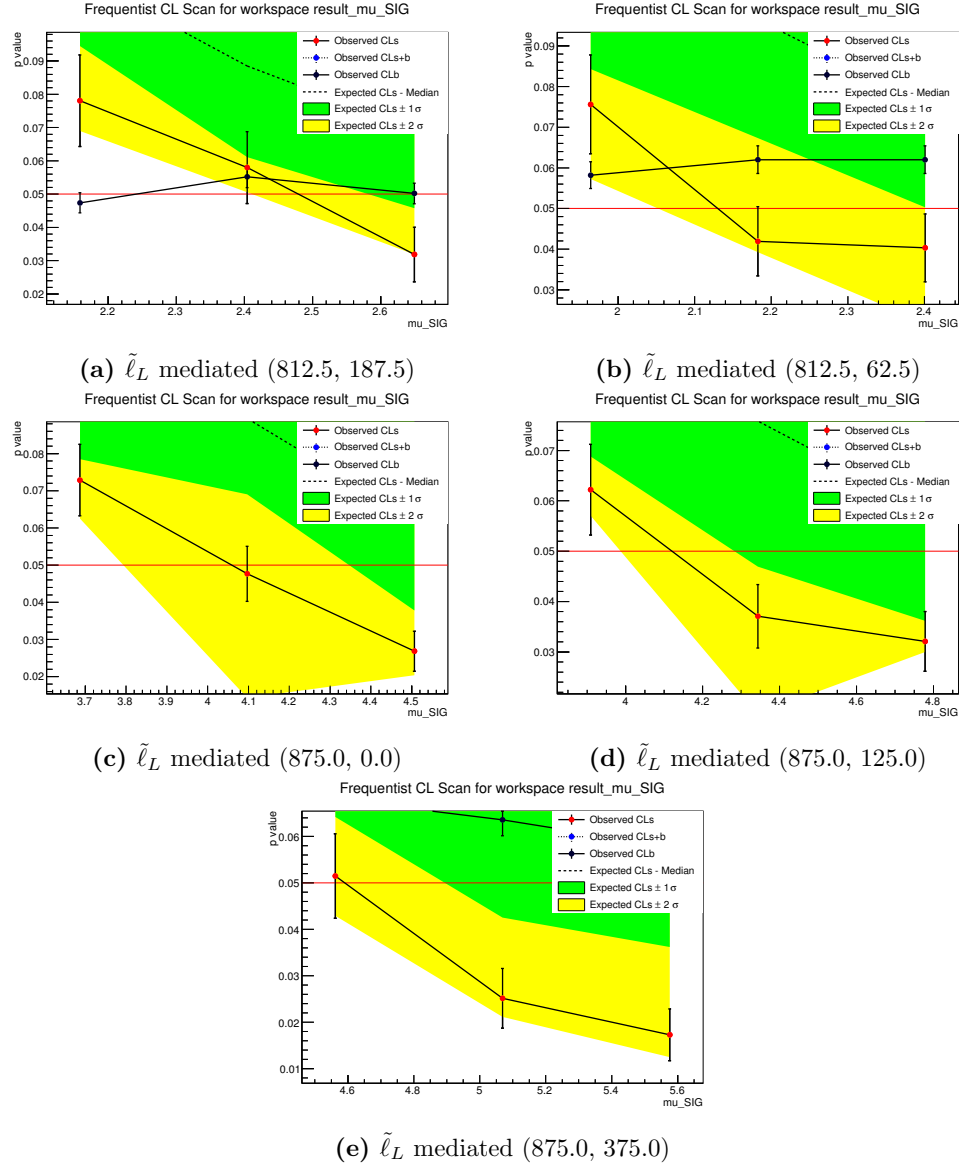


Figure 177: Scan for different values of μ for upper limits on model cross-sections. The numbers in parentheses are $(m_{\tilde{\chi}_1^\pm}, m_{\tilde{\chi}_1^0})$

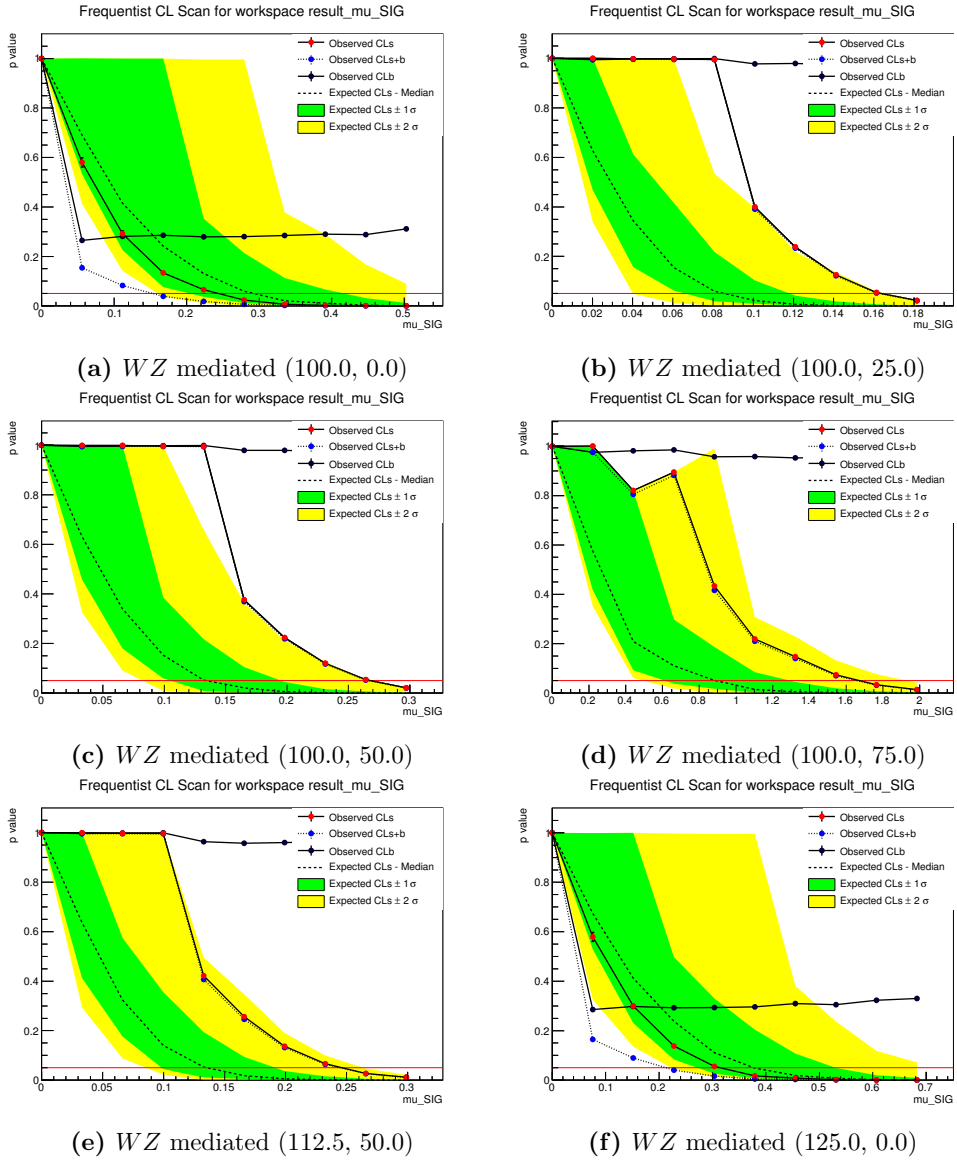


Figure 178: Scan for different values of μ for upper limits on model cross-sections. The numbers in parentheses are $(m_{\tilde{\chi}_1^\pm}, m_{\tilde{\chi}_1^0})$

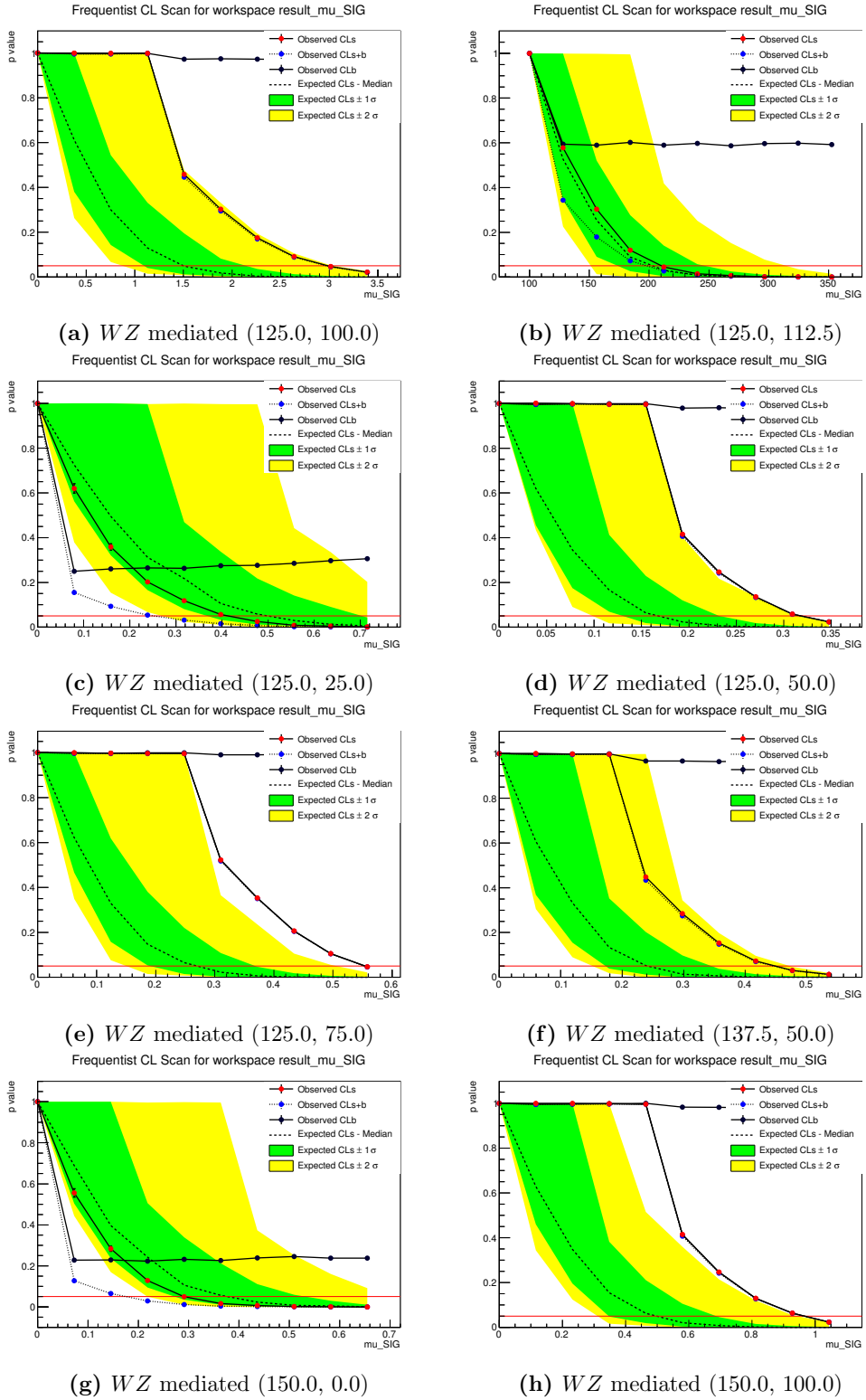


Figure 179: Scan for different values of μ for upper limits on model cross-sections. The numbers in parentheses are $(m_{\tilde{\chi}_1^\pm}, m_{\tilde{\chi}_1^0})$

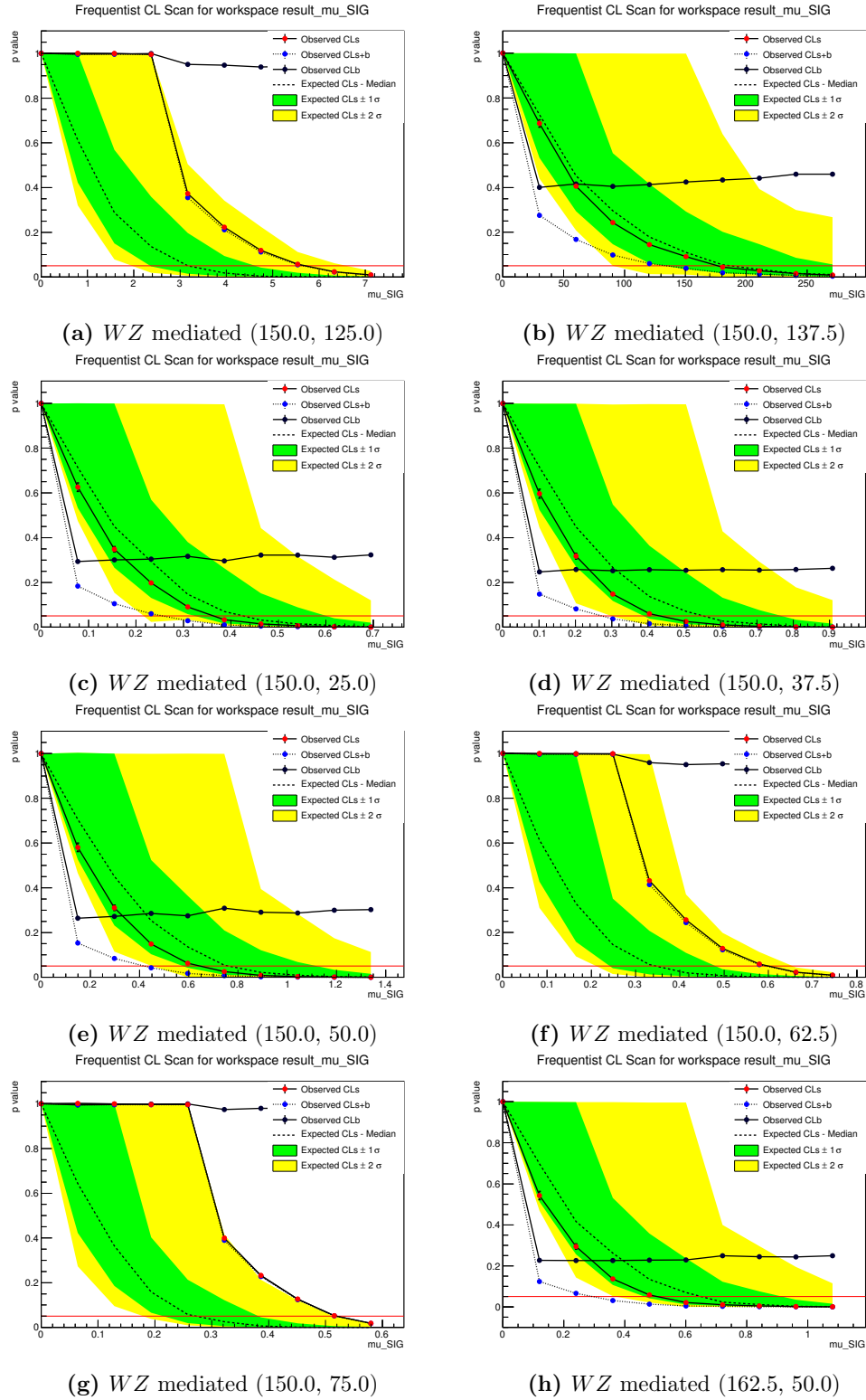


Figure 180: Scan for different values of μ for upper limits on model cross-sections. The numbers in parentheses are $(m_{\tilde{\chi}_1^\pm}, m_{\tilde{\chi}_1^0})$

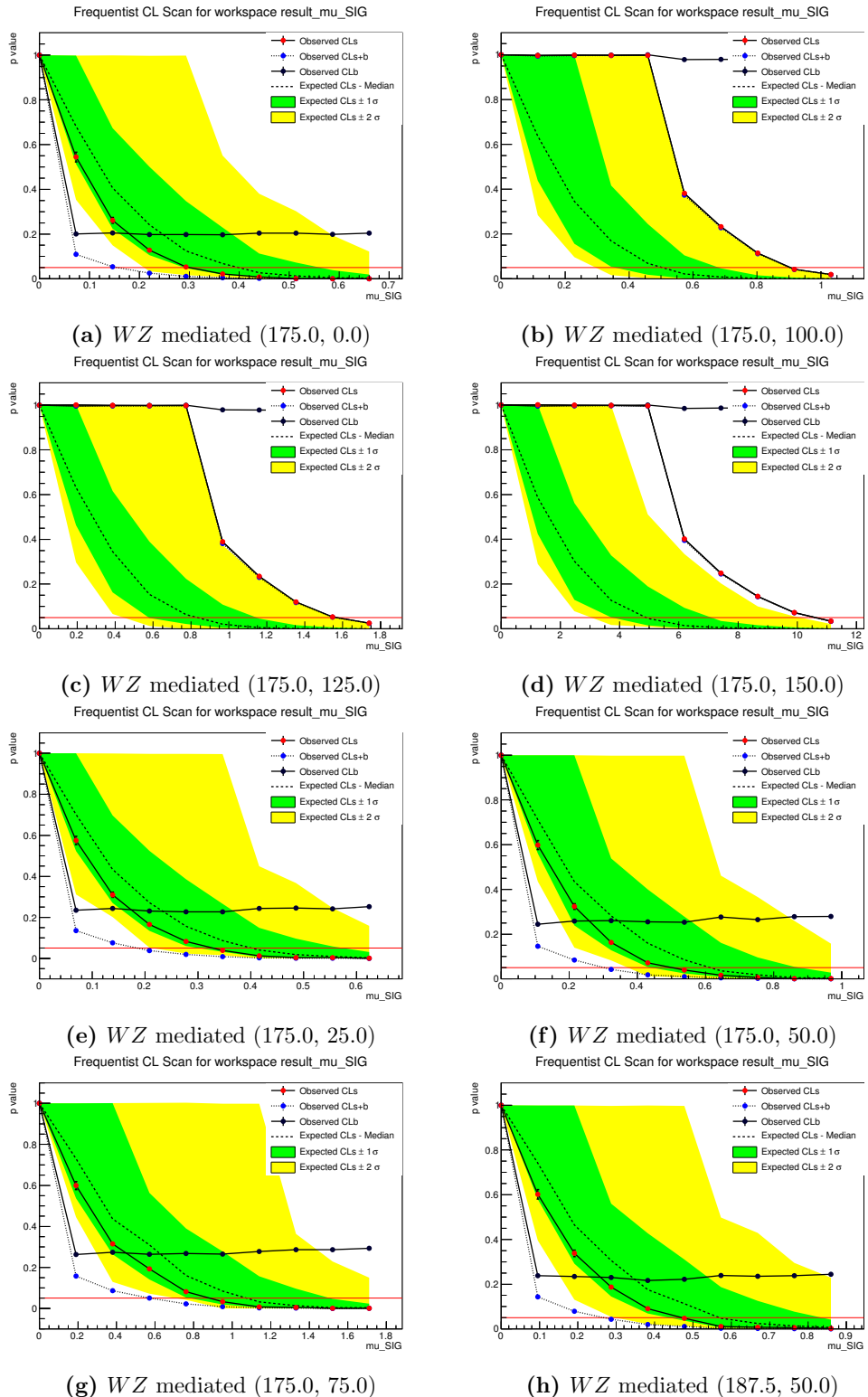


Figure 181: Scan for different values of μ for upper limits on model cross-sections. The numbers in parentheses are $(m_{\tilde{\chi}_1^\pm}, m_{\tilde{\chi}_1^0})$

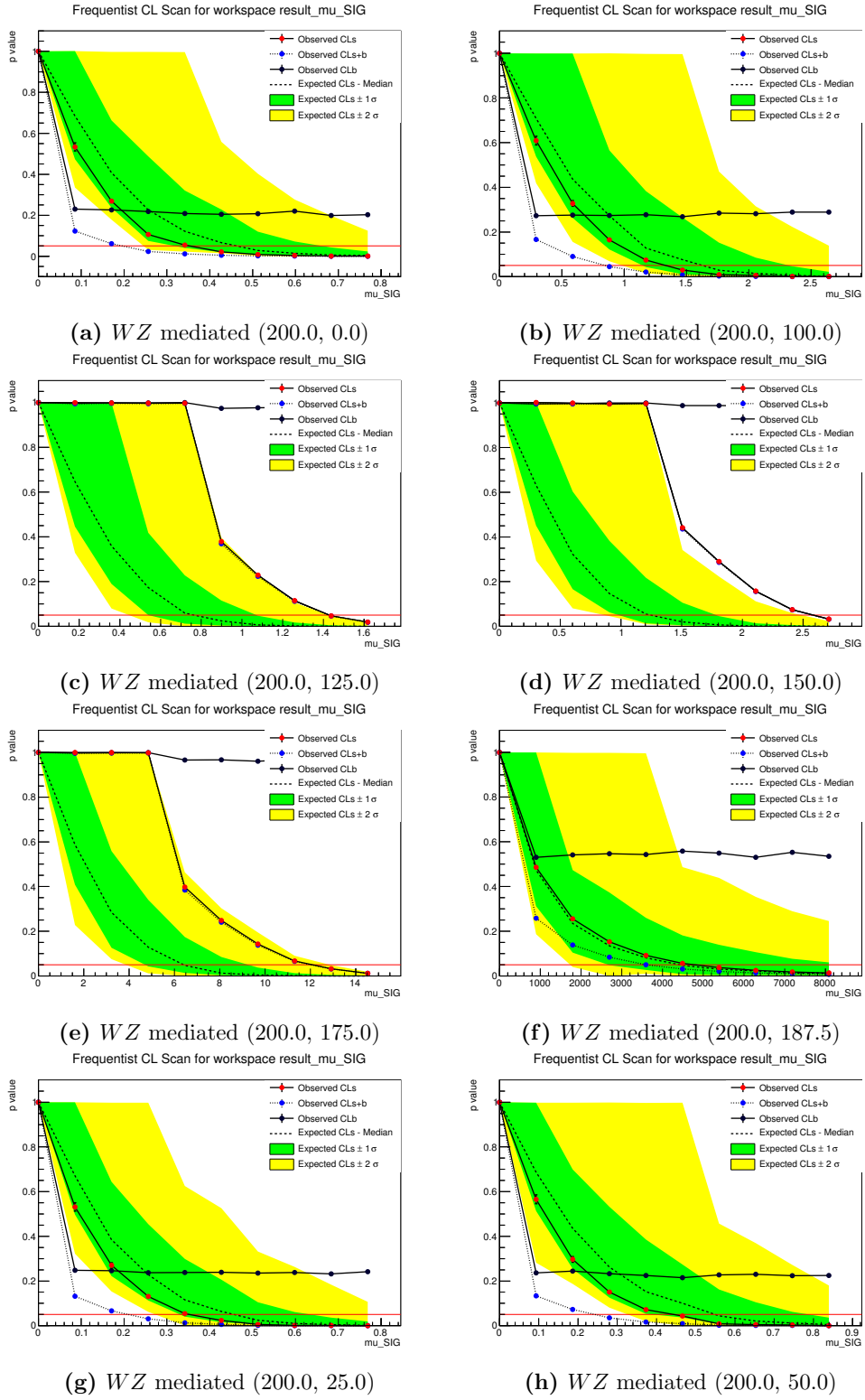


Figure 182: Scan for different values of μ for upper limits on model cross-sections. The numbers in parentheses are $(m_{\tilde{\chi}_1^\pm}, m_{\tilde{\chi}_1^0})$

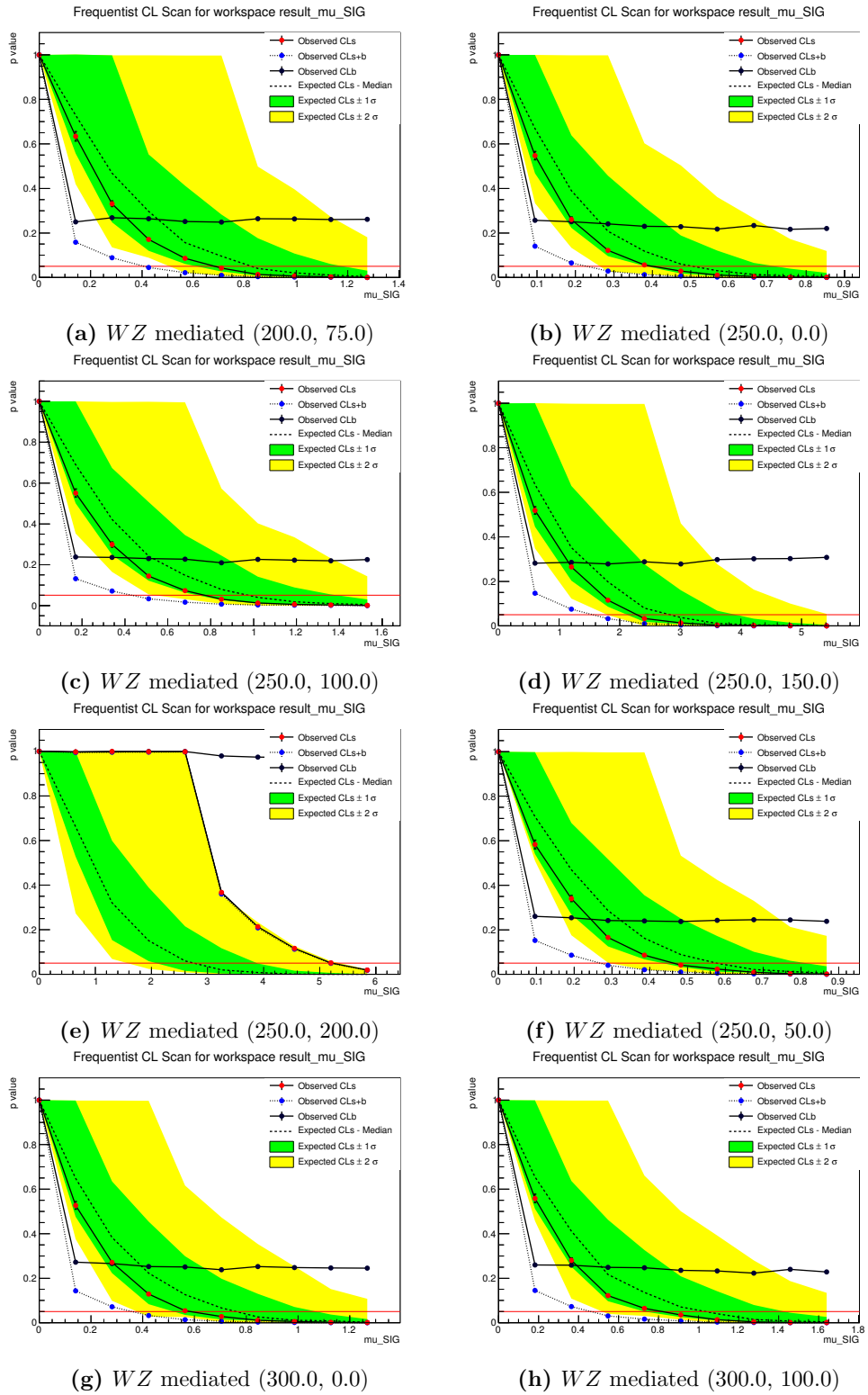


Figure 183: Scan for different values of μ for upper limits on model cross-sections. The numbers in parentheses are $(m_{\tilde{\chi}_1^\pm}, m_{\tilde{\chi}_1^0})$

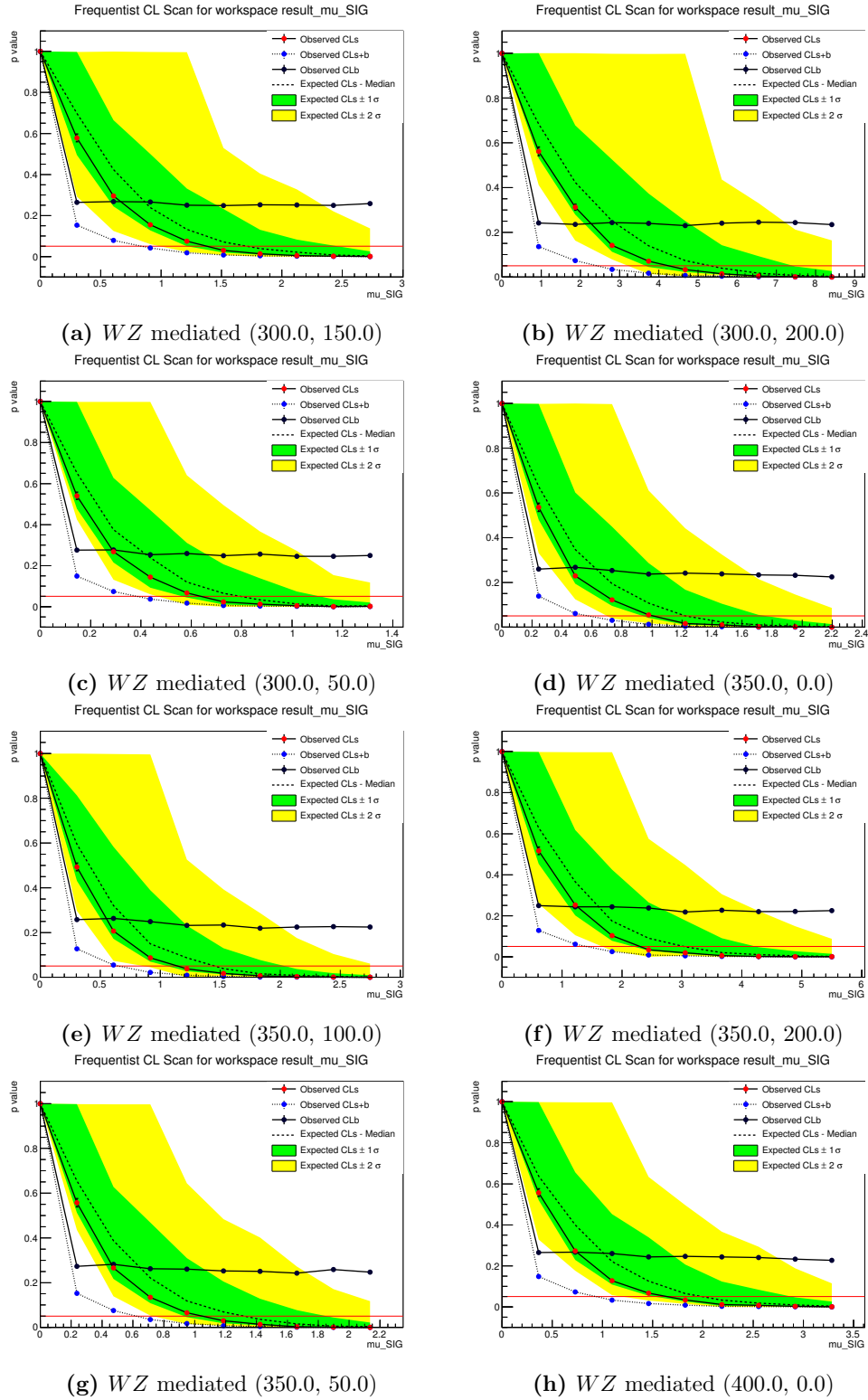


Figure 184: Scan for different values of μ for upper limits on model cross-sections. The numbers in parentheses are $(m_{\tilde{\chi}_1^\pm}, m_{\tilde{\chi}_1^0})$

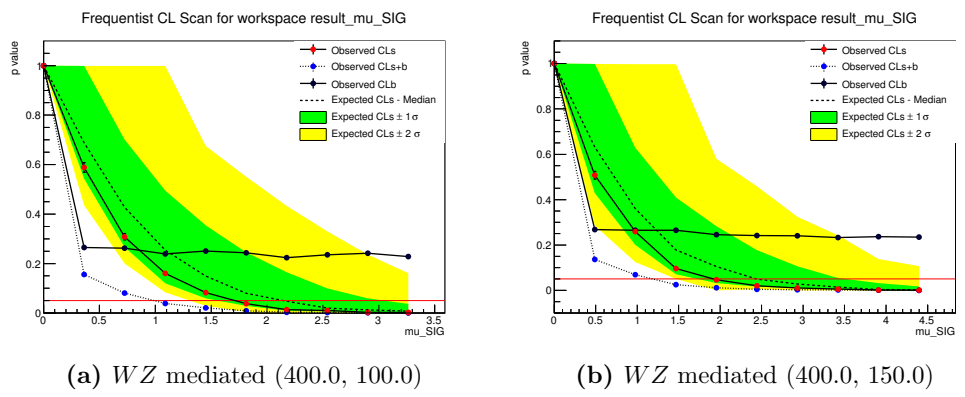


Figure 185: Scan for different values of μ for upper limits on model cross-sections. The numbers in parentheses are $(m_{\tilde{\chi}_1^\pm}, m_{\tilde{\chi}_1^0})$

List of Tables

1	Insertion loss (IL) of the different cables used.	27
2	WZ samples used in this analysis. Given are the LO cross-sections, the k -factors, the filter efficiencies and the integrated luminosities per sample. The leptons in the square brackets indicate the applied Powheg filter. All samples are generated with Powheg and showered with Pythia8	38
3	ZZ samples used in this analysis. Given are the LO cross-sections, the k -factors, the filter efficiencies and the integrated luminosities per sample. The leptons in the square brackets indicate the applied Powheg filter. All samples are generated with Powheg and showered with Pythia8 , except the $gg2ZZ$ samples which are generated with JIMMY	40
4	top + V samples used in this analysis. Given are the LO cross-sections, the k -factors and the integrated luminosities per sample. All top + V samples are generated with ALPGEN , the top + Z and the $t\bar{t} + WW$ samples are generated with MADGRAPH . Np gives the number of partons.	40
5	Tribosons samples used in this analysis. Given are the LO cross-sections, the k -factors and the integrated luminosities per sample.	41
6	Higgs samples used in this analysis. Given are the cross-sections, the filter efficiencies and the integrated luminosities per sample. The gluon fusion and the vector boson fusion samples are generated with Powheg and showered with Pythia8 , all other samples are generated and showered with Pythia8 . The cross-sections are calculated at NNLO QCD and NLO electroweak precision, except for $pp \rightarrow t\bar{t} + h$, which is calculated at NLO QCD precision [82].	42
7	$t\bar{t}$ sample used in this analysis. Given is the LO cross-section, the k -factor, the filter efficiency and the integrated luminosity of the sample. It was generated with Powheg , showered with Pythia8 . The filter requests at least one leptonically decaying W boson.	43
8	Single top samples used in this analysis. Given are the LO cross-sections, the k -factors and the integrated luminosities per sample. For all samples, HERWIG is used for fragmentation and hadronisation while JIMMY is used for the underlying event.	43
9	$V + \text{jets}$ samples used in this analysis. Given are the NNLO cross-sections and the integrated luminosities per sample. Np gives the number of partons.	44
10	$V + \gamma$ samples used in this analysis. Given are the LO cross-sections and the integrated luminosities per sample.	45
11	Triggers used in this analysis. Offline threshold is a cut applied on the p_T of the lepton passing the trigger to avoid the turn-on curve and ensure the lepton is on the plateau of the trigger efficiency.	46
12	Different steps of the overlap removal. Steps at the top are performed first. SFOS stands for same flavour opposite sign lepton pair.	49
13	Example of different binnings that are analyzed during signal region optimization scan. Table is best read from top down. Overlapping combinations have not been removed in this Table but during optimization process.	63
14	Summary of the bins in m_{SFOS} , m_T , and E_T^{miss} . The $3\ell Z$ veto is described in 5.6. All units are in GeV.	64
15	Numbers of expected background events splitted by contributions for the 4 bins where $12 < m_{\text{SFOS}} < 40$ GeV. All estimates are taken purely from Monte Carlo. Uncertainties are from limited Monte Carlo statistics only.	72

16	Numbers of expected background events splitted by contributions for the 4 bins where $40 < m_{\text{SFOS}} < 60$ GeV. All estimates are taken purely from Monte Carlo. Uncertainties are from limited Monte Carlo statistics only.	72
17	Numbers of expected background events splitted by contributions for the 4 bins where $60 < m_{\text{SFOS}} < 81.2$ GeV. All estimates are taken purely from Monte Carlo. Uncertainties are from limited Monte Carlo statistics only.	73
18	Numbers of expected background events splitted by contributions for the 4 bins where $81.2 < m_{\text{SFOS}} < 101.2$ GeV. All estimates are taken purely from Monte Carlo. Uncertainties are from limited Monte Carlo statistics only.	73
19	Numbers of expected background events splitted by contributions for the 4 bins where $101.2 < m_{\text{SFOS}} < \infty$ GeV. All estimates are taken purely from Monte Carlo. Uncertainties are from limited Monte Carlo statistics only.	76
20	The other signal regions defined in [2] and [60]. All signal regions shown here are orthogonal to the binned signal region by either selecting at least one τ (SR1 τ , SR2 τ a and SR2 τ b) or by vetoing a same flavour opposite sign lepton pair (SR0 τ b). Except SR2 τ a and SR2 τ b, all signal regions are also orthogonal to each other.	77
21	Summary of the selection requirements for the validation regions. All units are in GeV. Z^* stands for an off-shell Z . The binned validation region VR0 τ b is not in this table.	89
22	Data and background yields in the validation regions, except the binned validation region. Irreducible background components are derived purely from Monte Carlo; reducible components have been computed with the Matrix Method. Uncertainties are statistical and systematic.	91
23	Data and background yields in the binned validation region. Irreducible background components are derived purely from Monte Carlo; reducible components have been computed with the Matrix Method. Uncertainties are statistical and systematic. Only the total Standard Model background Σ SM is shown, not the separate contributions.	92
24	Total irreducible background in the binned signal region. All components are derived purely from Monte Carlo. Uncertainties are statistical and systematic.	103
25	Expected Standard Model background and observed number of events in data in the binned signal region. Irreducible background components are derived purely from Monte Carlo, the numbers split up in components are shown in Table 24. Reducible background is computed with the Matrix Method. Uncertainties are statistical and systematic. A graphical representation of this table is given in Figure 60.	104
26	Discovery p -value of each bin and in case of an overfluctuation the significance in σ 's. Using the definition of a one-sided p -value, the probability density function is capped and every underfluctuation has a p -value of 0.5. 100 000 pseudo-experiments have been run for each bin with an overfluctuation. The number of expected (N_{exp}) and the number of observed events (N_{obs}) are also given.	120
27	Observed and expected number of signal events excluded at the 95 % confidence level. All results derived with Monte Carlo pseudo-experiments. 50 000 pseudo-experiments have been run per bin. The number of expected (N_{exp}) and the number of observed events (N_{obs}) are also given.	121

28	Background only fit results of the simultaneous fit of the 20 bins, SR0 τ b, SR1 τ and SR2 τ a. This table shows the first 10 bins. Errors shown are statistical plus systematic, but symmetrized.	150
29	Background only fit results of the simultaneous fit of the 20 bins, SR0 τ b, SR1 τ and SR2 τ a. This table shows the last 10 bins. Errors shown are statistical plus systematic, but symmetrized.	151
30	Background only fit results of the simultaneous fit of the 20 bins, SR0 τ b, SR1 τ and SR2 τ a. This table shows SR0 τ b, SR1 τ and SR2 τ a. Errors shown are statistical plus systematic, but symmetrized.	152
31	Discovery p -value of each bin and in case of an overfluctuation the significance in σ 's. Using the definition of a one-sided p -value, the probability density function is capped and every underfluctuation has a p -value of 0.5. Asymptotic and pseudo-experiments results are given, “asymptotic” refers to asymptotic formulae introduced in Section 8.5, “toys” refers to an ensemble of Monte Carlo pseudo-experiments. The official result is the one from the pseudo-experiments. 100 000 pseudo-experiments have been run for each bin with an overfluctuation.	153

List of Figures

1	Schematic overview of the accelerator complex at CERN [21]. Shown are accelerators, in case of synchrotrons their circumferences, year of construction, and the four large LHC experiments ALICE, ATLAS, CMS and LHCb. Sizes not to scale.	10
2	Cumulative luminosity as a function of the date in 2012. Green is collision data delivered by the LHC, yellow the collision data recorded by the ATLAS detector and blue the collision data which is certified as good quality by all detector subsystems.	11
3	Scheme of filling, magnetic field and particle current in Proton Synchrotron Booster (PSB), Proton Synchrotron (PS), Super Proton Synchrotron (SPS) and LHC, as published in [22]. Green lines are the particle current, black lines the magnetic field. (a) is a zoomed in version of (b).	12
4	Schematic view of the ATLAS detector [37] and its subsystems.	13
5	Schematic view of the inner detector, consisting of (from inside out) pixel detector (see Figure 6), semiconductor tracker and transition radiation tracker [38].	14
6	Schematic view of the pixel detector [39].	14
7	Schematic view of the different layers of the inner detector. Pixels are part of the pixel detector, SCT stands for semiconductor tracker and TRT for transition radiation tracker. The tube at the bottom is the beampipe. R is the distance from the centre of the beampipe, the designated interaction axis [38].	15
8	Schematic view of the calorimeters [40].	16
9	Schematic view of the muon chambers [41].	17
10	Installation of the IBL. (a) shows the present pixel detector and beampipe; (b) shows a schematic view of the present pixel detector without present beampipe and the new beampipe with the IBL mounted on it.	21
11	Partial cross-section view through the IBL and its staves [52].	22
12	The ATLAS readout chain. Abbreviations explained in the text.	23
13	SNAP12's from different manufacturers: (from left to right) Avago, Reflex Photonics, Tyco Electronics.	23
14	Mezzanine board with FMC connector (1) and two slots for a SNAP12 Tx (2) and a SNAP12 Rx (3), respectively.	24
15	USB Jig with VCSEL mounted on the right side and plugged in optical fibre.	25
16	Input signal (pink) and output signal (blue) after routing it via a SNAP12 device at 300 kHz (a) and at 10 kHz (b).	25
17	Amplitude of each channel with respect to the input value in the USB Jig Tool (UJT).	26
18	Amplitude of channel 2 with respect to the input value in the USB Jig Tool (UJT) and linear fit.	27
19	Amplitude of electrical output after conversion from an optical signal by a SNAP12 device (Avago)	28
20	Amplitude of electrical output after conversion from an optical signal by a SNAP12 device (Reflex Photonics)	29
21	Amplitude of electrical output after conversion from an optical signal by a SNAP12 device (Tyco Electronics)	29

22	95 % confidence level lower limits on various SUSY particle masses in different models. Some assumptions are made for the SUSY specific parameters, to come up with these lower limits, nonetheless it can be seen that the limits on colored particles are higher in general than the ones on electroweak particles. Naturalness asks for SUSY particles at $\lesssim 1$ TeV. This summary plot includes the results described in this thesis, which are the two EW direct (direct electroweak production of SUSY) limits with three leptons at 700 GeV and 420 GeV, respectively.	32
23	Cross sections for producing SUSY particles in pp collisions at $\sqrt{s} = 7$ TeV computed with PROSPINO. The cross-sections at $\sqrt{s} = 8$ TeV look similar.	33
24	The Feynman diagrams for the four $\tilde{\chi}_1^\pm \tilde{\chi}_2^0$ simplified models. $\tilde{\chi}_1^\pm$ and $\tilde{\chi}_2^0$ are always degenerate. The dashed line in (d) depicts the inclusion of decays via intermediate particles, like $\tau\tau$, WW or ZZ	35
25	The cross-sections of the four simplified models, given in fb. The figures also show the granularity of the grid.	36
26	Diagrams contributing to the WZ background with a final state of 3 leptons and E_T^{miss}	37
27	Diagrams contributing to the ZZ production. Not shown are u-channel diagrams.	39
28	Feynman diagram of $t\bar{t}$ production with subsequent decay into a final state with two charged leptons and two b quarks. The leading diagram at the LHC involves gluon fusion rather than $q\bar{q}$ annihilation.	42
29	One of many diagrams that contribute to $Z + \text{jets}$ events.	43
30	Different exclusion contours for the WZ mediated simplified model as presented at different physics conferences. Exclusion is at the 95 % confidence level. The yellow band around the expected limit shows the $\pm 1\sigma$ variations of the expected limit. Both expected and observed exclusion limits include all uncertainties except theoretical signal uncertainties. The dotted lines around the observed exclusion limit correspond to the $\pm 1\sigma$ variations of these theoretical uncertainties on the signal cross-section. Linear interpolation is used to account for the discrete nature of the signal grids.	54
31	Background distribution in m_{SFOS} from Monte Carlo after a basic three lepton selection. Vertical black lines indicate bin edges. Two exemplary signal distributions are also shown.	58
32	Different possibilities how a binning with one cut in m_T and one cut in E_T^{miss} inside an m_{SFOS} slice could be conducted. The axes are in arbitrary units.	59
33	A comparison of a full-fledged profile likelihood calculation of the significances (a) and one by using the approximative Z_N formula (37) and combining the different regions by adding them in quadrature (b) in the WZ mediated simplified model. (a) is exact, (b) is the approximation of which its validity is tested. In (a), no significance goes above 4.75. This is only due to a technical limitation. Wherever a significance of $Z = 4.75$ is reported, this should read as $Z \geq 4.75$	61
34	The E_T^{miss} and m_T distributions for the first three m_{SFOS} bins. The vertical black lines indicate bin edges.	65
35	The E_T^{miss} and m_T distributions for the last two m_{SFOS} bins. The vertical black lines indicate bin edges.	66

36	$m_{3\ell}$ distributions for $m_{\text{SFOS}} \in [12, 40]$ GeV. The Z window is indicated by vertical black lines. No contribution of $Z + \text{jets}$ is seen in the Z window.	67
37	$m_{3\ell}$ distributions for $m_{\text{SFOS}} \in [40, 60]$ GeV. The Z window is indicated by vertical black lines. Bin 05 (a) shows a contribution of $Z + \text{jets}$ within the Z window.	68
38	$m_{3\ell}$ distributions for $m_{\text{SFOS}} \in [60, 81.2]$ GeV. The Z window is indicated by vertical black lines. Bin 09 (a) shows a contribution of $Z + \text{jets}$ within the Z window.	69
39	$m_{3\ell}$ distributions for $m_{\text{SFOS}} \in [81.2, 101.2]$ GeV. The Z window is indicated by vertical black lines. Bin 13 (a) shows a contribution of $Z + \text{jets}$ within the Z window.	70
40	$m_{3\ell}$ distributions for $m_{\text{SFOS}} \in [101.2, \infty]$ GeV. The Z window is indicated by vertical black lines. As m_{SFOS} is already above the Z window, no contribution of $Z + \text{jets}$ is possible within the Z window.	71
41	Expected number of signal events for the whole signal region, i.e. all 20 bins summed up and expected significances for the statistical combination of the 20 bins in the $\tilde{\ell}_L$ mediated simplified model. All numbers are estimated with Monte Carlo only. The red line indicates exclusion at the 95 % confidence level $\approx 1.64\sigma$	74
42	Expected number of signal events for the whole signal region, i.e. all 20 bins summed up and expected significances for the statistical combination of the 20 bins in the WZ mediated simplified model. All numbers are estimated with Monte Carlo only. The red line indicates exclusion at the 95 % confidence level $\approx 1.64\sigma$	75
43	Total experimental uncertainty, not including Monte Carlo statistics for the most sensitive regions, i.e. bin 20 for the $\tilde{\ell}_L$ mediated and bin 16 for the WZ mediated simplified model.	81
44	Total experimental uncertainty, not including Monte Carlo statistics for the most sensitive regions, i.e. SR2 τ_a for the $\tilde{\tau}_L$ mediated and SR2 τ_b for the Wh mediated simplified model.	82
45	Acceptance in the most sensitive regions, i.e. bin 20 for the $\tilde{\ell}_L$ mediated, bin 16 for the WZ mediated simplified model.	84
46	Acceptance in the most sensitive regions, i.e. SR2 τ_a for the $\tilde{\tau}_L$ mediated and SR2 τ_b for the Wh mediated simplified model.	85
47	Efficiency in the most sensitive regions, i.e. bin 20 for the $\tilde{\ell}_L$ mediated, bin 16 for the WZ mediated simplified model.	86
48	Efficiency in the most sensitive regions, i.e. SR2 τ_a for the $\tilde{\tau}_L$ mediated and SR2 τ_b for the Wh mediated simplified model.	87
49	The observed excess in the distribution of number of b -tagged jets in the VR0 τ noZb region where at least one b -tagged jet is requested. As opposed to the validation region ultimately used in this analysis, where exactly one b -tagged jet is requested. The excess is especially visible in the bin with three b -tagged jets.	90
50	Number of observed and expected events in all bins of the binned validation region. Uncertainty bands include statistical and systematic uncertainties.	93
51	Distributions in VR0 τ noZa. Uncertainty bands include statistical and systematic uncertainties.	94
52	Distributions (continued) in VR0 τ noZa. Uncertainty bands include statistical and systematic uncertainties.	95

53	Distributions in VR0 τ Za. Uncertainty bands include statistical and systematic uncertainties.	96
54	Distributions (continued) in VR0 τ Za. Uncertainty bands include statistical and systematic uncertainties.	97
55	Distributions in VR0 τ noZb. Uncertainty bands include statistical and systematic uncertainties.	98
56	Distributions (continued) in VR0 τ noZb. Uncertainty bands include statistical and systematic uncertainties.	99
57	Distributions in VR0 τ Zb. Uncertainty bands include statistical and systematic uncertainties.	100
58	Distributions (continued) in VR0 τ Zb. Uncertainty bands include statistical and systematic uncertainties.	101
59	Signal contamination in the validation regions; only the simplified models in combination with the validation regions with the largest signal contamination are shown. (a) is the signal contamination from the WZ mediated simplified model in VR0 τ noZa, (b) is the signal contamination from the $\tilde{\ell}_L$ mediated simplified model in VR0 τ noZa.	102
60	Number of expected and observed events in each bin of the binned signal region.	104
61	Distributions in the 20 bins of the binned signal region joined together. The uncertainties are statistical and systematic.	105
62	A standard normal distribution (= a Gaussian distribution with mean $\mu = 0$ and standard deviation $\sigma = 1$). The filled area corresponds to a p -value of 5 %.	108
63	Exemplary distributions with different separations between the background-only and the background + signal hypotheses. (a) has a small separation between these two hypotheses and therefore a low sensitivity to the signal. (b) has a larger separation between these two hypotheses and therefore a higher sensitivity to the signal. Note that the test statistic has a smaller value for more signal-like data.	113
64	Comparisons for the asymptotic limit formula and Monte Carlo pseudo-experiments. Only the discovery test statistic (52) with no signal present in data is shown. (a) shows the probability density function $f(q_0 0)$ for three different values of b and the curve from the asymptotic limit as a function of q_0 . (b) shows the discovery significance Z_0 from Equation (64) with a fixed asymptotic value of $Z_0 = \sqrt{q_{0,obs}} = 4$ and derived with Monte Carlo pseudo-experiments as a function of b	114
65	Illustration of observed and expected discovery p -value.	116
66	A regular dataset (a) and the “Asimov dataset” (b) for 1000 events standard normally distributed. The “Asimov dataset” shows no fluctuations.	116
67	Observed and expected exclusion limit contours at the 95 % confidence level. (a) is the $\tilde{\ell}_L$ mediated and (b) the WZ mediated simplified model.	122
68	Observed and expected exclusion limit contours at the 95 % confidence level. (a) is the $\tilde{\tau}_L$ mediated and (b) the Wh mediated simplified model.	123
69	Observed and expected exclusion limit contours at the 95 % confidence level in the pMSSMs with light sleptons. (a) is with $M_1 = 100$ GeV, (b) is with $M_1 = 140$ GeV.	124
70	Observed and expected exclusion limit contours at the 95 % confidence level in the pMSSMs with light sleptons and $M_1 = 250$ GeV.	125

71	Observed and expected exclusion limit contours at the 95 % confidence level in the pMSSMs. (a) is the staus model and (b) the model without sleptons.	126
72	Observed (a) and expected (b) CL_s at each grid point for the $\tilde{\ell}_L$ mediated simplified model. Exclusion is at $CL_s < 5 \%$.	128
73	Observed (a) and expected (b) CL_s at each grid point for the WZ mediated simplified model. Exclusion is at $CL_s < 5 \%$.	129
74	Observed (a) and expected (b) CL_s at each grid point for the $\tilde{\tau}_L$ mediated simplified model. Exclusion is at $CL_s < 5 \%$.	130
75	Observed (a) and expected (b) CL_s at each grid point for the Wh mediated simplified model. Exclusion is at $CL_s < 5 \%$.	131
76	Observed (a) and expected (b) CL_s at each grid point for the pMSSMs with $\tan \beta = 6$ and $M_1 = 100$ GeV. Exclusion is at $CL_s < 5 \%$.	132
77	Observed (a) and expected (b) CL_s at each grid point for the pMSSMs with $\tan \beta = 6$ and $M_1 = 140$ GeV. Exclusion is at $CL_s < 5 \%$.	133
78	Observed (a) and expected (b) CL_s at each grid point for the pMSSMs with $\tan \beta = 6$ and $M_1 = 250$ GeV. Exclusion is at $CL_s < 5 \%$.	134
79	Observed (a) and expected (b) CL_s at each grid point for the pMSSMs with $\tan \beta = 50$ and $M_1 = 75$ GeV. Exclusion is at $CL_s < 5 \%$.	135
80	Observed (a) and expected (b) CL_s at each grid point for the pMSSMs with $\tan \beta = 10$ and $M_1 = 50$ GeV. Exclusion is at $CL_s < 5 \%$.	136
81	Comparing the exclusion limit contours of the conference note published in March 2013 [8] and the paper published in March 2014 [2]. Both use the full 8 TeV dataset (but see footnote on page 53), both analyses use signal regions that were optimized on these grids. From [8], the nominal expected and observed are shown. [8] used six signal regions, while [2] uses the binned signal region.	137
82	Observed and expected exclusion contours at the 95 % confidence level for the two and three leptons final state combination in the WZ mediated simplified model (a) and the pMSSM with $M_1 = 250$ GeV (b). The exclusion limits are published in [3]. The green contour in (a) corresponds to the 7 TeV limit of the three lepton search, the blue contour in (b) corresponds to the 7 TeV two and three lepton combined search [5]. Asymptotic formulae are used for these results, as opposed to Figures 67 and 70.	138
83	Exclusion limit contours in the $\tilde{\ell}_L$ mediated simplified model (a) and the WZ mediated simplified model (b) as published in [108].	139
84	Comparing my exclusion limit contours with the ones from CMS as published in [108]. The CMS results are drawn by hand and may not be 100 % accurate, see Figure 83 for the official results. (a) is the $\tilde{\ell}_L$ mediated simplified model. The results are comparable, but CMS published a combination of two searches. One search in a final state with two leptons and one search in a final state with three leptons. I only used data in a final state with three leptons. (b) is the WZ mediated simplified model. Both analyses use a combination of two and three lepton final state searches. In this grid, the usage of the binned signal region pays off, my exclusion contour is much stronger, especially in the WZ like region.	140
85	Limit derived as a combination of different detectors at the LEP accelerator at CERN. The limit is set on the $\tilde{\chi}_1^\pm$ masses as a function of $\Delta m = m_{\tilde{\chi}_1^\pm} - m_{\tilde{\chi}_1^0}$ (a). Δm in the pMSSM with $M_1 = 250$ GeV (b).	141

86	Upper limit scan for varying μ . 10 different values for μ have been tried. The dashed line is the expected CL_s including 1σ and 2σ uncertainty band. The observed CL_s are the red dots, as ratio between the blue dots (CL_{s+b}) and the black dots (CL_b). The uncertainties on the observed CL_s are also shown but usually too small to spot. Once the observed CL_s goes below the predefined value of 0.05, the excluded value of μ at the 95 % confidence level is found with linear interpolation. 10 000 pseudo-experiments are run for each point.	142
87	Upper limit scan for the WZ mediated point with $m_{\tilde{\chi}_1^\pm} = 150$ GeV and $m_{\tilde{\chi}_1^0} = 50$ GeV. In (a) asymptotic formulae have been used, in (b) 10 · 10 000 Monte Carlo pseudo-experiments have been used.	143
88	Upper limit scan for the $\tilde{\tau}_L$ mediated point with $m_{\tilde{\chi}_1^\pm} = 150$ GeV and $m_{\tilde{\chi}_1^0} = 50$ GeV. In (a) the values for μ are set to $0.99 \cdot \mu_{asym}$, $1.22 \cdot \mu_{asym}$ and $1.45 \cdot \mu_{asym}$. In (b) the values for μ are set to $0.9 \cdot \mu_{toys,est.}$, $1.0 \cdot \mu_{toys,est.}$ and $1.1 \cdot \mu_{toys,est.}$, where $\mu_{toys,est.}$ is the approximation from (a). For all points, 10 · 10 000 Monte Carlo pseudo-experiments have been used.	143
89	The excluded signal strength μ from the upper limit scan. The values for μ in the test statistic \tilde{q}_μ are the ones that are excluded at the 95 % confidence level.	145
90	The excluded signal strength μ from the upper limit scan. The values for μ in the test statistic \tilde{q}_μ are the ones that are excluded at the 95 % confidence level.	146
91	The excluded model cross-sections at the 95% confidence level from the upper limit scan. Cross-sections are in fb for the $\tilde{\ell}_L$ mediated simplified model and in pb for the WZ mediated simplified model.	147
92	The excluded model cross-sections at the 95% confidence level from the upper limit scan. Cross-sections are in pb.	148
93	The excluded model cross-sections at the 95% confidence level from the conference note published in March 2013 [8]. Both analyses use the full 8 TeV dataset (but see footnote on page 53), both analyses use signal regions that were optimized on these grids. [8] used six signal regions, while [2] uses the binned signal region.	149
94	Observed CL_s values derived with asymptotic formulae (a) and with Monte Carlo pseudo-experiments (b).	155
97	Expected number of signal events and expected significances in the four bins where $m_{SFOS} \in [12, 40]$ GeV for the $\tilde{\ell}_L$ mediated simplified model . . .	166
98	Expected number of signal events and expected significances in the four bins where $m_{SFOS} \in [40, 60]$ GeV for the $\tilde{\ell}_L$ mediated simplified model . . .	167
99	Expected number of signal events and expected significances in the four bins where $m_{SFOS} \in [60, 81.2]$ GeV for the $\tilde{\ell}_L$ mediated simplified model . .	168
100	Expected number of signal events and expected significances in the four bins where $m_{SFOS} \in [81.2, 101.2]$ GeV for the $\tilde{\ell}_L$ mediated simplified model .	169
101	Expected number of signal events and expected significances in the four bins where $m_{SFOS} \in [101.2, \infty]$ GeV for the $\tilde{\ell}_L$ mediated simplified model .	170
102	Expected number of signal events and expected significances in the four bins where $m_{SFOS} \in [12, 40]$ GeV for the WZ mediated simplified model . .	171
103	Expected number of signal events and expected significances in the four bins where $m_{SFOS} \in [40, 60]$ GeV for the WZ mediated simplified model . .	172

104	Expected number of signal events and expected significances in the four bins where $m_{\text{SFOS}} \in [60, 81.2]$ GeV for the WZ mediated simplified model .	173
105	Expected number of signal events and expected significances in the four bins where $m_{\text{SFOS}} \in [81.2, 101.2]$ GeV for the WZ mediated simplified model	174
106	Expected number of signal events and expected significances in the four bins where $m_{\text{SFOS}} \in [101.2, \infty]$ GeV for the WZ mediated simplified model	175
107	Systematic uncertainties in bin 1 and 2 of the signal region. The abbreviations are given in the text.	178
108	Systematic uncertainties in bin 3 and 4 of the signal region. The abbreviations are given in the text.	179
109	Systematic uncertainties in bin 5 and 6 of the signal region. The abbreviations are given in the text.	180
110	Systematic uncertainties in bin 7 and 8 of the signal region. The abbreviations are given in the text.	181
111	Systematic uncertainties in bin 9 and 10 of the signal region. The abbreviations are given in the text.	182
112	Systematic uncertainties in bin 11 and 12 of the signal region. The abbreviations are given in the text.	183
113	Systematic uncertainties in bin 13 and 14 of the signal region. The abbreviations are given in the text.	184
114	Systematic uncertainties in bin 15 and 16 of the signal region. The abbreviations are given in the text.	185
115	Systematic uncertainties in bin 17 and 18 of the signal region. The abbreviations are given in the text.	186
116	Systematic uncertainties in bin 19 and 20 of the signal region. The abbreviations are given in the text.	187
117	Distributions in VR0 τb -bin1. The uncertainties are statistical and systematic.	189
118	Distributions in VR0 τb -bin2. The uncertainties are statistical and systematic.	190
119	Distributions in VR0 τb -bin3. The uncertainties are statistical and systematic.	191
120	Distributions in VR0 τb -bin4. The uncertainties are statistical and systematic.	192
121	Distributions in VR0 τb -bin5. The uncertainties are statistical and systematic.	193
122	Distributions in VR0 τb -bin6. The uncertainties are statistical and systematic.	194
123	Distributions in VR0 τb -bin7. The uncertainties are statistical and systematic.	195
124	Distributions in VR0 τb -bin8. The uncertainties are statistical and systematic.	196
125	Distributions in VR0 τb -bin9. The uncertainties are statistical and systematic.	197
126	Distributions in VR0 τb -bin10. The uncertainties are statistical and systematic.	198
127	Distributions in VR0 τb -bin11. The uncertainties are statistical and systematic.	199
128	Distributions in VR0 τb -bin12. The uncertainties are statistical and systematic.	200
129	Distributions in VR0 τb -bin13. The uncertainties are statistical and systematic.	201
130	Distributions in VR0 τb -bin14. The uncertainties are statistical and systematic.	202
131	Distributions in VR0 τb -bin15. The uncertainties are statistical and systematic.	203
132	Distributions in VR0 τb -bin16. The uncertainties are statistical and systematic.	204

133	Distributions in VR0 τb -bin17. The uncertainties are statistical and systematic.	205
134	Distributions in VR0 τb -bin18. The uncertainties are statistical and systematic.	206
135	Distributions in VR0 τb -bin19. The uncertainties are statistical and systematic.	207
136	Distributions in VR0 τb -bin20. The uncertainties are statistical and systematic.	208
137	Distributions in bin 1. The uncertainties are statistical and systematic.	209
138	Distributions in bin 2. The uncertainties are statistical and systematic.	210
139	Distributions in bin 3. The uncertainties are statistical and systematic.	211
140	Distributions in bin 4. The uncertainties are statistical and systematic.	212
141	Distributions in bin 5. The uncertainties are statistical and systematic.	213
142	Distributions in bin 6. The uncertainties are statistical and systematic.	214
143	Distributions in bin 7. The uncertainties are statistical and systematic.	215
144	Distributions in bin 8. The uncertainties are statistical and systematic.	216
145	Distributions in bin 9. The uncertainties are statistical and systematic.	217
146	Distributions in bin 10. The uncertainties are statistical and systematic.	218
147	Distributions in bin 11. The uncertainties are statistical and systematic.	219
148	Distributions in bin 12. The uncertainties are statistical and systematic.	220
149	Distributions in bin 13. The uncertainties are statistical and systematic.	221
150	Distributions in bin 14. The uncertainties are statistical and systematic.	222
151	Distributions in bin 15. The uncertainties are statistical and systematic.	223
152	Distributions in bin 16. The uncertainties are statistical and systematic.	224
153	Distributions in bin 17. The uncertainties are statistical and systematic.	225
154	Distributions in bin 18. The uncertainties are statistical and systematic.	226
155	Distributions in bin 19. The uncertainties are statistical and systematic.	227
156	Distributions in bin 20. The uncertainties are statistical and systematic.	228
157	Expected (left) and observed (right) CL_s values for the $\tilde{\ell}_L$ mediated simplified model in the four bins where $m_{\text{SFOS}} \in [12, 40]$ GeV.	230
158	Expected (left) and observed (right) CL_s values for the $\tilde{\ell}_L$ mediated simplified model in the four bins where $m_{\text{SFOS}} \in [40, 60]$ GeV.	231
159	Expected (left) and observed (right) CL_s values for the $\tilde{\ell}_L$ mediated simplified model in the four bins where $m_{\text{SFOS}} \in [60, 81.2]$ GeV.	232
160	Expected (left) and observed (right) CL_s values for the $\tilde{\ell}_L$ mediated simplified model in the four bins where $m_{\text{SFOS}} \in [81.2, 101.2]$ GeV.	233
161	Expected (left) and observed (right) CL_s values for the $\tilde{\ell}_L$ mediated simplified model in the four bins where $m_{\text{SFOS}} \in [81.2, \infty]$ GeV.	234
162	Expected (left) and observed (right) CL_s values for the $\tilde{\ell}_L$ mediated simplified model in the unbinned signal regions.	235
163	Expected (left) and observed (right) CL_s values for the WZ mediated simplified model in the four bins where $m_{\text{SFOS}} \in [12, 40]$ GeV.	236
164	Expected (left) and observed (right) CL_s values for the WZ mediated simplified model in the four bins where $m_{\text{SFOS}} \in [40, 60]$ GeV.	237
165	Expected (left) and observed (right) CL_s values for the WZ mediated simplified model in the four bins where $m_{\text{SFOS}} \in [60, 81.2]$ GeV.	238
166	Expected (left) and observed (right) CL_s values for the WZ mediated simplified model in the four bins where $m_{\text{SFOS}} \in [81.2, 101.2]$ GeV.	239

167	Expected (left) and observed (right) CL_s values for the WZ mediated simplified model in the four bins where $m_{\text{SFOS}} \in [101.2, \infty]$ GeV.	240
168	Expected (left) and observed (right) CL_s values for the WZ mediated simplified model in the unbinned signal regions.	241
169	Scan for different values of μ for upper limits on model cross-sections. The numbers in parantheses are $(m_{\tilde{\chi}_1^\pm}, m_{\tilde{\chi}_1^0})$	243
170	Scan for different values of μ for upper limits on model cross-sections. The numbers in parantheses are $(m_{\tilde{\chi}_1^\pm}, m_{\tilde{\chi}_1^0})$	244
171	Scan for different values of μ for upper limits on model cross-sections. The numbers in parantheses are $(m_{\tilde{\chi}_1^\pm}, m_{\tilde{\chi}_1^0})$	245
172	Scan for different values of μ for upper limits on model cross-sections. The numbers in parantheses are $(m_{\tilde{\chi}_1^\pm}, m_{\tilde{\chi}_1^0})$	246
173	Scan for different values of μ for upper limits on model cross-sections. The numbers in parantheses are $(m_{\tilde{\chi}_1^\pm}, m_{\tilde{\chi}_1^0})$	247
174	Scan for different values of μ for upper limits on model cross-sections. The numbers in parantheses are $(m_{\tilde{\chi}_1^\pm}, m_{\tilde{\chi}_1^0})$	248
175	Scan for different values of μ for upper limits on model cross-sections. The numbers in parantheses are $(m_{\tilde{\chi}_1^\pm}, m_{\tilde{\chi}_1^0})$	249
176	Scan for different values of μ for upper limits on model cross-sections. The numbers in parantheses are $(m_{\tilde{\chi}_1^\pm}, m_{\tilde{\chi}_1^0})$	250
177	Scan for different values of μ for upper limits on model cross-sections. The numbers in parantheses are $(m_{\tilde{\chi}_1^\pm}, m_{\tilde{\chi}_1^0})$	251
178	Scan for different values of μ for upper limits on model cross-sections. The numbers in parantheses are $(m_{\tilde{\chi}_1^\pm}, m_{\tilde{\chi}_1^0})$	252
179	Scan for different values of μ for upper limits on model cross-sections. The numbers in parantheses are $(m_{\tilde{\chi}_1^\pm}, m_{\tilde{\chi}_1^0})$	253
180	Scan for different values of μ for upper limits on model cross-sections. The numbers in parantheses are $(m_{\tilde{\chi}_1^\pm}, m_{\tilde{\chi}_1^0})$	254
181	Scan for different values of μ for upper limits on model cross-sections. The numbers in parantheses are $(m_{\tilde{\chi}_1^\pm}, m_{\tilde{\chi}_1^0})$	255
182	Scan for different values of μ for upper limits on model cross-sections. The numbers in parantheses are $(m_{\tilde{\chi}_1^\pm}, m_{\tilde{\chi}_1^0})$	256
183	Scan for different values of μ for upper limits on model cross-sections. The numbers in parantheses are $(m_{\tilde{\chi}_1^\pm}, m_{\tilde{\chi}_1^0})$	257
184	Scan for different values of μ for upper limits on model cross-sections. The numbers in parantheses are $(m_{\tilde{\chi}_1^\pm}, m_{\tilde{\chi}_1^0})$	258
185	Scan for different values of μ for upper limits on model cross-sections. The numbers in parantheses are $(m_{\tilde{\chi}_1^\pm}, m_{\tilde{\chi}_1^0})$	259

References

- [1] <https://twiki.cern.ch/twiki/bin/view/Atlas/SNAP12RxTesting>.
- [2] ATLAS Collaboration, G. Aad et al., *Search for direct production of charginos and neutralinos in events with three leptons and missing transverse momentum in $\sqrt{s} = 8$ TeV pp collisions with the ATLAS detector*, JHEP **1404** (2014) 169, 10.1007/JHEP04(2014)169, arXiv:1402.7029 [hep-ex].
- [3] ATLAS Collaboration, G. Aad et al., *Search for direct production of charginos, neutralinos and sleptons in final states with two leptons and missing transverse momentum in pp collisions at $\sqrt{s} = 8$ TeV with the ATLAS detector*, arXiv:1403.5294 [hep-ex].
- [4] <http://cerncourier.com/cws/article/cern/57289>.
- [5] ATLAS Collaboration Collaboration, G. Aad et al., *Search for direct production of charginos and neutralinos in events with three leptons and missing transverse momentum in $\sqrt{s} = 7$ TeV pp collisions with the ATLAS detector*, Phys.Lett. **B718** (2013) 841–859, 10.1016/j.physletb.2012.11.039, arXiv:1208.3144 [hep-ex].
- [6] ATLAS Collaboration, *Search for direct production of charginos and neutralinos in events with three leptons and missing transverse momentum in 13.0 fb^{-1} of pp collisions at $\sqrt{s} = 8$ TeV with the ATLAS detector*, ATLAS-CONF-2012-154. <http://cdsweb.cern.ch/record/1493493>.
- [7] ATLAS Collaboration, *Search for Supersymmetry in events with four or more leptons in 13 fb^{-1} pp collisions at $s = 8$ TeV with the ATLAS detector*, ATLAS-CONF-2012-153. <https://cds.cern.ch/record/1493492>.
- [8] ATLAS Collaboration, *Search for direct production of charginos and neutralinos in events with three leptons and missing transverse momentum in 21 fb^{-1} of pp collisions at $\sqrt{s} = 8$ TeV with the ATLAS detector*, ATLAS-CONF-2013-035. <http://cdsweb.cern.ch/record/1532426>.
- [9] ATLAS Collaboration, *Search for supersymmetry in events with four or more leptons in 21 fb^{-1} of pp collisions at $\sqrt{s} = 8$ TeV with the ATLAS detector*, ATLAS-CONF-2013-036. <https://cds.cern.ch/record/1532429>.
- [10] ATLAS Collaboration, G. Aad et al., *Search for supersymmetry in events with four or more leptons in $\sqrt{s} = 8$ TeV pp collisions with the ATLAS detector*, arXiv:1405.5086 [hep-ex].
- [11] <https://svnweb.cern.ch/trac/atlasphys/browser/Physics/SUSY/Analyses/WeakProduction/HistFitterTree>.
- [12] <https://svnweb.cern.ch/trac/atlasphys/browser/Physics/SUSY/Analyses/WeakProduction/Limits>.
- [13] <https://twiki.cern.ch/twiki/bin/view/AtlasProtected/SusyFitter>.
- [14] B. Schneider, *SUSY Searches at ATLAS in Multilepton Final States with Jets and Missing Transverse Energy*, ATL-PHYS-SLIDE-2011-423. <https://cds.cern.ch/record/1371922>.

- [15] B. Schneider, *Search for direct production of charginos and neutralinos in events with three leptons and missing transverse momentum in 21 fb⁻¹ of pp collisions at s = 8 TeV with the ATLAS detector*, ATL-PHYS-SLIDE-2013-350. <https://cds.cern.ch/record/1555743>.
- [16] ATLAS Collaboration, *Observation of a new particle in the search for the Standard Model Higgs boson with the ATLAS detector at the LHC*, Phys.Lett. **B716** (2012) 1–29, arXiv:1207.7214 [hep-ex].
- [17] S. P. Martin, *A Supersymmetry primer*, arXiv:hep-ph/9709356 [hep-ph].
- [18] Particle Data Group Collaboration, J. Beringer et al., *Review of Particle Physics (RPP)*, Phys.Rev. **86** (2012) 010001, 10.1103/PhysRevD.86.010001.
- [19] ATLAS Collaboration, G. Aad et al., *The ATLAS Experiment at the CERN Large Hadron Collider*, JINST **3** (2008) S08003, 10.1088/1748-0221/3/08/S08003.
- [20] L. Evans and P. Bryant, *LHC Machine*, JINST **3** (2008) S08001, 10.1088/1748-0221/3/08/S08001.
- [21] J. Haffner, *The CERN accelerator complex*, OPEN-PHO-ACCEL-2013-056-1 (2013). <https://cds.cern.ch/record/1621894>.
- [22] C. Lefevre, “LHC: the guide (English version).” Feb, 2009.
- [23] ATLAS Collaboration. <http://atlas.ch>.
- [24] CMS Collaboration, S. Chatrchyan et al., *The CMS experiment at the CERN LHC*, JINST **3** (2008) S08004, 10.1088/1748-0221/3/08/S08004.
- [25] CMS Collaboration. <http://cms.web.cern.ch>.
- [26] ALICE Collaboration, K. Aamodt et al., *The ALICE experiment at the CERN LHC*, JINST **3** (2008) S08002, 10.1088/1748-0221/3/08/S08002.
- [27] ALICE Collaboration. <http://aliweb.cern.ch>.
- [28] LHCb Collaboration, J. Alves, A. Augusto et al., *The LHCb Detector at the LHC*, JINST **3** (2008) S08005, 10.1088/1748-0221/3/08/S08005.
- [29] LHCb Collaboration. <http://lhcb.web.cern.ch/lhcb>.
- [30] TOTEM Collaboration, G. Anelli et al., *The TOTEM experiment at the CERN Large Hadron Collider*, JINST **3** (2008) S08007, 10.1088/1748-0221/3/08/S08007.
- [31] TOTEM Collaboration. <http://totem.web.cern.ch/Totem>.
- [32] LHCf Collaboration, O. Adriani et al., *The LHCf detector at the CERN Large Hadron Collider*, JINST **3** (2008) S08006, 10.1088/1748-0221/3/08/S08006.
- [33] J. L. Pinfold, *The MoEDAL Experiment Searching for Highly Ionizing Particles at the LHC*,
- [34] MoEDAL Collaboration. <http://moedal.web.cern.ch>.

- [35] ATLAS Collaboration, G. Aad et al., *Observation of a new particle in the search for the Standard Model Higgs boson with the ATLAS detector at the LHC*, Phys.Lett. **B716** (2012) 1–29, 10.1016/j.physletb.2012.08.020, arXiv:1207.7214 [hep-ex].
- [36] CMS Collaboration, S. Chatrchyan et al., *Observation of a new boson at a mass of 125 GeV with the CMS experiment at the LHC*, Phys.Lett. **B716** (2012) 30–61, 10.1016/j.physletb.2012.08.021, arXiv:1207.7235 [hep-ex].
- [37] J. Pequenao, “Computer generated image of the whole ATLAS detector.” Mar, 2008.
- [38] J. Pequenao, “Computer generated image of the ATLAS inner detector.” Mar, 2008.
- [39] J. Pequenao, “Computer generated images of the Pixel, part of the ATLAS inner detector..” Mar, 2008.
- [40] J. Pequenao, “Computer Generated image of the ATLAS calorimeter.” Mar, 2008.
- [41] J. Pequenao, “Computer generated image of the ATLAS Muons subsystem.” Mar, 2008.
- [42] W. Lampl, S. Laplace, D. Lelas, P. Loch, H. Ma, S. Menke, S. Rajagopalan, D. Rousseau, S. Snyder, and G. Unal, *Calorimeter Clustering Algorithms: Description and Performance*.
- [43] *Expected electron performance in the ATLAS experiment*, ATL-PHYS-PUB-2011-006 (2011). <https://cds.cern.ch/record/1345327>.
- [44] R. Nicolaidou, L. Chevalier, S. Hassani, J. Laporte, E. Le Menedeu, et al., *Muon identification procedure for the ATLAS detector at the LHC using Muonboy reconstruction package and tests of its performance using cosmic rays and single beam data*, J.Phys.Conf.Ser. **219** (2010), 10.1088/1742-6596/219/3/032052.
- [45] *Preliminary results on the muon reconstruction efficiency, momentum resolution, and momentum scale in ATLAS 2012 pp collision data*, ATLAS-CONF-2013-088 (2013). <https://cds.cern.ch/record/1580207>.
- [46] M. Cacciari, G. P. Salam, and G. Soyez, *The Anti- $k(t)$ jet clustering algorithm*, JHEP **0804** (2008) 063, 10.1088/1126-6708/2008/04/063, arXiv:0802.1189 [hep-ph].
- [47] ATLAS Collaboration, *Jet energy measurement with the ATLAS detector in proton-proton collisions at $\sqrt{s} = 7$ TeV*, arXiv:1112.6426 [hep-ex].
- [48] ATLAS Collaboration, *Performance of the Reconstruction and Identification of Hadronic Tau Decays with ATLAS*, ATLAS-CONF-2011-152. <http://cdsweb.cern.ch/record/1398195>.
- [49] ATLAS Collaboration, *Performance of Missing Transverse Momentum Reconstruction in Proton-Proton Collisions at 7 TeV with ATLAS*, Eur. Phys. J. **C 72** (2012) 1844, 10.1140/epjc/s10052-011-1844-6, arXiv:1108.5602 [hep-ex].

- [50] *Expected photon performance in the ATLAS experiment*, ATL-PHYS-PUB-2011-007 (2011). <https://cds.cern.ch/record/1345329>.
- [51] M. Capeans, G. Darbo, K. Einsweiller, M. Elsing, T. Flick, M. Garcia-Sciveres, C. Gemme, H. Pernegger, O. Rohne, and R. Vuillermet, *ATLAS Insertable B-Layer Technical Design Report*, CERN-LHCC-2010-013. ATLAS-TDR-19 (2010). <https://cds.cern.ch/record/1291633>.
- [52] ATLAS IBL Collaboration, J. Albert et al., *Prototype ATLAS IBL Modules using the FE-I4A Front-End Readout Chip*, JINST **7** (2012) P11010, 10.1088/1748-0221/7/11/P11010, arXiv:1209.1906 [physics.ins-det].
- [53] D. Wiedner, “private communication.” 2011.
- [54] M. S. Cooke, *Studies of VCSEL Failures in the Optical Readout Systems of the ATLAS Silicon Trackers and Liquid Argon Calorimeters*, arXiv:1109.6679 [physics.ins-det].
- [55] “SNAP12: 12 channel pluggable optical module MSA Specifications - Appendix to SNAP12 Multi-Source Agreement.” http://www.physik.uzh.ch/~avollhar/snap12msa_051502.pdf, May, 2002.
- [56] “Pluggable Parallel Fiber Optic Modules, Transmitter and Receiver: Data Sheet.” <http://www.avagotech.com/docs/AV02-1158EN>, May, 2008.
- [57] “InterBOARDTM 40 Gbps SNAP12 Parallel Fiber Optic Transmitter and Receiver Board Edge Modules.” http://reflexphotonics.com/PDFs/SN-970-004-00_Rev_3-6_InterBoard_Board-Edge_Data_Sheet.pdf, Dec, 2010.
- [58] “Tyco Electronics SNAP12 ZL60102MLDL Product Details.” <http://www.te.com/catalog/pn/en/ZL60102MLDL?RQPN=ZL60102MLDL>.
- [59] M. Goodrick, “ATLAS SCT Optical Links - USB Jig.” http://www.hep.phy.cam.ac.uk/~goodrick/PlugIns/USB_Jig, Aug, 2011.
- [60] L. Ancu, A. Canepa, A. De Santo, S. Farrell, C. Gay, Z. Gesce, M. Gignac, S. Haug, O. Jinnouchi, L. Marti, R. Nagai, A. Mete, C. Potter, P. Salvatore, I. Santoyo Castillo, B. Schneider, A. Taffard, and M. Weber, *Search for supersymmetry in events with three leptons and missing transverse momentum in 20.3 fb⁻¹ pp collisions at √s = 8 TeV with the ATLAS detector*, ATL-COM-PHYS-2013-888 (2013). <https://cds.cern.ch/record/1558985>.
- [61] W. Beenakker, R. Hopker, and M. Spira, *PROSPINO: A Program for the production of supersymmetric particles in next-to-leading order QCD*, arXiv:hep-ph/9611232 [hep-ph].
- [62] W. Beenakker et al., *Squark and gluino production at hadron colliders*, Nucl. Phys. **B 492** (1997) 51–103, 10.1016/S0550-3213(97)00084-9, arXiv:hep-ph/9610490.
- [63] W. Beenakker, M. Kramer, T. Plehn, M. Spira, and P. Zerwas, *Stop production at hadron colliders*, Nucl.Phys. **B515** (1998) 3–14, 10.1016/S0550-3213(98)00014-5, arXiv:hep-ph/9710451 [hep-ph].

- [64] W. Beenakker, M. Klasen, M. Kramer, T. Plehn, M. Spira, et al., *The Production of charginos, neutralinos and sleptons at hadron colliders*, Phys. Rev. Lett. **83** (1999) 3780–3783, 10.1103/PhysRevLett.100.029901, 10.1103/PhysRevLett.83.3780, arXiv:hep-ph/9906298 [hep-ph].
- [65] ATLAS Collaboration, *ATLAS tunes of PYTHIA 6 and Pythia 8 for MC11*, ATL-PHYS-PUB-2011-009. <http://cdsweb.cern.ch/record/1363300>.
- [66] H.-L. Lai et al., *New parton distributions for collider physics*, Phys. Rev. **D 82** (2010) 074024, 10.1103/PhysRevD.82.074024, arXiv:1007.2241 [hep-ph].
- [67] M. Bahr, S. Gieseke, M. Gigg, D. Grellscheid, K. Hamilton, et al., *Herwig++ Physics and Manual*, Eur. Phys. J. **C 58** (2008) 639–707, 10.1140/epjc/s10052-008-0798-9, arXiv:0803.0883 [hep-ph].
- [68] P. Nason, *A New method for combining NLO QCD with shower Monte Carlo algorithms*, JHEP **0411** (2004) 040, 10.1088/1126-6708/2004/11/040, arXiv:hep-ph/0409146.
- [69] T. Sjostrand, S. Mrenna, and P. Z. Skands, *PYTHIA 6.4 Physics and Manual*, JHEP **0605** (2006) 026, 10.1088/1126-6708/2006/05/026, arXiv:hep-ph/0603175 [hep-ph].
- [70] J. M. Campbell and R. K. Ellis, *An Update on vector boson pair production at hadron colliders*, Phys. Rev. **D 60** (1999) 113006, 10.1103/PhysRevD.60.113006, arXiv:hep-ph/9905386 [hep-ph].
- [71] J. M. Campbell, R. K. Ellis, and C. Williams, *Vector boson pair production at the LHC*, JHEP **1107** (2011) 018, 10.1007/JHEP07(2011)018, arXiv:1105.0020 [hep-ph].
- [72] ATLAS Collaboration, G. Aad et al., *Measurement of WZ production in proton-proton collisions at $\sqrt{s} = 7$ TeV with the ATLAS detector*, Eur.Phys.J. **C72** (2012) 2173, 10.1140/epjc/s10052-012-2173-0, arXiv:1208.1390 [hep-ex].
- [73] ATLAS Collaboration, *A Measurement of WZ Production in Proton-Proton Collisions at $\sqrt{s} = 8$ TeV with the ATLAS Detector*, ATLAS-CONF-2013-021. <http://cdsweb.cern.ch/record/1525557>.
- [74] J. Butterworth et al., *Multiparton interactions in photoproduction at HERA*, Z. Phys. **C 72** (1996) 637–646, 10.1007/s002880050286, arXiv:hep-ph/9601371 [hep-ph].
- [75] ATLAS Collaboration, G. Aad et al., *Measurement of the ZZ production cross section and limits on anomalous neutral triple gauge couplings in proton-proton collisions at $\sqrt{s} = 7$ TeV with the ATLAS detector*, Phys.Rev.Lett. **108** (2012) 041804, 10.1103/PhysRevLett.108.041804, arXiv:1110.5016 [hep-ex].
- [76] ATLAS Collaboration, G. Aad et al., *Measurement of ZZ production in pp collisions at $\sqrt{s} = 7$ TeV and limits on anomalous ZZZ and $ZZ\gamma$ couplings with the ATLAS detector*, JHEP **1303** (2013) 128, 10.1007/JHEP03(2013)128, arXiv:1211.6096 [hep-ex].

- [77] ATLAS Collaboration, *Measurement of the total ZZ production cross section in proton-proton collisions at $s = 8$ TeV in 20 fb^{-1} with the ATLAS detector*, ATLAS-CONF-2013-020. <http://cdsweb.cern.ch/record/1525555>.
- [78] *ATLAS measurements of the 7 and 8 TeV cross sections for $Z \rightarrow 4\ell$ in pp collisions*, ATLAS-CONF-2013-055 (2013). <https://cds.cern.ch/record/1551514>.
- [79] M. L. Mangano et al., *ALPGEN, a generator for hard multiparton processes in hadronic collisions*, JHEP **0307** (2003) 001, <arXiv:hep-ph/0206293>.
- [80] J. Alwall et al., *MadGraph/MadEvent v4: The New Web Generation*, JHEP **09** (2007) 028, [arXiv:0706.2334 \[hep-ph\]](arXiv:0706.2334).
- [81] F. Campanario et al., *QCD corrections to charged triple vector boson production with leptonic decay*, Phys. Rev. **D 78** (2008) 094012, 10.1103/PhysRevD.78.094012, [arXiv:0809.0790 \[hep-ph\]](arXiv:0809.0790).
- [82] S. Dittmaier et al., *Handbook of LHC Higgs Cross Sections: 2. Differential Distributions*, [arXiv:1201.3084 \[hep-ph\]](arXiv:1201.3084).
- [83] S. Frixione and B. R. Webber, *The MC@NLO 3.2 event generator*, <arXiv:hep-ph/0601192>.
- [84] G. Corcella, I. Knowles, G. Marchesini, S. Moretti, K. Odagiri, et al., *HERWIG 6: An Event generator for hadron emission reactions with interfering gluons (including supersymmetric processes)*, JHEP **0101** (2001) 010, <arXiv:hep-ph/0011363>.
- [85] *Atlas Offline Software Release Status*, February, 2014. <http://atlas-computing.web.cern.ch/atlas-computing/projects/releases/status/>.
- [86] <http://twiki.cern.ch/twiki/bin/view/AtlasProtected/TechnicalitiesForMedium1>.
- [87] ATLAS Collaboration, *Muon Momentum Resolution in First Pass Reconstruction of pp Collision Data Recorded by ATLAS in 2010*, ATLAS-CONF-2011-046. <http://cdsweb.cern.ch/record/1338575>.
- [88] D0 Collaboration, V. Abazov et al., *Measurement of the $p\bar{p} \rightarrow t\bar{t}$ production cross section at $\sqrt{s} = 1.96$ TeV in the fully hadronic decay channel.*, Phys.Rev. **D76** (2007) 072007, 10.1103/PhysRevD.76.072007, [arXiv:hep-ex/0612040 \[hep-ex\]](arXiv:hep-ex/0612040).
- [89] ATLAS Collaboration, *Measuring the b-tag efficiency in a top-pair sample with 4.7 fb^{-1} of data from the ATLAS detector*, ATLAS-CONF-2012-097 (2012). <https://cds.cern.ch/record/1460443>.
- [90] C. Rogan, *Kinematical variables towards new dynamics at the LHC*, [arXiv:1006.2727 \[hep-ph\]](arXiv:1006.2727).
- [91] G. Cowan et al., *Asymptotic formulae for likelihood-based tests of new physics*, EPJC **71** (2011) 1–19, 10.1140/epjc/s10052-011-1554-0.
- [92] ATLAS Collaboration, G. Cowan, *Discussion and guidelines on significance*, https://twiki.cern.ch/twiki/pub/AtlasProtected/ATLASStatisticsFAQ/SigRec_v1.pdf.

- [93] ATLAS Collaboration, *Electron performance measurements with the ATLAS detector using the 2010 LHC proton-proton collision data*, Eur. Phys. J. **C 72** (2012) 1909, 10.1140/epjc/s10052-012-1909-1, arXiv:1110.3174 [hep-ex].
- [94] *Identification of the Hadronic Decays of Tau Leptons in 2012 Data with the ATLAS Detector*, ATLAS-CONF-2013-064 (2013).
<https://cds.cern.ch/record/1562839>.
- [95] *Determination of the tau energy scale and the associated systematic uncertainty in proton-proton collisions at $\sqrt{s} = 8$ TeV with the ATLAS detector at the LHC in 2012.* <https://cds.cern.ch/record/1544036>.
- [96] ATLAS Collaboration, *Jet energy scale and its systematic uncertainty for jets produced in proton-proton collisions at $\sqrt{s} = 7$ TeV and measured with the ATLAS detector*, ATLAS-CONF-2010-056. <http://cdsweb.cern.ch/record/1281329>.
- [97] W. Verkerke, *Guide to parametrized likelihood analyses*, April, 2012.
https://twiki.cern.ch/twiki/pub/AtlasProtected/ATLASStatisticsFAQ/pllguide_draft.pdf.
- [98] ATLAS Collaboration, *Luminosity Determination in pp Collisions at $\sqrt{s} = 7$ TeV Using the ATLAS Detector at the LHC*, Eur. Phys. J. **C 71** (2011) 1630, 10.1140/epjc/s10052-011-1630-5, arXiv:1101.2185 [hep-ex].
- [99] ATLAS Collaboration, *Luminosity Determination in pp Collisions at $\sqrt{s} = 7$ TeV using the ATLAS Detector in 2011*, ATLAS-CONF-2011-116.
<http://cdsweb.cern.ch/record/1376384>.
- [100] J. M. Campbell and R. K. Ellis, *$t\bar{t}W^{+-}$ production and decay at NLO*, JHEP **1207** (2012) 052, 10.1007/JHEP07(2012)052, arXiv:1204.5678 [hep-ph].
- [101] A. Kardos, Z. Trocsanyi, and C. Papadopoulos, *Top quark pair production in association with a Z-boson at NLO accuracy*, Phys. Rev. **D 85** (2012) 054015, 10.1103/PhysRevD.85.054015, arXiv:1111.0610 [hep-ph].
- [102] J. Boyd, G. Conti, M. D’Onofrio, O. Ducu, T. Eifert, S. Farrell, T. Gillam, A. Marzin, J. Manurer, B. Nachman, A. Paramonov, J. Poveda, K. Suruliz, and T. Yamanaka, *Studies of events with three leptons and three b-tagged jets observed in the full 2012 ATLAS dataset*, ATL-COM-PHYS-2014-030 (2014).
<https://cds.cern.ch/record/1643516>.
- [103] ATLAS Collaboration, A. statistics forum, *Frequentist Limit Recommendation.*, <http://indico.cern.ch/event/126652/contribution/0/material/2/0.pdf>.
- [104] A. L. Read, *Presentation of search results: the CL s technique*, J. Phys. G: Nucl. Part. Phys. **28** (2002) 2693, 10.1088/0954-3899/28/10/313.
- [105] A. L. Read, *Modified frequentist analysis of search results (The CL(s) method)*, CERN-OPEN-2000-205 (2000). <http://cds.cern.ch/record/451614>.
- [106] E. Gross, *LHC Statistics for Pedestrians*, (2008).
<https://cds.cern.ch/record/1099994>.
- [107] *Procedure for the LHC Higgs boson search combination in summer 2011*, ATL-PHYS-PUB-2011-011 (2011). <https://cds.cern.ch/record/1375842>.

- [108] CMS Collaboration, V. Khachatryan et al., *Searches for electroweak production of charginos, neutralinos, and sleptons decaying to leptons and W, Z, and Higgs bosons in pp collisions at 8 TeV*, arXiv:1405.7570 [hep-ex].
- [109] *SUSY limit plotting recommendations*,. <https://twiki.cern.ch/twiki/bin/view/AtlasProtected/SUSYLimitPlotting>.
- [110] S. Gori, S. Jung, and L.-T. Wang, *Cornering electroweakinos at the LHC*, JHEP **1310** (2013) 191, 10.1007/JHEP10(2013)191, arXiv:1307.5952 [hep-ph].